Dissertation

SIMULATION OF SALT AND ORGANIC FINGERPRINTS IN MASS SPECTRA OF ICE GRAINS IN THE EXOSPHERES OF THE ICY OCEAN MOONS EUROPA AND ENCELADUS

Maryse Napoleoni
Planetary Sciences and Remote Sensing,
Freie Universität Berlin,
Malteserstr. 74-100, 12249 Berlin, Germany
m.napoleoni@fu-berlin.de

FIRST REVIEWER:

Prof. Dr. Frank Postberg
Institute of Geological Sciences, Freie Universität Berlin
Malteserstraße 74-100
12249 Berlin, Germany

SECOND REVIEWER:

Prof. Dr. Grégoire Danger
Laboratoire Physique des Intéractions Ioniques et Moléculaires (PIIM)
Campus Etoile, Av. Escadrille Normandie Niemen
13897 Marseille, France

Other members of the doctoral committee:

Prof. Dr. Lena Noack
Institute of Geological Sciences, Freie Universität Berlin
Malteserstraße 74-100
12249 Berlin, Germany

Prof. Dr. Harry Becker
Institute of Geological Sciences, Freie Universität Berlin
Malteserstraße 74-100
12249 Berlin, Germany

Prof. Dr. Bernd Abel
Institut für Technische Chemie, Universität Leipzig
Permoserstraße 15
04318 Leipzig, Germany

Dr. Nozair Khawaja
Institute of Geological Sciences, Freie Universität Berlin
Malteserstraße 74-100
12249 Berlin, Germany

Date of defence: January 30th, 2024

ABSTRACT.

In the Solar System, the saturnian moon Enceladus and the jovian moon Europa are potentially habitable and the most promising candidates for space missions searching for extraterrestrial life. The subsurface oceans of these moons constitute the long-lived presence of large amounts of liquid water, a common component of icy moons throughout the outer Solar System. In addition, the rocky seafloors of both moons allow for rich geochemistry in their subsurface oceans, potentially including the formation of complex organic material at hydrothermal vent systems, which could also provide an energy source for another emergence of life. The exploration of icy ocean moons can be performed using impact ionization mass spectrometry, a powerful technique to thoroughly analyse the composition of ice grains ejected from both the surface ice shell and subsurface liquid reservoirs.

The Cosmic Dust Analyzer (CDA) onboard the Cassini mission detected a variety of salts, complex and reactive organic compounds, as well as bioessential elements in ice grains ejected by the plume of Enceladus into space. CDA mass spectra provided strong evidence for habitable conditions at the seafloor of the moon. These discoveries greatly benefitted from laboratory analogue mass spectra complementing the CDA data, obtained from a laboratory setup using Laser Induced Liquid Beam Ion Desorption (LILBID) as an ionisation source coupled to time-of-flight mass spectrometry. CDA paved the way for the SUrface Dust Analyzer (SUDA), its improved successor instrument onboard the upcoming Europa Clipper mission, which will provide a deeper understanding of Europa's habitability. SUDA aims to characterize the composition of the subsurface ocean or liquid inclusions in the icy crust by analysing young endogenic surface material or possible cryovolcanic plume material.

Preparation for SUDA's mission and related data analysis requires considerable laboratory work. This thesis describes LILBID experiments simulating the mass spectral signatures of both salt- and organic-rich ices, as expected to be encountered by SUDA or similar instruments on a future mission to Enceladus.

After a description of the current state of research into the habitability and astrobiological potential of both Europa and Enceladus in Part I, Part II details how SUDA-type instruments could detect organic molecules embedded in salt-rich ice grains. LILBID mass spectra were recorded for several organic species with various properties, derived from a range of functional groups, together with either NaCl, $MgSO_4$ or H_2SO_4 at concentrations relevant for the surfaces of icy moons. Mass spectrometric signatures of the organic species can be detected via their molecular ions and a range of cluster species with Na^+, Mg^{2+}, Cl^-, OH^-, HSO_4^- ions, and NaCl, $MgSO_4$ and H_2SO_4 molecules. The presence and intensity of these characteristic organic-rich peaks depends on the inorganic matrix and its concentration. The intensities of analyte signatures decrease with increasing salt concentrations due to suppression effects. In contrast, they are increased by the presence of sulfuric acid matrices in cation mode. Moreover, the sensitivity to different organic species strongly depends on the instrument polarity (cation or anion mode of the spectrometer) and on molecular properties, especially the functional groups present. The recorded spectra are an important foundation to characterise both the organic and salt composition in ice grains from Europa and Enceladus and, by extension, potential constituents of the subsurface oceans.

Part III reveals a previously unknown capability of SUDA-type instruments: the ability to determine the oxidation state of iron in iron-bearing salts (or other minerals) embedded in ice grains. Such analytical capability may, in the near future, allow the elucidation of key parameters related to the geochemistry of subsurface oceans on icy moons, notably their redox chemistry and pH. These factors may have implications for hydrothermal mineralogy as well as possible metabolic activity of putative microbial life.

Further ongoing projects that have been conducted in the framework of this PhD project are briefly described in Part IV. They cover the irradiation of (i) icy samples containing molecular biosignatures to evaluate their degradation under the harsh radiation environment of Europa's surface, and (ii) simple compounds ($CH_3OH:NH_3:H_2O$ ice) leading to the synthesis of a variety of complex organic structures. Moreover, an outlook is given on a future expedition to acquire samples in Antarctica - the best icy moon analogue on Earth - that has been planned during this PhD project. Finally, this work concludes with a summary of the most relevant results of this thesis (Part V).

Abstract.

In unserem Sonnensystem sind der Saturnmond Enceladus und der Jupitermond Europa die aussichtsreichsten Kandidaten für Missionen, um nach extraterrestrischen Leben zu suchen. Dort verfügen die subkrustalen Ozeane über einen langen Zeitraum über große Mengen flüssigen Wassers, ein häufiger Bestandteil von Eismonden im gesamten äußeren Sonnensystem. Darüber hinaus erlaubt der Ozeanboden aus Gestein auf beiden Monden eine reichhaltige Geochemie, die möglicherweise die Bildung von komplexem organischem Material in hydrothermalen Schloten einschließt. Solche Schlote würden darüber hinaus eine Energiequelle für das Entstehen von Leben bieten. Die Erforschung eisiger Ozeanmonde kann mit Hilfe der Einschlagsionisations-Massenspektrometrie durchgeführt werden, einer leistungsstarken Technik zur detaillierten Analyse der Zusammensetzung von Eiskörnern, die sowohl von der oberirdischen Eiskruste als auch aus den unterirdischen Flüssigkeitsreservoirs emittiert werden.

Der Cosmic Dust Analyzer (CDA) an Bord der Cassini-Mission wies eine Vielzahl von Salzen, komplexen und reaktiven organischen Verbindungen und bioessentiellen Elementen in Eiskörnern nach, die in den Eisfontänen von Enceladus ins All geschleudert werden. Die Daten lieferten deutliche Hinweise auf habitable Bedingungen am Meeresboden des Mondes. Dabei profitierten diese Entdeckungen von Labormassenspektren mit Analogmaterialien, die die CDA-Daten ergänzten und im Labor unter Verwendung der Laserinduzierten Flüssigstrahl-Ionendesorption (d. h. der LILBID-Ionisierungsmethode) in Verbindung mit Flugzeit-Massenspektrometrie gewonnen wurden. CDA ebnete den Weg für den SUrface Dust Analyzer (SUDA), sein verbessertes Nachfolgeinstrument an Bord der bevorstehenden Europa Clipper Mission, das ein tieferes Verständnis der Habitabilität Europas ermöglichen wird. SUDA zielt darauf ab, die Zusammensetzung des Ozeans, bzw. flüssiger Einschlüsse in der Eiskruste, durch die Analyse von jungem endogenen Oberflächenmaterial oder cryovulkanischen Auswurffontänen zu charakterisieren. Zur Vorbereitung der SUDA-Mission und der Datenanalyse sind erhebliche Laborarbeiten notwendig. In dieser Arbeit werden LILBID-Experimente zur Vorhersage massenspektrometrischer Signaturen von salz- und organik-haltigem Eis auf der Oberfläche von Europa durchgeführt, wie sie von SUDA beobachtet werden können oder einem ähnlichen Instrument auf einer zukünftigen Enceladus Mission.

Nach einer Beschreibung des aktuellen Wissenstandes über die Habitabilität und das astrobiologische Potenzial von Europa und Enceladus in Teil I, wird in Teil II erläutert, wie Instrumente vom SUDA-Typ organische Moleküle aufspüren könnten, die in salzreichen Eiskörnern eingebettet sind. Zu diesem Zweck wurden LILBID-Massenspektren für mehrere organische Substanzen mit verschiedenen Eigenschaften aufgenommen, die von den jeweiligen funktionellen Gruppen abgeleitet wurden. Diese Stoffe wurden zusammen mit NaCl, MgSO$_4$ oder H$_2$SO$_4$ in Konzentrationen gemessen, die für die Oberflächen von Eismonden relevant sind. Massenspektrometrische Signaturen der organischen Substanzen können über molekulare Ionen und eine Reihe von Clustern mit Na$^+$, Mg^{2+}, Cl$^-$, OH$^-$, HSO$_4^-$ Ionen und NaCl-, MgSO$_4$- und H$_2$SO$_4$-Molekülen nachgewiesen werden. Das Vorkommen und die Intensität dieser charakteristischen organischen Peaks hängen von der anorganischen Matrix und deren Konzentration ab. Die Intensität der Analytensignaturen nimmt mit steigender Salzkonzentration aufgrund von Unterdrückungseffekten ab. Hingegen ist sie im Kationenmodus in einer Schwefelsäure-Matrix erhöht. Darüber hinaus variiert die Empfindlichkeit für organische Substanzen oft stark mit der Polarität (Kationen- oder Anionenmodus des Spektrometers) und hängt stark von deren molekularen Eigenschaften ab, insbesondere von ihren funktionellen Gruppen. Die hier aufgenommenen Spektren stellen eine wichtige Grundlage dar, um mit SUDA sowohl organisches Material als auch Salze in Eispartikeln von Europa und Enceladus - und damit mögliche Bestandteile der Ozeane - zu charakterisieren.

Teil III zeigt eine bisher unbekannte Fähigkeit von Instrumenten des SUDA-Typs auf, nämlich die Oxidationszahl von Eisen in im Eis befindlichen eisenhaltigen Mineralen zu bestimmen. Diese analytische Methode könnte es in naher Zukunft ermöglichen, Schlüsselparameter der unterirdischen Ozeane auf Eismonden, insbesondere ihre Redox-Chemie und ihren pH-Wert, zu bestimmen. Diese Faktoren könnten Auswirkungen sowohl auf die hydrothermale Mineralogie als auch mögliche Stoffwechselaktivitäten mikrobiellen Lebens haben.

Weitere laufende Projekte, die im Rahmen dieses Promotionsprojektes durchgeführt wurden, sind in Teil IV kurz beschrieben. Sie umfassen die Bestrahlung von Eisproben, die zum einen biogene Substanzen enthalten, um die Modifikation von massenspektrometrischen Biosignaturen zu erfassen, und zum anderen einfache organische Substanzen, um die mögliche Synthese komplexerer Strukturen zu untersuchen. Darüber hinaus wird in einem Ausblick die anstehende Expedition zur Beschaffung natürlicher Eisproben aus der Antarktis - dem besten irdischen Analoga für Eismonde - beschrieben, die im Rahmen meiner Promotionstätigkeit geplant wurde. Schließlich wird die Arbeit mit einer Zusammenfassung der wichtigsten Ergebnisse abgeschlossen (Teil V).

CONTENTS

9

LIST OF TABLES

Nomenclature

CAB, Centre de Astrobiologia; **CDA**, Cosmic Dust Analyzer; **DA**, Dust Analyser; **DNA**, Deoxyribonucleic Acid; **ECM**, Europa Clipper Magnetometer; **ELF**, Enceladus Life Finder; **ELSI**, Earth Life Science Institute; **ENIJA**, Enceladus Icy Jet Analyzer; **EOS**, Enceladus Ocean Simulant; **Europa-UVS**, Europa Ultraviolet Spectrograph; **ESA**, European Space Agency; **EI**, Electron Ionization; **EIS**, Europa Imaging System; **ESI**, electrospray ionization; **E-THEMIS**, Europa Thermal Imaging System; **FUB**, Freie Universität Berlin; **FT-ICR**, Fourier Transform Ion Cyclotron Resonance; **GC-MS**, Gas Chromatography Mass Spectrometry; **HIFI**, High Ice Flux Instrument; **HMOC**, High Mass Organic Cations; **HRD**, High Rate Detector; **INMS**, Ion and Neutral Mass Spectrometer; **IOM**, Institut für Oberflächenmodifizierung; **IR**, Infrared; **JUICE**, JUpiter ICy Moon Explorer; **JWST**, James Webb Space Telescope; **LDI**, Laser Desorption Ionization; **LILBID**, Laser Induced Liquid Beam Ion Desorption; **LPC2E**, Laboratoire de Physique et Chimie de l'Environment et de l'Espace; **LUCA**, Last Universal Common Ancestor; **MALDI**, Matrix Assisted Laser Desorption Ionization; **MASPEX**, MAss Spectrometer for Planetary EXploration; **MISE**, Mapping Imaging Spectrometer for Europa; **MS**, Mass Spectrometry; **NASA**, National Aeronautics and Space Administration; **NIMS**, Near-Infrared Mapping Spectrometer; **NIST**, National Institute of Standards and Technology; **OLYMPIA**, Orbitrap anaLYser MultiPle IonisAtion; **PIIM**, Physique des Interactions Ioniques et Moléculaires; **PIMS**, Plasma Instrument for Magnetic Sounding; **QLEIT**, Quadro-Logarithmic Electrostatic Ion Trap; **REASON**, Radar for Europa Assessment and Sounding: Ocean to Near-surface; **SELINA**, SELected Ice Nanoparticle Accelerator; **SUDA**, SUrface Dust Analyzer; **ToF**, Time-of-Flight; **VUV**, Vacuum Ultraviolet.

I Introduction

1 The Search For Extraterrestrial Life

The fundamental question "Are we alone?" is as old as humankind itself. For centuries, humans have turned their eyes towards the night sky and the stars, wondering about our place in the cosmos and if there are "others" somewhere else. The question of whether or not life beyond Earth exists brings even more intriguing questions: If extraterrestrial life exists, is it similar to that in our own planet? Could we detect it on other planetary bodies? Beyond our Solar System? Where and how should we search for signs of past or present life? Is the origin and evolution of life an inevitable and ubiquitous process? Does biology follow universal laws (such as the laws of chemistry and physics)?

The field of Astrobiology has its roots in trying to understand the origin(s) of life, both on our own planet Earth and potentially on other places. This cross-disciplinary field, combining biology, geology, planetology, chemistry and astronomy, requires not only a broad-scale understanding of life and its functioning mechanisms, but also of the environments that support it, at scales ranging from planetary systems to microscopic dimensions. Astrobiology brings fundamental insights into our current understanding of the universe by connecting the formation of stars and planetary systems, with the universal laws of physics and chemistry, and with geological processes and the evolution of life from prebiotic chemistry to complex multicellular life. Understanding Earth, its geochemical history and coevolution with life sheds light on the necessary conditions for our planet to be habitable. This leads to a better understanding of habitability in other worlds in the Solar System and beyond.

1.1 Habitability across the Solar System and beyond

Life and Earth have co-evolved for at least 3.7 billion years [1] (i.e., for most of the history of the planet) and thus Earth has maintained the conditions required for planetary habitability over geological timescales. The term "habitability" describes the potential of a particular (extraterrestrial) environment to sustain life based on the known limits of life (that is, terrestrial life). Important aspects to consider about habitability include the potential of an environment to generate life, the timescales over which life can be sustained and its spatial distribution. Habitable planetary bodies are therefore defined as able to develop and maintain environments hospitable to life. However, the exact conditions for life to emerge are highly debated [2]. Moreover, the current definition of life is shaped, and therefore limited, by our understanding of life on Earth, and by the fact that we know of only one example of life (i.e., life on Earth, which has evolved from a last common ancestor, LUCA [3]). To try to go beyond this limitation, universal laws of physics and chemistry can be used as a potential way to understand life fully, including the requirements for it to emerge.

Studying life through the prism of universality has led to the consensus that it requires three essential components [4]: (i) an energy source to drive metabolic reactions, (ii) a liquid solvent to mediate these reactions, (iii) essential chemical elements (the so-called CHNOPS: Carbon, Hydrogen, Nitrogen, Oxygen, Phosphorus and Sulfur) both to build biomass and catalyze metabolic reactions with enzymes. Additionally, appropriate physicochemical conditions can also be regarded as a necessary component for life to emerge and perpetuate (Figure 1). The availability of the solvent is considered to be the key limiting factor for life, both on Earth (where it is the main factor controlling the distribution of life [5]) and potentially on other planetary bodies. While other liquid solvents could theoretically sustain extraterrestrial life [6], water is considered the most likely solvent, because of both its high cosmic abundance and its distinct physicochemical properties that make it a highly suitable medium for macromolecular interactions [7]. Water has the ability to act both as a solvent for polar molecules and as a reactant in biochemical reactions; it also plays an essential role in metabolic processes such as protein folding, enzymatic processes, and maintenance of the structural stability of proteins, DNA and RNA [8, 9]. Liquid water's unique physicochemical properties are thought to have profoundly shaped the emergence and evolution of life on our planet. As a general rule, liquid water is considered as the first potential indicator of habitability, and a main target in the search for places that may be suitable for carbon-based life [10]. This has led Mars (due to the past presence of liquid water on its surface [11, 12, 13]) and icy ocean worlds in the outer Solar System (due to the current presence of subsurface oceans) to be considered as prime targets of space exploration focusing on the search for extraterrestrial life.
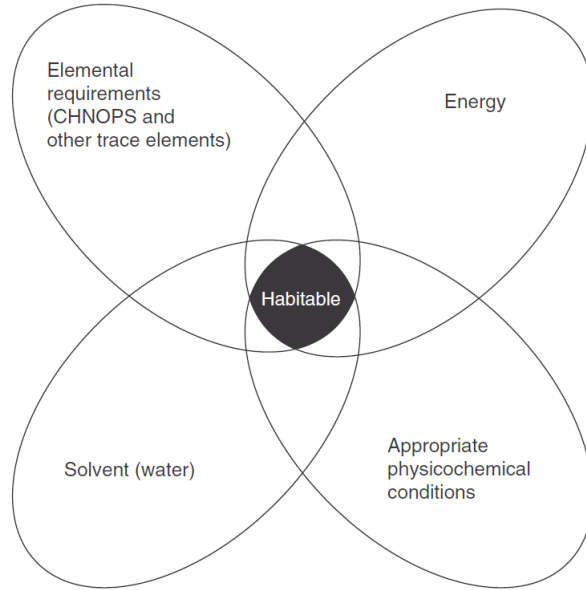
FIGURE 1. The pillars of habitability. From Cockell et al. [4].

Beyond the Solar System, the definition of "habitability" is not exactly comparable to the one used in the discussion of habitability in the Solar System. While the search for life has been driving research focusing on the detection and characterisation of exoplanets, it is not yet technically possible to know whether liquid water, CHNOPS, or energy sources are available on most exoplanets (or exomoons) detected so far. Instead of "habitability", the concept of "Habitable Zone" is typically used in the field of exoplanets and astronomy. The circumstellar habitable zone refers to the location around a star where a planet could sustain water in its liquid form at its surface, based on predicted temperatures (calculated from the modelled amount of energy that the planet receives from its star); and therefore varies with parameters such as the distance to the star, the type of star, and the size of the planet [14]. Only a few dozen exoplanets have been detected to date in habitable zones (e.g., [15]). However, the detection of exoplanets is a rather recent but exponentially growing field: since the first exoplanet orbiting a star was discovered in 1995 [16], over 5000 exoplanets have been detected[1], and thousands of planet candidates are under consideration [17]. Due to inherent technical difficulties, the detection of exoplanets (and exomoons) is limited to certain bodies, potentially excluding others that could possibly be more promising for life. For example, detection bias (typically, with the transit method) can favour the discovery of large exoplanets which are close to their star (so called "hot Jupiters"). Because of the tremendous abundance of exoplanets, future instrumentation is likely to enable the detection and characterisation of more potentially habitable bodies. The characterisation of exoplanetary surfaces and atmospheres in search of remotely detectable biosignatures is now key to astrobiology research programmes [18].

While the detection of exomoons has not been confirmed yet, they are expected to be numerous and likely to be discovered soon [19]. The concept of a habitable zone is not relevant for exomoons - or at least not the most relevant parameter. Indeed, exomoons do not need to orbit a planet in the habitable zone of its star to be habitable [20]. Tidal heating may allow a moon to sustain a subsurface ocean far beyond the planetary habitable zone [21]. In fact, habitable exomoons may outnumber habitable exoplanets.

Astrobiology in the context of exoplanet research reminds us that habitability is a complex notion, which is defined differently by astronomers, planetary scientists or biologists (e.g., [22, 23]). Combining these different approaches is necessary to answer the difficult questions that the multidisciplinary field of Astrobiology tries to investigate.

---

[1]According the NASA Exoplanet Archive, already 5,535 confirmed exoplanets have been detected on 24th October 2023.

1.2 Looking for life as we know it

The search for life in the Solar System is mostly based on the detection and characterisation of environments where the minimal requirements for habitability (Figure 1) are present, but it also involves the direct search for signatures of life. In Astrobiology, the term "biosignature" is of common use, although it is ambiguously defined and used differently depending on the scientific community (e.g, morphological, molecular, chemical, atmospheric, spectroscopic biosignatures). A widespread definition of biosignatures refers to them as an "object, substance, and/or pattern whose origin specifically requires a biological agent" [24]. In other words, it is a measure or feature that can be interpreted as evidence of past or present life. However, the observation of such "object, substance, and/or pattern", to fully qualify as biosignature, should be much more likely to be produced by biotic processes than by abiotic processes (i.e., it cannot be produced in the absence of life). The qualification as a biosignature therefore needs to (*i*) define the precise type of biosignature (e.g., structure, substance, pattern) (*ii*) be contextualised in the particular conditions, theories or models of a disciplinary field (e.g., [exo]planetary science, paleobiology, microbiology) and (*iii*) be subjected to varying degrees of confirmation [25].

Some examples of substances that can be considered as biosignatures with a high level of confidence, and are relevant for the instrumental technique described in this thesis (i.e., mass spectrometry), are amino acids and fatty acids. Amino acids are considered as some of the simplest molecules that could be a biosignature of life as we know it, because they are both ubiquitous (as the building blocks of proteins) and at the core of terrestrial biochemistry. However, they can also have an abiotic origin (e.g., [26]), thus amino acids alone will not be considered as rigorous evidence of life [27]. Nonetheless, a specific ratio of different amino acid concentrations can be considered a biosignature, since biotic processes induce an increase of the abundance of more complex amino acids as compared to those formed by abiotic processes [28]. Lipids are generally considered as universal biomarkers of extraterrestrial life [29] owing to their membrane-forming properties which are effective even under geochemically hostile conditions. While most organic species would be easily degraded on many planetary environments (e.g., by hydrothermalism or exposure to radiation), the provenance of lipid fragments such as fatty acids could be easily recognized as biological in origin [30]. Fatty acids of biogenic origin can be differentiated from abiotic origin owing to distribution patterns in their relative concentrations. In a biogenic synthesis, fatty acids are generated by the addition of two carbon atoms at a time, leading to an excess of fatty acids with an even number of carbon atoms [31]. On the contrary, in an abiotic synthesis (e.g., Fischer-Tropsch reactions), carbon atoms are added one at a time, therefore lacking such as characteristic pattern in fatty acid abundances. Lipids are also the only biomarkers that survived long enough to provide insights into the early history of life on Earth (e.g., terpenoids, specifically hopanes and steranes, in the Archaean rock record) [32]. While biosignatures are detectable with a wide range of laboratory techniques, mass spectrometry appears as one of the most relevant spaceborne technique to reach this goal: biosignatures detectable with mass spectrometry include specific biosignature molecules, distribution patterns indicative of selection by biotic processes and isotopic signatures [33]; and those are highly characteristic as compared to morphological biosignatures such as fossils, which can be highly debatable [34].

Studying and evaluating the validity of biosignatures is crucial for detecting them on extraterrestrial worlds. Therefore, accurately defining and identifying life on Earth is a major first step to ensure that space exploration will not fail to detect extraterrestrial life (i.e., false negative life detection) nor detect wrong signals (i.e., false positive). However, this is not an easy task, as "life" is a complex phenomenon and some uncertainty remains in our understanding of what it exactly is [35]. Because of this uncertainty, the quest for extraterrestrial life mainly focuses on signs of "life as we know it", which is defined as a self-organized, self-replicating, and metabolically active molecular system that is carbon-based and uses water as a solvent [36]. Alternative forms of life may be possible e.g., using methane instead of water as a solvent, or silicon-based instead of carbon-based (e.g. [37]), therefore introducing the need to search for agnostic biosignatures (i.e., signs of life as we do not know it) [38]. However, these potential alternative forms of life will not be explored in more details here due to their rather speculative nature.

To know where to look for life on other planets, it seems necessary beforehand to understand the origin(s) and the limits of life on our own planet. Several scenarios for the origin of life have been proposed, the two main theories being an origin in oceanic hydrothermal vents (e.g., [39]) or in shallow continental pools (e.g., [40]). While these scenarios can be further investigated, including with laboratory experiments, it may be difficult to find a single, definitive answer, since the origin(s) of life on Earth may actually have been several distinct events, and the geological record is limited in time. Finding a distinct, second origin of life outside of Earth (e.g., on bodies in the outer Solar System, where life from Earth could not have been distributed by impact ejecta) would

surely bring invaluable information for a better understanding of the origins of life in the early history of Earth.

A perhaps easier way to get hints about where to look for extraterrestrial life is to study the limits of terrestrial life. In the last few decades, discoveries of so-called "extremophiles" have extended the boundary conditions under which life can thrive in many different directions. Extremophiles can inhabit (or tolerate) environments with high temperatures, pressures, radiation, salinity, extreme pH, and severe nutrient limitation. Extremophiles, as opposed to extremotolerant organisms, are highly adapted for specific "extreme" conditions, which are therefore the norm under which the organisms are able to function both metabolically and biochemically. Many environments on Earth's surface and subsurface exhibit extremes in one or more physical or chemical parameters. Therefore, many extremophiles are actually polyextremophiles, enduring multiple factors simultaneously. Some microorganisms can even survive the harsh conditions of space, an environment where they are simultaneously exposed to extreme radiation, vacuum, highly variable temperature, and microgravity [41, 42].

The main outcome of recent extremophile research is that life can adapt to a wide range of parameters, including previously thought insurmountable physical and chemical barriers, and that its true limits have yet to be found. It therefore implies that life could be more common than expected - including beyond Earth, where conditions similar to Earth's inhabited environments are present on many bodies in the Solar System (Figure 2) and beyond, where since the discovery of exoplanets, a wide diversity of worlds is expected. Establishing the boundaries of life as we know it could help to predict the boundaries of life in a broader context, including on other planets. The discoveries of the most extreme organisms make more plausible the case of life beyond Earth, and even maybe raise the possibility of panspermia (i.e., the transport of life from one planet to another). Moreover, the search for the true limits of terrestrial life could also provide insight into the processes that have led to its origin.
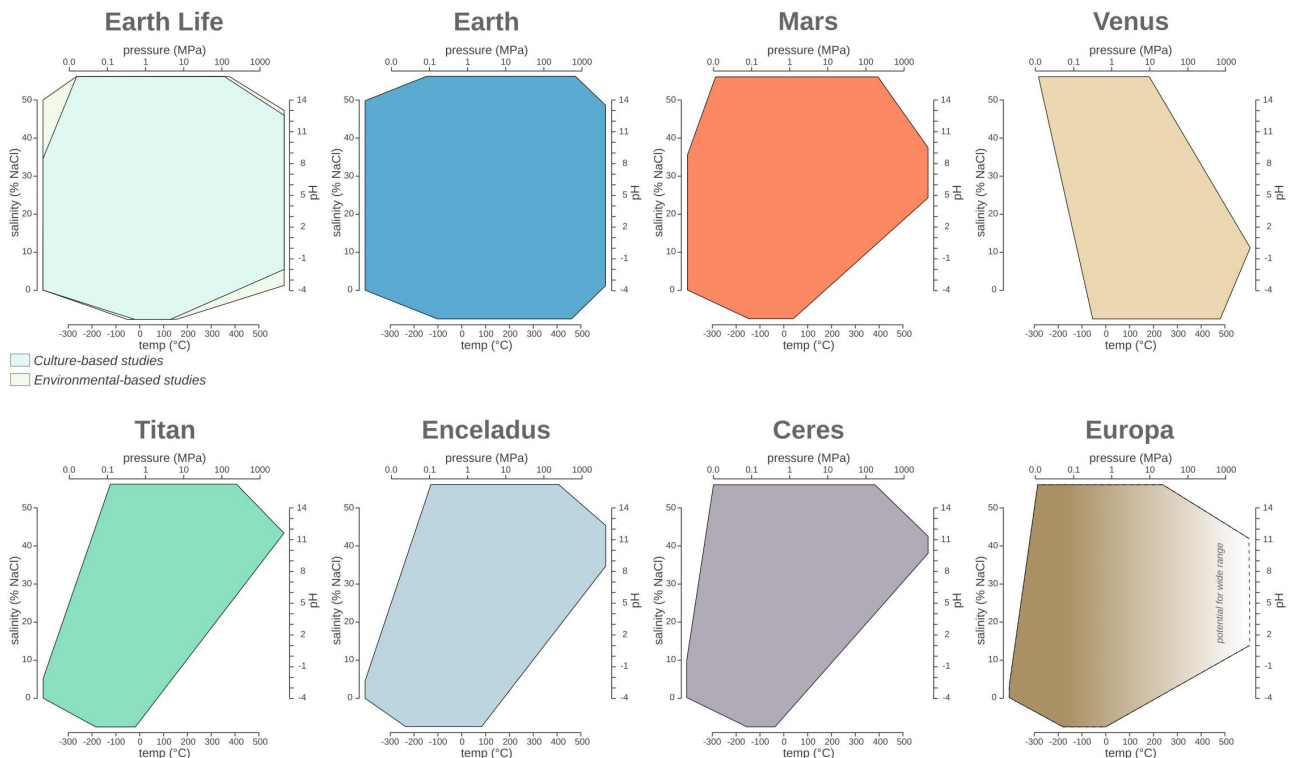
FIGURE 2. Ranges of temperature, pressure, pH, and salinity boundaries observed for life on Earth and estimated (from observations and models) on the environments of some potentially astrobiology-relevant planetary bodies in the Solar System. Each edge of the polygon chart represents the range for the specific parameter. From Merino et al. [43]

However, the definition of "extreme conditions" may be biased, as it is inherently based on anthropocentric criteria [44]. Species currently considered as extremophiles may actually have dominated the evolutionary history of life, since the current surface conditions on Earth (such as temperature, atmospheric composition, redox state) have only occurred for a short period of time compared to the time frame of the existence of terrestrial life [45]. Therefore, extremophile research should be used to gain insights into the origins of life on Earth, and possible similarities on other planetary bodies, while keeping in mind that extraterrestrial life may have evolved

in a way that makes it extremely hard to detect with the current techniques of space exploration.

1.3 Relevance of ocean worlds for Astrobiology

In the Solar System, the only bodies which are confidently thought to currently harbour the three minimal requirements for habitability are some of the ocean worlds in the outer Solar System. While Mars may have fulfilled these requirements in the past, surface conditions are presently harsh (e.g., radiation, lack of liquid water), suggesting that if life had developed on Early Mars, it may today only remains in limited areas of the subsurface, or in protected niches [46]. Other planetary systems might also harbour similar conditions on exoplanets (or exomoons), but our current knowledge of these systems is still very limited due to the large distances from Earth, and the difficulties to characterise them sufficiently only with telescopic methods (and without the possibility for investigations by spacecraft).

Some icy bodies in the outer Solar System currently host considerable amounts of liquid water, despite being millions of kilometres away from the "habitable zone" of our Solar System. These ocean worlds (i.e. bodies with a current, potentially global, liquid ocean) have been identified and characterised by several space missions [47] (Figure 3). The recent characterisation of moons of gas giants has shown that tidal heating makes them some of the most habitable environments in the Solar System (e.g., [48]), even small moons (e.g., Enceladus) which were not expected to be able to sustain global oceans due to the cold surface temperatures. While the moons Enceladus, Europa, Titan, Ganymede and Callisto are known to harbour subsurface liquid water reservoirs [49, 50, 51, 52, 53, 54], uncertainty remains for other bodies including Triton, some icy satellites of Saturn and Uranus [55, 56, 57]. The discovery of many ocean worlds in the outer Solar System also has implications for extrasolar systems, where many exomoons might have liquid water oceans due to tidal heating [58, 59].
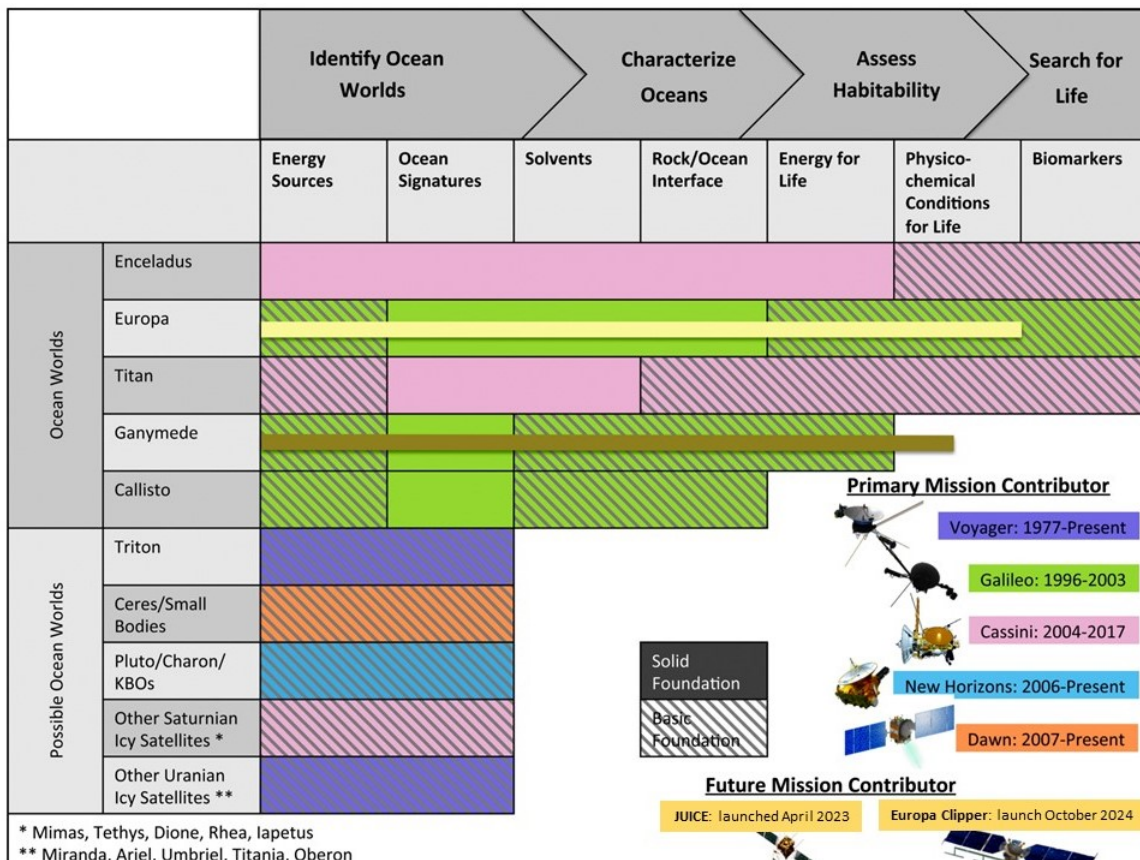
FIGURE 3. Investigations roadmap depicting the state of knowledge for (potential) ocean worlds. For each moon/body, the colours correspond to those of the missions that provided the majority of information about it. While solid colours show that the target is well understood, a hashed colour represents only a basic scientific foundation. Adapted from Hendrix et al. [47].

Ocean worlds are key to the search for traces of extraterrestrial life, due to the presence of large reservoirs of liquid water providing high potential for the emergence and development of life. Moreover, life needs a source

of energy to power chemical reactions, and the physicochemical gradients (e.g., redox conditions) present in icy moons could provide it. Such non-equilibrium conditions are thought to have played an important role in the origins, evolution, and diversity of life on Earth, with electron and proton exchanges (i.e., redox and pH gradients, respectively) initiating energy fluxes [60]. Another requirement for life as we know it, essential elements (i.e., CHNOPS; Figure 1), have also been identified in the ocean moon Enceladus [61], further supporting the idea that life may have all necessary components to start in ocean worlds.

In this thesis, I will focus mostly on Enceladus and Europa, as these two moons are the targets of ongoing, future and past international space missions (Figure 3). Most importantly, they are considered to have the greatest astrobiology potential of all extraterrestrial worlds explored to date in the Solar System. Past space missions such as Cassini or Galileo aroused extraordinary scientific interest by revealing that both moons possess a critical aspect for habitability, which is to have an ocean in contact with a rocky seafloor (and not sandwiched between ice layers). To date, only these two moons are confirmed to host this particular feature in their interiors.

Enceladus fulfils the three habitability criteria: (*i*) liquid water, with the presence of a global subsurface ocean [62, 63, 53]; (*ii*) essential elements, including the CHNOP(S?), and simple and complex organic molecules [64, 65, 66, 61]; (*iii*) energy sources, with tidal heating inducing hydrothermal processes such as serpentinization, which entail redox reactions [67, 64, 68]. The essential element Sulfur was tentatively detected as hydrogen sulfide in Enceladus' plume, and Sulfur is expected to be abundant in either the moon's core (as sulfides) or in the ocean (as sulfates).

Europa is currently less characterised than Enceladus, but is also considered to be potentially habitable, due to its long-term global liquid water ocean [51, 69], tidal forces generating heat in its interior [70, 71] and a high potential for water–rock interactions at the interface between its rocky core and subsurface ocean [72, 73], possibly promoting chemical disequilibria [74]. While hydrothermal activity has been detected on Enceladus, such process is uncertain for Europa, but predicted by modelling showing that seafloor magmatism could have been induced during most of Europa's history [73]. On the surface of Europa specifically, oxidants generated by an intense radiolytic chemistry (the moon orbiting within Jupiter's strong magnetosphere [75, 76, 77, 78]) could reach the subsurface ocean via tectonic processes, and these exchanges could potentially enable redox reactions with reductants in the subsurface ocean. Such exchanges may have provided the necessary ingredients for an independent origin of life in Europa's subsurface ocean [74].

Both **Enceladus and Europa** may currently host relatively evolved microbial life, originating from (potential) hydrothermal vents, as these are thought to be associated with the origin of life on Earth [79, 80]. Moreover, both moons might host a large organic inventory, as the synthesis of organic material has been shown to be viable in chondritic hydrothermal systems [81, 82, 83, 84]. Organic material concentrations can be enhanced in both hydrothermal vent structures [85] and in freezing phases [86] likely to occur during cycling at Europa's and Enceladus' overlying icy shell interfaces. Future space exploration might allow to determine more precisely the organic inventory, and its formation processes, of both Europa and Enceladus, as well as potentially discover traces of (microbial) life.

2 Icy Ocean Moons

2.1 Overview of icy ocean moons

Multiple icy moons orbit the gas and ice giant planets in the outer Solar System (Jupiter, Saturn, Uranus, and Neptune), and some dwarf planets such as Pluto and Eris. Their radii span a large range of values, from 2634km for the biggest (the galilean moon Ganymede) to only several tens of km for the smallest identified to date (e.g., Puck, a moon of Uranus [87]). Those with subsurface oceans of liquid water (i.e., icy ocean moons) rank among the most promising astrobiological targets in our Solar System. The current presence of oceans has been confirmed on the galilean moons Europa, Callisto [51, 50] and Ganymede [49], and on the saturnian moons Enceladus [52, 53] and Titan [88, 89, 90, 54]. More candidate planetary bodies are awaiting confirmation of ocean detection (e.g., Pluto [91], some Uranian satellites, and Triton). The dwarf planet Ceres is also thought to host a liquid water ocean (or at least liquid brine reservoirs), as shown by geological features and signs of aqueous alteration globally on the surface ([92], Figure 4). However, Ceres' ocean is likely to be in an advanced stage of freezing, because it does not have tidal heating as a major heat source. Indeed, tidal heating, generated by interactions between the moons and their giant planets, induces the melting of large amounts of water, thus forming (possibly global) oceans. Tidal heating of moons results from their slightly elliptical orbits around their planets, and is increased in the case of resonances between moons. This effect is particularly strong for the three inner galilean moons (Io, Europa and Ganymede), since the resonance between them maintain their eccentricities while simultaneously dissipating energy in the form of heat [94]. In the absence of resonance, dissipation leads to the circularization of a moon's orbit, therefore reducing its internal heat. Eccentricity of moons also varies with time, leading to oscillations of tidal heating in their interiors and of ice shell thickness in the case of icy moons [95]. Radiogenic elements can also heat their interiors, and dominates over tidal heating in the cases of e.g., Ganymede, Callisto and Titan [96, 97, 98]. Due to their different sizes, internal structures (Figure 4) and the different planets they orbit, icy ocean moons have a range of different chemistries, energy budgets and potentials for long-term heating.

While many similarities can be found with Earth oceans (e.g., presence of hydrothermal vents, similar physico-chemical parameters), a major difference is that the oceans of icy moons lie below several kilometres thick ice shells, thus shielded from the outside environment. However, material exchanges between the subsurface ocean and the surface have been observed for Enceladus (direct observations of plumes; e.g., [99]) and Europa and Ceres (geological features). Below their ice shells, icy ocean moons have a rocky mantle and/or core, which is either in direct contact with the ocean, or in contact with a high-pressure ice layer, itself surrounded by the ocean (Figure 4). The latter case of a liquid ocean sandwiched between two layers of ices has been proposed for Ganymede, Callisto and Titan [100, 101], and might induce global-scale planetary processes different from those with one ice shell at the surface only. Among the icy moons, Titan appears as a particularly special ocean world, as its surface is highly rich in both carbon and nitrogen, and hosts stable liquid material; it is also the only known moon with a dense atmosphere [102]. It will be further explored soon by the Dragonfly mission [103].

2.2 Enceladus

Enceladus, with an average diameter of 504 km, is one of the five mid-sized moons of Saturn, and tidally locked to the planet (i.e., it always presents the same face to the planet). Its libration amplitude (0.120° [53]) and ice to rock ratio (60:40 by mass) [104] indicate that (*i*) Enceladus hosts a global ocean completely differentiated from its rocky core and (*ii*) its thick ($\sim$40 km) ice shell is decoupled from the rest of the moon's mass [48, 105, 106]. Surface temperatures globally range from $\sim$50 K (night) to $\sim$80 K (day) [107], and may reach 130 to 185K at the anomalously warmer south polar terrain [108]. Enceladus is the brightest planetary body in the Solar System owing to its very young surface ice, showing many geological structures such as cracks and ridges, and its cryovolcanic activity (Figure 5). While Enceladus was expected to be completely frozen shortly after accretion, its cryovolcanic activity and heat emission at the south polar terrain (where the heat power is estimated to be $\sim$5–18 GW [109, 110, 111]) suggest strong and continuous heating processes, potentially operating for tens of millions to billions of years. Tidal friction in Enceladus' unconsolidated rocky core is the main process creating internal heat (estimated to be at least $\sim$20-25GW) [112, 48, 106], thus inducing strong water-rock interactions
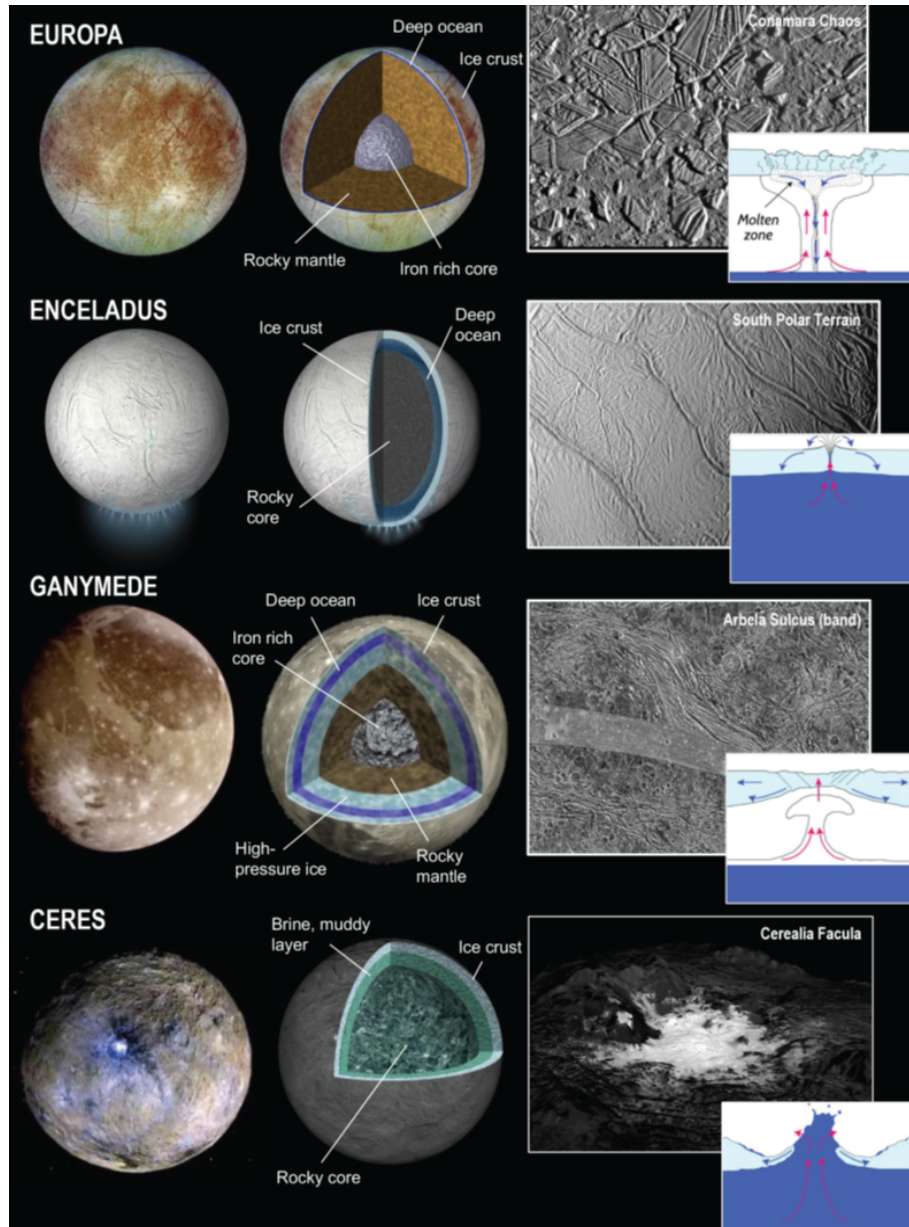
FIGURE 4. Illustration of some confirmed ocean worlds (the moons Europa, Enceladus and Ganymede and the dwarf planet Ceres), including their interior structures and the putative mechanisms of material exchange between subsurface ocean and surface. (*A*) Shallow melting and formation of chaos terrains (on Europa); (*B*) Plume activity and ejection of oceanic water through the ice shell to the surface (on Enceladus, possibly also on Europa); (*C*) Upwelling inducing the formation of bands on the surface (on Ganymede); (*D*) Excavation of oceanic water after an impact through the ice shell (observed on Ceres, but applicable to all icy bodies). From Castillo-Rodriguez & Kalousová [93].

(at the water-core boundary and deep in the water percolated core) and the transport of hydrothermal vent products from the ocean floor to the surface [83, 48, 113].

2.2.1 Exploration with the Cassini-Huygens mission

The Cassini-Huygens mission provided a much deeper understanding of the saturnian icy moons. A major discovery of the mission is that Enceladus possesses a global subsurface ocean containing organic compounds and hosting hydrothermal activity at the seafloor that sustains physicochemical disequilibria. The global, $\sim$37 km thick [106] ocean is surrounded by an ice shell, whose thickness varies from 21 to 26km globally, with a lower value of $\leq$ 5km at the south pole [53, 114] (Figure 6).
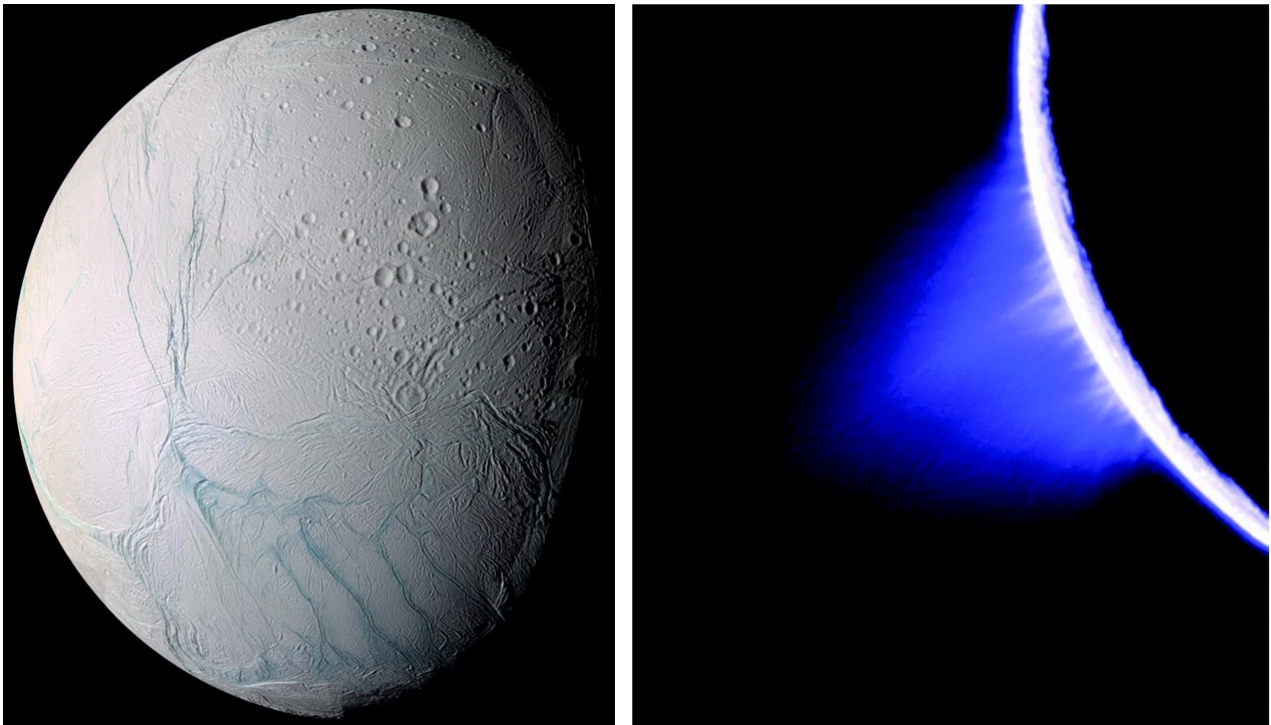
FIGURE 5. *Left*: The saturnian moon Enceladus. *Right*: Plume ejecting water vapour and ice grains from the "tiger stripes" at the south pole of Enceladus. (Credits: NASA/JPL/Space Science Institute).

Ice shell
(21-26 km thick, ≤5 km at south pole)

Global ocean
(~37 km thick, pH 8.5-9)

Rocky core
(density ~2400 kg/m^3)

Hydrothermal vents
(>90 °C)

Tiger Stripes
(~100 jets, total flux 100-1000 kg/s)

Collimated plume
(~20 km altitude; vapor, larger grains)

Mixed plume
(>40 km altitude; vapor, smaller grains)

Up to 93% of all grains fall back to the surface
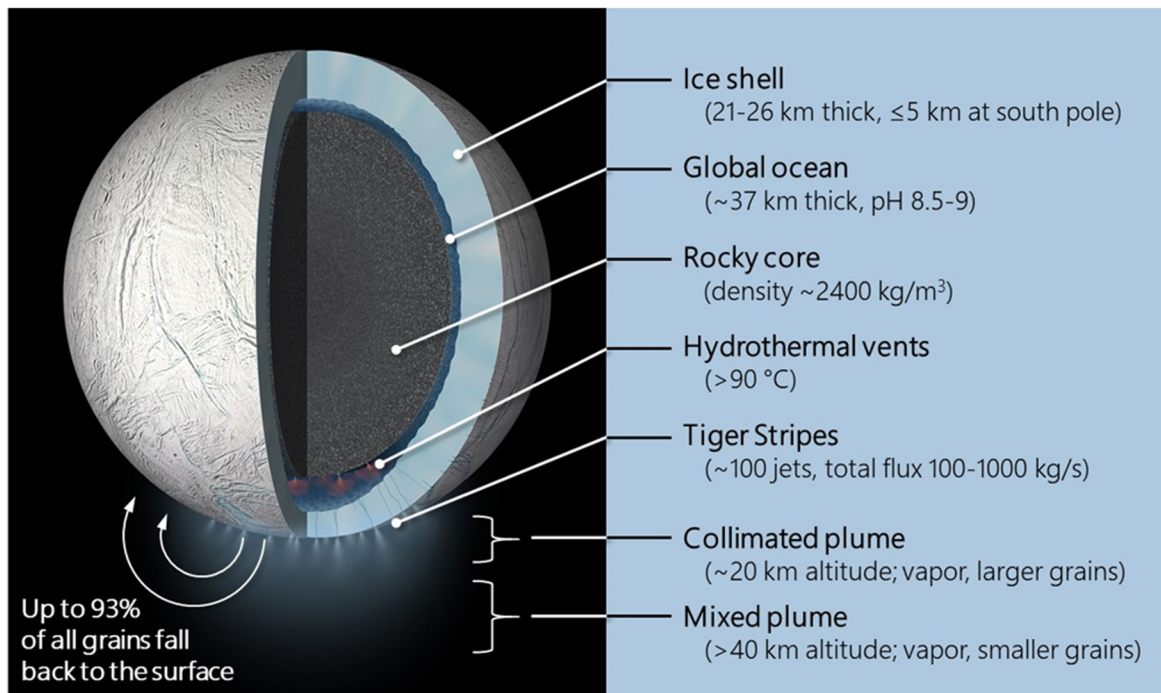
FIGURE 6. Illustration of the interior of Enceladus. From Cable et al. [115].

On July 14, 2005, the Cassini spacecraft detected a large plume of water vapour and icy particles at the south pole of Enceladus [116, 117, 118, 119, 120] (Figures 5, 6). The plume emanates from the so-called "tiger stripes", four parallel linear cracks associated with surface hot spots [99, 109], where oceanic material is ejected into space by ~ 100 high-speed narrow jets [121]. The plume is thought to be fed by evaporation of liquid water [122], extends thousands of kilometres from Enceladus, and have complex spatial variability and dynamics [123].

While its gaseous component has been characterised by Cassini's Ion and Neutral Mass Spectrometer (INMS), the icy particles have been characterised by the Cosmic Dust Analyzer (CDA) and are estimated to have sizes in the range of nanometres to micrometres (most grains having radii of 0.2-2 μm) and include a broad range of non-icy compounds [124, 65, 125].

Cassini's mass spectrometers results

The INMS and CDA mass spectrometers onboard Cassini both analysed plume material ejected from the subsurface ocean during close Enceladus flybys, as well as material in the E-ring of Saturn originating from the plume of Enceladus [118]. Indeed, while ∼68%–93% of the grains ejected in the plume fall ballistically back onto the surface [126, 127], the rest of the plume particles reaches circumplanetary space and supply material to Saturn's E-ring [128], due to the low gravitational pull of Enceladus. Measurements of neutral gases by the INMS indicated the dominance of H_2O, and the presence of CH_4, N_2, CO, CO_2, H_2, NH_3, and organic compounds ranging from C_2H_2 to C_6H_6 [120, 64]. CDA provided the compositional analysis of icy particles, and the identification of three main distinct classes of ice particles (type 1, 2, and 3):

• **Type 1** grains are almost exclusively composed of **water** ice, with occasional traces of sodium and potassium at the sub-ppm level [128, 124]. They are the smallest in size of all types, represent ∼60-70% of all spectra recorded in the E-ring and are thought to form by condensation of water vapour inside the icy vents [129, 122].

• **Type 2** grains contain significant amounts of **organic material**, and, like Type 1, are salt-poor. Two main types of organic material have been detected: (*i*) large macromolecular compounds with masses above 200 amu, the so-called High Mass Organic Cations (HMOC) [65] and (*ii*) low mass (<80 amu) frozen volatile organic compounds [66]. Type 2 grains bearing HMOC are thought to originate from an organic film on top of the ocean, where hydrophobic complex organic compounds separate by bursting of gas bubbles. The ejected solid phase organics are then coated by water ice, via condensation of water vapour around them, while rising through the icy vent system [65]. Type 2 grains with volatile organics are thought to form by condensation of these compounds together with the water vapour. They are highly reactive, bear aromatic moieties and O- and N-rich moieties which, by comparison with INMS data, are likely to be low-mass amines (e.g., (di)methylamine and/or ethylamine) and carbonyls (e.g., acetic acid and/or acetaldehyde) [66]. Type 2 grains are highly indicative of water/rock interactions and current geochemical processing on the porous seafloor. Indeed, the detected of H_2 and silica nanoparticles indicate exogenic serpentinisation and ongoing hydrothermal activity at temperatures greater than 90°C [64, 67, 130]. Such high temperatures in the interior of the moon are expected to promote chemical reactions and the formation of complex organic molecules, as observed by the detection of the HMOC.

• **Type 3** grains are rich in **salts**, including potassium and sodium salts [128]. They are thought to be frozen ocean spray and formed by bubble bursting (gas exsolution of CO_2, CH_4, or H_2). The detection of Type 3 grains requires the presence of both present-day liquid water and water-rock interactions to leach salts [131], therefore directly supporting the hypothesis of a subsurface ocean in direct contact with rocky material in Enceladus' interior. Type 3 grains allowed the Na concentrations in plume particles to be inferred and thus the overall salinity of Enceladus ocean to be estimated 3–8 g/kg, dominated by NaCl (0.05–0.2 mol/kg) [128].

The detailed characterisation of the different types of ice grains detected by CDA required laboratory analogue experiments, performed using the Laser Induced Liquid Beam Ion Desorption (LILBID) technique (described in detail in Section I.4.2). Together with the ice grains' compositions, the observed abundance of CO_2 in the plume indicates a pH value of 8.5 - 10.5 for Enceladus' ocean [131, 128, 67, 68]. The current model of the geochemistry of the interior of Enceladus, constrained by Cassini measurements, is shown in Figure 7. It also includes water-rock interactions at hydrothermal vents on the seafloor of Enceladus.

2.2.2 A hydrothermally active ocean world

Hydrothermal vents on the seafloor of Enceladus have been inferred from the detection and quantification of H_2 in Cassini's E21 flyby by INMS [64] and the detection of nanometre-sized SiO_2 particles by CDA [67]. The heat generated in the porous rocky core by tidal dissipation is transmitted to percolating fluids at the ocean-rock interface, thus inducing hydrothermal reactions. The presence of both H_2 and SiO_2 suggests a heterogeneous composition of the rocky core, with both ferrous-bearing rocks and carbonates [133]. Although H_2 could also be produced by other processes, such as the radiolysis of water ice by magnetospheric particles, the large quantities of H_2 observed make hydrothermalism a favoured hypothesis, due to the large yields that aqueous oxidation of
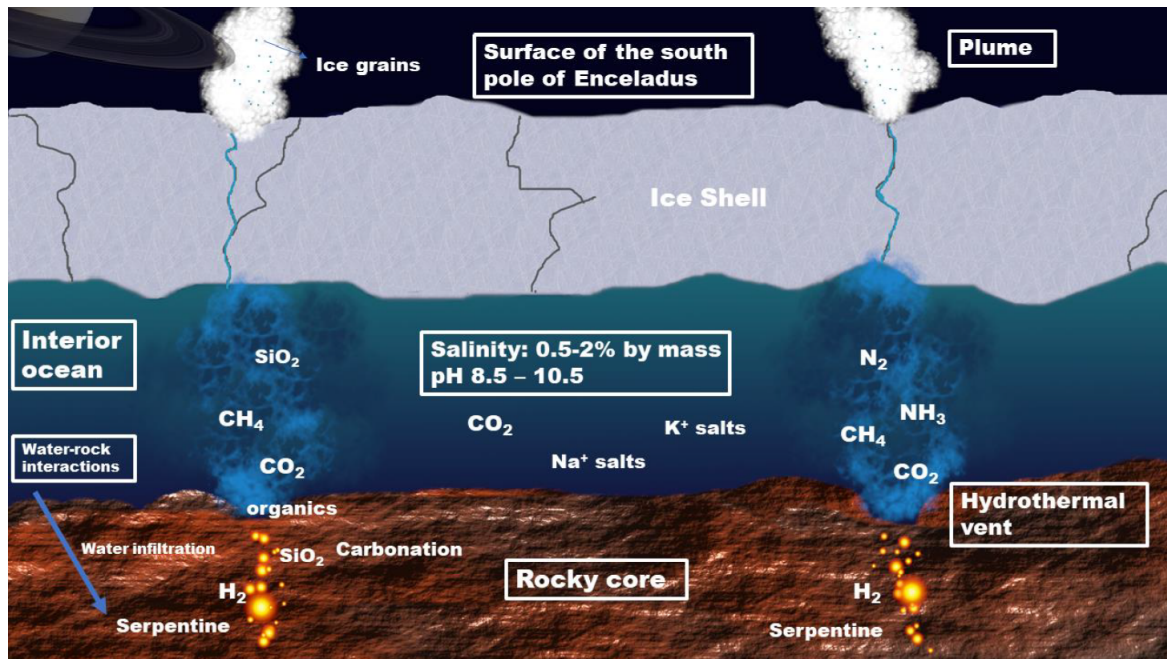
FIGURE 7. Illustration of the current geochemical model of the subsurface of Enceladus (not to scale). From Coelho et al. [132].

reduced minerals can produce. These lines of evidence for water/rock interactions and serpentinization reactions suggest that geochemical conditions are favourable for rich and complex chemistry at the bottom of the subsurface ocean.

The evidence for complex hydrothermal systems discovered on Enceladus show that this small moon is a geologically and hydrothermally active world, and its subsurface ocean bears similarities to those on Earth. Indeed, hydrothermal environments on Enceladus are highly analogous to alkaline hydrothermal vent systems on Earth, in particular to the Lost City Hydrothermal Field [67, 134, 135, 130] (Figure 8). The Lost City Hydrothermal Field is located on the Atlantic seafloor at the intersection between the Mid-Atlantic Ridge and the Atlantis Transform Fault. Carbonate chimney-like structures populate this long-lived site, where serpentinization of ultramafic rocks (i.e., igneous rocks mainly composed of mafic minerals and with a very low silica content, typical of Earth's mantle) abiotically produce simple compounds (e.g., CH_4, H_2) which feed a rich microbial life sustaining complex ecosystems that include unique animals [136].

Submarine hydrothermal vents are considered to be prime locations for investigating the origin of life on Earth, and potentially on Enceladus and other ocean worlds. Their discovery in 1977, with a first observation along the the Galapagos Rift in the Pacific ocean [138], changed the paradigm of habitability: until then, it was believed that all complex life on Earth was (directly or indirectly) linked to photosynthesis. The discovery of unique life endemic to hydrothermal vents, located deep underwater in the dark, and of many different types of hydrothermal vents (e.g., black smokers [139]), introduced a wider view of geologic, chemical, and biological diversity powered by chemosynthetic microorganisms. Overall, they provided a terrestrial example of how complex life might thrive on ocean worlds driven by internal heat and under a thick ice sheet which provides shielding from radiation.

2.2.3 Future missions

Enceladus is one of the main targets being considered for future in situ life-detection missions [140, 141, 142, 115]. Although no mission directly targeting Enceladus is currently under development, several mission concepts have been proposed to space agencies including both ESA and NASA. Among those proposed mission concepts, the **Enceladus Life Finder (ELF)** [141] is a Discovery-class mission proposed to NASA, which would directly search for evidence of life from the ocean of Enceladus. ELF's payload would comprise two state-of-the-art mass spectrometers, which would analyse the gas and ice grains ejected from the subsurface ocean in the plume: the Mass Spectrometer for Planetary Exploration (MASPEX) and the Enceladus Icy Jet Analyzer (ENIJA),
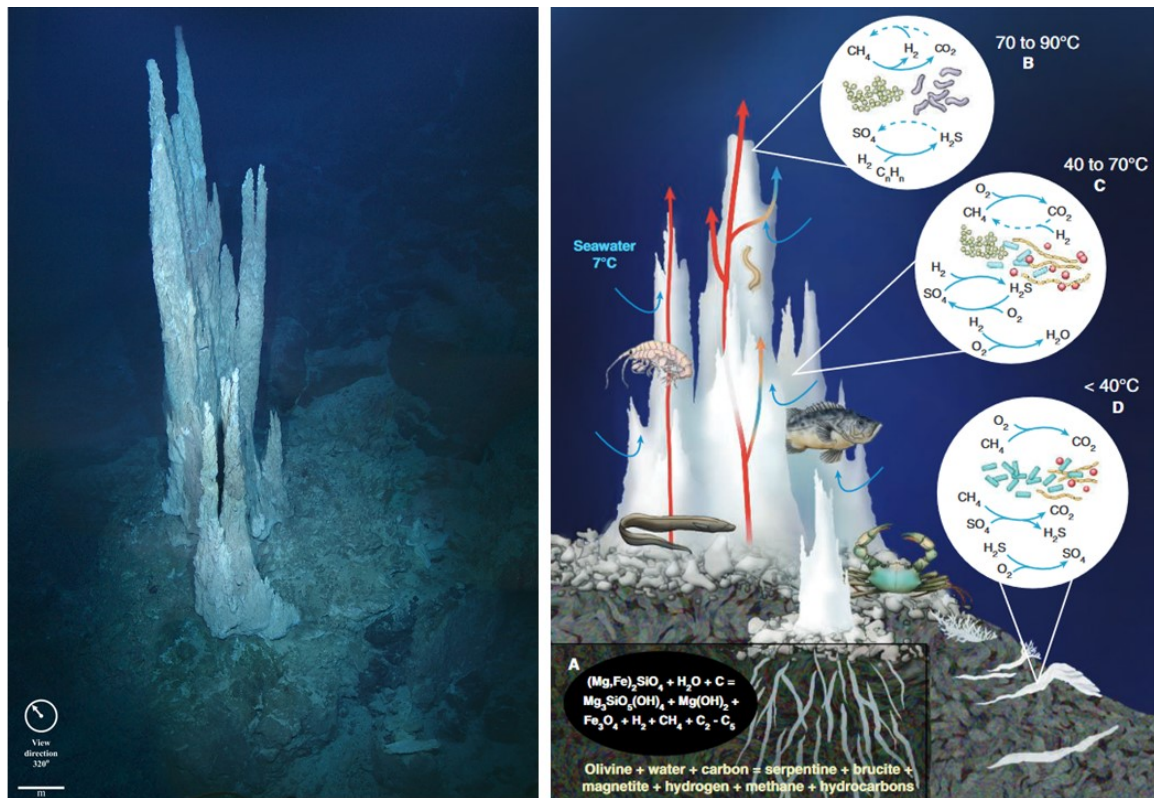
FIGURE 8. *Left*: Lost City hydrothermal vents, in the Atlantic ocean. Similar alkaline hydrothermal vents may be present on Enceladus' seafloor. (Credits: D. Kelley & M. Elend, University of Washington). *Right*: Illustration of ecosystems and microbial niches in Lost City hydrothermal vents. (A) Subsurface: serpentinization reactions. (B) Warm interior (hot hydrothermal fluids): archaea biofilms play a dominant role in methane production, methane oxidation and sulfate reduction. (C) Moderate-temperature zone: hydrothermal fluids mixed with seawater support a diverse microbial community including archaea and bacteria. Biochemical processes include the oxidation and reduction of sulfur compounds, the consumption and production of methane, and the oxidation of hydrogen. (D) Cooler zone: carbonate-filled fractures in serpentinized bedrocks, including archaea and bacterial populations. (Credits: Taina Litwak [137]).

respectively. ENIJA would be built from the heritage of the SUrface Dust Analyzer (SUDA) instrument (itself built from the heritage of CDA; Section I.3.2.2), with a higher sensitivity and resolution, and be able to detect both cations and anions [143]. Besides the higher performance of the payload, when compared to Cassini's mass spectrometers, ELF would be dedicated to characterising Enceladus' habitability and geochemical evolution. The spacecraft would conduct eight plume fly-throughs over 3 years, with closest approaches targetting the plume over the south-polar region at 50 km altitude.

More recently, the **Moonraker mission** [144] was proposed as an ESA M-class mission designed to perform multiple flybys of Enceladus and analyse its plume and surface over 13.5 years. Its payload consists of a suite of instruments dedicated to three major science goals (Figure 9) aiming at investigating (*i*) the habitability conditions of present-day Enceladus and its subsurface ocean; (*ii*) the mechanisms of communication between the subsurface ocean and the surface through the south polar terrain; and (*iii*) the origin and formation conditions of Enceladus (in the context of the formation of the Saturnian system). The performances of the payload would be significantly improved over Cassini's instruments. Notably, it would contain a modern impact ionization mass spectrometer, the High Ice Flux Instrument (HIFI), designed to surpass the capabilities of CDA (with a resolution ∼100 times better, and a mass range extending up to >2000 amu) and provide a significantly better determination of the composition of the salt- and organic-rich ice grains (Figure 9). HIFI and other Moonraker's instruments would have the capability to quantify the abundance and isotopic ratios of key species in the plume, and characterise physical parameters (e.g., composition) of the plume and the surface with an unprecedented precision.

Science Goals	Science Objectives	Measurement requirements		Instrument	Progress with regard to available data
		Physical parameter	Observables		
I. Habitability conditions of present-day Enceladus	1. Determine the abundances of key species related to habitability (CHNOPS, pH and redox state, hydrothermal interactions, organic inventory)	A. Mixing ratio in the plume with respect to water	H_2, CH_4, CO_2, NH_3, CO, N_2, H_2S, PH_3, ^4He, ^{40}Ar, volatile organics	INMS	Sensitivity > 50000 x Cassini INMS $M/\Delta M$ > 50 x Cassini INMS
				SWI	Allows remote measurements of the whole plume
		B. Abundance in icy grains	Refractory organics: HMOC, amino and fatty acids	HIFI, INMS, SWI (some organics such as AA condensed on grains)	HIFI: $M/\Delta M$ > 100 x Cassini CDA (distinction of inorganic ion clusters); 3.85 km/s flyby velocity prevents organic fragmentation SWI allows for detection of some organics condensed on grains
			Salts (incl. Mg, Ca, Na, K), carbonates, sulfates, SiO_2, phosphates		
		C. Energetic particles altering the surface	Abundance and energy of ions and electrons	Plasma spectrometer	$M/\Delta M$ for ions = 5 x Cassini CAPS Time resol. =45 x Cassini CAPS $E/\Delta E$ = 10 x Cassini CAPS
	2. Key properties of Enceladus' hydrosphere	A. Structure of the interior	Gravity field	Radio science	Close flybys at 3.85 km/s and <100 km altitude (at least 5 dedicated RS flybys, vs only 3 in Cassini)
II. Communication between the ocean and the surface through the South Polar Terrain	3. Determine the mechanisms of production of the plume	A. Size, distribution, shape of vents and fractures, temperature distribution	High resolution imaging	Camera	Multiple close flybys at 3.85 km/s and <100 km altitude
			Heat flux mapping	SWI	Multiple close flybys at 3.85 km/s and <100 km altitude, pixel 4 times smaller than Cassini CIRS, sensitivity to T as low as 20K
			Ions + charged grains in fine structure jets	Plasma spectrometer	$M/\Delta M$ for ions = 5 x Cassini CAPS Time resol. =45 x Cassini CAPS $E/\Delta E$ = 10 x Cassini CAPS
		B. Relative abundance and spatial distribution of the vapor and solid phase in the plume, variation over time	Abundance + size distribution of icy grains	HIFI, Nephelometer	HIFI measures flux, density, velocity No nephelometer on Cassini Large number of 3.85 km/s flybys provide spatial resolution and allow for monitoring over time of plume variations
				Plasma spectrometer	
			Velocity distribution of icy grains	HIFI, Nephelometer	
			Abundance, distribution of water vapor	INMS, SWI	Large number of 3.85 km/s flybys provide spatial resolution
			Gas kinematics	SWI	
III. Origin of Enceladus in the context of the formation of Saturn's system	4. Measure the isotopic and chemical composition of key tracers in the plume that are related to the origin of Enceladus	A. Relative elemental abundances	Ar, Ne, Kr, Xe /H_2O	INMS	Sensitivity > 50000 x Cassini INMS
		B. Isotopic ratios	$^{14}N/^{15}N$, $^{12}C/^{13}C$, $^{16}O/^{18}O$	INMS, TLS	INMS $M/\Delta M$ > 50 x Cassini INMS TLS
				SWI	Gives value for whole plume
			D/H in H_2O, CH_4, NH_3	INMS, TLS, HIFI (grains D/H), SWI	$M/\Delta M$ for INMS (> 50x Cassini INMS) and HIFI (>100 x Cassini CDA) removes ambiguity (D/H in H_2O) or enables detection (other isotopes), INMS sensitivity (>50000 Cassini INMS) enables detection of low-abundance species, TLS
			$^{38}Ar/^{36}Ar$	INMS	
			^{82}Kr, ^{83}Kr, ^{86}Kr /^{84}Kr		
			^{129}Xe, ^{131}Xe /^{132}Xe		

INMS = Ion and Neutral Mass Spectrometer. HIFI= High Ice Flux Instrument. SWI= Sub-mm Wave Instrument. TLS =

FIGURE 9. Overview of the scientific goals and intruments of the proposed Moonraker mission to Enceladus. Measurement requirements of the HIFI impact ionization mass spectrometer are highlighted in yellow. HIFI may allow the direct characterisation of oceanic composition with an unprecedented precision, going far beyond CDA's results. Adapted from Mousis et al. [144]

A possible future lander mission, such as the proposed **Enceladus Orbilander** [145], could include even more detailed science operations, such as a suite of life detection instruments with complex sampling systems. The proposed **Exobiology Extant Life Surveyor (EELS)** [146] would go even deeper and dive through the conduits in the icy crust at the south pole of Enceladus, where the plume is erupting. This snake-like robot would be able to explore the interior ocean of Enceladus. Future missions may reach areas of Enceladus that were once unattainable and thus open up new science opportunities for a better understanding of this fascinating small moon.

2.3 Europa

Europa was discovered near Jupiter by Galileo Galilei in 1610, together with the other jovian moons Io, Ganymede, and Callisto. While Jupiter has overall more than 90 moons, these four so-called galilean moons are the largest moons around Jupiter, with environments ranging from the volcanic and rocky Io to the icy moons Europa, Ganymede, and heavily cratered Callisto. Europa is the sixth closest to the planet, and the fourth largest, with a radius of 1561 km. Most of what is known today about Europa was discovered by the Voyager 2 spacecraft, the Galileo mission and the Hubble and James Webb space telescopes. In 1979, Voyager 2 was the first spacecraft to provide close images of Europa (captured from a distance of 250 000 km), revealing a surface full of unexpected features such as cracks and ridges, hinting at extent geological activity. Two decades later, the Galileo spacecraft orbiting Jupiter delivered even closer views of the surface (Figure 10) owing to 12 close flybys of Europa. Galileo provided the most detailed surface images to date, and strong evidence of a global subsurface ocean beneath the icy surface (e.g., [50]) containing two to three times the volume of Earth's oceans. Gravitational and magnetic Galileo data showed the interior ocean is in contact with a silicate core, all under an ice shell (whose thickness is still under debate). Insights into the composition of this ice shell have been revealed by Galileo instruments, but more recently, new data has been provided on this topic by the Hubble and James Webb telescopes. Another major input from Hubble is the tentative detection of cryogenic plumes (e.g., [147]); however, the difficulties associated with these detections might suggest that cryovolcanic plume activity on Europa may be limited in time and space.
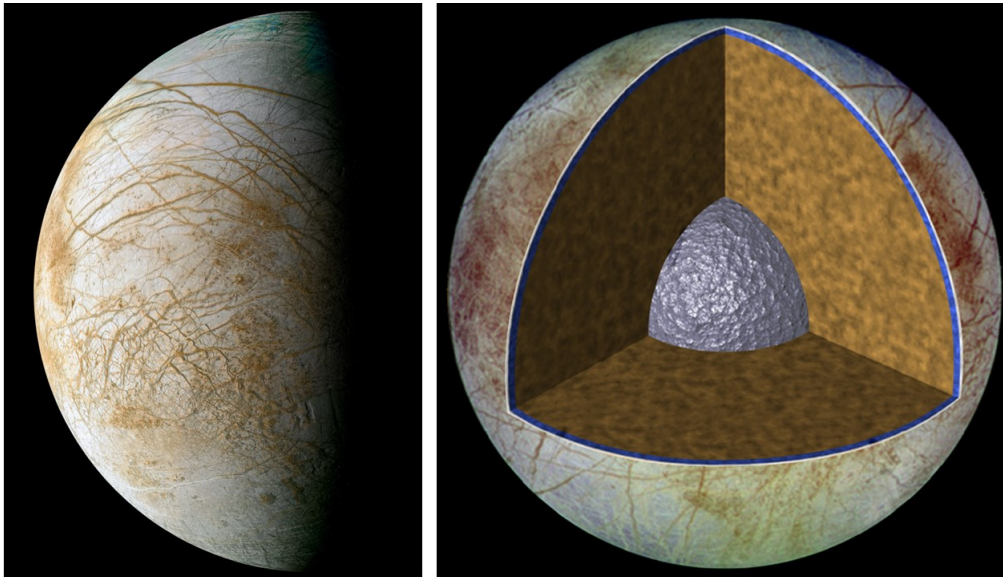
FIGURE 10. Left: View of Europa captured by Galileo on its 14th orbit of Jupiter, in March 1998 (Credit : NASA/JPL/Ted Stryk). Right: Internal structure of Europa, as inferred from Galileo observations, at approximately relative scales. Its metallic core is surrounded by a rocky mantle, a shell of liquid water and an outer ice shell. (Credits: NASA/JPL).

2.3.1 A geologically active moon

With a mean radius of ∼1561 km, Europa has a multi-layer internal structure (Figure 10): a metallic (iron and nickel) core surrounded by a rocky mantle, itself surrounded by a shell of liquid water and an ice shell estimated to be 15-30 km thick [148, 149], or less than 15 km thick [150]. Observations of the ice shell, including (limited) crater counting, indicate a young and active surface, estimated to be only 30 − 90 Ma old on average [51, 151, 152, 153]. Europa has one of the youngest surfaces in the Solar System, proof of active (or at last recent) tectonic processes. Indeed, Europa's surface bears many signs of significant geological activity, such as chaos terrains, domes, pits (lenticulae), and bands [51, 154]. Chaos terrains (Figure 11) represent around a quarter of the surface [155, 156] and are believed to be large-scale markers of shallow liquid water reservoirs [157, 158]. They are regions where irregular tilted plates, depressions, and discontinuous ridges form disorganized surface features, with polygonal blocks of older material set in younger ice [156]. At a smaller scale (∼10 km diameter), lenticulae are elliptical surface features suggested to form above small and shallow (up to ∼1km) bodies of liquid water emplaced in the ice shell [159, 160]. Bands form series of dark intersecting lineae on Europa's surface of

up to $\sim$1000 km in length, and $\sim$30km in width. They correspond to zones of dilation in the ice shell, with intrusion of crustal material inside the cracks [161].

Regions with compressional tectonic activity are thought to contribute to the downward transport of surface material to the ocean (e.g., [162]). In contrast, ubiquitous extensional and strike-slip faulting provide possible pathways from the interior to the surface [163]. A possible "recycling" of the surface has been suggested by surface reconstruction work, showing local regions with missing areas and possible episodic plate-like behaviour [162, 164]. Overall, both material exchange from the surface to the subsurface and vice-versa have astrobiological implications: (i) exchange processes [165] could bring material of astrobiological interest to the surface, where it could more easily be sampled than in the ocean; (ii) they could provide surface oxidants to the subsurface, potentially supplying a rich redox chemistry in the ocean [166, 74]. Shallow liquid reservoirs may also include potentially habitable brines pockets [167].

The high rock content of Europa's core is thought to produce significant heat [168], inducing water-rock interactions. Models show that Europa could produce enough energy to have extant volcanic activity at the seafloor [73]. Geological activity has also been reported on the surface, with tentative evidence for episodic or sporadic plume activity provided by both ground-based observations and spacecraft data [147, 169, 170, 171, 172, 173]. If those observations are confirmed, Europa would be the second moon in the Solar System found to eject a plume of water from the icy surface; however, because of the higher gravity (1.3 m/s^2 for Europa, as compared to 0.11m/s^2 for Enceladus), the plume is expected to be smaller in altitude than the Enceladus plume [174]. Future measurements of the topography, gravity and surface composition (e.g., from the upcoming JUICE and Clipper missions) will help to improve models of Europa's ice shell and interior, and better understand its evolution and habitability over geological times.
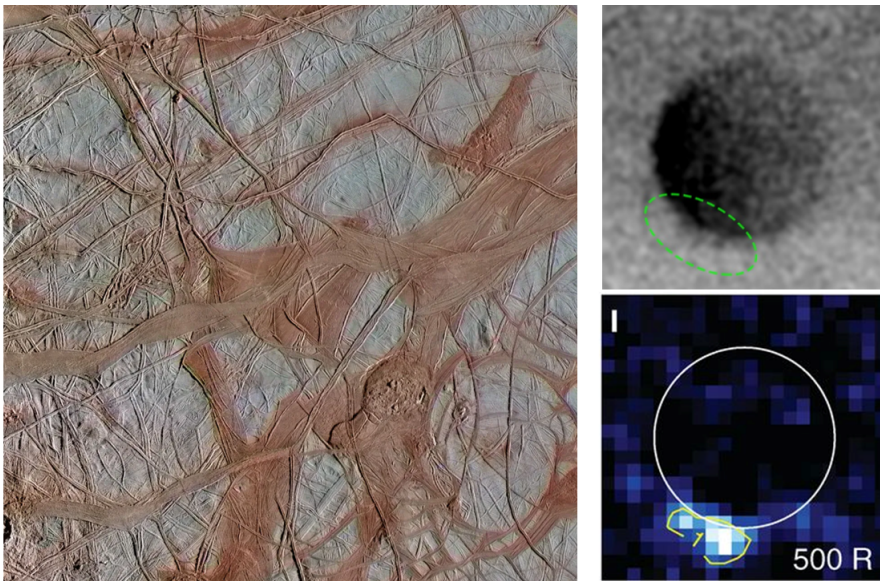
FIGURE 11. *Left*: The "Crisscrossing Bands" chaos terrains on Europa, exhibiting ridges and large smooth features. While ridges are thought to form by the repeated opening and closing of the icy surface, the flat smooth features might form when cracks are pulled apart horizontally for a long time (Credits: NASA/JPL-Caltech/SETI Institute). *Right*: Two plume candidate detections on Europa, located at similar areas in the southern hemisphere: (*top*) Transit continuum absorption image from January 2014 (Credits: Sparks et al. [169]); (*bottom*) Residual Lyman-α emission in an image from December 2012 (Credits: Roth et al. [147]).

2.3.2 A complex chemical composition

Europa's surface composition has been partially constrained by both spacecraft measurements, including Galileo's Near-Infrared Mapping Spectrometer (NIMS) observations, and Hubble and James Webb Space Telescope (JWST) observations. The surface is dominated by water, sulfuric acid hydrate (e.g., [151]) and a variety of other non-icy material: SO_2 [175]; CO_2 [176, 177]; O_2, H_2O_2 [178] and several salts such as NaCl [179, 180] and sulfates (including mirabilite $Na_2SO_4 \cdot 10H_2O$, bloedite $Na_2Mg(SO_4)_2 \cdot 4H_2O$, epsomite $MgSO_4 \cdot 7H_2O$ [151,

181, 182, 183, 184, 185]). Moreover, O_2 was detected in the very thin atmosphere [186].

Sulfuric acid hydrate is the largest component of the non-ice material. It is a product of radiolytic chemistry which dominates the surface composition of the heavily irradiated and sulfur-bombarded trailing hemisphere [187, 188, 189, 184, 190, 191]. Indeed, the Io plasma torus affects the surface of Europa with sulfur ions (originating from Io's volcanoes), combining with water to produce sulfuric acid [192, 193, 187]). The total mass transfer of material from Io to Europa is estimated to be 10^{14} g/Myr [194]). Hydrogen peroxide (H_2O_2) is another product of radiation (of water ice) [76, 195]. The detection of sulfuric acid is spatially coincident with magnesium sulfate salts, suggesting a radiolytic origin of the sulfates [184, 151]; but these may also be radiation products of exogenic sulfur ions and magnesium salts already present on Europa's surface [196]. Magnesium sulfates are likely some of the major salts in Europa's ice composition and estimated concentrations range from 0.04 to 4.2 mol/kg H_2O [197, 198]; but NaCl and KCl [184] or a mixture of Mg-chloride, chlorate, and perchlorate [190] have also been proposed to be the dominant salt material.

A better understanding of the composition of salts on Europa's surface has been undertaken with reinterpretations of NIMS data, which has low spectral resolution [183, 185]. Although these studies have brought significant constraints on the possible (combinations of) mixtures, large uncertainties remains and the data and a variety of different composition still fits some of the data. Moreover, the origins of most surface components are still highly debated, as the surface composition reflect both endogenic and exogenic processes (e.g., [184]). NaCl, MgCl salts and possibly sulfate salts on Europa's surface are believed to be endogenous salts originating from the subsurface ocean [181, 182, 199, 200, 190, 180]. The surface might be a combination of endogenic frozen material, including brines, and implanted surface material, with relative proportions varying spatially over Europa's hemispheres. The CO_2 ice on Europa is thought to originate from a source of carbon within Europa's subsurface, probably from the ocean. While CO_2 may also be produced by irradiation of organic material, so far the lack of correlation with irradiation on the surface excludes a radiolytic production of CO_2 [177].

Chaos terrains in the leading hemisphere may best reflect the composition of the interior ocean, since they are geologically young regions suggested to be formed from upwelling or melt-through, [201, 202] and are shielded from the iogenic sulfur ion implantation of the trailing hemisphere. Their high NaCl concentration [151, 180, 203, 204] hints towards a NaCl-dominated ocean composition. However, the ocean composition is highly uncertain as it is hidden beneath a thick ice shell and was never directly sampled. Modelling efforts have provided estimates of its composition, based on water-rock interactions betweeen candidate silicate core compositions and volatile components that may have accreted during Europa's formation [205]. Chondritic meteorite composition is typically assumed to represent the silicate interior. Europa's silicate interior is differentiated (at least partially) [206]. The composition of Europa's ocean also influences, and is influenced by, the seafloor rock composition, which is only constrained by models. It may contain carbonates, phyllosilicates, Fe-sulfides, Ca-sulfates, and organic material [205]. Although highly unconstrained, pH estimated values for Europa's ocean are ∼6-7 units [207]. Galileo magnetic measurements suggested a salinity of ∼50 g/kg [150], but this value is still uncertain as it strongly depends on the thickness of the ocean.

Like the surface, the ocean may also be a mixture of both endogenous and exogenous materials, since it may have incorporated products from reactions with rocky material at the seafloor, and surface material including oxidative species from the highly irradiated surface and volcanic products from Io deposited on the surface.

Further constraining the salt composition of Europa's ice shell is key to better understanding this moon, as salts play a key role in the evolution of the ice shell. Indeed, they influence the colligative properties of water and decrease its freezing point, thus changing the dynamics and longevity of liquids within the ice shell; they are associated (in endogenic material) with geologically young surface features, and play a key role in the habitability of salt-rich ice and brines. Moreover, identifying endogenic surface material through a good understanding of cyrovolcanic and tectonic processes is key to determining the habitability of the subsurface ocean [208].

2.3.3   A highly irradiated moon

The surface of Europa is highly irradiated by Jupiter's magnetosphere [209, 77], thus creating a highly oxidative surface. Magnetospheric electrons, protons, and ions constantly bombard it, with a high flux and relatively low energies on the trailing hemisphere and with a relatively lower flux and higher energies on the leading hemisphere [210, 211]. Because Europa is tidally locked to Jupiter, the global pattern of magnetospheric particle irradiation on Europa's surface induces a difference of colour between the leading and the trailing hemisphere: the trailing hemisphere is much darker (higher irradiation flux) than the leading hemisphere (enhanced impact

gardening[2]). Electrons are the dominant carriers of energy for radiation chemistry on Europa [209], with energies ranging from $\sim$10 keV to >10 MeV, and with high energy electrons (extending to >10 MeV) dominating the surface irradiation flux. The radiation doses received on Europa's surface ice have been estimated by Paterson et al. [211] to be 6.6×10^{-2} Gy per second for electrons up to energies >10 MeV and to be reduced by two orders of magnitude at a depth of 1 cm. A study by Nordheim et al. [210], including the variations with the surface location and the depth in water ice, showed that the yearly global average of irradiation that ice at 1 μm depth ($\sim$size of ejecta ice grains detectable by SUDA; Section I.3.2.2) receives is $\sim$60 MGy. They showed that radiation processing of organics and potential biosignatures is strongly dependent on the surface location and that the highest radiation doses are received by shallow material on the trailing hemisphere near the equator. Recently, Tsareva et al. [212] modelled the dose distribution of electron radiation on the surface Europa, thus creating accurate maps of radiation doses across the moon.

2.3.4 Europa Clipper

NASA's Europa Clipper mission [213] will be launched in October 2024 from the Kennedy Space Center (Florida, USA) and is designed to assess Europa's habitability, focusing on the ice shell and ocean, the composition and the geology. Gravity assists with Mars and Earth will increase Clipper's velocity, and allow it to reach the Jupiter system in April 2030. It will then orbit Jupiter and perform $\sim$50 flybys of Europa at altitudes of typically 25 – 100 km, over around 3 years. The spacecraft has a complementary suite of nine dedicated remote-sensing and in-situ science instruments (Figure 5): the Europa Ultraviolet Spectrograph (Europa-UVS), the Europa Imaging System (EIS), the Mapping Imaging Spectrometer for Europa (MISE), the Europa Thermal Imaging System (E-THEMIS), the Radar for Europa Assessment and Sounding: Ocean to Near-surface (REASON), the Europa Clipper Magnetometer (ECM), the Plasma Instrument for Magnetic Sounding (PIMS), the SUrface Dust Analyzer (SUDA), and the MAss Spectrometer for Planetary EXploration (MASPEX). They will
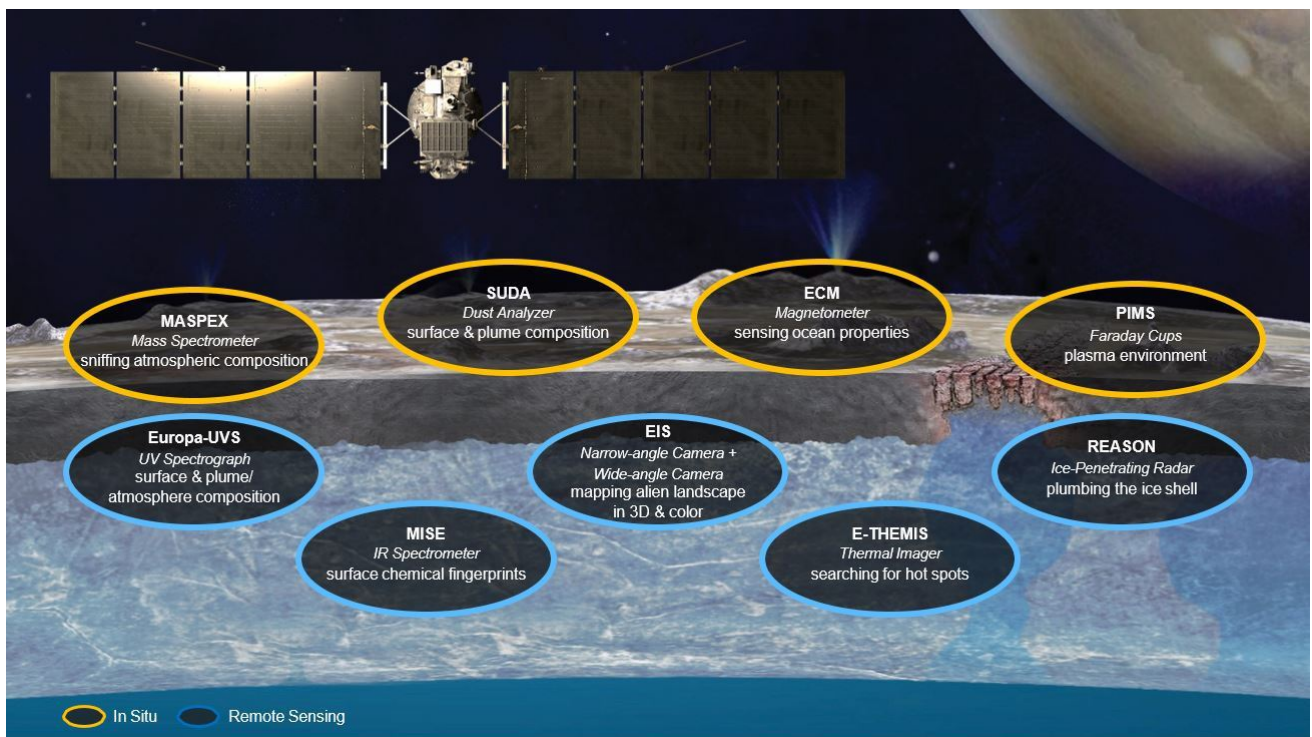
FIGURE 12. Illustration of the science instruments onboard Europa Clipper. In situ instruments are labelled in yellow, and remote sensing instruments in blue. They will both scan Europa from above and directly sample the moon's tenuous atmosphere and ejected dust grains. (Credits: NASA / JHUAPL)

collect remote-sensing and in situ data on Europa's interior, surface, atmosphere, and near-space environment. The low altitude flybys may allow Europa's potential plumes to be sampled, as this is expected to require low

---

[2]Impact gardening is the process by which frequent small impacts stochastically excavate the uppermost regolith of planetary surface.

altitudes (<100 km) [214, 174].

Two mass spectrometers are included in the payload: SUDA [215] (Section I.3.2.2), which will measure the composition of small icy particles ejected from Europa's surface and in potential plumes; and MASPEX [216], a neutral gas mass spectrometer which will sample the exosphere including possible plume gases, and neutral torus to detect and quantify major, minor, and trace compounds and isotopic ratios. Surface remote sensing equipment includes an imaging system in the visible range (EIS) consisting of both a wide-angle camera and narrow-angle camera; an imaging near-IR spectrometer (MISE) to probe the surface composition; a UV spectrograph (UVS) to look for potential plumes and characterize the composition, chemistry, and structure of the exosphere; and a thermal imaging system to locate geological activity. The ice-penetrating radar (REASON) will sound Europa's ice shell from the surface to the ocean to determine its structure and identify shallow liquid reservoirs. Both plasma and magnetometer instruments (PIMS and ECM) will help to determine the ocean depth and salinity, as well as the thickness of the ice shell. This suite of instruments will provide highly detailed and complementary data about Europa, which will be of great value for the determination of a potential landing site for a future Europa lander mission [217] or other proposed mission concepts.

Besides the dedicated instruments, gravity and radio science will be achieved using the spacecraft's telecommunication system (Doppler data) and antennas; and its radiation monitoring system will bring information about the radiation environment of the jovian system. Collaborations between Europa Clipper and the JUpiter ICy moons Explorer (JUICE) mission should provide synergistic science of high value, as both spacecraft are expected to be in the Jovian system at the same time. Simultaneous joint observations should allow unique scientific opportunities to enhance the science return from both missions. They might include simultaneous measurements of the solar wind and of the jovian magnetosphere (inside and outside of the magnetosphere), but also cross-calibrations of instruments over similar regions of Europa.

2.3.5   JUpiter ICy moons Explorer (JUICE)

Addressing key science questions about the jovian moons as an interconnected system is necessary to better understand each of its moons individually. With this goal in mind, the JUpiter ICy moons Explorer (JUICE) mission from ESA will open a new era of missions to the jovian icy moons [218]. JUICE was successfully launched on 14 April 2023 from Kourou, and will be inserted in orbit around Jupiter in July 2031. During a minimum of four years in the jovian system, it will mainly perform flybys of Europa, Ganymede and Callisto, but will avoid Io due to the high radiation environment. Two flybys will be dedicated to Europa, focusing on characterising the composition of the non water-ice material. JUICE's payload includes ten instruments dedicated to characterising the jovian icy satellites and the potential emergence of habitable environments. The payload (Figure 13) comprises remote sensing instruments (JANUS, MAJIS, UVS, SWI), a geophysical package (GALA, RIME, 3GM) and an in situ package (PEP, J-MAG, RPWI).

2.3.6   Mission concepts for a future exploration of Europa

A mission concept to the Jupiter system named Gan De, led by Chinese research institutes, is in development [219]. Its main objective is to characterise and study the formation of the jovian system, with a particular focus on its satellites. This mission has been proposed to have both a Jupiter orbiter and a Callisto lander, and its payload could include plasma and dust instruments, imaging systems and a sampling system. While this mission concept is still at preliminary stages, it could greatly benefit from synergies with previous missions from larger space agencies (ESA, NASA), as international collaborations are key to successful space missions.

The proposed Europa Lander mission concept [217] would be the first landed mission to search for biosignatures on an extraterrestrial ocean world. The lander's payload would include a microscope, a vibrational spectrometer, an organic compositional analyser and a geophysical sounding system. While the Europa lander would collect samples from ∼10 cm below the surface, some other mission concepts aim to go even deeper through the ice and cross through the ice shell [220]. However, under-ice exploration represents major technical challenges (including communication and resistance of the instruments to e.g., cold, vacuum, unknown salinity and porosity) which might, through several years of instrumentation development, delay their feasibility.

To conclude, many mission concepts are currently in development to orbit, land on or even dive into Europa. Such missions are extremely challenging due to the technologies and instrumentations they require [221], but they might become reality in the near future owing to the detailed characterisation that JUICE and Europa Clipper will bring at the very beginning of the next decade. Although JUICE and Clipper may not be able to

Instruments inside the spacecraft:
3GM:
 - KaT
 - USO
 - HAA
Gravity & Geophysics of Jupiter and Galilean Moons

Sub-millimeter Wave Instrument

GAnymede Laser Altimeter

SWI
GALA
MAJIS

Moons and Jupiter Imaging Spectrometer

PEP

Particle Environment Package

RPWI

RIME

Radar for Icy Moon Exploration

Magnetometer boom (J-MAG, RPWI)

Magnetometer

RIME

RPWI — Radio & Plasma Wave Investigation
PEP
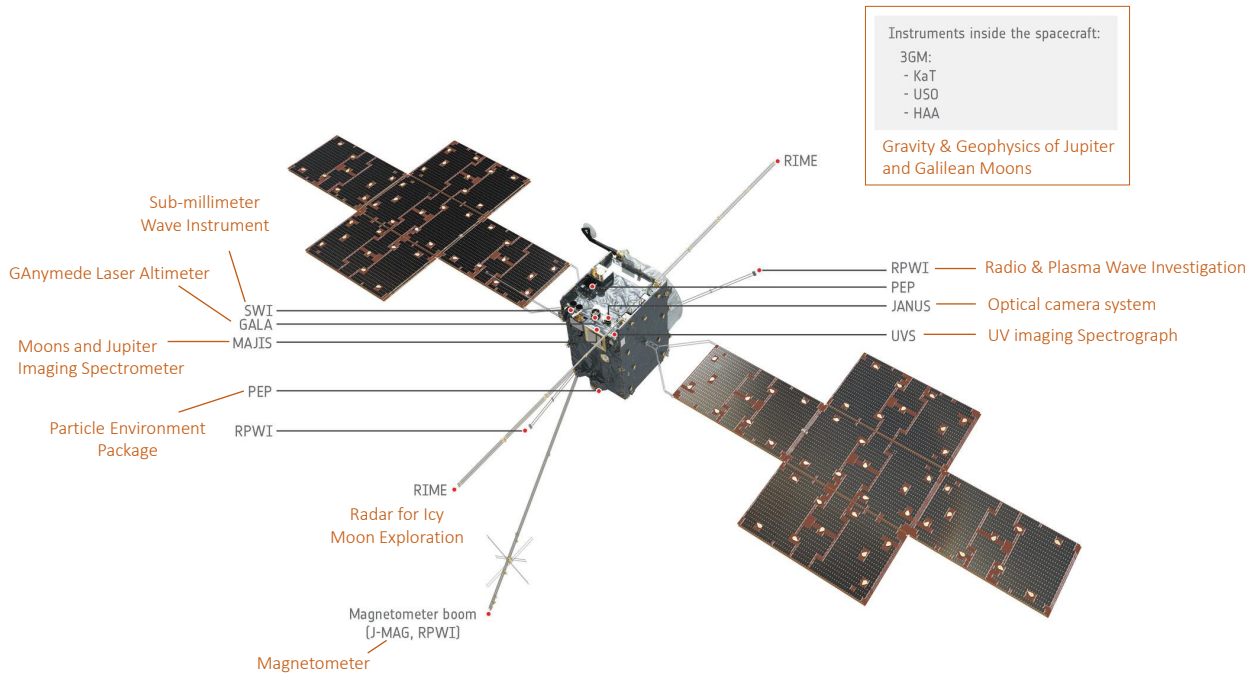JANUS — Optical camera system
UVS — UV imaging Spectrograph

FIGURE 13. Payload of the Jupiter Icy Moons Explorer (JUICE). The full names of the instruments, reflecting their functionality, are written in orange. Adapted from ESA/ATG medialab.

detect direct signatures of life on Europa, they will pave the way to that goal with a deeper understanding of this fascinating moon, with notably the expected identification of endogenous material arising from the ocean.

3 Spaceborne Impact Ionization Mass Spectrometry

3.1 General overview of mass spectrometry

Mass spectrometry (MS) is a powerful analytical technique that is widely used both in laboratories, with many fields of application (chemistry, biochemistry, pharmacy, medicine...), and in space instrumentation as an in situ technique. It aims to identify a compound (or compounds) from the molecular or atomic mass(es) of its constituents, and is particularly beneficial for the study of complex analytes. The basic principle of MS is to generate ions from the analyte, separate them according to their mass-to-charge ratios (m/z) and to measure them with their respective m/z and abundance. A mass spectrometer therefore always combines an ion source, a mass analyzer, and a detector; and is operated in high vacuum. Many different types of mass spectrometers exist, combining different interconnected fundamental (e.g., nature of ionization processes), and technical aspects with instrumentation (e.g., nature of the sample, ionization technique, type of mass analyzer and detector, vacuum systems, performance characteristics, mode of operation, data acquisition) [222]. The most common types of mass analysers include Time of Flight (ToF), Fourier Transform Ion Cyclotron Resonance (FT-ICR), and Quadrupole and Orbitrap 14. Combining two MS techniques in a 2-step analysis is also possible (so-called tandem mass spectrometry), and is especially useful for analyzing complex mixtures. The principle of ToF is that ions of different mass-to-charge ratio (m/z) are dispersed in time during their flight along a field-free drift path of known length, with the lighter ones will arrive earlier at the detector than the heavier ones [223]. This technique is used in impact ionization mass spectrometers onboard space missions (sections I.2.2.1 and I.3.2.2). Mass spectral interpretation involves the identification of characteristic ions, but also potentially the

Type	Acronym	Principle
Time-of-flight	TOF	Time dispersion of a pulsed ion beam; separation by time-of-flight
Magnetic sector	B	Deflection of a continuous ion beam; separation by momentum in magnetic field due to Lorentz force
Linear quadrupole	Q	Continuous ion beam in linear radio frequency quadrupole field; s due to instability of ion trajectories
Linear quadrupole ion trap	LIT	Continuous ion beam delivers ions for trapping; storage, and eventually separation in linear radio frequency quadrupole field by resonant excitation
Quadrupole ion trap	QIT	Trapped ions; separation in three-dimensional radio frequency quadrupole field by resonant excitation
Fourier transform-ion cyclotron resonance	FT-ICR	Trapped ions in magnetic field (Lorentz force); separation by cyclotron frequency, image current detection and Fourier transformation of a transient signal
Orbitrap	Orbitrap	Axial oscillation in inhomogeneous electric field; detection of frequency after Fourier transformation of a transient signal

FIGURE 14. Overview of different mass analyzers commonly used in mass spectrometry. Time-of-Flight (ToF) is highlighted as the method typically used in impact ionization mass spectrometers onboard spacecrafts. Adapted from [223].

identification of fragmentation (and recombination) pathways, which can provide valuable information on ionic structures. Ionization of the analyte can be initiated using a variety of techniques of varying hardness, typically chosen depending on the analyte's properties (Figure 15). Among all those techniques, Matrix-Assisted Laser Desorption and Ionization (MALDI) is highlighted as a soft ionization method that can be used to ionise organic molecules with minimal fragmentation; and will be mentioned in more detail in Section I.4.2. In MALDI, the analyte is mixed in a suitable solid matrix, where it is irradiated with a pulsed laser thus creating cations, anions, electrons, and neutral molecules. Mass spectrometry can also be combined with a separation method to target specific material e.g., using a Gas Chromatograph Mass Spectrometer (GC-MS).
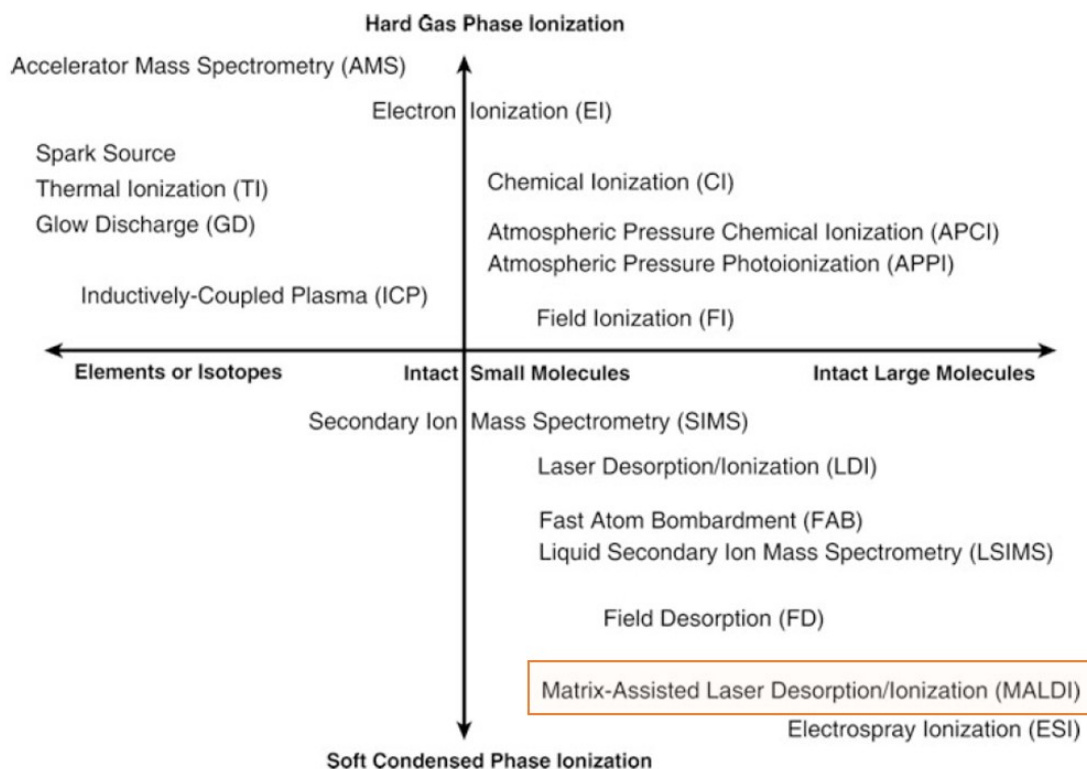
Hard Gas Phase Ionization

Accelerator Mass Spectrometry (AMS)

Electron Ionization (EI)

Spark Source
Thermal Ionization (TI)
Glow Discharge (GD)

Chemical Ionization (CI)

Atmospheric Pressure Chemical Ionization (APCI)
Atmospheric Pressure Photoionization (APPI)

Inductively-Coupled Plasma (ICP)

Field Ionization (FI)

Elements or Isotopes | Intact **Small Molecules** | **Intact Large Molecules**

Secondary Ion Mass Spectrometry (SIMS)

Laser Desorption/Ionization (LDI)

Fast Atom Bombardment (FAB)
Liquid Secondary Ion Mass Spectrometry (LSIMS)

Field Desorption (FD)

Matrix-Assisted Laser Desorption/Ionization (MALDI)

Electrospray Ionization (ESI)

Soft Condensed Phase Ionization

FIGURE 15. Overview of different ionization techniques used in mass spectrometry, classified by their estimated relative hardness or softness, and suitability for analytes depending on their molecular mass. Matrix-Assisted Laser Desorption and Ionization (MALDI) is highlighted as a soft ionization method suitable to ionize (large) organic molecules with minimal fragmentation. Adapted from [223].

3.2 Impact ionization mass spectrometry: past and future space instruments

Since MS is one of the few available techniques to provide a thorough analysis of the chemical composition of samples, mass spectrometers have both a rich history and a promising future in planetary exploration. Mass spectrometers that are typically part of the payload of space missions include impact ionization mass spectrometers. Impact ionization mass spectrometry is powerful technique for space applications, as utilised from the 1960s onwards for micrometeroids and cosmic dust analysis (e.g., [224, 225, 226]). The principle of impact ionization involves the hypervelocity (>1 km/s) impact of small particles (dust and icy grains) onto a target, thus producing neutral atoms, ions and electrons. The ions are subsequently analyzed with ToF-MS. The first generation of dust detectors included the instruments onboard the Galileo [227], Ulysses [228], Helios [229], Giotto [230] and VeGa [231] spacecrafts. The Cosmic Dust Analyser (CDA) and SUrface Dust Analyzer (SUDA) instruments, two more recent instruments, will be described below, as well as the implications of these instruments for past and future space exploration.

3.2.1 The Cosmic Dust Analyser (CDA)

The Cosmic Dust Analyser (CDA; Figure 16) was the impact ionization mass spectrometer onboard the Cassini mission [232]. It characterised the dust and micrometeoroid environment in the Saturnian system, by measuring the properties of micron and submicron dust particles at impact velocities of the order of km/s. CDA was developed and built at the Max Planck Institute for Nuclear Physics (Heidelberg, Germany), and operated from 1999 (even before Cassini reached the Saturnian system) until the end of the Cassini mission in 2017. The Cassini mission was extended twice, thus giving CDA more than a decade to collect cosmic dust particles, including interstellar and interplanetary dust, E-ring and Enceladus plume particles. One of its major achievements is that it enabled some of the most significant discoveries related to the geochemistry of Enceladus' ocean, including the detection of salts, organic molecules and of bio-essential elements (see section I.2.2.1). In

fact, the detection of salts was perceived as the first real evidence for a present-day subsurface ocean in Enceladus [128].

CDA had two independent sensor heads (Figure 16): (i) the High Rate Detector (HRD), to detect particle impacts and their masses at very high impact rates (up to 10^4 particles per second); (ii) the Dust Analyser (DA) to analyse dust particles' properties i.e., the electric charge, impact direction, speed, and composition. The DA was itself composed of three main subsystems: the Entrance Grid (EG), the Impact Ionization Detector (IID) and the Chemical Analyser (CA). The included ToF mass spectrometer could measure cations with a mass resolution m/Δm of 20-50 and a mass range from 1 to $>\sim$200 u, depending on triggering [232]. The HRD and DA subsystems functioned simultaneously, providing complementary data about populations of dust grains with impact speeds ranging from 1 to $>$100 km/s [232].
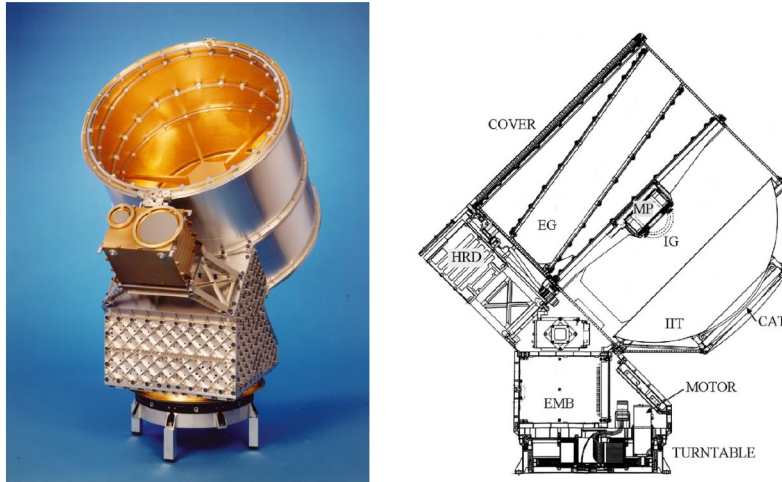
FIGURE 16. The Cosmic Dust Analyser (CDA). Figure from Srama et al. [232]. *Left*: Picture of the CDA instrument. *Right*: Technical drawing of CDA. HRD: High Rate Detector; EG: Entrance Grid; EMB: Electronics Main Box; MP: Multiplier; IG: Ion Grid; IIT: Impact Ionization Target; CAT: Chemical Analyser Target

3.2.2 SUDA

The SUrface Dust Analyzer (SUDA; Figure 17) [215] is the impact ionization mass spectrometer onboard Europa Clipper. It was built at the University of Colorado, USA. Based on the strong heritage of the CDA in-

FIGURE 17. The SUrface Dust Analyzer (SUDA) flight model. From Kempf et al. [215].

strument, SUDA combines several state-of-the-art features. Unlike CDA, SUDA is able to measure both cationic and anionic mass spectra (although not at the same time). While both CDA and SUDA are time-of-flight mass spectrometers, SUDA uses a Reflectron ToF (while CDA had a linear ion path), which extends the ion path and reduces the effects of the ions' initial energies, leading to a better mass resolution (m/Δm = 150-250). SUDA's high mass resolution and sensitivity will allow it to detect compounds even at trace concentrations (< 1 ppm), in the mass range m = 1-500 u.

SUDA's operation principle is shown in Figure 18. Incoming ejecta particles enter the instrument from the top, go through a set of grid electrodes (e.g., velocity grid), and impact the target at the bottom of the instrument. The entrance grids (located at the top) allow the mass and speed vector of the incoming particles to be measured sensitive down to 0.3 μm particle size. The iridium target, located at the bottom of the instrument, is held at a potential of ±2.5 kV, depending on the chosen ion mode. After impact of dust particles onto the target, ions resulting from the impact are repelled from the target, reflected by a reflecting grid (±3 kV) and focused towards the detector (Ion Sensor). Detection of the cations' or anions' masses is therefore achieved via their times of flight. The target is made with iridium, which has excellent impact ionization properties, is chemically inert and has two isotope lines (191 u and 193 u) which don't interfere with mass lines of interest in the mass spectra. Decontamination of the impact target will be performed after each close Europa flyby, via heating to
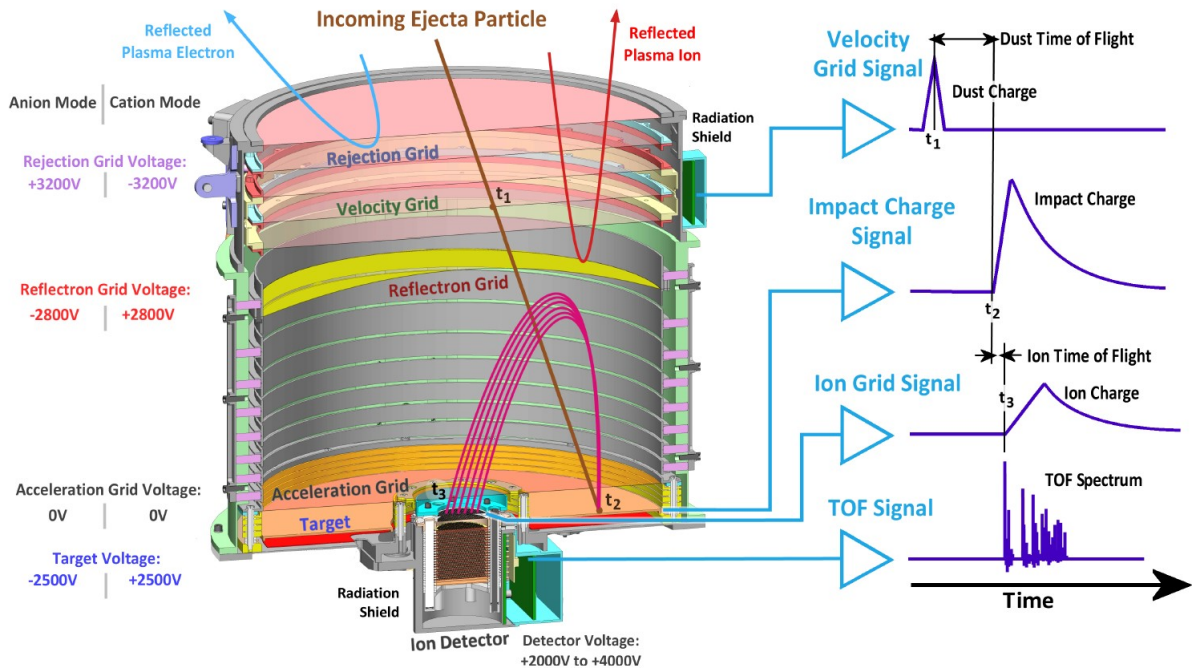

FIGURE 18. View of the SUrface Dust Analyzer (SUDA). On the right are displayed the operating principles for the different signals produced by incoming particles. From Kempf et al. [215].

110°C for 8 hours, to eliminate molecular deposition (e.g., of salts) that could degrade SUDA's performance.

SUDA will analyse ice grains ejected from the surface of Europa by micrometeorite bombardments [233, 234, 235] and from potential plumes [147, 169, 171, 172]. Micrometeorites impacting icy surfaces can eject a large amount of particles, up to few thousand times their own masses [236]. Most ejecta particles have ballistic trajectories, feeding a dust cloud around Europa, and will fall back to the surface. SUDA will be able to determine the trajectories of detected ejecta particles owing to information from the entrance grids combined with the attitude and position of the spacecraft, therefore constraining a spatial origin on the surface for each particle. With a spatial resolution roughly equal to the instantaneous altitude of the spacecraft, back-tracking of ejecta trajectories will enable the compositional mapping of Europa's surface [234, 237, 238].

Geological features of interest on Europa's surface, such as the chaos terrains Thera and Thrace Macula, will be specifically targetted and characterised in both cation and anion modes owing to repeated flybys by the Clipper spacecraft. SUDA will analyze up to 250 particles per second above geological features of interest during flybys at the lowest altitude of 25km (Figure 19). Ice grain compositions measured by SUDA will be associated

with observable surface features (i.e., geology, structures, albedo, grain sizes), as well as with compositional data from other instruments onboard Clipper, such as MASPEX and MISE. Future results from MISE and SUDA will be highly complementary, as SUDA will provide highly detailed composition from targeted surface features, while MISE will provide the inventory and distribution of surface compounds in a large-scale mapping. Such combined measurements will allow to better characterise the global composition of Europa, which is currently poorly constrained (Section I.2.3.2).
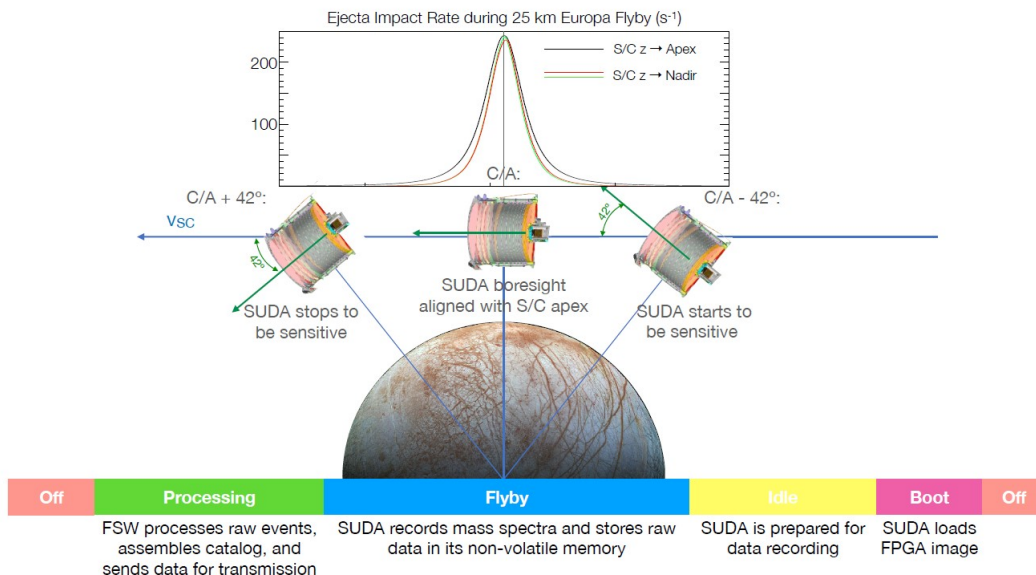
FIGURE 19. Data acquisition by SUDA during a flyby of Europa Clipper. From Kempf et al. [215].

During calibration campaigns, SUDA will attempt to characterise the surface composition of both Ganymede and Callisto, with the collection of ∼200 and ∼100 samples of their respective surfaces. Campaigns to characterise galilean ring particles and the Io nanograin flux are also planned [215]. The latter campaign will be used to determine the deposition flux of dust grains from Io on to the neighbouring galilean moons, and to monitor Io's volcanic activity over the duration of the Clipper mission.

4 Analogue Experiments to Study Icy Moons with Impact Ionization Mass Spectrometry

To reliably characterise the composition of material from icy moons with SUDA-type instruments, whether as ejecta or plume particles, terrestrial instrument calibration is required.

4.1 Simulations of hypervelocity impacts: laboratory work and modelling

Hypervelocity impacts involve particles undergoing extreme physical and chemical conditions, including high energies (10s to 100s of eV), extreme pressures (>MPa), and high local temperatures (>1000 K), over extremely fast (femto to picosecond) timescales [239]. Such events are therefore challenging to reproduce using current laboratory techniques, but this has been achieved for µm-sized siliceous, metallic and organic particles, by using electrostatic accelerators [240, 241, 242, 243, 244, 245, 246]. Such experiments have notably shown that organic compounds such as amino acids and peptides can be identified with ToF-MS and that they can fragment in high velocity impacts [246]. However, for water ice grains, hypervelocity impacts are extremely challenging to reproduce in laboratory experiments [239].

Some recent laboratory experiments have managed to accelerate water ice grains to velocities up to 7.4 km/s [247, 248]. Such experiments can be done by using a light-gas gun firing water ice, in which organic and biogenic material can be included [248], but these experiments present several drawbacks: (*i*) they are not performed in vacuum, (*ii*) the impacted grains cannot be analysed in situ, but they must be extracted from the chamber, (*iii*) the size of the accelerated grains is typically much larger than the actual size of cosmic dust grains.

Another technique that can be used to accelerate particles is electrostatic acceleration. This technique works with even smaller particles than light-gas guns (because small particles can more easily achieve a sufficient charge to mass ratio) and allows possible velocities in the order of km/s to be reached with the use of high-voltages. Recently, Spesyvyi et al. [249] developed the apparatus "SELINA" (SELected Ice Nanoparticle Accelerator"), an accelerator of water ice nanoparticles, coupled to a mass spectrometer, aiming at achieving speeds of $\geq$3–4 km/s. Ice particles are produced via electrospray ionization of water and subsequent cooling when transferred to vacuum. SELINA can select charged ice particles (50–1000 nm in diameter) based on their properties (e.g., mass, charge, and kinetic energy). Hypervelocity acceleration of water ice grains in laboratory experiments have also been demonstrated recently by Adamson et al. [250] and Belousov et al. [251].

Other laboratory systems are under development to accelerate µm-sized water ice grains in vacuum at hypervelocities of up to >6km/s and analyze the ions produced by their impact with TOF-MS [252, 247]. Different compositions relevant to icy moons (i.e., water ice grains rich in salts and/or organics) will be experimentally reproduced and will try to accurately simulate sampling by a spacecraft in a plume flyby.

Modelling work can bring valuable information to complement these challenging laboratory experiments. Recent work by Jaramillo-Botero et al. [239] has investigated atomic-scale fragmentation processes of molecules during hypervelocity impacts. They simulated the fragmentation of small organic molecules at impact velocities of 1-12 km/s (Figure 20). They determined that the best spacecraft encounter velocities for the measurement of amino and fatty acids embedded in ice grains are 4–6 km/s, because the organics are protected from fragmentation by the ice matrix. While they predict the onset of organic fragmentation at >5 km/s, a relatively high speed range is best because the ion yield increases with speed.

While significant work has been done to reproduce hypervelocity impacts of grains in the laboratory, serious limitations still exist to consider such experiments as accurate analogues for impact ionization in space. Notably, most experiments do not reach the appropriate size range (i.e., µm-size) of ice grains, or can only accelerate charged grains (and not neutral grains). To date, the only technique to accurately reproduce the hypervelocity impacts of water-rich ice grains at speeds relevant for SUDA- or CDA-type instruments, is the Laser Induced Liquid Beam Ion Desorption (LILBID) laboratory technique [128, 253] (Section I.4.2). To further improve laboratory hypervelocity impact experiments, comparing their results with those of LILBID should allow to better understand the processes at play in both methods, which have their own specific limitations as analogues for impact ionization in space. Such detailed comparisons would improve the ability to interpret measurements of SUDA-type instruments made at hypervelocity in past and future space missions.
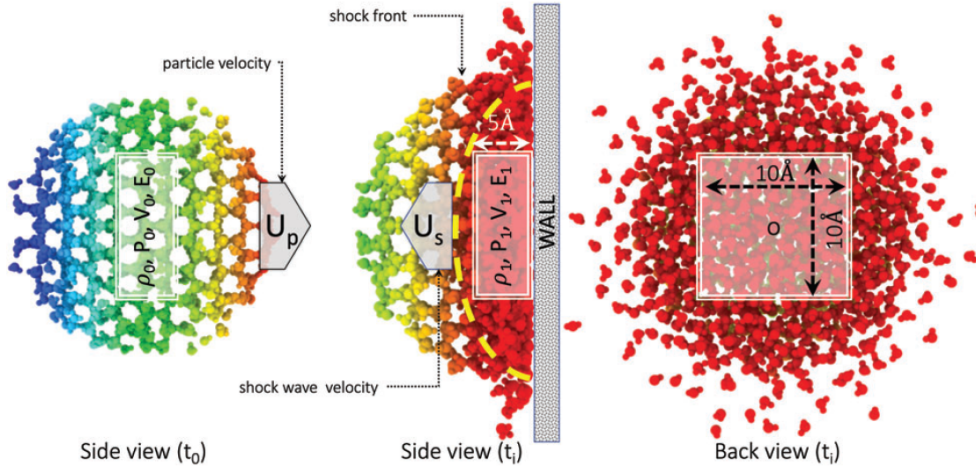
FIGURE 20. Model of a water ice particle before (t_0) and during (t_1) a hypervelocity impact, showing the uncompressed and compressed regions and the shock-front propagation (in the opposite direction to the particle velocity). From Jaramillo-Botero et al. [239].

4.2 The Laser Induced Liquid Beam Ion Desorption (LILBID) technique

The LILBID laboratory technique (Figure 21) at Freie Universität Berlin (FUB) was used in this work. This cost-effective method is a powerful tool for the preparation of future exploration missions to icy moons, as it accurately simulates the mass spectra produced by the ionization process of hypervelocity impacts of ice grains [253]. Analogue LILBID experiments have significantly improved the characterisation of cosmic water ice grains compositions. The composition and impact speed (onto the spaceborne mass spectrometer) of ice grains are the main parameter controlling their mass spectral appearance, and both can be simulated with LILBID. This technique is similar to Matrix-Assisted Laser Desorption and Ionization (MALDI) and both perform a soft ionization of analyte molecules, with minimal fragmentation. While MALDI is used to ionize analytes mixed in a solid matrix, LILBID uses a similar process but with liquid matrices [254, 255, 256].

The LILBID setup comprises a vacuum chamber, where the sample (a liquid solution) is ionized, and a time-of-flight mass spectrometer, which detects and analyses the created ions. In the vacuum chamber, the impact ionization process is simulated by irradiating a micrometre-sized liquid water beam and dissolved substances therein with a pulsed (20 Hz, 7 ns pulse length) infrared laser (λ =2840 nm) at variable laser energies (up to 4 mJ). The laser energy is absorbed by the water molecules, creates a thermal explosion, and breaks the analyte solution into charged and uncharged atomic, molecular and macroscopic fragments (Figure 22, [257, 258]). The formed charged fragments usually carry a single charge. After passing through a field-free drift region, the created ions (cations or anions, depending on the chosen polarity) are then accelerated and analyzed in the TOF mass spectrometer with a mass resolution m/Δm of 600-800 (for comparison, CDA's resolution was 20-50, while SUDA's is 150-250). The principle of delayed extraction allows ions to be selected for analysis as a function of their initial velocities. Ions cross a field-free drift region before reaching the acceleration (or extraction) region. When the acceleration electrodes (repeller and extractor) are switched on (after a predefined delay time), fast ions have already crossed more of the acceleration region than slow ions, so they experience a weaker potential difference than slow ions. Ions within a defined range of initial velocities can thus be selected for analysis by adjusting the delay time. Ions arriving later than the delay time are blocked by the repeller applying a potential (with the opposite polarity to the selected ions) that prevents them entering the mass spectrometer. The delay time is therefore defined as the time between the laser shot (T_0) and the ion acceleration. Selecting a range of ion velocities allows the selection of ions of a specific range of masses, since ion velocities are related to their masses and the amount of energy imparted by the laser:

$$v \sim \sqrt{\frac{E_{laser}}{m}}$$

Impact speeds ranging from 3 km/s to 21 km/s can be simulated using delay time values from 3.2 to 7.5 µs, with lower delay time values corresponding to higher speeds. The conversion from TOF to m/z is performed using a second order calibration equation. This mass calibration is done with the LabView software on the measurement computer. The spectra are recalibrated to reduce possible mass shifts [259, 260] (i.e., deviances up to
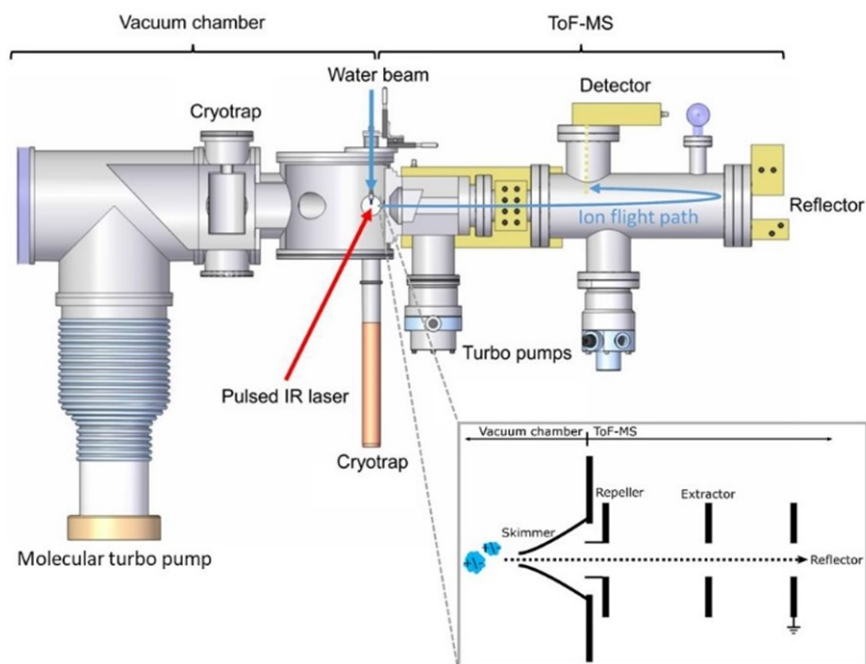
FIGURE 21. The Laser Induced Liquid Beam Ion Desorption (LILBID) laboratory setup. The LILBID method is used to reproduce the impact ionization mass spectra of ice grains recorded in space (figure reproduced from Klenner et al. [253]. The principle of delayed extraction of the ions as a function of their initial velocities is shown on the bottom right insert.

>1 amu due to the delayed extraction method and variable initial ion velocities) with a Python script that calculates a polynomial function based on real peak masses and assigns the corresponding data file with this function. Both impact ionization and the laser desorption experiment almost exclusively produce singly-charged ions. Ion signals are amplified, digitised (Analogue-to-Digital converter) and recorded with a LabVIEW-controlled computer. Each mass spectrum presented in Parts II, III and IV of this thesis is the average of 300 individual spectra, which were co-added to account for variations in laser intensity and to achieve a signal-to-noise similar to spectra from space instruments. The recorded spectra are archived in a comprehensive database containing analogue data for impact ionization mass spectrometers, available at https://lilbid-db.planet.fu-berlin.de [259]. Thousands of LILBID mass spectra have already been recorded, for a wide range of compounds, providing valuable data points for past and future data from space missions.

4.3   Previous LILBID experiments

While MALDI has been used for numerous applications (e.g., biochemistry, medicine, microbiology) since 1985 [261], the optimization of laser desorption/ionization for applications in space sciences started more recently. In 2009, Postberg et al. [128] showed that CDA mass spectra of Enceladean ice grains are strikingly similar to LILBID mass spectra of salty samples. Compositional variations of Enceladus ice grains could be understood by measuring different salt rich solutions, including sodium, potassium, chlorides and carbonates, with LILBID. In subsequent works, several types of organic compounds were identified in CDA mass spectra owing to LILBID analogue data: high molecular mass (> 200 u) refractory insoluble organic material [65] and low molecular mass (< 100 u) volatiles including various moieties bearing oxygen, nitrogen, aryl groups [66] as well as tentatively identified alkene and acyl groups [262]. Simulation of different impact speeds of ice grains onto CDA was performed by using combinations of different delay times and laser energies (Section I.4.2 and Klenner et al. [253]), allowing the reproduction of spectral variations for a wide range of ice grains detected by CDA.

Several LILBID experiments have already been performed to predict the mass spectral appearances of astrobiology-relevant material, and could certainly help in detecting and identifying biosignatures during future space missions. Previous work demonstrated that bioessential molecules (such as amino acids, fatty acids and peptides [263]) including their specific abiotic and biotic mass spectral fingerprints [264], and microbial
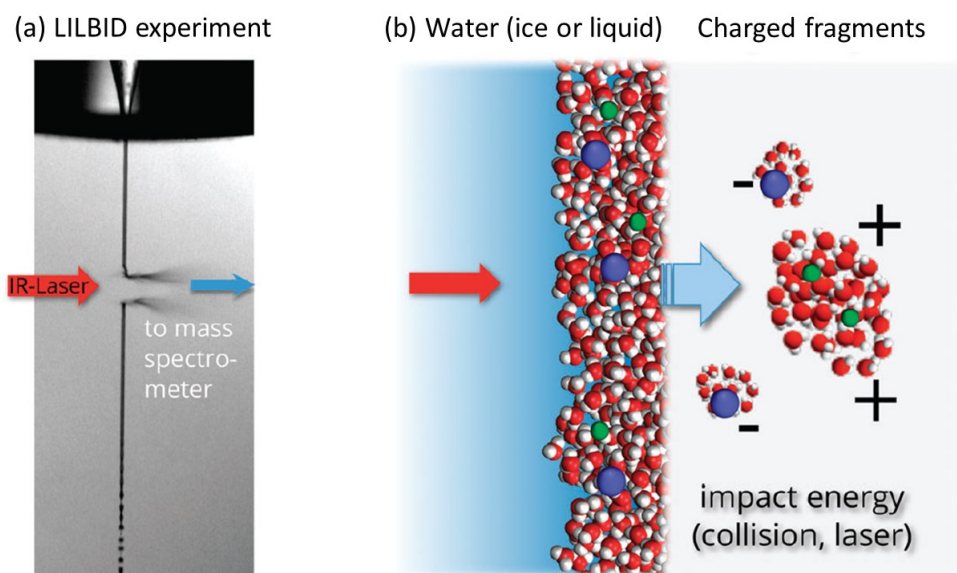
FIGURE 22. (a) Photograph of an IR laser irradiating a µm beam of liquid water in vacuum, as used in the LILBID method. The liquid beam is dispersed and the charged droplets are analyzed with mass spectrometry. (b) Schematic of the process shown in (a), depicting the formation and dispersion of charged droplets. Adapted from Wiederschein et al. [258].

biosignatures extracted from bacteria [265] could be detected down to the ppm or ppb level. These experiments have also included up to 0.1 mol/L of NaCl in the analytes solutions (to be representative of icy moons' salty ocean compositions) and notably showed that (*i*) the sensitivity to biosignatures decreases with increasing salt concentration, and (*ii*) amino acids and fatty acids form sodiated (i.e., sodium-complexed) molecular peaks in salty solutions (Figure 23).

In a scenario for Enceladus, where microbial cells would be encased in ice grains as nucleation cores, Klenner et al. [266] showed that the detection limits of characteristic spectral signatures (both amino acids and metabolites in cation mode, and fatty acids in anion mode) correspond to low cell densities of below 10^7 cells/mL. Even if only a small fraction (0.01%) of the cell's constituents were contained in an ice grain (of typical size for Enceladus as measured by CDA, i.e., 2µm in diameter), the bacterial signatures would be detectable by SUDA-type instruments. They used *Sphingopyxis alaskensis* cells, a highly relevant analogue species for potential lifeforms on Enceladus, as these are cold micotrophic marine bacteria, thriving in oligotrophic waters, and whose ultramicrosize [<0.1 µm^3] would allow it to fit in Enceladean ice grains. These experiments emphasize the outstanding capabilities of SUDA-type instruments to (*i*) detect very low levels of microbial material, without the need of a lander or extraction techniques to increase biosignatures' concentrations, (*ii*) characterise the composition of individual ice grains, rather than the entire plume where biosignatures could be scarce (i.e., higher local concentrations in targetted ice grains than in a diluted entire plume) and (*iii*) assess the compositional heterogeneity of the plume, owing to the high number of individual ice grains sampled per flyby (e.g., 10,000-100,000 grains [141]).

In their work with benzoic acid and its derivative isomers, Khawaja et al. [267] found that significant spectral differences between the isomers can be seen, but they don't appear for all experimental parameters (e.g., they appear particularly in negative ion mode and at simulated intermediate and high impact velocities). Future laboratory investigations focusing on how to characterise isomeric biosignatures with spaceborne instruments will be highly significant for missions to ocean worlds, as the capacity to identify subtle differences in molecular structure in isomeric species is a valuable tool for astrobiology investigations.

Recently, Khawaja et al. [268] measured with LILBID the mass spectral fingerprints of low-mass aldehydes and ketones, and compared the obtained spectral signatures and fragmentation patterns with electron ionization (EI) mass spectra from the National Institute of Standards and Technology (NIST). They showed that these two different mass spectrometry techniques can complement each other's compositional analysis, and therefore can help constrain the structural properties of organic species in data from mass spectrometers onboard space missions.
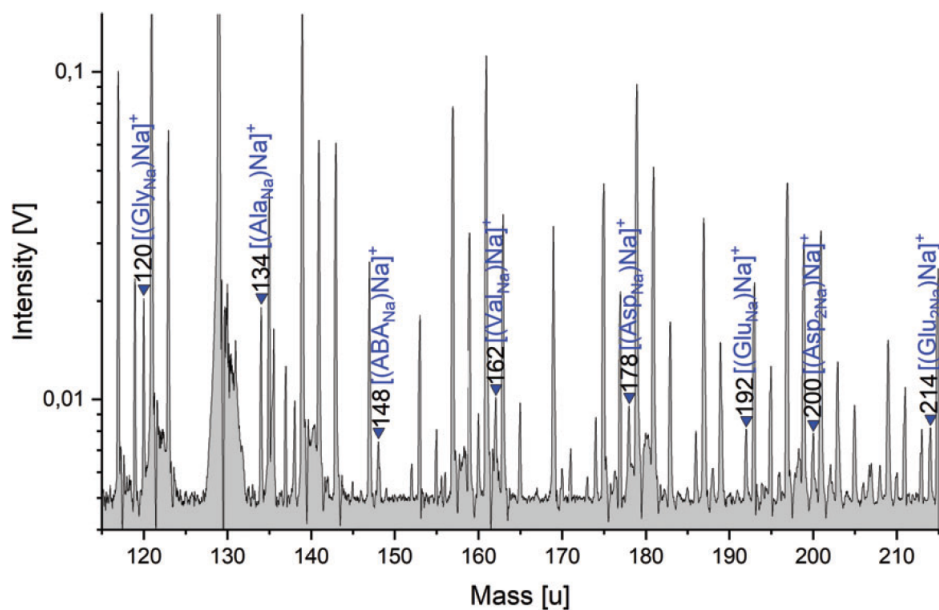
FIGURE 23. Cation LILBID mass spectrum of amino acids (Gly, Ala, ABA, Ser, Val, Asp, and Glu) in a salty Enceladus-like solution. Characteristic amino acid peaks are labelled in blue and showed that these compounds form sodiated complexes. Unlabelled peaks correspond to NaCl–water and Na_2CO_3–water peaks from the matrix solution. From Klenner et al. [264].

Building on the strong knowledge from previous LILBID experiments described above, I have undertaken several experimental projects. In this thesis, I describe the work I have performed with LILBID during my three years of PhD, and which have led to three peer-reviewed publications (Parts II and III). Additionally, I have taken part in additional ongoing projects, which are reported in Part IV.

5 Scientific Objectives and Thesis Outline

The main objective of this thesis is to reach a better understanding of Europa and Enceladus by improving the performance of spaceborne mass spectrometers onboard exploration missions, via a comprehensive experimental analysis of analogue target material. This involves providing analogue mass spectra applicable to the SUDA instrument onboard Europa Clipper, to be launched in less than a year, and to a possible (re)interpretation of past results from the data of Cassini's CDA but also future Enceladus missions. This thesis focuses on both organic material, since this is the main target of astrobiology investigations (as some organic molecules are considered to be the building blocks of life); and on several inorganic salts which are major components of the composition of both the ocean and the ice shell of Europa and Enceladus, and important to consider in mass spectrometry. This thesis is a cumulative thesis, comprising three peer-reviewed articles which have been already published or accepted in relevant scientific journals (with the corresponding bibliographic information here below). After the present introduction (Part I), the parts of this thesis are the following:

Part II - Analogue Experiments for the Detection of Organic Compounds in Salt-rich Ice Grains from Ocean Worlds:

Part II investigates the characteristic mass spectral signatures of several water-soluble organics in salt-rich and sulfuric acid-rich ice grains reflecting the compositions of Europa and Enceladus. Data collected from LILBID analogue experiments in which we examine the effects of sodium chloride (NaCl), magnesium sulfate ($MgSO_4$) and sulfuric acid (H_2SO_4) at concentrations of 0.01, 0.1 and 1M, is used to determine the spectral appearance of organic molecules and their detectability with SUDA-type instruments. The organic species 5-amino-1-pentanol, acetic acid, benzoic acid, butylamine, glucose, methanol, and pyridine were measured in both cation and anion mode. The following research questions are targeted:

- What are the mass spectral signatures of a variety of representative organic compounds in salt-rich ice grains reflecting the composition of Europa and Enceladus, as obtained with SUDA-type instruments?
- How do these signatures change with the properties of the organic compounds (e.g., functional groups)?
- What are the effects of increasing concentrations of different salts and inorganic acids on the mass spectral features of organic compounds? Can organic material be detected through mass spectrometry despite the high concentrations of inorganic material in the surface ice of these moons?
- What analyte suppression and matrix effects involving salts, inorganic acids and different organic species, are expected for SUDA's future measurements?

This Part resulted in two published manuscripts:

Napoleoni, M., Klenner, F., Khawaja, N., Hillier, J. K., & Postberg, F. (2023) Mass Spectrometric Fingerprints of Organic Compounds in NaCl-Rich Ice Grains from Europa and Enceladus. *ACS Earth and Space Chemistry*, 7(4), 735-752.

Napoleoni, M., Klenner, F., Hortal Sánchez, L., Khawaja, N., Hillier, J. K., Gudipati, M. S., Hand, K.P., Kempf, S., & Postberg, F. (2023) Mass Spectrometric Fingerprints of Organic Compounds in Sulfate-Rich Ice Grains: Implications for Europa Clipper. *ACS Earth and Space Chemistry*, 7(9), 1675-1693.

Part III - Probing the Oxidation State of Ocean Worlds with SUDA: Fe (II) and Fe (III) in Ice Grains:

Part III investigates differences in the cation and anion LILBID mass spectra of both iron (II) and iron (III) chlorides and sulfates. We draw implications for the geochemistries of subsurface oceans, including deciphering their pH values and oxidation states, but also potentially to characterise hydrothermal systems and the metabolisms of possible lifeforms. The following research questions are targeted:

- What are the spectral signatures of iron (Fe), a metallic element, in different oxidation states in the impact ionization mass spectra of SUDA-type instruments onboard space missions to icy ocean moons?

• Could the oxidations states of Fe in iron-bearing minerals be determined if present in water-rich ice grains ejected from these moons?

• What implications would such detections have for the geochemistry and habitability of subsurface oceans?

This Part resulted in one accepted manuscript:

Napoleoni, M., Hortal Sánchez L., Khawaja N., Abel, B., Glein, C., Hillier J.K., & Frank Postberg (2023) Probing the oxidation state of ocean worlds with SUDA: Fe (II) and Fe (III) in ice grains. *The Planetary Science Journal.*

Part IV - Complementary Analogue Experiments for the Detection of Organics and Biosignatures on Ocean Worlds

Part IV describes additional analogue experiments using both LILBID and other analytical techniques, which provide highly complementary information to the main objective of this thesis. New techniques and approaches are considered, such as the use of irradiation and the collection of natural samples from analogue fields in an expedition to Antarctica. These complementary experiments of high scientific value will surely open up new research fields at Freie Universität Berlin and increase the scientific return of upcoming missions equipped with impact ionization mass spectrometers.

In Parts II and III, all the experimental work, data analysis and most of the writing of publications have been done by myself, with only minor contributions from co-authors. Part IV includes collaborative projects where the experimental work and/or data analysis are performed by myself and collaborators, with a strong personal involvement from my side.

Part V - General Conclusions and Outlook

This work concludes with a summary of the most relevant results of this thesis, and some final perspectives for the exploration of ocean worlds.

At the end of this dissertation, an appendix contains the supplementary material mentioned in Parts II and III. A list of publications is also provided.

II Analogue Experiments for the Detection of Organic Compounds in Salt-rich Ice Grains from Ocean Worlds

1 Mass Spectrometric Fingerprints of Organic Compounds in NaCl-rich Ice Grains from Europa and Enceladus

1.1 Summary

Europa and Enceladus, respective moons of Jupiter and Saturn, are prime targets in the exploration of potentially habitable extraterrestrial ocean worlds. Organic material could be incorporated from the ocean into ice grains ejected from the surface or in potential plumes and detected via spacecraft flybys with impact ionization mass spectrometers, such as the SUrface Dust Analyzer (SUDA) onboard Europa Clipper or the Cosmic Dust Analyzer (CDA) onboard the past Cassini mission. Ice grains ejected from both Europa and Enceladus are expected to contain sodium salts, specifically sodium chloride (NaCl), in varying concentrations. Consequently, it is important to understand its effects on the mass spectrometric signatures of organic material in salt-rich ice grains. Previous studies have only focused on the detection of biosignatures, such as amino acids, in salt-rich ice grains. We here perform analogue experiments using the Laser Induced Liquid Beam Ion Desorption (LILBID) technique to study how a wide variety of abiotic and potentially biotic organic molecules could be identified by SUDA-type instruments. We investigate their mass spectral characteristics and detectability at various typical NaCl concentrations expected for salt-rich ice grains and in both cation and anion modes. Results show that organics in salt-rich ice grains can still be detected because of the formation of molecular ions and sodiated and chlorinated species. However, high salt concentrations induce compound- and concentration-dependent suppression effects, depending on the chemical properties and functional groups of the analytes. Our results emphasize the need of both ion modes to detect a wide range of organics embedded in complex matrices and to discriminate between abiotic and potentially biotic species. This work complements a spectral reference library for Europa Clipper and other ocean world missions.

1.2 Introduction

Ocean worlds are of growing interest for life detection missions. In particular, Jupiter's moon Europa and Saturn's moon Enceladus both have a high potential to host extant biological life in their global subsurface water oceans [50, 69, 74, 53] with uniquely hospitable chemistry[269]. Europa's ocean is thought to be in contact on its lower part with a rocky silicate seafloor, and on its upper part with an ice shell that may have tectonic activity allowing reductant-oxidant cycling [270, 197]; and it might have been present for much of the history of

the Solar System, providing a long-term stable environment with geochemical interactions, essential elements, and energy sources for an independent origin of life [271, 168, 208, 272]. Enceladus's subsurface ocean of salty water [128, 124] is also thought to be long lived and hosts a variety of organic material, including compounds made of the biologically essential elements carbon, hydrogen, oxygen, nitrogen, and phosphorus [273, 65, 66, 61] potentially acting as building blocks or byproducts of life. The discovery of hydrothermal processes at the interface between the ocean and the rocky core of Enceladus was deduced from the detections of nanometer-scale silica particles [67] and of molecular hydrogen (H_2) [64], a product of serpentinization reactions, in a large plume of icy particles emanating from cracks in the southern pole [99, 117]. These jets of water provide a source of potentially life-bearing material being ejected from the subsurface ocean and emitted to space in icy particles.

Europa's subsurface ocean may be communicating material to the surface through tectonic activity, resurfacing or other forms of upwelling [274], rendering subsurface material analyzable by spacecraft flybys. Organic material possibly related to bioactivity in Europa's subsurface ocean might therefore reach the surface ice and be sputtered to high altitudes by micrometeorite bombardment [233, 235] and by energetic heavy ions trapped in Jupiter's magnetosphere [275]. Organics could also be incorporated in potential plumes ejecting gas and water ice grains from the subsurface ocean into space [147, 169, 171, 172]. The detection and identification of organics in Enceladus plume ice grains allowed the interpretation of ice grains' origins, their formation mechanisms, and the presence of an organic-rich layer at the upper ocean-ice interface [65, 66]. Diverse complex organic species including hydrocarbons, amino acids and carboxylic acids, could be geochemically synthesized in icy moons' oceans by serpentinization reactions and reduction of inorganic precursors [276, 277, 278] in potential hydrothermal systems. Processes such as bubble-scrubbing may increase the concentration of organic material and lead to enriched particles allowing the detection of organic biosignatures in ice grains at a much higher level than expected in the bulk ocean [126].

Dust analyzers are powerful instruments for the analysis of extraterrestrial ice grains and the identification of molecules therein. A dust analyzer detects individual particles impacting its target at hypervelocities (several km/s), creating an impact plasma whose composition is measured via time-of-flight (TOF) mass spectrometry (MS). Such instruments can detect chemical species embedded in ice at the ppm level, including organic compounds [65, 279] and salts [128], and have revealed some of the most significant advances about the chemistry of the plume of Enceladus [65, 133]. The Cosmic Dust Analyzer (CDA) onboard the Cassini spacecraft allowed the discovery of complex organic macromolecules with molecular masses above 200 u [65], as well as smaller reactive nitrogen- and oxygen-bearing molecules [66] from the ocean of Enceladus. Onboard NASA's upcoming Europa Clipper mission [213], the SUrface Dust Analyzer (SUDA) will capture and analyze dust particles released from Europa's surface by impacts and in its potential plumes [215]. During close flybys, SUDA will map the composition of encountered ejecta particles onto certain surface features of Europa [237]. The SUDA instrument is a TOF reflectron-type mass spectrometer optimized for a high mass resolution in the mass range m=1-500u. As compared to the CDA instrument that could only detect cations, the SUDA instrument will be able to record both cation and anion mass spectra, aiming to target a wider range of compounds.

The search for organic material and molecular biosignatures in ice grains ejected from ocean worlds with SUDA-type instruments might be challenged by the complex chemistry and salty composition of their ice and oceans. The salinity of Enceladus's ocean is assumed to be roughly similar to Earth's ocean or lower [280], at around 20 g/kg [281] and dominated by NaCl at a concentration of 0.05–0.2 mol/kg [128]. At Europa, the strong magnetic induction field measured by Galileo suggested a salinity perhaps in excess of 50 g/kg [150]. Analysis of the Galileo Near-Infrared Mapping Spectrometer (NIMS) data showed that the Europa's icy surface is dominated by water, sulfuric acid hydrate and other non-ice material. Sulfuric acid hydrate is an expected product of radiolytic chemistry occurring on the heavily irradiated and sulfur-bombarded trailing hemisphere [187, 188, 189]. Its detection was confirmed on the trailing hemisphere by telescopic observations, which also detected spatially coincident magnesium sulfate salts, suggesting a radiolytic origin of the sulfate salts [184, 151]. The non-ice material identified by NIMS has been first interpreted as endogenous sulfate salts originating from the subsurface ocean [181, 182, 199, 200]. Ground-based spectroscopic observations have proposed sodium chloride and potassium chloride [184] or a mixture of magnesium chloride, chlorate, and perchlorate [190] as the dominant non-ice component of the leading hemisphere. The non-ice material is likely a combination of multiple materials, including frozen brines, sulfate salts and chlorides or chlorates, with relative proportions varying spatially over Europa's leading and trailing hemispheres. Endogenous material reflecting the composition of the interior ocean is thought to be particularly abundant in the chaos terrains of the leading hemisphere, as these terrains are geologically young, are potential regions of subsurface upwelling or melt-through [201, 202] and are shielded from the sulfur ion implantation of the trailing hemisphere. Chaos terrains are rich in sodium chloride [151, 180, 203, 204], an inorganic salt likely to be a major component of Europa's ocean, as this salt is expected

to dominate in an ocean with an extensive hydrothermal circulation [282]. Sodium chloride is estimated to be present at a mean concentration of 0.1-1.2 mol/kg H_2O [197], but surface ice inhomogeneities could even increase the salt concentrations, leading the Europa lander mission concept to request that onboard instruments should be prepared for samples containing up to 30% salt [217]. Analytical instruments aiming at investigating the chemical composition and possible biosignature content of ocean worlds will therefore have to deal with native samples containing significant amounts of salts.

Interpreting mass spectra acquired in space from SUDA-type instruments requires terrestrial calibration by analogue experiments. Spaceborne impact ionization mass spectrometers analyze projectile ions from ice grains impacting onto metal targets. It is challenging to recreate this impact process in laboratories, because micrometer-sized ice grains cannot currently be easily accelerated at relevant speeds [251, 283]. Therefore, the Laser Induced Liquid Beam Ion Desorption (LILBID) technique has been developed to simulate the impact ionization mass spectra of ice grains recorded in space at impact speeds from 3 to >20km/s [255, 254, 253] without the need of a dust accelerator. This technique has been used to reproduce compositional differences of ice grains detected from Enceladus with the CDA instrument [128, 65, 66], and to investigate the mass spectral characteristics and fragmentation patterns of organics between different ionization methods [268]. Klenner et al. [263, 264] used LILBID analogue experiments to investigate the detection of amino acids, fatty acids, and peptides in water-rich and salt-rich ice grains in an ocean world scenario, as they could be identified by future spaceborne mass spectrometers such as SUDA or the Enceladus Ice Analyzer (ENIA)[143]. They found that these bioessential compounds can be detected down to the micro- or nanomolar level, with optimal encounter velocities of 4-6 km/s, and that these complex organic molecules remained largely intact up to encounter velocities of 8 km/s. Moreover, characteristic abiotic and biotic fingerprints could be discriminated in the mass spectra. Recently, the investigation of bacterial extracts showed that microbial biosignatures could be reliably identified at the ppm level in salt-rich ice grains, and that the sensitivity to biosignatures decreases with increasing salt concentration [265].

In impact ionization mass spectrometry, the matrix from which a sample is analyzed can increase or decrease the ionization process, hence influencing ion formation and the resulting spectra [284, 285]. In particular, salts in the analyte solution can cause a significant degradation of the signal-to-noise ratio and lead to ion suppression and adduct formation, which may mask or complicate the ion signals with interferences. Matrix effects can therefore limit the quantitative and qualitative analysis of SUDA-type instruments, which are likely to analyze salty and oxidant-rich ice grains reflecting icy moons' compositions. To prevent these difficulties, laboratory analogue experiments investigating salt-rich matrices are required. A previous study by Klenner et al. [264] investigated the spectral appearance of amino acids in salt-rich solutions. They found that, although high salt concentrations suppress characteristic organic peaks, amino acids typically form sodiated (sodium-complexed) molecules in which a sodium ion replaces a hydrogen ion and could be detected down to micromolar concentrations.

This work investigates the characteristic mass spectral signatures of several water-soluble organics in salt-rich ice grains reflecting the composition of Europa and Enceladus. We discuss data collected from LILBID analogue experiments in which we examine the effects of sodium chloride (NaCl), at concentrations of 0.01, 0.1 and 1M NaCl, on the spectral appearance of organic molecules and their detectability with SUDA-type instruments. We focus on the mass spectral signatures of 5-amino-1-pentanol, acetic acid, benzoic acid, butylamine, glucose, methanol, and pyridine, in both cation and anion mode, to infer general rules predicting the behavior of organic species containing a wide range of functional groups, namely hydroxyl, azine, (aromatic) carboxylic acid, (aromatic) amine, and alkanolamine. Such functional groups are especially relevant for icy moons, because oxygen- and nitrogen-bearing as well as aromatics compounds have been detected on Enceladus ice grains [65, 66]. Sugars and N-heterocycles are especially relevant for astrobiology investigations as they are essential to biological processes in all terrestrial life and may have played an important role in the origin and evolution of life [286, 287, 288]. The purpose of this study is to form a better understanding of peak suppression and matrix effects involving salts and different organic species as if detected in icy moons' ice grains by impact ionization mass spectrometers.

1.3   Experimental Section

The experimental LILBID setup (Figure 21) was used to record mass spectra of several solutions of organic compounds in salt-rich water matrices. It has been described in detail in section I.4.2 (and by Klenner et al. [253]).

Seven organic species containing a wide range of functional groups, namely hydroxyl, azine, (aromatic) carboxylic acid, (aromatic) amine, and alkanolamine, were investigated (Table 1): 5-amino-1-pentanol ($C_5H_{13}NO$), acetic acid ($C_2H_4O_2$), benzoic acid ($C_7H_6O_2$), butylamine ($C_4H_{11}N$), glucose ($C_6H_{12}O_6$), methanol (CH_4O), and pyridine (C_5H_5N). Each compound was dissolved in distilled, deionized Milli-Q purified water and NaCl-

		5-amino-1-pentanol	Acetic acid	Benzoic acid	Butylamine	Glucose	Methanol	Pyridine
Formula		$C_5H_{13}NO$	$C_2H_4O_2$	$C_7H_6O_2$	$C_4H_{11}N$	$C_6H_{12}O_6$	CH_4O	C_5H_5N
Molecular weight (u)		103	60	122	73	180	32	79
pKa		15	4.7	4.2	11	12	15	5
pH in solution	H_2O	12.1	2.4	3.3	12.3	7.1	9.0	8.6
	0.01M NaCl	11.7	2.4	3.0	12.4	7.3	7.1	9.3
	0.1M NaCl	12.0	2.4	2.9	12.3	6.9	6.1	8.4
	1M NaCl	12.0	2.2	2.9	12.1	6.0	5.3	9.3

TABLE 1. Organic compounds investigated in this work, their molecular weight, molecular concentrations used in the experiments, values of pKa and measured pH in the different solutions investigated.

rich solutions at a concentration of 5wt% of the organic species, except for benzoic acid that was dissolved at a concentration of 0.17wt% due to its low solubility in water. Each organic compound was measured in pure water and in three solutions of different NaCl concentration (0.01M, 0.1M and 1M NaCl) with the LILBID setup. Because of the low purity of the glucose sample, the Na ion exchange resin amberlite was added to the "pure water" glucose solution to record cation mode spectra. The LILBID setup was checked for contamination and cleaned between sample measurements.

1.4 Results

1.4.1 NaCl background matrix

Several salt ions and clusters were identified in the mass spectra of the NaCl background matrix without any organics. In cation mode, the clusters $[Na(H_2O)_n]^+$, $[Na(NaOH)_n]^+$, $[Na(NaCl)_n]^+$, $[Na(NaCl)_n(H_2O)_m]^+$, $[Na(NaCl)_n(NaOH)_m]^+$ were identified (Figure 24). These species were also observed by Postberg et al. [128] in analogue LILBID data with pure salt solutions. The spectra with the lowest salt concentration (0.01M NaCl; Figure S1) show a predominance of $[Na(H_2O)_n]^+$ clusters, whereas $[Na(NaCl)_n]^+$ clusters are predominant in 0.1M NaCl and 1M NaCl spectra (Figure 25 and Figure S2). In anion mode, the clusters $[Cl(H_2O)_n]^-$, $[Cl(NaOH)_n]^-$, $[Cl(NaCl)_n]^-$, $[Cl(NaCl)_n(H_2O)_m]^-$, and $[Cl(NaOH)(NaCl)_n]^-$ were identified (Figure 25). At 0.01M NaCl, $[Cl(H_2O)_n]^-$ clusters are predominant (Figure S3), whereas $[Cl(NaCl)_n]^-$ clusters become predominant at 0.1M and 1M NaCl (Figure 25 and Figure S4). In both ion modes, peaks corresponding to ions containing Cl atom(s) show characteristic ^{37}Cl isotopes.

1.4.2 Organic compounds in water matrix

We measured all the organic species in pure water matrices without any salts (Figures S37-S50). We detected protonated molecular peaks ($[M+H]^+$) and deprotonated molecular peaks ($[M-H]^-$) for all organic species, except butylamine, for which no deprotonated molecular peak was observed. We detected prominent $[M-3H]^-$ peaks in the anion spectra of 5-amino-1-pentanol (Figure S38). Positively and negatively charged organic fragments were detected for all compounds except methanol, for which only positively charged fragments were observed (Tables S1 and S2). We detected clusters of the organic species and charged fragments thereof ($[M+M-x]^+$ and $[M+M-x]^-$, with x a fragment of the organic species) or fragmented polymers of the organics (e.g., $[2M-x]^+$
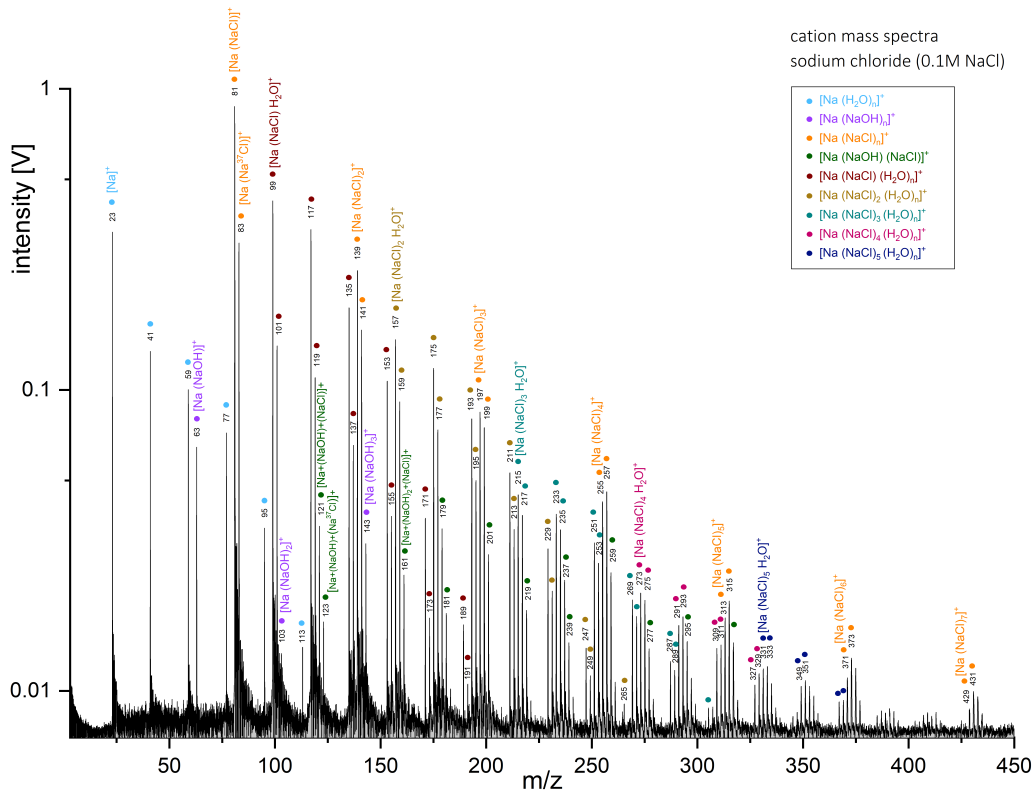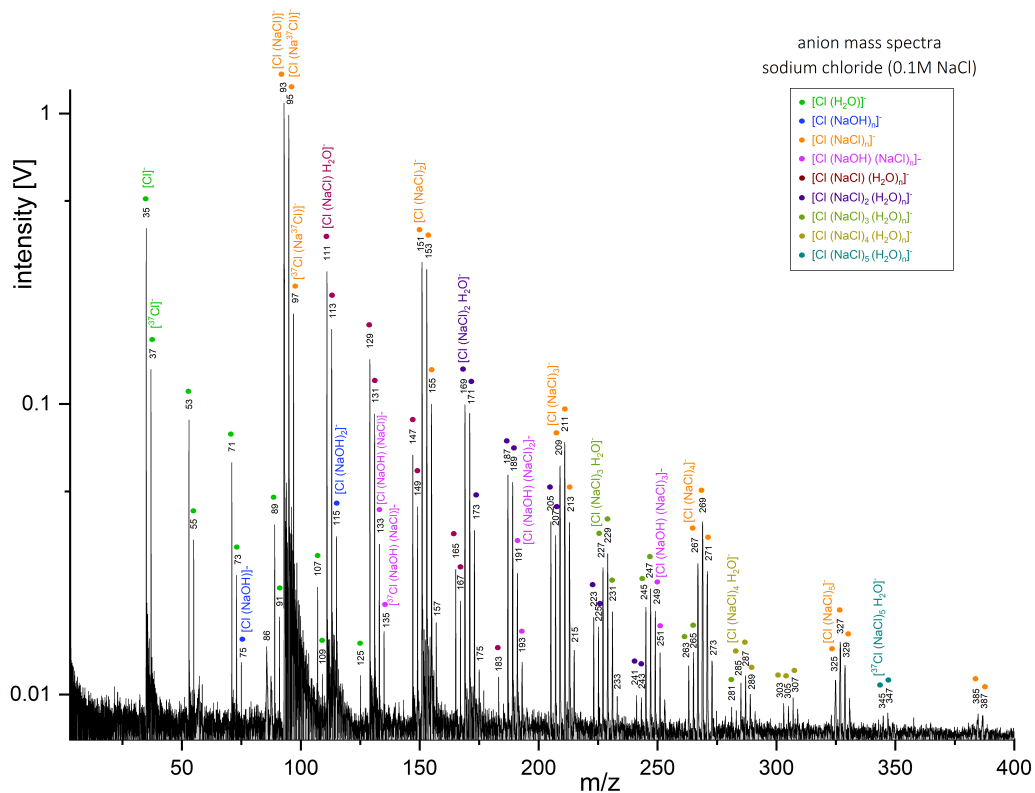
FIGURE 24. Baseline corrected cation mass spectrum of sodium chloride (NaCl) at a concentration of 0.1M. The spectrum was recorded with a delay time of 6.1µs. Sodiated cations are identified and labelled with their corresponding water clusters.

FIGURE 25. Baseline corrected anion mass spectrum of sodium chloride (NaCl) at a concentration of 0.1M. The spectrum was recorded with a delay time of 6.1µs. Chlorinated anions are identified and labelled with their corresponding water clusters.

and $[2M-x]^-$, with x a fragment of the organic species) in both cation and anion spectra of 5-amino-1-pentanol (e.g., $[M+(M-OH-NH_3)]^+$; Figures S37 and S38) and pyridine (Figures S49 and S50), in the cation spectra of butylamine (Figure S43) and in the anion spectra of glucose (Figure S46).

1.4.3 Organic compounds in NaCl-rich matrix

Low salt concentration (0.01M NaCl)

At a concentration of 0.01M NaCl, all the investigated organics form both protonated molecular ions ($[M+H]^+$, with M the molecular mass of the organic compound) and sodiated ions ($[M+Na]^+$) (Table 2), as well as water clusters ($+(H_2O)_n$) of these ions. The intensities of sodiated peaks are usually higher than those of protonated molecular peaks (e.g., Figure 26 and Figures S7, S13, S26 and S31). Positively charged clusters of sodiated organic molecules with NaCl ($[M(NaCl)+Na]^+$) were detected for all organics. Clusters of sodiated organic molecules with NaOH ($[M(NaOH)+Na]^+$) were detected for 5-amino-1-pentanol, butylamine and pyridine, and tentatively detected for both acetic acid and benzoic acid. $[M(NaCl)_n+H]^+$ was detected for benzoic acid and tentatively detected for acetic acid at high delay time (Figures S13 and S8). Disodiated molecules ($[M-H+2Na]^+$) were detected in cation mass spectra of 5-amino-1-pentanol, acetic acid, benzoic acid and glucose, and trisodiated species were detected for glucose ($[M-2H+3Na]^+$) and acetic acid dimers and trimers($[2M-2H+3Na]^+$, $[3M-2H+3Na]^+$). Clusters of disodiated organic molecules with NaCl ($[M(NaCl)-H+2Na]^+$) were detected only for benzoic acid and acetic acid. Organic fragments were detected for five organics (5-amino-1-pentanol, acetic acid, benzoic acid, butylamine and glucose) in the cation mode (table S1). An adduct of the organic molecule and a charged fragment thereof, $[M+NH_4]^+$, was detected for 5-amino-1-pentanol (Figure 26).
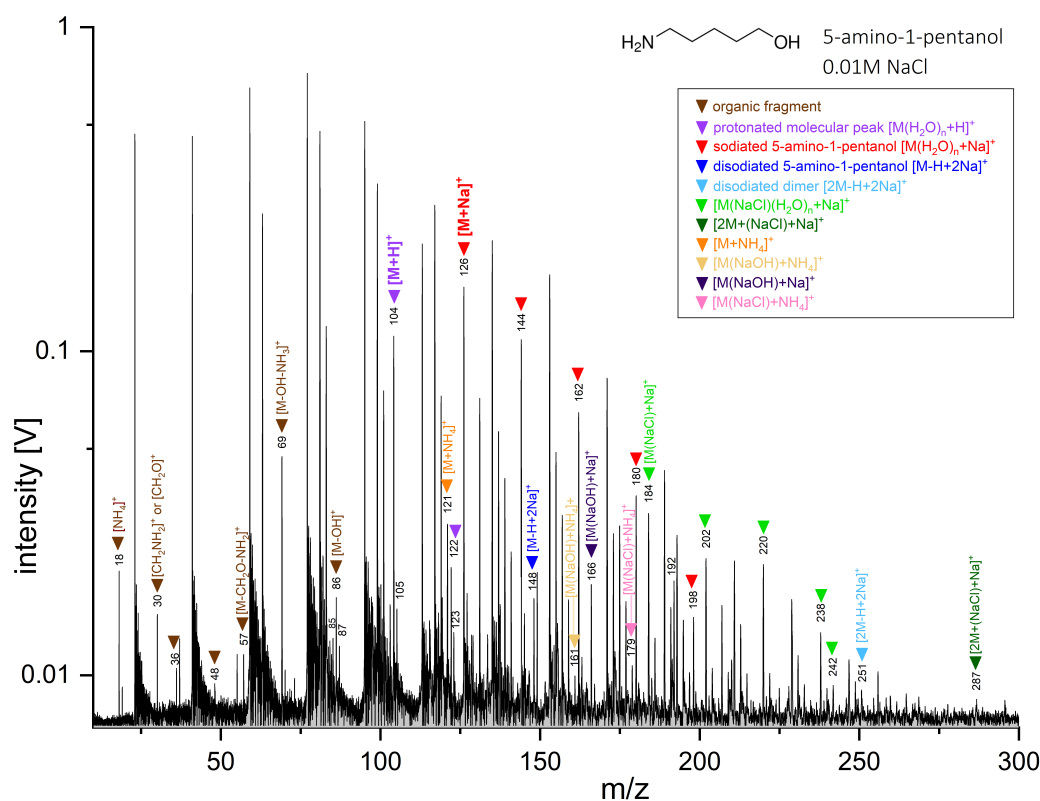
FIGURE 26. Baseline corrected cation mass spectrum of 5-amino-1-pentanol at a concentration of 5wt% in a 0.01M NaCl matrix. The spectrum was recorded with a delay time of 6.2µs. Unlabeled peaks originate exclusively from the salty matrix.

In anion mode, 5-amino-1-pentanol, acetic acid, benzoic acid and glucose were identified as deprotonated molecular ions ($[M-H]^-$), and 5-amino-1-pentanol, benzoic acid, glucose, methanol and pyridine form chlorinated ions ($[M+Cl]^-$) (Table 3). Salt adducts were detected: $[M(NaCl)_n+Cl]^-$ for 5-amino-1-pentanol and glucose, tentatively for both benzoic acid and methanol; $[M(NaOH)_n+Cl]^-$ tentatively for glucose; $[M(NaCl)_n-H]^-$ for 5-amino-1-pentanol, acetic acid, benzoic acid, and glucose; and $[M(NaOH)-H]^-$ and $[M(NaCl)(NaOH)-H]^-$ for glucose. Dichlorinated anions $[M+H+2Cl]^-$ were tentatively identified for glucose, but this peak interferes with

possible $[2M-H-(H_2O)_6]^-$ peaks. Sodiated anion dimers were detected as $[2M-2H+Na]^-$ for acetic acid, benzoic acid and methanol, and disodiated anion oligomers ($[3M-3H+2Na]^-$, $[4M-3H+2Na]^-$) were detected for acetic acid. Negatively charged organic fragments were detected for acetic acid, benzoic acid, butylamine and glucose (Figure 27; Figure S5; Figures S11, S15 and S21; and Table S2).
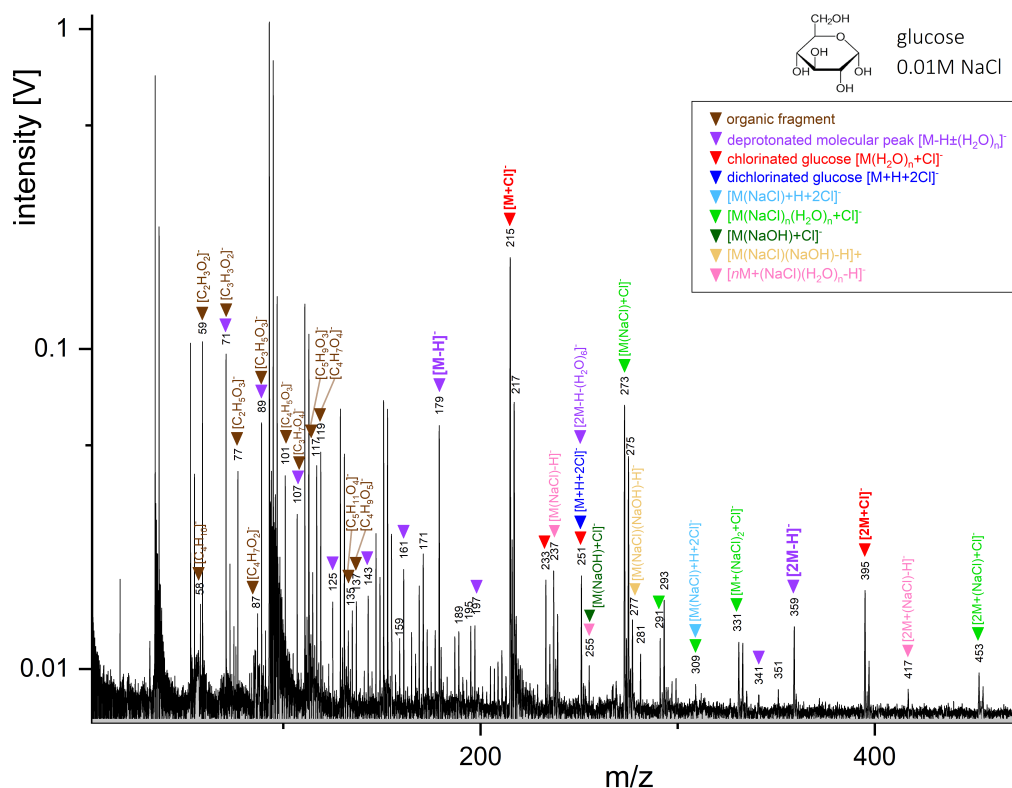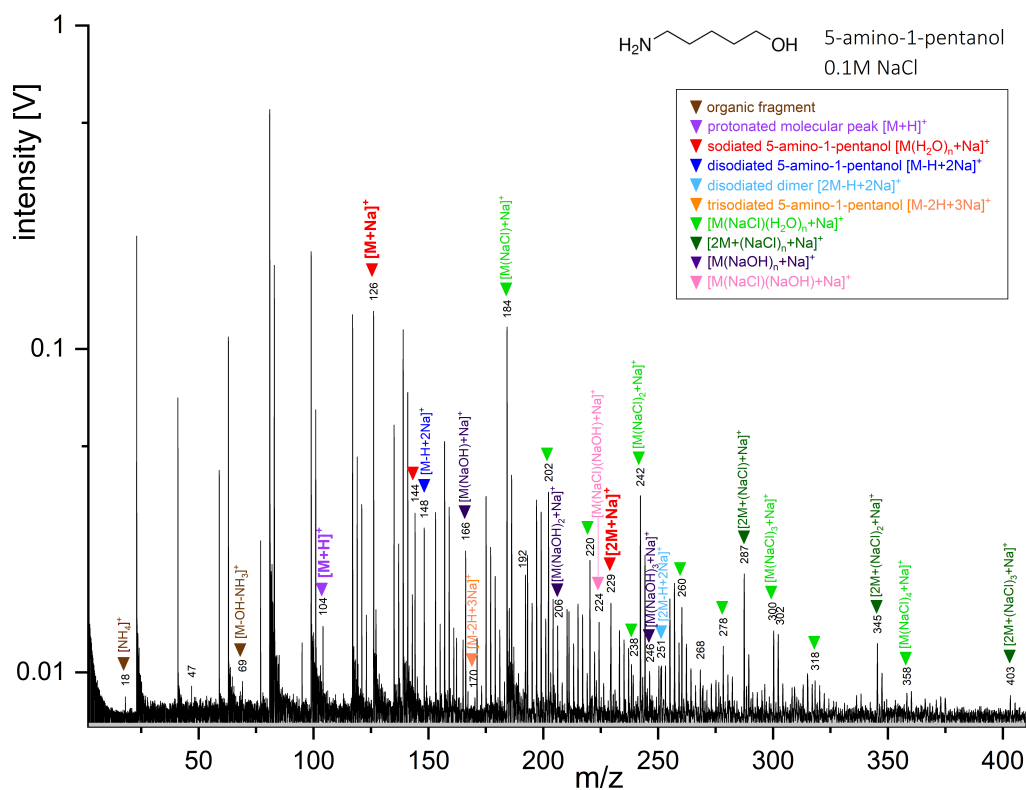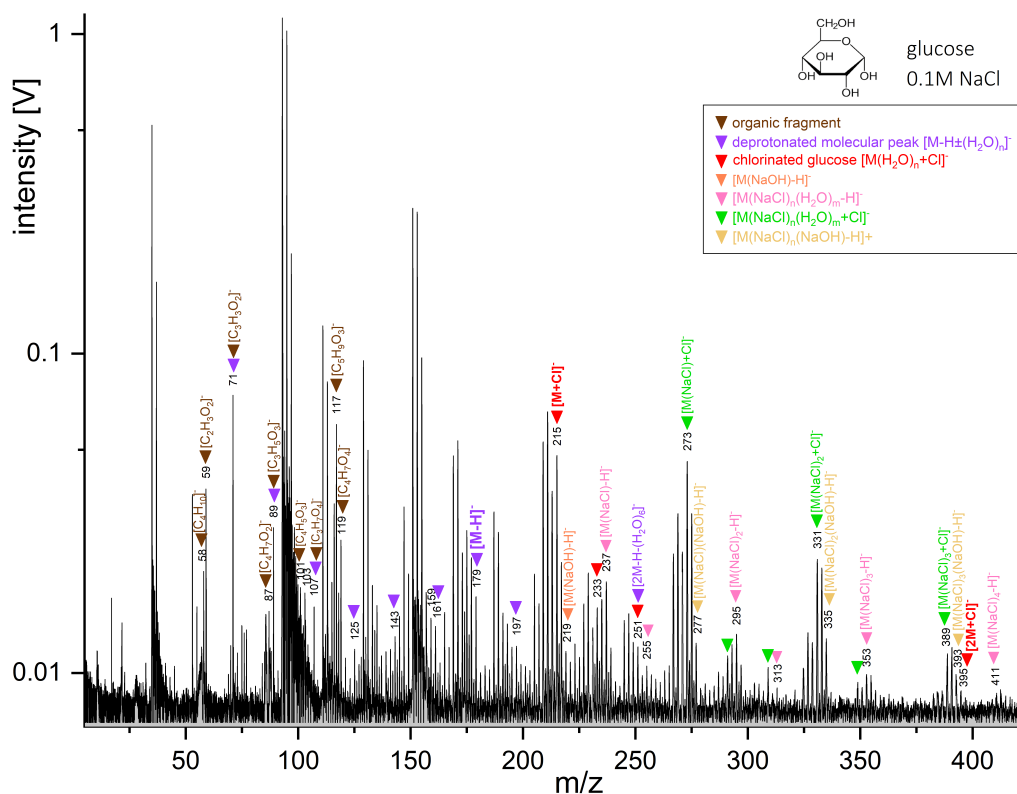

FIGURE 27. Baseline corrected anion mass spectrum of glucose at a concentration of 5wt% in a 0.01M NaCl matrix. The spectrum was recorded with a delay time of 6.1μs. Characteristic deprotonated molecular peak $[M-H]^-$ and chlorinated peak $[M+Cl]^-$ are labelled in purple and red, respectively, with their corresponding water clusters. Unlabeled peaks originate exclusively from the salty matrix. Peaks labelled in brown correspond to glucose fragments. Peaks labelled in all other colors were identified as salt adducts.

Intermediate salt concentration (0.1M NaCl)

At a concentration of 0.1M NaCl in the matrix solution, protonated molecular peaks ($[M+H]^+$) are much weaker than in a 0.01M NaCl matrix (e.g., Figures 26 and 28) but are still detectable for 5-amino-1-pentanol, butylamine and glucose (Table 2). Protonated molecular peaks are not detected anymore for acetic acid, benzoic acid, methanol, and pyridine. Sodiated molecular ions ($[M+Na]^+$) are detectable for all organics except acetic acid, at intensities lower than in 0.01M NaCl matrices (e.g., Figures S18 and S19). Clusters of sodiated organic molecules with NaCl ($[M(NaCl)+Na]^+$) were detected for all organics except acetic acid, usually at higher intensities than in 0.01M NaCl matrices (e.g., Figures 26 and 28). Clusters of sodiated organic molecules with NaOH ($[M(NaOH)+Na]^+$) were detected for 5-amino-1-pentanol, butylamine and pyridine, and tentatively detected for benzoic acid, at roughly similar intensities as compared to 0.01M NaCl matrices. Disodiated peaks ($[M-H+2Na]^+$) were detected in the cation mass spectra of 5-amino-1-pentanol, acetic acid, benzoic acid and glucose (Figure 28; Figures S9, S14 and S23), and trisodiated peak were detected for 5-amino-1-pentanol ($[M-2H+3Na]^+$) and acetic acid dimers ($[2M-2H+3Na]^+$). Whereas the disodiated peaks of benzoic acid had weaker intensities in 0.1M NaCl than in 0.01M NaCl matrices, the intensities of disodiated glucose peak were roughly similar in both matrices, and those of 5-amino-1-pentanol and acetic acid were stronger in 0.1M NaCl matrices. The trisodiated peak of 5-amino-1-pentanol was not present in 0.01M NaCl matrices, and that of the acetic acid dimer is much higher in 0.1M NaCl than in 0.01M NaCl matrices. Clusters of disodiated organic molecules with NaCl ($[M(NaCl)-H+2Na]^+$) were detected for acetic and benzoic acids. Compared to 0.01M matrices, a smaller number of fragments at lower intensities are usually detected (e.g. Figures 26 and 28). No $[M(NaCl)_n+H]^+$ peak was detected.
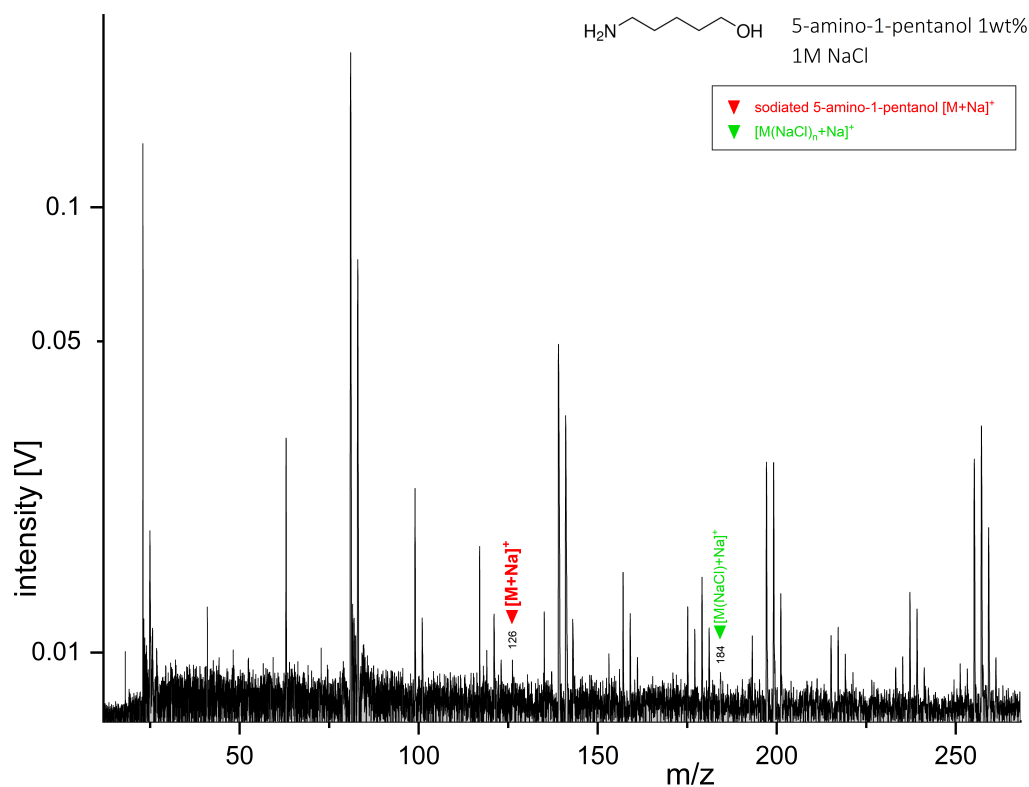
FIGURE 28. Baseline corrected cation mass spectrum of 5-amino-1-pentanol at a concentration of 5wt% in a 0.1M NaCl matrix. The spectrum was recorded with a delay time of 6.3µs. Unlabeled peaks originate exclusively from the salty matrix.

In anion mode, acetic acid, benzoic acid, and glucose were identified as deprotonated molecular ions ($[M-H]^-$), and 5-amino-1-pentanol, glucose, and methanol were identified as chlorinated ions ($[M+Cl]^-$) (Table 3), all at lower intensities as compared to 0.01M NaCl matrices (Figures 27 and 29; Figures S5, S6, S11, S12, S15, S16, S29, and S30). Salt adducts were detected for 5-amino-1-pentanol, acetic acid, benzoic acid, glucose, and methanol at intensities roughly similar to 0.01M NaCl matrices: $[M(NaCl)_n+Cl]^-$ for 5-amino-1-pentanol, glucose and methanol; $[M(NaCl)_n-H]^-$ for 5-amino-1-pentanol, acetic acid, benzoic acid and glucose; and $[M(NaOH)-H]^-$ and $[M(NaCl)_n(NaOH)-H]^-$ for glucose. As in the 0.01M NaCl matrix, sodiated anion dimers $[2M-2H+Na]^-$ and disodiated anion trimers $[3M-3H+2Na]^-$ were detected in the spectra of acetic acid, at higher intensities as compared to 0.01M NaCl. Fragments of acetic acid, benzoic acid, butylamine and glucose were detected (Table S2).

High salt concentration (1M NaCl)

At a concentration of 1M NaCl, protonated molecular peaks ($[M+H]^+$) are detectable for 5-amino-1-pentanol (Figure 30) and glucose despite an interference with a salt cluster (Figure S25). Sodiated molecular ions ($[M+Na]^+$) are detected for 5-amino-1-pentanol, glucose, methanol and pyridine (Figure 26; Figures S25, S28 and S33). As compared to the 0.1M NaCl matrix, protonated molecular peaks are not detected anymore for butylamine and sodiated peaks are not detected anymore for benzoic acid and butylamine. All detected protonated and sodiated peaks have lower intensities than in 0.1M NaCl matrices (e.g., Figures 28 and 30). Clusters of sodiated organic molecules with NaCl ($[M(NaCl)+Na]^+$) were detected for all organics except acetic and benzoic acid, and at lower intensities than in 0.1M NaCl matrices. In the mass spectra of butylamine (Figure S20), $[M(NaCl)_{1-2}+Na]^+$ clusters were detected although no $[M+Na]^+$ peaks were detected. $[M(NaCl)+Na]^+$ clusters are the highest organic-related peaks in the mass spectra of 5-amino-1-pentanol, butylamine, pyridine, and methanol. Clusters of sodiated organic molecules with NaOH ($[M(NaOH)+Na]^+$) were detected for 5-amino-1-pentanol, at lower intensities as compared to 0.1M NaCl matrices (Figures 28 and 30). Disodiated peaks ($[M-H+2Na]^+$) were detected in the cation mass spectra of 5-amino-1-pentanol, acetic acid, and glucose at similar (for acetic acid) or lower intensities as compared to 0.1M NaCl matrices. As compared to the 0.1M NaCl matrix, disodiated peaks were not detected for benzoic acid anymore. Trisodiated dimers ($[2M-2H+3Na]^+$) and clusters of disodiated organic molecules with NaCl ($[M(NaCl)-H+2Na]^+$) were detected for acetic acid, both at lower intensities as compared to 0.1M NaCl matrices. Cationic fragments were only detected for glucose and

FIGURE 29. Baseline corrected anion mass spectrum of glucose at a concentration of 5wt% in a 0.1M NaCl matrix. The spectrum was recorded with a delay time of 6.2µs. Unlabeled peaks originate exclusively from the salty matrix.

5-amino-1-pentanol (Figure S2 and Table S1). Similarly to 0.1M NaCl matrices, $[M(NaCl)+H]^+$ cations were not detected.

In anion mode, only acetic acid and benzoic acid showed characteristic organic signatures, whereas the spectra of all other organics are similar to pure 1M NaCl spectra. For both acetic acid and benzoic acid, deprotonated molecular peaks were detected with a high sensitivity (Figure 31 and Figure S17), but at lower intensities than in 0.01M NaCl matrices. Salt adducts ($[M(NaCl)_n-H]^-$) were detected for both acetic acid and benzoic acid, for both at lower intensities as compared to 0.01M NaCl matrices. Clusters $[2M-H+(NaCl)_n]^-$, $[3M-H+(NaCl)_n]^-$, $[2M-2H+(NaCl)_n+Na]^-$ and $[3M-H+(NaCl)_n]^-$, were detected for acetic acid (Figure 31). One organic fragment was detected for acetic acid ($[CH_3]^-$) and benzoic acid (deprotonated benzene).

Detection limits were estimated in 1M NaCl matrices for the compounds with the highest sensitivities (i.e., 5-amino-1-pentanol in cation mode and acetic acid in anion mode). Deprotonated molecular ions of acetic acid were identified in a 1M NaCl matrix at a concentration as low as 0.1wt% (Figure S35). In cation mode, 5-amino-1-pentanol and glucose were the only organics that could be surely identified at 1M NaCl as a protonated molecular peak, at a concentration of 5wt% (Figure 30 and Figure S25). The protonated molecular peak of 5-amino-1-pentanol could not be observed at lower concentrations than 5wt%, but the sodiated peak was detected down to a concentration of 1wt% (Figure S36).

1.4.4 Detection of organic fragments

Organic fragments are crucial for spectral interpretation as they provide structural information and might help to resolve ambiguities from the molecular or cluster peaks alone. In water matrices, fragments were detected for all organic species in both ion modes, except for methanol in anion mode (Tables S1 and S2). In salt-rich matrices, organic fragments were detected in at least one ion mode for all the investigated organics except methanol and pyridine (Tables S1 and S2). The number of characteristic organic fragments, as well as their intensities, decreased with increasing NaCl concentration (Tables S1 and S2). The fragments observed at high NaCl concentrations were usually also observed at low NaCl concentrations.

Both 5-amino-1-pentanol and butylamine formed cationic fragments by losing their functional groups, typically forming $[NH_4]^+$, $[CH_2NH_2]^+$ and/or $[CH_2O]^+$, $[M-OH-NH_3]^+$ and $[M-OH]^+$ fragments for 5-amino-1-pentanol,
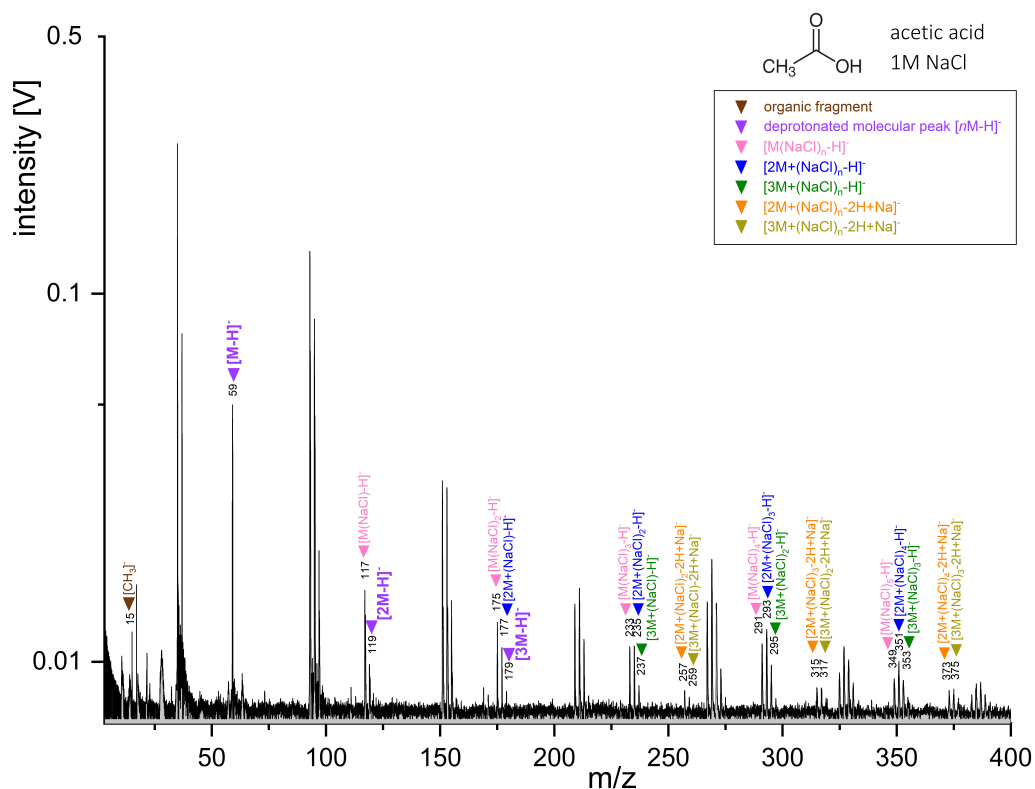
FIGURE 30. Baseline corrected cation mass spectrum of 5-amino-1-pentanol at a concentration of 5wt% in a 1M NaCl matrix. The spectrum was recorded with a delay time of 6.5µs. Characteristic protonated molecular peak $[M+H]^+$ and sodiated peak $[M+Na]^+$ are labelled in purple and red, respectively. Unlabeled peaks originate exclusively from the salty matrix. Peaks labeled in all other colors were identified as salt adducts.

			5-amino-1-pentanol	Acetic acid	Benzoic acid	Butylamine	Glucose	Methanol	Pyridine
0.01M NaCl	$[M+H]^+$	M+1 u	✓	✓	✓	✓	✓	✓	✓
	$[M+Na]^+$	M+23 u	✓	✓	✓	✓	✓	✓	✓
	$[M(NaCl)+H]^+$	M+59 u		✓	✓				
	$[M(NaCl)+Na]^+$	M+81 u	✓	✓	✓	✓	✓	✓	✓
	$[M(NaOH)+Na]^+$	M+63 u	✓	✓	✓	✓			✓
	$[M-H+2Na]^+$	M+45 u	✓	✓	✓		✓		
	$[M-2H+3Na]^+$	M+67 u					✓		
	$[2M-2H+3Na]^+$	2M+67 u		✓					
	$[M(NaCl)-H+2Na]^+$	M+103 u		✓	✓				
0.1M NaCl	$[M+H]^+$	M+1 u	✓			✓	✓		
	$[M+Na]^+$	M+23 u	✓		✓	✓	✓	✓	✓
	$[M(NaCl)+H]^+$	M+59 u							
	$[M(NaCl)+Na]^+$	M+81 u	✓		✓	✓	✓	✓	✓
	$[M(NaOH)+Na]^+$	M+63 u	✓		✓	✓			✓
	$[M-H+2Na]^+$	M+45 u	✓	✓	✓		✓		
	$[M-2H+3Na]^+$	M+67 u	✓						
	$[2M-2H+3Na]^+$	2M+67 u		✓					
	$[M(NaCl)-H+2Na]^+$	M+103 u		✓	✓				
1M NaCl	$[M+H]^+$	M+1 u	✓				✓		
	$[M+Na]^+$	M+23 u	✓				✓	✓	✓
	$[M(NaCl)+H]^+$	M+59 u							
	$[M(NaCl)+Na]^+$	M+81 u	✓			✓	✓	✓	✓
	$[M(NaOH)+Na]^+$	M+63 u	✓						
	$[M-H+2Na]^+$	M+45 u	✓	✓			✓		
	$[M-2H+3Na]^+$	M+67 u							
	$[2M-2H+3Na]^+$	2M+67 u		✓					
	$[M(NaCl)-H+2Na]^+$	M+103 u		✓					

TABLE 2. Detected peaks, and their respective m/z values, in cation mode for the investigated organics at 0.01M, 0.1M and 1M NaCl concentrations. Blue symbols (✓) represent tentative identifications.

FIGURE 31. Baseline corrected anion mass spectrum of acetic acid at a concentration of 5wt% in a 1M NaCl matrix. The spectrum was recorded with a delay time of 6.5µs. Characteristic deprotonated molecular peaks [M-H]$^-$ are labelled in purple. Unlabeled peaks originate exclusively from the salty matrix. Peaks labelled in brown correspond to organic fragments. Peaks labeled in all other colors were identified as salt adducts.

			5-amino-1-pentanol	Acetic acid	Benzoic acid	Butylamine	Glucose	Methanol	Pyridine
0.01M NaCl	[M-H]⁻	M-1 u	✓	✓	✓		✓		
	[M+Cl]⁻	M+35 u	✓		✓		✓	✓	✓
	[M(NaCl)-H]⁻	M+57 u	✓	✓	✓		✓		
	[M(NaOH)-H]⁻	M+39 u					✓		
	[M(NaCl)+Cl]⁻	M+93 u	✓		✓		✓	✓	
	[M(NaOH)+Cl]⁻	M+75 u					✓		
	[M+H+2Cl]⁻	M+71 u					✓		
	[2M-2H+Na]⁻	2M+21 u		✓	✓			✓	
	[3M-3H+2Na]⁻	3M+43 u		✓					
0.1M NaCl	[M-H]⁻	M-1 u		✓	✓		✓		
	[M+Cl]⁻	M+35 u	✓				✓	✓	
	[M(NaCl)-H]⁻	M+57 u	✓	✓	✓		✓		
	[M(NaOH)-H]⁻	M+39 u					✓		
	[M(NaCl)+Cl]⁻	M+93 u	✓				✓	✓	
	[M(NaOH)+Cl]⁻	M+75 u							
	[M+H+2Cl]⁻	M+71 u							
	[2M-2H+Na]⁻	2M+21 u		✓					
	[3M-3H+2Na]⁻	3M+43 u		✓					
1M NaCl	[M-H]⁻	M-1 u		✓	✓				
	[M+Cl]⁻	M+35 u							
	[M(NaCl)-H]⁻	M+57 u		✓	✓				
	[M(NaOH)-H]⁻	M+39 u							
	[M(NaCl)+Cl]⁻	M+93 u							
	[M(NaOH)+Cl]⁻	M+75 u							
	[M+H+2Cl]⁻	M+71 u							
	[2M-2H+Na]⁻	2M+21 u							
	[3M-3H+2Na]⁻	3M+43 u							

TABLE 3. Detected peaks, and their respective m/z values, in anion mode for the investigated organics at 0.01M, 0.1M and 1M NaCl concentrations. Blue symbols (✓) represent tentative identifications.

and $[NH_4]^+$ and $[M-NH_2]^+$ fragments for butylamine.

Both acetic acid and benzoic acid formed $[M-OH]^+$ peaks in 0.01M NaCl matrices, but different cationic fragments are detected at higher NaCl concentrations: at 0.1M NaCl, $[CO]^+$ is detected for acetic acid and $[C_3H_3]^+$ for benzoic acid. No fragments are detected at higher NaCl concentration in cation mode. In the anion mass spectra of acetic acid, $[CH_3]^-$ fragments were detected at all NaCl concentrations at approximately similar intensities (Figure 31 and Figures S11, S12). Deprotonated benzene ($[M-COOH]^-$) was detected in the anion mass spectra of benzoic acid at all NaCl concentrations, at intensities decreasing with increasing NaCl concentrations (Figures S15-S17).

A high number of glucose fragments were detected in cation mode at all NaCl concentrations (Table S1), and in anion mode at 0.01M and 0.1M NaCl (Table S2). Fragments resulted from the successive loss of water from the alcohol functional groups of the deprotonated glucose molecule and other fragmentation pathways (e.g., Figure 32). As other compounds containing hydroxyl (-OH) groups, glucose typically form $[M-OH]^+$ fragments. Glucose is the only organic for which a high number of fragments was detected in 1M NaCl matrices.
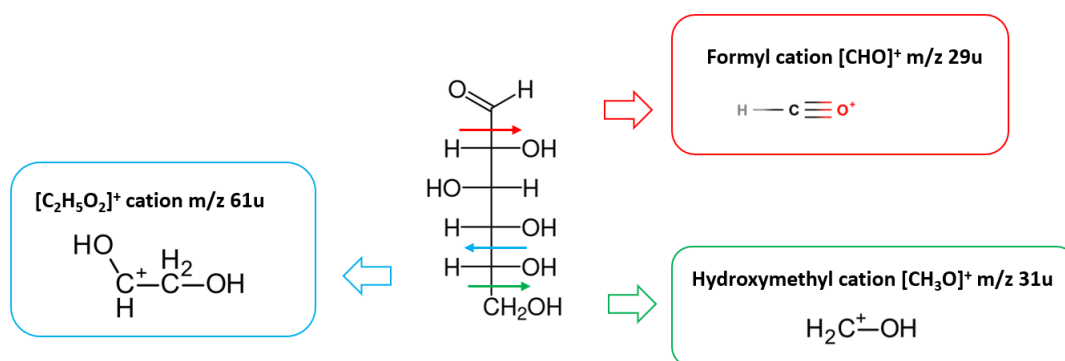
FIGURE 32. Examples of fragmentation pathways of some detected cation fragments of glucose. The arrows represent bond cleavage.

1.4.5 General trends

Our results show that organics embedded in high-salinity ice grains can still be detected because of the formation of molecular ions and sodiated and chlorinated adducts. However, the spectral appearance of the organics fundamentally changes from relatively low (0.01M) to high (1M) NaCl matrices. The formation, and relative intensities, of different ions and salt adducts at varying salt concentrations strongly influence the resulting spectra. Organic molecular peaks but also sodiated and chlorinated organic adducts are effectively suppressed with increasing NaCl concentrations, and the relative intensities of peaks change with varying salt concentrations.

Suppression Effects.

Effective suppression effects by the salt [264, 285] provoked a general decrease of the absolute number and intensities of organic-related peaks, including molecular peaks, fragment peaks and sodiated and chlorinated peaks, with increasing NaCl concentration in both ion modes (Figures 33 and 34, Tables 2 and 3, and Tables S1 and S2). We investigated the trends of the amplitudes of protonated and sodiated peaks (Figure 33) and of (de)protonated molecular peaks (Figure 34) in matrices of increasing NaCl concentration, by normalizing these peaks' integrals against the total integrated ions. This analysis showed that the degree of suppression of molecular peaks as well as some sodiated and chlorinated peaks by the salt is highly dependent on the organic species and ranges from less than a factor of 2 up to several orders of magnitude. Figures 33 and 34 should nonetheless be treated cautiously, because they don't represent true comparisons of ionization efficiencies between the different organic species: multiple variables have an influence on the peak amplitudes (e.g., the organic/NaCl ratio is decreasing in the solution as [NaCl] increases; the different organic samples have different molecular densities). Rather than an absolute quantitative comparison, Figures 33 and 34 provide valuable trends representative of suppression effects for a variety of organic species. The amount of water clusters, in the spectra of both pure NaCl matrix and organic-rich salty solutions, decreased with increasing NaCl concentration. Counterintuitively, the number and intensities of both sodiated and chlorinated peaks were also found to likewise decrease with increasing NaCl concentration (e.g., Figures 4-8). By contrast, intensities increased with salinity for clusters of

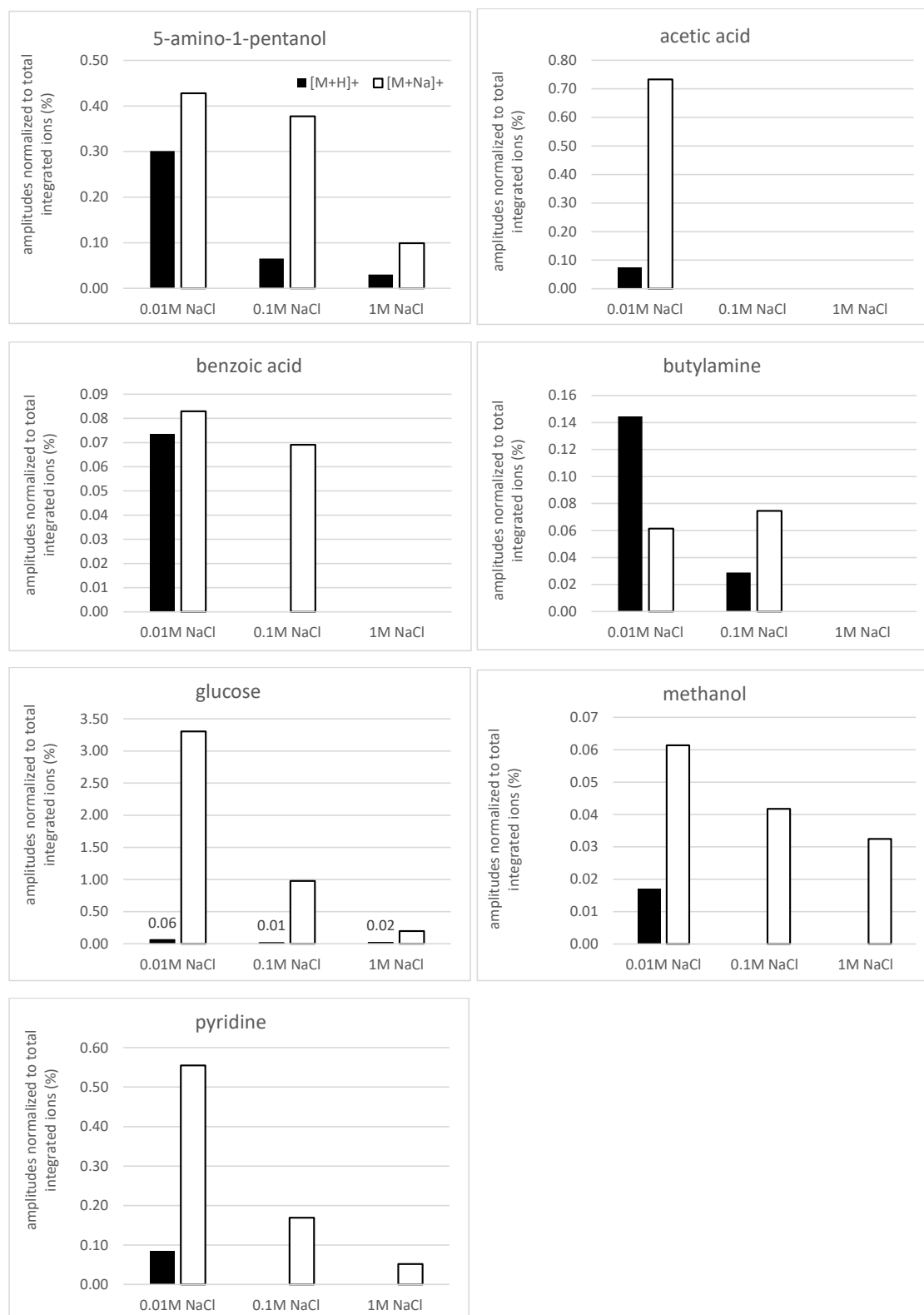sodiated organic molecules with NaCl ([M(NaCl)+Na]$^+$.

FIGURE 33. Relative amplitudes of protonated molecular peaks [M+H]$^+$ and sodiated peaks [M+Na]$^+$ in 0.01M, 0.1M and 1M NaCl matrices for the seven measured organic species. Peak amplitudes were normalized to the total integrated ions.
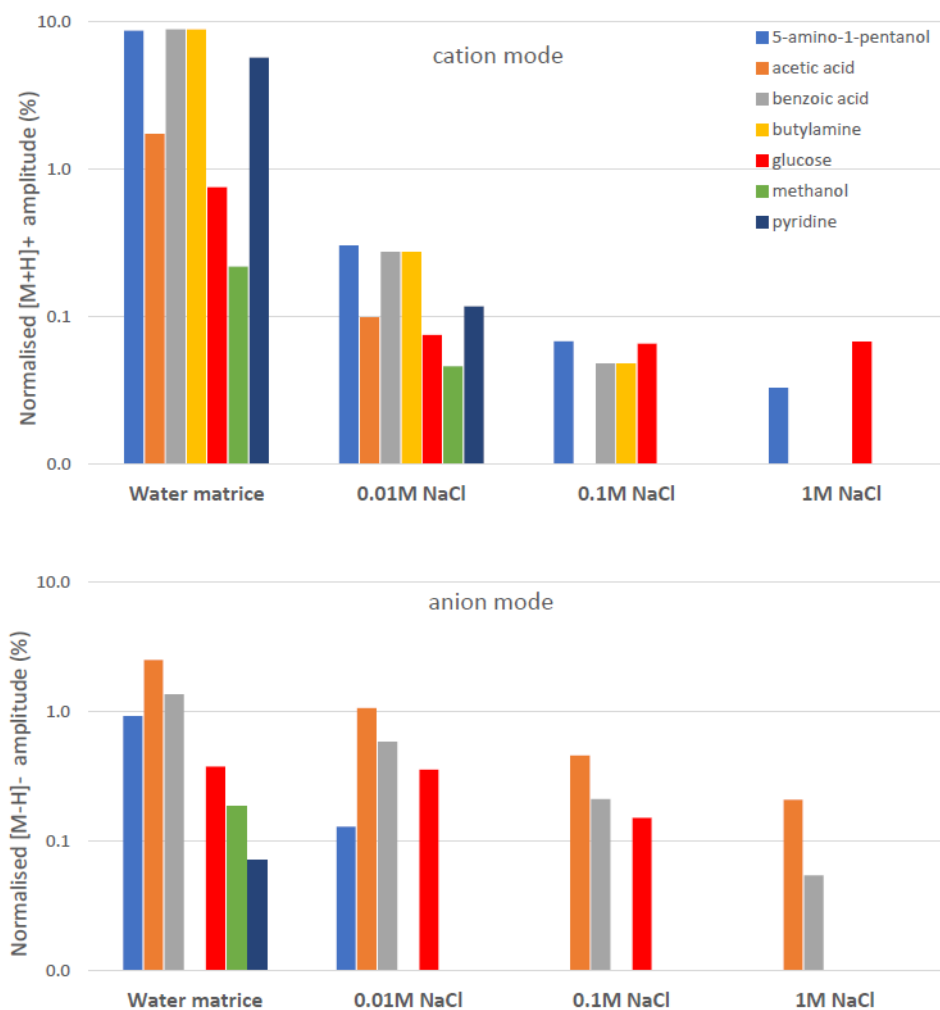
FIGURE 34. Relative amplitudes of protonated molecular peaks [M+H]$^+$ (top) and deprotonated molecular peaks [M-H]$^-$ (bottom) in water matrices, 0.01M NaCl, 0.1M NaCl and 1M NaCl matrices for the seven organic species measured in cation and anion mode. Amplitudes were normalized against the integral of the whole spectra and plotted on a logarithmic scale.

Ion Mode.

Most of the organics investigated typically formed a larger number of peaks in cation mode than in anion mode (Tables 2 and 3). Generally, we observe a trend of lower response of the organics in anion mode as compared to cation mode. Whereas all organics formed protonated and sodiated molecular peaks (at least in 0.01M NaCl matrices), only some of the organics formed deprotonated or chlorinated peaks. The intensities of organic peaks are usually higher in cation mode than anion mode, except for the two carboxylic acids, to which the sensitivity was much higher in anion mode than cation mode. These two species are the only organics that were detected at the highest NaCl concentration (1M) in anion mode, thanks to highly significant deprotonated molecular peaks (Figure 31 and Figure S17). In anion mode, the response of the different organics varied greatly from one organic species to another. In particular, butylamine and pyridine are not or barely detectable even at low NaCl concentrations.

Sodiation and Chlorination Processes.

Sodiation appears to play a major role in the spectral appearance of the organics in salt-rich matrices. In cation mode spectra, the most prevalent characteristic peaks are sodiated peaks ([M+Na]$^+$) for all organics, except for acetic acid and benzoic acid for which disodiated peaks [M-H+2Na]$^+$ dominate (Figures S7-S10, S13 and S14). A higher absolute number of sodiated species have been detected for acetic acid and benzoic acid (e.g., [M(NaCl)-H+2Na]$^+$, [2M-2H+Na]$^-$; Tables 2 and 3), and for acetic acid only ([3M-3H+2Na]$^-$, [4M-3H+2Na]$^-$, [xM-2H+Na]$^-$, [xM-3H+2Na]$^-$ and [4M-4H+3Na]$^-$; Table 3, Figures S11 and S12), as compared to other

organics. Disodiated cations $[M-H+2Na]^+$ have been detected for all species containing hydroxyl (-OH) functional group(s) except methanol (i.e., 5-amino-1-pentanol, acetic acid, benzoic acid and glucose), but at much higher intensities for acetic acid and benzoic acid as compared to the other organics. Trisodiated cations have been detected for glucose ($[M-2H+3Na]^+$) and acetic acid dimers and trimers ($[2M-2H+3Na^+, [3M-2H+3Na]^+$). Chlorination processes (i.e., addition of a chloride anion) were also observed: chlorinated peaks ($[M+Cl]^-$) were detected in 0.01M NaCl matrices for most organics, and dichlorinated peaks ($[M+H+2Cl]^-$) were tentatively detected for glucose in 0.01M NaCl matrix.

Salt Clusters with NaCl and NaOH.

A variety of salt clusters were observed in both ion modes. Clustering of NaCl onto cations or anions was observed more frequently, and create higher intensity peaks, than clustering of NaOH in both ion modes. This is consistent with the spectra of the pure NaCl matrix, where clusters of $[Na(NaCl)_n]^+$ and $[Cl(NaCl)]^-$ are much more significant than $[Na(NaOH)_n]^+$ and $[Cl(NaOH)_n]^-$ (Figures 24 and 25 and Figures S1-S4). Clustering of NaCl onto sodiated molecules ($[M(NaCl)_n+Na]^+$) appeared to be more frequent than onto protonated molecules ($[M(NaCl)_n+H]^+$). The relative intensity of $[M(NaCl)_n+Na]^+$ in many cases increased with NaCl concentrations (e.g., Figures 26, 28 and 30), although the intensities of $[M+Na]^+$ peaks decreased. Conversely, clusters of protonated organics with NaCl ($[M(NaCl)+H]^+$) were detected only in 0.01M matrices but not at higher NaCl concentrations. At 1M NaCl concentrations, $[M(NaCl)+Na]^+$ peaks were detected for butylamine although sodiated peaks $[M+Na]^+$ were not detected. In anion mode, both $[M(NaCl)_n-H]^-$ and $[M(NaCl)_n+Cl]^-$ clusters were detected for many organics, but clustering of anions with NaOH was only observed for glucose.

1.5 Discussion

In this work, we performed analogue experiments for the detection of organic molecules in salt-rich ice grains from icy moons with impact ionization mass spectrometry. A range of organic compounds were measured with the LILBID setup in water and NaCl-rich matrices at different salt concentrations (0.01, 0.1 and 1M NaCl). Our results show that our laboratory setup is more sensitive to the majority of the measured organics and their fragments in the cation mode than in the anion mode. The sensitivity in negative ion mode has also been reported to be generally lower than that in positive ion mode in both Matrix Assisted Laser Desorption Ionization mass spectrometry (MALDI)-MS [289, 290] and electrospray ionization (ESI)-MS [291]. The lower sensitivity in anion mode must be due to differences in mechanisms leading to the formation of charged analyte molecules during the ionization process, which are not yet very well understood. Anions can be generated by (*i*) deprotonation from the analyte, (*ii*) fragmentation during the ionization process, (*iii*) adduct formation with anions, or (*iv*) simultaneous deprotonation and adduct formation with cations (e.g., $[2M-2H+Na]^-$ ions). Analytes with free electron pairs can be easily ionized by the attachment of protons and cations (e.g., $[M+Na]^+$).

Different organic species have different ionization efficiency that depends on the organic's intrinsic properties [292]. The organic response depends on its molecular structure and on its physicochemical properties. Using the LILBID setup, Klenner et al. [263] found a better sensitivity to amino acids in the cation mode than in the anion mode. Basic amino acids with high proton affinities have efficient proton transfer and therefore promote an efficient formation of cations. Generally, basic analytes often have lower sensitivities in negative ion mode than their corresponding protonated species in cation mode [293]. On the contrary, strong acids have higher ionization efficiency and give higher signals in the negative mode than in the positive mode, as shown by Kruve et al. [294] using ESI-MS. We found that the molecular structure of the organic species and the presence of functional groups influence the ionization efficiency, the fragmentation pathways, and the formation of adducts:

• **hydroxyl (-OH)** functional groups increase the ionization efficiency to form molecular anions. They also promote the formation of sodiated species, with protons from the hydroxyl functional groups being easily replaced by Na^+, and allow the formation of characteristic $[M-OH]^+$ fragments, which often have a very prominent intensity, even higher than molecular peaks in some cases (e.g., for glucose; Figures S24 and S25).

• **carboxylic acid (-COOH)** functional groups greatly increase the ionization efficiency to form deprotonated molecular anions. Such functional groups can be easily cleaved from the carboxylic acid-bearing molecule, leading to the formation of $[M-COOH]^-$ anions. They also promote sodiation processes, leading to the formation of both sodiated cations and anions. In cation mode, $[M-H+2Na]^+$ peaks are highly prominent, and much higher than $[M+Na]^+$. In water matrices, $[M-OH]^+$ fragments are the most prominent peaks in cation mass spectra (Figures S39 and S41).

- **amine (-NH$_2$)** functional groups were found to decrease the ionization efficiency of molecular species in anion mode. Similarly to hydroxyl groups, they also promote the formation of sodiated species, with protons from the NH$_2$ being easily replaced by Na$^+$.
- the presence of **aromatic rings** increases the stability of the molecular structure, inhibiting its fragmentation and the formation of respective fragment ions.
- **species with a low pH** show a very high signal in the anion mode and show significantly high deprotonated molecular peaks, even at high salt concentration.
- **high pH species** might be better detected in cation mode than anion mode, as seen in the anion mass spectra of 5-amino-1-pentanol, butylamine and pyridine that show very low signal.

Comparing butylamine and 5-amino-1-pentanol, i.e., two species with the same pH value of 12, we suggest that 5-amino-1-pentanol might have a better detectability than butylamine owing to its hydroxyl functional group. With the aim to detect specific types of organics, their pH values are a first important consideration when preferring negative or positive mode analysis. However, we could not establish a straightforward trend of detectability of all organics in relation to the pH, suggesting that the pH is only one important parameter among others, such as the presence of functional groups or the ion mode. This is in accordance with a study by Liigand et al. [295] that showed that decreasing pH can significantly increase the ionization efficiency of a compound, although other physicochemical properties, such as the pka, the number of potential charge center and the hydrogen bonding acceptor capacity were also found to play an important role in the analyte behavior. In our experiments, the ionization efficiency of an organic species is related to the molecular density in the ionization region of the sample, therefore it depends on the organic's molecular concentration. The organics investigated have molar masses ranging from 32 to 180 g/mol (Table 1). In a constant volume V, the molecular density D of an organic species of mass m decreases when the molecular mass M increases (D=m/(M×V)), e.g., glucose (M=180 g/mol) has a lower molecular density than methanol (M=32 g/mol). Molecular densities of the investigated organics therefore vary by a factor of ∼6 between the lowest and the highest molecular masses organics. However, we believe that this effect has a second-order significance on the sensitivity as compared to the organics' intrinsic properties such as the pH or some specific functional groups.

Our results emphasize the need of both ion modes for future spaceborne impact ionization mass spectrometers because different organic families have different sensitivities in cation compared to anion mode. For example, the sensitivity to carboxylic acids is very high in anion mode even at the highest salt concentration (Figure 31 and Figure S17); whereas butylamine, and pyridine at C$_{NaCl}$ > 0.01M, could be detected in cation mode but not in anion mode (Tables 2 and 3). Measurements in both ion mode are therefore necessary to cover the complete range of the characteristic spectral signatures investigated here. Severe ion suppression as described here could result in false-negative results for samples containing organics. Both SUDA and ENIA will be capable of detecting both cations and anions [215, 143].

Whereas (de)protonated molecular peaks are the strongest peaks in pure water solutions, salt adducts instead form the strongest signals when salts are added to the matrix. Our results indicate that uncomplexed organics may be less stable than respective sodium complexes formed in a salt-rich solution, in agreement with previous mass spectrometry studies showing that sodium adducts can be difficult to fragment [296, 297]. Sodiation of organic species is a well-known process in mass spectrometry [264, 298]. The presence of hydroxyl (OH) and amine (NH$_2$) functional groups in the organic species' molecular structure promotes sodiation processes, as the protons from these functional groups can easily be replaced by a sodium cation (Na$^+$), forming disodiated cations ([M-H+2Na]$^+$) or in the case of several functional groups, polysodiated cations [M-mH+nNa]$^+$ with $m=n$-1, e.g., trisodiated cations [M-2H+3Na]$^+$. Sodiated organics [M-nH+mNa]$^{(m-n)+}$ have been observed in ESI-MS and MALDI-MS, on a number of functional groups including amines, carboxylic groups and amides [299, 300, 301]. Interestingly, we detected a disodiated monomer ([M-H+2Na]$^+$) and a trisodiated dimer ([2M-2H+3Na]$^+$) in the mass spectra of acetic acid, and trisodiated cations were detected also for glucose ([M-2H+3Na]$^+$), confirming that multiple functional groups are needed for multiple replacement of H atoms with Na$^+$. Generally, the degree of sodiation of organic molecules depends on the number of hydroxyl and amine functional groups available in the organic molecule. The spectra of the two carboxylic acids show especially prominent disodiated cation peaks ([M-H+2Na]$^+$) as compared to other organics and sodiated anions were not detected for any other organics, suggesting that carboxylic functional groups are even more efficient in incorporating Na$^+$ cations than hydroxyl groups that do not belong to carboxyl groups.

We observed chlorinated species for the first time with the LILBID, where a chloride anion is added in the molecular structure. Chlorinated species were detected for different families of organic species, but they were

particularly prominent for glucose and methanol. Moreover, dichlorinated peaks ($[M+H+2Cl]^-$) were tentatively identified for glucose (Figure 27), suggesting that hydroxyl functional groups may offer favorable sites for chlorination to happen. Chlorination of organic species has also been previously observed in ESI and Orbitrap mass spectrometry [302, 303]. The chlorinated peaks we observed were not as strong as sodiated peaks. Chloride attachment and more generally ionization by addition of anions, is a substantially softer form of ionization than with cations [304], because bonds between anions and molecules are usually weaker than corresponding bonds to cations (i.e., molecular proton affinities are usually higher than anion affinities).

Organic-related peaks tend to be fewer and have smaller intensities with increasing NaCl concentrations, due to suppression effects (so-called "salt-in" effects) [264, 285, 305]. The degree of suppression varied from one sample to another, consistent with the expectation that suppression effects by salts are compound-dependent and concentration-dependent [306]. Severe ion suppression has led to the non-detection of some organics, especially in anion mode and at high NaCl concentrations. We evaluated the strength of ion suppression by comparing the signal of molecular peaks of the analytes measured in pure water to their signal in increasing NaCl concentration matrices (Figure 34). The signal decreased by several orders of magnitude between pure water matrices and 1M NaCl matrices in both ion modes. The signals of sodiated peaks were also found to decrease drastically with increasing NaCl matrix concentration (Figure 33). However, the ion suppression cannot strictly be quantitatively estimated as in Figures 33 and 34, the decrease in amplitude is likely to be due not solely to suppression effects, but also to other intertwined factors (e.g., the molar concentration). Suppression effects are caused by the general inhibition of ion formation at high salinities [258] and by the formation of sodiated and chlorinated adducts, which contributes to the reduction of signal of the (de)protonated organic species and results in loss of resolution and sensitivity [307]. The formation of salt adducts spreads the un-sodiated molecular organic ions' signal over multiple different masses, causing a suppression of the signal of the analyte together with reduced detection abilities. Salt clusters can also increase the baseline noise, further lowering the signal-to-noise ratio.

Our results indicate that the detection and identification of organics in the mass spectra of salty grains are likely to be more difficult than for the salt-poor grains. At the highest NaCl concentration investigated (1M), most organics can only be detected as sodiated complex in cation mode, and cannot be detected at all in anion mode. However, several organic species i.e. low pH organics can still be detected even at 1M NaCl. High concentrations of salts as expected on Europa (0.1-1.2M NaCl) [197] or Enceladus (0.05–0.2M NaCl) [128] could therefore degrade the spectral quality of organic-rich ice grains measured by impact ionization mass spectrometers. However, salts are not expected to always be present in every ice grain that carries organics (e.g., "Type 2" salt-poor, organic-rich ice grains from Enceladus ocean) [308], so the salt-in effects we describe are not be applicable to all mass spectra recorded by spaceborne mass spectrometers. Ion suppression effects influencing the measurements of SUDA-type instruments might be stronger in cases where organic analytes are present only in trace amounts, because the potential for ion suppression in complex matrices is higher at low organic concentrations [309]. However, high organic concentrations, perhaps on the order of several %, are expected on certain regions on Europa [310] i.e., chaos terrains [311]. Moreover, the SUDA instrument will have a substantially higher dynamic range, together with a higher sensitivity, than the mass spectrometer of our LILBID setup [215], meaning that detection limits can be expected to be at least 1 order of magnitude lower than the detection limits we estimated and this might help counteracting the degradation of the spectral quality by salt-in effects. This increase in sensitivity would be even higher for future instruments investigating ice grains in the Enceladus plume, such as ENIA [143, 141, 312].

During impact ionization processes, kinetic energy is imparted to the molecules, and can be effectively released by the molecule breaking into fragments. Fragments have been detected for most of the investigated organics and in some cases, even at high salt concentrations (Tables S1 and S2). This is a new result as compared to previous studies by Klenner et al. [263, 264], where characteristic amino acid fragments were observed in salt-poor solutions but not in salt-rich solutions with a similar salinity (0.1M NaCl + 0.015M Na_2CO_3 + 0.015M $NaHCO_3$) as in our cases with fragment detection – but Klenner et al. [264] investigated amino acids at concentrations < 0.1%, which might be the reason why they did not observe fragments. However, we detected fewer characteristic organic ionic fragments with increasing salt concentrations. Judging from our results, the effectivity of the suppression of fragment ions depends on the analyte species, on its molecular structure and functional groups, and on the matrix salt concentration: fragmentation is inhibited for smaller organic molecules, with few functional groups, and is less likely at high NaCl concentrations. Among the investigated organics, glucose was found to form many fragments even at high NaCl concentrations. This may be due to its large molecular mass allowing the cleavage of many different bonds, and to its numerous hydroxyl functional groups that can easily be cleaved in an ionic form from the deprotonated glucose molecule. Both 5-amino-1-pentanol and butylamine were observed to form some of the same fragments reported by Klenner et al. [263] for amino

acids, such as $[NH_4]^+$ at m/z 18 and $[CH_2NH_2]^+$ at m/z 30. Benzoic acid formed deprotonated benzene at m/z 77, consistent with the results of Klenner et al. [263] who showed that several amino acids typically cleaved their carboxylic group to form $[M-COOH]^-$ anions. $[M-OH]^+$ fragments are typically detected for species containing hydroxyl functional groups. Fragments of pyridine and methanol were not detected in any salt-rich matrices. In the case of pyridine, the stability of its aromatic ring structure prevents fragmentation processes of the pyridine molecule. In the case of methanol, the small size of this compound (CH_3OH, 46u) does not allow the formation of many fragments, as compared to larger molecules.

The suppression of organic fragment ions at high salinities might be because the ionization of fragments is suppressed - alternatively, charged fragments may be neutralized by the salts, or the fragmentation process of the organics may be suppressed. NaCl has been shown to have a stabilizing effect against fragmentation in ESI mass spectrometry [313]. Besides, we detected more fragments in cation than anion mode (Tables S1 and S2). This is consistent with the generally higher sensitivity to organic cations than organic anions that we observed, which then also applies to fragments. We did not detect sodiated fragments, although we expected them to form as results of the loss of water and functional groups from sodiated organics. Sodiated fragments have been observed in ESI mass spectrometry experiments [314]. Chlorinated fragments have also not been detected. This may suggest that sodiated and chlorinated species are more resistant to fragmentation than protonated and deprotonated molecular species, thanks to a stabilization by the salt that, in turn, hinder fragmentation; or that, alternatively, they form neutral fragments that we could not detect.

The sensitivity to the signal of the organics and their detection limits vary with the simulated impact speeds (i.e., combination of delay time and laser energy) [253], the organic species, the salt concentration, and the ion mode. Detection limits were found to increase with increasing NaCl concentrations and were estimated at the highest salt concentration (1M NaCl). In anion mode, the most sensitive compounds were the two carboxylic acids, with acetic acid (the lowest pH species) forming a deprotonated molecular peak at a concentration as low as 0.1 wt% (Figure S35). In cation mode, a save detection was established at 1wt% for 5-amino-1-pentanol. Our estimated detection limits in 1M NaCl (1000 ppmw in best case scenario) are, as expected, higher than those found by Klenner et al. [264] for amino acids in 0.1M NaCl matrices (between 0.5ppmw and 1000ppmw). Whereas Dannenmann et al. [265] detected bacterial biosignatures in low concentrations in salt-rich solutions up to 10^{-2}M NaCl, our results show that the detection of other organics and potentially other types of biosignatures is possible at higher salt concentrations.

Our results provide insights into the behavior of organics in salt-rich solutions and therefore might help in the potential detection of organic biosignatures from ocean worlds. In particular, we investigated a sugar, glucose, and a N-heterocycle, pyridine, which are from important families for astrobiology investigations as they are typically found in biogenic material. Results from Dannenmann et al. [265] showed that deprotonated biomolecules can be unambiguously detected in 0.01M NaCl solutions. Salt-complexed adducts appear as reliable biosignatures that are more likely to be detected than (de)protonated biomolecules in an ocean world scenario. The wide range of compounds that we investigated allowed for a broader characterisation applicable to other classes of (potentially yet unknown) biosignature molecules. The salt adducts we recurrently identified (Tables 1 and 2) for organics in NaCl-rich solutions, together with typical fragments (Tables S1 and S2), can allow the identification of unknown species in complex salt matrices. Larger organic molecules than the species we investigated could potentially be detected as organics contained in ice grains as they should be able to survive impact processes at velocities comparable to Europa Clipper flybys speeds [65, 264, 239], i.e., 4-5 km/s. Thanks to the protective effect of the ice matrix for large organics, even slightly higher impact speeds might be suitable.

Different impact speeds of ice grains onto impact ionization mass spectrometer detectors can be reproduced by selecting appropriate laser power density and ion extraction parameters (i.e., delay time of the gating system) on the LILBID setup 64. The experimental parameters used here (laser intensities 97-100%; delay time 5.5-6.8 µs) are compared to those required to simulate different impact speeds of water ice grains and are representative of a speed regime of around 4-8 km/s. This range of equivalent impact speeds lies within the range matching the maximum of detection sensitivity of amino acids, fatty acids and peptides [264, 263].

1.6 Conclusion and Outlook

Both Europa and Enceladus have perhaps the highest potential of any extraterrestrial bodies in our Solar System to host extant biological life. Their oceans and surface ice are expected to contain sodium chloride (NaCl) salt among their major non-water constituents [128, 180, 179], potentially complicating the search for

organic compounds including biosignatures with mass spectrometers such as the SUDA instrument onboard the upcoming Europa Clipper mission or a future Enceladus mission [141]. Using the LILBID setup to simulate the process of impact ionization of organic- and salt-rich ice grains in space, we showed that a wide variety of individual organic species could be detected by SUDA-type mass spectrometers although these samples can be analytically demanding. The presence of functional groups and the molecular structure and physico-chemical properties of the organics play a major role in the detectability of the organic species. The recorded mass spectra allowed us to establish general rules for the identification of organic species in a NaCl-rich matrix:

• protonated and deprotonated molecular peaks are usually suppressed because of "salt-in" effects with increasing NaCl concentrations, as observed in both ion mode. Organic species can still be detected by the identification of molecular ions and sodiated and chlorinated adducts.

• carboxylic acids, due to their high acidity, have highly characteristic mass spectral signatures with signals of high intensity especially in anion mass spectra. They tend to form $[M-H]^-$ in the presence of water [315] and therefore are detectable by prominent deprotonated molecular peaks $[M-H]^-$ in anion mode even with high salt concentrations. In cation mode, they can be detected by highly prominent disodiated $[M-H+2Na]^+$ peaks.

• organic species bearing hydroxyl (-OH) groups typically form abundant molecular anions, allowing a good detectability in anion mode. They are usually also well detected in cation mode owing to their sodiated adducts.

• organic species bearing amine ($-NH_2$) groups tend to have a low response in anion mode and an intermediate response in cation mode. Other functional groups or other properties of the organic species may increase their sensitivity (e.g. amino acids have a high sensitivity in salt-rich ice grains with impact ionization mass spectrometry [264]).

• highly acidic compounds are expected to be highly responsive in anion analysis. However, we believe that acidity alone cannot predict the sensitivity of anions, which is also influenced by other physicochemical factors such as the molecular structure, its polarity or the presence of functional groups.

• polysodiated complexes formed from the substitution of carboxylic or amidic protons by Na^+ are expected for organic species containing hydroxyl and/or amine functional groups.

• organic fragments are expected to form from organic species having hydroxyl, amine and carboxylic groups by the cleavage of these groups. Typical fragments include for hydroxyl-bearing organics $[M-OH]^+$; for amine-bearing organics $[M-NH_2]^+$, $[NH_4]^+$, and $[CH_2NH_2]^+$; and, for carboxylic acids $[M-COOH]^-$ and $[M-OH]^+$. On the contrary, aromatic ring systems significantly inhibit fragmentation processes.

• the mass spectrometric signal of organics in anion mode is usually lower than that in cation mode (except for acidic species) and greatly depends on the organics' physicochemical properties.

Although these rules were established from investigations on a limited range of representative organic species, we believe that they are transferrable to different organic compounds having similar pH values and functional groups. Whereas we investigated rather "simple" samples composed of only one organic species in NaCl matrix, the targets of SUDA-type instruments are natural samples from icy moons likely to be mixtures of several compounds. On the one hand, the effects of inorganic content of the ice grains require more laboratory investigations focusing on the spectral signatures of different types of salts and other non-ice components of icy moons' surfaces. We currently also perform experiments with inorganic components expected to be found in the matrix of ice grains ejected from Europa or Enceladus, including sulfates [184], sulfuric acid [187, 188], and magnesium salts. On the other hand, definitive identification of organic species can be complicated by potential interferences in complex mixtures. To resolve such ambiguities, comparison of isobaric masses can be performed with the high mass resolution of mass spectrometers to establish mass differences <1u as shown in Klenner et al. [264]. Besides, the rules established here can allow the identification of functional groups in a sample, if not the definitive identification of an organic species. The recorded LILBID mass spectra complement a comprehensive spectral reference library for impact ionization mass spectrometers onboard Europa Clipper and other ocean world missions [259], which will undoubtedly help to resolve the ambiguities encountered with complex salt-rich ice matrices and allow a better characterisation of icy moons' oceanic and surface composition in the next decades.

2 Mass Spectrometric Fingerprints of Organic Compounds in Sulfate-Rich Ice Grains: Implications for Europa Clipper

2.1 Summary

The surface ice of Europa is known to contain high proportions of inorganic material that could heavily influence the compositional analysis of organic compounds in ejecta ice grains by the SUrface Dust Analyzer (SUDA) impact ionization mass spectrometer onboard NASA's Europa Clipper mission. We previously have analyzed the effects of NaCl [264, 316] on the mass spectral appearance of organic-rich ice grains. Here we present analogue experiments for SUDA simulating cation and anion mass spectra of organic-rich ice grains together with sulfates, one of the most abundant inorganic compounds on Europa's surface. Using the Laser Induced Liquid Beam Ion Desorption (LILBID) technique a diverse range of representative organic species in $MgSO_4$- and H_2SO_4-rich matrices at concentrations ranging from 0.01M to 1M were measured. Results show that mass spectrometric signatures of organic species can be detected in $MgSO_4$-rich and H_2SO_4-rich ice grains via molecular ions, although the mass spectral appearance changes from molecular ions to a range of adducts with Mg^{2+}, OH^-, HSO_4^- ions, and $MgSO_4$ and H_2SO_4 molecules depending on the matrix and the matrix concentration. Sensitivity to the organics is typically higher in cation mode than anion mode in both matrices. Due to suppression effects, the sensitivity to detect the organics decreases with increasing $MgSO_4$ concentration; but it does not decrease in H_2SO_4 matrices in cation mode. We establish generic rules for the detection of organics in Europan ice grains by SUDA, applicable to a wide range of organic species in complex ice matrices. The recorded mass spectra complement a spectral reference database for Europa Clipper and other ocean world missions.

2.2 Introduction

Subsurface oceans have been detected in several icy satellites in the outer Solar System, such as Europa [69, 51], Enceladus [317], Ganymede [318] and Callisto [50]. As potentially habitable environments they are at the center of attention of planetary exploration and astrobiology investigations [47, 319]. On Europa, there is intriguing evidence of erupting plumes [147] that might eject water ice grains from subsurface reservoirs to high altitudes. A similar plume has previously been observed at the south pole of Enceladus [116, 117, 99, 118]. Bombardment by micrometeorites also ejects ice particles from the surface, continuously supplying dust clouds around atmosphereless bodies such as the Galilean moons of Jupiter [233, 235].

The compositional analysis of such ice grains from Europa will be accomplished by the Surface Dust Analyzer (SUDA) [215] onboard NASA's upcoming Europa Clipper mission [213]. SUDA is an impact ionization time-of-flight mass spectrometer (TOF-MS) and the successor instrument of the Cosmic Dust Analyzer (CDA) [232] which detected water [320], salts [128, 124, 61] and organic material [308, 65, 66] in dust grains from Enceladus during the Cassini mission, thus characterising properties of an extraterrestrial water reservoir. SUDA will be able to detect both cations and anions at a high mass resolution ($m/\Delta m$ =200-250) in the mass range m = 1-500 u, and will potentially sample freshly ejected plume material at Europa, enabling the compositional mapping of geological surface features by analysis of surface ejecta [234, 321, 238, 237].

SUDA will be able to detect organic material encased in Europan ice grains. This material may originate from the subsurface ocean and be transported to the surface by tectonic processes (e.g., resurfacing) but it will also be exposed to surface conditions such as radiation processing and S-ion implantation and mixed with salts and other inorganic compounds present in the subsurface ocean and ice crust. Europa's subsurface ocean and surface ice are rich in salts, such as NaCl e.g., [179, 180] and sulfates e.g., [181, 182, 183]. Magnesium sulfates are likely some of the major salts in Europa's ice composition and, although exact concentrations are not yet constrained, estimates range from 0.04 to 4.2 mol/kg H_2O [197, 198]. Whereas their distribution has been broadly determined e.g., [184, 185], their origin is still debated. On the one hand, the Io plasma torus that interacts with and affects the surface of Europa [192, 193] was found to lack magnesium ions [198], suggesting that magnesium ions are likely to originate directly from the subsurface ocean [322]. Generally, sulfates could be

formed abundantly through the differentiation of a subsurface ocean and leaching of chondritic material [323]. On the other hand, they could be a radiation product of exogenic sulfur ions and magnesium salts already present on Europa's surface [196, 184]. Regions experiencing sulfur radiolysis may therefore contain particularly high concentrations of sulfate salts.

Europa's surface ice is exposed to substantial ionizing radiation due to the strong magnetosphere of Jupiter [209, 324]. Several studies have shown that irradiating water ice leads to the production of a variety of radiolytic products, such as H_2 and O_2 [76, 325, 326, 327]. The production of strong oxidants such as H_2O_2 and O_3 is expected on Europa [328, 329] but so far only H_2O_2 has been observed on Europa's leading hemisphere [184, 75]. Oxidation reactions are presumed to play a major role in the surface chemistry of Europa's ice [330]. Due to the bombardment of sulfur ions onto the surface, another expected product of radiolytic chemistry is sulfuric acid hydrate $H_2SO_4(H_2O)$ [75, 188, 189, 331]. Indeed, sulfuric acid hydrates mixed with water ice dominate the surface composition in the trailing hemisphere of Europa, as they are the main product of the surface radiolysis reactions [189, 184, 190, 191]. Recent ground-based observations at high spectral resolution have confirmed the presence of sulfuric acid on the trailing hemisphere [184, 151]. The concentration of H_2SO_4 in Europa's ice has been estimated to be up to 2.5–3.6 mol/kg H_2O [198], but these values are strongly location-dependent [190, 332].

Laboratory experiments reproducing the impact ionization mass spectra of icy dust grains as produced by SUDA- or CDA-type instruments have been conducted with the Laser Induced Liquid Beam Ion Desorption (LILBID) [254, 255] technique. This technique has been used to calibrate spaceborne mass spectrometers and reproduce the compositional variations seen in icy moons' water ice particles [253, 128, 65, 66]. LILBID analog experiments have also been conducted to investigate the mass spectral characteristics of different biosignatures, such as amino acids, fatty acids, peptides and bacterial material, as if enclosed in sampled water ice grains [263, 264, 265]. In both LILBID and impact ionization, the analyzed material is exposed to very high energy densities and undergoes a high degree of macroscopic and molecular fragmentation, leading to the formation of charged molecular fragment clusters detectable by time-of-flight mass spectrometry. In both cases, the chemical composition - and not the phase, i.e., liquid or solid – is key in the formation of molecular and elemental ions due to the very high energy density applied to the analyzed material [128, 61, 66]. The main difference between the populations of ions created by LILBID vs by impact ionization (for a similar composition of analyzed material) is due to differences in the electric field environment in which the ionization and the formation of molecular clusters and fragments occurs: ions are collected and rapidly accelerated towards the detector in spaceborne impact ionization mass spectrometers, while in LILBID ions drift through a field-free region after they are generated. The selection of ions crossing this field-free region at a certain speed therefore allows the simulation of the speed at which the impact cloud expands in spaceborne impact ionization mass spectrometers and with that the kinetic energy of the impact. This can be achieved by combining variations in laser power density with delay time [253].

Recently, the LILBID technique was used to investigate the mass spectral fingerprints of a wide range of organic compounds in NaCl-rich water ice grains [316] as present at Enceladus [128] and probably Europa [180]. We showed that despite high salt concentrations, organic material - depending on the NaCl concentration - can be detected via molecular peaks or sodiated and chlorinated adducts [316]. Matrix effects were shown to play an important role on the detectability of organics and were dependent on the structural and compositional properties of the organic compounds, including the presence of functional groups, and the salt concentration.

Building on these experiments [316], we here measured LILBID spectra of the same range of organic species (5-amino-1-pentanol, acetic acid, benzoic acid, butylamine, glucose, methanol, pyridine) in both cation and anion mode, to investigate their mass spectral signatures in 0.01, 0.1 and 1M concentration $MgSO_4$- and H_2SO_4-rich matrices, i.e., concentrations representative of those expected at the surface of Europa and similar as those used for NaCl matrices [316]. The goal of this work is to understand the interactions between salts or sulfuric acid and organics in simulated impact mass spectra of SUDA, for organic content on the order of several % in concentration. We here complement the general rules inferred to predict the mass spectral appearance of organic species in salt-rich ice grains with matrix compound specifically relevant on Europa's surface ($MgSO_4$ and H_2SO_4) for the analysis of ice grains by SUDA-type impact ionization mass spectrometers.

2.3   Experimental Section

The LILBID technique (Figure 21), used here to record mass spectra of the different solutions of organic compounds in $MgSO_4$- and H_2SO_4-rich matrices, is described in detail in Section I.4.2 (and by Klenner et al. [253]).

Solutions containing both an organic species and $MgSO_4$ or H_2SO_4 were prepared. The solutions were made in 18.2 MΩ.cm ultrapure water, to which was added either $MgSO_4$ or H_2SO_4 at different concentrations (0.01M [mol/L], 0.1M and 1M – i.e., concentrations of 1.2 g/L, 12 g/L and 120 g/L for $MgSO_4$ and of 0.98 g/L, 9.8 g/L, and 98 g/L for H_2SO_4, respectively). Seven organic species (Table 4), namely 5-amino-1-pentanol ($C_5H_{13}NO$), acetic acid ($C_2H_4O_2$), benzoic acid ($C_7H_6O_2$), butylamine ($C_4H_{11}N$), glucose ($C_6H_{12}O_6$), methanol (CH_4O), and pyridine (C_5H_5N), were measured individually. Among those, four species (acetic acid, glucose, methanol,
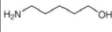
		5-amino-1-pentanol	Acetic acid	Benzoic acid	Butylamine	Glucose	Methanol	Pyridine
Formula		$C_5H_{13}NO$	$C_2H_4O_2$	$C_7H_6O_2$	$C_4H_{11}N$	$C_6H_{12}O_6$	CH_4O	C_5H_5N
Molecular weight (u)		103	60	122	73	180	32	79
Molecular concentrations (mmol/L)	All $MgSO_4$ matrices & 0.01M, 0.1M H_2SO_4	485	833	13.9	685	278	1563	633
	1M H_2SO_4 matrix	126	833	13.9	14	278	1563	633
pH in solution	H_2O	12.1	2.4	3.3	12.3	7.1	9.0	8.6
	0.01M $MgSO_4$	11.9	2.5	3.2	12.1	5.5	7.6	8.7
	0.1M $MgSO_4$	10.9	2.5	3.2	11.5	5.6	7.6	8.6
	1M $MgSO_4$	9.3	4.16	3.3	9.4	6.2	6.7	8.8
	0.01M H_2SO_4	12.0	2.0	2.1	12.2	1.9	2.0	6.8
	0.1M H_2SO_4	11.0	0.9	1.2	11.2	1.3	1.2	5.8
	1M H_2SO_4	0.4	0.2	0.8	0.4	0.2	0.8	0.8

TABLE 4. Organic species investigated in the LILBID experiments, their molecular weights, their molecular concentrations and the resulting pH values of the different matrix solutions investigated.

and pyridine) were measured at concentrations of 5 wt% in both matrices; two species (butylamine and 5-amino-1-pentanol) at reduced concentrations of 0.1wt% and 1.3wt% respectively when in 1 M H_2SO_4 due to the formation of precipitates; and one species, benzoic acid, measured at 0.17 wt% in all concentrations of both matrices as it is poorly soluble in water. The organic species we investigated cover a wide range of functional groups, namely: hydroxyl, azine, (aromatic) carboxylic acid, (aromatic) amine, and alkanolamine.

2.4 Results

We here present the results of the LILBID measurements of the organic species (Table 4) in $MgSO_4$- and H_2SO_4-rich matrices at 0.01, 0.1 and 1M $MgSO_4$ or H_2SO_4. Due to the high number of spectra recorded, only part of the data is presented in this manuscript and the supplementary material, with the remainder available in the LILBID database (https://lilbid-db.planet.fu-berlin.de). The same organic compounds were previously measured in pure water and NaCl matrices at similar concentrations [316].

2.4.1 Spectra of the $MgSO_4$ Background Matrix

The cation spectra of magnesium sulfate at 0.01M concentration (Figure 35) show a wide range of Mg-bearing cations: $[Mg(OH)]^+$, $[nMg+(OH)_{2n-1}]^+$ (i.e., $[2Mg+(OH)_3]^+$, $[3Mg+(OH)_5]^+$, $[4Mg+(OH)_7]^+$, $[5Mg+(OH)_9]^+...$), $[(MgSO_4)_{1-2}+H]^+$, $[Mg(OH)(MgSO_4)_{1-2}]^+$ and $[nMg+(OH)_{2n-1}+(MgSO_4)]^+$ species, with $n > 1$. All peaks corresponding to Mg-bearing cations show characteristic Mg isotope patterns (^{24}Mg, ^{25}Mg and ^{26}Mg with intensities of 79%, 10% and 11% respectively). The cation mass spectra of the 0.1M $MgSO_4$ solution
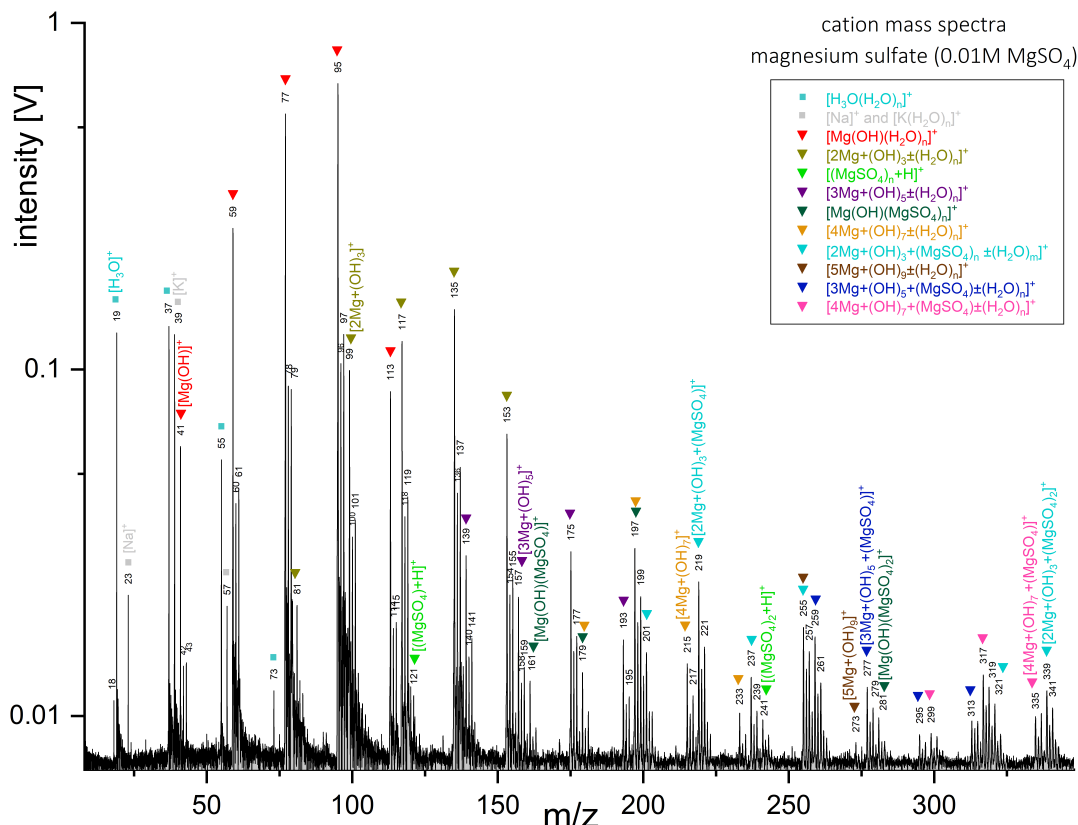
FIGURE 35. Baseline-corrected cation mass spectrum of magnesium sulfate (MgSO$_4$) at a concentration of 0.01M. The mass spectrum was generated with a delay time of 5.0 μs.

(Figure S51) show similar peaks of Mg-bearing cations, but at lower intensities and with a smaller number of water clusters. Fewer peaks were detected in 1M MgSO$_4$ (Figure S52), but [Mg(OH)]$^+$ and [nMg+(OH)$_{2n-1}$]$^+$ peaks are still identified. In anion mode, peaks from deprotonated sulfate ions [(H$_2$SO$_4$)$_n$-H]$^-$ and a range of magnesium-containing species were present in the mass spectra of 0.01M and 0.1M MgSO$_4$ (Figure 36 and Figure S53): [(MgSO4)$_n$ (OH)]$^-$, [(MgSO$_4$)$_n$ HSO$_4$]$^-$, and [(MgSO$_4$)$_n$ (H$_2$SO$_4$)$_m$ (HSO$_4$)]$^-$. In 1M MgSO$_4$ the intensities of these peaks were reduced. The sulfite anion [SO$_3$]$^-$, or the [S$_2$O]$^-$ anion, was tentatively detected at m/z 80 in the spectra of 0.1M and 1M MgSO$_4$ (Figure S53).

2.4.2 Spectra of Organic Compounds in MgSO$_4$-rich Matrix

Cation mode

In cation mode, protonated molecular peaks [M+H]$^+$ were detected for all organic species in 0.01M MgSO$_4$, for all species except benzoic acid in 0.1M MgSO$_4$ and only for 5-amino-1-pentanol, methanol and pyridine in 1M MgSO$_4$ (Table 5). These are the highest intensity peaks in the spectra of 5-amino-1-pentanol (Figure 37, Figures S54 and S55) and pyridine (Figure S56) at all MgSO$_4$ concentrations, and of butylamine in 0.01M (Figure S57) and 0.1M MgSO$_4$. A wide range of other organic cations containing Mg atoms were detected (Table 5, Figure 37, Figures S54-S62):

- [M-H+Mg]$^+$ cations for all species except 5-amino-1-pentanol, methanol and pyridine;
- [M+Mg(OH)]$^+$ cations for all species except methanol (but tentatively for butylamine);
- [M+2Mg+(OH)-2H]$^+$ (M+63u), [M+3Mg+(OH)$_2$-H]$^+$ (M+105u), [M+4Mg+(OH)$_5$-H]$^+$ (M+180u) cations in the spectra of acetic acid in 0.01M and 0.1M MgSO$_4$;
- [M+2Mg+(OH)$_3$]$^+$ and [M+3Mg+(OH)$_5$]$^+$ cations in the spectra of benzoic acid in 0.01M MgSO$_4$;
- [M(SO$_3$)+3H]$^+$, [M(SO$_3$)+Mg+H]$^+$, [M(SO$_3$)(MgSO$_4$)+Mg+H]$^+$ in the spectra of glucose in 0.01M MgSO$_4$;
- [M+Mg+(OH)$_2$+H]$^+$ and [2M+Mg+(OH)$_2$+H]$^+$ cations in the spectra of methanol in 0.01M MgSO$_4$.

The number and intensities of these peaks typically decreased with increasing MgSO$_4$ concentration (Table 5; e.g., Figures S58 and S59). Addition of MgSO$_4$ molecules onto organic cations was observed in 0.01M MgSO$_4$ for all species except butylamine and methanol, with cations such as [M(MgSO$_4$)+H]$^+$, [M(MgSO$_4$)+Mg-H]$^+$ and [M(MgSO$_4$) (OH)+Mg]$^+$ (Table 5). These species are suppressed at higher MgSO$_4$ concentrations and have
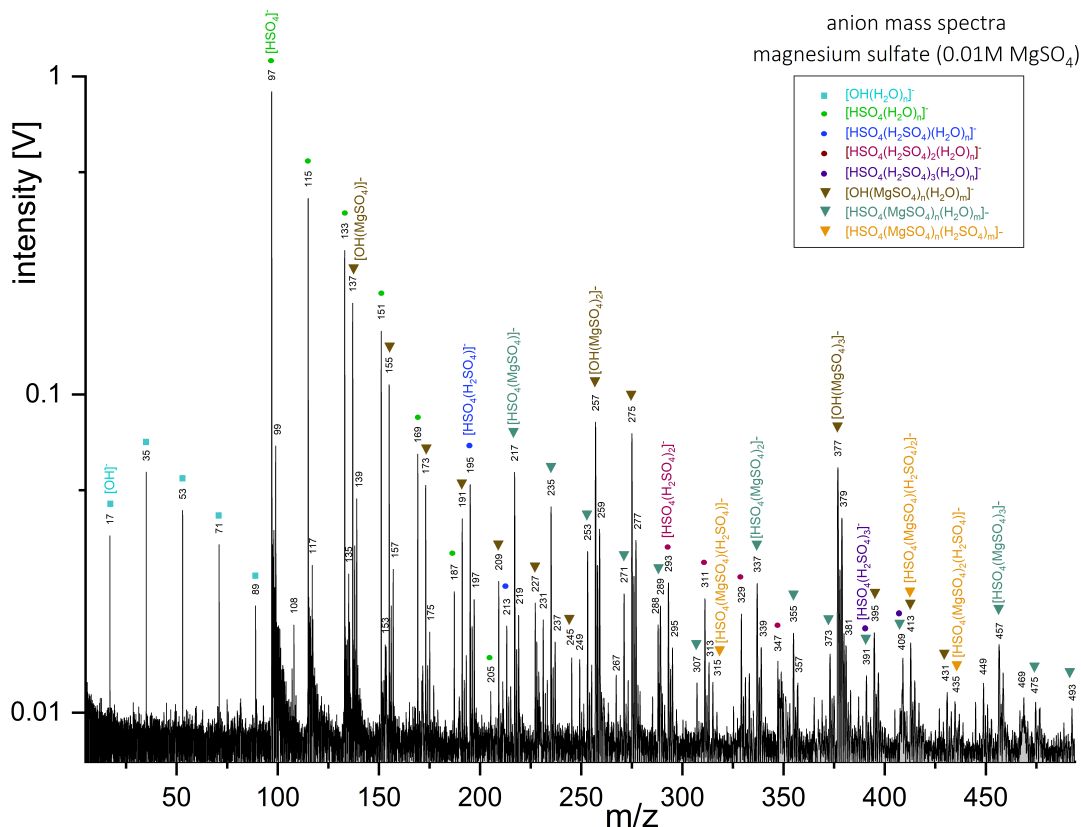
FIGURE 36. LILBID anion mass spectrum of MgSO$_4$ at a concentration of 0.01M. The mass spectrum was generated with a delay time of 6.3 µs. All peaks related to sulfate only are labeled with circles whereas all species containing magnesium sulfate are labeled with triangles.

			5-amino-1-pentanol	Acetic acid	Benzoic acid	Butylamine	Glucose	Methanol	Pyridine
0.01M MgSO$_4$	[M+H]$^+$	M+1 u	✓	✓	✓	✓	✓	✓	✓
	[M-H+Mg]$^+$	M+23 u		✓	✓	✓	✓		
	[M+Mg(OH)]$^+$	M+41 u	✓	✓	✓	?	✓		✓
	[nM+(H$_2$SO$_4$)+H]$^+$	M+99 u	✓	?	?				
	[M+(MgSO$_4$)+H]$^+$	M+121 u	✓	✓			✓		✓
	[M+(MgSO$_4$)+Mg-H]$^+$	M+143 u		?	✓		✓		
	[M+(MgSO$_4$)+Mg(OH)]$^+$	M+161 u	✓	?	✓		✓		✓
0.1M MgSO4	[M+H]$^+$	M+1 u	✓	✓		✓	✓	✓	✓
	[M-H+Mg]$^+$	M+23 u		✓		✓	✓		
	[M+Mg(OH)]$^+$	M+41 u	✓	✓		?			
	[nM+(H$_2$SO$_4$)+H]$^+$	M+99 u	✓						✓
	[M+(MgSO$_4$)+H]$^+$	M+121 u		✓					
	[M+(MgSO$_4$)+Mg-H]$^+$	M+143 u		?					
	[M+(MgSO$_4$)+Mg(OH)]$^+$	M+161 u	✓	?					
1M MgSO$_4$	[M+H]$^+$	M+1 u	✓					✓	✓
	[M-H+Mg]$^+$	M+23 u							
	[M+Mg(OH)]$^+$	M+41 u							✓
	[nM+(H$_2$SO$_4$)+H]$^+$	M+99 u							
	[M+(MgSO$_4$)+H]$^+$	M+121 u	✓						
	[M+(MgSO$_4$)+Mg-H]$^+$	M+143 u							
	[M+(MgSO$_4$)+Mg(OH)]$^+$	M+161 u							
Figures			S4, 4, S5	S8, S9	S10	S7	S12	S11	S6

TABLE 5. Characteristic detected peaks, and their respective m/z values, in cation mode for the investigated organics at 0.01M, 0.1M and 1M MgSO$_4$. In case of multiple species for a given concentration, the most prominent species are represented by bold checkmarks (✓). Question marks represent tentative identifications.
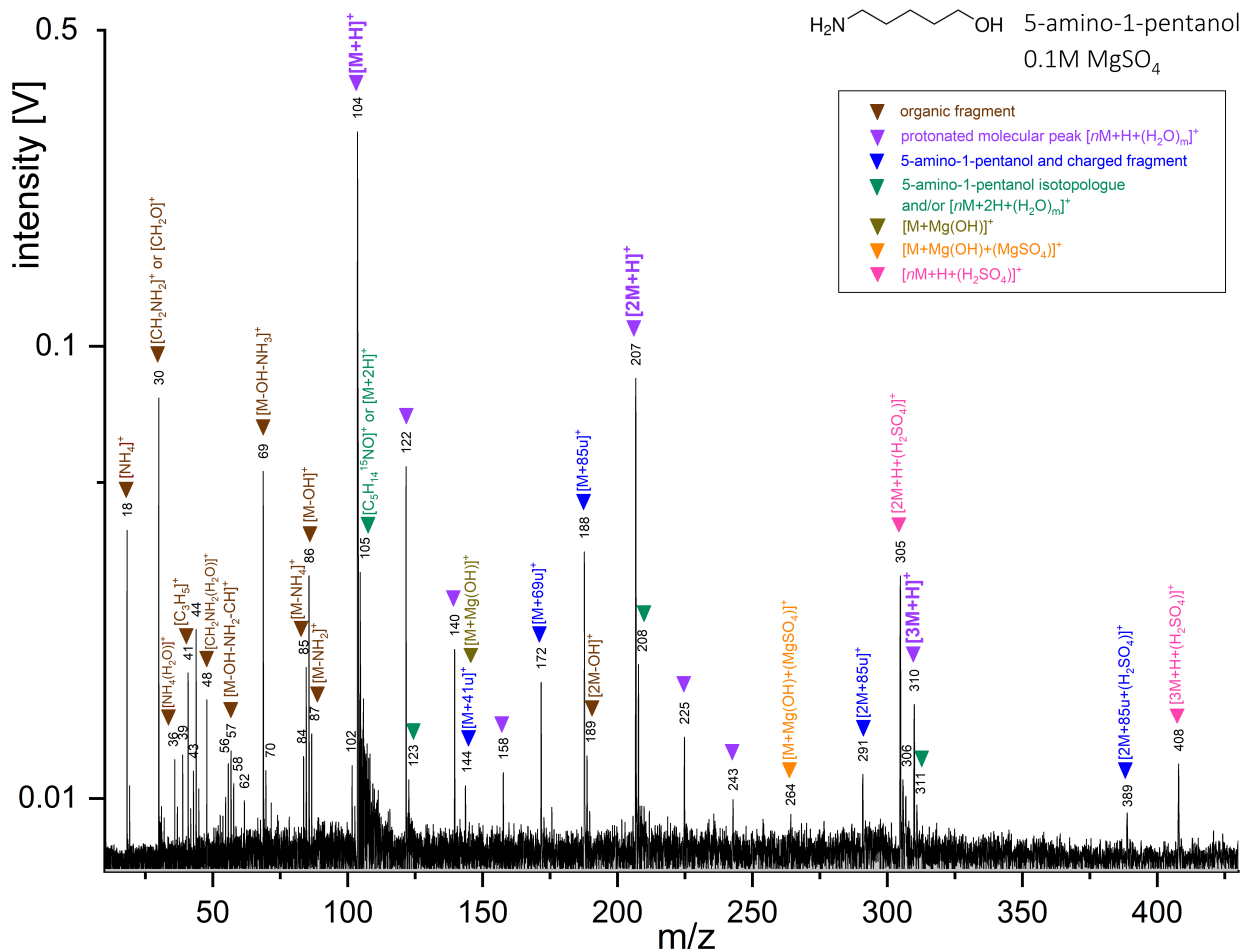
FIGURE 37. Cation mass spectrum of 5-amino-1-pentanol (concentration 5 wt%) in 0.1M magnesium sulfate (MgSO$_4$).The mass spectrum was generated with a delay time of 7.0 µs.

only been observed for 5-amino-1-pentanol and tentatively for acetic acid in 0.1M and 1M MgSO$_4$. Addition of H$_2$SO$_4$ molecules onto organic cations (i.e., $[n$M+(H$_2$SO$_4$)+H$]^+$ peaks with n $\geq$ 1) was observed for 5-amino-1-pentanol in 0.01M and 0.1M MgSO$_4$ (Figures 37, S4), for pyridine in 0.1M MgSO$_4$ and tentatively for acetic acid and benzoic acid in 0.01M MgSO$_4$. Adducts of molecular organic species and charged fragments thereof ($[$M+M-$x]^+$ with x a fragment of the organic species) or fragmented polymers of the organics ($[n$M-$x]^+$ with $n > 1$) were observed in the cation spectra of 5-amino-1-pentanol in 0.01M and 0.1M MgSO$_4$ (Figures S54, 4), butylamine in 0.01M and 0.1M MgSO$_4$ (Figure S57), acetic acid in 0.01M MgSO$_4$ (Figure S58), and glucose in 0.01M MgSO$_4$ (Figure S62).

Anion mode

In anion mode, deprotonated molecular peaks $[$M-H$]^-$ were detected for five organic species (acetic acid, benzoic acid, glucose, methanol and pyridine) in 0.01M MgSO$_4$, for three organic species (acetic acid, benzoic acid and glucose) in 0.1M MgSO$_4$ and only for acetic acid and benzoic acid in 1M MgSO$_4$ (Table 6; Figures S63-S67). Deprotonated molecular peaks have highly prominent intensities in the spectra of acetic acid and benzoic acid in all MgSO$_4$ concentrations (Figures S63 and S64), and in the spectra of glucose and methanol in 0.01M MgSO$_4$ (Figures S65 and S66). Ionization by addition of hydrogen sulfate anion onto organic molecules was observed with the detection of $[$M(HSO$_4$)$]^-$ peaks in the spectra of 5-amino-1-pentanol, acetic acid, glucose and methanol, and $[$M(H$_2$SO$_4$)(HSO$_4$)$]^-$ peaks for 5-amino-1-pentanol and acetic acid (Table 6; Figure 37, Figures S63, S65, S66 and S68). The intensity of the $[$M(HSO$_4$)$]^-$ and $[$M(H$_2$SO$_4$)(HSO$_4$)$]^-$ peaks typically decreased with increasing MgSO$_4$ concentration (e.g., Figure 38 and Figure S68, Table 6).

Addition of MgSO$_4$ molecules onto deprotonated organic anions ($[$M(MgSO$_4$)-H$]^-$ anions) has been observed for acetic acid, benzoic acid and glucose in 0.01M MgSO$_4$, and acetic acid, benzoic acid and glucose in 0.1M MgSO$_4$, and acetic acid in 1M MgSO$_4$ (Table 63, Figures S63-S65). Adducts of magnesium sulfate and sulfate molecules onto the organic species ($[$M(MgSO$_4$)(HSO$_4$)$]^-$ anions) were detected for glucose in 0.01M MgSO$_4$ (Figure S65). Other Mg-bearing species detected in the spectra of acetic acid in 0.01M and 0.1M MgSO$_4$ include
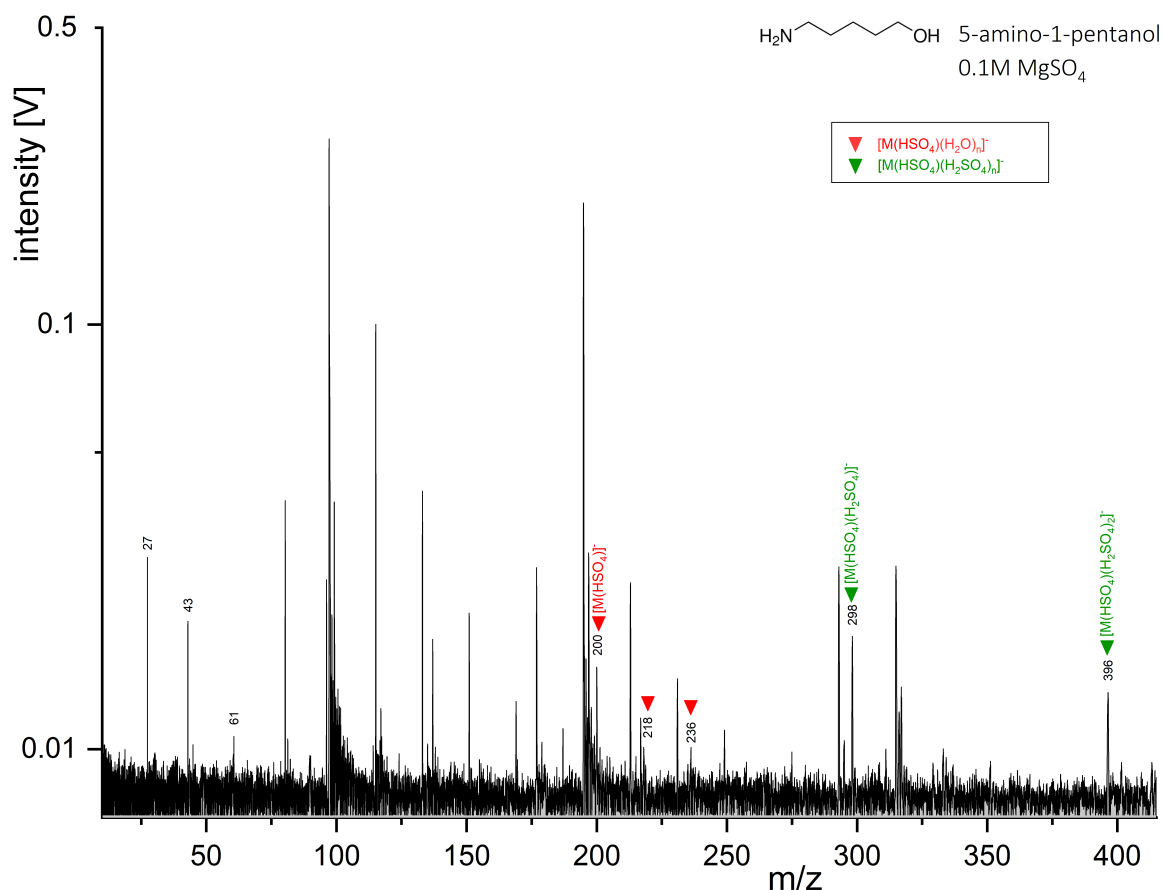
FIGURE 38. LILBID anion mass spectrum of 5-amino-1-pentanol (concentration 5 wt%) in 0.1M magnesium sulfate ($MgSO_4$). The mass spectrum was generated with a delay time of 7.3 µs. Unlabeled peaks originate exclusively from the $MgSO_4$ matrix.

			5-amino-1-pentanol	Acetic acid	Benzoic acid	Butylamine	Glucose	Methanol	Pyridine
0.01M MgSO₄	[M-H]⁻	M-1 u		✓	✓		✓	✓	✓
	[M(HSO₄)]⁻	M+97 u	✓	✓			✓	✓	
	[M(MgSO₄)-H]⁻	M+119u	✓	✓	✓		✓		
	[M(HSO₄)(H₂SO₄)]⁻	M+195 u	✓	✓					
	[M(HSO₄)(MgSO₄)]⁻	M+217 u					✓		
0.1M MgSO₄	[M-H]⁻	M-1 u		✓	✓		✓		
	[M(HSO₄)]⁻	M+97 u	✓	✓			✓		
	[M(MgSO₄)-H]⁻	M+119u		✓	✓		✓		
	[M(HSO₄)(H₂SO₄)]⁻	M+195 u	✓	✓					
	[M(HSO₄)(MgSO₄)]⁻	M+217 u							
1M MgSO₄	[M-H]⁻	M-1 u		✓	✓				
	[M(HSO₄)]⁻	M+97 u						✓	
	[M(MgSO₄)-H]⁻	M+119u		✓					
	[M(HSO₄)(H₂SO₄)]⁻	M+195 u							
	[M(HSO₄)(MgSO₄)]⁻	M+217 u							
Figures			S18, 5	S13	S14	S20	S15	S16, S19	S17

TABLE 6. Characteristic detected peaks, and their respective m/z values, in anion mode for the investigated organics at 0.01M, 0.1M and 1M $MgSO_4$. In case of multiple species for a given concentration, the most prominent species are represented by bold checkmarks (✓).

$[M(OH)_2+Mg-H]^-$, $[M(OH)_3+Mg]^-$, $[M(OH)_5+2Mg]^-$, $[2M+(OH)+Mg-2H]^-$ and $[2M+(OH)+(MgSO_4)+Mg-2H]^-$ anions (Figure S63). In the mass spectrum of glucose in 0.01M $MgSO_4$, a peak at m/z 261 (i.e., M+81u) was identified as $[M(HSO_3)]^-$ anion (Figure S65). In the mass spectra of methanol in 0.1M and 1M $MgSO_4$, a peak at m/z 111 (i.e., M+79u) was identified as $[M(SO_4)-OH]^-$ anion (Figure S69). Peaks at m/z 124 were

detected in the mass spectra of butylamine in 0.01M and 0.1M MgSO$_4$ (Figure S70), which correspond to [C$_2$H$_2$(H$_2$SO$_4$)]$^-$ or [CN(H$_2$SO$_4$)]$^-$, i.e., a sulfuric acid molecule added to butylamine fragments. An adduct of glucose and a charged fragment thereof ([M(C$_2$H$_3$O$_2$)]$^-$ at m/z 239 u) in the cation spectra of glucose in 0.01M and 0.1M MgSO$_4$ (Figure S65) was also identified.

Detection of organic fragments.

In summary, the number and intensity of fragment peaks typically decreased with increasing MgSO$_4$ concentration in both ion modes (Table S1, Figures S53, S55). Organic fragment cations (e.g., [M-OH-NH$_3$]$^+$) were detected for 5-amino-1-pentanol in 0.01M, 0.1M and 1M MgSO$_4$; for acetic acid, benzoic acid, butylamine and glucose in 0.01M and 0.1M MgSO$_4$; and pyridine in the 0.01M MgSO$_4$ (Table S3). In anion mode, organic fragments were detected for 5-amino-1-pentanol in 0.01M and 0.1M MgSO$_4$; for acetic acid, benzoic acid, butylamine and glucose at all MgSO$_4$ concentrations; and pyridine in 0.01M MgSO$_4$ (Table S4). No fragments were detected for methanol in any of the MgSO$_4$ matrices investigated in neither ion mode, except a tentative fragment of methanol with sulfuric acid [M(SO$_4$)-OH]$^-$ or [M(SO$_3$)-H]$^-$ (Figure S69).

2.4.3 Spectra of the H$_2$SO$_4$ Background Matrix

All cation mass spectra of sulfuric acid show strong water cluster peaks [H$_3$O(H$_2$O)$_n$]$^+$, as well as protonated sulfuric acid peaks [H$_3$SO$_4$]$^+$ and their water clusters [H$_3$SO$_4$(H$_2$O)$_n$]$^+$, with n defined as n $\geq$ 1 (Figures 39 and S71). In 0.01M H$_2$SO$_4$, water cluster peaks are much higher than those from sulfuric acid (Figure S71). In
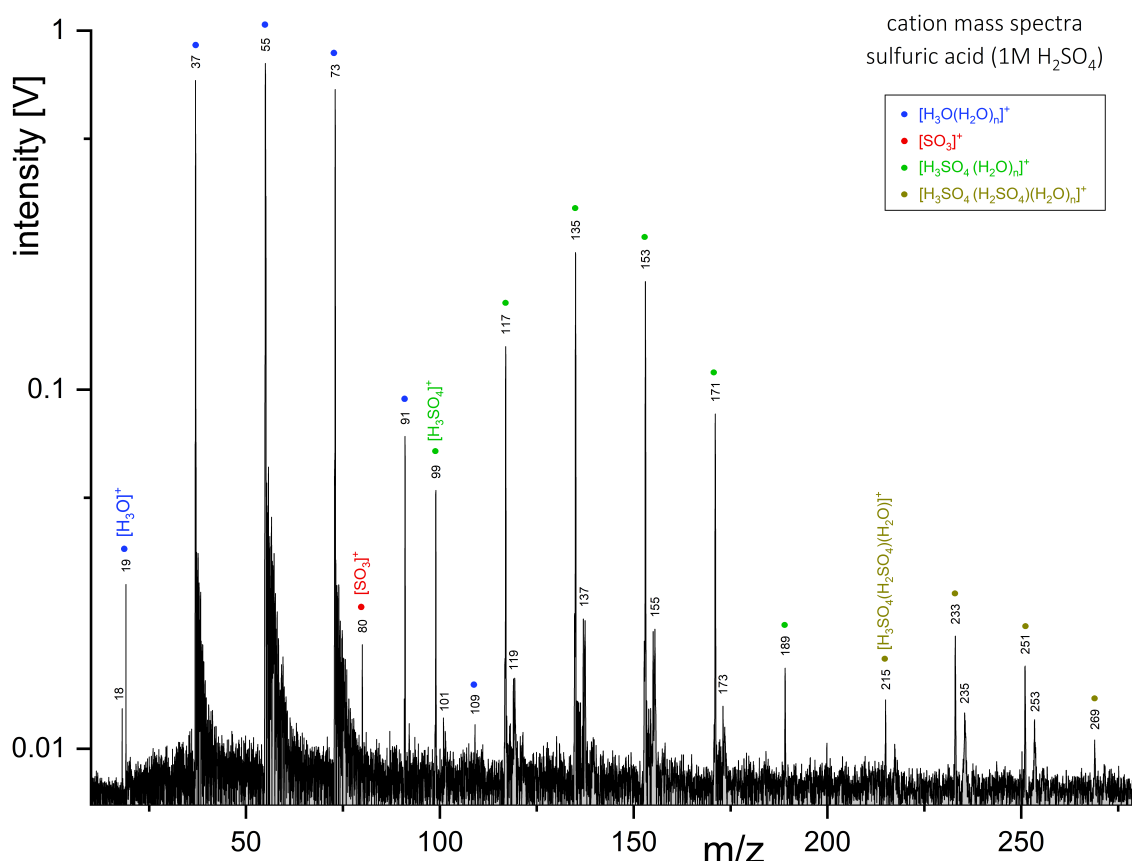
FIGURE 39. LILBID cation mass spectrum of sulfuric acid (H$_2$SO$_4$) at a concentration of 1M. The mass spectrum was generated with a delay time of 6.0 μs.

0.1M and 1M H$_2$SO$_4$, peaks corresponding to sulfuric acid polymers [(H$_2$SO$_4$)$_n$+H]$^+$ and their water clusters [(H$_2$SO$_4$)$_n$ (H$_2$O)$_m$ +H]$^+$ were detected (with m defined as m $\geq$ 1), with n increasing with the H$_2$SO$_4$ concentration of the sample (Figure 39). Peaks at m/z 80, tentatively identified as [SO$_3$]$^+$ cations (see Discussion), were detected in 0.01M, 0.1M, and 1M H$_2$SO$_4$ spectra.

In anion mode, all mass spectra of sulfuric acid show prominent deprotonated sulfuric acid peaks $[HSO_4]^-$, as well as sulfuric acid polymers $[(HSO_4)(H_2SO_4)_n]^-$ and their respective water clusters $[(HSO_4)(H_2SO_4)_n(H_2O)_m]^-$ (Figure 40 and Figure S72). The maximum number n of sulfuric acid molecules increased with the H_2SO_4 concentration, whereas the maximum number m of water clusters sulfuric acid polymers decreased with increasing H_2SO_4 concentration (Figure 40 and Figure S72). We did not detect any pure water cluster ions in any anion
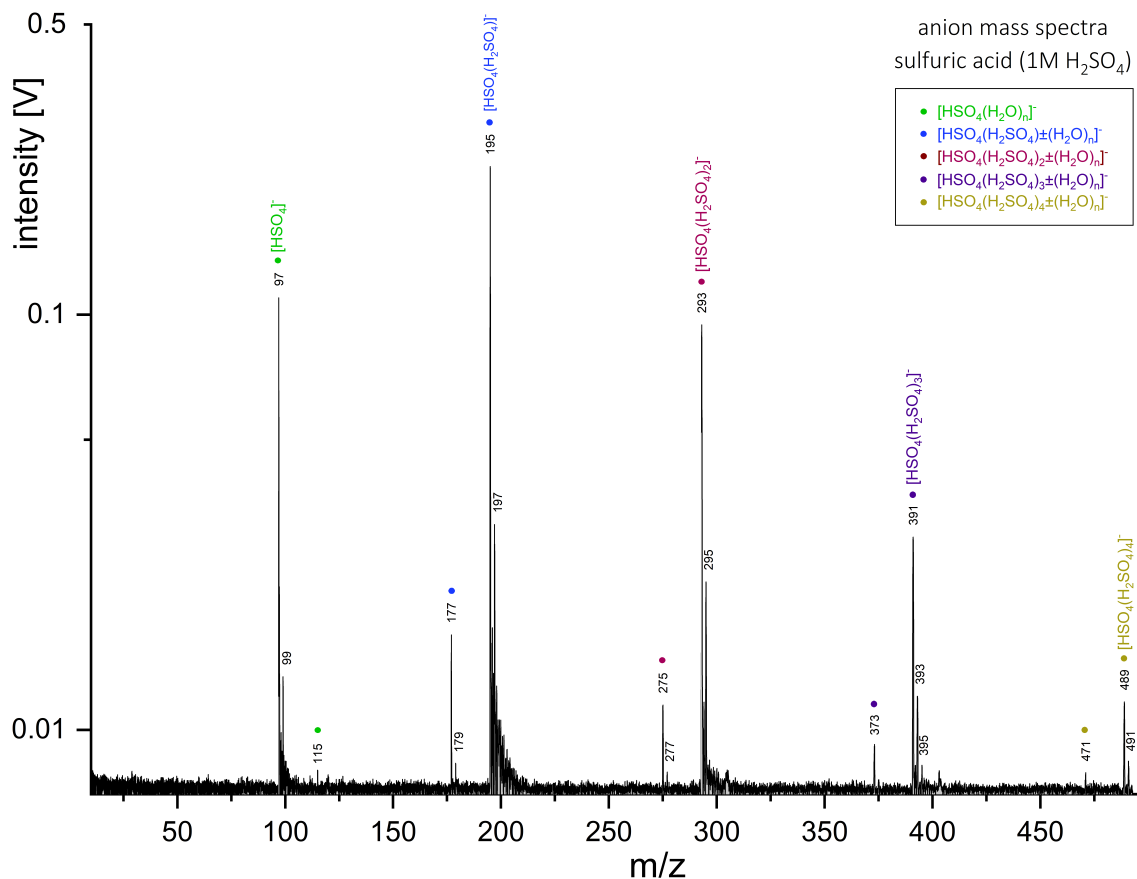
FIGURE 40. LILBID anion mass spectrum of sulfuric acid (H_2SO_4) at a concentration of 1M. The mass spectrum was generated with a delay time of 6.4 µs.

sulfuric acid spectrum, even at the lowest H_2SO_4 concentrations. The sulfite anion $[SO_3]^-$, or the $[S_2O]^-$ anion, was tentatively detected at m/z 80 in the spectra of 0.01M H_2SO_4 (Figure S72).

2.4.4 Spectra of Organic Compounds in H_2SO_4-rich Matrix

In cation mode, protonated molecular peaks $[M+H]^+$ were detected for all organic species at all H_2SO_4 concentrations (Table 7). Protonated molecular peaks are the highest intensity peaks in the spectra of 5-amino-1-pentanol, butylamine, methanol and pyridine, and are highly prominent in acetic acid, benzoic acid and glucose spectra (e.g., Figure 41 and Figures S73-S80), at all H_2SO_4 concentrations. We observed the addition of H_2SO_4 molecules onto protonated organic species ($[nM+(H_2SO_4)_m+H]^+$), with the intensity and number ($m \geq 1$) of H_2SO_4 molecules increasing with the H_2SO_4 concentration of the sample (e.g., Figure 41 and Figures S73 and S74). Such $[nM+(H_2SO_4)_m+H]^+$ peaks were detected for all organic species in 0.1M and 1M H_2SO_4 (Table 7), and for four species (5-amino-1-pentanol, butylamine, glucose, pyridine) in 0.01M H_2SO_4, and they have particularly high intensities for 5-amino-1-pentanol and butylamine (Figure 41, Figures S73, S74 and S80). The spectra of both glucose and methanol in 0.01M H_2SO_4 (Figures S78 and S79) show similar patterns of water clusters as those seen in the pure H_2SO_4 matrix spectra (Figure 39 and Figure S71).

5-amino-1-pentanol and butylamine both have much higher $[2M+(H_2SO_4)+H]^+$ peaks than $[M+(H_2SO_4)+H]^+$ peaks at all H_2SO_4 concentrations (Figure 41 and Figures S73, S74, and S80). This is also observed to a lower extent for acetic acid in 1M H_2SO_4 (Figure S76), pyridine in 0.01M and 0.1M H_2SO_4 (Figure S75), and methanol in 0.1M H_2SO_4.

|			5-amino-1-pentanol	Acetic acid	Benzoic acid	Butylamine	Glucose	Methanol	Pyridine
0.01M H₂SO₄	[M+H]⁺	M+1 u	**✓**	**✓**	✓	**✓**	**✓**	✓	**✓**
	[M+H+(H₂SO₄)]⁺	M+99 u	✓				✓		✓
	[2M+H+(H₂SO₄)]⁺	2M+99 u	✓				✓		✓
	[M+H+(H₂SO₄)₂]⁺	M+197 u							✓
0.1M H₂SO₄	[M+H]⁺	M+1 u	**✓**	**✓**	**✓**	**✓**	**✓**	**✓**	**✓**
	[M+H+(H₂SO₄)]⁺	M+99 u	✓	✓	✓	✓	✓	✓	✓
	[2M+H+(H₂SO₄)]⁺	2M+99 u	✓				✓		✓
	[M+H+(H₂SO₄)₂]⁺	M+197 u					✓		
1M H₂SO₄	[M+H]⁺	M+1 u	**✓**	**✓**	**✓**	**✓**	**✓**	**✓**	**✓**
	[M+H+(H₂SO₄)]⁺	M+99 u	✓	✓	✓	✓	✓	✓	✓
	[2M+H+(H₂SO₄)]⁺	2M+99 u	✓	✓		✓	✓	✓	✓
	[M+H+(H₂SO₄)₂]⁺	M+197 u	✓	✓		✓	✓		
Figures			S23, S24, 8	S26	S27	S30	S28	S29	S25

TABLE 7. Characteristic detected peaks and their respective m/z values in cation mode for the investigated organics at 0.01M, 0.1M and 1M H_2SO_4. In case of multiple species for a given concentration, the most prominent species are represented by bold checkmarks (✓).
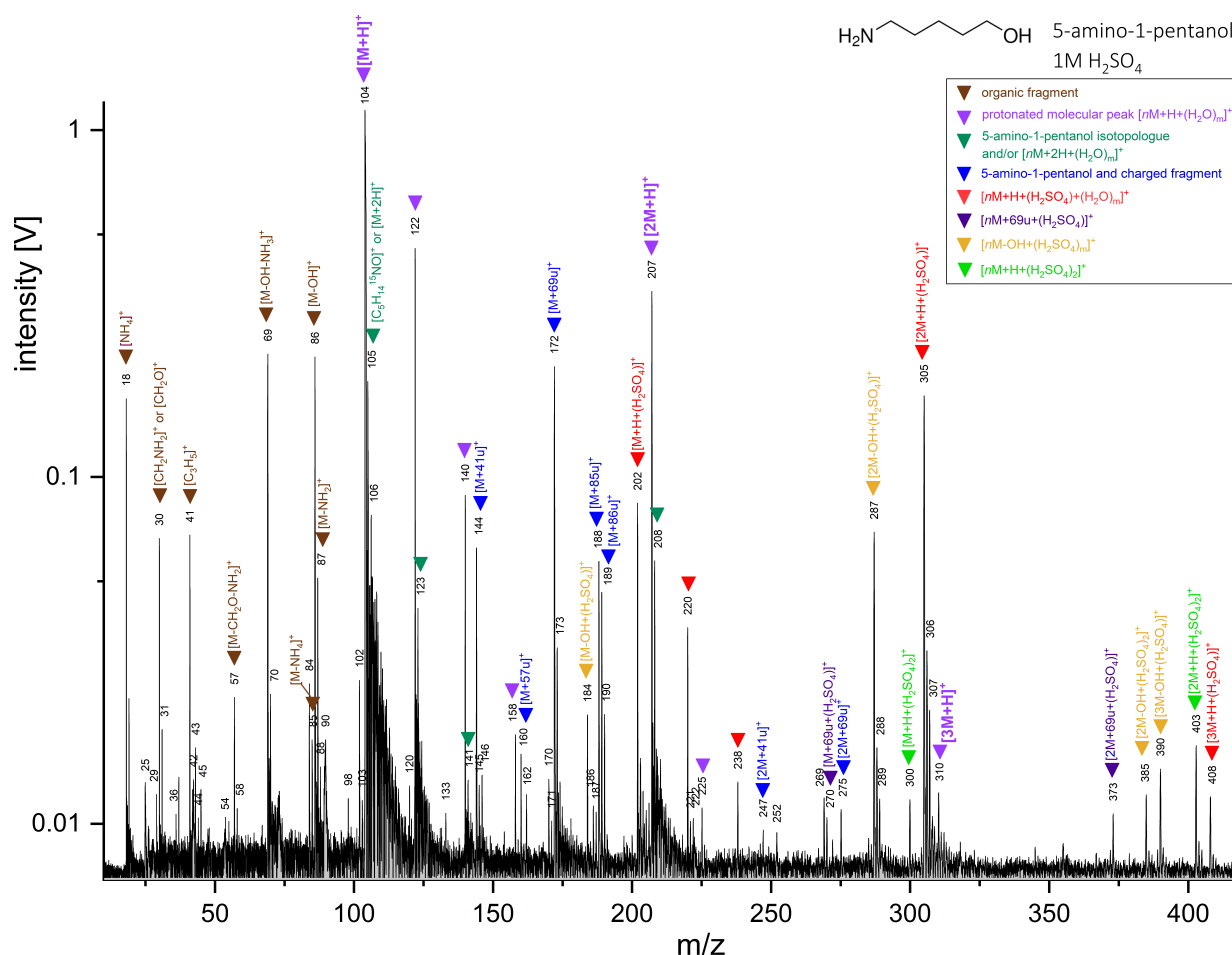
FIGURE 41. Cation mass spectrum of 5-amino-1-pentanol (concentration 5 wt%) in 1M sulfuric acid (H_2SO_4). The mass spectrum was generated with a delay time of 6.9 µs.

Adducts of the organic species and charged fragments thereof ($[M(M-x)]^+$ with x as a fragment of the organic species) or fragmented polymers of the organics ($[nM-x]^+$ with $n > 1$) were detected in the cation spectra of 5-amino-1-pentanol (e.g., $[M(M-OH-NH_3)]^+$; Figure 41, Figures S73 and S74), acetic acid (Figure S76), butylamine (Figure S80), and glucose (Figure S78) at all H_2SO_4 concentrations, and in the spectra of methanol in 0.1 and 1M H_2SO_4. Adducts of the organic species and charged fragments together with sulfuric acid ($[M(M-x)(H_2SO_4)]^+$)

74

were observed for 5-amino-1-pentanol in 0.1M and 1M H_2SO_4 (Figure 41 and Figure S74); butylamine, benzoic acid, and methanol in 1M H_2SO_4 (Figure S77).

In anion mode, deprotonated molecular peaks $[M\text{-}H]^-$ were detected for three organic species (5-amino-1-pentanol, acetic acid and benzoic acid; Table 8, Figures S81-S83). A higher number of organic species can be detected by their $[M(HSO_4)]^-$ peaks (Table 8): in 0.01M and 0.1M H_2SO_4, all organics except butylamine and pyridine; in 1M H_2SO_4, glucose and tentatively acetic acid. $[M(H_2SO_4)_n(HSO_4)]^-$ peaks were detected for 5-amino-1-pentanol, acetic acid, glucose and methanol in 0.01M and 0.1M H_2SO_4 (Table 8, Figures S64-S86), and for 5-amino-1-pentanol (Figure 37) and methanol in 1M H_2SO_4. The observable number, n, of polymers of sulfuric acid $[M(H_2SO_4)_n(HSO_4)]^-$ increased with the H_2SO_4 concentration (e.g., Figure 42 and Figure S31). $[M(HSO_4)(SO_3)]^-$ peaks have been detected for glucose in 0.01M and 0.1M H_2SO_4 (Figure S85); and for 5-
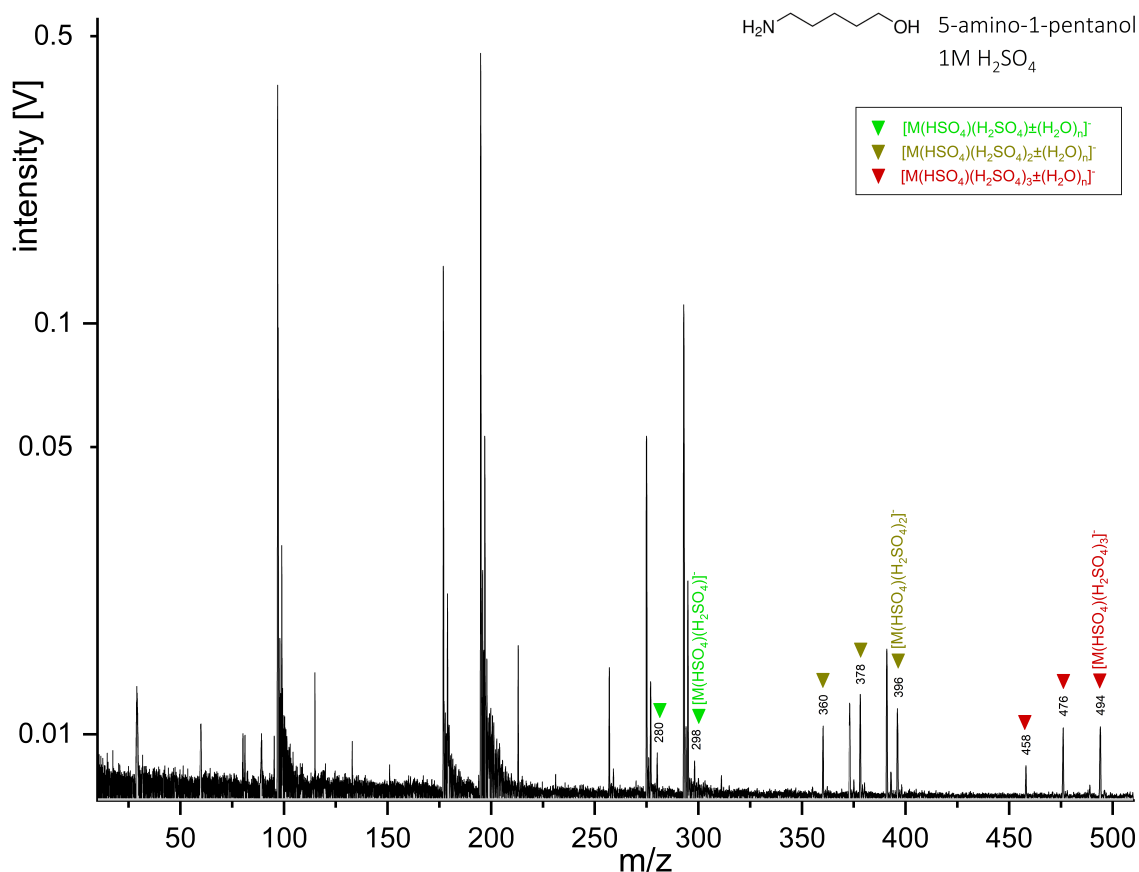
FIGURE 42. Anion mass spectrum of 5-amino-1-pentanol (concentration 5 wt%) in 1M sulfuric acid (H_2SO_4). The mass spectrum was generated with a delay time of 6.9 μs. Unlabeled peaks originate exclusively from the H_2SO_4 matrix.

amino-1-pentanol and glucose in 1M H_2SO_4 (Figure 42).

Detection of organic fragments.

Organic fragment cations were detected for 5-amino-1-pentanol, acetic acid, benzoic acid, butylamine and glucose at all H_2SO_4 concentrations, and for methanol and pyridine in 1M H_2SO_4 (Tables S3, S4). In contrast to the observations in the NaCl and $MgSO_4$ matrices, both the intensity and number of detected cationic fragments is usually unchanged or even increase with the H_2SO_4 concentration (e.g., Figure 41, Figures S73 and S74; Table S3). In anion mode, organic fragments were only detected for 5-amino-1-pentanol and butylamine in 0.01M H_2SO_4 (Table S4).

2.4.5 Summary of General Trends
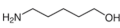
			5-amino-1-pentanol	Acetic acid	Benzoic acid	Butylamine	Glucose	Methanol	Pyridine
0.01M H₂SO₄	[M-H]⁻	M-1 u	✓	✓	✓				
	[M(HSO₄)]⁻	M+97 u	✓	✓	✓		✓	✓	
	[M(H₂SO₄)ₙ(HSO₄)]⁻	M+195 u	✓	✓		✓	✓		
0.1M H₂SO₄	[M-H]⁻	M-1 u							
	[M(HSO₄)]⁻	M+97 u	✓	✓	✓		✓	✓	
	[M(H₂SO₄)ₙ(HSO₄)]⁻	M+195 u	✓	✓		✓	✓	✓	
1M H₂SO₄	[M-H]⁻	M-1 u							
	[M(HSO₄)]⁻	M+97 u		?			✓		
	[M(H₂SO₄)ₙ(HSO₄)]⁻	M+195 u	✓			✓	?	✓	
	Figures		S31, S34, 9	S32	S33	S37	S35	S36	

TABLE 8. Characteristic detected peaks, and their respective m/z values, in anion mode for the investigated organics at 0.01M, 0.1M and 1M H_2SO_4. In case of multiple species for a given concentration, the most prominent species are represented by bold checkmarks (✓). Question marks represent tentative identifications.

Our results show that organic species can be detected in ice grains rich in magnesium sulfate and sulfuric acid, due to the formation of molecular ions, fragment ions and a range of adducts with Mg^{2+}, OH^-, HSO_4^- ions, and $MgSO_4$ and H_2SO_4 molecules. The mass spectral appearance of the organics fundamentally changes depending on the matrix ($MgSO_4$ or H_2SO_4) and the matrix concentration. Similar to NaCl matrices, strong suppression effects by the salt [264, 285] were observed in $MgSO_4$ matrices in both ion modes, i.e., the absolute number and intensities of organic-related peaks decrease with increasing $MgSO_4$ concentration (Tables 5, 6, Figure 38, Figures S54, S55, S68). Suppression effects were also observed in H_2SO_4 matrices in anion mode, but to a lower extent than in $MgSO_4$ matrices (Table 8, Figure 42, Figures S81, S84). However, no suppression effects were observed in H_2SO_4 matrices in cation mode. The intensity of suppression effects was characterised for organics in NaCl, $MgSO_4$ and H_2SO_4 matrices in both ion modes (Table 9). Detection limits were established in pure water matrix (Table 9) for the (de)protonated molecular peaks of all organic species in the most sensitive ion mode. Detection limits are estimated to be similar in pure water and in H_2SO_4 matrices for organics in cation mode.

Cation mode is generally more sensitive than anion mode to organics in $MgSO_4$ solutions (Tables 5 and 6), especially for butylamine and pyridine – two species for which the sensitivity is very low in anion mode. However, acetic acid and benzoic acid in $MgSO_4$ matrices are more easily detected in anion mode than cation mode. Cation mode is preferred over anion mode for the detection of all organic species in H_2SO_4 matrices because organic species can be unambiguously detected via protonated molecular peaks even at the highest sulfuric acid concentrations (Table 7).

In both $MgSO_4$ and H_2SO_4 matrices, interactions of the organic species with sulfates lead to the detection of $[M(HSO_4)]^-$ anions for four organic species (5-amino-1-pentanol, acetic acid, glucose and methanol). $[M(HSO_4)]^-$ anions were also detected in the spectra of benzoic acid only in H_2SO_4 solutions. These anion peaks are suppressed with increasing matrix concentration in both $MgSO_4$ and H_2SO_4 matrices. $[M(H_2SO_4)n(HSO_4)]^-$ anions (with $n \geq 1$) were detected in both $MgSO_4$ and H_2SO_4 matrices: for 5-amino-1-pentanol and acetic acid in $MgSO_4$ matrices, and all organics except benzoic acid and pyridine in H_2SO_4 matrices. The maximum number, n, of (H_2SO_4) molecules in $[M(H_2SO_4)_n(HSO_4)]^-$ peaks typically increased with increasing matrix concentration.

Adducts of organics with H_2SO_4 molecules were observed in both matrices and in both ion modes, although more frequently in H_2SO_4 matrices (e.g., $[M(H_2SO_4)+H]^+$ peaks were observed for one, and tentatively for two, organic species in $MgSO_4$ matrices, and for all organic species in H_2SO_4 matrices). In H_2SO_4 matrices, the intensities and number of $[M(H_2SO_4)_n+H]^+$ peaks typically increased with increasing H_2SO_4 concentrations, whereas these peaks are suppressed in $MgSO_4$ matrices with increasing $MgSO_4$ concentration. We observe $[nM+(H_2SO_4)_m+H]^+$ peaks for all species at H_2SO_4 concentrations $\geq 0.1M$, and for most species at an H_2SO_4 concentration of 0.01M. The $[nM(H_2SO_4)_m+H]^+$ peaks are especially prominent for basic species (i.e., 5-amino-1-pentanol and butylamine). In $MgSO_4$ matrices, adducts of $MgSO_4$ molecules with organic ions were observed in both ion modes, with the detection of $[M(MgSO_4)+H]^+$, $[M(MgSO_4)-H]^-$, $[M(MgSO_4)+Mg-H]^+$ and $[M(MgSO_4)(OH)+Mg]^+$ ions.

	LOD in pure H$_2$O matrix in best ion mode	NaCl			MgSO$_4$			H$_2$SO$_4$		
		Best ion mode	suppression effects		Best ion mode	suppression effects		Best ion mode	suppression effects	
			cation mode	anion mode		cation mode	anion mode		cation mode	anion mode
5-amino-1-pentanol	1 ppb [+] (10^{-7} wt%)	+	Low: 2 orders of magnitude	High: >2 orders of magnitude	+	Low: 1 order of magnitude	High: >2 orders of magnitude	+	None	Intermediate: 1 order of magnitude
acetic acid	<1 ppb* [-] (< 10^{-7} wt%)	-	Intermediate: 2 orders of magnitude	Low: 1 order of magnitude	-	High: >2 orders of magnitude	Low: 1 order of magnitude	+	None	Intermediate: 2 orders of magnitude
benzoic acid	1 ppb [-] (10^{-7} wt%)	-	High: >2 orders of magnitude	Low: 1 order of magnitude	-	High: >2 orders of magnitude	Low: 1 order of magnitude	+	None	High: >2 orders of magnitude
butylamine	<1 ppb* [+] (< 10^{-7} wt%)	+	Intermediate: 2 orders of magnitude	High: >2 orders of magnitude	+	High: >2 orders of magnitude	Intermediate: <1 order of magnitude	+	None	Intermediate: <1 order of magnitude
glucose	100 ppm [+] (10^{-2} wt%)	+	Low: 1 order of magnitude	High: >2 orders of magnitude	-	High: >2 orders of magnitude	Intermediate: 1 orders of magnitude	+	None	Intermediate: 1 order of magnitude
methanol	500 ppm [+] (5×10^{-2} wt%)	+	Intermediate: 1 order of magnitude	High: >2 orders of magnitude	+	Low: 1 order of magnitude	Intermediate: <1 order of magnitude	+	None	Intermediate: 1 order of magnitude
pyridine	1 ppb [+] (10^{-7} wt%)	+	Intermediate: 2 orders of magnitude	High: >3 orders of magnitude	+	None	High: >3 orders of magnitude	+	None	High: >3 orders of magnitude

* the exact LOD of acetic acid and butylamine in water matrix was not determined, but this value is lower than 1 ppb.

TABLE 9. Limits of detection (LOD) of (de)protonated molecular peaks of the organic species in pure water matrix with LILBID, and the estimated intensities of suppression effects for all organic species in the different matrices (NaCl, MgSO$_4$, H$_2$SO$_4$). The (+) or (-) in the first column gathering the LODs indicate the ion mode in which the LOD was measured – cation mode for (+) or anion mode for (-). No suppression effects were observed for organics in H$_2$SO$_4$ matrices in cation mode, and pyridine in MgSO$_4$ matrix. For all other matrices, the suppression effects are considered "low" when organics' (de)protonated molecular peaks were detected in all matrix concentrations (from 0.01M to 1M); "intermediate" when any organic ions (including organic fragments and clusters) were detected in all matrix concentrations; and "high" when no organic ions were detected at the highest matrix concentration of 1M. Additionally, the strength of the suppression effects was quantified - with order of magnitude accuracy - by comparing the ion abundances of the highest organic-bearing ion between the spectra of organics in the pure water matrix, and in the NaCl, MgSO$_4$, or H$_2$SO$_4$ matrices at 1M concentration.

Generally, a lower degree of fragmentation was observed in NaCl matrices as compared to MgSO$_4$ and H$_2$SO$_4$ matrices in cation mode for most species (i.e., 5-amino-1-pentanol, acetic acid, benzoic acid, glucose, pyridine). The absolute number and intensities of fragment peaks are higher in cation mode than anion mode for all organic species in all three matrices.

Comparing organic fragments detected in sulfate matrices of this work (Tables S3, S4) with fragments detected in NaCl matrices [316], the following trends can be established:
- **5-amino-1-pentanol**: the type and abundance of cationic fragments of 5-amino-1-pentanol detected in MgSO$_4$ and H$_2$SO$_4$ matrices were roughly similar in both matrices, but a much smaller number of fragments were detected in NaCl matrices.
- **Carboxylic acids**: highly prominent [M-OH]$^+$ fragments were detected in the mass spectra of both acetic acid and benzoic acid in MgSO$_4$ and H$_2$SO$_4$ matrices (at all matrix concentrations), whereas in NaCl matrices, they were detected only at low NaCl concentrations and at much lower intensities. Such peaks were also very prominent in the cation mass spectra of acetic acid and benzoic acid in pure water matrices [316].
  - o **Acetic acid**: more cationic fragments of acetic acid were detected in MgSO$_4$ matrices than in H$_2$SO$_4$ matrices, and very few in NaCl matrices. In the anion spectra, [CH$_3$]$^-$ fragments were detected in both MgSO$_4$ and NaCl matrices, but no fragments were detected in H$_2$SO$_4$ matrices.
  - o **Benzoic acid**: more cationic fragments of benzoic acid were detected in H$_2$SO$_4$ matrices than in MgSO$_4$ matrices, and very few in NaCl matrices. In anion mode, deprotonated benzene was detected in both MgSO$_4$ and NaCl matrices, but no benzoic acid fragments were detected in H$_2$SO$_4$ matrices.
- **Butylamine**: a decreasing trend with matrix composition was found in the number and intensities of cationic fragments of butylamine: MgSO$_4$ > H$_2$SO$_4$ > NaCl. In anion mode, only one anionic fragment was detected in H$_2$SO$_4$ matrices, whereas many more anionic fragments were detected in MgSO$_4$ and NaCl matrices.

Very prominent fragment peaks (e.g., $[C_2H_2]^-$ or $[CN]^-$ at m/z 26; Figure S20) were detected in the anion spectra of butylamine in $MgSO_4$ matrices at all $MgSO_4$ concentrations.

- **Glucose**: many cationic fragments of glucose, but no anionic fragments, were detected in H_2SO_4 matrices. Fewer cationic fragments were detected in $MgSO_4$ matrices than H_2SO_4 matrices, and even less in NaCl matrices. Anionic fragments were detected in $MgSO_4$ and NaCl matrices, with more fragments and at higher intensities in NaCl matrices.

- **Methanol**: the only methanol fragment detected was $[CH_3]^+$ in the 1M H_2SO_4 matrix, and together with sulfate $[CH_3(SO_4)]^-$ in 0.1M and 1M $MgSO_4$.

- **Pyridine**: small fragment peaks of pyridine were detected in the 1M H_2SO_4 matrix and in 0.01M $MgSO_4$ matrix in cation mode, and in the 0.01M $MgSO_4$ matrix in anion mode whereas no fragments were detected in the NaCl matrices.

2.5   Discussion

Suppression effects. Suppression effects are described as the decrease in the mass spectrometric response of an analyte due to matrix effects [333]. In the H_2SO_4 matrix, no ionization suppression effects occurred in cation mode (because the only cation species sulfuric acid releases in water is H^+), whereas suppression effects were observed in anion mode. The mass spectra of organics in $MgSO_4$ matrices show suppression effects with increasing matrix concentration, a phenomenon frequently seen for the detection of analytes in salt-rich matrices [264, 285]. This effect (in $MgSO_4$ matrices) is similar or stronger than that seen for the same organic compounds in NaCl matrices [316]. While detection limits can typically drop by orders of magnitude with high concentrations of salts, this effect is strongly compound-dependent and was mild for some organic species (e.g., for 5-amino-1-pentanol in 1M $MgSO_4$ as seen in Figure S55). The origins and mechanisms of ionization suppression in mass spectrometry are poorly understood. King et al. [334] showed that the presence of nonvolatile solutes is the main cause of ionization suppression in electrospray ionization (ESI) due to induced changes in the droplet solution properties. They suggested that nonvolatile materials inhibit the formation of small droplets and therefore the release of analytes into the gas phase. In the LILBID setup, the analyte is converted from the liquid water beam into gas phase ions, so coprecipitation of organic molecules (before the formation of gaseous ions) with nonvolatile sample components could be an efficient mechanism of ionization suppression. Gas phase reactions, such as acid-base neutralization or charge transfer to another gas phase species, could also lead to a loss of charge in the total ions created in the LILBID experiments. Both explanations are consistent with the fact that suppression effects are compound-dependent (i.e., they have different intensities for different organic species in a given matrix).

Fragmentation of the organic species. In $MgSO_4$ matrices, the number and the intensities of organic fragment peaks typically decrease with increasing $MgSO_4$ concentration in both ion modes (Table S3, Figures S53, S55), a trend similar to that observed in NaCl matrices [316]. This result reinforces our hypotheses that high salinity matrices might provoke the suppression of the fragmentation process (i.e., adducts of organics and salts are more stable than the pure organics) or the neutralization of charged fragments (or neutral fragments are produced). Sulfuric acid does not appear to inhibit the formation of cationic fragments since (1) we detected a high number of cationic fragments (Table S3), which in some cases increased with increasing H_2SO_4 concentration (2) almost all cationic fragments detected in water matrices were also detected in H_2SO_4 matrices. However, anionic fragments were only detected via infrequent, low amplitude, peaks and at low H_2SO_4 concentrations, probably due to a lower sensitivity to organic species with increasing H_2SO_4 concentration. Comparing the organic fragments detected in $MgSO_4$, H_2SO_4 and NaCl matrices (Section II.2.4.5), we observe a wide diversity of fragments varying with the matrix's nature and concentration. Each matrix induced different fragmentation patterns, e.g., the cation spectra of organics in NaCl matrices show fewer fragments compared to $MgSO_4$ and H_2SO_4 matrices and entirely inhibited fragmentation of hydroxyl groups in carboxylic acids (a typical cleavage of carboxylic acids; section II.2.4.5). Fragment peaks are also subject to suppression effects with increasing salt concentration in $MgSO_4$ and NaCl matrices. This variability of fragmentation patterns might be due to differences in the energetics of the fragmentation mechanisms induced by the varying matrix. For SUDA's analysis, many other factors than the matrix's composition will influence the level of fragmentation of organics embedded in ice grains, such as the impact velocity, the pH of the ice matrix and the spatial distribution of the organic species inside the ice grain [239, 335]. Schulze et al. [335] showed that in extreme saline ice (>1M), salting-out effects (i.e., a decrease in solubility at high salt concentrations leading to phase separation of organics, salts, and water) shield organic species from the impact energy, therefore further limiting fragmentation by alteration of the ice's mechanical behavior.

We detected $[M+M-x]^+$ and $[M+M-x]^-$ species where x is a fragment of the organic species (e.g., [2M-OH-NH_3]$^+$; Figure 37). They might form by fragmentation of an organic polymer rather than by addition of a

charged fragment onto a neutral organic molecule, because we observe fragmented polymers (e.g., ([3M-OH-NH$_3$]$^+$ in 5-amino-1-pentanol in 0.01M MgSO$_4$ matrix; Figure S54) but no addition of several charged fragments onto an organic molecule. We observed oxygen-carrying fragment ions in the spectra of 5-amino-1-pentanol, acetic acid, benzoic acid and glucose, and nitrogen-carrying fragment ions in the spectra of 5-amino-1-pentanol, butylamine and pyridine. Khawaja et al. [268] measured a range of aldehydes and ketones with the LILBID technique, and showed that oxygen-carrying fragment ions (e.g., [CHO]$^+$, [CH$_3$O]$^+$, [C$_2$H$_3$O]$^+$, [C$_2$H$_5$O]$^+$...) were also typically produced. Some fragments were observed in MgSO$_4$ and/or H$_2$SO$_4$ matrices, but not in the spectra of the organic species in pure water (e.g., [C$_2$H$_4$N]$^-$ was observed only for butylamine in MgSO$_4$ matrices, [NH$_4$]$^+$ for pyridine in 1M H$_2$SO$_4$ matrix, [C$_3$H$_3$]$^+$ or [HCCN]$^+$ for butylamine in H$_2$SO$_4$ matrices, [CHO]$^+$ for acetic acid in MgSO$_4$ matrices; Tables S3, S2). These species may therefore indicate that different fragmentation patterns appear due to compositional differences in the matrix; or they might be products of interactions of organic fragments with matrix compounds.

In mass spectrometry experiments, organic fragments can interact with ions from the matrix, thus forming for example sodiated or chlorinated fragments in NaCl matrices [314]. Although we did not detect sodiated or chlorinated fragments with LILBID (potentially because of the suppression of fragmentation processes or the neutralization of charged fragments2), we detected a few species formed by the interaction of organic fragments with ions from the MgSO$_4$ or H$_2$SO$_4$ matrix:
- a species consisting of a charged butylamine fragment and a sulfuric acid molecule ([C$_2$H$_2$(H$_2$SO$_4$)]$^-$ or [CN(H$_2$SO$_4$)]$^-$ at m/z 124) in the anion spectra of butylamine in 0.01 and 0.1M MgSO$_4$ matrices (Figure S70)
- [nM+(H$_2$SO$_4$)$_m$-OH]$^+$ and [2M+(H$_2$SO$_4$)$_m$-OH-NH$_3$]$^+$ cations in the spectra of 5-amino-1-pentanol in 1M H$_2$SO$_4$ matrix (Figure 41) • [C$_2$H$_4$N+Mg+SO$_3$]$^-$ anions in the spectra of 5-amino-1-pentanol in 0.01M H$_2$SO$_4$ matrix (Figure S81)
- a fragment of methanol with sulfuric acid [M(SO$_4$)-OH]$^-$ in MgSO$_4$ matrix.

Ion formation from organic/matrix interaction. In MgSO$_4$ solutions, we observed the addition of Mg^{2+} cations onto both deprotonated organic species ([M-H+Mg]$^+$) and together with OH$^-$ groups (e.g., [M(OH)$_2$+3Mg-H]$^+$, [M(OH)$_3$+2Mg]$^+$, [M(OH)$_2$+Mg+H]$^+$...). Magnesium adducts including [M+Mg-H]$^+$ cations have previously been observed by Han et al. [336] with electrospray ionization (ESI) mass spectrometry. As the LILBID ionization method tends to produce singly charged ions, and magnesium (Mg^{2+}) and sodium (Na$^+$) ions have different charges, the organic cations formed in MgSO$_4$ matrices are different from the species observed in NaCl matrices, where sodium adducts form with organic molecules via sodiation processes [264, 316, 298]. The replacement of structural elements by Na$^+$ cations (i.e., sodiation) seems to be more efficient than by Mg^{2+} cations, as protonated organic species typically dominate the cation spectra of MgSO$_4$ matrices whereas sodiated cations typically dominate in NaCl matrices [264, 316]. In organic molecules, it is easier to replace H$^+$ with Na$^+$ than with Mg^{2+} because Na$^+$ and H$^+$ have the same charge. Additionally, the larger size of Mg^{2+} ions compared to Na$^+$ slows down the attachment to organic molecules by steric hindrance.

In anion mode, we observe the addition of hydrogen sulfate anions HSO$_4$$^-$ to organic species (i.e., bisulfate adducts [M(HSO$_4$)]$^-$) in both MgSO$_4$ and H$_2$SO$_4$ solutions. Bisulfate adducts [M(HSO$_4$)]$^-$ were previously observed by other mass spectrometry methods e.g., with Matrix Assisted Laser Desorption Ionization (MALDI) [337] and with ESI-MS [338]. The formation of bisulfate adducts is comparable to the chlorination of organics (i.e., addition of a chloride anion) in NaCl matrices [316, 302, 303]. In both ion modes, we observed the addition of MgSO$_4$ and H$_2$SO$_4$ molecules to organic ions in MgSO$_4$ matrices and the addition of H$_2$SO$_4$ molecules in H$_2$SO$_4$ matrices. Addition of H$_2$SO$_4$ molecules is therefore a common characteristic pattern in sulfate-rich matrices. The addition of MgSO$_4$ molecules onto organic cations was observed for all organic species except butylamine and methanol, suggesting that linear molecules having few functional groups might be less prone to the addition of MgSO$_4$ molecules. The observed addition of NaCl and NaOH molecules in NaCl matrices [264, 316] is consistent with these mechanisms. The number of added H$_2$SO$_4$ and NaCl molecules often increased with increasing matrix concentration. Attachment of sulfuric acid molecules onto peptides and proteins have been previously reported by using ESI-MS [339], together with a decrease of the mass spectrometric signal.

In the cation spectra of the sulfuric acid matrix without organics (Figures 39, S71), cations at m/z 80 were identified as [SO$_3$]$^+$ as seen in the electron ionization spectra retrieved from the National Institute of Standards and Technology (NIST). The [SO$_3$]$^+$ cation can form by the loss of water from H$_2$SO$_4$. Although sulfuric acid is intrinsically different from salts, mass spectral similarities can be found in the spectra of organics in MgSO$_4$ and H$_2$SO$_4$ matrices. This is due to the presence of sulfates in both MgSO$_4$ and H$_2$SO$_4$ matrices, therefore inducing the formation of similar species in both matrices.

In the cation mass spectra of 5-amino-1-pentanol and butylamine in H$_2$SO$_4$ matrices (Figures 41, S73, S74, S80), and to a lesser extent in the spectra of 5-amino-1-pentanol in the MgSO$_4$ matrix (Figures 37, S54), we observe [2M+(H$_2$SO$_4$)+H]$^+$ in higher abundance than [M+(H$_2$SO$_4$)+H]$^+$. As shown in Figure 43, this could be because [2M+(H$_2$SO$_4$)+H]$^+$ cations preferentially form as [2(M+H)+(SO$_4$)+H]$^+$ cations (i.e., two

protonated organic molecules interact with one SO_4^{2-} anion, and the adduct thus formed is protonated), and $[M+(H_2SO_4)+H]^+$ cations are rather formed as $[(M+H)+(HSO_4)+H]^+$ cations (i.e., a protonated organic molecule interacts with HSO_4^-, and the adduct thus formed is protonated). This formation mechanism is explained
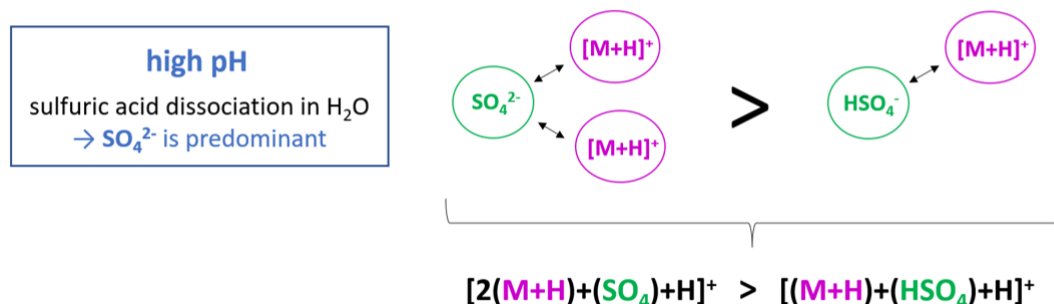

FIGURE 43. Possible interaction of basic organic species with sulfate ions, explaining the higher intensities of $[2(M+H)+(SO_4)+H]^+$ cations as compared to $[(M+H)+(HSO_4)+H]^+$ cations.

by the dissociation of sulfuric acid in water into different ions including hydrogen sulfate HSO_4^- and sulfate SO_4^{2-}: the sulfate ion has two negative charges making it more likely to interact with two other positively charged molecules. If sulfuric acid is predominantly present as SO_4^{2-}- (i.e., at high pH), then $[2(M+H)+(SO_4)+H]^+$ cations are more likely to form than $[(M+H)+(HSO_4)+H]^+$ cations. This mass spectral pattern was observed for the two most basic species we measured (i.e., 5-amino-1-pentanol and butylamine; Table 1).

The differences in sensitivity to the organics between different matrices is primarily due to the organics' properties (e.g., pH, the presence of functional groups). The molar concentration of the organic species in solution can also play a role (since the organic species were investigated at similar weight percentages but consequently at different molar concentrations; Table 1), but no direct correlation was observed between the sensitivity to an organic species and its molar concentration in solution. This suggests that the difference in molecular densities in the ionization region of the LILBID only plays a minor role in the sensitivity to the organics.

Liquid phase reactions. Liquid phase reactions can occur in solution when mixing organic species with salts or sulfuric acid. Reactions involving high concentrations of sulfuric acid played a significant role in our experiments, e.g., amines participated in acid-base reactions with sulfuric acid in solution and were partially precipitated as salts in the samples of butylamine and 5-amino-1-pentanol in H_2SO_4 matrices (especially at high H_2SO_4 concentrations). Matrices such as sulfuric acid could also induce liquid-phase fragmentation of the organic species. Although the formation of salt crystals in solution is thought to negatively perturb the mass spectrometric response of the analytes [334], no suppression effects were observed in cation mode despite the strong ion pairs formed between sulfuric acid and basic organic species, and all organics could be identified even in 1M H_2SO_4 matrices. High concentrations of strong acids in the matrix therefore do not restrict the detection of organics in cation mode with impact ionization mass spectrometers at the concentrations investigated.

General rules for the mass spectral appearance of organic species in Europa-like ice grains. In Napoleoni et al. [316], we established generic rules for the detection of organics in NaCl-rich matrices using LILBID, and by extension, impact ionization mass spectrometry. We here summarize the list of rules established with salts (NaCl, MgSO$_4$) and H_2SO_4 matrices, to provide a complete set for the detection of organics in ice grains of typical Europa composition with SUDA:
- **sulfuric acid**
  o sulfuric acid does not inhibit the detection of organics in cation mode even at high sulfuric acid concentrations. Indeed, all organic species in H_2SO_4 matrices show highly prominent protonated $[M+H]^+$ peaks at all H_2SO_4 concentrations (0.01M-1M). The cation mass spectra of all organics in H_2SO_4 matrices are quite similar to the spectra of those organics in pure water matrices, with additional signatures due to the addition of H_2SO_4 molecules onto organic cations with increasing H_2SO_4 concentration.
  o organic species in H_2SO_4 matrices typically form bisulfate adducts $[M(HSO_4)]^-$ and/or $[M(HSO_4)(H_2SO_4)_n]^-$ species, whereas deprotonated molecular peaks $[M-H]^-$ are only observed for a few species in low H_2SO_4 concentrations. Bisulfate adducts can also form in MgSO$_4$ matrices for some organic species. Generally, low pH

matrices (i.e., having a high concentration of H$^+$) are expected to inhibit the formation of deprotonated molecular peaks [M-H]$^-$.

- **NaCl and MgSO$_4$ salts**

    o in salt-rich matrices, protonated and deprotonated molecular peaks are usually suppressed with increasing salt concentrations, but organic species can still be detected via the presence of molecular ions and adducts with salt ions.

    o in salt-rich samples, organic species form adducts with Na$^+$ and Mg^{2+} ions, but adduct formation with these two ions occurs via different mechanisms and results in different ions with different mass spectral properties. Sodiation seems more efficient than Magnesium-adduct formation and can lead to the formation of polysodiated adducts for organic species that contain hydroxyl and/or amine functional groups (i.e., carboxylic or amidic protons are replaced by Na$^+$). The formation of Mg-adducts accompanies the loss of a proton or addition of a negatively charged group (e.g., OH$^-$), thus forming singly charged ionic species. A wide variety of Mg-adducts can be formed.

- **Fragments.**

We expect to detect a range of organic fragments in future SUDA mass spectra of Europan organic-rich ice grains, providing valuable structural information for the identification of parent organic species. Extensive fragmentation can be expected in sulfuric acid-rich ice grains (in cation mode), whereas the fragmentation will be limited with increasing matrix concentration in salt-rich ice grains and in sulfuric acid-rich ice grains in anion mode. The extent of the organic fragmentation will also be determined by the organic's structure and the presence of functional groups likely to be cleaved (e.g., hydroxyl, amine groups), and other parameters e.g., the impact velocity of the ice grain, the crystallinity of the water ice, and the spatial distribution of the organics and ions inside the water ice [239, 335].

The mass spectrometric signal of most organics is generally higher in cation mode than in anion mode. However, the response greatly depends on the organics' chemical family and physicochemical properties. The pH is an important parameter that influences the formation and detectability of organic molecular ions, adducts and fragments, together with other physicochemical factors such as the organics' molecular structure or the presence of functional groups. We established **characteristic mass spectral signatures of different organic families**:

- **carboxylic acids**

    o form highly prominent deprotonated molecular peaks [M-H]$^-$ in salt-rich matrices even at high salt concentration. Such peaks are also detected in H$_2$SO$_4$ matrices but with a lower intensity. Among the investigated compounds, this chemical family is the one to which anion polarity LILBID-MS is most sensitive in salt-rich matrices, although it is only moderately sensitive in H$_2$SO$_4$ solutions. Generally, we expect highly acidic compounds to be highly responsive in anion mode analysis thanks to a strong tendency to form deprotonated molecular peaks.

    o typically form highly prominent [M-OH]$^+$ fragment peaks, as observed here in MgSO$_4$ and H$_2$SO$_4$ matrices and by Khawaja et al. [267] in similar experiments with pure water matrix. This differs from the case of NaCl matrices where [M-OH]$^+$ peaks have a low intensity, but highly prominent disodiated [M-H+2Na]$^+$ peaks are observed [316].

    o typically form a range of highly prominent Mg-adduct cations (e.g., [M-H+Mg]$^+$, [M+Mg+OH]$^+$...) in MgSO$_4$ matrices.

- **N-bearing organics**

    o produce abundant characteristic peaks in cation mode in MgSO$_4$ and H$_2$SO$_4$ matrices, with highly prominent [M+H]$^+$ peaks, and have a moderate response in NaCl matrices.

    o these compounds have a much better response in cation mode than in anion mode in all investigated matrices (pure H$_2$O, NaCl, MgSO$_4$, H$_2$SO$_4$).

- **high pH organics** typically form highly prominent [2M+H+H$_2$SO$_4$]$^+$ peaks in H$_2$SO$_4$ matrices.

- **aromatic rings** in organic species typically undergo a low degree of fragmentation, as seen for example with benzoic acid fragmenting to form highly prominent peaks of protonated benzene in H$_2$SO$_4$ matrices and of deprotonated benzene in MgSO$_4$ matrices.

Implications for Europa Clipper. SUDA's measurements will allow a compositional mapping of the surface by trajectory reconstruction of the ejecta particles [237, 238] providing accurate locations of measured/interpreted compositions. Together with the potential identification of organics, the analogue spectra presented here and in Napoleoni et al. [316] will help to determine the concentrations of NaCl, MgSO$_4$ and H$_2$SO$_4$ on the surface, by comparing the presence and relative abundances of ions in SUDA's mass spectra.

As Europa's trailing hemisphere is likely dominated by sulfuric acid hydrate (a product of surface radiolytic chemistry e.g., [184, 188, 189]), SUDA's measurements in cation mode in this hemisphere, with potentially lower

salt concentrations, should undergo no suppression effects and therefore the assessment of organics on Europa's surface should be of high sensitivity and quality.

Europan ice grains are likely to have a more complex composition than the compositions investigated here, i.e., they may contain a variety of salts and organics instead of a binary mixture of species. In matrices composed of complex mixtures, information can be deduced from mass spectral characteristics such as isotope patterns to help reduce ambiguities due to interferences. For example, for an organic species of molecular mass M, the $[M-H+Mg]^+$ and $[M+Na]^+$ cations have the same mass (M+23u). In the case of $[M-H+Mg]^+$, these two species can be differentiated from each other by Mg-isotope peaks at M+24u and M+25u at characteristic intensities. The identification of characteristic fragments could also help to constrain ambiguous identifications of organic species, as shown in this work by the identification of fragmentation patterns for typical functional groups.

The LILBID setup simulates different impact speeds of ice grains onto impact ionization mass spectrometers' detectors by adjustment of the laser power density and ion extraction parameters [253]. The analogue mass spectra presented here were recorded with laser intensities of 95% to 100% and delay times of the gating system of 5.0 μs to 9.3 μs, which is representative of a speed regime of around 4 to 10 km/s. This speed regime includes the sampling speeds previously recommended [239, 263] for a maximum sensitivity to organic species and biosignatures (4 to 6 km/s). The speed of SUDA flybys is planned to be between 4 and 5 km/s [238].

The limits of detection (LODs) of organics in pure water matrix (Table 6) established in this work and the inferred suppression effects are a good approximation for SUDA or similar space detectors. In fact, detection limits of these space instruments are expected to be improved by at least one magnitude compared to our laboratory setup by the use of more efficient ion detectors (SUDA has a much higher dynamic range and therefore a higher sensitivity than the LILBID-ToF used here).

The results of our laboratory analogue experiments are applicable to other ocean worlds visited by Europa Clipper. For example, the icy surface of Ganymede is thought to contain large proportions of sulfuric acid and salts, likely sulfates [340]. Sulfates might be recurring components of icy ocean worlds, as they can be dominant products formed through the differentiation and evolution of subsurface oceans [341]. Sulfuric acid hydrates are thought to be generally abundant material on the surface of the Galilean moons due to their formation mechanisms [342]. The analogue mass spectra recorded with the LILBID experiment are stored in a database (https://lilbid-db.planet.fu-berlin.de) [259] that supports both Europa Clipper and the development of future ocean world missions, such as the proposed mission concept Enceladus Life Finder (ELF) [141], with the Enceladus Ice Analyzer (ENIA) [143] onboard.

Relevance for biosignature detection. Our analogue experiments established rules for the detection of organic material in Europan ice grains and include organic species that are relevant to astrobiology – e.g., sugars and N-heterocycles which play essential roles in all known biological processes [286, 287, 288]. The range of investigated organic species cover relevant functional groups for astrobiological investigations of icy moons, since oxygen- and nitrogen-bearing as well as aromatics compounds have been detected in Enceladean ice grains [65, 66]. The experiments covered general classes of organic compounds in a generic approach, so that results are potentially applicable to a variety of diverse agnostic biosignatures. Previous LILBID experiments targeting terrestrial biosignatures were conducted with bacterial extracts, amino acids, fatty acids and peptides and showed that these materials are detectable by SUDA-type mass spectrometers even at low concentrations [264, 263, 265]. The rules established here could help the detection of more, and potentially yet unknown, organic biosignatures of alien lifeforms.

2.6   Conclusion and Outlook

Europa's ocean and ice crust are expected to contain high proportions of non-water constituents such as sulfates and sulfuric acid [181, 182, 196, 183, 184, 189, 190]. In this work, we simulated the mass spectra of organic-rich ice grains mixed with these compounds as expected to be produced by SUDA-type impact ionization mass spectrometers. We performed analogue experiments with the LILBID technique and measured seven organic species, representative of a wide range of chemical families, in magnesium sulfate and sulfuric acid liquid matrices at 0.01M, 0.1M and 1M concentrations.

Our results showed that SUDA will be more sensitive to the majority of the measured organics and their fragments in cation mode than in anion mode. The higher sensitivity in cation mode is particularly enhanced for sulfuric acid matrices (i.e., no suppression effects were observed in cation mode and the organic signal was as high as in pure water). The reason is that the only cation species sulfuric acid releases in water is H^+, whereas salt matrices release cations such as alkali metals (e.g., Na^+) which induce suppression effects. A better

sensitivity in cation mode than anion mode was also previously found for organics in NaCl matrices [316].

The cation mode enhanced sensitivity to organics in sulfuric acid matrices may serendipitously serve the Europa Clipper observations well. Endogenous organics should be associated with oceanic salts, such as NaCl and $MgSO_4$, and thus we predict that if organics are to be found on Europa, they would likely be associated with those salts. Conversely, sulfuric acid is an exogenous radiolytic product and there is no a priori reason to expect a direct association with endogenous organics. In addition, the radiolytic processing that generates sulfuric acid may also modify any organics that are present [343]. As a result, it is reasonable to predict that lower concentrations of organics might be associated with sulfuric acid-rich regions, relative to salt-rich regions. Thus, SUDA's enhanced organic sensitivity in cation mode to organics associated with sulfuric acid is advantageous, given the above considerations for the Europan environment. Importantly, we emphasize the necessity of both ion modes in spaceborne impact ionization mass spectrometers to cover a wide range of organic families (e.g., anion mode is more sensitive to non-polar compounds such lipids). Both SUDA [215] and the Enceladus Ice Analyzer instrument (ENIA) [143], in a proposed astrobiology mission concept to Enceladus (Enceladus Life Finder)[141], will be capable of detecting cations and anions.

Our experiments show that the detection of organic species in ice grains by SUDA can be possible despite the potentially complex inorganic ice matrices. Suppression effects reduce the sensitivity to the organics in the presence of Na-chlorides [316] and Mg-sulfates, but not in the presence of sulfuric acid. We established generic rules applicable to a wide range of organic species, which may allow the discovery of organic biosignatures in Europan ice grains. This study provides valuable experimental context for the interpretation of impact ionization mass spectra of SUDA-type instruments at relevant impact speeds, and for space mission planning (e.g., use of cation or anion modes, compositional locations to target). This work will also significantly enhance our ability to interpret the origin and evolution of organic material on Europa, possibly providing insights into hydrothermal sources in the subsurface ocean, interactions with salts and inorganic material, transport from the subsurface ocean to the surface and lastly modification via surface processes such as irradiation by magnetospheric particles. These processes may all be part of the pathway of organic material toward finally be detected in a dust cloud of ice particles by the Europa Clipper mission.

III Probing the Oxidation State of Ocean Worlds with SUDA: Fe (II) and Fe (III) in Ice Grains

1 Summary

Characterising the geochemistry of Europa and Enceladus is a key step for astrobiology investigations looking for evidence of life in their subsurface oceans. Transition metals [3] with several oxidation states, such as iron, may be tracers of the oxidation state of icy ocean moon interiors. Their detection, and the characterisation of their oxidation states, on the moons' (plume) ice grains would bring valuable new information about the geochemistry of both the subsurface oceans and surface processes. Impact ionization mass spectrometers such as the SUDA instrument onboard Europa Clipper can analyze ice grains ejected from icy moons' surfaces and detect ocean-derived salts therein. Here we record mass spectra analogues for SUDA using the Laser Induced Liquid Beam Ion Desorption (LILBID) technique for Fe^{2+} and Fe^{3+} salts (both sulfates and chlorides). We show that impact ionization mass spectrometers have the capability to detect and differentiate ferrous (Fe^{2+}) from ferric (Fe^{3+}) ions in both cation and anion modes owing to their tendency to form distinct ionic complexes with characteristic spectral features. Peaks bearing Fe^{3+}, such as $[Fe^{3+}(OH)_2]^+$ and $[Fe^{3+}(OH)_a Cl_b]^-$ are particularly important to discriminate between the two oxidation states of iron in the sample. The recorded analogue spectra may allow the characterisation of the oxidation state of the oceans of Europa and Enceladus with implications for hydrothermal processes and potential metabolic pathways for lifeforms in their subsurface oceans.

2 Introduction

The subsurface oceans of several icy moons (e.g., Enceladus and Europa) are in direct contact with their silicate interiors, making them some of the most likely candidates in the Solar System to support habitable conditions (e.g., [166, 344, 345]) and therefore compelling targets in the search for life beyond Earth. A better understanding of the geochemistry of icy moons' subsurface oceans is needed for astrobiology investigations looking for traces of life there. Icy moons' surfaces hold clues to the composition of their subsurface oceans, as they are shaped by both internal processes (e.g., resurfacing, plume activity) and external processes (e.g., space weathering). Their characterisation is key to understanding icy moons' evolution over geological timescales as well as their current habitability.

The subsurface ocean of Enceladus, one of the moons of Saturn, is presently the best characterised extraterrestrial ocean in the Solar System and accessible owing to the active plume at its south pole which ejects water vapor and ice grains into space [120, 118, 346, 347]. Enceladus' ocean is global, with an ice shell decoupled from its core and heated at the ocean–core interface [348, 53], where hydrothermal reactions occur between the porous chondritic bedrock and percolating oceanic water [67, 130, 64, 48]. The material detected from the plume (e.g., silica nanoparticles and molecular hydrogen [130, 64]) is consistent with the presence of alkaline, Lost city type hydrothermal vents, with exothermic serpentinization reactions between sea water and rocks [134]. The detected molecular H_2 is thought to be a major species of the plume [64], suggesting an overall reducing Enceladus ocean. The ocean is rich in salts including sodium chlorides, carbonates [128], and phosphates [61] and has a pH estimated to be around 8.5 – 10.5 [131, 128, 67, 68, 349]. It also contains a variety of organic molecules, including high molecular mass (> 200 u) refractory insoluble organic material [65] and low molecular mass (< 100 u) volatiles including various moieties bearing oxygen, nitrogen, aryl groups [66] as well as tentative alkene and acyl groups [262].

---

[3]Transition metals are the chemical elements in the d-block of the periodic table (groups 3 to 12).

Europa, one of the Galilean moons, also possesses a global salty ocean [50, 69], which lays beneath a 3 – 47 km ice shell (e.g., [206, 350]) and may be communicating material to the surface through plume activity or other forms of upwelling [147, 170, 171, 202, 351, 176]. Europa likely contains a solid iron-rich metal core [272]. Its subsurface ocean could be anoxic or even significantly oxygenated [74], and the surface ice is rich in salts including chlorides (e.g., [179, 180]) and sulfates (e.g., [181, 182, 196, 183]). Its young surface age ($\sim 40 - 90$ My [352]) implies that recent endogenic resurfacing events could provide material from the subsurface ocean onto the surface, potentially including organic material. This material may originate from hydrothermal systems, which may be present due to the considerable heat generated by tidal interactions between Europa, Jupiter and the other Galilean satellites, and transmitted through the liquid ocean [73, 72]. Hydrothermal plumes may be implicated in the formation of chaos terrains by melting or by inducing convection in the ice shell [353]. Chaos terrains such as Thrace Macula are prime targets of the Europa Clipper and JUICE missions, as they may provide the freshest material for sampling by future spacecraft [163].

The detection and quantification of dissolved salts in icy moons' subsurface oceans can provide information about water-rock interactions, which are necessary for habitability, and the geochemical reactions involved. Enceladus' core is thought to have a composition close to CI or CM carbonaceous chondrites [130], and Europa close to L/LL-type chondrites [354]. Both moons' interiors should therefore host a range of iron-bearing minerals including phyllosilicates (e.g., serpentine), olivine, iron oxides (e.g., magnetite, ferrihydrite), pyroxene and sulfides [130, 355, 356]. A variety of Fe^{2+} and Fe^{3+} bearing mineral phases are expected to be present (some being formed by hydrothermal water–rock interactions) and their dissolution could supply Fe^{2+} and Fe^{3+} ions to the ocean. The oceanic abundances of Fe^{2+} and Fe^{3+} ions are likely limited by both the bulk Fe content and the precipitation of ferrous and ferric minerals (i.e., by the solubility of Fe^{2+} and Fe^{3+}), which is tightly linked to key geochemical parameters of the ocean, notably its oxidation state and pH. While the oceans of Europa and Enceladus may contain several iron species in a variety of oxidation states, concentrations are still unconstrained [131, 130, 68]. However, under the assumed redox state of Enceladus's ocean, Fe should always be in the form of Fe^{2+} [357]. Ray et al. [355] estimated the concentrations of dissolved ferrous ions in Enceladus' ocean, as determined by the dissolution of stable minerals, to be $\sim 10^{-7}$ to 10^{-9} mol/L for oceanic pH values of 9 and 11, respectively, and Hao et al. [358] estimated concentrations from 10^{-5} to 10^{-8} mol/L for pH values ranging from 8.5 to 11.

On Europa's surface, iron (if present) would likely be in its ferric form due to the intense radiation chemistry that oxidizes the surface ice. Iron compounds have been suggested for Europa's surface [198], particularly ferric oxides and ferric sulfate given the oxidizing nature of the surface, but there is currently no strong evidence for these compounds at observable amounts. Ferrous iron could be oxidized radiolytically (by oxidants originating from the radiation-induced dissociation of water), producing ferric iron. Exchanges between the ice shell and the subsurface ocean (e.g., a recycling of the ice shell) could provide Fe^{3+} to the ocean and provoke the precipitation of ferric oxyhydroxide and/or a reduction of Fe^{3+} to Fe^{2+} if the ocean is sufficiently reduced.

The detection of Fe^{2+} and/or Fe^{3+} (in molecular complexes) in fresh material from Europa and Enceladus would bring insight into the geochemistry of their subsurface oceans, thus constraining the concentrations of ionic species and therefore geochemical models. It could allow the evaluation of redox disequilibria, a prerequisite for the origin of life, and may also bring insight into potential metabolic processes that may happen in the oceans [355].

On both Enceladus and Europa, regional heating [359, 48] hints towards chemical and thermal disequilibria on a global scale, which is essential for the appearance of life and entails the presence of multiple physicochemical gradients of diverse nature [360]. One example of these are redox gradients, expected to arise between a reducing rocky core and oxidized oceanic water (and on Europa between the ocean and more oxidized surface ice), thus potentially providing abundant chemical energy for life to develop [166, 82, 74, 361, 362]. Hydrothermal vents are prime candidates for observing prebiotic chemistry at play, as they gather a large variety of redox gradients and are regarded as the most likely environment for a putative origin of life both on early Earth and icy moons (e.g., Russell et al., 2010, 2014). Under hydrothermal conditions, iron minerals provide a rich source of both Fe^{2+} and Fe^{3+}. This redox imbalance can promote chemical reactions among simple carbon-containing substrates found in hydrothermal vents giving rise to molecules relevant for prebiotic chemistry, such as amino acids [363]. The abundance of iron minerals in hydrothermal systems on both early Earth and presently on icy moons could in both cases have triggered geochemical gradients perhaps driving prebiotic chemistry leading to more complex organic reaction networks.

On Earth, a major model for the origin of life is that life has started on a Fe^{2+}–rich early Earth (e.g., [364, 365]) within alkaline hydrothermal vents where thin mineral walls containing catalytic Fe(Ni)S minerals offered redox and pH gradients. Such gradients could drive prebiotic chemistry and are comparable to those needed in all cells to function [366], which makes a very strong case for hydrothermal vents being the site for the origin of life. Furthermore, inorganic cofactors utilized in ancient pathways such as the acetyl-CoA pathway (carbon fixation) and the reverse Krebs cycle (energy transduction) in cells share the same composition as catalytic Fe(Ni)S clusters from the redox-active minerals of the vents' walls [367, 368, 369, 370]. Therefore iron-based metabolisms could have been essential for the development of primitive life on early Earth and may also be of prime importance on icy moons. Several metabolisms have been proposed to be viable in hydrothermal environments on icy moons, such as methanogenesis [371, 372] and iron-based metabolisms [355, 373]. Iron oxidizing bacteria have also been documented in terrestrial alkaline hydrothermal systems analogous to those expected on Enceladus [374]. The detection of the oxidation state of metallic elements such as Fe on icy moons' oceans could constrain potential biogeochemical oceanic iron cycles [375] and the possible metabolic pathways of putative organisms.

Jupiter's icy moons are the targets of the upcoming JUICE mission from ESA and Europa Clipper from NASA. Several mission concepts have been proposed to explore Enceladus such as Moonraker [144] and Enceladus Life Finder [141]. To investigate the geochemistry of extraterrestrial ocean worlds, a powerful technique is impact ionization mass spectrometry (MS), using instruments such as the Cosmic Dust Analyzer (CDA [232]) onboard the past Cassini mission and its successor instruments, the SUrface Dust Analyzer (SUDA [215]) onboard Europa Clipper, and the proposed High Ice Flux Instrument (HIFI [144]) onboard Moonraker. Impact ionization mass spectrometers measure the ionized species created by the hypervelocity impact of dust grains onto a metal plate. Around icy ocean moons, they can provide compositional analysis of ice grains ejected from the surface ice by the ambient micrometeorite bombardment [234, 237] and of ice grains ejected from subsurface water reservoirs by plume activity [124].

The performance and data analysis of these instruments requires laboratory calibration, which may be done with analogue experiments such as the Laser Induced Liquid Beam Ion Desorption (LILBID) technique coupled to time-of-flight mass spectrometry (ToF MS) [258, 253]. This will be demonstrated and showcased in the present paper. Due to the technical difficulties linked to the hypervelocity acceleration of water ice grains in laboratory experiments [250, 251, 247, 249], LILBID is still the only currently available method to accurately reproduce impact ionization mass spectra of water ice grains from icy moons. Various LILBID analogue experiments have already been performed with salts [128, 61, 316, 376], organic material [65, 66, 268, 316, 376] and biosignatures [263, 264, 266, 265].

Here we measure the cation and anion LILBID mass spectra of iron (II) and iron (III) chlorides and sulfates, to investigate the spectral signatures of iron in different oxidation states as detectable by impact ionization mass spectrometers onboard space missions to icy moons. The recorded LILBID spectra are analogue for the SUDA instrument and complement a database [259] for Europa Clipper and future Enceladus missions which might allow the detection and characterisation of iron on these icy moons, providing valuable information on their geochemistry and habitability.

3   Methods

Four types of aqueous solutions were prepared at concentrations of 0.1 wt%: (a) iron (II) chloride, (b) iron (III) chloride, (c) iron (II) sulfate and (d) iron (III) sulfate. Molar concentrations are $[FeCl_2]= 7.9 \times 10^{-2}$ mol/L, $[FeCl_3]= 6.2 \times 10^{-2}$ mol/L, $[FeSO_4]= 6.6 \times 10^{-2}$ mol/L and $[Fe_2(SO_4)_3]= 2.5 \times 10^{-2}$ mol/L. Additionally, iron (III) sulfate was measured at additional concentrations (1, 0.01, 0.005 and 0.0001 wt%) and its detection limit in cation mode was determined. The solutions were prepared only a few minutes before their measurement, to minimize oxidation reactions of Fe^{2+} to Fe^{3+}. The salts were measured both in solutions of argon-sparged deionized water and non-sparged deionized water, and no major differences were observed in the mass spectra (nor in the solutions' colors). The spectra presented here are therefore those of salts dissolved in non-sparged deionized water. The pH values of the solutions (measured at 20°C) are 3.9 for iron (II) chloride, 2.2 for iron (III) chloride, 4.9 for iron (II) sulfate and 2.5 for iron (III) sulfate.

The solutions were measured with Liquid Ion Beam Ion Desorption (LILBID) coupled to Time-of-Flight mass spectrometry (Figure 21) in a vacuum chamber (5×10^{-5} mbar). The aqueous sample solutions were injected a μm-sized liquid water beam irradiated by a pulsed infrared laser ($\lambda = 2840$ nm, energy up to 4mJ), which desorbs analyte molecules in a thermal explosion. This process is analogue to the impact ionization of dust

grains in space, when those impact the metal targets of spaceborne mass spectrometers at hypervelocities (i.e., > 1 km/s) [128, 253]. In both cases (i.e., LILBID and impact ionization in space), a cloud of neutral and ionized species is created from the sample/dust grain, and the fraction of ionized species is measured by ToF-MS. The LILBID ionization method tends to produce singly charged ions. Different impact speeds of the ice grains onto spaceborne mass spectrometers are simulated in LILBID by a delayed extraction of the ions: ions of specific velocities are selected thanks to a repeller electrode switched on after a defined delay time, preventing ions arriving later than the delay time to enter the mass spectrometer detector. Different impact speeds of the dust grains, ranging from 3 to >20km/s, can thus be simulated by adjusting the extraction delay time and the laser's power intensity [253].

Here, the samples were measured with LILBID in both cation and anion mode, rendering complementary mass spectra, with a mass resolution of 600-800 m/Δm. Each recorded spectrum was an average of three hundred individual spectra, co-added to improve the signal-to-noise ratio, and was both baseline-corrected and recalibrated. The LILBID setup was calibrated before each measurement session. The recorded mass spectra are stored in a database (https://lilbid-db.planet.fu-berlin.de [259]) in which LILBID analogue data for impact ionization mass spectrometers are available.

4 Results

Both cations and anions bearing Fe^{2+} and/or Fe^{3+} were identified in the recorded LILBID mass spectra of iron (II) and iron (III) chlorides and sulfates (Figures 44, 45, 46, and S88-S91). Distinctive spectral characteristics are highlighted in Table 10 for each type of sample in both ion modes and discussed in detail in the following subsections. Peaks corresponding to Fe-bearing and Cl-bearing cations show respectively characteristic Fe isotope patterns (^{54}Fe, ^{56}Fe and ^{57}Fe with intensities of 5.82%, 91.66% and 2.19%) and Cl isotope patterns (^{35}Cl and ^{37}Cl with intensities of 75.87% and 24.22%). Isotopic patterns were used to resolve ambiguities in identifying peaks (e.g., Figure 44b).

	Chlorides		Sulfates	
	Fe^{2+} (FeCl$_2$)	**Fe^{3+} (FeCl$_3$)**	**Fe^{2+} (FeSO$_4$)**	**Fe^{3+} (Fe$_2$[SO$_4$]$_3$)**
Characteristic peak(s) in cation mode	**[aFe^{2+} (OH)$_b$]$^+$** e.g., m/z 73 [Fe^{2+} (OH)]$^+$ m/z 163 [2Fe^{2+} (OH)$_3$]$^+$	**[aFe^{2+} (OH)$_b$]$^+$** e.g., m/z 73 [Fe^{2+} (OH)]$^+$, m/z 163 [2Fe^{2+} (OH)$_3$]$^+$ **[aFe^{3+} (OH)$_b$]$^+$** e.g., m/z 90 [Fe^{3+} (OH)$_2$]$^+$, m/z 197 [2Fe^{3+} (OH)$_5$]$^+$ **[Fe^{2+} Fe^{3+} (OH)$_4$]$^+$** m/z 180	**[aFe^{2+} (OH)$_b$]$^+$** e.g., m/z 73 [Fe^{2+} (OH)]$^+$, m/z 163 [2Fe^{2+} (OH)$_3$]$^+$	**[aFe^{2+} (OH)$_b$]$^+$** e.g., m/z 73 [Fe^{2+} (OH)]$^+$, m/z 163 [2Fe^{2+} (OH)$_3$]$^+$ **[aFe^{3+} (OH)$_b$]$^+$** e.g., m/z 90 [Fe^{3+} (OH)$_2$]$^+$, m/z 197 [2Fe^{3+} (OH)$_5$]$^+$ **[Fe^{2+} Fe^{3+} (OH)$_4$]$^+$** m/z 180
Characteristic peak(s) in anion mode	**[aFe^{2+} (OH)$_b$ Cl$_c$]$^-$** e.g., m/z 107 [Fe^{2+} (OH)$_3$]$^-$ m/z 125 [Fe^{2+} (OH)$_2$ Cl]$^-$ m/z 143 [Fe^{2+} (OH) Cl$_2$]$^-$ m/z 161 [Fe^{2+} Cl$_3$]$^-$ m/z 197 [2Fe^{2+} (OH)$_5$]$^-$	**[aFe^{3+} (OH)$_b$ Cl$_c$]$^-$** e.g., m/z 124 [Fe^{3+} (OH)$_4$]$^-$ m/z 142 [Fe^{3+} (OH)$_3$ Cl]$^-$ m/z 160 [Fe^{3+} (OH)$_2$Cl$_2$]$^-$ m/z 231 [2Fe^{3+} (OH)$_7$]$^-$	**[aFe^{2+} (SO$_4$)$_b$ (OH)$_c$]$^-$** e.g., m/z 169 [Fe^{2+} (SO$_4$)(OH)]$^-$ m/z 321 [2Fe^{2+}(SO$_4$)$_2$(OH)]$^-$	**[aFe^{3+} (SO$_4$)$_b$ (OH)$_c$]$^-$** e.g., m/z 186 [Fe^{3+} (SO$_4$) (OH)$_2$]$^-$ m/z 248 [Fe^{3+} (SO$_4$)$_2$]$^-$ **[aFe^{3+} (SO$_4$)$_b$ (OH)$_c$ -H]$^-$** e.g., m/z 168 [Fe^{3+} (SO$_4$) (OH) -H]$^-$ m/z 275 [2Fe^{3+} (SO$_4$) (OH)$_4$ -H]$^-$ m/z 337 [2Fe^{3+} (SO$_4$)$_2$(OH)$_2$ -H]$^-$

TABLE 10. Characteristic peaks for Fe^{2+} and Fe^{3+} chlorides and sulfates, highlighting distinctive spectral appearance between the Fe^{2+} and Fe^{3+} salt solutions. Interestingly, in cation mode Fe(III) salts show characteristic molecular cations related to both Fe^{2+} and Fe^{3+}.

4.1 Cation mode spectra

4.1.1 iron (II) chloride

In the cation mass spectrum of Fe(II) chloride solution (Figure 44), [Fe^{2+} (OH)]$^+$, [2Fe^{2+} (OH)$_3$]$^+$ cations and water cluster peaks corresponding to [aFe^{2+} (OH)$_b$ (H$_2$O)$_c$]$^+$ cations are highly prominent (with a, b, and c $\geq$ 0). Minor peaks at m/z 90 and 108 are attributed to [Fe^{3+} (OH)$_2$]$^+$ and [Fe^{3+} (OH)$_2$ (H$_2$O)]$^+$ cations. These peaks vanish completely in the cation mass spectra of the same solution at lower delay time (Figure S88). The low intensities of these characteristic peaks indicate very low concentrations of Fe^{3+} in this sample, as compared to Fe^{2+}.

4.1.2 iron (III) chloride

In the cation mass spectra of Fe(III) chloride solution (Figure 44), ions bearing Fe^{2+} and/or Fe^{3+} were detected. Both $[Fe^{2+} (OH)]^+$ (interfering with a pure water cluster peak, as seen in Figure S2) and $[Fe^{3+} (OH)_2]^+$ cations are highly prominent. Cations identified as $[2Fe^{2+} (OH)_3]^+$, $[2Fe^{3+} (OH)_5]^+$ and water cluster peaks $[aFe^{2+} (OH)_b (H_2O)_c]^+$ and $[aFe^{3+} (OH)_b (H_2O)_c]^+$ were detected. $[aF^{3+} (OH)_b (H_2O)_c]^+$ cations are drastically increased compared to the Fe(II) solution and - in contrast to the Fe(II) solution - are still present at a lower delay time, indicating a much higher concentration of Fe^{3+} in this sample. Cations including both Fe^{2+} and Fe^{3+}, i.e., $[Fe^{2+}Fe^{3+}(OH)_4 (H_2O)_a]^+$, were detected at lower intensity.

4.1.3 iron (II) sulfate

The cation mass spectrum of iron (II) sulfate (Figure S90) is quite similar to those of iron (II) chloride (Figure 44), in the sense that in both spectra, $[Fe^{2+} (OH)]^+$ cations show high intensities, together with $[2Fe^{2+} (OH)_3]^+$ and $[aFe^{2+} (OH)_b (H_2O)_c]^+$ water clusters peaks, and small $[Fe^{3+} (OH)_2 (H_2O)_a]^+$ peaks. In the cation mass spectra of Fe(II) sulfate (Figure S3), a small number of additional cations were detected at lower intensities: $[Fe^{2+} Fe^{3+} (OH)_4]+$ (m/z 180) and unidentified peaks at m/z 269 and m/z 307.

4.1.4 iron (III) sulfate

Similarly to the Fe (II) sulfate, the cation mass spectrum of Fe (III) sulfate (Figure S91) shares many similarities with the respective chloride (Figure 44): in both spectra, (1) both $[Fe^{2+} (OH)]^+$ and $[Fe^{3+} (OH)_2]^+$ cations are highly prominent, as well as their water cluster peaks $[Fe^{2+} (OH) (H_2O)a]^+$ and $[Fe^{3+} (OH)_2 (H_2O)_a]^+$ (2) $[2Fe^{2+} (OH)_3]^+$, $[2Fe^{3+} (OH)_5]^+$ and $[Fe^{2+} Fe^{3+} (OH)_4]^+$ cations are detected at lower intensities, (3) water clusters are detected for most species (i.e., $[aFe^{2+} (OH)_b (H_2O)_c]^+$, $[aFe^{3+} (OH)_b (H_2O)_c]^+$, $[aFe^{2+} bFe^{3+} (OH)_c (H_2O)_d]^+$) and (4) a peak at m/z 286 was identified as $[3Fe^{3+} (OH)_8\text{-}H_2O]^+$ cations. In the cation mass spectra of Fe(III) sulfate (Figure S91), a few additional cations are detected: $[2Fe^{3+} (OH) (SO_4)_2]^+$ at m/z 304, $[2Fe^{3+} (OH) (SO_4)_2]^+$ at m/z 321, and unidentified peaks at m/z 268 and 269. Additionally, the detection limit of Fe(III) sulfate in cation mode was determined to be 0.0001wt% i.e., 2.5×10^{-6} mol/L.

4.2 Anion mode spectra

In contrast to positive mode, the negative mode spectra show fundamentally different spectra between sulfate and chloride solutions.

4.2.1 iron (II) chloride

In the anion mass spectra of Fe(II) chloride (Figure 45), $[Fe^{2+} (OH)_a Cl_b]^-$ anions are detected at very prominent intensities, and $[2Fe^{2+} (OH)_a Cl_b]^-$ and $[3Fe^{2+} (OH)_a Cl_b]^-$ anions at lower intensity. Peaks at m/z 125, 143 and 161 could also be a water cluster series of $[Fe^{2+} (OH)_3]^-$ (m/z 107), but the presence of smaller peaks at m/z 127, 145, 163 and 165 confirms the presence of chlorine atoms in those anions. A small peak corresponding to $[Fe^{3+} (OH)_4]^-$ was detected at m/z 124 (Figure 45) but it was not detected at lower delay time (Figure S92), indicating a very low concentration of Fe^{3+} in this sample.

4.2.2 iron (III) chloride

In the anion mass spectra of Fe(III) chloride (Figure 45), $[Fe^{3+} (OH)_a Cl_b]^-$ anions are detected at prominent intensities, and $[2Fe^{3+} (OH)_a Cl_b]^-$ and $[3Fe^{3+} (OH)_{10}]^-$ anions at lower intensities. $[Fe^{2+} (OH)_a Cl_b]^-$ anions were also detected but at lower intensities than $[Fe^{3+} (OH)_a Cl_b]^-$ anions.

4.2.3 iron (II) sulfate

The anion mass spectra of iron (II) sulfate (Figure 46) show prominent sulfate peaks $[HSO_4 (H_2O)_a]^-$ and Fe^{2+} bearing anions: highly prominent $[Fe^{2+} (SO_4) (OH)]^-$ anions as well as smaller $[2Fe^{3+} (SO_4)_2 (OH)]^-$ peaks. Some smaller peaks were identified as Fe^{3+} bearing species: $[aFe^{3+} (SO_4) (OH)_b \text{-}cH]^-$ anions.

4.2.4 iron (III) sulfate

In the anion mass spectra of iron (III) sulfate (Figure 46), $[aFe^{3+} (SO_4)_b (OH)_c \text{-}dH]^-$ anions are detected at high intensity, as well as $[Fe^{2+} (SO_4) (OH)]^-$ anions at m/z 169.
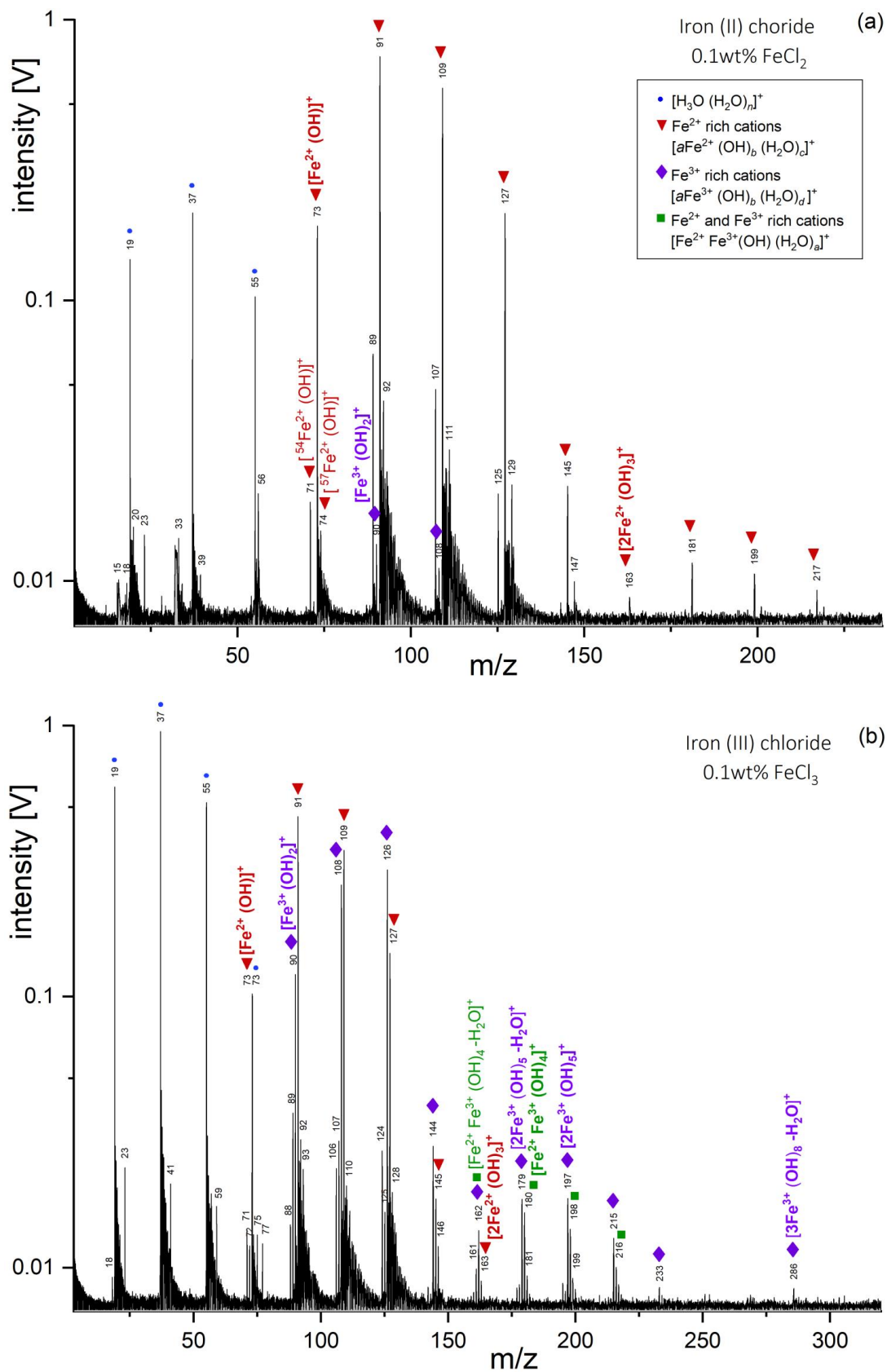
FIGURE 44. LILBID cation mass spectra recorded with a delay time of 5.1 µs for (a) iron (II) chloride ($FeCl_2$), with an example of the iron isotope pattern for $[Fe^{2+} (OH)]^+$ and (b) iron (III) chloride ($FeCl_3$). In the spectrum (b), two distinct peaks are observed at m/z 73 at a similar intensity, corresponding to a pure water cluster $[H_3O(H_2O)_3]^+$ and to $[Fe^{2+}(OH)]^+$ (Figure S89).
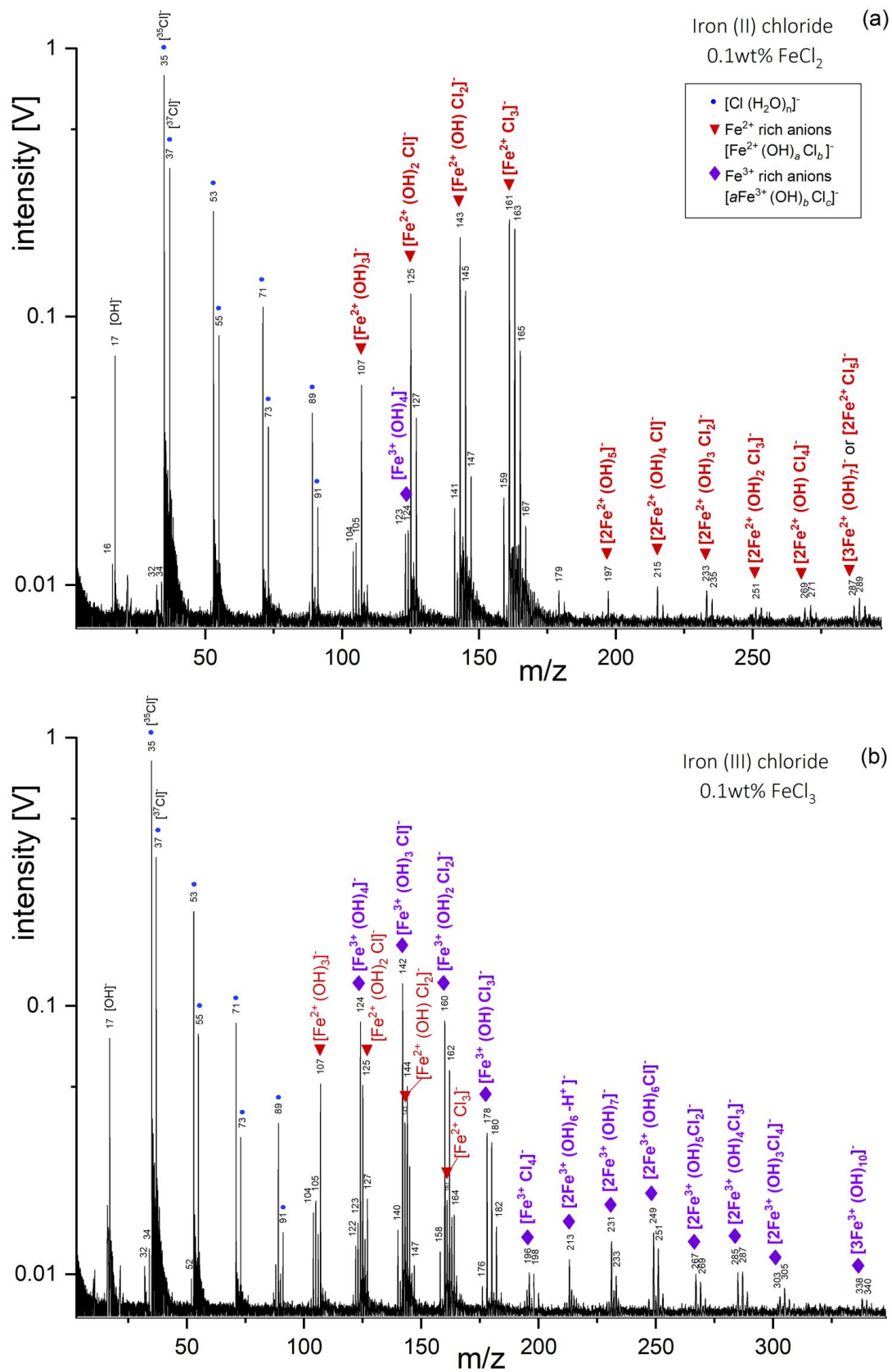
FIGURE 45. LILBID anion mass spectra recorded with a delay time of 6.0 μs for (a) of iron (II) chloride (FeCl$_2$), and (b) iron (III) chloride (FeCl$_3$).
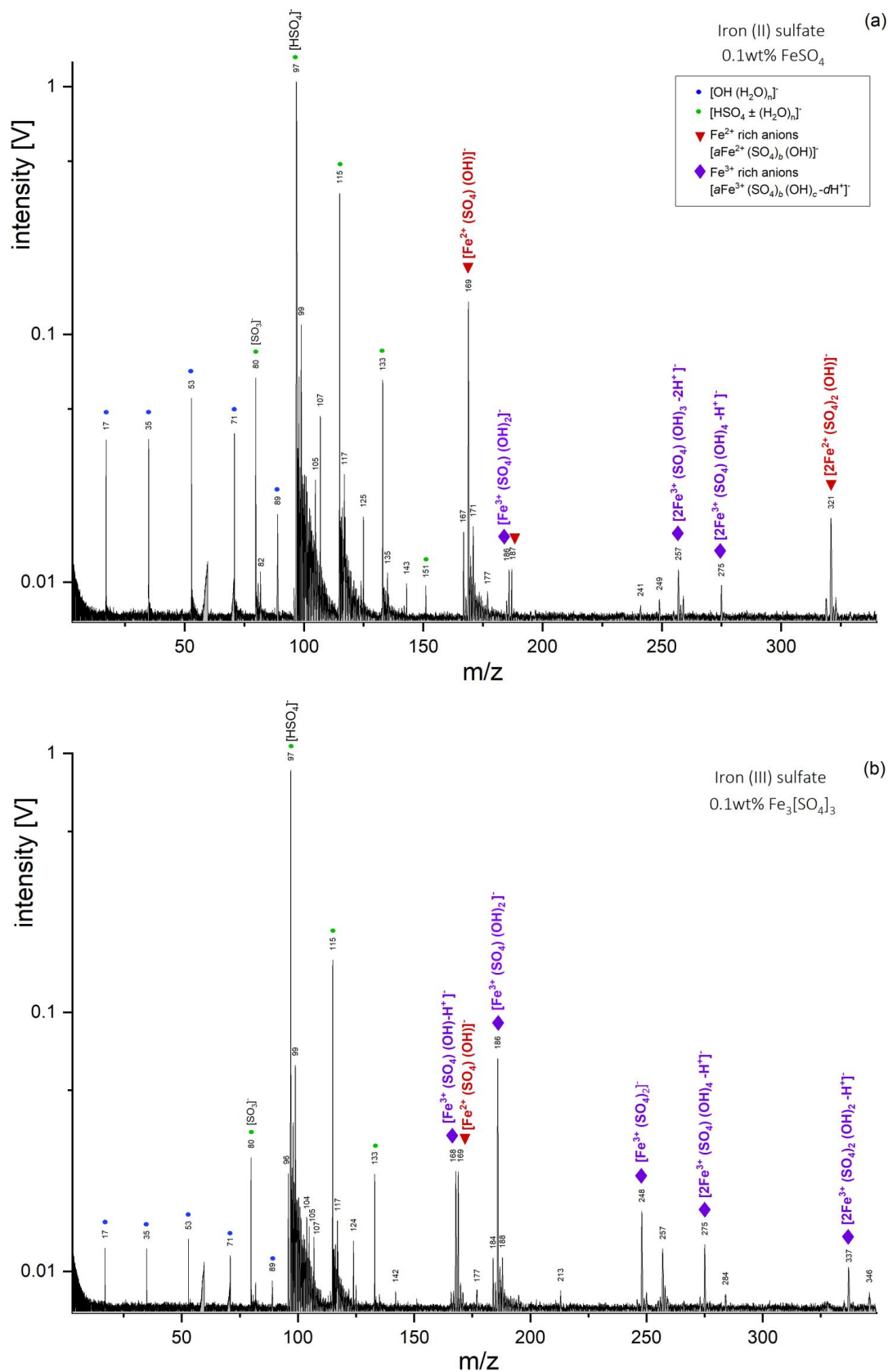
FIGURE 46. LILBID anion mass spectra recorded with a delay time of 5.4 μs for (a) of iron (II) sulfate ($FeSO_4$) and (b) iron (III) sulfate ($Fe_2[SO_4]_3$).

5 Discussion

5.1 Spectral Analysis

While our work focuses on applications for spaceborne instruments, previous laboratory work by Charvat & Abel [257] and Mayer et al. [377] performed comparable experiments and shown different applications and mechanistic details of laser assisted liquid phase dispersion mass spectrometry when analyzing iron at different oxidation states. Both studies have highlighted the possibility to measure oxidation states of ions in complexes with IR laser dispersion MS. In these two papers, aqueous solutions containing Fe in different oxidation states (in both organic and inorganic complexes) were measured. It was shown that IR laser desorption of ions combined with TOF-MS detects the "situation" (concentrations of species) in solution, i.e., the solution concentration with a linear response over several orders of magnitude. This result is of prime importance as it shows that the method is suitable to measure Fe ion concentrations in solutions and/or in the condensed phase (e.g., ice), making it a powerful technique to work in analogue experiments also for ions in different oxidation states. Other techniques such as electrospray (ESI) and UV-MALDI change oxidation states through electrochemistry at the ESI tip or through electron transfer and plasma chemistry during ablation. Still, other mass spectrometry methods obtained some results comparable to ours, which must be treated with caution in the context of analog experiments for space missions, however. Hellman et al. [378] measured $FeCl_3$ (0.1mM) in aqueous solution with electrospray ionization (ESI) MS and identified a range of $[Fe_a\, O_b\, (OH)_c\, Cl_d]$ ions, including species containing both Fe^{2+} and Fe^{3+}. In cation mode, they detected $[Fe^{3+}Cl_2]^+$ (m/z 126) and $[Fe^{2+}\, 2(OH)\, Cl_2]^+$ (m/z 160) cations. We haven't detected these two species in every cation mass spectrum of Fe^{2+} nor Fe^{3+} chlorides, despite the presence of a peak at m/z 126 (Figure 2) which has been attributed to $[Fe^{3+}(OH)_2(H_2O)_2]^+$ due to the lack of characteristic ^{37}Cl isotopologue peak at m/z 128. In anion mode, Hellmann et al [378] detected $[Fe^{2+}\, Cl_3]^-$ (m/z 161), $[2Fe^{2+}\, Cl_5]^-$ (m/z 287), $[Fe^{3+}\, (OH)\, Cl_3]^-$ (m/z 178) and $[Fe^{3+}\, Cl_4]^-$ (m/z 196) anions, species that we also identified (Fig. 3). Radisavljević et al. [379] studied $FeCl_3$ with matrix-assisted laser desorption (MALDI) and Laser Desorption Ionization (LDI) ToF-MS and also identified $[Fe^{2+}\, Cl_3]^-$ and $[Fe^{3+}\, Cl_4]^-$ anions. The hydrolysis of Fe(II) in water leads to an acid solution where $[Fe(H_2O)_6]^{2+}$ is the predominant species, and another hydrolysis product is $[Fe(OH)_3]^-$ [380], which we observe at high intensity in the anion mass spectra of Fe(II) and Fe(III) chlorides (Figure 45).

Moreover, our present results show that it is possible to detect and discriminate Fe^{2+} from Fe^{3+} with impact ionization mass spectrometers such as SUDA. The determination of the oxidation state (II or III) of iron is done by the identification of Fe^{2+} and/or Fe^{3+} bearing ions at different relative intensities. While Fe^{2+} and Fe^{3+} have practically the same mass, they form different characteristic clusters due to their different charges. While peaks from Fe^{2+} species appear in both Fe (II) and Fe (III) samples, major peaks bearing Fe^{3+}, such as $[Fe^{3+}\, (OH)_2]^+$, $[Fe^{3+}\, (OH)_a\, Cl^b]^-$ and $[aFe^{3+}\, (SO_4)_b\, (OH)_c\, -dH]^-$ only appear in Fe (III) samples and thus are particularly important to discriminate between the two oxidation states of iron (Figures 2, 3, 4). Our results, combined to those of Mayer et al. [377] showing the complexation of iron ions in different organic complexes, suggest that organic clusters with Fe^{2+} or with Fe^{3+} might also display characteristic spectral differences in SUDA-type mass spectra.

In the mass spectra of Fe(III) chlorides and Fe(III) sulfates, we observe iron in two oxidation states (Fe^{2+} and Fe^{3+}) although we used only Fe^{3+} salts. This was also previously observed by Mayer et al. [377], who observed Fe(I), Fe(II) and Fe(III) in solutions of Fe(III) with organic complex partners (e.g., oxalate). This can be explained by the fact that Fe(III) is not very stable in solution (it is a strong oxidation agent). A reduction of Fe^{3+} to Fe^{2+} upon laser-induced desorption and ionization has been previously observed in MALDI-MS with iron (III) [379] and with other metal ions such as Cu [381]; however, contrary to our ionization method, in MALDI the oxidation state can change through electrochemistry at the ESI tip or through electron transfer and plasma chemistry during ablation.

We find that cation mass spectra of both Fe (II) and Fe (III) chloride are quite similar to those from respective sulfates (Figures 44, S90, S91). This result was expected since similar cations are present in those samples. An important lesson for impact ionization mass spectrometers is that the anion mode is much better in discriminating sulfates from chlorides, even in small quantities (Figures 44, 45, 46 and S88-S92) – therefore SUDA's ability to use both ion modes provides great improvement over CDA, which only was able to detect cations. Indeed, in contrast to positive mode, the negative mode spectra show fundamentally different spectra between sulfate and chloride solutions. However, the detection of the oxidations state of iron can be done in both ion modes.

Several ionic species detected in this work have been also described in previous mass spectrometry experiments. In Napoleoni et al. [376], sulfate anions were identified with the LILBID technique, in the anion mass spectra of both magnesium sulfates ($MgSO_4$) and sulfuric acid (H_2SO_4). We here observe similar sulfate anions, such as $[SO_3]^-$ and $[HSO_4]^-$ (Figures 45 and 46). We conclude that anion spectra always show characteristic sulfate peaks, regardless of the cation these were previously bound to, together with unique molecular peaks that allow the identification of such cations.

5.2 Implications for Europa and Enceladus

Iron could be present as soluble ions in the oceans of Europa and Enceladus over a wide range of pH (0-10) and oxidation states (Figure 47). Soluble iron-bearing species could be transported from depths to the surface of the ocean helped by the buoyancy of hydrothermal plumes of hot fluids [113] containing metal species and/or upwelling bubbles of volatile gases [65]. The detection of Fe^{2+} and/or Fe^{3+} on Enceladus' and Europa' surfaces
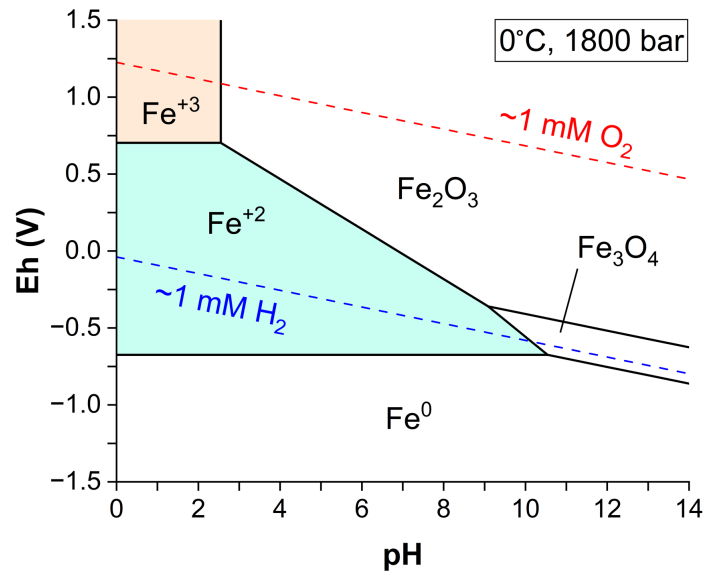
FIGURE 47. Example of a Pourbaix diagram of the Fe-O-H system. The driving variables are the pH and reduction potential Eh; the latter values are expressed relative to the standard hydrogen electrode. Eh is a measure of the oxidation state of the system. Within a region demarcated by black lines, the indicated species/mineral is the most stable form of iron. The aqueous species regions are shaded in color to highlight that they are of greatest interest in the present application of measuring soluble salts from samples of ocean water. The sizes of their regions depends on the activity of the species. Here, they are assumed to have activities of 10^{-6} – close to our experimentally determined detection limit for ferric sulfate. Dashed lines show cases of strongly oxidized and reduced conditions as points of reference. This diagram was constructed using thermodynamic data from the SUPCRT database [382, 383], together with the Nernst equation. Note: Fe_2O_3 = hematite, Fe_3O_4 = magnetite, Fe^0 = native iron.

would therefore have implications for the characterisation of their subsurface oceans, potentially including hydrothermal systems, but surface processes could also play an important role. Both Fe^{2+} and Fe^{3+} are expected to be present on hydrothermal vents minerals and released as ions into the ocean by hydrolysis of these minerals. While (some) Fe^{3+} may cross the ocean and reach the surface in the same oxidation state, Fe^{2+} would likely be transformed to Fe^{3+} during its journey to the exterior of the moon because the redox gradients created between the reduced core's interior and the more oxidized subsurface ocean entails that all ionic ferrous compounds are subject to mildly oxidizing conditions. Thus, the detection of Fe^{2+} ions (or simultaneous presence of both ferrous and ferric ions) in freshly ejected material might hint at the presence of protective mechanisms taking place at the hydrothermal vents and hydrothermal plumes, preventing the oxidation of Fe^{2+} ions. These protective mechanisms may be achieved by complexation of Fe^{2+} by organic compounds, as observed in terrestrial hydrothermal systems [384, 385]. Besides, a lack of detection of Fe^{2+} in the surface of these moons does not imply the absence of Fe^{2+} in the subsurface ocean of the moon.

Generally, it is important to remember that the oxidation state of Fe in solution, including in the subsurface oceans of icy moons, is highly dependent on the surrounding conditions such as the dissolved O_2 or H_2 and pH (Figure 47). Fe (III) in solution can act as an oxidizing agent, which makes both Fe (II) and Fe (III) ions available in aqueous solution. A detection of the Fe(II) / Fe(III) ratio, combined with related modelling work, might be an effective tool to provide information about the geochemistry of subsurface oceans.

On Europa specifically, the surface is highly oxidizing due to radiation, thus if Fe^{2+} reaches the surface, it would be quickly oxidized – forming Fe^{3+}, or reacting with water or other compounds in its environment. Therefore, if Fe^{2+} is detected in surface ejecta by spacecraft measurement, it is an indicator that the ejecta is coming from fresh surface deposits that have not been exposed to radiation for a long time. A ratio of Fe(II) / Fe(III) may also bring information about the timescales of exposition of iron-bearing material to surface irradiation. In the case of plume ejecting frozen material to high altitudes, SUDA could sample material which has been exposed to radiation less than a few minutes, and thus it may be possible to sample Fe^{2+} in concentrations accurately reflecting those present in Europa's subsurface liquid reservoirs. For Enceladus specifically, fresh plume material - as sampled by the Cassini spacecraft in the vicinity of Enceladus - should not undergo considerable modifications of the oxidation state due to radiation. On the contrary, the E-ring of Saturn is mainly fed by Enceladus plume [308], so its material might have been exposed to space weathering [386] for much longer timescales, up to hundreds of years.

The detection and quantification of Fe^{2+} and/or Fe^{3+} in ejected ice grains could allow to constrain the geochemistry of the subsurface oceans of Enceladus and Europa. The pH of oceanic water plays a decisive role in the solubility of ferric and ferrous ions (Figure 47). Ferrous ions would have a substantial dissolved concentration ($\sim$1μM) if the ocean water is relatively reduced and the pH is neutral to low. Ferric iron has a much lower solubility unless the pH is quite low. The pH of Enceladus, currently thought to be mildly alkaline [133], may therefore not allow for a high solubility of any form of iron. As shown in Figure 48, the characterisation (or a lack of detection) of iron would have implications for the geochemistry of subsurface oceans, depending on the origin (plume or surface) of the sampled ice grains. For example, a detection of Fe(III)-dominated plume ice grains (i.e., with a direct origin from subsurface fluids) would indicate an oxidized, acidic ocean (i.e., bottom left of Figure 47). Besides iron, a detection of aluminum ions (Al^{3+}) would hint at an acidic ocean composition, as this ion only occurs under acidic conditions. Other ions, such as Mg-ions, could also be used similarly to get indications about the pH range of the original liquid source.

In Figure 48, we assumed that the iron in the detected ice grains once resided in liquid water (i.e., the sampled source material - either plume or surface ice - developed from a liquid). However, another possible scenario would be that Fe ions have never been dissolved in a liquid and occur from the depositions of meteoritic material such as interplanetary dust particles. In this putative case, Fe might be associated with Ni.

Currently, Fe-bearing species have not been detected in ice grains from Enceladus with the CDA instrument. However, due to the large amount of CDA data yet to analyze, it may be that Fe-bearing species are only present in a small number of ice grains sampled by Cassini (similarly to phosphates; [61]) and that the spectra showing Fe-bearing species have just not been characterised yet. It may otherwise hint that iron is preferentially present as insoluble hydroxide compounds, thus suggesting that the pH tends to more alkaline values (Figure 47). On the contrary, a finding of Fe-bearing species in Enceladan ice grains would be an indication of lower pH values. Even if not detected in Enceladean ice grains, establishing the detection limit of Fe^{2+} and Fe^{3+} bearing salts in Enceladus ice grains would yield a lower limit for their concentrations, and therefore could allow to constrain the solubility of these ions and thus the pH. Some complementary measurements of other elements could bring additional constraint, such as Al^{3+} in chloride or sulfate salts (Figure 48).

While salts were thoroughly studied in previous LILBID experiments [257, 377, 316, 376, 128, 61], this is the first time that a metallic element with multiple oxidation states was analyzed with LILBID serving as an analog experiment relevant for Europa and Enceladus missions. We showed that Fe^{2+} and Fe^{3+} display characteristic mass patterns, due to the formation of different charged clusters and molecular aggregates, and expect similar results for other transition metals with oxidation states comparable to those of iron, e.g., nickel (oxidation state of +2 is most common, but +3 occurs as well), which could also be relevant for the origin of life in icy moons [387]. This work is also a first step towards further characterisation of different transition metals with a greater number of possible oxidation states, such as manganese (oxidation states from +2 to +7).
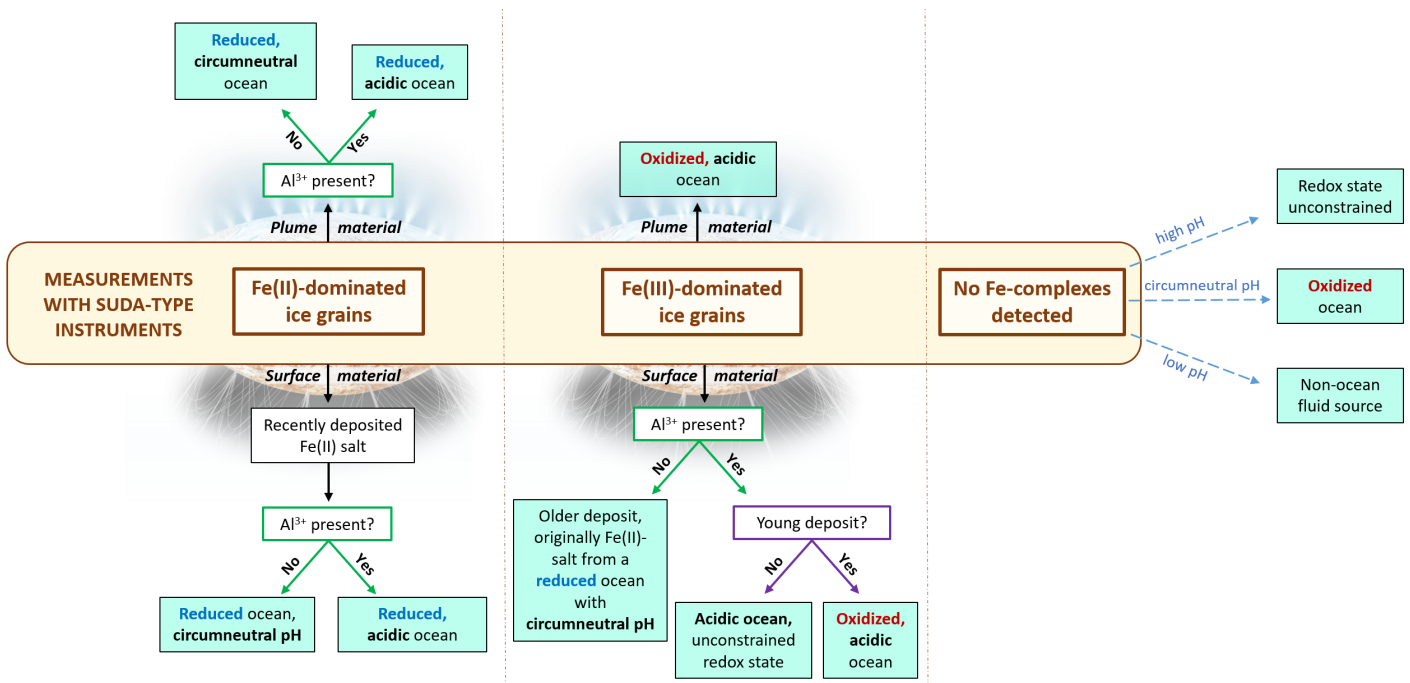
FIGURE 48. Simplified interpretations of the (non) detection and characterisation of iron in ice grains from ocean worlds with SUDA-type instruments. Three scenarios are considered: (a) detection of Fe(II)-dominated grains; (b) detection of significant Fe(III) in ice grains; (c) no Fe detection. In addition to iron, the detection of aluminum ions (Al^{3+}) in ice grains would support a salt source from an acidic ocean composition. In both scenarios (a) and (b), the case of ice grains originating from a plume, implying fresh subsurface material, is distinct from ice grains originating from the surface, therefore probably much older material that has undergone oxidation. In the case of surface material, the age of this material may be constrained by investigating its surface appearance, including its color (e.g., darkened material might indicate older ages) and geological features. In case (c), the characterisation of the pH (e.g., by detection in the grains of other ions, like hydroxide) could bring constraints on the oxidation state in the case of a circumneutral pH, while the case of a low pH would hint towards a non-oceanic fluid origin (e.g., a perched melt of water and sulfuric acid) of the ice grains (as seen in Figure 47, iron is soluble at low pH, whatever the oxidation state of the ocean). In the case of a high pH ocean, iron would not be present as ions (but incorporated in very poorly soluble minerals; Figure 47) therefore not detectable in ice grains.

6 Conclusion

This study indicates that impact ionization mass spectrometers - like SUDA - could be useful tools for the characterisation of the oxidation state of subsurface oceans by quantification of iron-bearing salts in Enceladus' and Europa's ice grains. In both our analogue experiment and future flight-data (e.g., SUDA mass spectra), the intensities of Fe-bearing ions of different oxidation states and the isotope distribution patterns are informative features that can be used to determine the presence and oxidation state of iron-bearing compounds.

While Fe-rich samples have been measured with the laser dispersion MS before [257, 377], our experiments complement these previous results showing that LILBID appears as a reliable technique to characterise the oxidation state of the analyte (contrary to ESI and MALDI, where the oxidation state is (possibly) changed during the ionization process). This is an especially important result as detecting oxidation states via mass spectrometry is very challenging. Moreover, the consistency of our results with those of Charvat & Abel [257] and Mayer et al. [377] shows that our experiments can specifically serve as relevant analogues for ice grain analysis emitted by icy moons in future and past space missions.

The LILBID spectra recorded in this work could allow the detection of iron and the characterisation of its oxidation state on the surface of icy moons (and potentially from their subsurface oceans in the case of ice grains ejected by plumes). The recorded LILBID spectra are stored in a database [259] providing analogue data for space missions targeting dust grains from icy moons, such as Europa Clipper and potential future Enceladus

missions. Future laboratory work will investigate whether characteristic spectral differences between organic clusters with Fe^{2+} or with Fe^{3+} could also be detected [377].

The characterisation of the oxidation states of Fe in icy moons' ice grains with SUDA-type instruments may provide major insight into the geochemistry of subsurface oceans. A quantification of the oxidation states of iron for Enceladus or Europa may be used to constrain the concentrations of reduced iron in the ocean and thus the likelihood of different models of redox chemistry in the ocean [355]. In perspective, such results would also constrain potential metabolic pathways, such as iron reduction metabolisms [373], that may be used by possible extant life in icy moons' oceans, where the necessary ingredients and environmental conditions favorable for sustaining life seem to be present. Future space missions to icy moons such as the upcoming Europa Clipper may detect the chemical signatures of a biogeochemical iron cycling, providing information about extant life that may have started in extraterrestrial hydrothermal systems.

IV Complementary Analogue Experiments for the Detection of Organics and Biosignatures on Ocean Worlds

1 Destruction and Modifications of Potential Molecular Biosignatures on Europa's Irradiated Surface

In parallel of the work presented in Parts II and III of this thesis, irradiation experiments were conducted in cooperation with the Leibniz-Institut für Oberflächenmodifizierung (IOM) in Leipzig, Germany. The goal of these experiments is to provide analogue mass spectra of irradiated material for the upcoming Europa Clipper mission, and to study the evolution of organic material and potential molecular biosignatures under the surface conditions of Europa. Results from these experiments will be published in 2024.

1.1 Goals & Methods

1.1.1 Europa's radiation environment: a destructive agent for biosignatures?

A powerful way to look for life on Europa involves searching for universal biochemical signatures at the molecular level. This approach could include both specific biosignature molecules and distribution patterns indicative of selection by biotic processes (Section I.1.2). All known (terrestrial) lifeforms share a common biochemistry based on an invariant set of organic molecules which includes **amino acids and long-chain fatty acids** [31], making them likely targets of life detection missions. Lipids are generally considered as universal biomarkers of extraterrestrial life. Amino acids, although not unambiguously indicative of life, are considered as some of the simplest molecules that could constitute a biosignature. The detection and quantification of amino acids and fatty acids on icy moons is therefore a powerful tool for the search for life there. Both have been previously analysed with LILBID by Klenner et al. [263, 264], in analogue experiments showing that SUDA could detect and identify these biosignatures.

However, if molecular biosignatures are exposed to surface conditions for a long time, they may undergo chemical modifications and/or degradation due to radiation. Indeed, the survival of potential lifeforms and preservation of chemical biosignatures on Europa's surface is mainly limited by the sterilizing irradiation environment, as they would be exposed to the harsh radiation of Jupiter's magnetosphere (Section I.2.3.3). Radiation can break apart large molecules and could thus be a destructive agent for potential biomolecules on Europa's surface. For lipids specifically, it was shown that they can be destroyed by ionizing radiation due to direct ionization or by oxidative fragmentation (e.g., by hydroxyl free radicals), and that the concentration of lipid membrane biomarkers decreases when exposed to radiation [388]. Amino acids also undergo degradation if exposed to ionizing radiation, as shown by many experimental studies studying their preservation in the context of Mars (e.g., [389]).

The detection by SUDA of such material may therefore be complicated or reduced to the detection of degradation products of these organics. Radiation-induced degradation would be mitigated in the case of plumes ejecting ocean material directly to high altitudes, where it could be sampled during Europa Clipper's flybys only a few minutes after its ejection, or in the case of recent surface material where grains of fresh ice are ejected by micrometeorites (e.g., in chaos terrains [163, 158]). However, it is currently unclear if such an opportunity can be realised for Europa Clipper.

1.1.2 Experimental

We assessed the effects of electron irradiation on the mass spectral appearances of molecular biosignatures embedded in ice, as detectable by SUDA-type mass spectrometers. Irradiation was performed with high energy

(10 MeV) electrons i.e., the dominant carriers of energy for radiation chemistry on Europa's surface [209]. We irradiated amino acids and fatty acids in water ice with high-energy (10 MeV) electrons and recorded analogue mass spectra using LILBID. The icy samples were prepared by mixing the biosignature compounds (amino acids and fatty acids) with water ice powder in solid state to prevent exsolution of the compounds and assure a homogenous repartition in each sample.

Samples consisted of:

(*i*) 4 amino acids - alanine, aspartic acid, glycine, lysine - at a concentration of 0.01 wt% for each amino acid;

(*ii*) fatty acids at simulated abiotic concentrations: all fatty acids at the same concentration of 5.5×10^{-5}M;

(*iii*) fatty acids at simulated biotic concentrations: odd carbon number fatty acids at the concentration of 5.5×10^{-5}M, while abundances for even carbon number fatty acids were increased to 5.5×10^{-4}M, and C16 and C18 fatty acids increased to 2.75×10^{-3}M.

Samples were irradiated with doses from about 300 Gy to 3.5 MGy, i.e., exposure on the timescale of minutes up to around a year on Europa's surface at 0.1mm depth [210], with 10 MeV electrons from a linear electron accelerator (Mevex), performed with pulsed irradiation with a dose rate of 69 Gy/pulse, a frequency of 4 Hz and a current of 50 mA. The irradiation experiments were conducted at conditions similar to those experienced by Europa's surface ice (10^{-5}mbar and temperatures between 110-130K).

1.2 Preliminary Results & Discussion

We show that characteristic signals can be identified from both amino acids and fatty acids (Figure 49) even at the highest tested dose of 3.5MGy, indicating that these biosignatures could persist under Europan surface conditions over at least one year and remain easily detectable by SUDA.
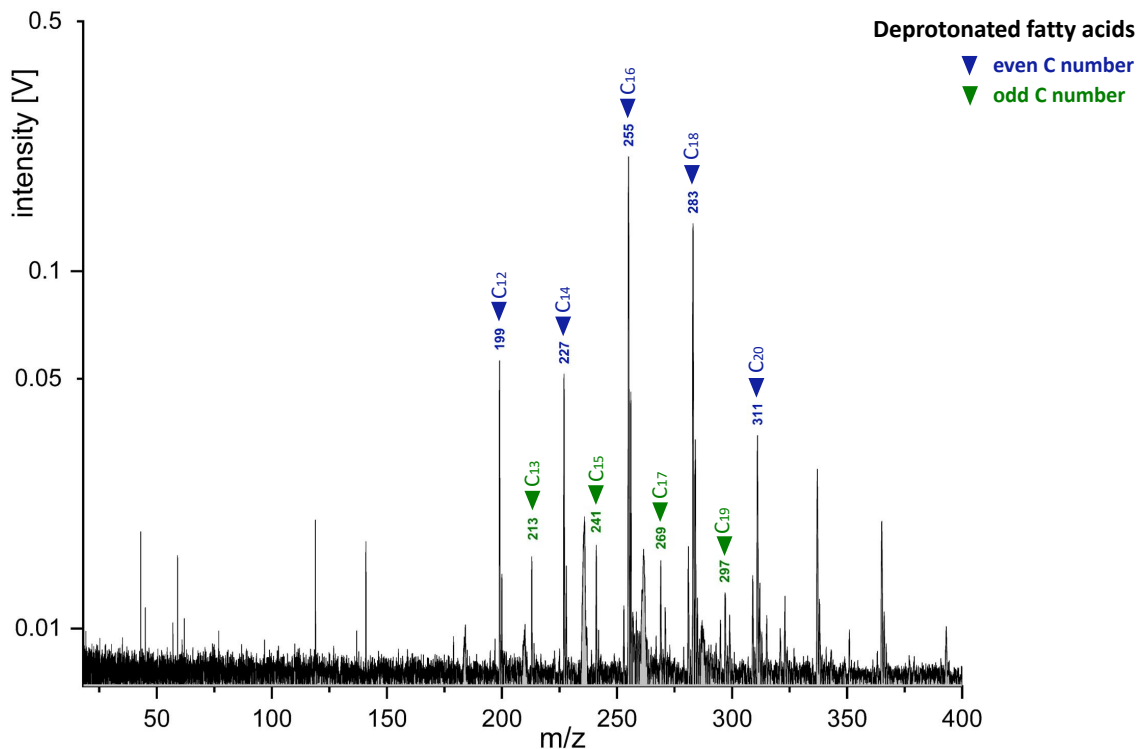
FIGURE 49. LILBID anion mass spectrum of fatty acids irradiated in water ice with 10MeV electrons with a dose of 1.2 MGy, at simulated biotic concentrations: odd Carbon number fatty acids at the concentration of 5.5×10^{-5}M, while abundances for even carbon number fatty acids were increased to 5.5×10^{-4}M, and C16 and C18 fatty acids increased to 2.75×10^{-3}M. The irradiated ice was thawed, and isopropanol was added to the melted sample to ensure the dissolution of fatty acid (a necessary step for the preparation of solution containing hydrophobic compounds).

The intensities of peaks corresponding to high molecular mass amino acids were found to decrease with increasing radiation dose, indicating that these compounds undergo destruction due to the radiation. However, peaks' intensities decreased to a lower degree than expected, hinting at protective mechanisms of organic compounds when embedded in water ice matrix, maybe due to a 'cage effect' trapping organic molecules in the matrix. Such mechanisms have been previously observed in irradiation experiments of interstellar ice analogues [390, 391].

Future experiments at lower amino acids concentrations should allow us to correlate the destructions of these organics with concentrations and irradiation doses. The results of ongoing spectral analysis will be discussed in the context of surface location and depth on Europa, as radiation exposure can vary significantly with these variables [210] - with the most critical parameter being the surface age - and will have direct implications for the detection of organic biosignatures with missions such as Europa Clipper and future visits to other icy moons.

Although our experiments were performed with electrons at a specific energy (10MeV), Europa's surface is exposed to a range of particles of different nature and energies. However, our experiments are relevant to correlate with surface locations because the type of radiation particles is not as important as the dose [392].

Further laboratory experiments will complement these results, such as irradiation of more complex samples including different organic mixtures in a salty ice matrix of relevant composition for Europa. These experiments including salts will be a logic continuation of Part II of this thesis. Additional samples for irradiation will also include microbial material, either whole cells or extracted material (such as lipids, DNA or pigments), to investigate the spectral signatures of biogenic compounds and potential microbial biosignatures exposed to simulated surface conditions of Europa.

In particular, extremophile organisms adapted to Europa-like environments (Figure 2 & section I.1.2) may have distinctive spectrometric fingerprints that could be detected with LILBID. For example, the abundances of fatty acids from psychrophilic microorganisms typically reflect a common adaptation of these microorganisms to cold temperatures, which is an increase in the ratio of (poly)unsaturated to saturated fatty acids in the membrane lipids [393]. Such differences in the abundances of fatty acids from psychrophilic as compared to mesophilic bacteria have been detected with LILBID by Dannenmann et al. [265], and could be detectable even after irradiation simulating long-term exposure on Europa's surface.

2 Perspectives: Additional Analogue Experiments

Further laboratory campaigns could provide great benefit to the study of icy ocean worlds. Such work can also be coupled with - and provide essential data points for - modelling work, which is imperative to our understanding of these worlds. The following sections summarize other ongoing research projects in which I participated, or initiated, during my PhD years, and which we expect to bring interesting results in the coming months to years.

2.1 A rich chemistry driven by irradiation on the surface of icy moons

In Section IV.1, we showed that radiation (in particular, high energy electrons) is generally perceived as a damaging agent for potential organic biosignatures. However, radiation processes can also be the driver of complex organic chemistry, as shown by a wealth of laboratory experiments with astrophysical ices (e.g., [394, 395, 396, 397]). In fact, irradiation of small molecules in ice could lead to the synthesis of bigger molecules of prebiotic interest, even at very low temperatures (e.g., [398]). Such reactions could occur on the heavily irradiated surface of Europa [399, 400], thereby likely enriching the surface ice with a variety of organic compounds.

In the context of astrobiology investigations, it is vital to identify the complex organic compounds that can form by irradiation on Europa's surface, as those could easily be mistaken for (possibly unfamiliar) features and chemistries of life (i.e., false-positive detection of biosignatures). Indeed, if SUDA detects organic material on Europa, the origin of this material will have to be discriminated between possible biotic or abiotic radiolytic chemistry. The experiments presented here are complementary to the irradiation experiments described in Section IV.1, as they both reflect processes that are thought to affect organic material embedded in ice on Europa's surface.

Ongoing irradiation experiments are conducted in a collaboration with the Physique des Interactions Ioniques et Moléculaires (PIIM) laboratory in Aix-Marseille Université, France. The goals are (i) to simulate the complex chemistry that could be driven by radiation on Europa's surface ice, starting from simple compounds, and (ii) to determine how the resulting products would be observed by SUDA-type mass spectrometers. To this end, irradiation experiments are performed with a $CH_3OH:NH_3:H_2O$ ice mixture, irradiated with Vacuum Ultraviolet (VUV) and warmed to room temperature. The warming of the ice induced the sublimation of volatile species and the formation of a residue, which is then dissolved in water and analysed with LILBID, providing analogue mass spectra for SUDA-type instruments.

Danger et al. [401] previously analysed a similar ice analogue with in situ infrared (IR) monitoring and the produced residue with high resolution mass spectrometry (FT-Orbitrap). While the IR analysis mainly showed the presence of functional groups such as alcohols and carboxylic acids, and -NH and C-N bonds, the Orbitrap results allowed a detailed characterisation of the sample's high organic diversity, and the detection of a large number of molecules formed of CHNO elements including amino acids, hexamethylenetetramine and macromolecules of molar masses >4000 Da. By comparing these results with those obtained with LILBID, we will determine similarities and complementarity in these two mass spectrometry techniques on the same organic residue. However, this comparison might also highlight some of the possible limitations of LILBID as compared to higher resolution mass spectrometry. This might suggest that the highly complex composition of the residue may be challenging to analyse with SUDA-type instruments, thus hinting at the need for superior resolution mass spectrometers onboard space missions (e.g., Orbitrap mass spectrometry [402, 403]).

2.2 Experiments with natural samples from polar locations

Many LILBID analogue experiments have already been conducted with a wide variety of inorganic, organic, and biogenic compounds (Section I.4.3). However, all these experiments were reflecting expected scenarios based on our current understanding of icy moons, but reality is rarely as "simple" as the scenario created in the laboratory, where experimental parameters can be precisely controlled (or at least monitored). Natural samples have not yet been analyzed with LILBID, despite the fact that planetary field analogues with extreme conditions offer the best comparable samples to icy moons. An ambitious new project, lead by Lucía Hortal Sánchez and myself at Freie Universität Berlin (FUB), will involve the LILBID analysis of environmental samples collected from polar locations analogous to icy moons. The polar regions proposed for sampling include Antarctica, the Greenland highlands and the Patagonian Southern Ice Field. These locations hold several unique characteristics relevant to icy moons, including very dry and cold climates, high exposure to radiation, high salt concentrations, unique biogeochemistries and the presence of extremophilic ecosystems. Ices from such locations are exposed to extreme shifting physico-chemical conditions over long periods of time, which limits the microorganisms capable of thriving in it to extremophiles[4]. Therefore, they offer a unique inventory and distribution of organics that cannot be attained when using synthetic samples.

A first field work campaign (partially funded by a START grant from FUB) will be undertaken in February-March 2024 on King George Island in Antarctica. A spectrum of samples will be collected in several locations on the Collins Glacier, at different altitudes and in various terrains (e.g., cryoconite[5], organic-poor ices). Deep ($\sim$1m) ice cores will be collected, as well as surficial ice samples and several replicas to ensure the reproducibility of our results. An extensive protocol designed to avoid and monitor contamination will be followed [404]. Part of the collected ice samples will be submitted to intense radiation (10 MeV electrons) to simulate Europa's high radiation environment.

A comprehensive analysis of the samples will be performed at both FUB and the Centro de Astrobiología in Madrid (CAB) to characterise the organic material present in these ices, with a focus on lipid biosignatures (i.e., CAB's expertise [405, 406]). Two complementary analytical techniques will be used:

(*i*) standard Gas Chromatography coupled to Mass Spectrometry (GC-MS) including a lipid extraction step, to provide a highly detailed and quantitative characterisation of the organic and lipid content,

(*ii*) LILBID coupled to ToF-MS to provide analogue mass spectra for SUDA-type impact ionization mass spectrometers for space missions to icy moons.

The detailed compositional data provided by GC-MS will allow a better interpretation of the LILBID mass spectra, which might be complicated in the case of complex samples due to the limited resolution of the ToF-MS. Indeed, environmental samples are challenging to analyze due to the unknown organics that they might contain, and thus require a full characterisation with complementary methods. Moreover, the comparison of the results of these two methods (GC-MS and LILBID) for the same sample will allow us to highlight possible limitations that spaceborne SUDA-type instruments could encounter with ices of complex composition - which is likely to be the case for the upcoming Europa Clipper mission. This project will allow the development of novel goals and suggestion of improvements for future spaceborne dust analyzers.

Future campaigns of field work could focus on areas especially relevant for Europa, with the goal to prepare for the upcoming Europa Clipper mission. For example, ices containing sulfur inclusions could serve as specific analogues of the Europan chaos terrains. On Earth, this element is usually not associated with ice and the known terrestrial locations where sulfur is present in ices are limited to the Blood Falls on Taylor Glacier in Antarctica (Figure 50) [407] and the Borup Fiord Pass [408, 409] on Ellesmere Island in the Canadian Arctic, where a sulfur-rich spring circulates under the glacier.

Other target areas for field work campaigns focusing on Enceladus analogues could include the ice-covered lake Untersee (Eastern Antarctica) and the Gypsum Hill Springs in Axel Heiberg Island (Canadian Arctic). Lake Untersee has anoxic, methane rich, stratified waters representative of Enceladus' subsurface ocean. Gypsum Hill Springs is adjacent to highly saline ice rich in perennial saline springs [410] that could serve as a highly relevant analogue of the saline ice of Enceladus. All of these locations offer not only different types of environmental ices,

---

[4]See Section I.1.2 for a definition of extremophiles, and their relevance to the search for life on extraterrestrial environments.

[5]Cryoconites are dark terrains composed of rocky material, soot and microbes

FIGURE 50. Blood Falls: a saline subglacial discharge from the Taylor Glacier (Antarctica). Such a location is a relevant analogue for the chaos terrains on Europa. Credits: Alasdair Turner, National Geographic.

thus providing a varied set of samples, but also a unique and extreme biochemistry that should ultimately be reflected in the analyzed mass spectra.

V   General Conclusions and Outlook

In the last few decades, many space missions have been launched to collect information about the environments of different bodies in the Solar System and to evaluate the habitability of these places. Building on this important knowledge, one of the main goals of contemporary planetary exploration is to find signs of extraterrestrial life, focusing on bodies which are deemed to be potentially habitable. Icy ocean moons are some of the most promising targets for astrobiology research, and will be explored in great detail in the near future by several space missions, including NASA's Europa Clipper. In this context, this thesis aims to bring valuable new results to the field of planetary exploration with impact ionization mass spectrometry, providing relevant implications for astrobiology investigations. The core of the thesis gathers two peer-reviewed articles and one submitted manuscript which describe comprehensive analogue experiments for the detection of organic- and salt-rich material with instruments similar to the SUrface Dust Analyzer (SUDA) onboard Europa Clipper. Further analogue experiments relevant for SUDA are detailed in the following Part IV, and bring complementary information on the detectability organic material and potential molecular biosignatures on Europa and Enceladus. Such analogue experiments are necessary tools to improve space exploration e.g., by calibrating instrumentation, improving mission planning based on instrumental capabilities determined in terrestrial laboratories (where environmental conditions are well-monitored), and increasing possibilities of data analysis and subsequent discoveries. Based on supporting laboratory preparation, future space exploration missions are the ultimate approach that might soon provide definitive answers to the questions that the field of astrobiology addresses.

Exploration of the Solar System targeting organic material brings valuable knowledge to the search for biosignatures beyond Earth. On Europa and Enceladus, the composition and distribution of organic material in the ocean, or in the surface, could reveal the presence of life as we know it. The SUDA instrument onboard the upcoming Europa Clipper mission could facilitate the identification and quantification of a wide range of organic compounds originating from both the surface and subsurface liquid water reservoirs. In Part II of this thesis, we determined the characteristic mass spectral signatures of several organic species with varied physicochemical properties, to provide key data points for similar detections by SUDA. Because Europa's surface contains high amounts of salts and sulfuric acid, we also evaluated the effects of these inorganic components on each organic compound's spectral fingerprints. We showed that, at concentrations relevant for Europa, these organic compounds can typically be detected by the presence of their molecular ions and a range of different adducts of the organics with inorganic ions. However, the sensitivity of SUDA to detect organic material typically decreases with increasing salt concentrations due to suppression effects, which may (in worst case concentration values) prevent the detection of organic material hidden by the salts. On the contrary, sulfuric acid, one of the most abundant non-water-ice compounds on Europa, does not at all inhibit the identification of organic cations. The results of these analogue experiments (especially with salts) are also highly relevant for Enceladus in the context of a possible future mission to the saturnian moon with an impact ionization mass spectrometer onboard.

While the characterisation of organic material on icy ocean moons may provide direct information about (bio)chemistry in the subsurface, the detection of inorganic compounds can be used to derive key parameters about the geochemistry of subsurface oceans. This was shown by the partial characterisation of the pH, salinity and hydrothermal processes within Enceladus based on Cassini's mass spectrometry data. Moreover, detection capabilities of SUDA-type mass spectrometers usually support higher sensitivity for salts than for organic compounds. Salts bearing metallic elements (such as iron) which exist in different oxidation states depending on their environmental conditions, are key tracers of the geochemistry of subsurface oceans. In Part III, we investigated the mass spectral signatures of Fe (II) as compared to Fe (III) salts, and demonstrated that SUDA has the capability to differentiate between these two oxidation states of iron. This valuable feature could allow the quantification of the oxidation states of iron in both plume grains and surface ejecta on Enceladus and Europa, thus possibly constraining the pH and oxidation state of their subsurface oceans. Such results have strong implications for the characterisation of subsurface oceans' geochemistry and habitability, as they would allow to investigate the likelihood of different models of redox chemistry, as well as possible types of hydrothermal activity and metabolic pathways (e.g., iron reduction) of putative lifeforms.

The set of experimental parameters used in this work correspond to different simulated impact speeds of ice grains, which can be linked to spacecraft velocities. Indeed, ice grains' impact speeds are usually estimated with

the velocity grid (i.e., a charge sensitive grid system at the entrance of SUDA-type instruments), but this can also be done (*i*) with the rise times of the charge signals on the target or the ion grids, (*ii*) by spectral appearance (e.g., abundance of clusters) and (*iii*) by dynamical calculations (i.e., estimation of the orbital speed of particles at the known spacecraft position) [253]. Mass spectra recorded for different impact speeds display significant differences: not only different ions are formed, but also different fragments reflect characteristic fragmentation patterns. The present LILBID analogue experiments lead to a better understanding of the mechanisms of impact fragmentation of organic compounds for specific spacecraft velocities, as well as the formation of different clusters for inorganic ions.

The large number of LILBID mass spectra presented in this thesis provide key data to an existing database [259] gathering analogue data for space missions targeting dust grains from icy moons. Such mass spectral libraries are of vital importance in the interpretation of data from spaceborne instruments. They can also help to better understand hypervelocity impacts of icy particles, including the mechanisms of impact-induced fragmentation of molecules. Such results could be included in theoretical investigations for these phenomenons, obtained by modelling efforts. This would allow to extrapolate the theory to analytes, or conditions, which are difficult (or even impossible) to obtain in laboratory experiments. Combining theoretical work, LILBID experiments and hypervelocity impact experiments will enable advanced science investigations to be included on flyby missions, which have the significant advantage to be cost-effective as compared to lander missions.

The analogue experiments presented in this work have direct implications for the (re)interpretation of impact ionization mass spectra from past and future missions, and for the identification and quantification of the organic and inorganic inventory of the possible plume(s) and icy surfaces of Europa and Enceladus. Characterising the compositional inventory of Europa and Enceladus brings valuable information about both the jovian and saturnian systems, and can bring insight into the evolution of these systems, including the material exchanges between their different moons.

History has showed that mass spectrometry is an invaluable tool for planetary exploration [411]. The design of a new generation of instruments adapted for spacecraft could revolutionise space missions and would allow an improved characterisation of icy ocean moons (e.g., [412]). In fact, instruments carried onboard missions are considerably less performant than those currently used in terrestrial laboratories, which have low limits of detection, are capable of measuring the abundances of molecular and elemental species, and can precisely determine isotopic compositions.

One effective method of improving planetary exploration using mass spectrometry would be to include high-resolution mass spectrometers on space missions, such as Orbitrap instruments. An Orbitrap mass spectrometer combines a miniature design with analytical capabilities far exceeding those of ToF mass spectrometers [413, 414], including a mass resolution reaching values of up to 1,000,000 [415]. In the future, state-of-the art successor instruments to SUDA could be hypervelocity ice grain detectors using high resolution mass spectrometry. This promising concept is currently undergoing calibration in the laboratory at FU Berlin with the Orbitrap anaLYser MultiPle IonisAtion (OLYMPIA) [416]. Aiming for a similar goal, the CosmOrbitrap (an Orbitrap mass analyzer coupled with a laser ablation ionization system) is currently in development as an adaptation for space exploration [402, 403].

Spaceborne Orbitrap instruments would be of significant value in the search for biosignatures, and especially relevant for agnostic biosignatures (i.e., life as we do not know it) [33]. In fact, it seems today necessary to broaden the search for biosignatures outside of the framework of terrestrial biosignatures. Indeed, as life has a high capacity for evolution (which is needed to adapt organisms to changing environmental conditions), biosignatures may therefore be different on extraterrestrial planetary environments, and very challenging to detect. A high resolution mass spectrometer onboard a space mission would therefore be an invaluable tool for astrobiology investigations searching for extraterrestrial forms of life.

VI   Bibliography and Supplementary material

1   Bibliography

References

[1] M. S. Dodd, D. Papineau, T. Grenne, J. F. Slack, M. Rittner, F. Pirajno, J. O'Neil, and C. T. Little, "Evidence for early life in earth's oldest hydrothermal vent precipitates," *Nature*, vol. 543, no. 7643, pp. 60–64, 2017.

[2] E. Camprubi, J. De Leeuw, C. House, F. Raulin, M. Russell, A. Spang, M. Tirumalai, and F. Westall, "The emergence of life," *Space Science Reviews*, vol. 215, no. 8, pp. 1–53, 2019.

[3] N. Glansdorff, Y. Xu, and B. Labedan, "The last universal common ancestor: emergence, constitution and genetic legacy of an elusive forerunner," *Biology direct*, vol. 3, no. 1, pp. 1–35, 2008.

[4] C. S. Cockell, T. Bush, C. Bryce, S. Direito, M. Fox-Powell, J. P. Harrison, H. Lammer, H. Landenmark, J. Martin-Torres, N. Nicholson, *et al.*, "Habitability: a review," *Astrobiology*, vol. 16, no. 1, pp. 89–117, 2016.

[5] J. P. Harrison, N. Gheeraert, D. Tsigelnitskiy, and C. S. Cockell, "The limits for life under multiple extremes," *Trends in microbiology*, vol. 21, no. 4, pp. 204–212, 2013.

[6] S. A. Benner, A. Ricardo, and M. A. Carrigan, "Is there a common chemical model for life in the universe?," *Current opinion in chemical biology*, vol. 8, no. 6, pp. 672–689, 2004.

[7] D. Schulze-Makuch, L. N. Irwin, D. Schulze-Makuch, and L. N. Irwin, "Life and the need for a solvent," *Life in the universe: Expectations and constraints*, pp. 123–147, 2018.

[8] P. Ball, "Water as an active constituent in cell biology," *Chemical reviews*, vol. 108, no. 1, pp. 74–108, 2008.

[9] P. Ball, "The importance of water," in *Astrochemistry and Astrobiology*, pp. 169–210, Springer, 2012.

[10] M. Gargaud and R. Amils, *Encyclopedia of astrobiology*, vol. 1. Springer Science & Business Media, 2011.

[11] R. A. Craddock and A. D. Howard, "The case for rainfall on a warm, wet early mars," *Journal of Geophysical Research: Planets*, vol. 107, no. E11, pp. 21–1, 2002.

[12] A. D. Howard, J. M. Moore, and R. P. Irwin III, "An intense terminal epoch of widespread fluvial activity on early mars: 1. valley network incision and associated deposits," *Journal of Geophysical Research: Planets*, vol. 110, no. E12, 2005.

[13] C. I. Fassett and J. W. Head III, "Valley network-fed, open-basin lakes on mars: Distribution and implications for noachian surface and subsurface hydrology," *Icarus*, vol. 198, no. 1, pp. 37–56, 2008.

[14] R. K. Kopparapu, R. M. Ramirez, J. SchottelKotte, J. F. Kasting, S. Domagal-Goldman, and V. Eymet, "Habitable zones around main-sequence stars: dependence on planetary mass," *The Astrophysical Journal Letters*, vol. 787, no. 2, p. L29, 2014.

[15] L. Kaltenegger, "How to characterize habitable worlds and signs of life," *Annual Review of Astronomy and Astrophysics*, vol. 55, pp. 433–485, 2017.

[16] M. Mayor and D. Queloz, "A jupiter-mass companion to a solar-type star," *nature*, vol. 378, no. 6555, pp. 355–359, 1995.

[17] B. Rojas-Ayala, "Twenty-five years of exoplanet discoveries: The exoplanet hosts," in *Planetary Systems Now*, pp. 71–95, World Scientific, 2023.

[18] M. A. Voytek, "Nasa astrobiology strategy 2015," 2016.

[19] A. C. Barr, "Formation of exomoons: a solar system perspective," *Astronomical Review*, vol. 12, no. 1-4, pp. 24–52, 2016.

[20] N. R. Hinkel and S. R. Kane, "Habitability of exomoons at the hill or tidal locking radius," *The Astrophysical Journal*, vol. 774, no. 1, p. 27, 2013.

[21] J. Tjoa, M. Mueller, and F. van der Tak, "The subsurface habitability of small, icy exomoons," *Astronomy & Astrophysics*, vol. 636, p. A50, 2020.

[22] P. Mason and P. Biermann, "Astrophysical and cosmological constraints on life," *Habitability of the Universe before Earth. Elsevier BV, Amsterdam*, pp. 89–126, 2018.

[23] A. Méndez, E. G. Rivera-Valentín, D. Schulze-Makuch, J. Filiberto, R. M. Ramírez, T. E. Wood, A. Dávila, C. McKay, K. N. O. Ceballos, M. Jusino-Maldonado, *et al.*, "Habitability models for astrobiology," *Astrobiology*, vol. 21, no. 8, pp. 1017–1027, 2021.

[24] D. J. Des Marais, J. A. Nuth III, L. J. Allamandola, A. P. Boss, J. D. Farmer, T. M. Hoehler, B. M. Jakosky, V. S. Meadows, A. Pohorille, B. Runnegar, *et al.*, "The nasa astrobiology roadmap," *Astrobiology*, vol. 8, no. 4, pp. 715–730, 2008.

[25] C. Malaterre, I. L. ten Kate, M. Baqué, V. Debaille, J. L. Grenfell, E. J. Javaux, , N. Khawaja, F. Klenner, Y. J. Lara, *et al.*, "Is there such a thing as a biosignature?," *Astrobiology*, 2023.

[26] B. Ménez, C. Pisapia, M. Andreani, F. Jamme, Q. P. Vanbellingen, A. Brunelle, L. Richard, P. Dumas, and M. Réfrégiers, "Abiotic synthesis of amino acids in the recesses of the oceanic lithosphere," *Nature*, vol. 564, no. 7734, pp. 59–63, 2018.

[27] P. Schwendner, A. Riedo, D. J. Melton, P. Horvath, R. Lindner, P. Ehrenfreund, K. Beblo-Vranesevic, P. Rettberg, E. Rabbow, F. Westall, *et al.*, "Microbial metabolism of amino acids—biologically induced removal of glycine and the resulting fingerprint as a potential biosignature," *Frontiers in Astronomy and Space Sciences*, vol. 9, p. 781542, 2022.

[28] A. F. Davila and C. P. McKay, "Chance and necessity in biochemistry: implications for the search for extraterrestrial biomarkers in earth-like environments," *Astrobiology*, vol. 14, no. 6, pp. 534–540, 2014.

[29] C. D. Georgiou and D. W. Deamer, "Lipids as universal biomarkers of extraterrestrial life," *Astrobiology*, vol. 14, no. 6, pp. 541–549, 2014.

[30] T. L. Salter, J. S. Watson, J. H. Waite, and M. A. Sephton, "Hydrothermal processing of microorganisms: Mass spectral signals of degraded biosignatures for life detection on icy moons," *ACS Earth and Space Chemistry*, vol. 6, no. 10, pp. 2508–2518, 2022.

[31] C. P. McKay, "What is life—and how do we search for it in other worlds?," *PLoS biology*, vol. 2, no. 9, p. e302, 2004.

[32] J. J. Brocks, R. Buick, R. E. Summons, and G. A. Logan, "A reconstruction of archean biological diversity based on molecular fossils from the 2.78 to 2.45 billion-year-old mount bruce supergroup, hamersley basin, western australia," *Geochimica et Cosmochimica Acta*, vol. 67, no. 22, pp. 4321–4335, 2003.

[33] L. Chou, P. Mahaffy, M. Trainer, J. Eigenbrode, R. Arevalo, W. Brinckerhoff, S. Getty, N. Grefenstette, V. Da Poian, G. M. Fricke, *et al.*, "Planetary mass spectrometry for agnostic life detection in the solar system," *Frontiers in Astronomy and Space Sciences*, vol. 8, p. 755100, 2021.

[34] D. S. McKay, E. K. Gibson Jr, K. L. Thomas-Keprta, H. Vali, C. S. Romanek, S. J. Clemett, X. D. Chillier, C. R. Maechling, and R. N. Zare, "Search for past life on mars: possible relic biogenic activity in martian meteorite alh84001," *Science*, vol. 273, no. 5277, pp. 924–930, 1996.

[35] C. E. Cleland and C. F. Chyba, "Defining 'life'," *Origins of Life and Evolution of the Biosphere*, vol. 32, pp. 387–393, 2002.

[36] N. R. Pace, "The universal nature of biochemistry," *Proceedings of the National Academy of Sciences*, vol. 98, no. 3, pp. 805–808, 2001.

[37] J. Stevenson, J. Lunine, and P. Clancy, "Membrane alternatives in worlds without oxygen: Creation of an azotosome," *Science advances*, vol. 1, no. 1, p. e1400067, 2015.

[38] S. S. Johnson, E. V. Anslyn, H. V. Graham, P. R. Mahaffy, and A. D. Ellington, "Fingerprinting non-terran biosignatures," *Astrobiology*, vol. 18, no. 7, pp. 915–922, 2018.

[39] W. Martin, J. Baross, D. Kelley, and M. J. Russell, "Hydrothermal vents and the origin of life," *Nature Reviews Microbiology*, vol. 6, no. 11, pp. 805–814, 2008.

[40] B. Damer and D. Deamer, "The hot spring hypothesis for an origin of life," *Astrobiology*, vol. 20, no. 4, pp. 429–452, 2020.

[41] G. Horneck, D. M. Klaus, and R. L. Mancinelli, "Space microbiology," *Microbiology and molecular biology reviews*, vol. 74, no. 1, pp. 121–156, 2010.

[42] A. Yamagishi, Y. Kawaguchi, S.-i. Yokobori, H. Hashimoto, H. Yano, E. Imai, S. Kodaira, Y. Uchihori, and K. Nakagawa, "Environmental data and survival data of deinococcus aetherius from the exposure facility of the japan experimental module of the international space station obtained by the tanpopo mission," *Astrobiology*, vol. 18, no. 11, pp. 1369–1374, 2018.

[43] N. Merino, H. S. Aronson, D. P. Bojanova, J. Feyhl-Buska, M. L. Wong, S. Zhang, and D. Giovannelli, "Living at the extremes: extremophiles and the limits of life in a planetary context," *Frontiers in microbiology*, vol. 10, p. 780, 2019.

[44] L. J. Rothschild and R. L. Mancinelli, "Life in extreme environments," *Nature*, vol. 409, no. 6823, pp. 1092–1101, 2001.

[45] A. H. Knoll, *Life on a Young Planet: The First Three Billion Years of Evolution on Earth: The First Three Billion Years of Evolution on Earth*. Princeton University Press, 2015.

[46] P. Boston, M. Spilde, D. Northup, L. Melim, D. Soroka, L. Kleina, K. Lavoie, L. Hose, L. Mallory, C. Dahm, *et al.*, "Cave biosignature suites: microbes, minerals, and mars," *Astrobiology*, vol. 1, no. 1, pp. 25–55, 2001.

[47] A. R. Hendrix, T. A. Hurford, L. M. Barge, M. T. Bland, J. S. Bowman, W. Brinckerhoff, B. J. Buratti, M. L. Cable, J. Castillo-Rogez, G. C. Collins, *et al.*, "The nasa roadmap to ocean worlds," *Astrobiology*, vol. 19, no. 1, pp. 1–27, 2019.

[48] G. Choblet, G. Tobie, C. Sotin, M. Běhounková, O. Čadek, F. Postberg, and O. Souček, "Powering prolonged hydrothermal activity inside enceladus," *Nature Astronomy*, vol. 1, no. 12, pp. 841–847, 2017.

[49] J. Anderson, E. Lau, W. Sjogren, G. Schubert, and W. Moore, "Gravitational constraints on the internal structure of ganymede," *Nature*, vol. 384, no. 6609, pp. 541–543, 1996.

[50] K. Khurana, M. Kivelson, D. Stevenson, G. Schubert, C. Russell, R. Walker, and C. Polanskey, "Induced magnetic fields as evidence for subsurface oceans in europa and callisto," *Nature*, vol. 395, no. 6704, pp. 777–780, 1998.

[51] M. H. Carr, M. J. S. Belton, C. R. Chapman, M. E. Davies, P. Geissler, R. Greenberg, A. S. McEwen, B. R. Tufts, R. Greeley, R. Sullivan, J. W. Head, R. T. Pappalardo, K. P. Klaasen, T. V. Johnson, J. Kaufman, D. Senske, J. Moore, G. Neukum, G. Schubert, J. A. Burns, P. Thomas, and J. Veverka, "Evidence for a subsurface ocean on europa," *Nature*, vol. 391, no. 6665, pp. 363–365, 1998.

[52] L. Iess, D. Stevenson, M. Parisi, D. Hemingway, R. Jacobson, J. Lunine, F. Nimmo, J. Armstrong, S. Asmar, M. Ducci, *et al.*, "The gravity field and interior structure of enceladus," *Science*, vol. 344, no. 6179, pp. 78–80, 2014.

[53] P. Thomas, R. Tajeddine, M. Tiscareno, J. Burns, J. Joseph, T. Loredo, P. Helfenstein, and C. Porco, "Enceladus's measured physical libration requires a global subsurface ocean," *Icarus*, vol. 264, pp. 37–47, 2016.

[54] C. Béghin, O. Randriamboarison, M. Hamelin, E. Karkoschka, C. Sotin, R. C. Whitten, J.-J. Berthelier, R. Grard, and F. Simões, "Analytic theory of titan's schumann resonance: Constraints on ionospheric conductivity and buried water ocean," *Icarus*, vol. 218, no. 2, pp. 1028–1042, 2012.

[55] J. Gaeman, S. Hier-Majumder, and J. H. Roberts, "Sustainability of a subsurface ocean within triton's interior," *Icarus*, vol. 220, no. 2, pp. 339–347, 2012.

[56] A. R. Rhoden, "Mimas: Frozen fragment, ring relic, or emerging ocean world?," *Annual Review of Earth and Planetary Sciences*, vol. 51, pp. 367–387, 2023.

[57] H. Hussmann, F. Sohl, and T. Spohn, "Subsurface oceans and deep interiors of medium-sized outer planet satellites and large trans-neptunian objects," *Icarus*, vol. 185, no. 1, pp. 258–273, 2006.

[58] R. Heller and R. Barnes, "Exomoon habitability constrained by illumination and tidal heating," *Astrobiology*, vol. 13, no. 1, pp. 18–46, 2013.

[59] V. Dobos and E. L. Turner, "Viscoelastic models of tidally heated exomoons," *The Astrophysical Journal*, vol. 804, no. 1, p. 41, 2015.

[60] N. Lane, J. F. Allen, and W. Martin, "How did luca make a living? chemiosmosis in the origin of life," *BioEssays*, vol. 32, no. 4, pp. 271–280, 2010.

[61] F. Postberg, Y. Sekine, F. Klenner, C. R. Glein, Z. Zou, B. Abel, K. Furuya, J. K. Hillier, N. Khawaja, S. Kempf, *et al.*, "Detection of phosphates originating from enceladus's ocean," *Nature*, vol. 618, no. 7965, pp. 489–493, 2023.

[62] D. A. Patthoff and S. A. Kattenhorn, "A fracture history on enceladus provides evidence for a global ocean," *Geophysical Research Letters*, vol. 38, no. 18, 2011.

[63] W. B. McKinnon, "Effect of enceladus's rapid synchronous spin on interpretation of cassini gravity," *Geophysical Research Letters*, vol. 42, no. 7, pp. 2137–2143, 2015.

[64] J. H. Waite, C. R. Glein, R. S. Perryman, B. D. Teolis, B. A. Magee, G. Miller, J. Grimes, M. E. Perry, K. E. Miller, A. Bouquet, *et al.*, "Cassini finds molecular hydrogen in the enceladus plume: evidence for hydrothermal processes," *Science*, vol. 356, no. 6334, pp. 155–159, 2017.

[65] F. Postberg, N. Khawaja, B. Abel, G. Choblet, C. R. Glein, M. S. Gudipati, B. L. Henderson, H.-W. Hsu, S. Kempf, F. Klenner, G. Moragas-Klostermeyer, B. Magee, L. Nölle, M. Perry, R. Reviol, J. Schmidt, R. , F. Stolz, G. Tobie, M. Trieloff, and J. H. Waite, "Macromolecular organic compounds from the depths of Enceladus," *Nature*, vol. 558, no. 7711, pp. 564–568, 2018.

[66] N. Khawaja, F. Postberg, J. Hillier, F. Klenner, S. Kempf, L. Nölle, R. Reviol, Z. Zou, and R. Srama, "Low-mass nitrogen-, oxygen-bearing, and aromatic compounds in enceladean ice grains," *Monthly Notices of the Royal Astronomical Society*, vol. 489, no. 4, pp. 5231–5243, 2019.

[67] H.-W. Hsu, F. Postberg, Y. Sekine, T. Shibuya, S. Kempf, M. Horányi, A. Juhász, N. Altobelli, K. Suzuki, Y. Masaki, *et al.*, "Ongoing hydrothermal activities within enceladus," *Nature*, vol. 519, no. 7542, pp. 207–210, 2015.

[68] C. R. Glein and J. H. Waite, "The carbonate geochemistry of enceladus' ocean," *Geophysical Research Letters*, vol. 47, no. 3, p. e2019GL085885, 2020.

[69] M. G. Kivelson, K. K. Khurana, C. T. Russell, M. Volwerk, R. J. Walker, and C. Zimmer, "Galileo magnetometer measurements: A stronger case for a subsurface ocean at europa," *Science*, vol. 289, no. 5483, pp. 1340–1343, 2000.

[70] M. Ross and G. Schubert, "Tidal heating in an internal ocean model of europa," *Nature*, vol. 325, no. 6100, pp. 133–134, 1987.

[71] C. Sotin, G. Tobie, J. Wahr, W. B. McKinnon, W. McKinnon, and K. Khurana, "Tides and tidal heating on europa," *Europa*, vol. 11, 2009.

[72] R. P. Lowell and M. DuBose, "Hydrothermal systems on europa," *Geophysical Research Letters*, vol. 32, no. 5, 2005.

[73] M. Běhounková, G. Tobie, G. Choblet, M. Kervazo, M. Melwani Daswani, C. Dumoulin, and S. D. Vance, "Tidally induced magmatic pulses on the oceanic floor of jupiter's moon europa," *Geophysical Research Letters*, vol. 48, no. 3, p. e2020GL090077, 2021.

[74] K. P. Hand, R. W. Carlson, and C. F. Chyba, "Energy, chemical disequilibrium, and geological constraints on europa," *Astrobiology*, vol. 7, no. 6, pp. 1006–1022, 2007.

[75] R. W. Carlson, M. S. Anderson, R. E. Johnson, W. D. Smythe, A. R. Hendrix, C. A. Barth, L. A. Soderblom, G. B. Hansen, T. B. McCord, J. B. Dalton, R. N. Clark, J. H. Shirley, A. C. Ocampo, and D. L. Matson, "Hydrogen peroxide on the surface of europa," *Science*, vol. 283, no. 5410, pp. 2062–2064, 1999.

[76] M. Moore and R. Hudson, "Ir detection of h2o2 at 80 k in ion-irradiated laboratory ices relevant to europa," *Icarus*, vol. 145, no. 1, pp. 282–288, 2000.

[77] C. Paranicas, J. Cooper, H. Garrett, R. Johnson, and S. Sturner, "Europa's radiation environment and its effects on the surface," *Europa*, pp. 529–544, 2009.

[78] J. Li, M. S. Gudipati, Y. N. Mishra, M.-C. Liang, and Y. L. Yung, "Oxidant generation in the ice under electron irradiation: Simulation and application to europa," *Icarus*, vol. 373, p. 114760, 2022.

[79] S. L. Miller and J. L. Bada, "Submarine hot springs and the origin of life," *Nature*, vol. 334, no. 6183, pp. 609–611, 1988.

[80] M. J. Russell, L. M. Barge, R. Bhartia, D. Bocanegra, P. J. Bracher, E. Branscomb, R. Kidd, S. McGlynn, D. H. Meier, W. Nitschke, *et al.*, "The drive to life on wet and icy worlds," *Astrobiology*, vol. 14, no. 4, pp. 308–343, 2014.

[81] B. T. Burcar, L. M. Barge, D. Trail, E. B. Watson, M. J. Russell, and L. B. McGown, "Rna oligomerization in laboratory analogues of alkaline hydrothermal vent systems," *Astrobiology*, vol. 15, no. 7, pp. 509–522, 2015.

[82] D. Deamer and B. Damer, "Can life begin on enceladus? a perspective from hydrothermal chemistry," *Astrobiology*, vol. 17, no. 9, pp. 834–839, 2017.

[83] E. L. Steel, A. Davila, and C. P. McKay, "Abiotic and biotic formation of amino acids in the enceladus ocean," *Astrobiology*, vol. 17, no. 9, pp. 862–875, 2017.

[84] W. Takahagi, K. Seo, T. Shibuya, Y. Takano, K. Fujishima, M. Saitoh, S. Shimamura, Y. Matsui, M. Tomita, and K. Takai, "Peptide synthesis under the alkaline hydrothermal conditions on enceladus," *ACS Earth and Space Chemistry*, vol. 3, no. 11, pp. 2559–2568, 2019.

[85] A. Priye, Y. Yu, Y. A. Hassan, and V. M. Ugaz, "Synchronized chaotic targeting and acceleration of surface chemistry in prebiotic hydrothermal microenvironments," *Proceedings of the National Academy of Sciences*, vol. 114, no. 6, pp. 1275–1280, 2017.

[86] S. Miyakawa, H. J. Cleaves, and S. L. Miller, "The cold origin of life: B. implications based on pyrimidines and purines produced from frozen ammonium cyanide solutions," *Origins of Life and Evolution of the Biosphere*, vol. 32, pp. 209–218, 2002.

[87] C. Dumas, B. A. Smith, and R. J. Terrile, "Hubble space telescope nicmos multiband photometry of proteus and puck," *The Astronomical Journal*, vol. 126, no. 2, p. 1080, 2003.

[88] L. Iess, N. J. Rappaport, R. A. Jacobson, P. Racioppa, D. J. Stevenson, P. Tortora, J. W. Armstrong, and S. W. Asmar, "Gravity field, shape, and moment of inertia of titan," *science*, vol. 327, no. 5971, pp. 1367–1369, 2010.

[89] L. Iess, R. A. Jacobson, M. Ducci, D. J. Stevenson, J. I. Lunine, J. W. Armstrong, S. W. Asmar, P. Racioppa, N. J. Rappaport, and P. Tortora, "The tides of titan," *Science*, vol. 337, no. 6093, pp. 457–459, 2012.

[90] D. Durante, D. Hemingway, P. Racioppa, L. Iess, and D. Stevenson, "Titan's gravity field and interior structure after cassini," *Icarus*, vol. 326, pp. 123–132, 2019.

[91] S. A. Stern, W. M. Grundy, W. B. McKinnon, H. A. Weaver, and L. A. Young, "The pluto system after new horizons," *Annual Review of Astronomy and Astrophysics*, vol. 56, pp. 357–392, 2018.

[92] M. C. De Sanctis, G. Mitri, J. Castillo-Rogez, C. H. House, S. Marchi, C. A. Raymond, and Y. Sekine, "Relict ocean worlds: Ceres," *Space Science Reviews*, vol. 216, pp. 1–33, 2020.

[93] J. C. Castillo-Rogez and K. Kalousová, "Ocean worlds in our solar system," *Elements: An International Magazine of Mineralogy, Geochemistry, and Petrology*, vol. 18, no. 3, pp. 161–166, 2022.

[94] S. Peale, "Origin and evolution of the natural satellites," *Annual Review of Astronomy and Astrophysics*, vol. 37, no. 1, pp. 533–602, 1999.

[95] H. Hussmann and T. Spohn, "Thermal-orbital evolution of io and europa," *Icarus*, vol. 171, no. 2, pp. 391–410, 2004.

[96] F. Sohl, H. Hussmann, B. Schwentker, T. Spohn, and R. Lorenz, "Interior structure models and tidal love numbers of titan," *Journal of Geophysical Research: Planets*, vol. 108, no. E12, 2003.

[97] K. Nagel, D. Breuer, and T. Spohn, "A model for the interior structure, evolution, and differentiation of callisto," *Icarus*, vol. 169, no. 2, pp. 402–412, 2004.

[98] M. T. Bland, A. P. Showman, and G. Tobie, "The orbital–thermal evolution and global expansion of ganymede," *Icarus*, vol. 200, no. 1, pp. 207–221, 2009.

[99] C. C. Porco, P. Helfenstein, P. Thomas, A. Ingersoll, J. Wisdom, R. West, G. Neukum, T. Denk, R. Wagner, T. Roatsch, *et al.*, "Cassini observes the active south pole of enceladus," *science*, vol. 311, no. 5766, pp. 1393–1401, 2006.

[100] S. D. Vance, M. P. Panning, S. Stähler, F. Cammarano, B. G. Bills, G. Tobie, S. Kamata, S. Kedar, C. Sotin, W. T. Pike, *et al.*, "Geophysical investigations of habitability in ice-covered ocean worlds," *Journal of Geophysical Research: Planets*, vol. 123, no. 1, pp. 180–205, 2018.

[101] B. Journaux, K. Kalousová, C. Sotin, G. Tobie, S. Vance, J. Saur, O. Bollengier, L. Noack, T. Rückriemen-Bez, T. Van Hoolst, *et al.*, "Large ocean worlds with high-pressure ices," *Space Science Reviews*, vol. 216, pp. 1–36, 2020.

[102] C. Sotin, K. Kalousová, and G. Tobie, "Titan's interior structure and dynamics after the cassini-huygens mission," *Annual Review of Earth and Planetary Sciences*, vol. 49, pp. 579–607, 2021.

[103] R. D. Lorenz, E. P. Turtle, J. W. Barnes, M. G. Trainer, D. S. Adams, K. E. Hibbard, C. Z. Sheldon, K. Zacny, P. N. Peplowski, D. J. Lawrence, *et al.*, "Dragonfly: A rotorcraft lander concept for scientific exploration at titan," *Johns Hopkins APL Technical Digest*, vol. 34, no. 3, p. 14, 2018.

[104] G. Schubert, J. D. Anderson, B. J. Travis, and J. Palguta, "Enceladus: Present internal structure and differentiation by early and long-term radiogenic heating," *Icarus*, vol. 188, no. 2, pp. 345–355, 2007.

[105] P. M. Schenk, R. N. Clark, C. J. Howett, A. J. Verbiscer, and J. H. Waite, *Enceladus and the icy moons of Saturn*. University of Arizona Press, 2018.

[106] D. J. Hemingway and T. Mittal, "Enceladus's ice shell structure as a window on internal heat production," *Icarus*, vol. 332, pp. 111–131, 2019.

[107] C. Howett, J. Spencer, J. Pearl, and M. Segura, "Thermal inertia and bolometric bond albedo values for mimas, enceladus, tethys, dione, rhea and iapetus as derived from cassini/cirs measurements," *Icarus*, vol. 206, no. 2, pp. 573–593, 2010.

[108] J. P. Kay and A. J. Dombard, "Simulating spatial variations of lithospheric folding in the south polar terrain of enceladus," *Icarus*, vol. 394, p. 115431, 2023.

[109] J. Spencer, J. Pearl, M. Segura, F. Flasar, A. Mamoutkine, P. Romani, B. Buratti, A. Hendrix, L. Spilker, and R. Lopes, "Cassini encounters enceladus: Background and the discovery of a south polar hot spot," *science*, vol. 311, no. 5766, pp. 1401–1405, 2006.

[110] C. Howett, J. Spencer, J. Pearl, and M. Segura, "High heat flow from enceladus' south polar region measured using 10–600 cm- 1 cassini/cirs data," *Journal of Geophysical Research: Planets*, vol. 116, no. E3, 2011.

[111] C. Howett, F. Nimmo, and J. Spencer, "Constraining enceladus' heat flow between its tiger stripes," tech. rep., Copernicus Meetings, 2022.

[112] O. Čadek, G. Tobie, T. Van Hoolst, M. Massé, G. Choblet, A. Lefèvre, G. Mitri, R.-M. Baland, M. Běhounková, O. Bourgeois, *et al.*, "Enceladus's internal ocean and ice shell constrained from cassini gravity, shape, and libration data," *Geophysical Research Letters*, vol. 43, no. 11, pp. 5653–5660, 2016.

[113] A. M. Schoenfeld, E. K. Hawkins, K. M. Soderlund, S. D. Vance, E. Leonard, and A. Yin, "Particle entrainment and rotating convection in enceladus' ocean," *Communications Earth & Environment*, vol. 4, no. 1, p. 28, 2023.

[114] A. R. Rhoden, T. A. Hurford, J. Spitale, W. Henning, E. M. Huff, M. T. Bland, and S. Sajous, "The formation of enceladus' tiger stripe fractures from eccentricity tides," *Earth and Planetary Science Letters*, vol. 544, p. 116389, 2020.

[115] M. Cable, S. M. MacKenzie, M. Neveu, T. Hoehler, A. Hendrix, J. L. Eigenbrode, F. Postberg, C. Porco, C. R. Glein, L. Spilker, *et al.*, "The case for a return to enceladus," *Bulletin of the American Astronomical Society*, vol. 53, no. 4, p. 053, 2021.

[116] M. K. Dougherty, K. K. Khurana, F. M. Neubauer, C. T. Russell, J. Saur, J. S. Leisner, and M. E. Burton, "Identification of a dynamic atmosphere at enceladus with the cassini magnetometer," *Science*, vol. 311, no. 5766, pp. 1406–1409, 2006.

[117] C. J. Hansen, L. Esposito, A. I. F. Stewart, J. Colwell, A. Hendrix, W. Pryor, D. Shemansky, and R. West, "Enceladus' water vapor plume," *Science*, vol. 311, no. 5766, pp. 1422–1425, 2006.

[118] F. Spahn, J. Schmidt, N. Albers, M. Hörning, M. Makuch, M. Seiß, S. Kempf, R. Srama, V. Dikarev, S. Helfert, G. Moragas-Klostermeyer, A. V. Krivov, M. Sremčević, A. J. Tuzzolino, T. Economou, and E. Grün, "Cassini dust measurements at enceladus and implications for the origin of the e ring," *Science*, vol. 311, no. 5766, pp. 1416–1418, 2006.

[119] R. Tokar, R. Johnson, T. Hill, D. Pontius, W. Kurth, F. Crary, D. Young, M. Thomsen, D. Reisenfeld, A. Coates, *et al.*, "The interaction of the atmosphere of enceladus with saturn's plasma," *Science*, vol. 311, no. 5766, pp. 1409–1412, 2006.

[120] J. H. Waite Jr, M. R. Combi, W.-H. Ip, T. E. Cravens, R. L. McNutt Jr, W. Kasprzak, R. Yelle, J. Luhmann, H. Niemann, D. Gell, *et al.*, "Cassini ion and neutral mass spectrometer: Enceladus plume composition and structure," *science*, vol. 311, no. 5766, pp. 1419–1422, 2006.

[121] C. Porco, D. DiNino, and F. Nimmo, "How the geysers, tidal stresses, and thermal emission across the south polar terrain of enceladus are related," *The Astronomical Journal*, vol. 148, no. 3, p. 45, 2014.

[122] J. Schmidt, N. Brilliantov, F. Spahn, and S. Kempf, "Slow dust in enceladus' plume from condensation and wall collisions in tiger stripe fractures," *Nature*, vol. 451, no. 7179, pp. 685–688, 2008.

[123] B. D. Teolis, M. E. Perry, C. J. Hansen, J. H. Waite, C. C. Porco, J. R. Spencer, and C. J. Howett, "Enceladus plume structure and time variability: Comparison of cassini observations," *Astrobiology*, vol. 17, no. 9, pp. 926–940, 2017.

[124] F. Postberg, J. Schmidt, J. Hillier, S. Kempf, and R. Srama, "A salt-water reservoir as the source of a compositionally stratified plume on enceladus," *Nature*, vol. 474, no. 7353, pp. 620–622, 2011.

[125] S. Kempf, M. Horányi, H.-W. Hsu, T. W. Hill, A. Juhász, and H. T. Smith, "Saturn's diffuse e ring and its connection with enceladus," *Enceladus and the Icy Moons of Saturn*, pp. 195–210, 2018.

[126] C. C. Porco, L. Dones, and C. Mitchell, "Could it be snowing microbes on enceladus? assessing conditions in its plume and implications for future missions," *Astrobiology*, vol. 17, no. 9, pp. 876–901, 2017.

[127] A. P. Ingersoll and S. P. Ewald, "Total particulate mass in enceladus plumes and mass of saturn's e ring inferred from cassini iss images," *Icarus*, vol. 216, no. 2, pp. 492–506, 2011.

[128] F. Postberg, S. Kempf, J. Schmidt, N. Brilliantov, A. Beinsen, B. Abel, U. Buck, and R. Srama, "Sodium salts in e-ring ice grains from an ocean below the surface of enceladus," *Nature*, vol. 459, no. 7250, pp. 1098–1101, 2009.

[129] F. Postberg, R. N. Clark, C. J. Hansen, A. J. Coates, C. M. Dalle Ore, F. Scipioni, M. M. Hedman, and J. H. Waite, "Plume and surface composition of enceladus," *Enceladus and the icy moons of Saturn*, vol. 129, 2018.

[130] Y. Sekine, T. Shibuya, F. Postberg, H.-W. Hsu, K. Suzuki, Y. Masaki, T. Kuwatani, M. Mori, P. K. Hong, M. Yoshizaki, S. Tachibana, and S.-i. Sirono, "High-temperature water–rock interactions and hydrothermal environments in the chondrite-like core of enceladus," *Nature Communications*, vol. 6, no. 1, p. 8604, 2015.

[131] M. Y. Zolotov, "An oceanic composition on early and today's enceladus," *Geophysical Research Letters*, vol. 34, no. 23, 2007.

[132] L. F. Coelho and Z. Martins, "The geochemistry of icy moons," *Encycl. Geol*, vol. 1, pp. 207–216, 2021.

[133] C. R. Glein, F. Postberg, and S. D. Vance, "The geochemistry of enceladus: Composition and controls," *Enceladus and the icy moons of Saturn*, vol. 39, 2018.

[134] D. S. Kelley, t. A.-. S. Party, J. A. Karson, D. K. Blackman, G. L. Fruh-Green, D. A. Butterfield, M. D. Lilley, E. J. Olson, M. O. Schrenk, K. K. Roe, G. T. Lebon, and P. Rivizzigno, "An off-axis hydrothermal vent field near the mid-atlantic ridge at 30 deg n," *Nature*, vol. 412, no. 6843, pp. 145–149, 2001.

[135] D. S. Kelley, J. A. Karson, G. L. Fruh-Green, D. R. Yoerger, T. M. Shank, D. A. Butterfield, J. M. Hayes, M. O. Schrenk, E. J. Olson, G. Proskurowski, *et al.*, "A serpentinite-hosted ecosystem: the lost city hydrothermal field," *Science*, vol. 307, no. 5714, pp. 1428–1434, 2005.

[136] C. R. Fisher, K. Takai, and N. Le Bris, "Hydrothermal vent ecosystems," *Oceanography*, vol. 20, no. 1, pp. 14–23, 2007.

[137] A. Boetius, "Lost city life," *Science*, vol. 307, no. 5714, pp. 1420–1422, 2005.

[138] J. B. Corliss, J. Dymond, L. I. Gordon, J. M. Edmond, R. P. von Herzen, R. D. Ballard, K. Green, D. Williams, A. Bainbridge, K. Crane, *et al.*, "Submarine thermal springs on the galapagos rift," *Science*, vol. 203, no. 4385, pp. 1073–1083, 1979.

[139] K. Von Damm, "Seafloor hydrothermal activity: black smoker chemistry and chimneys," *Annual Review of Earth and Planetary Sciences*, vol. 18, no. 1, pp. 173–204, 1990.

[140] P. Tsou, D. E. Brownlee, C. P. McKay, A. D. Anbar, H. Yano, K. Altwegg, L. W. Beegle, R. Dissly, N. J. Strange, and I. Kanik, "Life: Life investigation for enceladus a sample return mission concept in search for evidence of life," *Astrobiology*, vol. 12, no. 8, pp. 730–742, 2012.

[141] K. Reh, L. Spilker, J. I. Lunine, J. H. Waite, M. L. Cable, F. Postberg, and K. Clark, "Enceladus life finder: The search for life in a habitable moon," in *2016 IEEE Aerospace Conference*, pp. 1–8, IEEE, 2016.

[142] J. Eigenbrode, R. E. Gold, C. P. McKay, T. Hurford, and A. Davila, "Searching for life in an ocean world: the enceladus life signatures and habitability (elsah) mission concept," *42nd COSPAR Scientific Assembly*, vol. 42, pp. F3–6, 2018.

[143] R. Srama, F. Postberg, H. Henkel, T. Klopfer, Y. Li, J. Simolka, S. Bugiel, S. Kempf, J. Hillier, N. Khawaja, *et al.*, "Enceladus icy jet analyzer (enija): Search for life with a high resolution tof-ms for in situ characterization of high dust density regions," *Eur. Planet. Sci. Congr*, vol. 10, 2015.

[144] O. Mousis, A. Bouquet, Y. Langevin, N. André, H. Boithias, G. Durry, F. Faye, P. Hartogh, J. Helbert, L. Iess, *et al.*, "Moonraker: enceladus multiple flyby mission," *The planetary science journal*, vol. 3, no. 12, p. 268, 2022.

[145] S. M. MacKenzie, M. Neveu, A. F. Davila, J. I. Lunine, K. L. Craft, M. L. Cable, C. M. Phillips-Lander, J. D. Hofgartner, J. L. Eigenbrode, J. H. Waite, *et al.*, "The enceladus orbilander mission concept: Balancing return and resources in the search for life," *The Planetary Science Journal*, vol. 2, no. 2, p. 77, 2021.

[146] K. Carpenter, A. Thoesen, D. Mick, J. Martia, M. Cable, K. Mitchell, S. Hovsepian, J. Jasper, N. Georgiev, R. Thakker, *et al.*, "Exobiology extant life surveyor (eels)," in *Earth and Space 2021*, pp. 328–338, 2021.

[147] L. Roth, J. Saur, K. D. Retherford, D. F. Strobel, P. D. Feldman, M. A. McGrath, and F. Nimmo, "Transient water vapor at europa's south pole," *Science*, vol. 343, no. 6167, pp. 171–174, 2014.

[148] G. Tobie, G. Choblet, and C. Sotin, "Tidally heated convection: Constraints on europa's ice shell thickness," *Journal of Geophysical Research: Planets*, vol. 108, no. E11, 2003.

[149] S. E. Billings and S. A. Kattenhorn, "The great thickness debate: Ice shell thickness models for europa and comparisons with estimates based on flexure at ridges," *Icarus*, vol. 177, no. 2, pp. 397–412, 2005.

[150] K. Hand and C. Chyba, "Empirical constraints on the salinity of the europan ocean and implications for a thin ice shell," *Icarus*, vol. 189, no. 2, pp. 424–438, 2007.

[151] P. D. Fischer, M. E. Brown, and K. P. Hand, "Spatially resolved spectroscopy of europa: The distinct spectrum of large-scale chaos," *The Astronomical Journal*, vol. 150, no. 5, p. 164, 2015.

[152] K. Zahnle, P. Schenk, H. Levison, and L. Dones, "Cratering rates in the outer solar system," *Icarus*, vol. 163, no. 2, pp. 263–289, 2003.

[153] T. Doggett, R. Greeley, P. Figueredo, and K. Tanaka, "Geologic stratigraphy and evolution of europa's surface," *Europa*, p. 137, 2009.

[154] R. Greeley, C. F. Chyba, J. Head, T. B. McCord, W. B. McKinnon, R. T. Pappalardo, P. H. Figueredo, *et al.*, "Geology of europa," *Jupiter: The planet, satellites and magnetosphere*, pp. 329–362, 2004.

[155] J. Riley, G. V. Hoppa, R. Greenberg, B. R. Tufts, and P. Geissler, "Distribution of chaotic terrain on europa," *Journal of Geophysical Research: Planets*, vol. 105, no. E9, pp. 22599–22615, 2000.

[156] G. Collins and F. Nimmo, "Chaotic terrain on europa," *Europa*, pp. 259–281, 2009.

[157] B. Schmidt, D. Blankenship, G. Patterson, and P. Schenk, "Active formation of 'chaos terrain'over shallow subsurface water on europa," *Nature*, vol. 479, no. 7374, pp. 502–505, 2011.

[158] P. Matteoni, A. Neesemann, R. Jaumann, J. Hillier, and F. Postberg, "Ménec fossae on europa: A strike-slip tectonics origin above a possible shallow water reservoir," *JGR: Planets*, vol. 128, 2023.

[159] C. Culha and M. Manga, "Geometry and spatial distribution of lenticulae on europa," *Icarus*, vol. 271, pp. 49–56, 2016.

[160] M. Manga and C. Michaut, "Formation of lenticulae on europa by saucer-shaped sills," *Icarus*, vol. 286, pp. 261–269, 2017.

[161] S. A. Kattenhorn and T. Hurford, "Tectonics of europa," *Europa*, pp. 199–236, 2009.

[162] S. A. Kattenhorn and L. M. Prockter, "Evidence for subduction in the ice shell of europa," *Nature Geoscience*, vol. 7, no. 10, pp. 762–767, 2014.

[163] P. Matteoni, A. Neesemann, R. Jaumann, J. Hillier, and F. Postberg, "Evolution of thrace macula on europa: Strike-slip tectonic control and identification of the youngest terrains," *Journal of Geophysical Research: Planets*, p. e2023JE007905, 2023.

[164] G. C. Collins, G. W. Patterson, C. E. Detelich, L. M. Prockter, S. A. Kattenhorn, C. M. Cooper, A. R. Rhoden, B. B. Cutler, S. R. Oldrid, R. P. Perkins, *et al.*, "Episodic plate tectonics on europa: Evidence for widespread patches of mobile-lid behavior in the antijovian hemisphere," *Journal of Geophysical Research. Planets*, vol. 127, no. 11, 2022.

[165] K. M. Soderlund, K. Kalousová, J. J. Buffo, C. R. Glein, J. C. Goodman, G. Mitri, G. W. Patterson, F. Postberg, M. Rovira-Navarro, T. Rückriemen, *et al.*, "Ice-ocean exchange processes in the jovian and saturnian satellites," *Space Science Reviews*, vol. 216, pp. 1–57, 2020.

[166] C. F. Chyba, "Energy for microbial life on europa," *Nature*, vol. 403, no. 6768, pp. 381–382, 2000.

[167] C. Chivers, J. Buffo, and B. Schmidt, "Thermal and chemical evolution of small, shallow water bodies in europa's ice shell," *Journal of Geophysical Research: Planets*, vol. 126, no. 5, p. e2020JE006692, 2021.

[168] S. D. Vance, K. P. Hand, and R. T. Pappalardo, "Geophysical controls of chemical disequilibria in europa," *Geophysical Research Letters*, vol. 43, no. 10, pp. 4871–4879, 2016.

[169] W. B. Sparks, K. P. Hand, M. A. McGrath, E. Bergeron, M. Cracraft, and S. E. Deustua, "PROBING FOR EVIDENCE OF PLUMES ON EUROPA WITH *HST* /STIS," *The Astrophysical Journal*, vol. 829, no. 2, p. 121, 2016.

[170] W. B. Sparks, B. E. Schmidt, M. A. McGrath, K. P. Hand, J. R. Spencer, M. Cracraft, and S. E. Deustua, "Active cryovolcanism on europa?," *The Astrophysical Journal Letters*, vol. 839, no. 2, p. L18, 2017.

[171] X. Jia, M. G. Kivelson, K. K. Khurana, and W. S. Kurth, "Evidence of a plume on europa from galileo magnetic and plasma wave signatures," *Nature Astronomy*, vol. 2, no. 6, pp. 459–464, 2018.

[172] L. Paganini, G. L. Villanueva, L. Roth, A. M. Mandell, T. A. Hurford, K. D. Retherford, and M. J. Mumma, "A measurement of water vapour amid a largely quiescent environment on europa," *Nature Astronomy*, vol. 4, no. 3, pp. 266–272, 2020.

[173] H. Huybrighs, E. Roussos, A. Blöcker, N. Krupp, Y. Futaana, S. Barabash, L. Hadid, M. Holmberg, O. Lomax, and O. Witasse, "An active plume eruption on europa during galileo flyby e26 as indicated by energetic proton depletions," *Geophysical Research Letters*, vol. 47, no. 10, p. e2020GL087806, 2020.

[174] B. Southworth, S. Kempf, and J. Schmidt, "Modeling europa's dust plumes," *Geophysical Research Letters*, vol. 42, no. 24, pp. 10–541, 2015.

[175] J. Dalton, D. P. Cruikshank, K. Stephan, T. B. Mccord, A. Coustenis, R. W. Carlson, and A. Coradini, "Chemical composition of icy satellite surfaces," *Space science reviews*, vol. 153, pp. 113–154, 2010.

[176] G. Villanueva, H. Hammel, S. Milam, S. Faggi, V. Kofman, L. Roth, K. Hand, L. Paganini, J. Stansberry, J. Spencer, *et al.*, "Endogenous co2 ice mixture on the surface of europa and no detection of plume activity," *Science*, vol. 381, no. 6664, pp. 1305–1308, 2023.

[177] S. K. Trumbo and M. E. Brown, "The distribution of co2 on europa indicates an internal source of carbon," *Science*, vol. 381, no. 6664, pp. 1308–1311, 2023.

[178] S. K. Trumbo, M. E. Brown, and K. P. Hand, "H2o2 within chaos terrain on europa's leading hemisphere," *The Astronomical Journal*, vol. 158, no. 3, p. 127, 2019.

[179] K. P. Hand and R. W. Carlson, "Europa's surface color suggests an ocean rich with sodium chloride: Sodium chloride on europa's surface," *Geophysical Research Letters*, vol. 42, no. 9, pp. 3174–3178, 2015.

[180] S. K. Trumbo, M. E. Brown, and K. P. Hand, "Sodium chloride on the surface of europa," *Science Advances*, vol. 5, no. 6, p. eaaw7123, 2019.

[181] T. B. McCord, G. B. Hansen, F. P. Fanale, R. W. Carlson, D. L. Matson, T. V. Johnson, W. D. Smythe, J. K. Crowley, P. D. Martin, A. Ocampo, C. A. Hibbitts, J. C. Granahan, and the NIMS Team, "Salts on europa's surface detected by galileo's near infrared mapping spectrometer," *Science*, vol. 280, no. 5367, pp. 1242–1245, 1998.

[182] J. B. Dalton, "Linear mixture modeling of europa's non-ice material based on cryogenic laboratory spectroscopy," *Geophysical Research Letters*, vol. 34, no. 21, p. L21205, 2007.

[183] G. C. Mermy, F. Schmidt, F. Andrieu, T. Cornet, I. Belgacem, and N. Altobelli, "Selection of chemical species for europa's surface using galileo/nims," *Icarus*, vol. 394, p. 115379, 2023.

[184] M. E. Brown and K. P. Hand, "Salts and radiation products on the surface of europa," *The Astronomical Journal*, vol. 145, no. 4, p. 110, 2013.

[185] O. King, L. N. Fletcher, and N. Ligier, "Compositional mapping of europa using mcmc modeling of near-ir vlt/sphere and galileo/nims observations," *The Planetary Science Journal*, vol. 3, no. 3, p. 72, 2022.

[186] D. T. Hall, D. Strobel, P. Feldman, M. McGrath, and H. Weaver, "Detection of an oxygen atmosphere on jupiter's moon europa," *Nature*, vol. 373, no. 6516, pp. 677–679, 1995.

[187] R. W. Carlson, R. E. Johnson, and M. S. Anderson, "Sulfuric acid on europa and the radiolytic sulfur cycle," *Science*, vol. 286, no. 5437, pp. 97–99, 1999.

[188] R. Carlson, M. Anderson, R. Johnson, M. Schulman, and A. Yavrouian, "Sulfuric acid production on europa: The radiolysis of sulfur in water ice," *Icarus*, vol. 157, no. 2, pp. 456–463, 2002.

[189] R. Carlson, M. Anderson, R. Mehlman, and R. Johnson, "Distribution of hydrate on europa: Further evidence for sulfuric acid hydrate," *Icarus*, vol. 177, no. 2, pp. 461–471, 2005.

[190] N. Ligier, F. Poulet, J. Carter, R. Brunetto, and F. Gourgeot, "Vlt/sinfoni observations of europa: new insights into the surface composition," *The Astronomical Journal*, vol. 151, no. 6, p. 163, 2016.

[191] I. Mishra, N. Lewis, J. Lunine, K. P. Hand, P. Helfenstein, R. W. Carlson, and R. J. MacDonald, "A comprehensive revisit of select galileo/nims observations of europa," *The Planetary Science Journal*, vol. 2, no. 5, p. 183, 2021.

[192] A. Eviatar, G. L. Siscoe, T. Johnson, and D. Matson, "Effects of io ejecta on europa," *Icarus*, vol. 47, no. 1, pp. 75–83, 1981.

[193] F. Bagenal and V. Dols, "The space environment of io and europa," *Journal of Geophysical Research: Space Physics*, vol. 125, no. 5, 2020.

[194] J. L. Alvarellos, K. J. Zahnle, A. R. Dobrovolskis, and P. Hamill, "Transfer of mass from io to europa and beyond due to cometary impacts," *Icarus*, vol. 194, no. 2, pp. 636–646, 2008.

[195] R. L. Hudson and M. H. Moore, "Infrared spectra and radiation stability of h2o2 ices relevant to europa," *Astrobiology*, vol. 6, no. 3, pp. 483–489, 2006.

[196] C. Hibbitts, K. Stockstill-Cahill, B. Wing, and C. Paranicas, "Color centers in salts - evidence for the presence of sulfates on europa," *Icarus*, vol. 326, pp. 37–47, 2019.

[197] M. Y. Zolotov and E. L. Shock, "Composition and stability of salts on the surface of europa and their oceanic origin," *Journal of Geophysical Research: Planets*, vol. 106, no. E12, pp. 32815–32827, 2001.

[198] R. Carlson, W. Calvin, J. Dalton, G. Hansen, R. Hudson, R. Johnson, T. McCord, and M. Moore, "Europa's surface composition," *Europa*, vol. 283, 2009.

[199] J. B. Dalton, J. H. Shirley, and L. W. Kamp, "Europa's icy bright plains and dark linea: Exogenic and endogenic contributions to composition and surface properties: Europa-icy bright plains and dark linea," *Journal of Geophysical Research: Planets*, vol. 117, 2012.

[200] J. Dalton, T. Cassidy, C. Paranicas, J. Shirley, L. Prockter, and L. Kamp, "Exogenic controls on sulfuric acid hydrate production at the surface of europa," *Planetary and Space Science*, vol. 77, pp. 45–63, 2013.

[201] D. O'Brien, "A melt-through model for chaos formation on europa," *Icarus*, vol. 156, no. 1, pp. 152–161, 2002.

[202] C. Sotin, J. W. Head, and G. Tobie, "Europa: Tidal heating of upwelling thermal plumes and the origin of lenticulae and chaos melting: TIDAL HEATING OF EUROPAN PLUMES," *Geophysical Research Letters*, vol. 29, no. 8, pp. 74–1–74–4, 2002.

[203] S. K. Trumbo, T. M. Becker, M. E. Brown, W. T. P. Denman, P. Molyneux, A. Hendrix, K. D. Retherford, L. Roth, and J. Alday, "A new UV spectral feature on europa: Confirmation of NaCl in leading-hemisphere chaos terrain," *The Planetary Science Journal*, vol. 3, no. 2, p. 27, 2022.

[204] M. E. Brown, W. T. P. Denman, and S. K. Trumbo, "The mid-uv spectrum of irradiated nacl at europa-like conditions," *The Planetary Science Journal*, vol. 3, no. 2, p. 28, 2022.

[205] M. Y. Zolotov and J. Kargel, *On the chemical composition of Europa's icy shell, ocean, and underlying rocks*, vol. 431. University of Arizona Press Tucson, AZ, 2009.

[206] G. Schubert, F. Sohl, and H. Hussmann, *Interior of Europa*, vol. Europa. Tucson: University of Arizona Press, in r. t pappalardo, w. b mckinnon and k khurana (eds.) ed., 2009.

[207] P. V. Johnson, R. Hodyss, T. H. Vu, and M. Choukroun, "Insights into europa's ocean composition derived from its surface expression," *Icarus*, vol. 321, pp. 857–865, 2019.

[208] M. J. Russell, A. E. Murray, and K. P. Hand, "The possible emergence of life and differentiation of a shallow biosphere on irradiated icy worlds: The example of europa," *Astrobiology*, vol. 17, no. 12, pp. 1265–1273, 2017.

[209] J. Cooper, "Energetic ion and electron irradiation of the icy galilean satellites," *Icarus*, vol. 149, no. 1, pp. 133–159, 2001.

[210] T. Nordheim, K. Hand, and C. Paranicas, "Preservation of potential biosignatures in the shallow subsurface of europa," *Nature Astronomy*, vol. 2, no. 8, pp. 673–679, 2018.

[211] G. W. Patterson, C. Paranicas, and L. M. Prockter, "Characterizing electron bombardment of europa's surface by location and depth," *Icarus*, vol. 220, no. 1, pp. 286–290, 2012.

[212] O. Tsareva, E. Popova, V. Y. Popov, H. Malova, and L. Zeleny, "Modeling the dose distribution of electron radiation on the surface of jupiter's satellite europa for different magnetic field models," *Solar System Research*, vol. 55, no. 4, pp. 335–340, 2021.

[213] S. M. Howell and R. T. Pappalardo, "Nasa's europa clipper - a mission to a potentially habitable ocean world," *Nature Communications*, vol. 11, no. 1, p. 1311, 2020.

[214] L. C. Quick, O. S. Barnouin, L. M. Prockter, and G. W. Patterson, "Constraints on the detection of cryovolcanic plumes on europa," *Planetary and Space Science*, vol. 86, pp. 1–9, 2013.

[215] S. Kempf, S. Tucker, N. Altobelli, *et al.*, "Suda: A surface dust analyser for compositional mapping of the galilean moon europa," *Science, Submitted*, 2023.

[216] J. H. Waite, T. Brockwell, C. Glein, E. Shock, M. McGrath, B. Teolis, D. Wyrick, W. McKinnon, O. Mousis, M. Sephton, *et al.*, "The europa clipper maspex europa investigation.," in *Geophysical Research Abstracts*, vol. 21, 2019.

[217] K. P. Hand, C. B. Phillips, and A. e. a. Murray, "Science goals and mission architecture of the europa lander mission concept," *The Planetary Science Journal*, vol. 3, no. 1, p. 22, 2022.

[218] O. Grasset, M. Dougherty, A. Coustenis, E. Bunce, C. Erd, D. Titov, M. Blanc, A. Coates, P. Drossart, L. Fletcher, *et al.*, "Jupiter icy moons explorer (juice): An esa mission to orbit ganymede and to characterise the jupiter system," *Planetary and Space Science*, vol. 78, pp. 1–21, 2013.

[219] M. Blanc, C. Wang, L. Li, M. Li, L. Wang, Y. Wang, Y. Wang, Q. Zong, N. Andre, O. Mousis, D. Hestroffer, and P. Vernazza, "Gan de: Science objectives and mission scenarios for china's mission to the jupiter system," in *EGU*, pp. EGU2020–20179, 2020.

[220] A. Spears, M. West, M. Meister, J. Buffo, C. Walker, T. R. Collins, A. Howard, and B. Schmidt, "Under ice in antarctica: The icefin unmanned underwater vehicle development and deployment," *IEEE Robotics & Automation Magazine*, vol. 23, no. 4, pp. 30–41, 2016.

[221] B. Dachwald, S. Ulamec, F. Postberg, F. Sohl, J.-P. de Vera, C. Waldmann, R. D. Lorenz, K. A. Zacny, H. Hellard, J. Biele, *et al.*, "Key technologies and instrumentation for subsurface exploration of ocean worlds," *Space Science Reviews*, vol. 216, no. 5, p. 83, 2020.

[222] J. H. Gross, *Mass spectrometry: a textbook*. Springer Science & Business Media, 2006.

[223] D. L. Andrews, *Encyclopedia of applied spectroscopy*. Wiley-VCH Weinheim, 2009.

[224] J. Friichtenicht, "Micrometeroid simulation using nuclear accelerator techniques," *Nuclear Instruments and Methods*, vol. 28, no. 1, pp. 70–78, 1964.

[225] A. Auer and K. Sitte, "Detection technique for micrometeoroids using impact ionization," *Earth and Planetary Science Letters*, vol. 4, no. 2, pp. 178–183, 1968.

[226] J. Friichtenicht, N. Roy, and D. Becker, "The cosmic dust analyzer: experimental evaluation of an impact ionization model," in *International Astronomical Union Colloquium*, vol. 13, pp. 299–310, Cambridge University Press, 1971.

[227] E. Grün, H. Fechtig, M. S. Hanner, J. Kissel, B.-A. Lindblad, D. Linkert, D. Maas, G. E. Morfill, and H. A. Zook, "The galileo dust detector," *Space Science Reviews*, vol. 60, pp. 317–340, 1992.

[228] E. Grün, H. Fechtig, J. Kissel, D. Linkert, D. Maas, J. McDonnell, G. Morfill, G. Schwehm, H. Zook, and R. Giese, "The ulysses dust experiment," *Astronomy and Astrophysics Supplement Series (ISSN 0365-0138), vol. 92, no. 2, Jan. 1992, p. 411-423.*, vol. 92, pp. 411–423, 1992.

[229] N. Altobelli, E. Grün, and M. Landgraf, "A new look into the helios dust experiment data: presence of interstellar dust inside the earth's orbit," *Astronomy & Astrophysics*, vol. 448, no. 1, pp. 243–252, 2006.

[230] J. McDonnell, "The giotto dust impact detection system," *Journal of Physics E: Scientific Instruments*, vol. 20, no. 6, p. 741, 1987.

[231] M. Perkins, J. Simpson, and A. Tuzzolino, "A cometary and interplanetary dust experiment on the vega spacecraft missions to halley's comet," *Nuclear Instruments and Methods in Physics Research Section A: Accelerators, Spectrometers, Detectors and Associated Equipment*, vol. 239, no. 2, pp. 310–323, 1985.

[232] R. Srama, T. J. Ahrens, and N. e. a. Altobelli, "The cassini cosmic dust analyzer," *Space Science Reviews*, vol. 114, no. 1-4, pp. 465–518, 2004.

[233] A. V. Krivov, M. Sremcevic, F. Spahn, V. V. Dikarev, and K. V. Kholshevnikov, "Impact-generated dust clouds around planetary satellites: spherically symmetric case," *Planetary and Space Science*, vol. 51, no. 3, pp. 251–269, 2003.

[234] F. Postberg, E. Grün, M. Horanyi, S. Kempf, H. Krüger, J. Schmidt, F. Spahn, R. Srama, Z. Sternovsky, and M. Trieloff, "Compositional mapping of planetary moons by mass spectrometry of dust ejecta," *Planetary and Space Science*, vol. 59, no. 14, pp. 1815–1825, 2011.

[235] K. Miljkovic, J. Hillier, N. Mason, and J. Zarnecki, "Models of dust around europa and ganymede," *Planetary and Space Science*, vol. 70, no. 1, pp. 20–27, 2012.

[236] D. Koschny and E. Grün, "Impacts into ice–silicate mixtures: Ejecta mass and size distributions," *Icarus*, vol. 154, no. 2, pp. 402–411, 2001.

[237] W. Goode, S. Kempf, and J. Schmidt, "Detecting the surface composition of geological features on europa and ganymede using a surface dust analyzer," *Planetary and Space Science*, vol. 208, p. 105343, 2021.

[238] W. Goode, S. Kempf, and J. Schmidt, "Mapping the surface composition of europa with suda," *Planetary and Space Science*, vol. 227, p. 105633, 2023.

[239] A. Jaramillo-Botero, M. L. Cable, A. E. Hofmann, M. Malaska, R. Hodyss, and J. Lunine, "Understanding hypervelocity sampling of biosignatures in space missions," *Astrobiology*, vol. 21, no. 4, pp. 421–442, 2021.

[240] M. J. Burchell, M. J. Cole, J. McDonnell, and J. C. Zarnecki, "Hypervelocity impact studies using the 2 mv van de graaff accelerator and two-stage light gas gun of the university of kent at canterbury," *Measurement Science and Technology*, vol. 10, no. 1, p. 41, 1999.

[241] M. J. Burchell, S. A. Bowden, M. Cole, M. C. Price, and J. Parnell, "Survival of organic materials in hypervelocity impacts of ice on sand, ice, and water in the laboratory," *Astrobiology*, vol. 14, no. 6, pp. 473–485, 2014.

[242] A. Shu, A. Collette, K. Drake, E. Grün, M. Horányi, S. Kempf, A. Mocker, T. Munsat, P. Northway, R. Srama, *et al.*, "3 mv hypervelocity dust accelerator at the colorado center for lunar dust and atmospheric studies," *Review of Scientific Instruments*, vol. 83, no. 7, 2012.

[243] A. Mocker, K. Hornung, E. Grün, S. Kempf, A. Collette, K. Drake, M. Horányi, T. Munsat, L. O'Brien, Z. Sternovsky, *et al.*, "On the application of a linear time-of-flight mass spectrometer for the investigation of hypervelocity impacts of micron and sub-micron sized dust particles," *Planetary and Space Science*, vol. 89, pp. 47–57, 2013.

[244] L. A. Fielding, J. K. Hillier, M. J. Burchell, and S. P. Armes, "Space science applications for conducting polymer particles: synthetic mimics for cosmic dust and micrometeorites," *Chemical Communications*, vol. 51, no. 95, pp. 16886–16899, 2015.

[245] J. S. New, R. Mathies, M. C. Price, M. J. Cole, M. Golozar, V. Spathis, M. Burchell, and A. Butterworth, "Characterizing organic particle impacts on inert metal surfaces: Foundations for capturing organic molecules during hypervelocity transits of enceladus plumes," *Meteoritics & Planetary Science*, vol. 55, no. 3, pp. 465–479, 2020.

[246] Z. Ulibarri, T. Munsat, M. Voss, J. Fontanese, M. Horányi, S. Kempf, and Z. Sternovsky, "Detection of the amino acid histidine and its breakup products in hypervelocity impact ice spectra," *Icarus*, vol. 391, p. 115319, 2023.

[247] M. E. Miller, S. E. Burke, and R. E. Continetti, "Production and impact characterization of enceladus ice grain analogues," *ACS Earth and Space Chemistry*, vol. 6, no. 7, pp. 1813–1822, 2022.

[248] M. C. Price, C. Solscheid, M. J. Burchell, L. Jossé, N. Adamek, and M. J. Cole, "Survival of yeast spores in hypervelocity impact events up to velocities of 7.4 km s- 1," *Icarus*, vol. 222, no. 1, pp. 263–272, 2013.

[249] A. Spesyvyi, J. Zabka, M. Polasek, A. Charvat, J. Schmidt, F. Postberg, and B. Abel, "Charged ice particle beams with selected narrow mass and kinetic energy distributions," *Journal of the American Society for Mass Spectrometry*, vol. 34, no. 5, pp. 878–892, 2023.

[250] B. D. Adamson, M. E. Miller, and R. E. Continetti, "The aerosol impact spectrometer: a versatile platform for studying the velocity dependence of nanoparticle-surface impact phenomena," *EPJ Techniques and Instrumentation*, vol. 4, pp. 1–17, 2017.

[251] A. Belousov, M. Miller, R. Continetti, S. Madzunkov, J. Simcic, D. Nikolic, F. Maiwald, S. Waller, M. Malaska, and M. Cable, "Sampling accelerated micron scale ice particles with a quadrupole ion trap mass spectrometer," *Journal of the American Society for Mass Spectrometry*, vol. 32, no. 5, pp. 1162–1168, 2021.

[252] M. Cable, S. E. Waller, R. Hodyss, A. E. Hofmann, M. J. Malaska, R. E. Continetti, A. Jaramillo-Botero, B. Abel, F. Postberg, M. E. Miller, *et al.*, "Plume grain sampling at hypervelocity: Implications for astrobiology investigations," *Bull. AAS*, vol. 53, 2021.

[253] F. Klenner, F. Postberg, J. Hillier, N. Khawaja, R. Reviol, R. Srama, B. Abel, F. Stolz, and S. Kempf, "Analogue spectra for impact ionization mass spectra of water ice grains obtained at different impact speeds in space," *Rapid Communications in Mass Spectrometry*, vol. 33, no. 22, pp. 1751–1760, 2019.

[254] W. Kleinekofort, J. Avdiev, and B. Brutschy, "A new method of laser desorption mass spectrometry for the study of biological macromolecules," *International Journal of Mass Spectrometry and Ion Processes*, vol. 152, no. 2, pp. 135–142, 1996.

[255] W. Kleinekofort, A. Pfenninger, T. Plomer, C. Griesinger, and B. Brutschy, "Observation of noncovalent complexes using laser-induced liquid beam ionization/desorption," *International Journal of Mass Spectrometry and Ion Processes*, vol. 156, no. 3, pp. 195–202, 1996.

[256] A. Wattenberg, F. Sobott, H.-D. Barth, and B. Brutschy, "Laser desorption mass spectrometry on liquid beams," *European Mass Spectrometry*, vol. 5, no. 2, pp. 71–76, 1999.

[257] A. Charvat and B. Abel, "How to make big molecules fly out of liquid water: applications, features and physics of laser assisted liquid phase dispersion mass spectrometry," *Physical Chemistry Chemical Physics*, vol. 9, no. 26, pp. 3335–3360, 2007.

[258] F. Wiederschein, E. Vohringer-Martinez, A. Beinsen, F. Postberg, J. Schmidt, R. Srama, F. Stolz, H. Grubmueller, and B. Abel, "Charge separation and isolation in strong water droplet impacts," *Physical Chemistry Chemical Physics*, vol. 17, no. 10, pp. 6858–6864, 2015.

[259] F. Klenner, M. Umair, S. H. Walter, N. Khawaja, J. Hillier, L. Nölle, Z. Zou, M. Napoleoni, A. Sanderink, W. Zuschneid, *et al.*, "Developing a laser induced liquid beam ion desorption spectral database as reference for spaceborne mass spectrometers," *Earth and Space Science*, vol. 9, no. 9, p. e2022EA002313, 2022.

[260] N. P. Christian, R. J. Arnold, and J. P. Reilly, "Improved calibration of time-of-flight mass spectra by simplex optimization of electrostatic ion calculations," *Analytical chemistry*, vol. 72, no. 14, pp. 3327–3337, 2000.

[261] D. Li, J. Yi, G. Han, and L. Qiao, "Maldi-tof mass spectrometry in clinical analysis and research," *ACS Measurement Science Au*, vol. 2, no. 5, pp. 385–404, 2022.

[262] N. Khawaja, J. Hillier, M. Napoleoni, and F. Postberg, "Composition of organic material in freshly ejected ice grains in enceladus' plume," *Eur. Planet. Sci. Congr*, 2023.

[263] F. Klenner, F. Postberg, J. Hillier, N. Khawaja, R. Reviol, F. Stolz, M. L. Cable, B. Abel, and L. Nölle, "Analog experiments for the identification of trace biosignatures in ice grains from extraterrestrial ocean worlds," *Astrobiology*, vol. 20, no. 2, pp. 179–189, 2020.

[264] F. Klenner, F. Postberg, J. Hillier, N. Khawaja, M. L. Cable, B. Abel, S. Kempf, C. R. Glein, J. I. Lunine, R. Hodyss, *et al.*, "Discriminating abiotic and biotic fingerprints of amino acids and fatty acids in ice grains relevant to ocean worlds," *Astrobiology*, vol. 20, no. 10, pp. 1168–1184, 2020.

[265] M. Dannenmann, F. Klenner, J. Boenigk, M. Pavlista, M. Napoleoni, J. Hillier, N. Khawaja, K. Olsson-Francis, M. L. Cable, M. J. Malaska, B. Abel, and F. Postberg, "Toward detecting biosignatures of DNA, lipids, and metabolic intermediates from bacteria in ice grains emitted by enceladus and europa," *Astrobiology*, vol. 23, no. 1, pp. 60–75, 2023.

[266] F. Klenner, J. Boenigk, M. Napoleoni, N. Khawaja, J. Hillier, K. Olsson-Francis, M. Cable, M. Malaska, S. Kempf, and F. Postberg, "Identifying cell material in a single ice grain emitted from enceladus or europa," *Eur. Planet. Sci. Congr*, 2023.

[267] N. Khawaja, T. R. O'Sullivan, F. Klenner, L. H. Sanchez, and J. Hillier, "Discriminating aromatic parent compounds and their derivative isomers in ice grains from enceladus and europa using a laboratory analogue for spaceborne mass spectrometers," *Earth and Space Science*, vol. 10, no. 4, p. e2022EA002807, 2023.

[268] N. Khawaja, J. Hillier, F. Klenner, L. Nölle, Z. Zou, M. Napoleoni, R. Reviol, and F. Postberg, "Complementary mass spectral analysis of isomeric o-bearing organic compounds and fragmentation differences through analog techniques for spaceborne mass spectrometers," *The Planetary Science Journal*, vol. 3, no. 11, p. 254, 2022.

[269] C. Chyba, "Correction: Energy for microbial life on europa," *Nature*, vol. 406, no. 6794, pp. 368–368, 2000.

[270] J. D. Anderson, G. Schubert, R. A. Jacobson, E. L. Lau, W. B. Moore, and W. L. Sjogren, "Europa's differentiated internal structure: Inferences from four galileo encounters," *Science*, vol. 281, no. 5385, pp. 2019–2022, 1998.

[271] R. M. Canup and W. R. Ward, "Formation of the galilean satellites: Conditions of accretion," *The Astronomical Journal*, vol. 124, no. 6, pp. 3404–3423, 2002.

[272] W. B. Moore, H. Hussmann, R. Pappalardo, W. McKinnon, and K. Khurana, "Thermal evolution of europa's silicate interior," *Europa*, pp. 369–380, 2009.

[273] J. H. Waite Jr, W. S. Lewis, B. A. Magee, J. I. Lunine, W. B. McKinnon, C. R. Glein, O. Mousis, D. T. Young, T. Brockwell, J. Westlake, M.-J. Nguyen, B. D. Teolis, H. B. Niemann, R. L. McNutt Jr, M. Perry, and W.-H. Ip, "Liquid water on enceladus from observations of ammonia and 40ar in the plume," *Nature*, vol. 460, no. 7254, pp. 487–490, 2009.

[274] P. H. Figueredo and R. Greeley, "Resurfacing history of europa from pole-to-pole geological mapping," *Icarus*, vol. 167, no. 2, pp. 287–312, 2004.

[275] R. Johnson and B. Sundqvist, "Sputtering and detection of large organic molecules from europa," *Icarus*, vol. 309, pp. 338–344, 2018.

[276] C. Huber, W. Eisenreich, S. Hecht, and G. Wächtershäuser, "A possible primordial peptide cycle," *Science*, vol. 301, no. 5635, pp. 938–940, 2003.

[277] G. Proskurowski, M. D. Lilley, J. S. Seewald, G. L. Früh-Green, E. J. Olson, J. E. Lupton, S. P. Sylva, and D. S. Kelley, "Abiogenic hydrocarbon production at lost city hydrothermal field," *Science*, vol. 319, no. 5863, pp. 604–607, 2008.

[278] Y. Novikov and S. D. Copley, "Reactivity landscape of pyruvate under simulated hydrothermal vent conditions," *Proceedings of the National Academy of Sciences*, vol. 110, no. 33, pp. 13283–13288, 2013.

[279] R. Srama, W. Woiwode, F. Postberg, S. P. Armes, S. Fujii, D. Dupin, J. Ormond-Prout, Z. Sternovsky, S. Kempf, G. Moragas-Klostermeyer, A. Mocker, and E. Grün, "Mass spectrometry of hyper-velocity impacts of organic micrograins: MS study of hyper-velocity impacts of organic micrograins," *Rapid Communications in Mass Spectrometry*, vol. 23, no. 24, pp. 3895–3906, 2009.

[280] Y. Zeng and M. F. Jansen, "Ocean circulation on enceladus with a high- versus low-salinity ocean," *The Planetary Science Journal*, vol. 2, no. 4, p. 151, 2021.

[281] W. Kang, T. Mittal, S. Bire, J.-M. Campin, and J. Marshall, "How does salinity shape ocean circulation and ice geometry on enceladus and other icy satellites?," *Science Advances*, vol. 8, no. 29, p. eabm4665, 2022.

[282] J. S. Kargel, J. Z. Kaye, J. W. Head, G. M. Marion, R. Sassen, J. K. Crowley, O. P. Ballesteros, S. A. Grant, and D. L. Hogenboom, "Europa's crust and ocean: Origin, composition, and the prospects for life," *Icarus*, vol. 148, no. 1, pp. 226–265, 2000.

[283] J. S. New, B. Kazemi, V. Spathis, M. C. Price, R. A. Mathies, and A. L. Butterworth, "Quantitative evaluation of the feasibility of sampling the ice plumes at enceladus for biomarkers of extraterrestrial life," *Proceedings of the National Academy of Sciences*, vol. 118, no. 37, p. e2106197118, 2021.

[284] T. M. Annesley, "Ion suppression in mass spectrometry," *Clinical Chemistry*, vol. 49, no. 7, pp. 1041–1044, 2003.

[285] A. M. Piwowar, N. P. Lockyer, and J. C. Vickerman, "Salt effects on ion formation in desorption mass spectrometry: An investigation into the role of alkali chlorides on peak suppression in time-of-flight-secondary ion mass spectrometry," *Analytical Chemistry*, vol. 81, no. 3, pp. 1040–1048, 2009.

[286] R. Stern and M. J. Jedrzejas, "Carbohydrate polymers at the center of life's origins: The importance of molecular processivity," *Chemical Reviews*, vol. 108, no. 12, pp. 5061–5085, 2008.

[287] Y. Furukawa, Y. Chikaraishi, N. Ohkouchi, N. O. Ogawa, D. P. Glavin, J. P. Dworkin, C. Abe, and T. Nakamura, "Extraterrestrial ribose and other sugars in primitive meteorites," *Proceedings of the National Academy of Sciences*, vol. 116, no. 49, pp. 24440–24445, 2019-12-03.

[288] L. E. Rodriguez, C. H. House, K. E. Smith, M. R. Roberts, and M. P. Callahan, "Nitrogen heterocycles form peptide nucleic acid precursors in complex prebiotic mixtures," *Scientific Reports*, vol. 9, no. 1, p. 9281, 2019.

[289] S. Maedler, K. Barylyuk, E. Boeri Erba, R. J. Nieckarz, and R. Zenobi, "Compelling advantages of negative ion mode detection in high-mass MALDI-MS for homomeric protein complexes," *Journal of the American Society for Mass Spectrometry*, vol. 23, no. 2, pp. 213–224, 2012.

[290] M. Dashtiev, E. Wafler, U. Rohling, M. Gorshkov, F. Hillenkamp, and R. Zenobi, "Positive and negative analyte ion yield in matrix-assisted laser desorption/ionization," *International Journal of Mass Spectrometry*, vol. 268, no. 2, pp. 122–130, 2007.

[291] N. B. Cech and C. G. Enke, "Practical implications of some recent studies in electrospray ionization fundamentals," *Mass Spectrometry Reviews*, vol. 20, no. 6, pp. 362–387, 2001.

[292] M. Oss, A. Kruve, K. Herodes, and I. Leito, "Electrospray ionization efficiency scale of organic compounds," *Analytical Chemistry*, vol. 82, no. 7, pp. 2865–2872, 2010.

[293] F. Hillenkamp and J. Peter-Katalinic, *MALDI MS: a practical guide to instrumentation, methods and applications*. john wiley & sons ed., 2013.

[294] A. Kruve, K. Kaupmees, J. Liigand, and I. Leito, "Negative electrospray ionization via deprotonation: Predicting the ionization efficiency," *Analytical Chemistry*, vol. 86, no. 10, pp. 4822–4830, 2014.

[295] J. Liigand, A. Laaniste, and A. Kruve, "ph effects on electrospray ionization efficiency," *Journal of the American Society for Mass Spectrometry*, vol. 28, no. 3, pp. 461–469, 2017.

[296] I. Ferrer, J. A. Zweigenbaum, and E. M. Thurman, "Analytical methodologies for the detection of sucralose in water," *Analytical Chemistry*, vol. 85, no. 20, pp. 9581–9587, 2013.

[297] P. Sales, K. de Souza, A. Bezerra, S. Ojala, S. de Oliveira, P. dos Santos, and M. T. Bara, "How sodiation influences the sucralose behavior under electrospray ionization mass spectrometry," *Brazilian Journal of Analytical Chemistry*, vol. 9, no. 36, 2022.

[298] K. A. Newton and S. A. McLuckey, "Generation and manipulation of sodium cationized peptides in the gas phase," *Journal of the American Society for Mass Spectrometry*, vol. 15, no. 4, pp. 607–615, 2004.

[299] R. Grewal, H. E. Aribi, J. C. Smith, C. F. Rodriquez, A. C. Hopkinson, and K. Siu, "Multiple substitution of protons by sodium ions in sodiated oligoglycines," *International Journal of Mass Spectrometry*, vol. 219, no. 1, pp. 89–99, 2002.

[300] W. C. Chang, L. C. L. Huang, Y.-S. Wang, W.-P. Peng, H. C. Chang, N. Y. Hsu, W. B. Yang, and C. H. Chen, "Matrix-assisted laser desorption/ionization (MALDI) mechanism revisited," *Analytica Chimica Acta*, vol. 582, no. 1, pp. 1–9, 2007.

[301] C. F. Rodriquez, X. Guo, T. Shoeib, A. C. Hopkinson, and K. M. Siu, "Formation of [m- n h+ m na](m- n)+ and [m- n h+ m k](m- n)+ ions in electrospray mass spectrometry of peptides and proteins," *Journal of the American Society for Mass Spectrometry*, vol. 11, no. 11, pp. 967–975, 2000.

[302] L. Boutegrabet, B. Kanawati, I. Gebefugi, D. Peyron, P. Cayot, R. D. Gougeon, and P. Schmitt-Kopplin, "Attachment of chloride anion to sugars: Mechanistic investigation and discovery of a new dopant for efficient sugar ionization/detection in mass spectrometers," *Chemistry - A European Journal*, vol. 18, no. 41, pp. 13059–13067, 2012.

[303] P. Phungsai, F. Kurisu, I. Kasuga, and H. Furumai, "Molecular characterization of low molecular weight dissolved organic matter in water reclamation processes using orbitrap mass spectrometry," *Water Research*, vol. 100, pp. 526–536, 2016.

[304] H. P. Tannenbaum, J. D. Roberts, and R. C. Dougherty, "Negative chemical ionization mass spectrometry. chloride attachment spectra," *Analytical Chemistry*, vol. 47, no. 1, pp. 49–54, 1975.

[305] M. F. Mora, M. G. Kok, A. Noell, and P. A. Willis, "Detection of biosignatures by capillary electrophoresis mass spectrometry in the presence of salts relevant to ocean worlds missions," *Astrobiology*, vol. 22, no. 8, pp. 914–925, 2022.

[306] T. L. Constantopoulos, G. S. Jackson, and C. G. Enke, "Effects of salt concentration on analyte response using electrospray ionization mass spectrometry," *Journal of the American Society for Mass Spectrometry*, vol. 10, no. 7, pp. 625–634, 1999.

[307] P. Pan and S. A. McLuckey, "The effect of small cations on the positive electrospray responses of proteins at low pH," *Analytical Chemistry*, vol. 75, no. 20, pp. 5468–5474, 2003.

[308] F. Postberg, S. Kempf, J. Hillier, R. Srama, S. Green, N. McBride, and E. Grün, "The e-ring in the vicinity of enceladus: Ii. probing the moon's interior—the composition of e-ring particles," *Icarus*, vol. 193, no. 2, pp. 438–454, 2008.

[309] A. Furey, M. Moriarty, V. Bane, B. Kinsella, and M. Lehane, "Ion suppression; a critical review on causes, evaluation, prevention and applications," *Talanta*, vol. 115, pp. 104–122, 2013.

[310] K. P. Hand, C. F. Chyba, J. C. Priscu, R. W. Carlson, and K. H. Nealson, "Astrobiology and the potential for life on europa," *Europa*, pp. 589–629, 2009.

[311] A. Kereszturi and Z. Keszthelyi, "Astrobiological implications of chaos terrains on europa to help targeting future missions," *Planetary and Space Science*, vol. 77, pp. 74–90, 2013.

[312] G. Mitri, F. Postberg, and J. M. e. a. Soderblom, "Explorer of enceladus and titan (e2t): Investigating ocean worlds' evolution and habitability in the solar system," *Planetary and Space Science*, vol. 155, pp. 73–90, 2018.

[313] G. Lusci, T. Pivetta, C. Carucci, D. F. Parsons, A. Salis, and M. Monduzzi, "BSA fragmentation specifically induced by added electrolytes: An electrospray ionization mass spectrometry investigation," *Colloids and Surfaces B: Biointerfaces*, vol. 218, p. 112726, 2022.

[314] T. Shi, J. Zhao, P. I. Shek, A. C. Hopkinson, and K. M. Siu, "Carbonate, carbamate, urea, and guanidine as model species for functional groups in biological molecules: A combined density functional theory and mass spectrometry examination of polysodiation and gas-phase dissociation," *Canadian Journal of Chemistry*, vol. 83, no. 11, pp. 1941–1952, 2005.

[315] T. Henriksen, R. K. Juhler, B. Svensmark, and N. B. Cech, "The relative influences of acidity and polarity on responsiveness of small organic molecules to analysis with negative ion electrospray ionization mass spectrometry (ESI-MS)," *Journal of the American Society for Mass Spectrometry*, vol. 16, no. 4, pp. 446–455, 2005.

[316] M. Napoleoni, F. Klenner, N. Khawaja, J. K. Hillier, and F. Postberg, "Mass spectrometric fingerprints of organic compounds in nacl-rich ice grains from europa and enceladus," *ACS Earth and Space Chemistry*, vol. 7, no. 4, pp. 735–752, 2023.

[317] G. C. Collins and J. C. Goodman, "Enceladus' south polar sea," *Icarus*, vol. 189, no. 1, pp. 72–82, 2007.

[318] T. Spohn and G. Schubert, "Oceans in the icy galilean satellites of jupiter?," *Icarus*, vol. 161, no. 2, pp. 456–467, 2003.

[319] J. I. Lunine, "Ocean worlds exploration," *Acta Astronautica*, vol. 131, pp. 123–130, 2017.

[320] J. Hillier, S. Green, N. Mcbride, N. Altobelli, F. Postberg, S. Kempf, J. Schwanethal, R. Srama, J. Mcdonnell, and E. Grun, "Interplanetary dust detected by the cassini cda chemical analyser," *Icarus*, vol. 190, no. 2, pp. 643–654, 2007.

[321] S. Kempf, R. Srama, E. Grün, A. Mocker, F. Postberg, J. K. Hillier, M. Horanyi, Z. Sternovsky, B. Abel, A. Beinsen, R. Thissen, J. Schmidt, F. Spahn, and N. Altobelli, "Linear high resolution dust mass spectrometer for a mission to the galilean satellites," *Planetary and Space Science*, vol. 65, no. 1, pp. 10–20, 2012.

[322] T. B. McCord, "Brines exposed to europa surface conditions," *Journal of Geophysical Research*, vol. 107, no. E1, p. 5004, 2002.

[323] F. Fanale, Y.-H. Li, E. De Carlo, C. Farley, S. Sharma, K. Horton, and J. Granahan, "An experimental estimate of europa's "ocean" composition independent of galileo orbital remote sensing," *Journal of Geophysical Research: Planets*, vol. 106, no. E7, pp. 14595–14600, 2001.

[324] T. A. Nordheim, J. M. Jasinski, and K. P. Hand, "Galactic cosmic-ray bombardment of europa's surface," *The Astrophysical Journal Letters*, vol. 881, no. 2, p. L29, 2019.

[325] T. Orlando and M. Sieger, "The role of electron-stimulated production of o2 from water ice in the radiation processing of outer solar system surfaces," *Surface Science*, vol. 528, no. 1-3, pp. 1–7, 2003.

[326] M. Loeffler, U. Raut, R. Vidal, R. Baragiola, and R. Carlson, "Synthesis of hydrogen peroxide in water ice by ion irradiation," *Icarus*, vol. 180, no. 1, pp. 265–273, 2006.

[327] W. Zheng, D. Jewitt, and R. I. Kaiser, "Formation of hydrogen, oxygen, and hydrogen peroxide in electron-irradiated crystalline water ice," *The Astrophysical Journal*, vol. 639, no. 1, pp. 534–548, 2006.

[328] B. D. Teolis, M. J. Loeffler, U. Raut, M. Famá, and R. A. Baragiola, "Ozone synthesis on the icy satellites," *The Astrophysical Journal*, vol. 644, no. 2, pp. L141–L144, 2006.

[329] K. P. Hand and R. W. Carlson, "H2o2 production by high-energy electrons on icy satellites as a function of surface temperature and electron flux," *Icarus*, vol. 215, no. 1, pp. 226–233, 2011.

[330] P. D. Tribbett and M. J. Loeffler, "Thermal reactions between h2s and o3: Implications for europa surface chemistry," *The Planetary Science Journal*, vol. 3, no. 10, p. 233, 2022.

[331] G. Strazzulla, G. Baratta, G. Leto, and O. Gomis, "Hydrate sulfuric acid after sulfur implantation in water ice," *Icarus*, vol. 192, no. 2, pp. 623–628, 2007.

[332] J. H. Shirley, J. B. Dalton, L. M. Prockter, and L. W. Kamp, "Europa's ridged plains and smooth low albedo plains: Distinctive compositions and compositional gradients at the leading side–trailing side boundary," *Icarus*, vol. 210, no. 1, pp. 358–384, 2010.

[333] R. Knochenmuss, F. Dubois, M. J. Dale, and R. Zenobi, "The matrix suppression effect and ionization mechanisms in matrix-assisted laser desorption/ionization," *Rapid Communications in Mass Spectrometry*, vol. 10, no. 8, pp. 871–877, 1996.

[334] R. King, R. Bonfiglio, C. Fernandez-Metzler, C. Miller-Stein, and T. Olah, "Mechanistic investigation of ionization suppression in electrospray ionization," *Journal of the American Society for Mass Spectrometry*, vol. 11, no. 11, pp. 942–950, 2000.

[335] J. A. Schulze, D. E. Yilmaz, M. L. Cable, M. Malaska, A. E. Hofmann, R. P. Hodyss, J. I. Lunine, A. C. T. van Duin, and A. Jaramillo-Botero, "Effect of salts on the formation and hypervelocity-induced fragmentation of icy clusters with embedded amino acids," *ACS Earth and Space Chemistry*, p. acsearthspacechem.2c00267, 2022.

[336] L. Han and C. E. Costello, "Electron transfer dissociation of milk oligosaccharides," *Journal of the American Society for Mass Spectrometry*, vol. 22, no. 6, pp. 997–1013, 2011.

[337] A. W. Wong, H. Wang, and C. B. Lebrilla, "Selection of anionic dopant for quantifying desialylation reactions with maldi-ftms," *Analytical Chemistry*, vol. 72, no. 7, pp. 1419–1425, 2000.

[338] Y. Jiang and R. B. Cole, "Oligosaccharide analysis using anion attachment in negative mode electrospray mass spectrometry," *Journal of the American Society for Mass Spectrometry*, vol. 16, no. 1, pp. 60–70, 2005.

[339] S. K. Chowdhury, V. Katta, R. C. Beavis, and B. T. Chait, "Origin and removal of adducts (molecular mass = 98 u) attached to peptide and protein ions in electrospray ionization mass spectra," *Journal of the American Society for Mass Spectrometry*, vol. 1, no. 5, pp. 382–388, 1990.

[340] N. Ligier, C. Paranicas, J. Carter, F. Poulet, W. Calvin, T. Nordheim, C. Snodgrass, and L. Ferellec, "Surface composition and properties of ganymede: Updates from ground-based observations with the near-infrared imaging spectrometer sinfoni/vlt/eso," *Icarus*, vol. 333, pp. 496–515, 2019.

[341] F. Sohl, M. Choukroun, J. Kargel, J. Kimura, R. Pappalardo, S. Vance, and M. Zolotov, "Subsurface water oceans on icy satellites: Chemical composition and exchange processes," *Space Science Reviews*, vol. 153, no. 1-4, pp. 485–510, 2010.

[342] H. E. Maynard-Casely, K. S. Wallwork, and M. Avdeev, "A new material for the icy galilean moons: The structure of sulfuric acid hexahydrate: A new material for the galilean moons," *Journal of Geophysical Research: Planets*, vol. 118, no. 9, pp. 1895–1902, 2013.

[343] K. P. Hand and R. W. Carlson, "Laboratory spectroscopic analyses of electron irradiated alkanes and alkenes in solar system ices: Irradiated hydrocarbons in ice," *Journal of Geophysical Research: Planets*, vol. 117, no. E3, pp. n/a–n/a, 2012.

[344] G. M. Marion, C. H. Fritsen, H. Eicken, and M. C. Payne, "The search for life on europa: limiting environmental factors, potential habitats, and earth analogues," *Astrobiology*, vol. 3, no. 4, pp. 785–811, 2003.

[345] L. M. Barge and L. E. Rodriguez, "Life on enceladus? it depends on its origin," *Nature Astronomy*, vol. 5, no. 8, pp. 740–741, 2021.

[346] F. Postberg, R. N. Clark, C. J. Hansen, A. J. Coates, C. M. Dalle Ore, F. Scipioni, M. M. Hedman, and J. H. Waite, "Plume and surface composition of enceladus," in *Enceladus and the Icy Moons of Saturn*, The University of Arizona Press, 2018.

[347] G. L. Villanueva, H. B. Hammel, S. N. Milam, V. Kofman, S. Faggi, C. R. Glein, R. Cartwright, L. Roth, K. P. Hand, L. Paganini, J. Spencer, J. Stansberry, B. Holler, N. Rowe-Gurney, S. Protopapa, G. Strazzulla, G. Liuzzi, G. Cruz-Mermy, M. El Moutamid, M. Hedman, and K. Denny, "Jwst molecular mapping and characterization of enceladus' water plume feeding its torus," *Nature Astronomy*, 2023.

[348] V. Lainey, Ö. Karatekin, J. Desmars, S. Charnoz, J.-E. Arlot, N. Emelyanov, C. Le Poncin-Lafitte, S. Mathis, F. Remus, G. Tobie, *et al.*, "Strong tidal dissipation in saturn and constraints on enceladus'thermal state from astrometry," *The Astrophysical Journal*, vol. 752, no. 1, p. 14, 2012.

[349] L. M. Fifer, D. C. Catling, and J. D. Toner, "Chemical fractionation modeling of plumes indicates a gas-rich, moderately alkaline enceladus ocean," *The Planetary Science Journal*, vol. 3, no. 8, p. 191, 2022.

[350] S. M. Howell, "The likely thickness of europa's icy shell," *The Planetary Science Journal*, vol. 2, no. 4, p. 129, 2021.

[351] K. N. Singer, W. B. McKinnon, and P. M. Schenk, "Pits, uplifts and small chaos features on europa: Morphologic and morphometric evidence for intrusive upwelling and lower limits to ice shell thickness," *Icarus*, vol. 364, p. 114465, 2021.

[352] E. B. Bierhaus, K. Zahnle, C. R. Chapman, R. Pappalardo, W. McKinnon, and K. Khurana, "Europa's crater distributions and surface ages," *Europa*, pp. 161–180, 2009.

[353] J. C. Goodman, "Hydrothermal plume dynamics on europa: Implications for chaos formation," *Journal of Geophysical Research*, vol. 109, no. E3, p. E03008, 2004.

[354] O. Kuskov and V. Kronrod, "Internal structure of europa and callisto," *Icarus*, vol. 177, no. 2, pp. 550–569, 2005.

[355] C. Ray, C. R. Glein, J. H. Waite, B. Teolis, T. Hoehler, J. A. Huber, J. Lunine, and F. Postberg, "Oxidation processes diversify the metabolic menu on enceladus," *Icarus*, vol. 364, p. 114248, 2021.

[356] R. E. Hamp, *Geochemical Cycling in the Subsurface Environment of Enceladus*. Open University (United Kingdom), 2022.

[357] C. L. Christ, *Solutions, minerals, and equilibria*. Harper & Row, 1965.

[358] J. Hao, C. R. Glein, F. Huang, N. Yee, D. C. Catling, F. Postberg, J. K. Hillier, and R. M. Hazen, "Abundant phosphorus expected for possible life in enceladus's ocean," *Proceedings of the National Academy of Sciences*, vol. 119, no. 39, p. e2201388119, 2022.

[359] K. M. Soderlund, B. E. Schmidt, J. Wicht, and D. D. Blankenship, "Ocean-driven heating of europa's icy shell at low latitudes," *Nature Geoscience*, vol. 7, no. 1, pp. 16–19, 2014.

[360] E. Shock and P. Canovas, "The potential for abiotic organic synthesis and biosynthesis at seafloor hydrothermal systems," *Geofluids*, 2010.

[361] L. M. Barge and L. M. White, "Experimentally testing hydrothermal vent origin of life on enceladus and other icy/ocean worlds," *Astrobiology*, vol. 17, no. 9, pp. 820–833, 2017.

[362] G. Angelis, G. G. Kordopati, E. Zingkou, A. Karioti, G. Sotiropoulou, and G. Pampalakis, "Plausible emergence of biochemistry in enceladus based on chemobrionics," *Chemistry – A European Journal*, vol. 27, no. 2, pp. 600–604, 2021.

[363] L. M. Barge, E. Flores, M. M. Baum, D. G. VanderVelde, and M. J. Russell, "Redox and ph gradients drive amino acid synthesis in iron oxyhydroxide mineral systems," *Proceedings of the National Academy of Sciences*, vol. 116, no. 11, pp. 4828–4833, 2019.

[364] M. J. Russell, A. J. Hall, and D. Turner, "In vitro growth of iron sulphide chimneys: possible culture chambers for origin-of-life experiments," *Terra Nova*, vol. 1, no. 3, pp. 238–241, 1989.

[365] M. J. Russell, R. M. Daniel, A. J. Hall, and J. A. Sherringham, "A hydrothermally precipitated catalytic iron sulphide membrane as a first step toward life," *Journal of Molecular Evolution*, vol. 39, pp. 231–243, 1994.

[366] V. Sojo, B. Herschy, A. Whicher, E. Camprubi, and N. Lane, "The origin of life in alkaline hydrothermal vents," *Astrobiology*, vol. 16, no. 2, pp. 181–197, 2016.

[367] R. V. Eck and M. O. Dayhoff, "Evolution of the structure of ferredoxin based on living relics of primitive amino acid sequences," *Science*, vol. 152, no. 3720, pp. 363–366, 1966.

[368] M. J. Russell and W. Martin, "The rocky roots of the acetyl-coa pathway," *Trends in Biochemical Sciences*, vol. 29, no. 7, pp. 358–363, 2004.

[369] G. Bender, E. Pierce, J. A. Hill, J. E. Darty, and S. W. Ragsdale, "Metal centers in the anaerobic microbial metabolism of co and co2," *Metallomics*, vol. 3, no. 8, p. 797, 2011.

[370] M. J. Russell and A. Hall, "The emergence of life from iron monosulphide bubbles at a submarine hydrothermal redox and ph front," *Journal of the Geological Society*, vol. 154, no. 3, pp. 377–402, 1997.

[371] R.-S. Taubner, P. Pappenreiter, J. Zwicker, D. Smrzka, C. Pruckner, P. Kolar, S. Bernacchi, A. H. Seifert, A. Krajete, W. Bach, J. Peckmann, C. Paulik, M. G. Firneis, C. Schleper, and S. K.-M. R. Rittmann, "Biological methane production under putative enceladus-like conditions," *Nature Communications*, vol. 9, no. 1, p. 748, 2018.

[372] L. I. Tenelanda-Osorio, J. L. Parra, P. Cuartas-Restrepo, and J. I. Zuluaga, "Enceladus as a potential niche for methanogens and estimation of its biomass," *Life*, vol. 11, no. 11, p. 1182, 2021.

[373] M. J. Roche, M. G. Fox-Powell, R. E. Hamp, and J. M. Byrne, "Iron reduction as a viable metabolic pathway in enceladus' ocean," *International Journal of Astrobiology*, pp. 1–20, 2023.

[374] J. J. Scott, J. A. Breier, G. W. Luther, and D. Emerson, "Microbial iron mats at the mid-atlantic ridge and evidence that zetaproteobacteria may be restricted to iron-oxidizing marine systems," *PLOS ONE*, vol. 10, no. 3, p. e0119284, 2015.

[375] M. Y. Zolotov, "A model for low-temperature biogeochemistry of sulfur, carbon, and iron on europa," *Journal of Geophysical Research*, vol. 109, no. E6, p. E06003, 2004.

[376] M. Napoleoni, F. Klenner, L. Hortal Sanchez, N. Khawaja, J. K. Hillier, M. S. Gudipati, K. P. Hand, S. Kempf, and F. Postberg, "Mass spectrometric fingerprints of organic compounds in sulfate-rich ice grains: Implications for europa clipper," *ACS Earth and Space Chemistry*, 2023.

[377] M. Mayer, N. Vankova, F. Stolz, B. Abel, T. Heine, and K. R. Asmis, "Identification of a two-coordinate iron (i)–oxalate complex," *Angewandte Chemie International Edition*, vol. 61, no. 16, p. e202117855, 2022.

[378] H. Hellman, R. S. Laitinen, L. Kaila, J. Jalonen, V. Hietapelto, J. Jokela, A. Sarpola, and J. Rämö, "Identification of hydrolysis products of fecl3· 6h2o by esi-ms," *Journal of mass spectrometry*, vol. 41, no. 11, pp. 1421–1429, 2006.

[379] M. Radisavljević, T. Kamčeva, I. Vukićević, M. Nišavić, M. Milovanović, and M. Petković, "Sensitivity and accuracy of organic matrix-assisted laser desorption and ionisation mass spectrometry of fecl3 is higher than in in matrix-free approach," *European Journal of Mass Spectrometry*, vol. 19, no. 2, pp. 77–89, 2013.

[380] L. Guimaraes, H. A. De Abreu, and H. A. Duarte, "Fe(ii) hydrolysis in aqueous solution: A dft study," *Chemical Physics*, vol. 333, no. 1, pp. 10–17, 2007.

[381] J. Zhang, V. Frankevich, R. Knochenmuss, S. D. Friess, and R. Zenobi, "Reduction of cu(ii) in matrix-assisted laser desorption/ionization mass spectrometry," *Journal of the American Society for Mass Spectrometry*, vol. 14, no. 1, pp. 42–50, 2003.

[382] H. C. Helgeson, "Summary and critique of the thermodynamic properties of rock-forming minerals," *American Journal of Science, A*, vol. 278, pp. 1–229, 1978.

[383] E. L. Shock, D. C. Sassani, M. Willis, and D. A. Sverjensky, "Inorganic species in geologic fluids: correlations among standard molal thermodynamic properties of aqueous ions and hydroxide complexes," *Geochimica et Cosmochimica Acta*, vol. 61, no. 5, pp. 907–950, 1997.

[384] B. M. Toner, S. C. Fakra, S. J. Manganini, C. M. Santelli, M. A. Marcus, J. W. Moffett, O. Rouxel, C. R. German, and K. J. Edwards, "Preservation of iron(ii) by carbon-rich matrices in a hydrothermal plume," *Nature Geoscience*, vol. 2, no. 3, pp. 197–201, 2009.

[385] S. G. Sander and A. Koschinsky, "Metal flux from hydrothermal vents increased by organic complexation," *Nature Geoscience*, vol. 4, no. 3, pp. 145–150, 2011.

[386] A. R. Hendrix, G. Filacchione, C. Paranicas, P. Schenk, and F. Scipioni, "Icy saturnian satellites: Disk-integrated uv-ir characteristics and links to exogenic processes," *Icarus*, vol. 300, pp. 103–114, 2018.

[387] E. Camprubi, S. F. Jordan, R. Vasiliadou, and N. Lane, "Iron catalysis at the origin of life," *IUBMB Life*, vol. 69, no. 6, pp. 373–381, 2017.

[388] P. Sundararaman and J. E. Dahl, "Depositional environment, thermal maturity and irradiation effects on porphyrin distribution: Alum shale, sweden," *Organic geochemistry*, vol. 20, no. 3, pp. 333–337, 1993.

[389] G. Kminek and J. L. Bada, "The effect of ionizing radiation on the preservation of amino acids on mars," *Earth and Planetary Science Letters*, vol. 245, no. 1-2, pp. 1–5, 2006.

[390] A. Gutiérrez-Quintanilla, Y. Layssac, T. Butscher, S. Henkel, Y. Tsegaw, D. Grote, W. Sander, F. Borget, T. Chiavassa, and F. Duvernay, "icom formation from radical chemistry: a mechanistic study from cryogenic matrix coupled with ir and epr spectroscopies," *Monthly Notices of the Royal Astronomical Society*, vol. 506, no. 3, pp. 3734–3750, 2021.

[391] M. E. Jacox and F. L. Rook, "Photodecomposition of methyl nitrite trapped in solid argon," *The Journal of Physical Chemistry*, vol. 86, no. 15, pp. 2899–2904, 1982.

[392] J.-W. Lee, J.-H. Seo, J.-H. Kim, S.-Y. Lee, and M.-W. Byun, "Comparison of the changes of the antigenicities of a hen's egg albumin by a gamma and an electron beam irradiation," *Radiation Physics and Chemistry*, vol. 76, no. 5, pp. 879–885, 2007.

[393] N. Russell, "Cold adaptation of microorganisms," *Philosophical Transactions of the Royal Society of London. B, Biological Sciences*, vol. 326, no. 1237, pp. 595–611, 1990.

[394] G. Munoz Caro, U. J. Meierhenrich, W. A. Schutte, B. Barbier, A. Arcones Segovia, H. Rosenbauer, W.-P. Thiemann, A. Brack, and J. M. Greenberg, "Amino acids from ultraviolet irradiation of interstellar ice analogues," *Nature*, vol. 416, no. 6879, pp. 403–406, 2002.

[395] S. Esmaili, A. D. Bass, P. Cloutier, L. Sanche, and M. A. Huels, "Glycine formation in co2: Ch4: Nh3 ices induced by 0-70 ev electrons," *The Journal of chemical physics*, vol. 148, no. 16, 2018.

[396] C. Meinert, I. Myrgorodska, P. De Marcellus, T. Buhse, L. Nahon, S. V. Hoffmann, L. L. S. d'Hendecourt, and U. J. Meierhenrich, "Ribose and related sugars from ultraviolet irradiation of interstellar ice analogs," *Science*, vol. 352, no. 6282, pp. 208–212, 2016.

[397] M. Nuevo, G. Cooper, and S. A. Sandford, "Deoxyribose and deoxysugar derivatives from photoprocessed astrophysical ice analogues and comparison to meteorites," *Nature Communications*, vol. 9, no. 1, p. 5276, 2018.

[398] Y. Oba, Y. Takano, H. Naraoka, N. Watanabe, and A. Kouchi, "Nucleobase synthesis in interstellar ices," *Nature communications*, vol. 10, no. 1, p. 4413, 2019.

[399] T. E. Madey, R. E. Johnson, and T. M. Orlando, "Far-out surface science: radiation-induced surface processes in the solar system," *Surface Science*, vol. 500, no. 1-3, pp. 838–858, 2002.

[400] C. K. Materese, D. P. Cruikshank, S. A. Sandford, H. Imanaka, and M. Nuevo, "Ice chemistry on outer solar system bodies: Electron radiolysis of n2-, ch4-, and co-containing ices," *The Astrophysical Journal*, vol. 812, no. 2, p. 150, 2015.

[401] G. Danger, F.-R. Orthous-Daunay, P. De Marcellus, P. Modica, V. Vuitton, F. Duvernay, L. Flandinet, L. L. S. d'Hendecourt, R. Thissen, and T. Chiavassa, "Characterization of laboratory analogs of interstellar/cometary organic residues using very high resolution mass spectrometry," *Geochimica et Cosmochimica Acta*, vol. 118, pp. 184–201, 2013.

[402] C. Briois, R. Thissen, L. Thirkell, K. Aradj, A. Bouabdellah, A. Boukrara, N. Carrasco, G. Chalumeau, O. Chapelon, F. Colin, *et al.*, "Orbitrap mass analyser for in situ characterisation of planetary environments: Performance evaluation of a laboratory prototype," *Planetary and Space Science*, vol. 131, pp. 33–45, 2016.

[403] R. Arevalo Jr, L. Selliez, C. Briois, N. Carrasco, L. Thirkell, B. Cherville, F. Colin, B. Gaubicher, B. Farcy, X. Li, *et al.*, "An orbitrap-based laser desorption/ablation mass spectrometer designed for spaceflight," *Rapid Communications in Mass Spectrometry*, vol. 32, no. 21, pp. 1875–1886, 2018.

[404] L. F. Coelho, M.-A. Blais, A. Matveev, T. Keller-Costa, W. F. Vincent, R. Costa, Z. Martins, and J. Canário, "Contamination analysis of arctic ice samples as planetary field analogs and implications for future life-detection missions to europa and enceladus," *Scientific Reports*, vol. 12, no. 1, p. 12379, 2022.

[405] L. Sánchez-García, M. A. Fernández-Martínez, M. Moreno-Paz, D. Carrizo, M. García-Villadangos, J. M. Manchado, C. R. Stoker, B. Glass, and V. Parro, "Simulating mars drilling mission for searching for life: ground-truthing lipids and other complex microbial biomarkers in the iron-sulfur rich río tinto analog," *Astrobiology*, vol. 20, no. 9, pp. 1029–1047, 2020.

[406] D. Carrizo, F. A. Vignale, L. Sánchez-García, and M. E. Farías, "Ecological variability based on lipid biomarkers in astrobiologically interesting wetlands from the argentinian central andes," *FEMS Microbiology Ecology*, vol. 98, no. 5, p. fiac049, 2022.

[407] J. A. Mikucki, C. M. Foreman, B. Sattler, W. Berry Lyons, and J. C. Priscu, "Geomicrobiology of blood falls: an iron-rich saline discharge at the terminus of the taylor glacier, antarctica," *Aquatic Geochemistry*, vol. 10, pp. 199–220, 2004.

[408] D. Gleeson, C. Williamson, S. Grasby, R. Pappalardo, J. Spear, and A. Templeton, "Low temperature s0 biomineralization at a supraglacial spring system in the canadian high arctic," *Geobiology*, vol. 9, no. 4, pp. 360–375, 2011.

[409] K. E. Wright, C. Williamson, S. E. Grasby, J. R. Spear, and A. S. Templeton, "Metagenomic evidence for sulfur lithotrophy by epsilonproteobacteria as the major energy source for primary productivity in a sub-aerial arctic glacial deposit, borup fiord pass," *Frontiers in microbiology*, vol. 4, p. 63, 2013.

[410] J. L. Heldmann, W. H. Pollard, C. P. McKay, D. T. Andersen, and O. B. Toon, "Annual development cycle of an icing deposit and associated perennial spring activity on axel heiberg island, canadian high arctic," *Arctic, Antarctic, and Alpine Research*, vol. 37, no. 1, pp. 127–135, 2005.

[411] R. Arevalo Jr, Z. Ni, and R. M. Danell, "Mass spectrometry and planetary exploration: A brief review and future projection," *Journal of mass spectrometry*, vol. 55, no. 1, p. e4454, 2020.

[412] B. Cherville, L. Thirkell, B. Gaubicher, F. Colin, and C. Briois, "Current progress in positive and negative ion modes of a laser ionization mass spectrometer equipped with cosmorbitrap development-applicability to in situ analysis of ocean worlds," *Planetary and Space Science*, p. 105675, 2023.

[413] Q. Hu, R. J. Noll, H. Li, A. Makarov, M. Hardman, and R. Graham Cooks, "The orbitrap: a new mass spectrometer," *Journal of mass spectrometry*, vol. 40, no. 4, pp. 430–443, 2005.

[414] A. Makarov, E. Denisov, A. Kholomeev, W. Balschun, O. Lange, K. Strupat, and S. Horning, "Performance evaluation of a hybrid linear ion trap/orbitrap mass spectrometer," *Analytical chemistry*, vol. 78, no. 7, pp. 2113–2120, 2006.

[415] E. Denisov, E. Damoc, O. Lange, and A. Makarov, "Orbitrap mass spectrometry with resolving powers above 1,000,000," *International Journal of Mass Spectrometry*, vol. 325, pp. 80–85, 2012.

[416] A. Sanderink, F. Klenner, I. Zymak, J. Zabka, F. Postberg, J.-P. Lebreton, B. Gaubicher, A. Charvat, B. Abel, M. Polasek, *et al.*, "Olympia-lilbid: A new laboratory setup to calibrate spaceborne hypervelocity ice grain detectors using high-resolution mass spectrometry," *Analytical Chemistry*, vol. 95, no. 7, pp. 3621–3628, 2023.

2 Scientific publications

Peer-reviewed publications gathered in this thesis:

Napoleoni, M., Klenner, F., Khawaja, N., Hillier, J. K., & Postberg, F. (2023) Mass Spectrometric Fingerprints of Organic Compounds in NaCl-Rich Ice Grains from Europa and Enceladus. *ACS Earth and Space Chemistry*, 7(4), 735-752.

Napoleoni, M., Klenner, F., Hortal Sánchez, L., Khawaja, N., Hillier, J. K., Gudipati, M. S., Hand, K.P., Kempf, S., & Postberg, F. (2023) Mass Spectrometric Fingerprints of Organic Compounds in Sulfate-Rich Ice Grains: Implications for Europa Clipper. *ACS Earth and Space Chemistry*, 7(9), 1675-1693.

Napoleoni, M., Hortal Sánchez L., Khawaja N., Abel, B., Glein, C., Hillier J.K., & Frank Postberg (2023) Probing the oxidation state of ocean worlds with SUDA: Fe (II) and Fe (III) in ice grains. *The Planetary Science Journal.* Submitted on 3rd November 2023; accepted with minor revisions in January 2024.

Additional, co-authorship publications:

Khawaja, N., Hillier, J., Klenner, F., Nölle, L., Zou, Z., Napoleoni, M., ... & Postberg, F. (2022). Complementary mass spectral analysis of isomeric O-bearing organic compounds and fragmentation differences through analog techniques for spaceborne mass spectrometers. *The Planetary Science Journal*, 3(11), 254.

Klenner, F., Umair, M., Walter, S. H., ... & Postberg, F. (2022). Developing a laser induced liquid beam ion desorption spectral database as reference for spaceborne mass spectrometers. *Earth and Space Science*, 9(9), e2022EA002313.

Dannenmann, M., Klenner, F., Bönigk, J., Pavlista, M., Napoleoni, M., ... & Postberg, F. (2023). Toward detecting biosignatures of DNA, lipids, and metabolic intermediates from bacteria in ice grains emitted by Enceladus and Europa. *Astrobiology*, 23(1), 60-75.

Klenner, F., Boenigk, J., Napoleoni, M., ... & Postberg, F. How to Identify Cell Material in a Single Ice Grain Emitted from Enceladus or Europa. *Science Advances*, submitted.

Kempf, S., Tucker, S., Altobelli, N., ... & Simolka, J. SUDA: A SUrface Dust Analyser for compositional mapping of the Galilean moon Europa. *Science*, submitted.

Khawaja, N., Hortal Sánchez, L., O'Sullivan, T., Bloema, J., Napoleoni, M., ... & Postberg, F. A novel approach to identify hydrothermally processed oligopeptides in Enceladus ice grains with mass spectrometry. *Philosophical Transactions of the Royal Society A* (Special Issue: Cosmic Dust in the Solar System and Beyond), submitted.

Bouquet, A., Aparecida Pires da Costa, C., Boduch, P., ... & Mousis, O. Energetic sulfur implantation into water ice with alkanes: implications for organic chemistry on the surface of Europa. *The Planetary Science Journal*, submitted.

Oral and poster presentations at conferences:

Napoleoni, M., Khawaja N., Klenner, F., Hillier J.K., Hortal Sánchez L., Gudipati, M., Hand, K.P., Kempf, S. & Frank Postberg (2023) "Mass Spectrometric Fingerprints of Organic Compounds in Salt-Rich Ice Grains: Implications for Europa Clipper". Galilean Moons workshop, Marseille 2023. Oral presentation.

Napoleoni, M., Khawaja N., Klenner, F., Hillier J.K., Hortal Sánchez L., Gudipati, M., Hand, K.P., Kempf, S. & Frank Postberg (2023) "Mass Spectrometric Fingerprints of Organic Compounds in Salt-Rich Ice Grains:

Implications for Europa Clipper" EPSC-DPS, San Antonio, TX, USA. Oral presentation.

Napoleoni, M.. Klenner, F., Khawaja N., Hillier J.K., Knolle, W., Lugovoy, E., Abel, B. & Frank Postberg (2023) "Experiments for the Detection of Biosignatures in Irradiated Ice Grains with Europa Clipper's SUDA Mass Spectrometer" DAbG meeting, DLR, Berlin 2023. Oral presentation.

Napoleoni, M.. Klenner, F., Khawaja N., Hortal Sanchez, L., Hillier J.K. & Frank Postberg (2023) "Mass spectrometric fingerprints of organics in salt rich ice grains: implications for Europa Clipper" Dusty Visions, Berlin 2023. Oral presentation.

Napoleoni, M.. Klenner, F., Khawaja N., Hillier J.K., Hortal Sánchez L. & Frank Postberg (2023) "Analysis of organics in salt rich ice grains with mass spectrometry: implications for Europa Clipper". BEACON 2023, La Palma, Spain. Oral presentation.

Napoleoni, M.. Klenner, F., Bönigk, J., Hillier J.K., Khawaja N., Olsson-Francis, K. & Frank Postberg (2023) "Analogue experiments for the detection of microbial biosignatures in ice grains from ocean worlds" AbGradE-PEC 2023, La Palma, Spain. Poster, granted the award for the best poster.

Napoleoni, M.. Klenner, F., Khawaja N., Hillier J.K. & Frank Postberg (2022) "Mass spectral analysis of organic compounds in salt-rich ice grains from Europa" DAbG meeting, Bremen 2022. Oral presentation.

Napoleoni, M.. Klenner, F., Bönigk, J., Pavlista, M., Dannenmann, M., Hillier J.K., Khawaja N., Olsson-Francis, K. & Frank Postberg (2022) "Analog experiments for the detection of bacterial biosignatures in ice grains from ocean worlds" Exobiologie Jeunes Chercheurs (EJC) 2022, Paris. Oral presentation granted the award of the Institut Origines (Marseille).

Napoleoni, M.. Klenner, F., Khawaja N., Hillier J.K. & Frank Postberg (2022) "Analogue Experiments for the Mass Spectral Analysis of Organic Compounds form the Salt-rich Surface of Europa" EPSC 2022, Granada, Spain. Oral presentation.

Napoleoni, M.. Klenner, F., Khawaja N., Hillier J.K. & Frank Postberg (2022) "ANALOGUE EXPERIMENTS FOR THE MASS SPECTRAL ANALYSIS OF ORGANIC COMPOUNDS FROM THE SURFACE OF EUROPA" COSPAR 2022, Athens, Greece. Oral presentation.

Napoleoni, M.. Klenner, F., Hillier J.K., Khawaja N., Hand, K.P. & Frank Postberg (2021) "Analogue Experiments for the Identification of Organics in Ice Grains from Europa Using Mass Spectrometry" AGU. Online poster.

Napoleoni, M.. Klenner, F., Hillier J.K., Khawaja N., Hand, K.P. & Frank Postberg (2021) "Analogue experiments for the identification of organics in ice grains from Europa using mass spectrometry" EPSC 2021. Online meeting. Oral presentation.

Napoleoni, M. (2021) "Analog experiments for the detection of bacterial biosignatures in ice grains from ocean worlds" AbGradCon 2021. Earth-Life Science Institute Tokyo, Japan. Online Meeting. Oral presentation.

Seminar talks:

Cornell University, NY, USA. October 16th, 2023.
Planetary science seminar talk, invited by Dr. Ligia F. Coelho and Prof. Dr. Lisa Kaltenegger.
"Laboratory simulations of possible biogenic and organic fingerprints in mass spectra of ice grains from ocean worlds".

Institut Origines, Marseille. June 22nd, 2023.
"Simulation of possible biogenic and organic fingerprints in mass spectra of ice grains from icy moons".

3 Appendix

Supplementary Material – Part II.

Analogue experiments for the detection of organic compounds in salt-rich ice grains from ocean worlds.

The spectra of solutions not included in the Part II of this thesis, i.e. anion mass spectrum of 5-amino-1-pentanol in 1M NaCl matrix, cation mass spectrum of benzoic acid in 1M NaCl, anion mass spectrum of butylamine in 1M NaCl, anion mass spectrum of glucose in 1M NaCl, anion mass spectrum of methanol in 1M NaCl matrix, and the anion mass spectra of pyridine in 0.1M and 1M NaCl matrix showed no peak related to the organics and are similar to the respective NaCl background matrix spectra. In the spectra of organics in NaCl-rich matrices (figure S5 to S36), unlabeled peaks originate exclusively from the salty matrix.
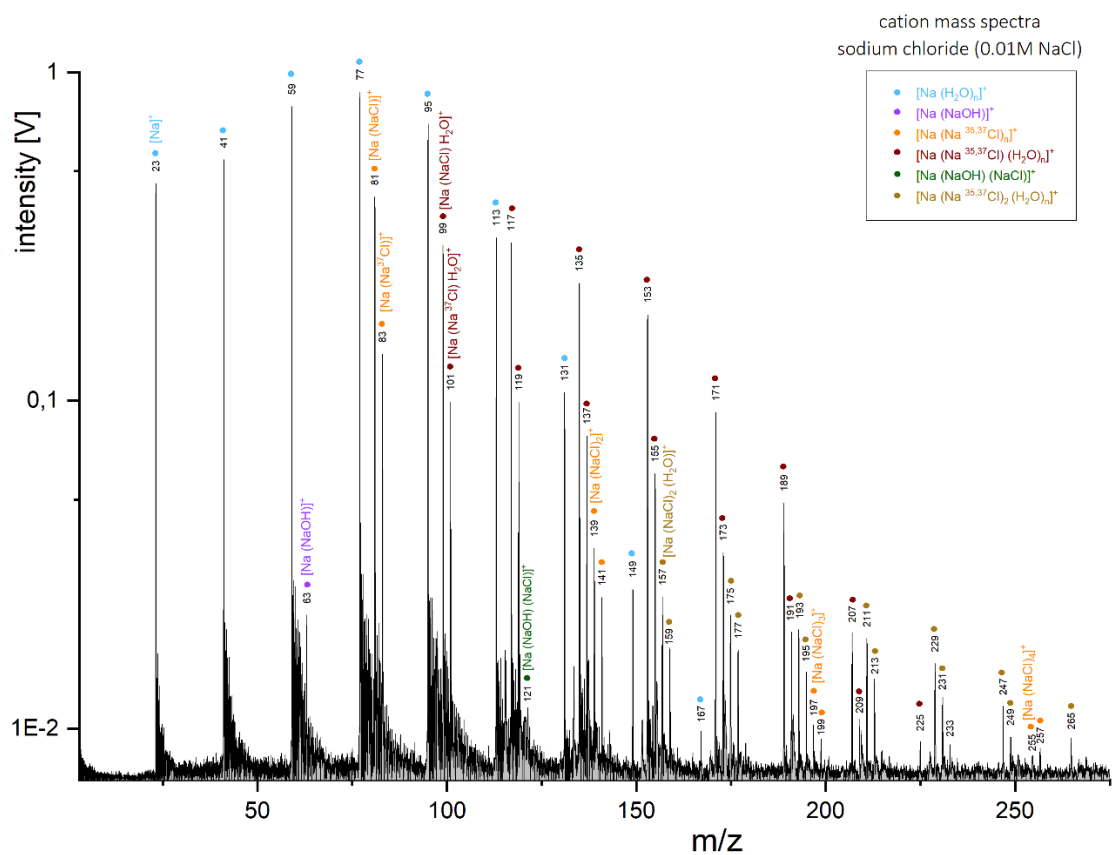
Figure S1. Baseline corrected cation mass spectrum of sodium chloride (NaCl) at a concentration of 0.01M, recorded at a delay time of 6.2μs.
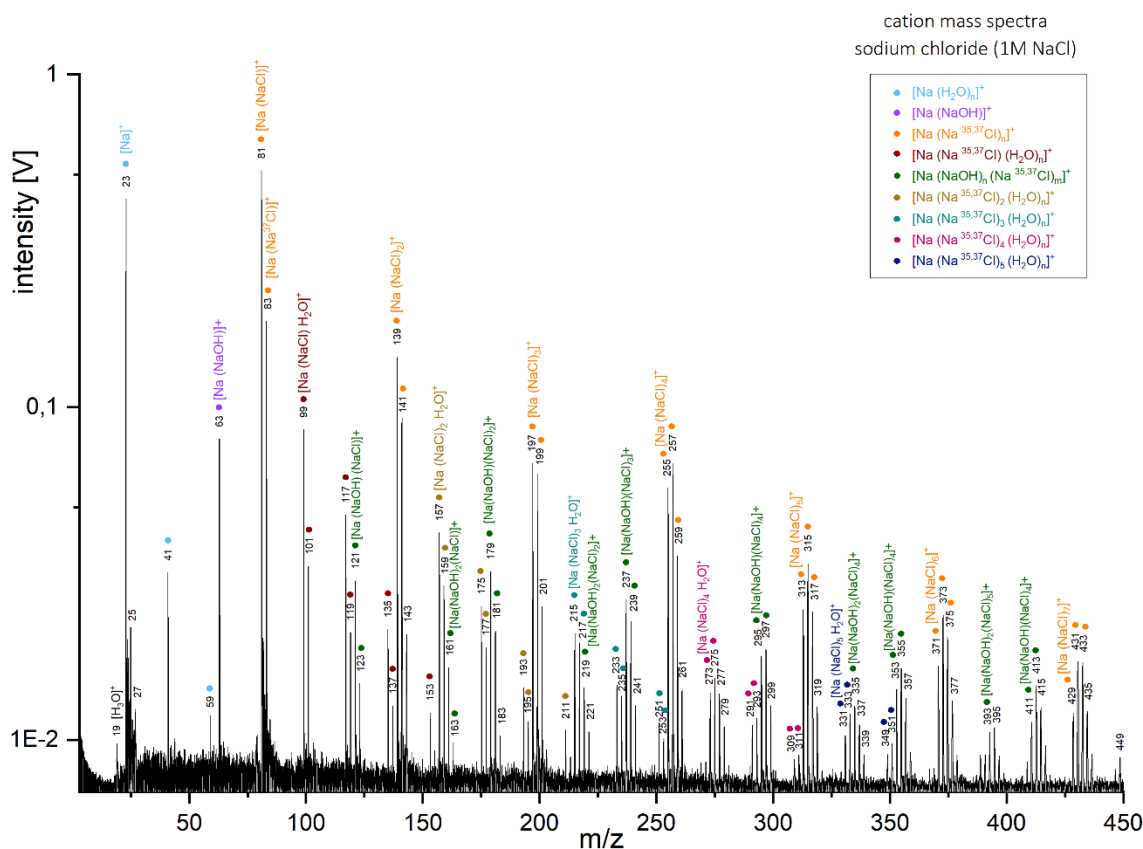
Figure S2. Baseline corrected cation mass spectrum of sodium chloride (NaCl) at a concentration of 1M, recorded at a delay time of 6.2μs.
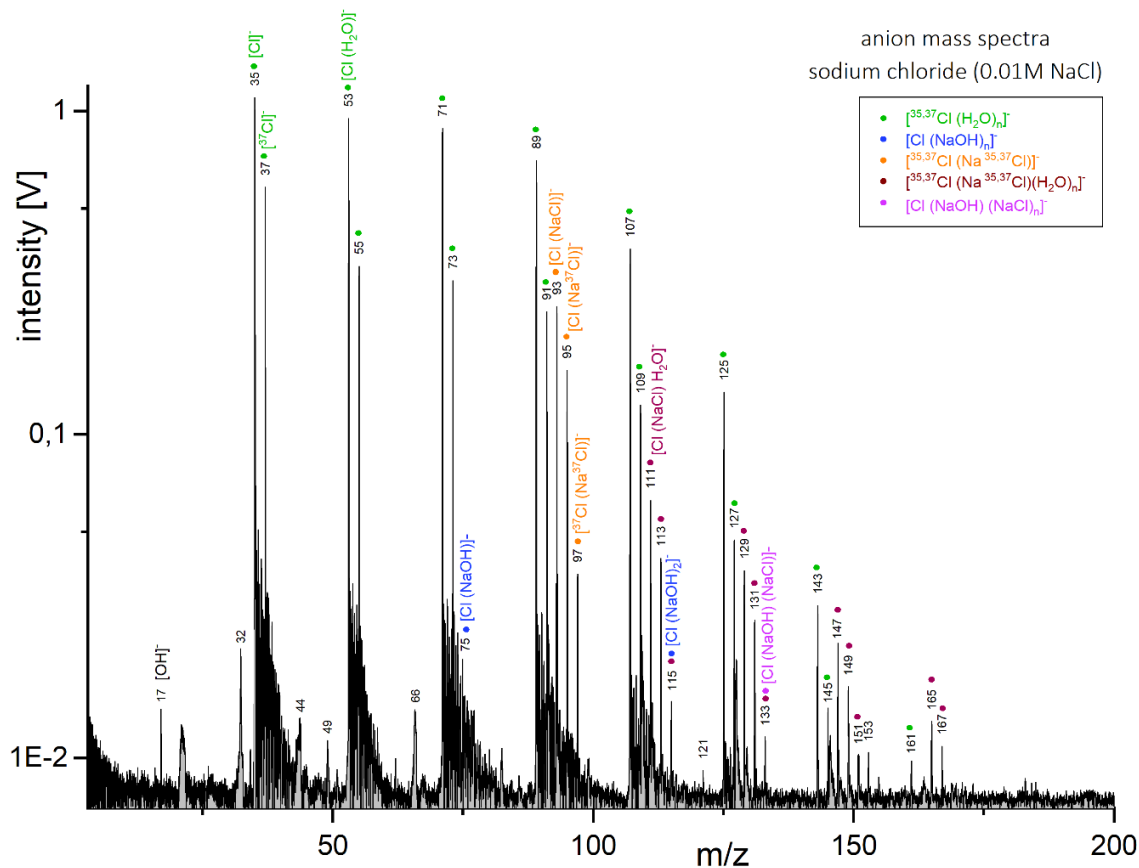
Figure S3. Baseline corrected anion mass spectrum of sodium chloride (NaCl) at a concentration of 0.01M, recorded at a delay time of 6.1μs.
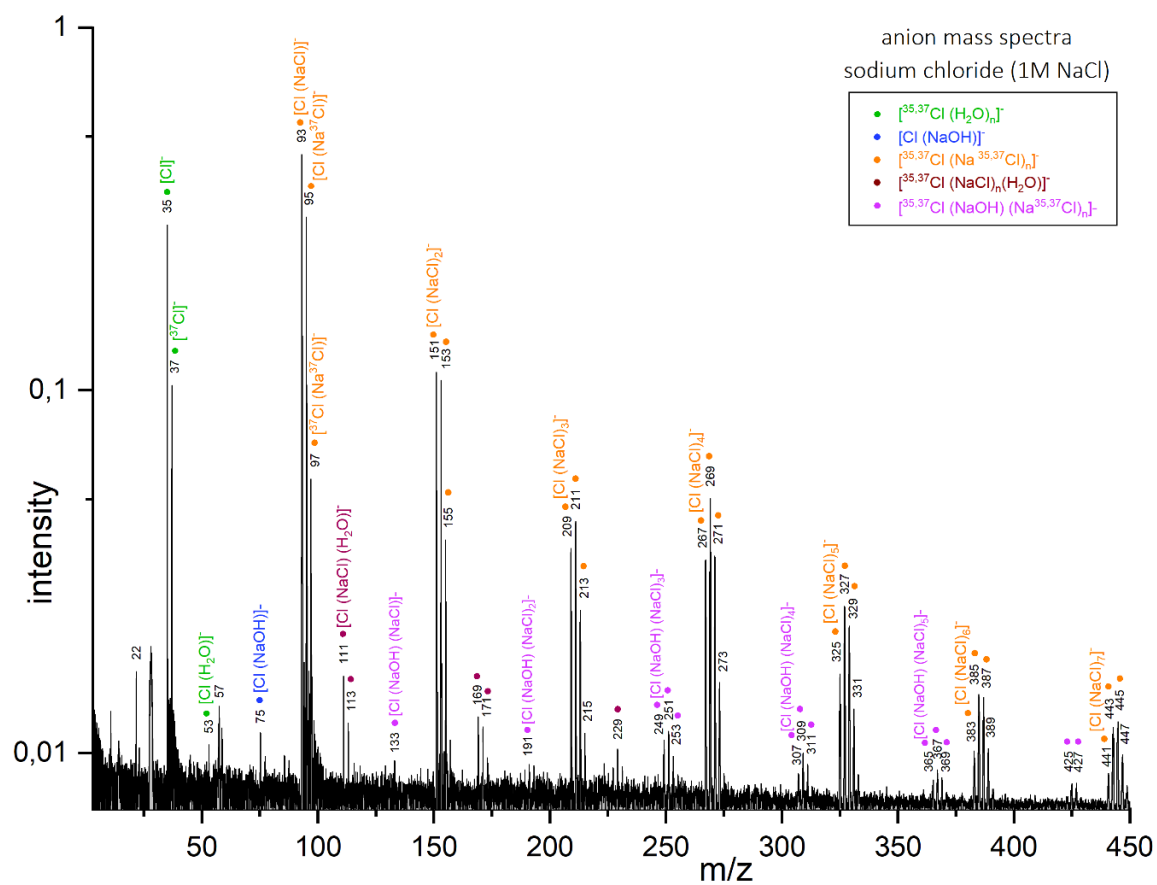
Figure S4. Baseline corrected anion mass spectrum of sodium chloride (NaCl) at a concentration of 1M, recorded at a delay time of 6.2μs.
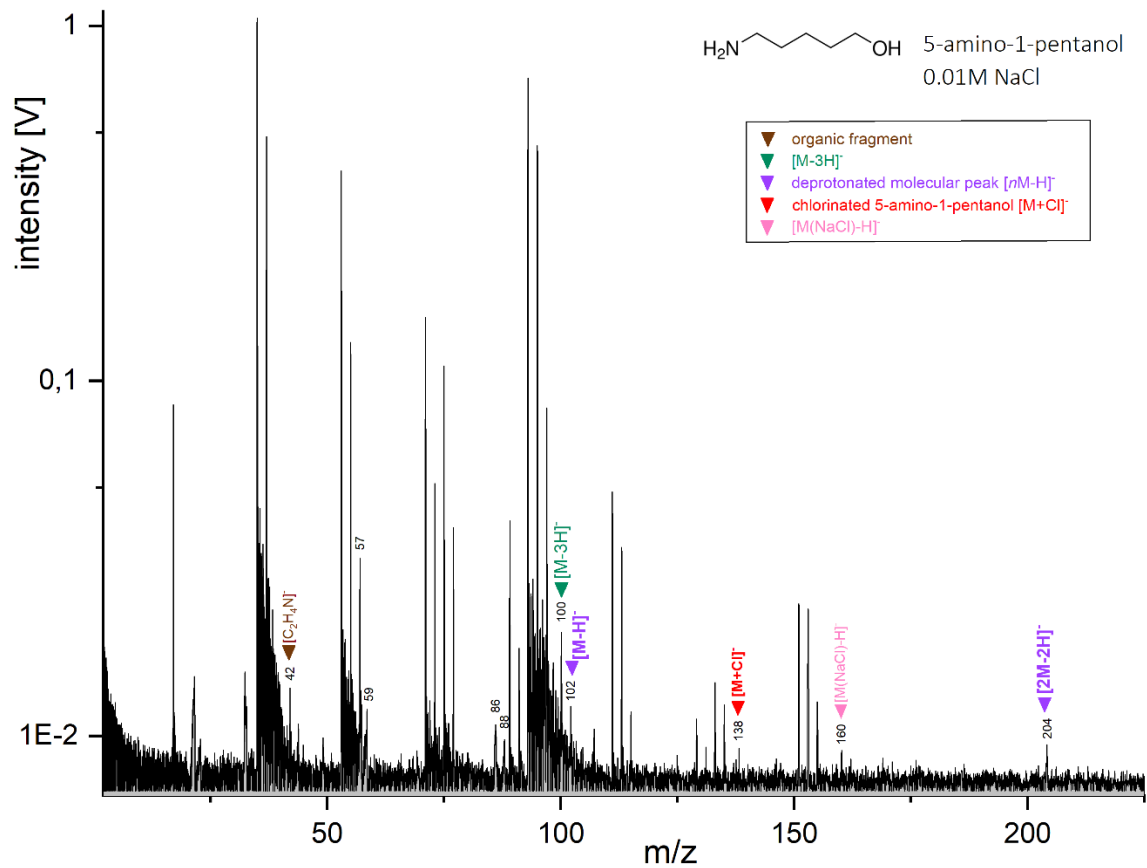
Figure S5. Baseline corrected anion mass spectrum of 5-amino-1-pentanol at a concentration of 5wt% in a H_2O and NaCl (0.01M) matrix, recorded at a delay time of 5.5µs.
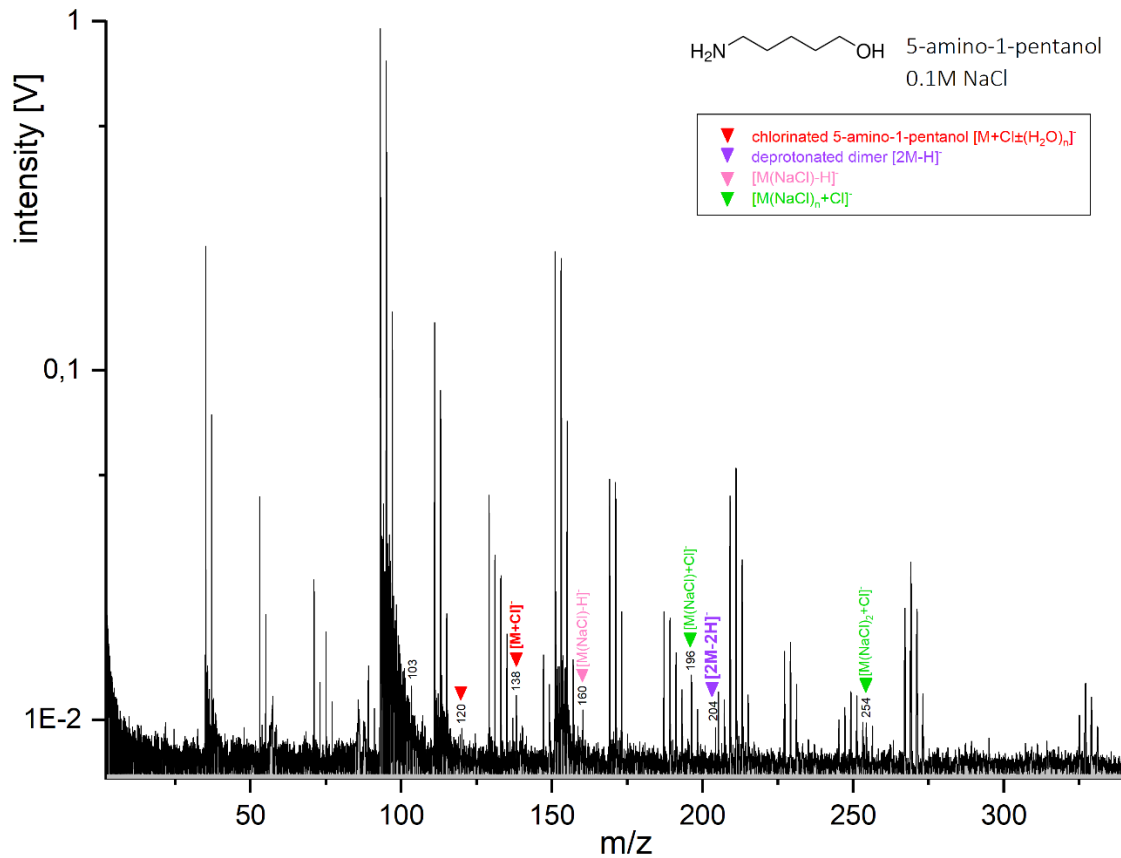
Figure S6. Baseline corrected anion mass spectrum of 5-amino-1-pentanol at a concentration of 5wt% in a H_2O and NaCl (0.1M) matrix, recorded at a delay time of 6.2µs.
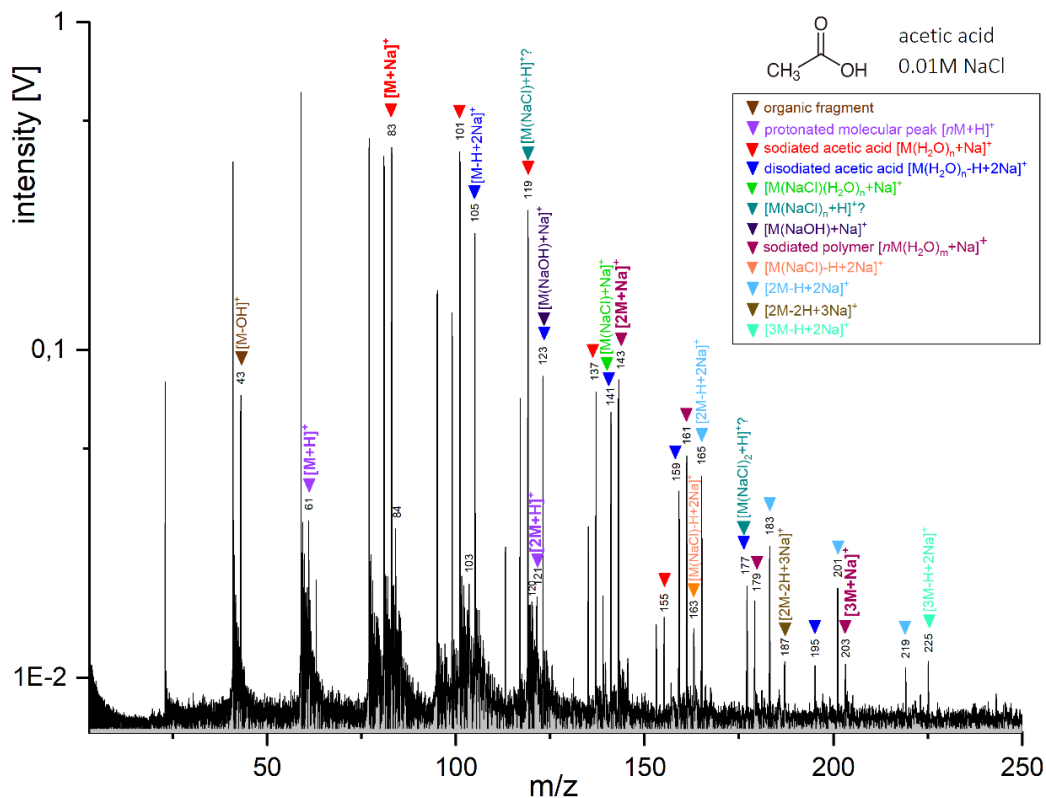
Figure S7. Baseline corrected cation mass spectrum of acetic acid at a concentration of 5wt% in a H_2O and NaCl (0.01M) matrix, recorded at a delay time of 6.0µs. The peak at m/z 83u (0.416 V) is assigned to both the salt cluster $[Na(Na^{37}Cl)]^+$ (0.125V) and sodiated acetic acid $[M+Na]^+$ (0.291 V). Peaks at m/z 123u and 141u have been tentatively assigned to acetic acid and salt clusters $[M+Na+NaOH]^+$ and $[M+Na+NaCl]^+$ but can also be water clusters of disodiated acetic acid.
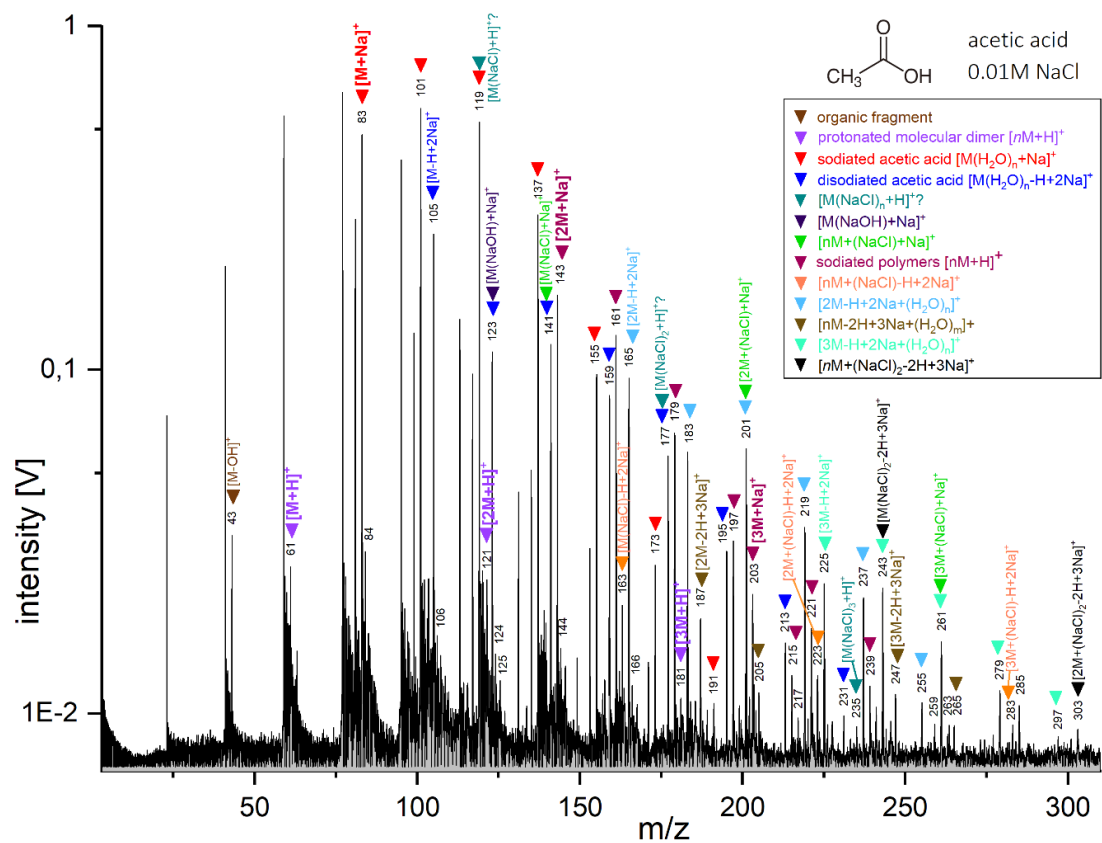
Figure S8. Baseline corrected cation mass spectrum of acetic acid at a concentration of 5wt% in a H_2O and NaCl (0.01M) matrix, recorded at a delay time of 6.5µs. Unlabeled peaks originate exclusively from the salty matrix.
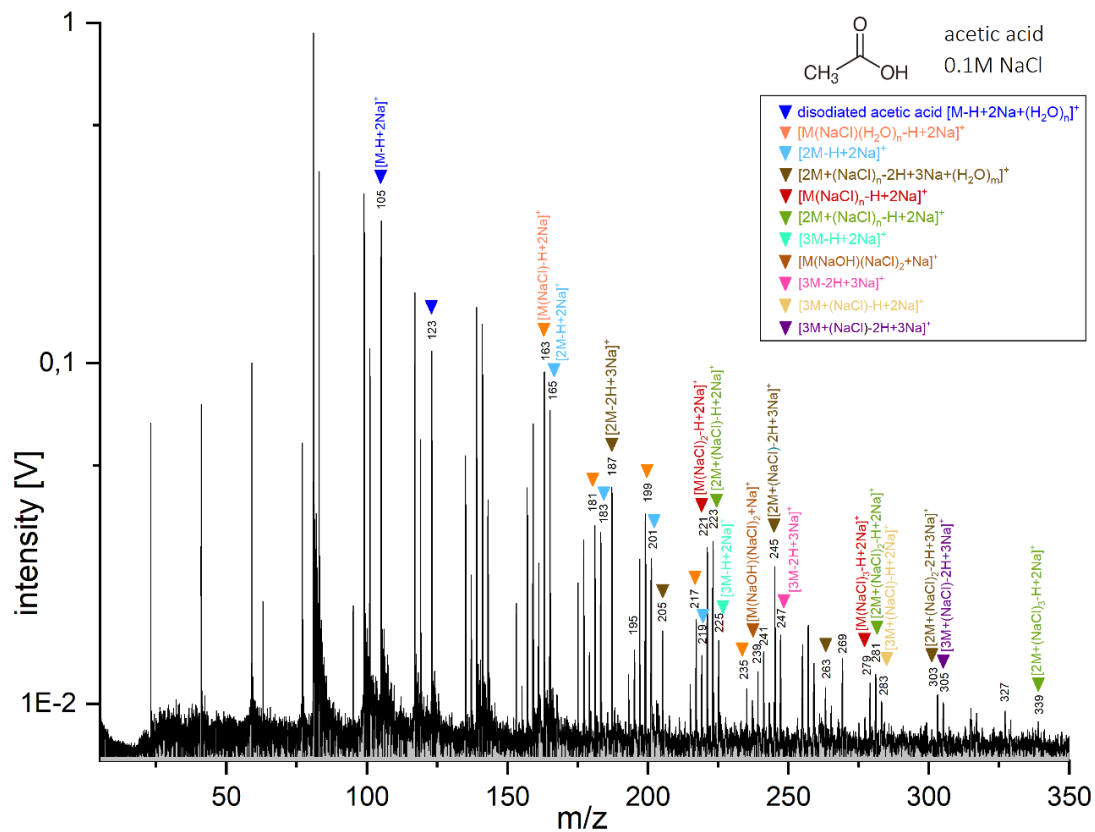
Figure S9. Baseline corrected cation mass spectrum of acetic acid at a concentration of 5wt% in a H_2O and NaCl (0.1M) matrix, recorded at a delay time of 6.0µs.
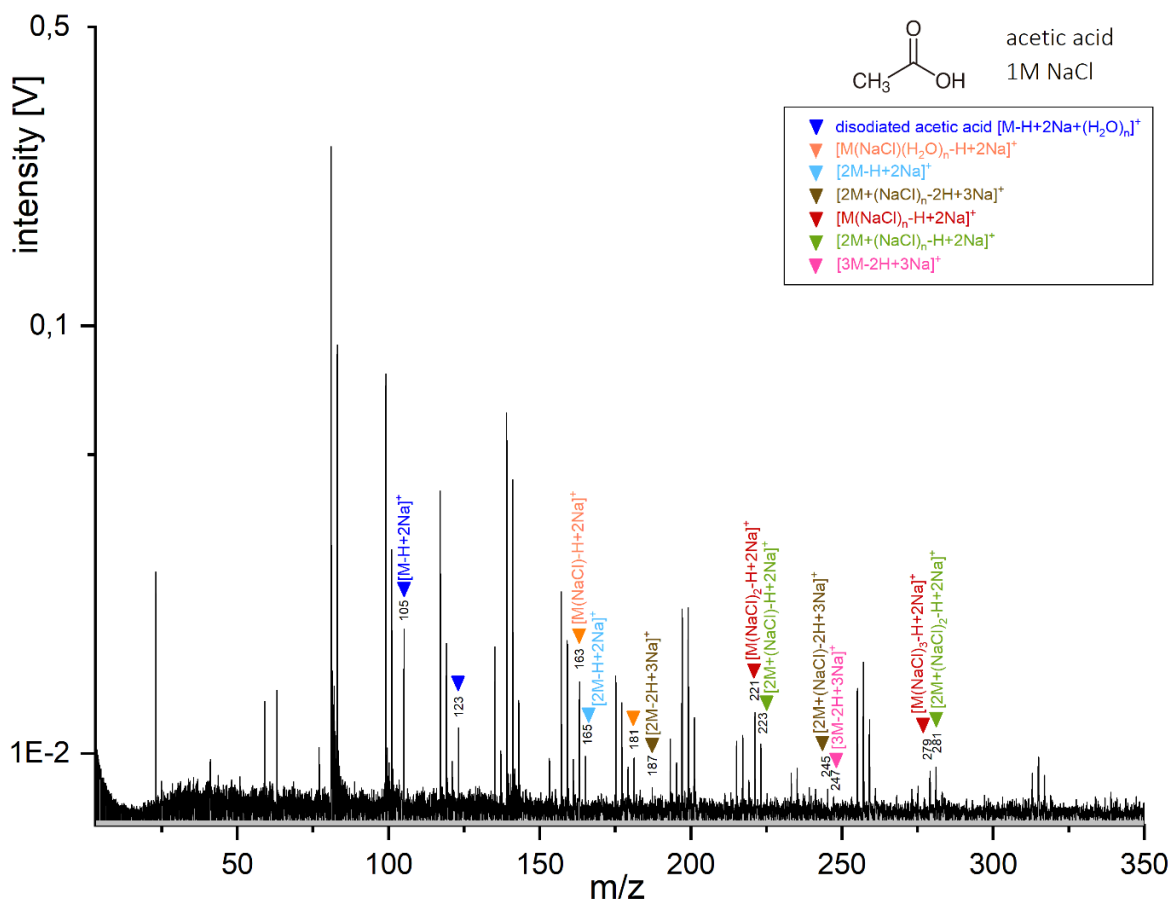
Figure S10. Baseline corrected cation mass spectrum of acetic acid at a concentration of 5wt% in a H_2O and NaCl (1M) matrix, recorded at a delay time of 6.0µs.
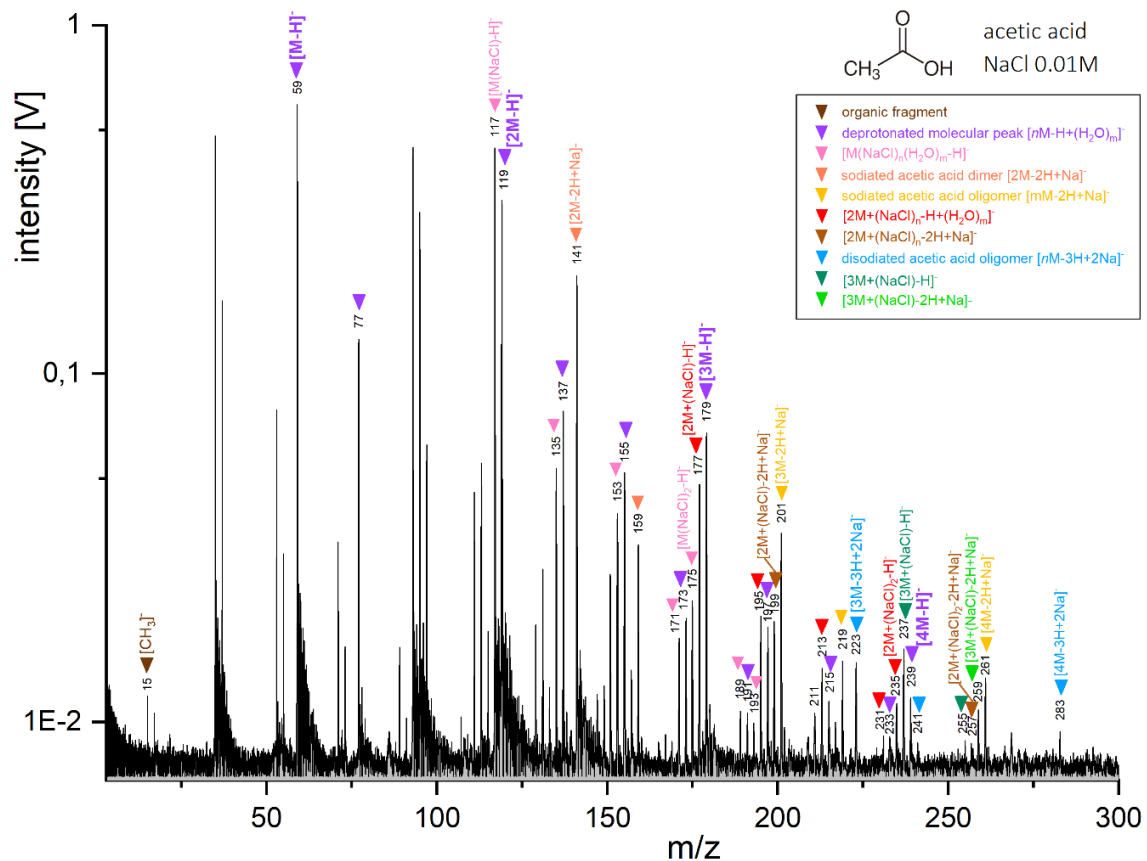
Figure S11. Baseline corrected anion mass spectrum of acetic acid at a concentration of 5wt% in a H_2O and NaCl (0.01M) matrix, recorded at a delay time of 6.5μs.
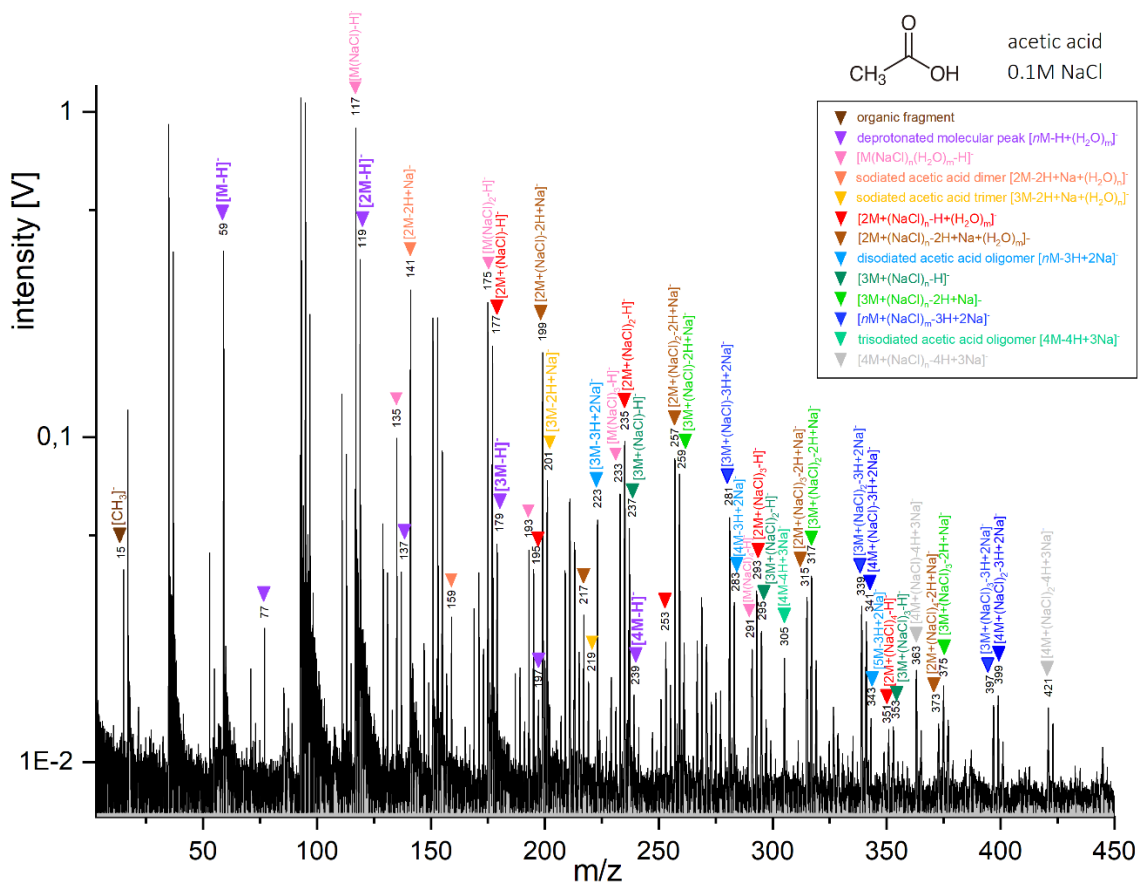
Figure S12. Baseline corrected anion mass spectrum of acetic acid at a concentration of 5wt% in a H_2O and NaCl (0.1M) matrix, recorded at a delay time of 6.5μs.
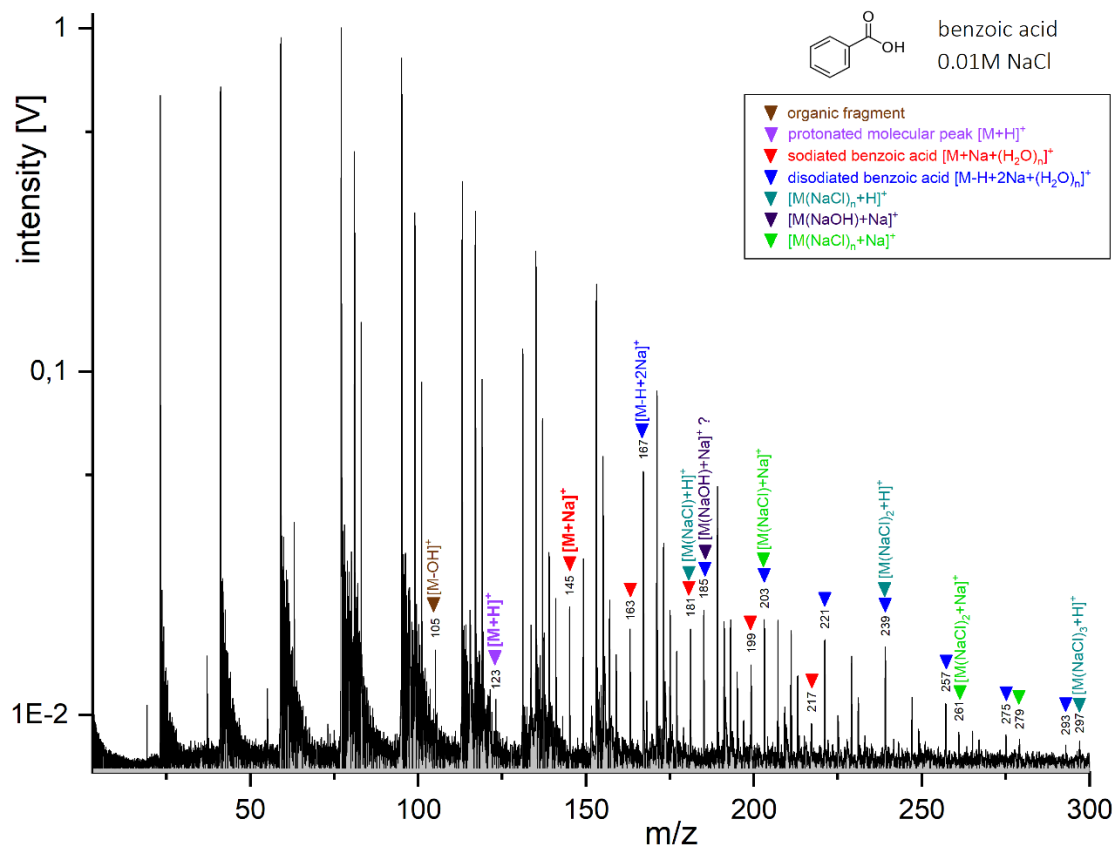
Figure S13. Baseline corrected cation mass spectrum of benzoic acid at a concentration of 0.17wt% in a H_2O and NaCl (0.01M) matrix, recorded at a delay time of 6.2µs.
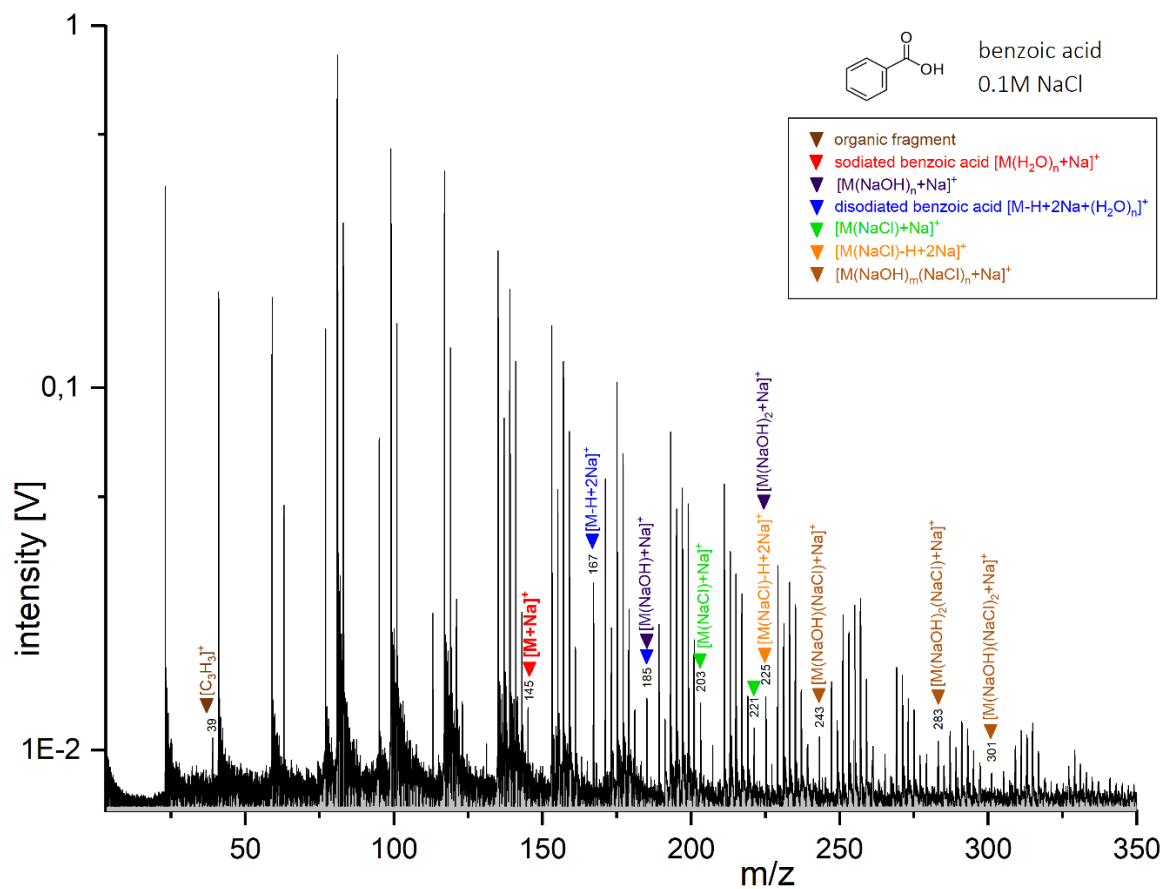
Figure S14. Baseline corrected cation mass spectrum of benzoic acid at a concentration of 0.17wt% in a H_2O and NaCl (0.1M) matrix, recorded at a delay time of 6.1µs.
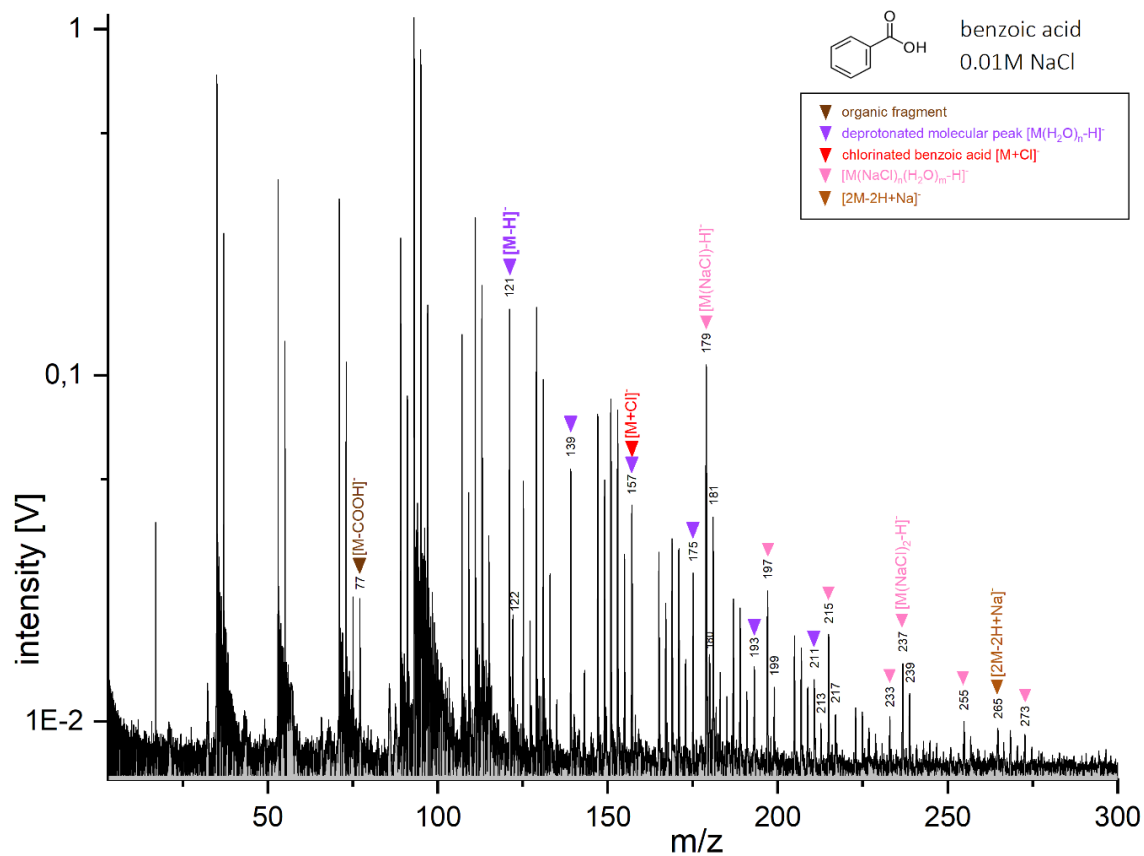
Figure S15. Baseline corrected anion mass spectrum of benzoic acid at a concentration of 0.17wt% in a H_2O and NaCl (0.01M) matrix, recorded at a delay time of 6.1µs.
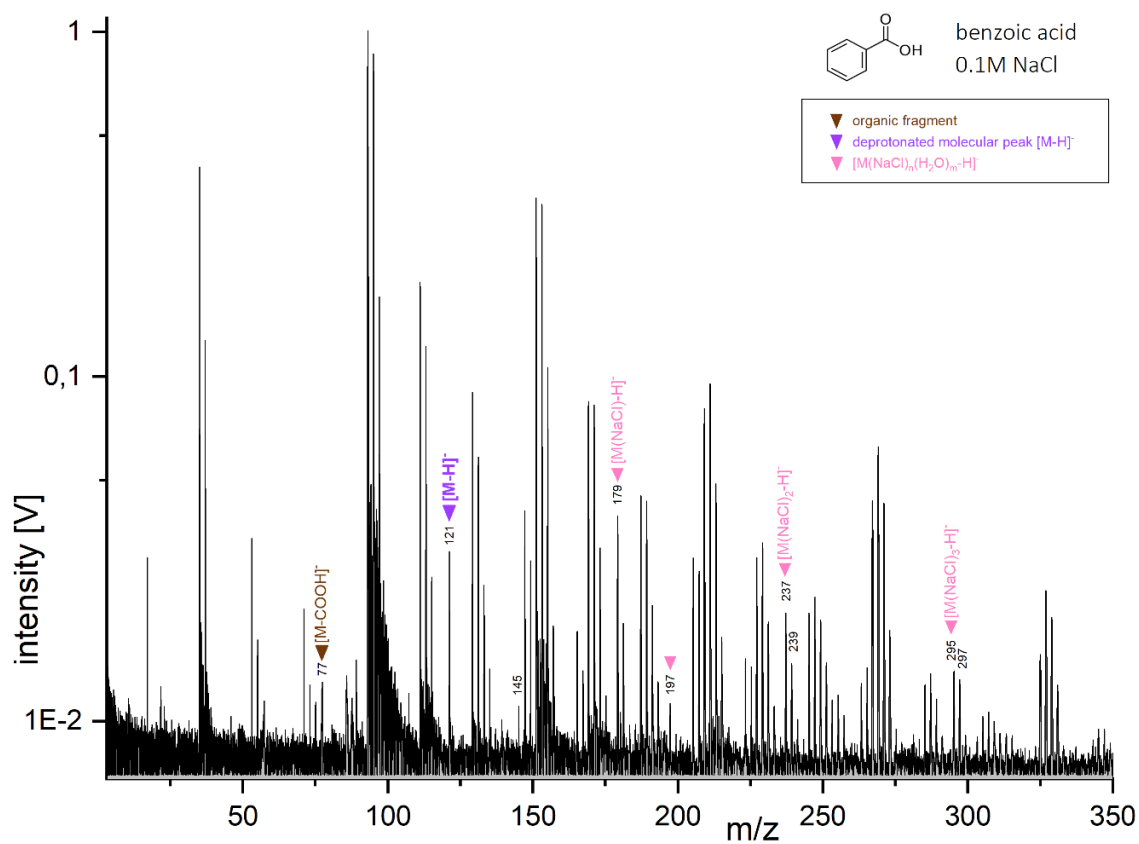
Figure S16. Baseline corrected anion mass spectrum of benzoic acid at a concentration of 0.17wt% in a H_2O and NaCl (0.1M) matrix, recorded at a delay time of 6.1µs.
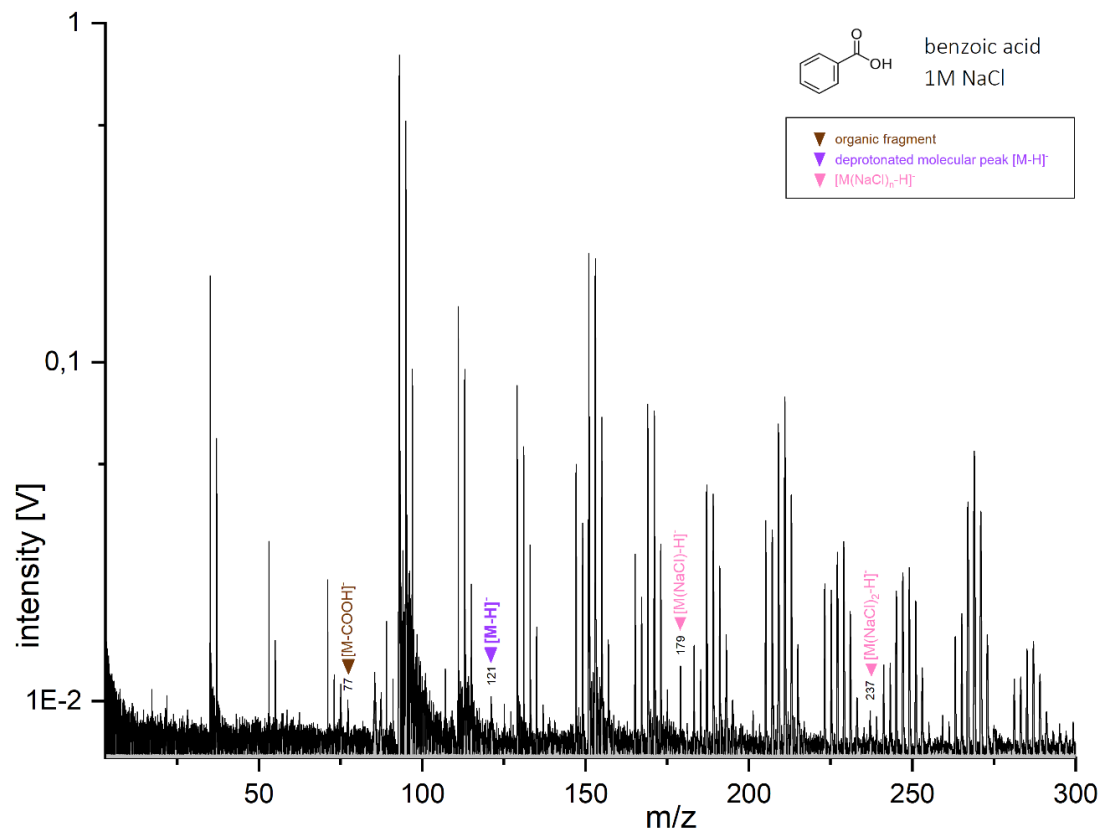
Figure S17. Baseline corrected anion mass spectrum of benzoic acid at a concentration of 0.14wt% in a H_2O and NaCl (1M) matrix, recorded at a delay time of 6.8µs.
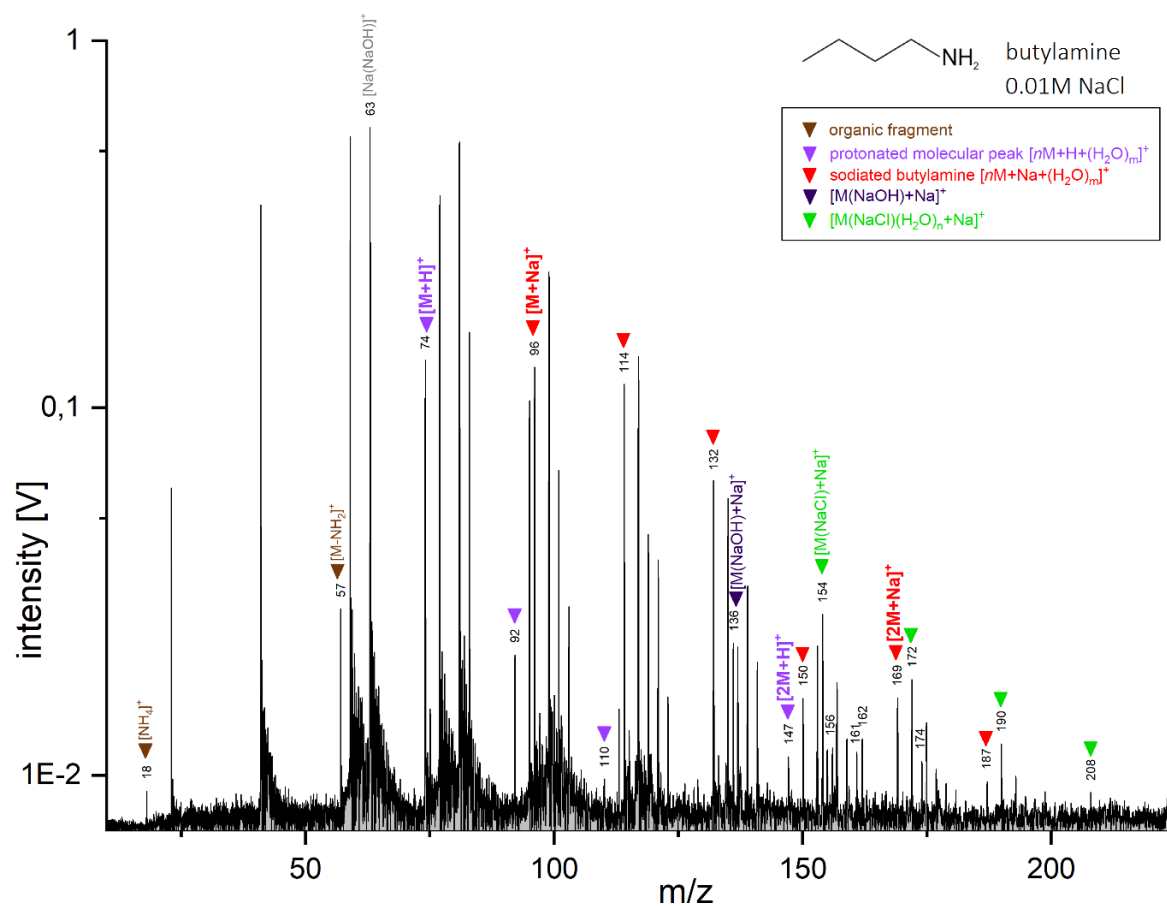
Figure S18. Baseline corrected cation mass spectrum of butylamine at a concentration of 5wt% in a H_2O and NaCl (0.01M) matrix, recorded at a delay time of 6.0µs.
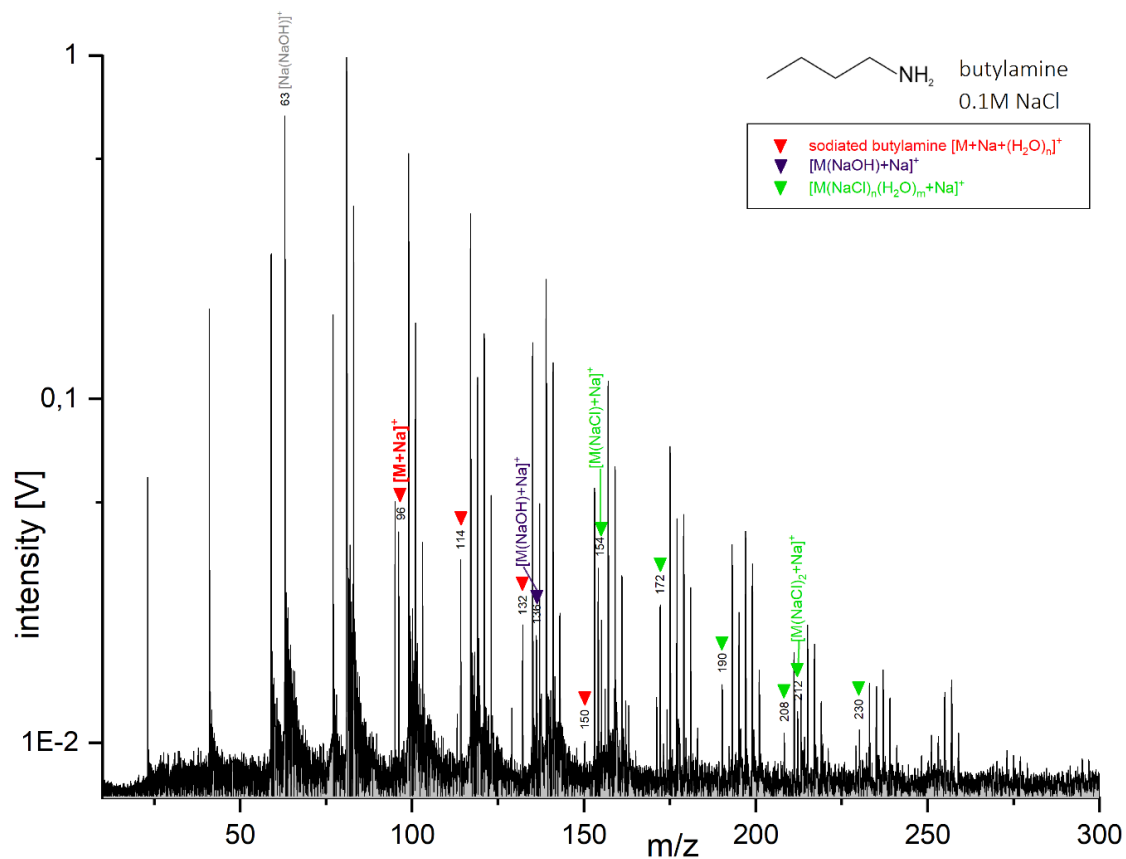
Figure S19. Baseline corrected cation mass spectrum of butylamine at a concentration of 5wt% in a H_2O and NaCl (0.1M) matrix, recorded at a delay time of 6.0µs. The peak at m/z 63 might have a contribution by organic species as it has a much higher amplitude than in the NaCl (0.1M) matrix spectra (Figure 2).
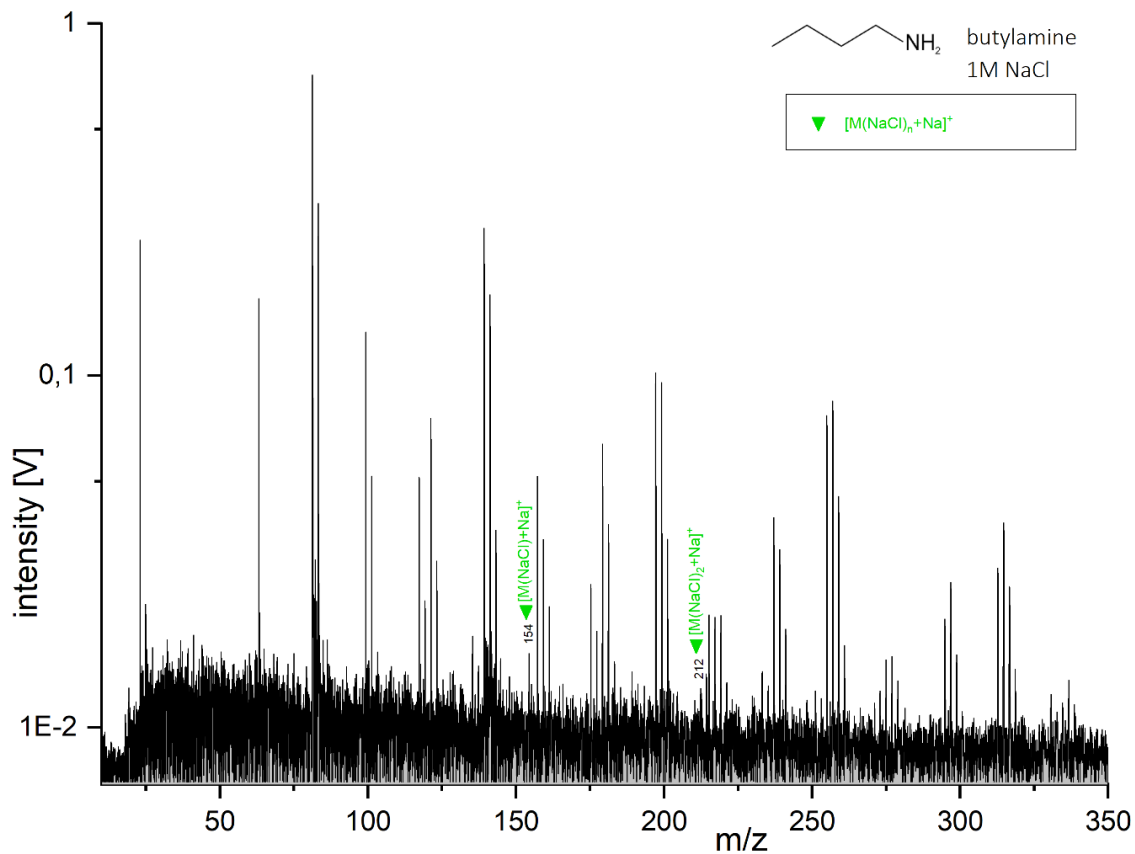
Figure S20. Baseline corrected cation mass spectrum of butylamine at a concentration of 5wt% in a H_2O and NaCl (1M) matrix, recorded at a delay time of 6.0µs.
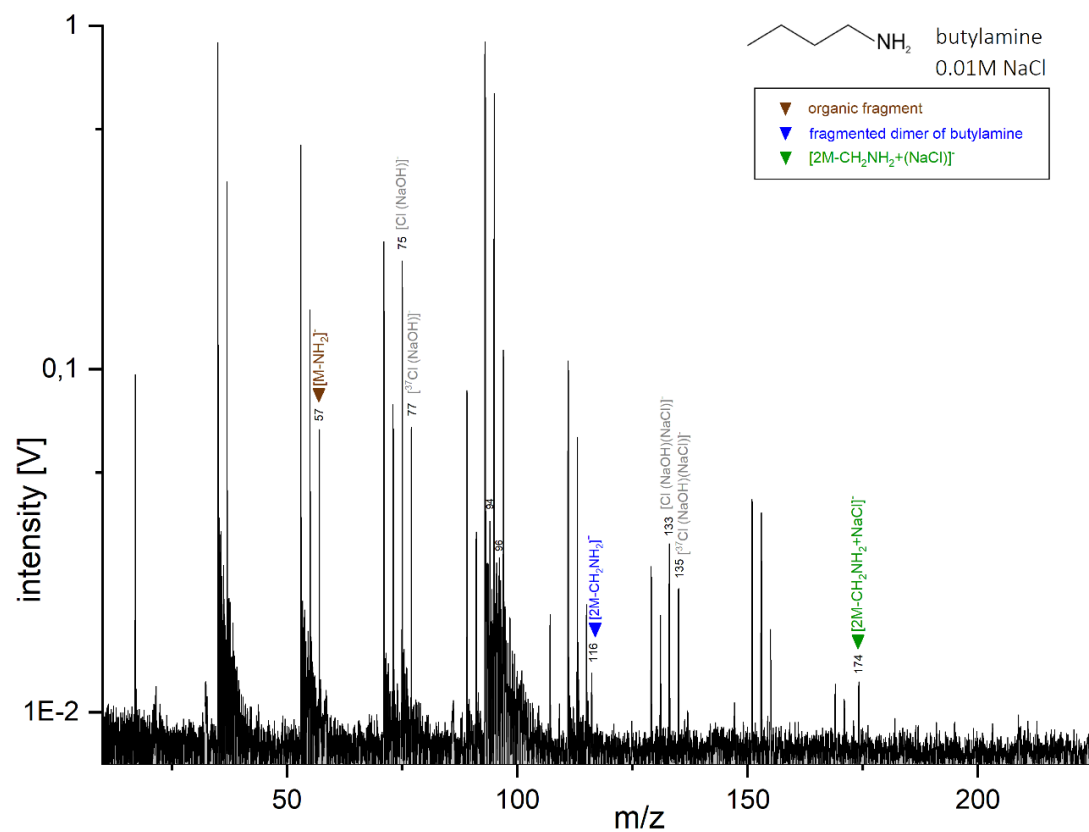
Figure S21. Baseline corrected anion mass spectrum of butylamine at a concentration of 5wt% in a H_2O and NaCl (0.01M) matrix, recorded at a delay time of 6.0µs. Peaks at m/z 75, 77, 133 and 135 may have a contribution by organic species as they have much higher amplitudes than in the NaCl (0.01M) matrix spectra (Figure S3).
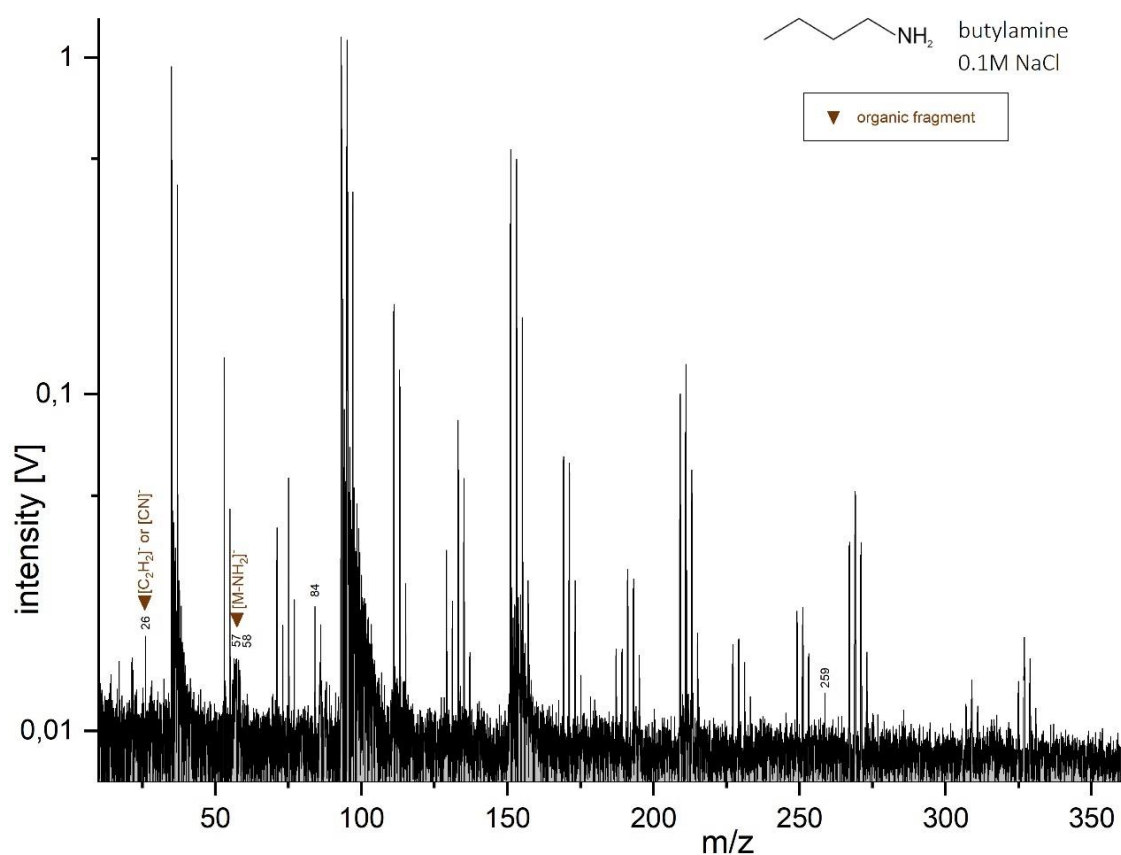
Figure S22. Baseline corrected anion mass spectrum of butylamine at a concentration of 5wt% in a H_2O and NaCl (0.1M) matrix, recorded at a delay time of 6.0µs.
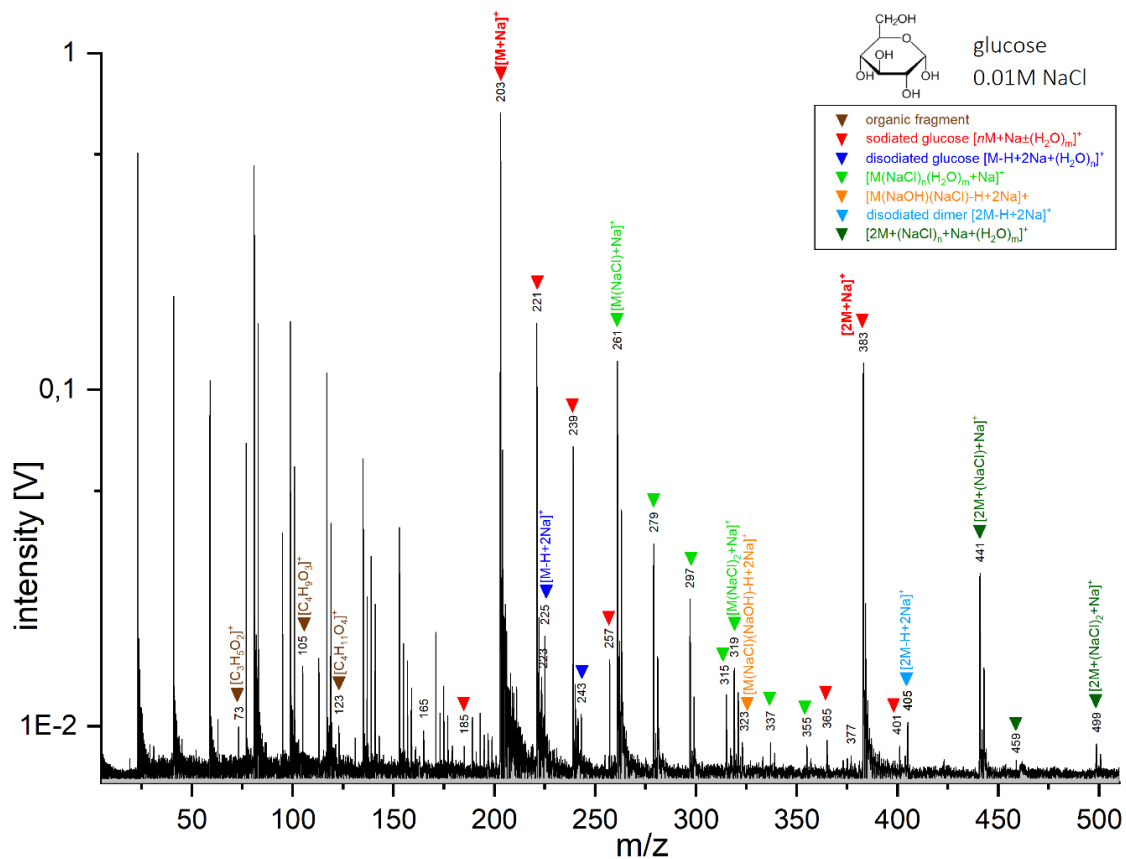
Figure S23. Baseline corrected cation mass spectrum of glucose at a concentration of 5wt% in a H_2O and NaCl (0.01M) matrix, recorded at a delay time of 6.2µs.
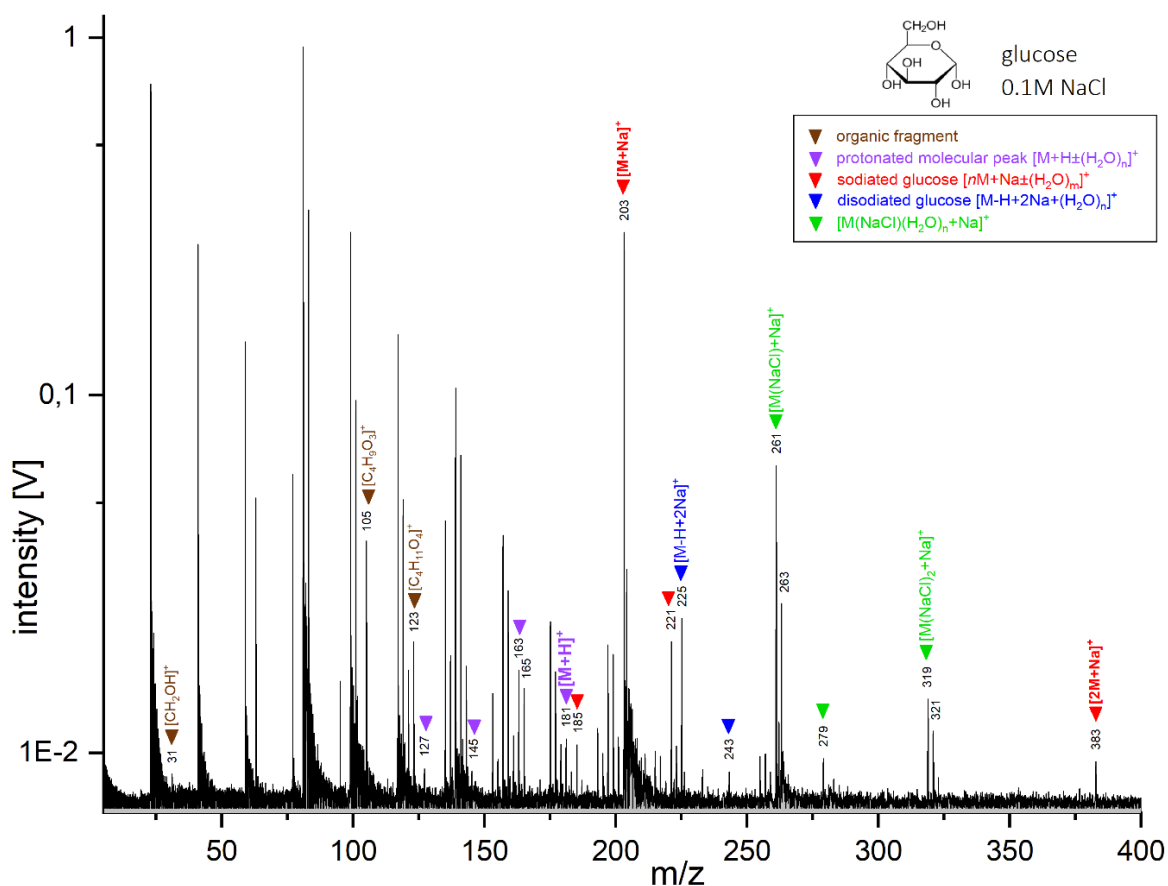
Figure S24. Baseline corrected cation mass spectrum of glucose at a concentration of 5wt% in a H_2O and NaCl (0.1M) matrix, recorded at a delay time of 5.7µs.
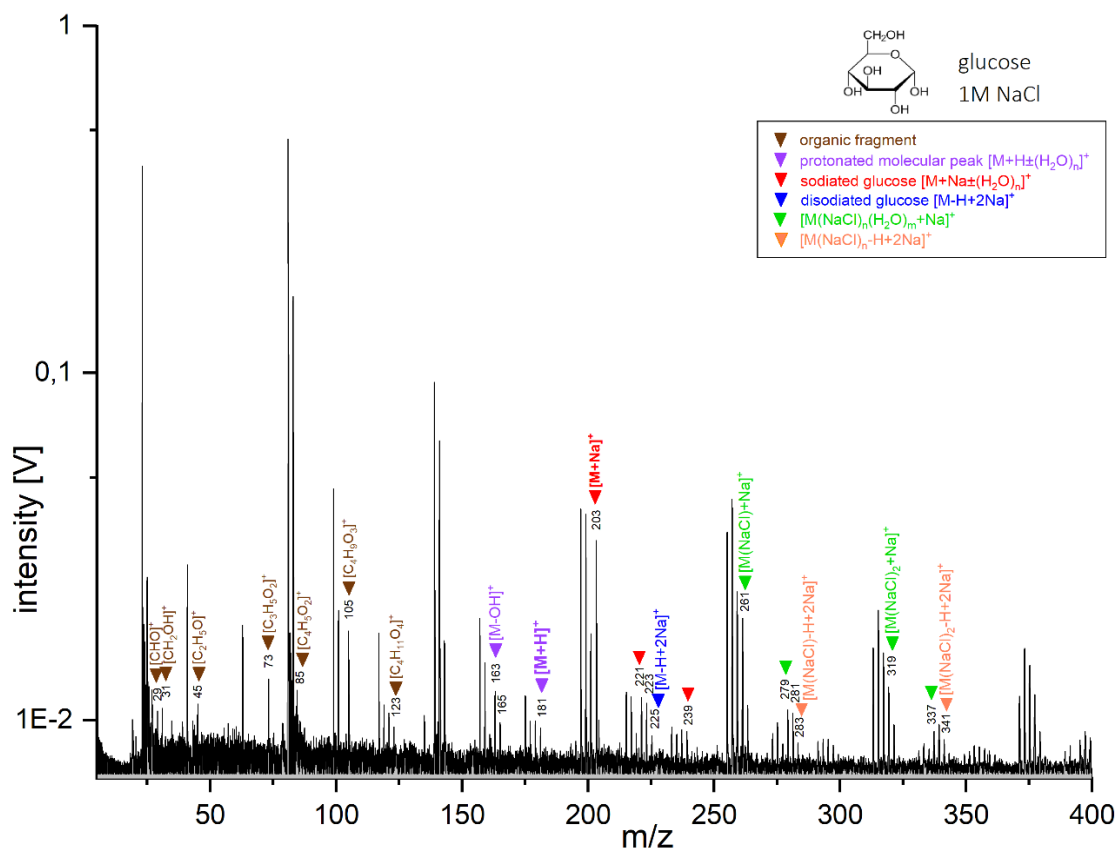
Figure S25. Baseline corrected cation mass spectrum of glucose at a concentration of 5wt% in a H_2O and NaCl (1M) matrix, recorded at a delay time of 6.2µs. The peak at m/z 181u (0.0095 V) is assigned to both the salt cluster $[Na(NaOH)(NaCl)_2]^+$ (0.0064 V) and protonated glucose $[M+H]^+$ (0.0031 V).
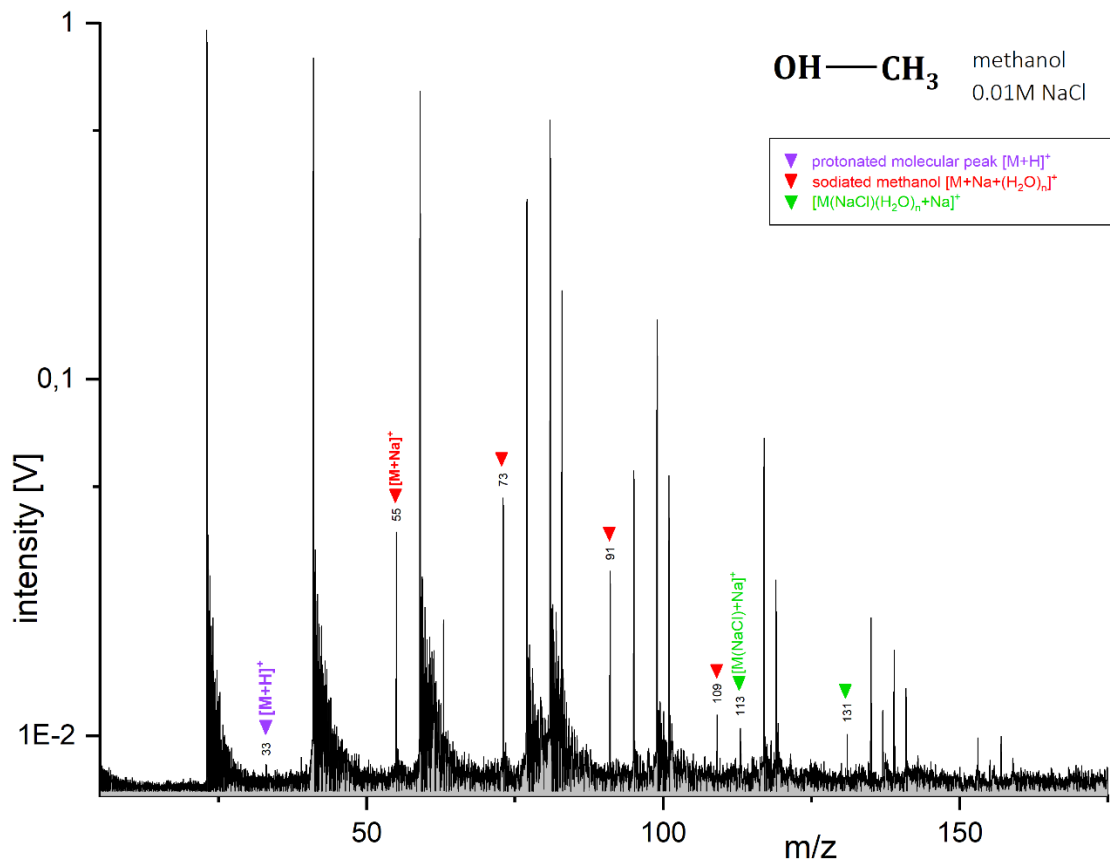
Figure S26. Baseline corrected cation mass spectrum of methanol at a concentration of 5wt% in a H_2O and NaCl (0.01M) matrix, recorded at a delay time of 5.5µs.
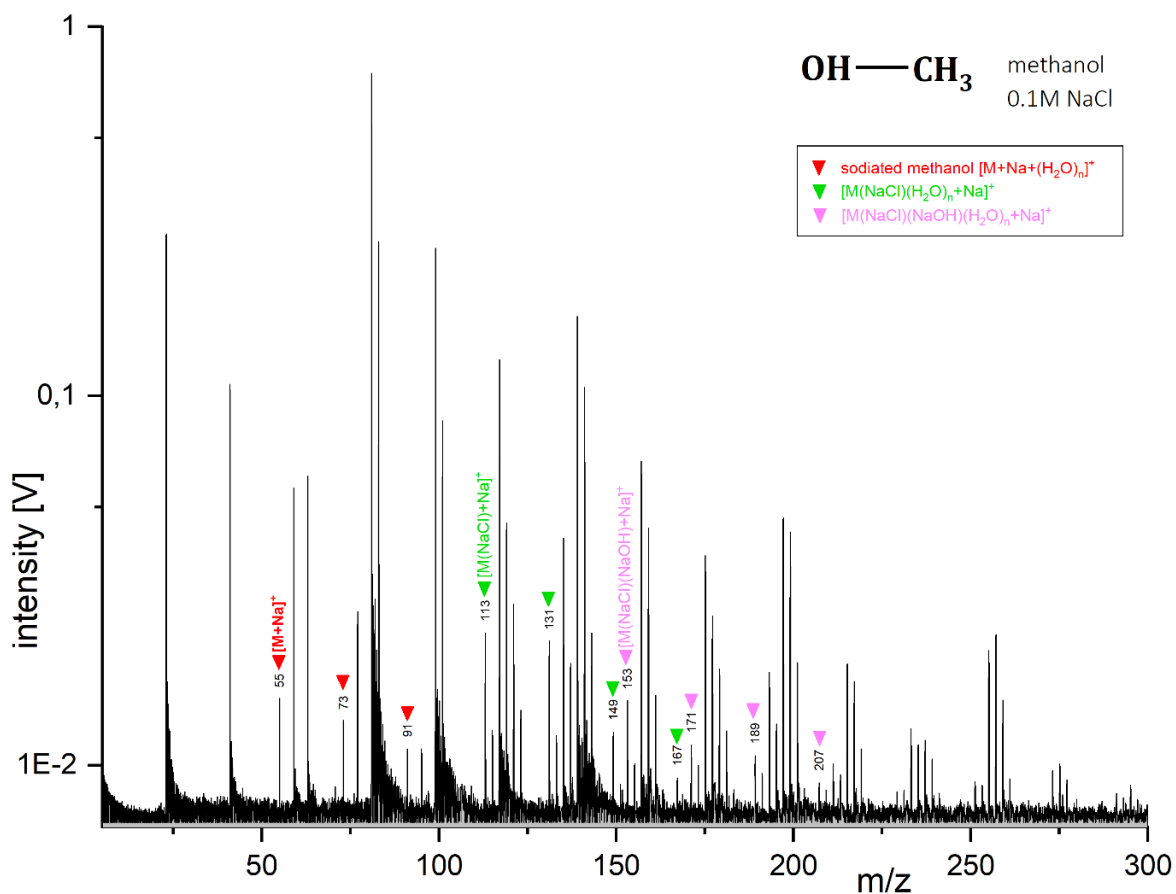
Figure S27. Baseline corrected cation mass spectrum of methanol at a concentration of 5wt% in a H_2O and NaCl (0.1M) matrix, recorded at a delay time of 5.9μs.
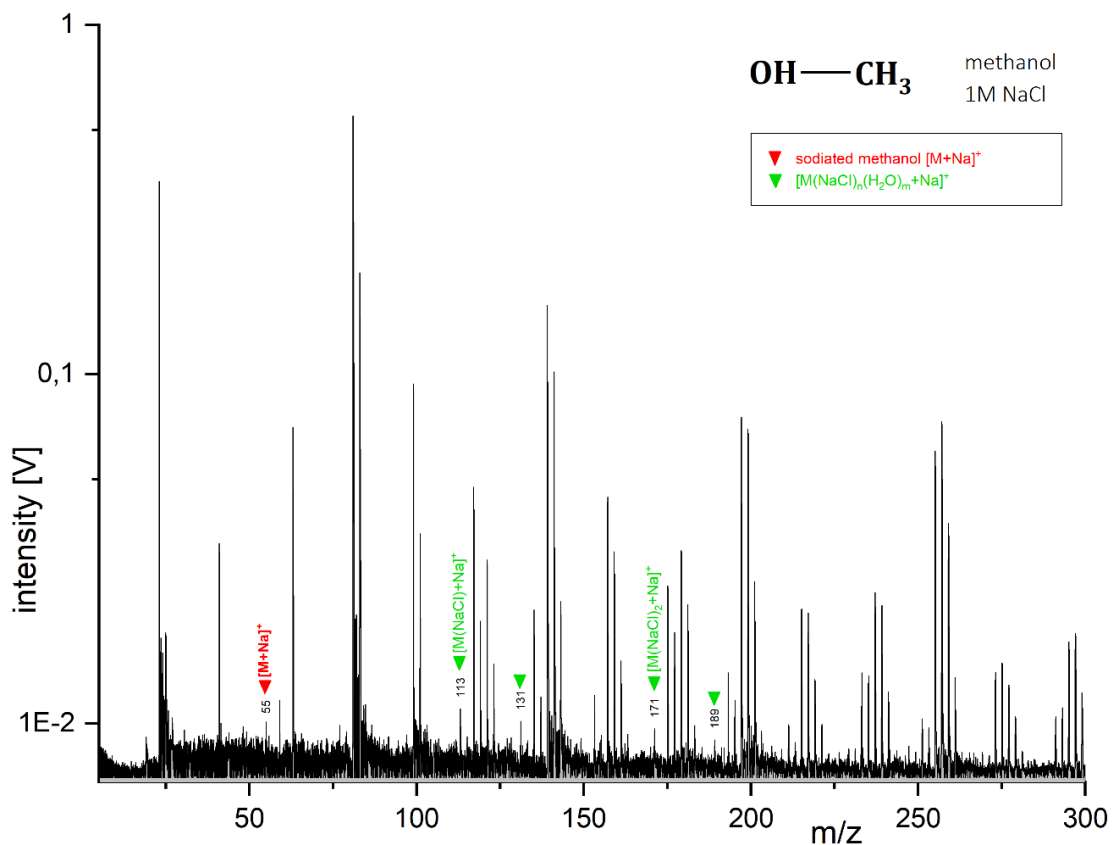
Figure S28. Baseline corrected cation mass spectrum of methanol at a concentration of 5wt% in a H_2O and NaCl (1M) matrix, recorded at a delay time of 6.2μs.
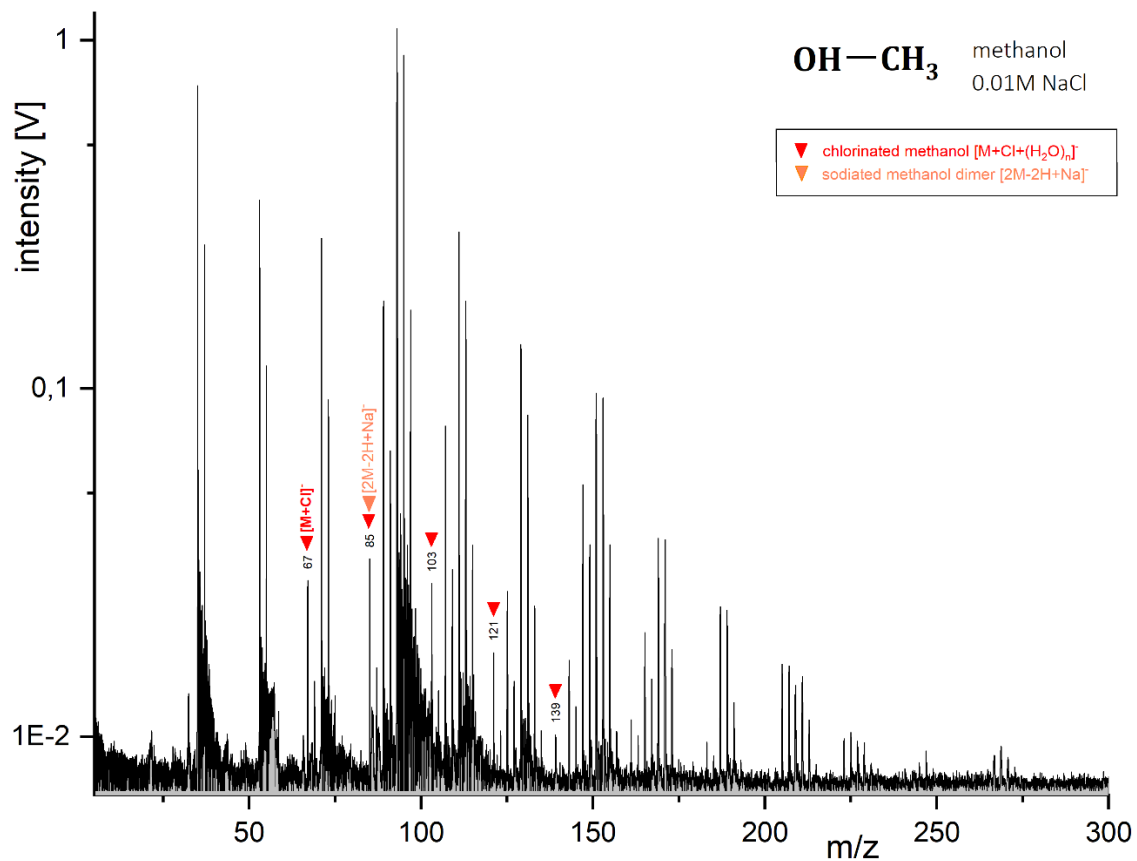
Figure S29. Baseline corrected anion mass spectrum of methanol at a concentration of 5wt% in a H_2O and NaCl (0.01M) matrix, recorded at a delay time of 6.1µs.
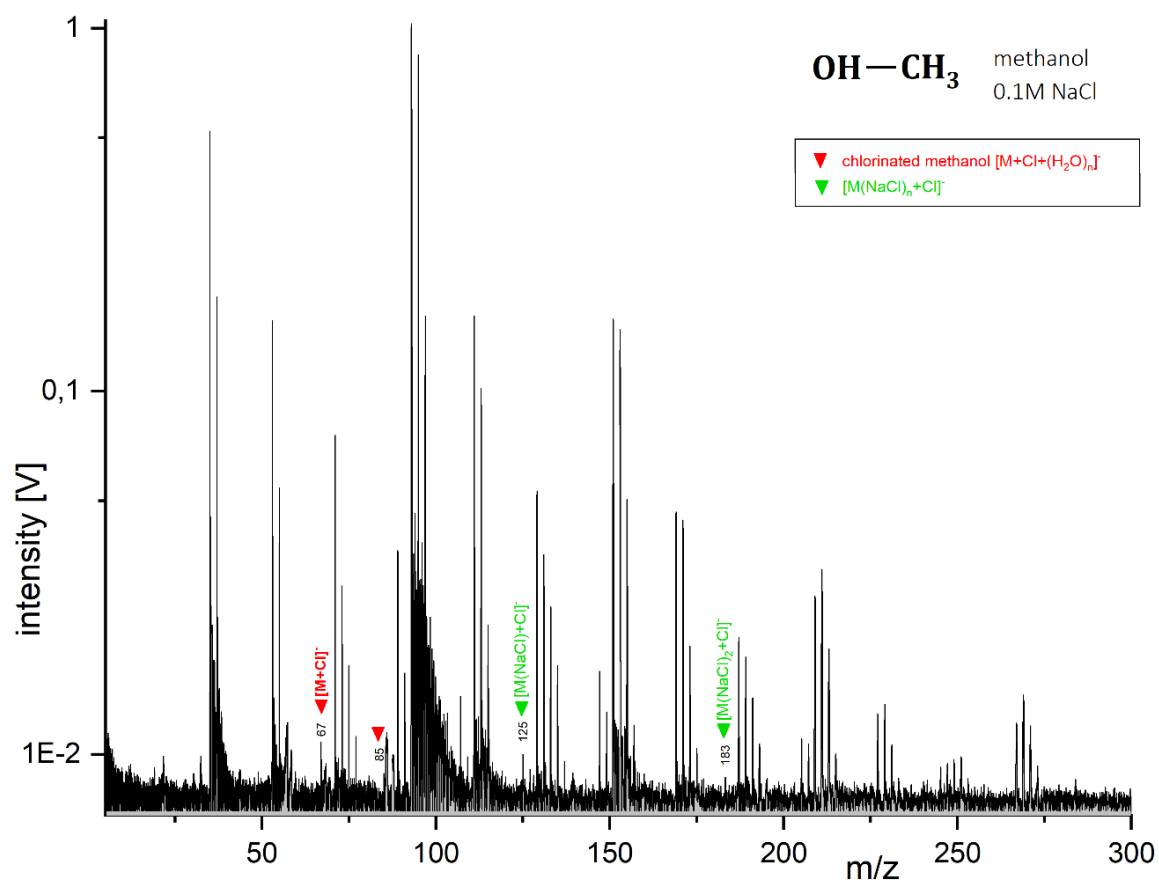
Figure S30. Baseline corrected anion mass spectrum of methanol at a concentration of 5wt% in a H_2O and NaCl (0.1M) matrix, recorded at a delay time of 6.0µs.
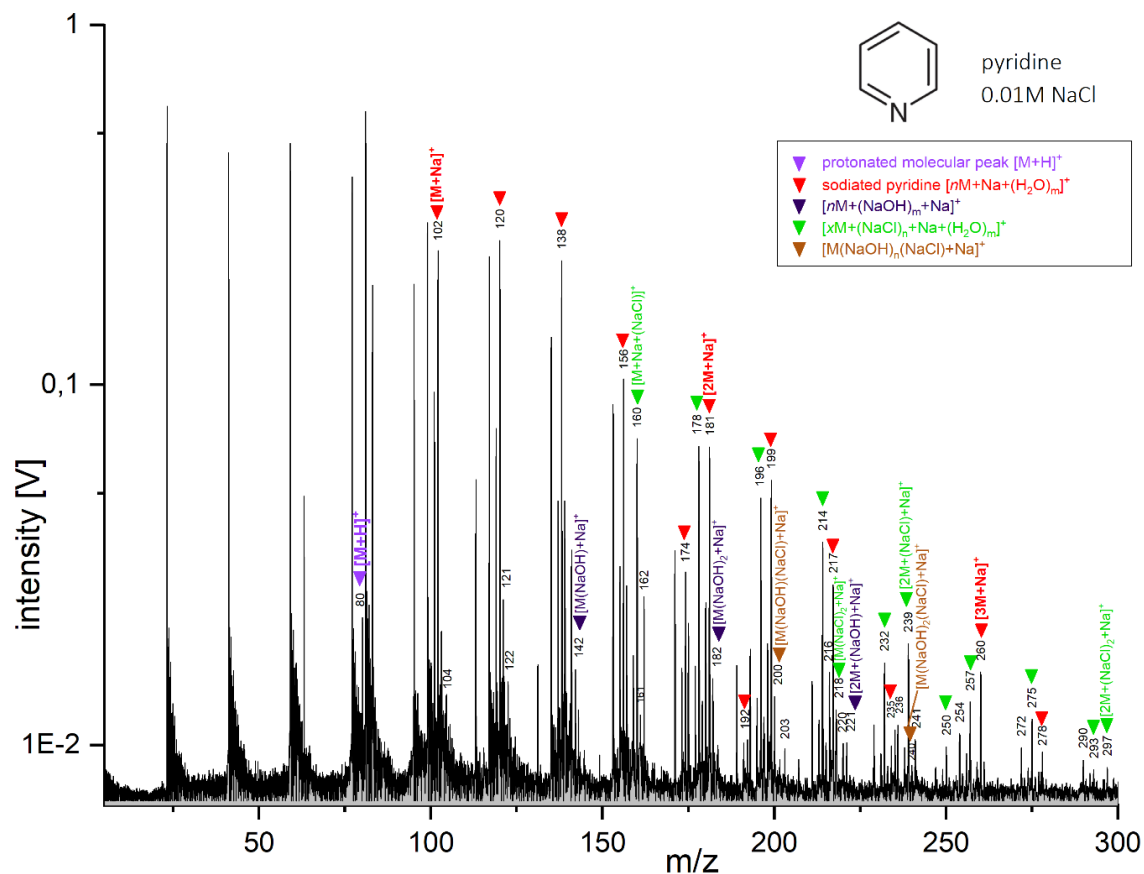
Figure S31. Baseline corrected cation mass spectrum of pyridine at a concentration of 5wt% in a H_2O and NaCl (0.01M) matrix, recorded at a delay time of 6.2μs.
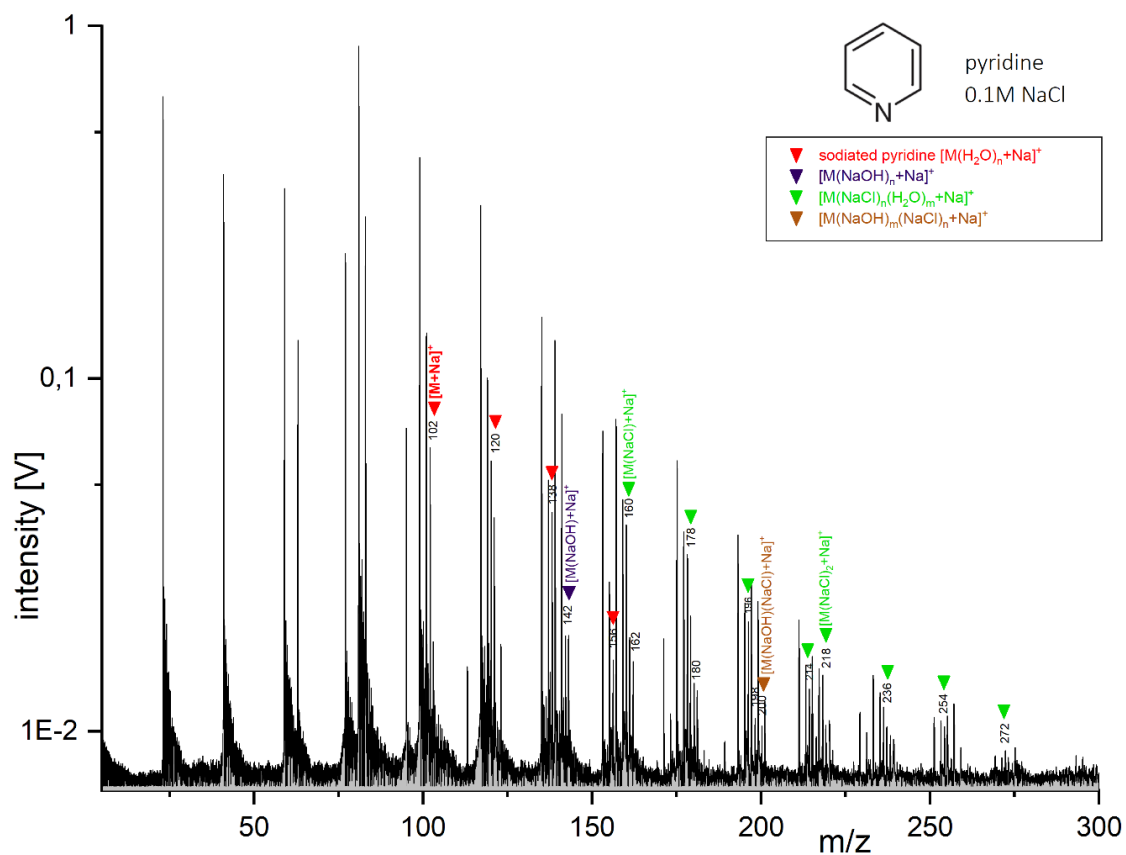
Figure S32. Baseline corrected cation mass spectrum of pyridine at a concentration of 5wt% in a H_2O and NaCl (0.1M) matrix, recorded at a delay time of 6.0μs.
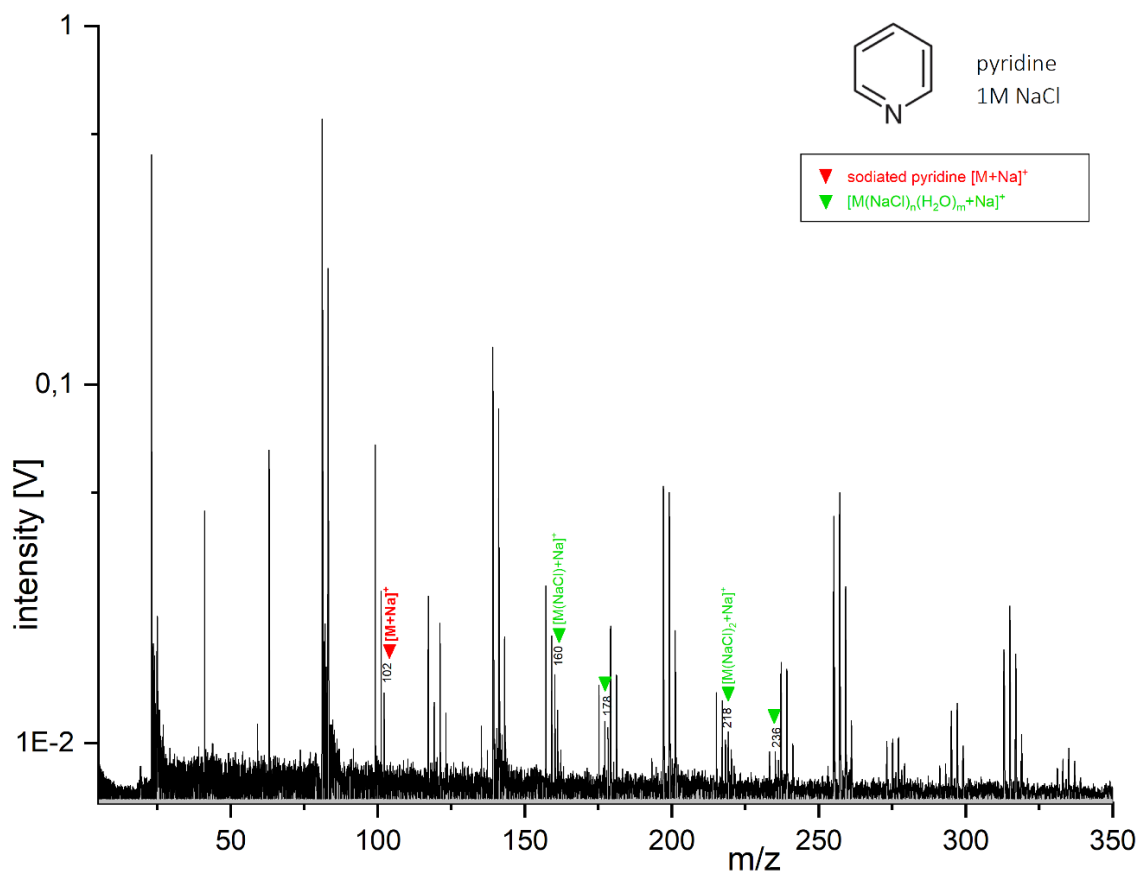
Figure S33. Baseline corrected cation mass spectrum of pyridine at a concentration of 5wt% in a H_2O and NaCl (1M) matrix, recorded at a delay time of 6.2μs.
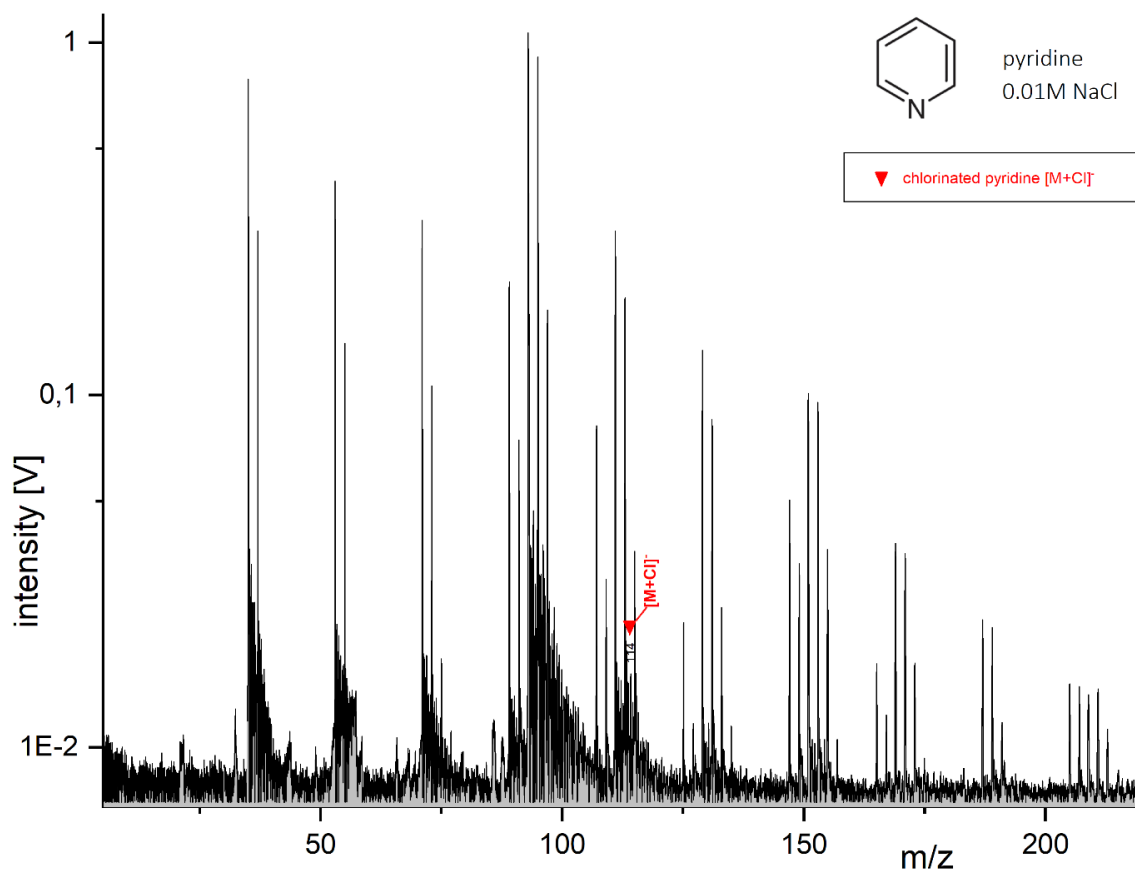
Figure S34. Baseline corrected anion mass spectrum of pyridine at a concentration of 5wt% in a H_2O and NaCl (0.01M) matrix, recorded at a delay time of 6.1μs.
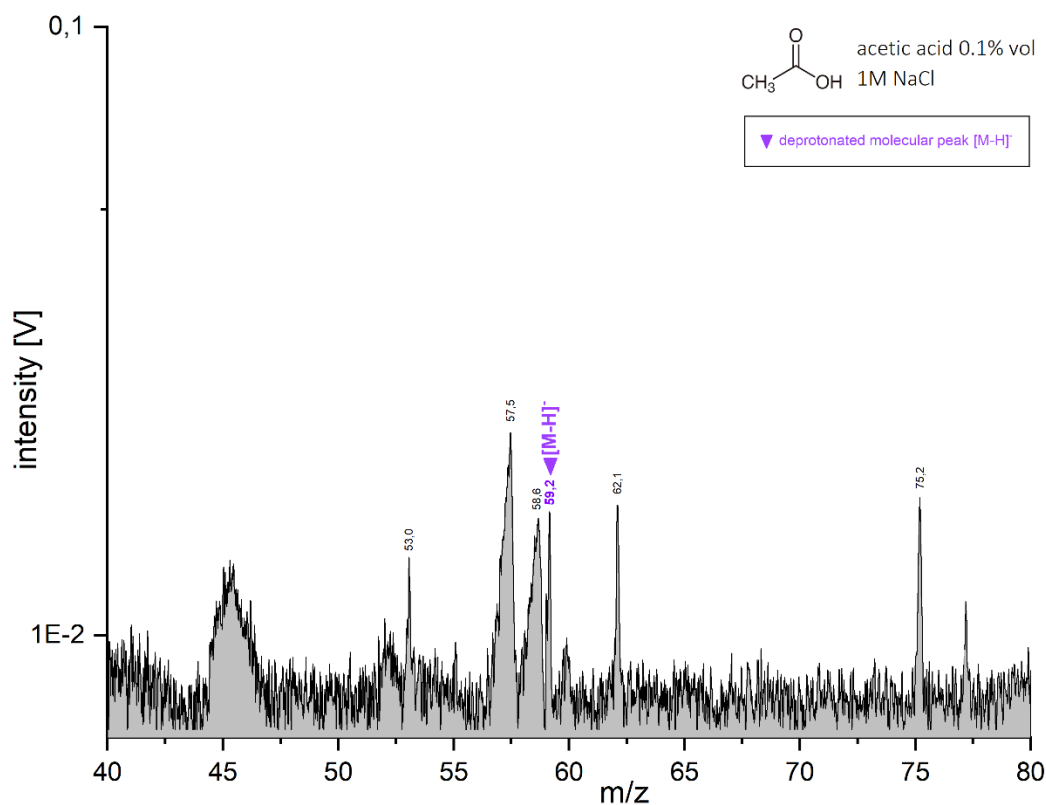
Figure S35. Section of a baseline corrected anion mass spectrum of acetic acid at a concentration of 0.1wt% in a H_2O and NaCl (1M) matrix, recorded at a delay time of 7.5µs. Peaks labelled in black originate exclusively from the salty matrix.
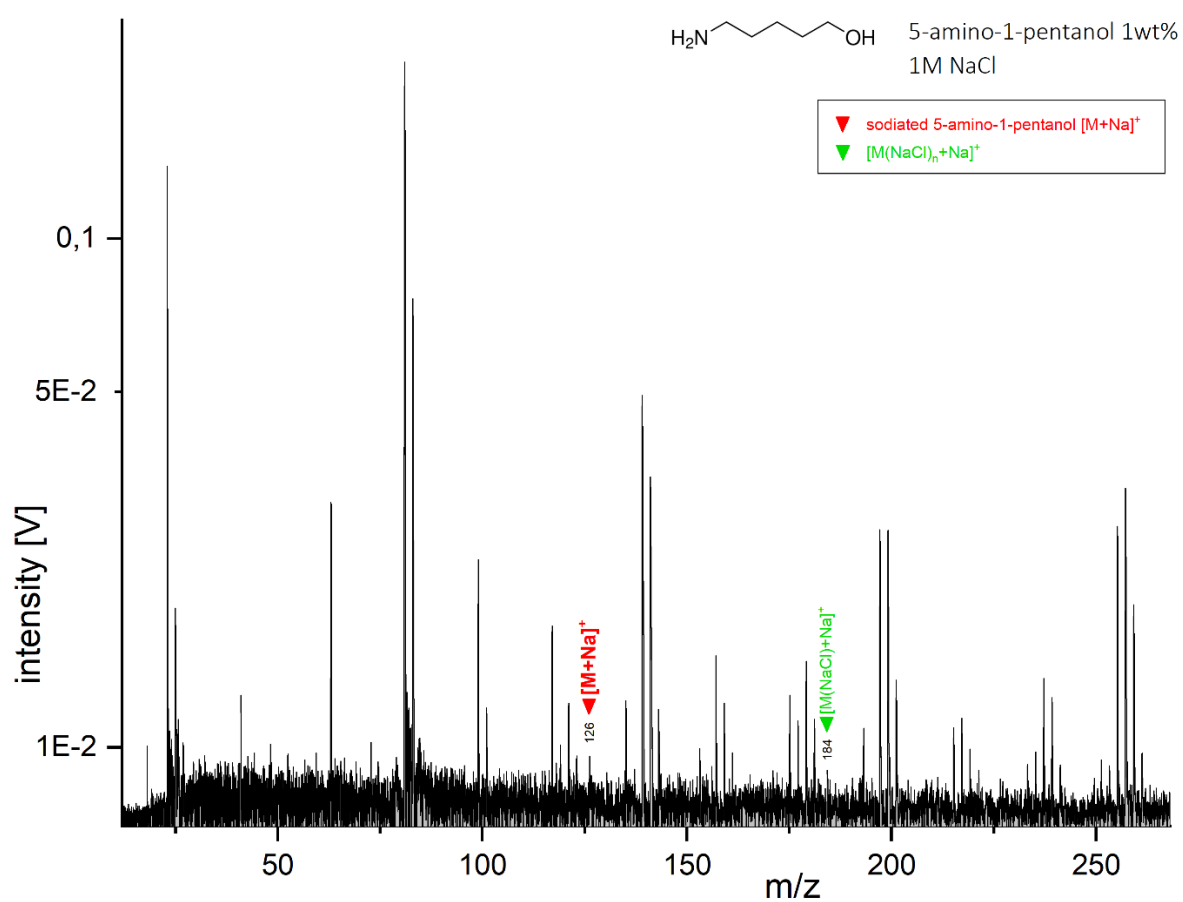
Figure S36. Baseline corrected cation mass spectrum of 5-amino-1-pentanol at a concentration of 1wt% in a H_2O and NaCl (1M) matrix, recorded at a delay time of 6.5µs.
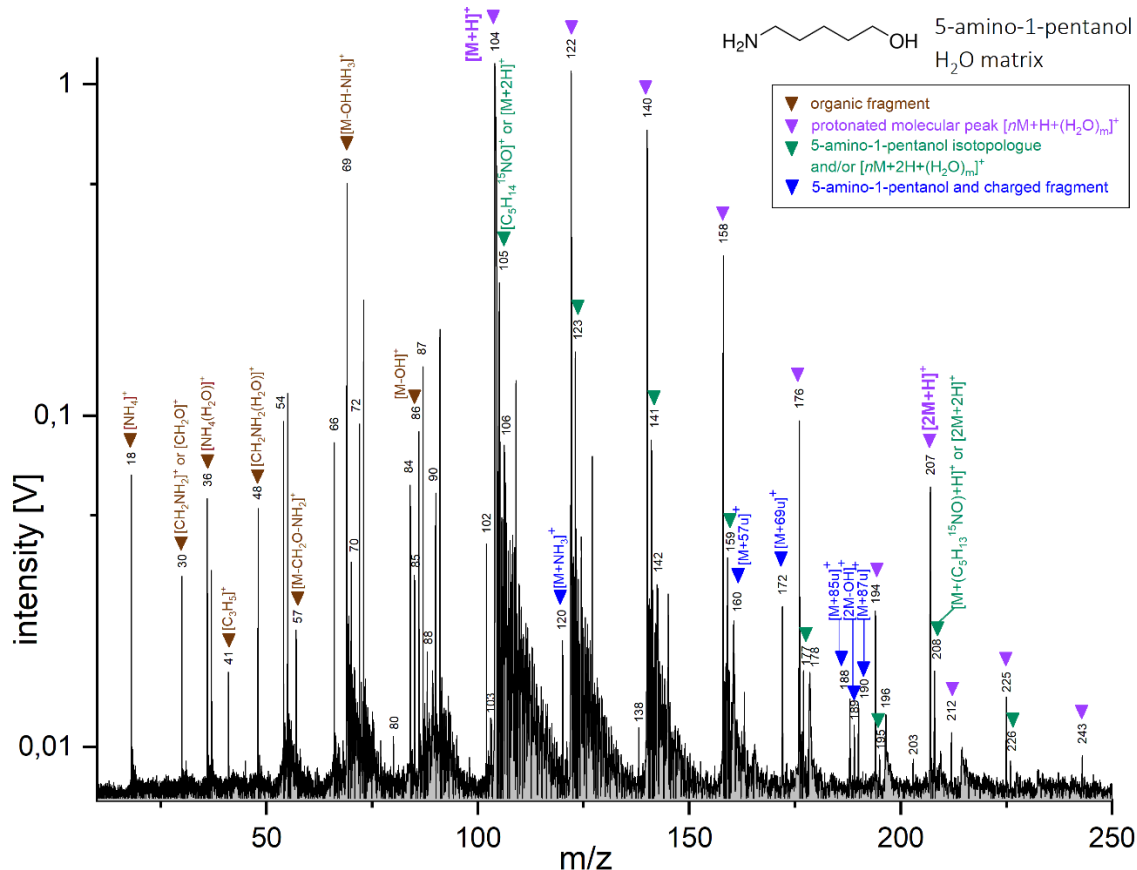
Figure S37. Baseline corrected cation mass spectrum of 5-amino-1-pentanol at a concentration of 5wt% in a pure H₂O matrix, recorded at a delay time of 6.3µs. Unlabeled peaks originate exclusively from the water matrix.
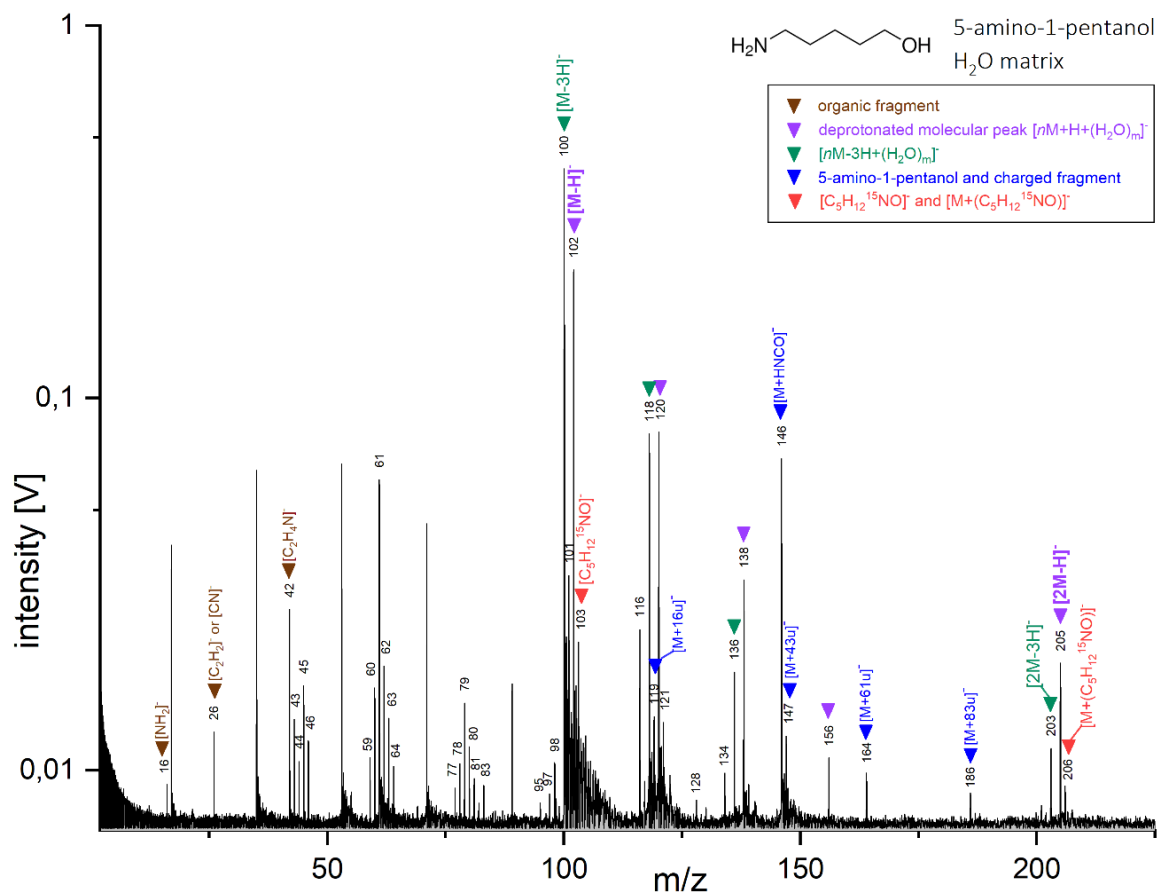
Figure S38. Baseline corrected anion mass spectrum of 5-amino-1-pentanol at a concentration of 5wt% in a pure H₂O matrix, recorded at a delay time of 5.7µs. Unlabeled peaks originate exclusively from the water matrix.
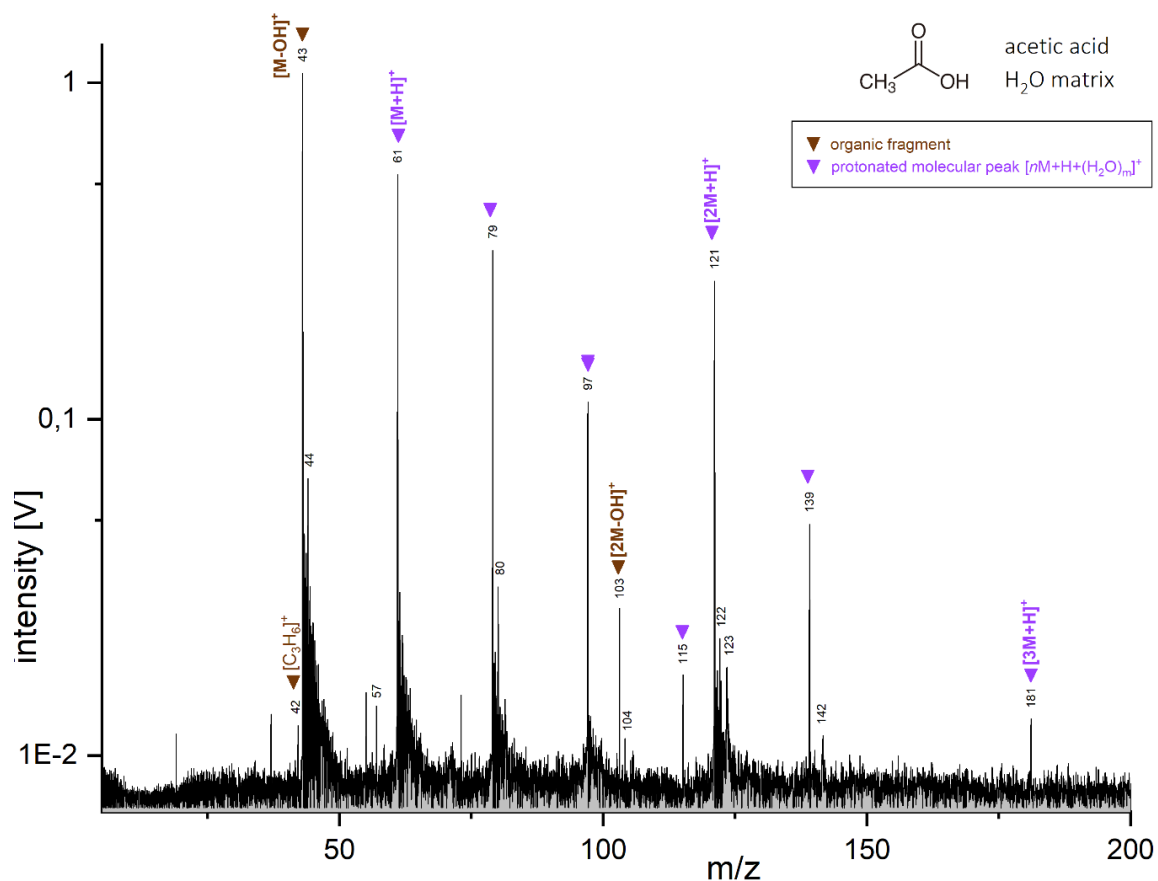
Figure S39. Baseline corrected cation mass spectrum of acetic acid at a concentration of 5wt% in a pure H_2O matrix, recorded at a delay time of 5.7µs. Unlabeled peaks originate exclusively from the water matrix.
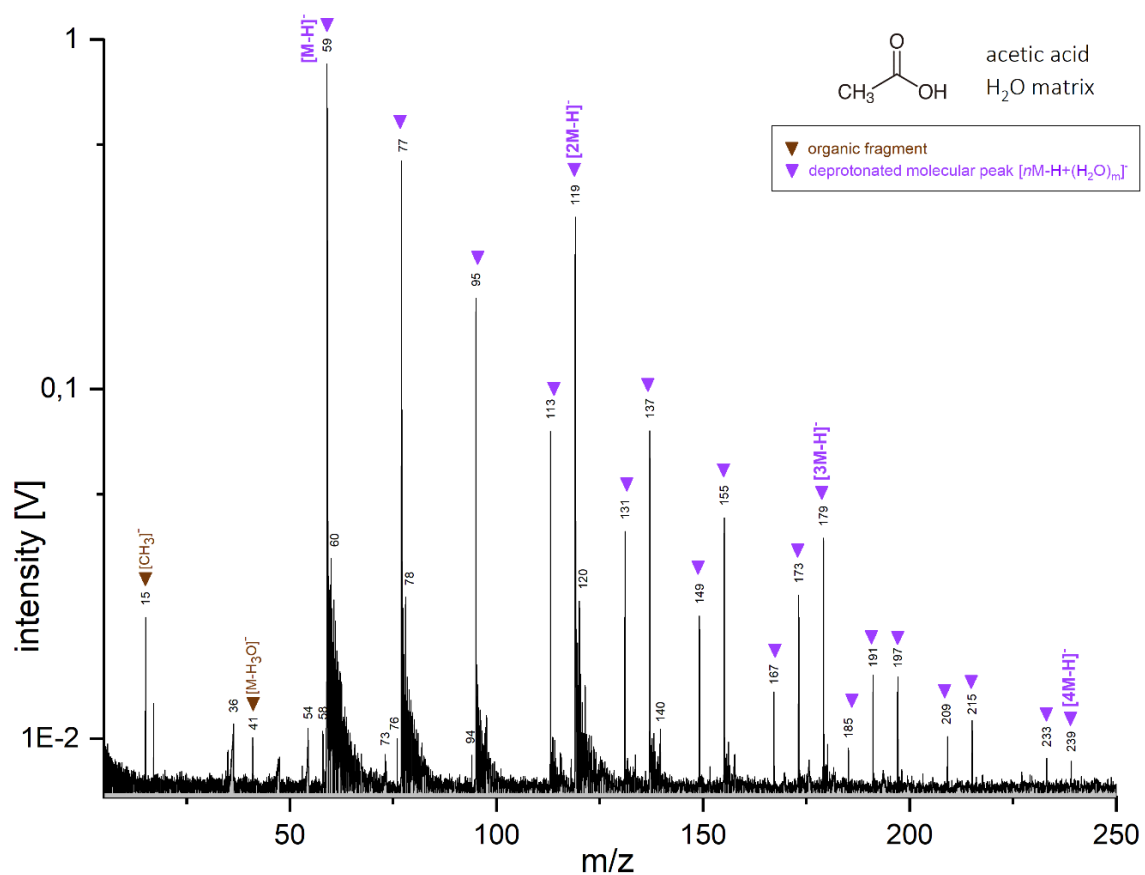
Figure S40. Baseline corrected anion mass spectrum of acetic acid at a concentration of 5wt% in a pure H_2O matrix, recorded at a delay time of 6.3µs. Unlabeled peaks originate exclusively from the water matrix.
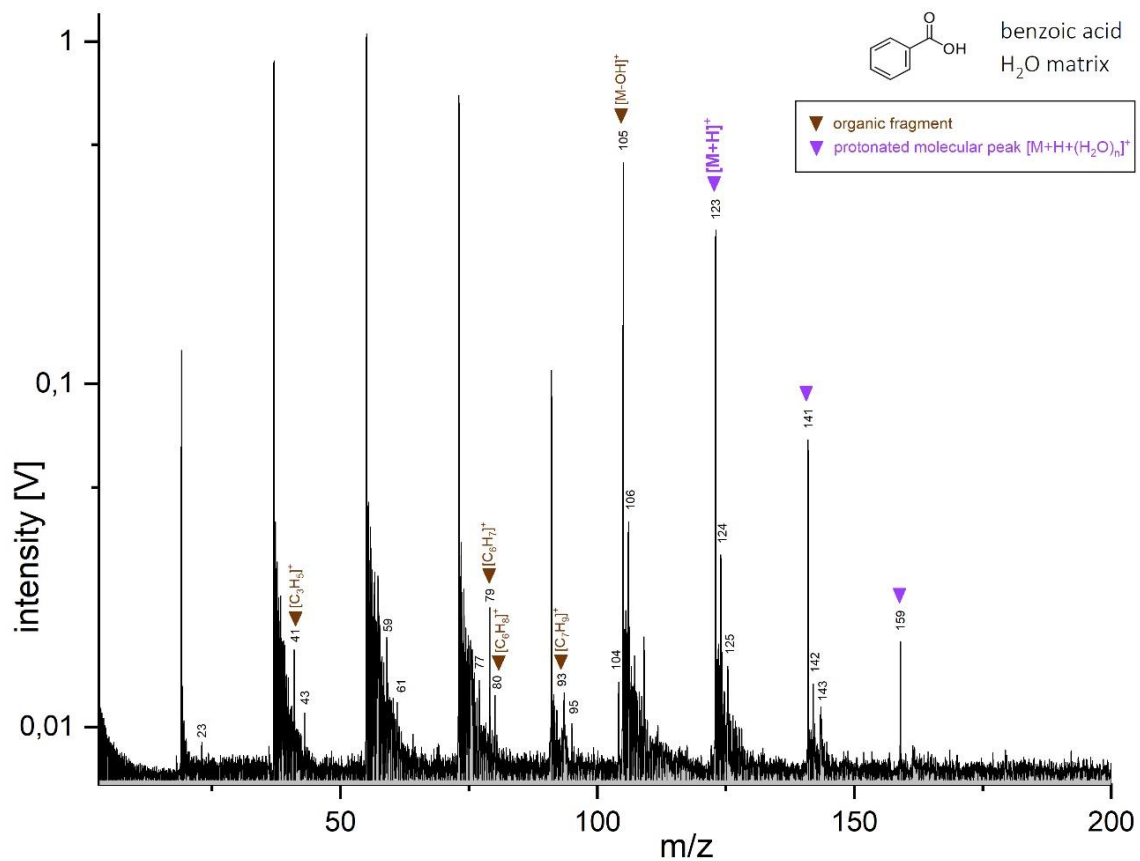
Figure S41. Baseline corrected cation mass spectrum of benzoic acid at a concentration of 0.17wt% in a pure H_2O matrix, recorded at a delay time of 5.7μs. Unlabeled peaks originate exclusively from the water matrix.
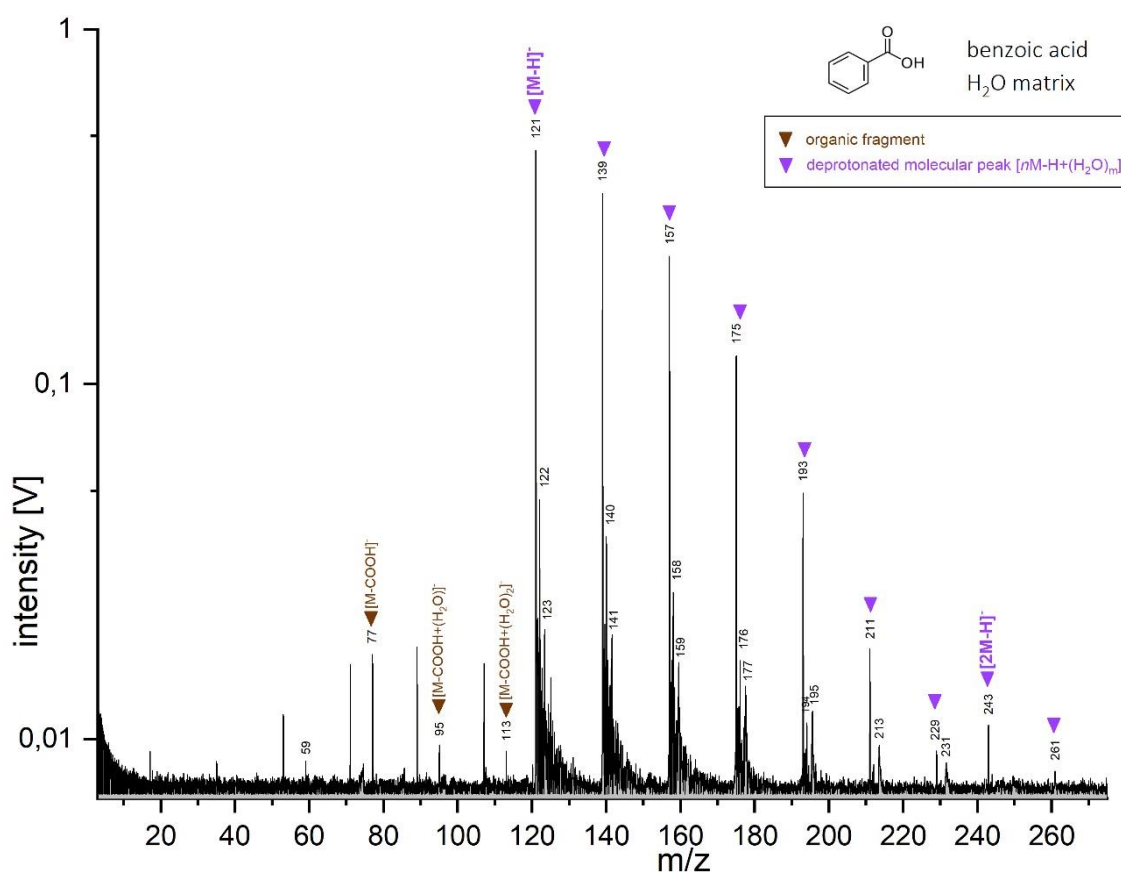
Figure S42. Baseline corrected anion mass spectrum of benzoic acid at a concentration of 0.17wt% in a pure H_2O matrix, recorded at a delay time of 6.3μs. Unlabeled peaks originate exclusively from the water matrix.
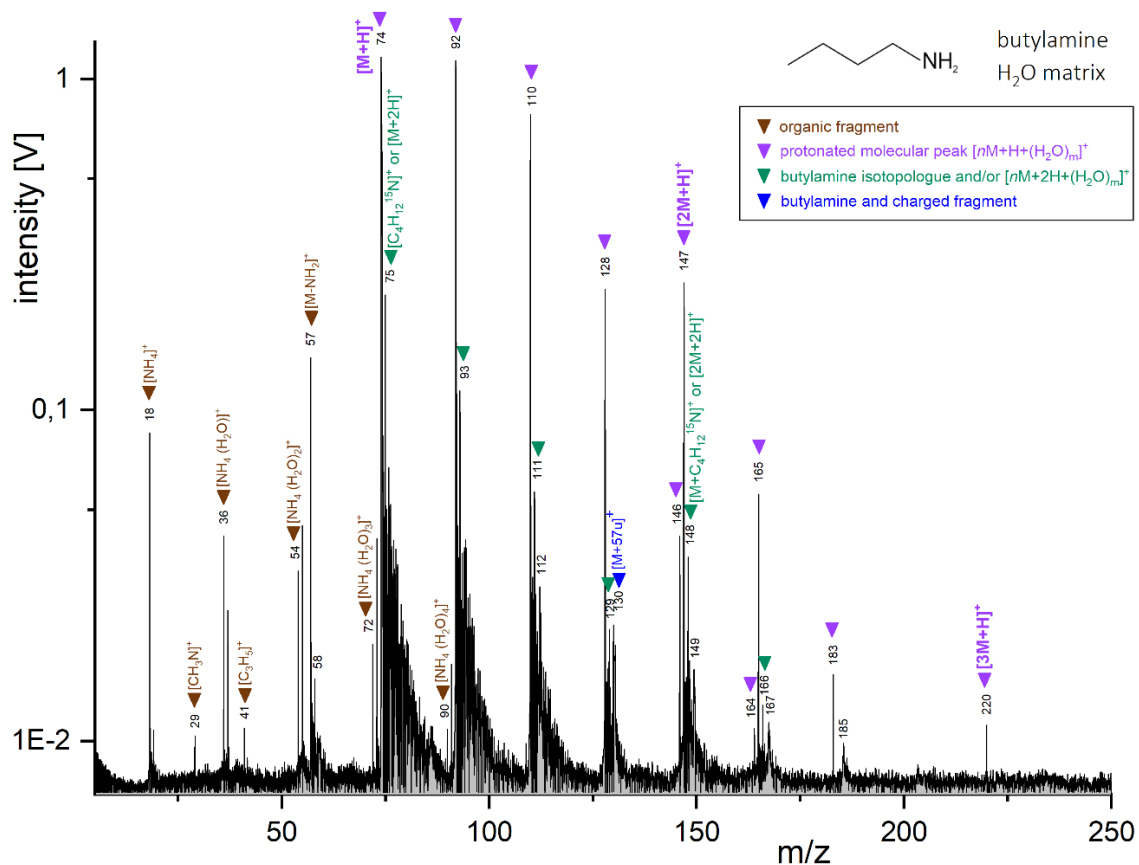
Figure S43. Baseline corrected cation mass spectrum of butylamine at a concentration of 5wt% in a pure H_2O matrix, recorded at a delay time of 6.0µs.
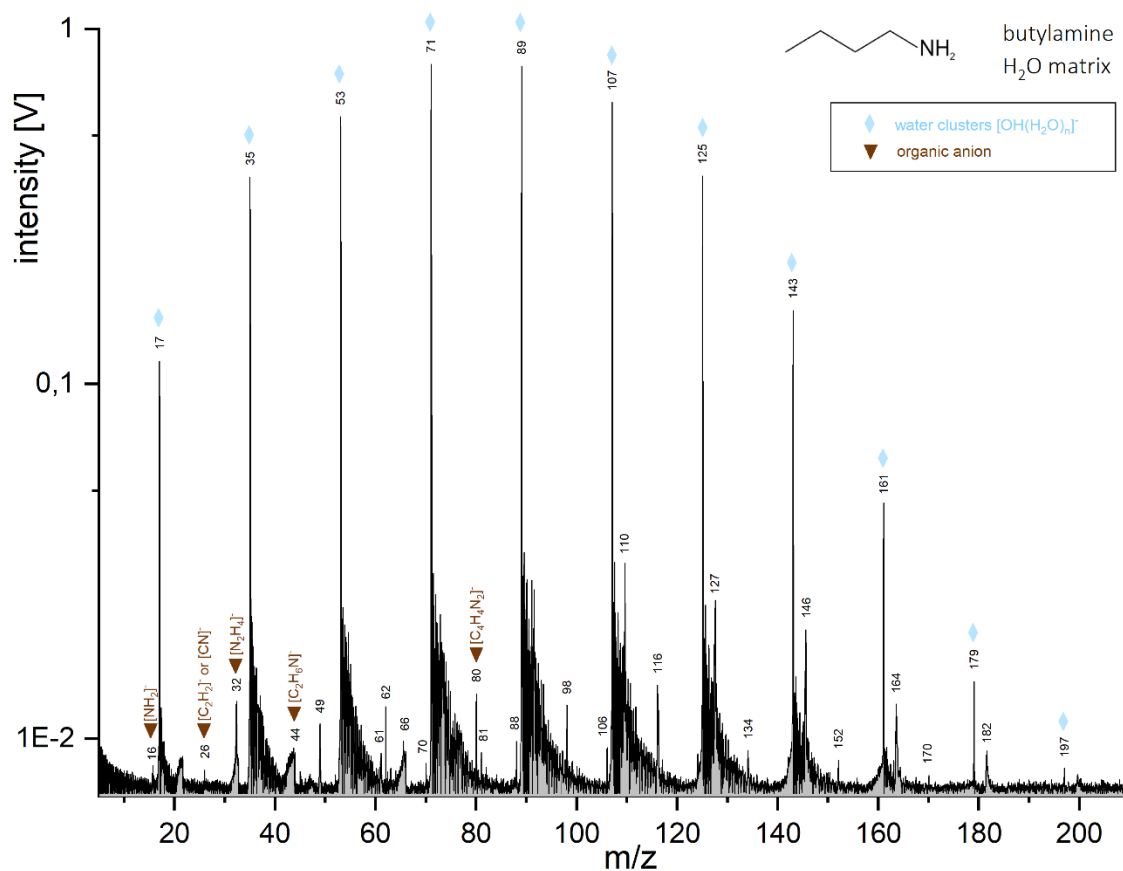
Figure S44. Baseline corrected anion mass spectrum of butylamine at a concentration of 5wt% in a pure H_2O matrix, recorded at a delay time of 6.5µs.

Figure S45. Baseline corrected cation mass spectrum of glucose at a concentration of 5wt% in a H_2O matrix with amberlite®, recorded at a delay time of 5.7µs. Unlabeled peaks originate exclusively from the water matrix.

Figure S46. Baseline corrected anion mass spectrum of glucose at a concentration of 5wt% in a pure H_2O matrix, recorded at a delay time of 6.3µs. Unlabeled peaks originate exclusively from the water matrix.
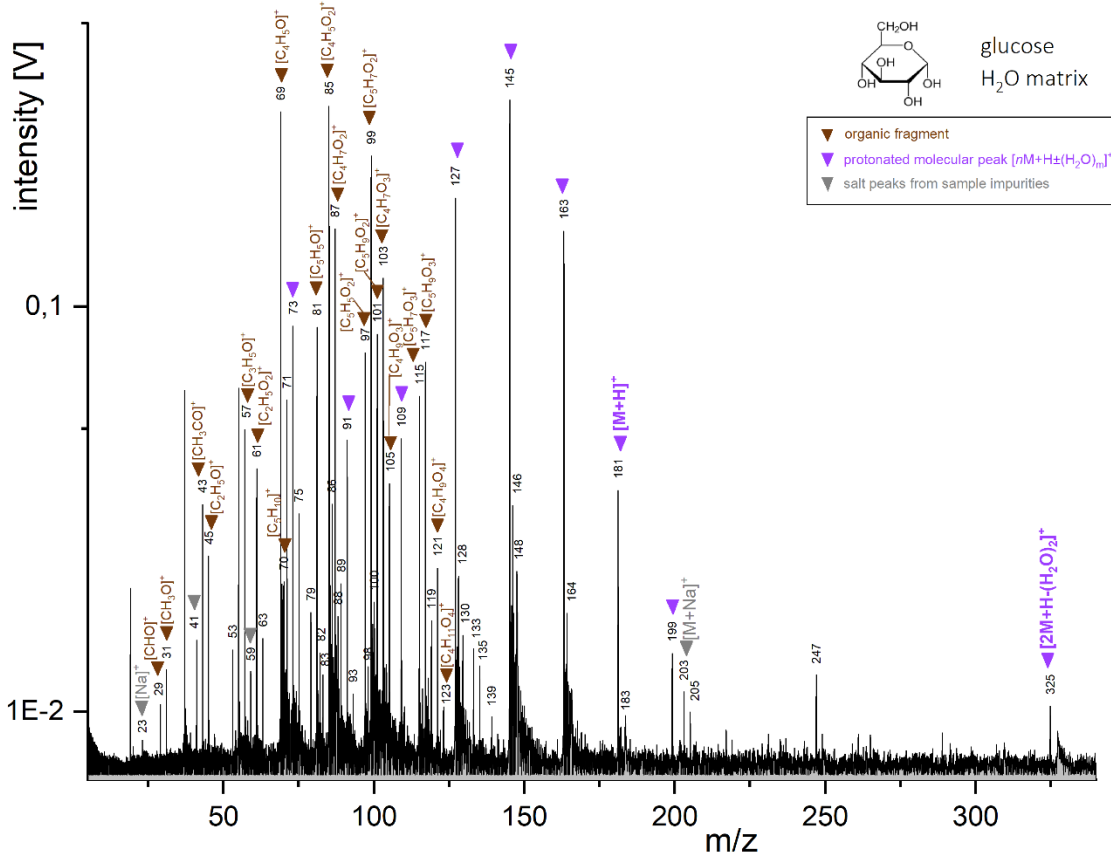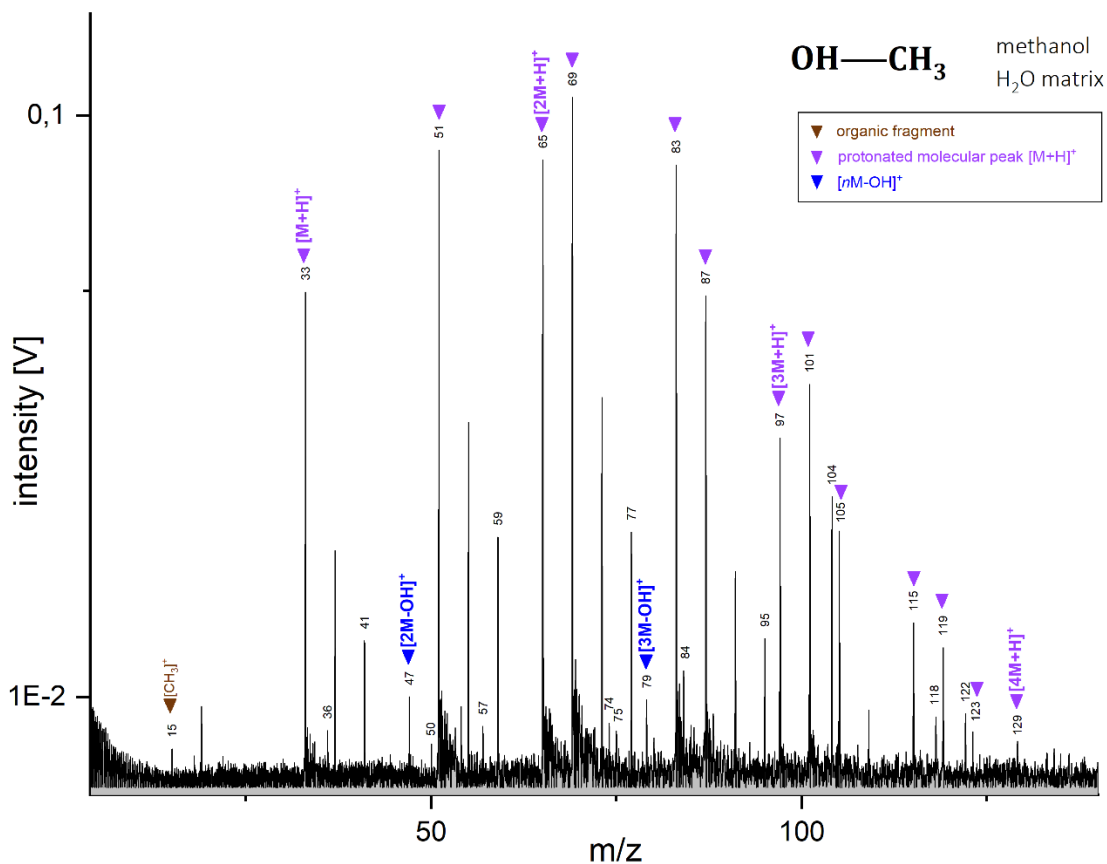
Figure S47. Baseline corrected cation mass spectrum of methanol at a concentration of 5wt% in a pure H_2O matrix, recorded at a delay time of 5.7μs. Unlabeled peaks originate exclusively from the water matrix.
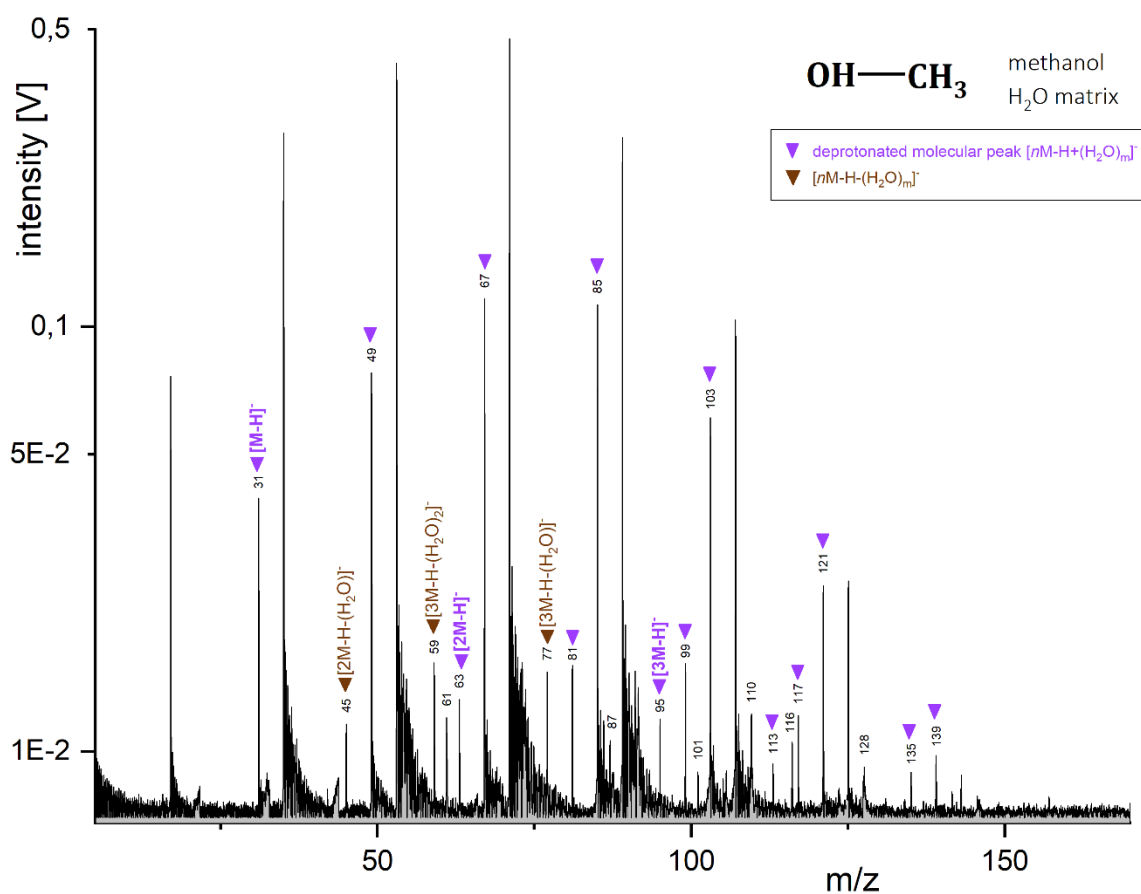
Figure S48. Baseline corrected anion mass spectrum of methanol at a concentration of 5wt% in a pure H_2O matrix, recorded at a delay time of 6.0μs. Unlabeled peaks originate exclusively from the water matrix.
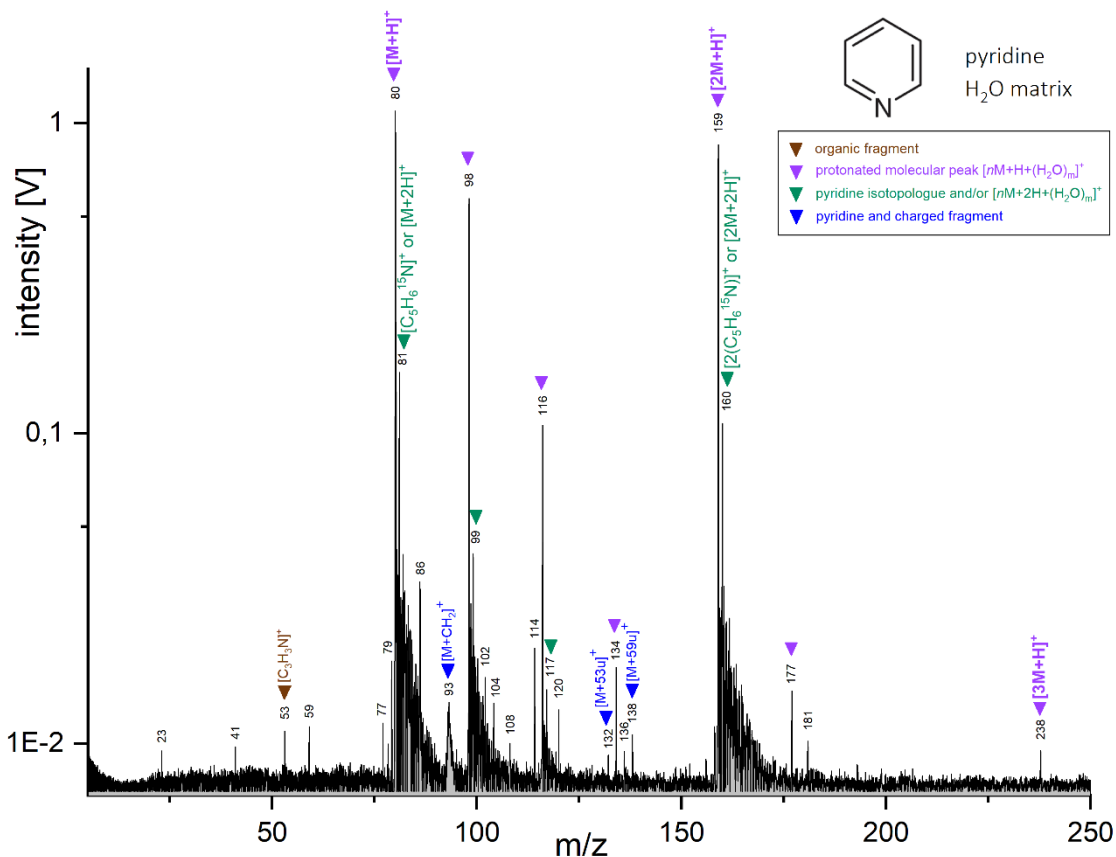
Figure S49. Baseline corrected cation mass spectrum of pyridine at a concentration of 5wt% in a pure H_2O matrix, recorded at a delay time of 6.3µs. Unlabeled peaks originate exclusively from the water matrix.
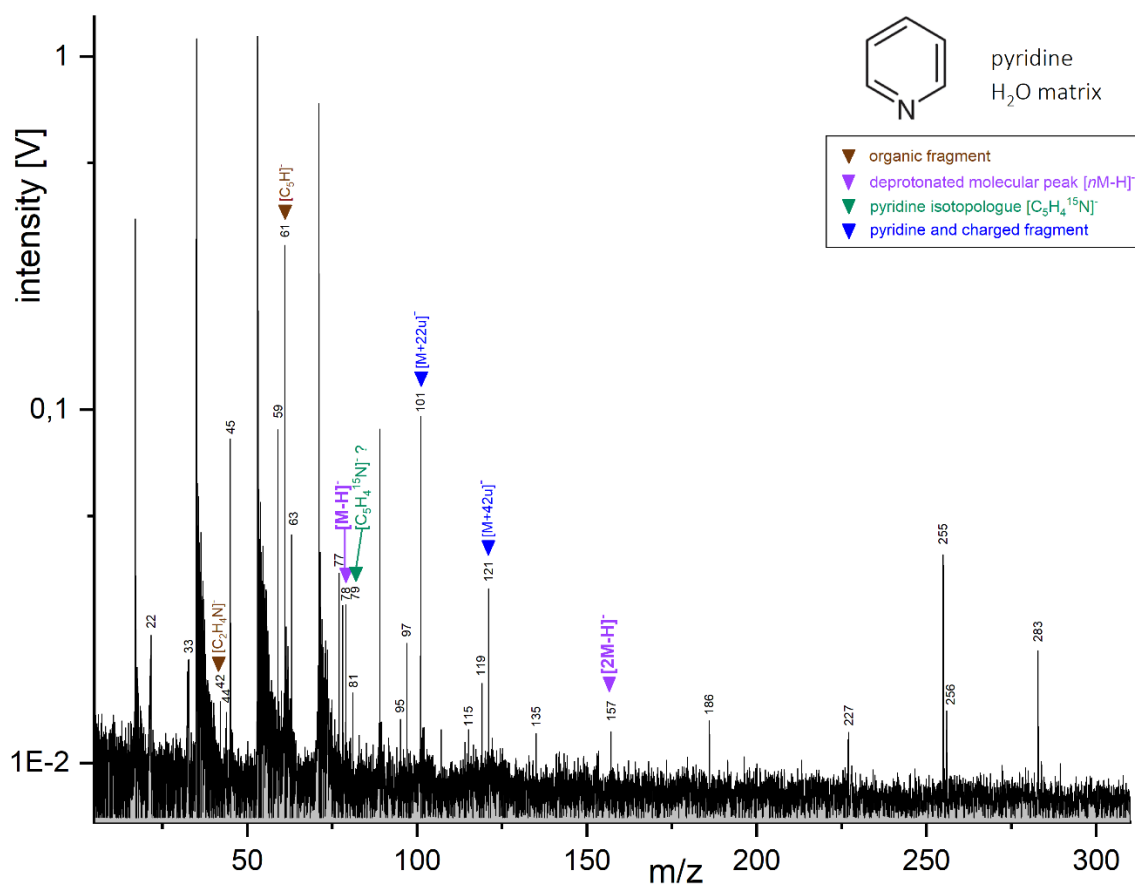
Figure S50. Baseline corrected anion mass spectrum of pyridine at a concentration of 5wt% in a pure H_2O matrix, recorded at a delay time of 6.3µs. Unlabeled peaks originate exclusively from the water matrix.
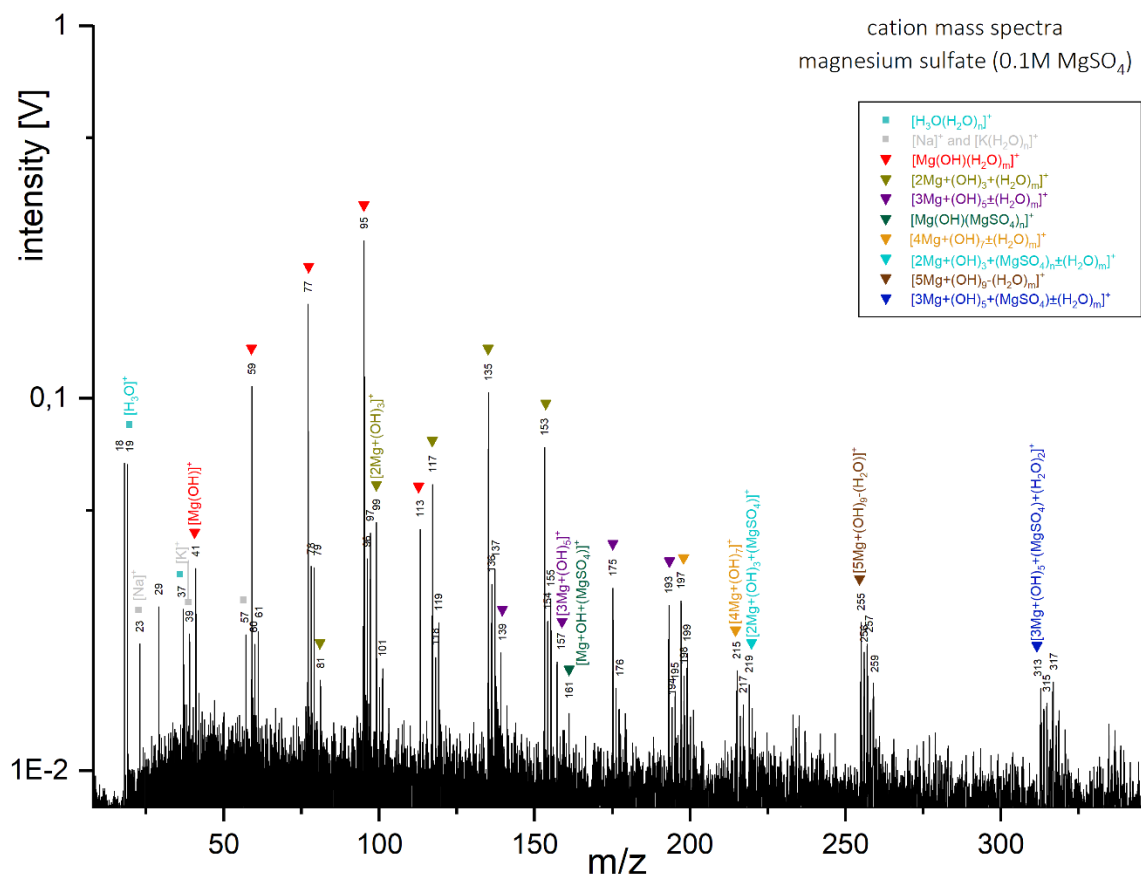
Figure S51. Baseline corrected cation mass spectrum of magnesium sulfate (MgSO₄) at a concentration of 0.1M, generated with a delay time of 5.0 μs.
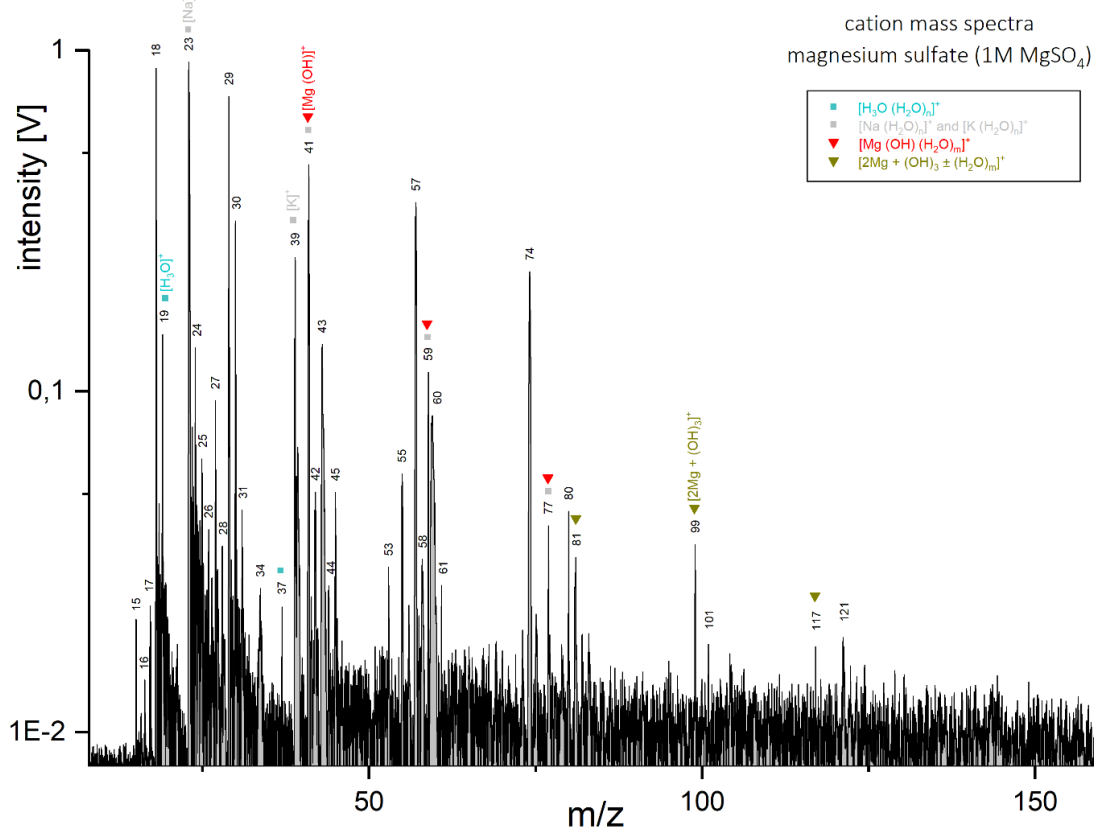
Figure S52. Baseline corrected cation mass spectrum of magnesium sulfate (MgSO₄) at a concentration of 1M, generated with a delay time of 6.0 μs.

Figure S53. Baseline corrected anion mass spectrum of magnesium sulfate (MgSO₄) at a concentration of 0.1M, generated with a delay time of 6.0 μs.

Figure S54. Baseline corrected cation mass spectrum of 5-amino-1-pentanol (concentration 5 wt%) in 0.01M magnesium sulfate (MgSO₄), generated with a delay time of 6.4 μs.
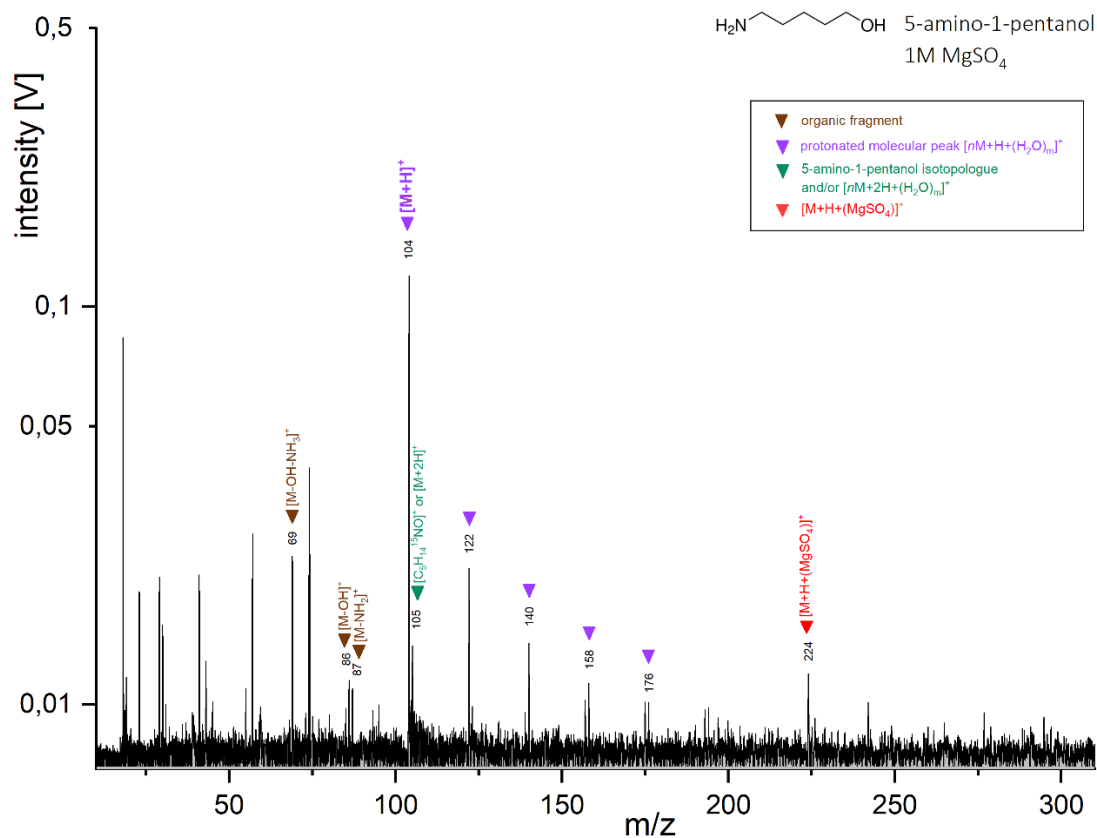
Figure S55. Baseline corrected cation mass spectrum of 5-amino-1-pentanol (concentration 0.1 wt%) in 1M magnesium sulfate ($MgSO_4$), generated with a delay time of 7.2 µs. Unlabeled peaks originate exclusively from the $MgSO_4$ matrix.
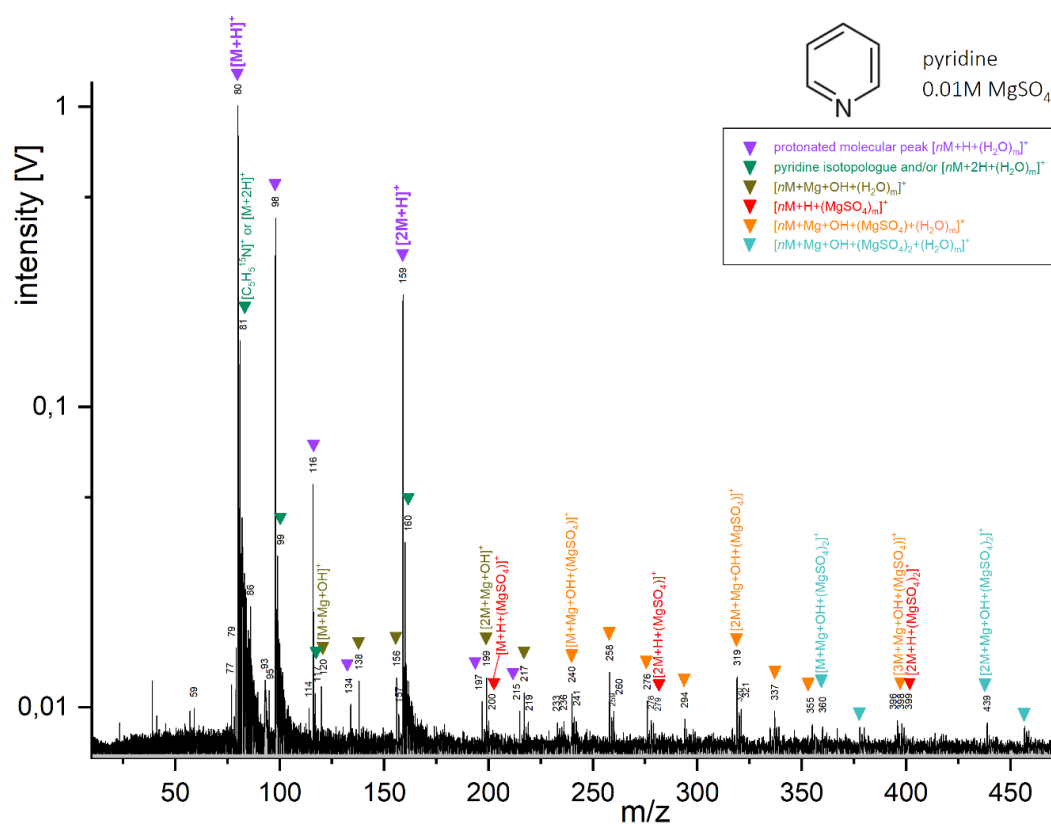
Figure S56. Baseline corrected cation mass spectrum of pyridine (concentration 5 wt%) in 0.01M magnesium sulfate ($MgSO_4$), generated with a delay time of 6.0 µs. Unlabeled peaks originate exclusively from the $MgSO_4$ matrix.
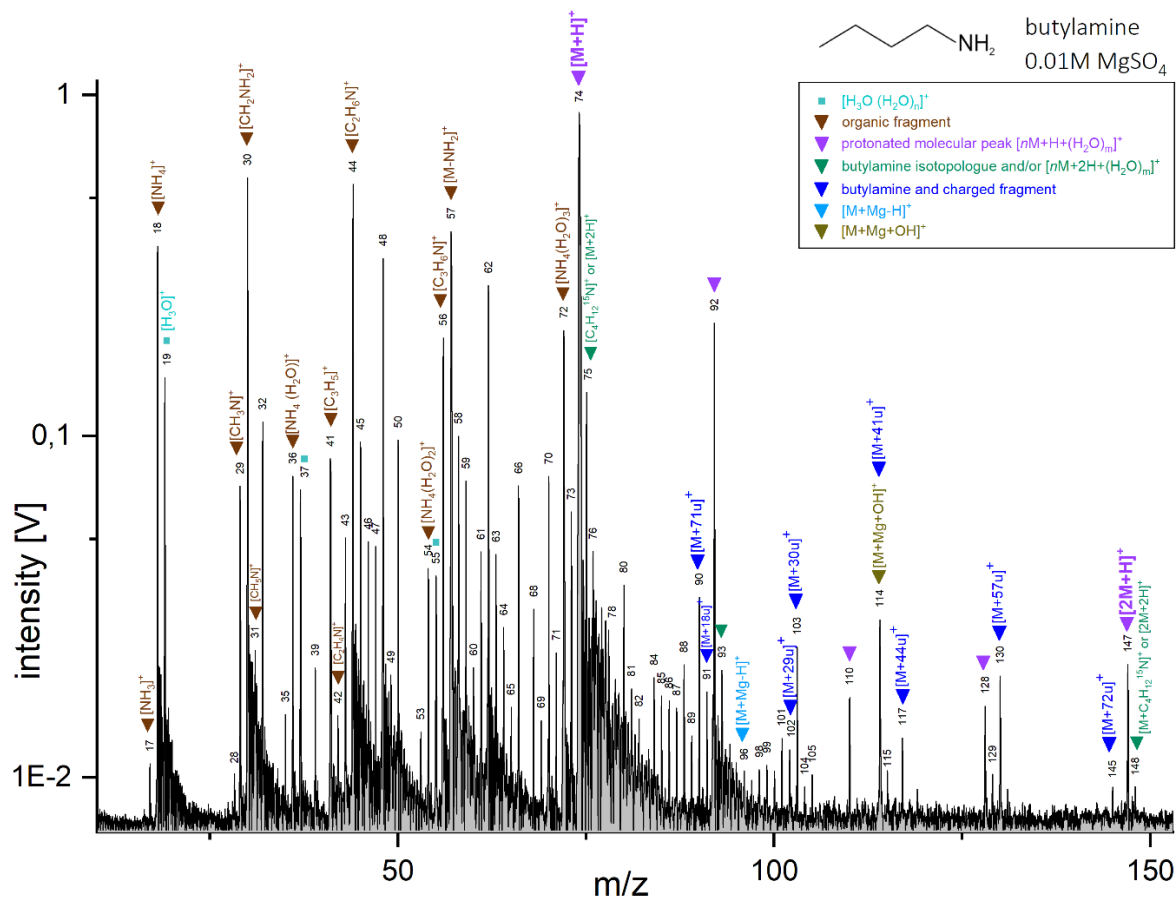
Figure S57. Baseline corrected cation mass spectrum of butylamine (concentration 5 wt%) in 0.01M magnesium sulfate (MgSO$_4$), generated with a delay time of 5.5 µs.
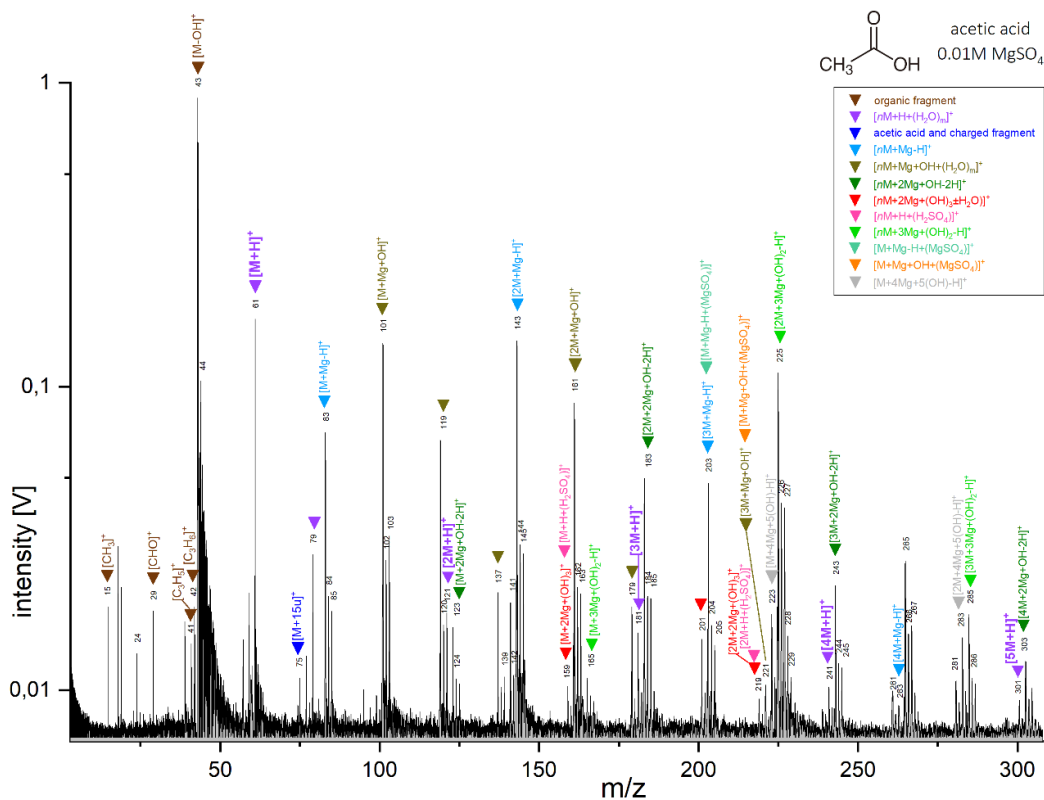
Figure S58. Baseline corrected cation mass spectrum of acetic acid (concentration 5 wt%) in 0.01M magnesium sulfate (MgSO$_4$), generated with a delay time of 5.0 µs. Unlabeled peaks originate exclusively from the MgSO$_4$ matrix.
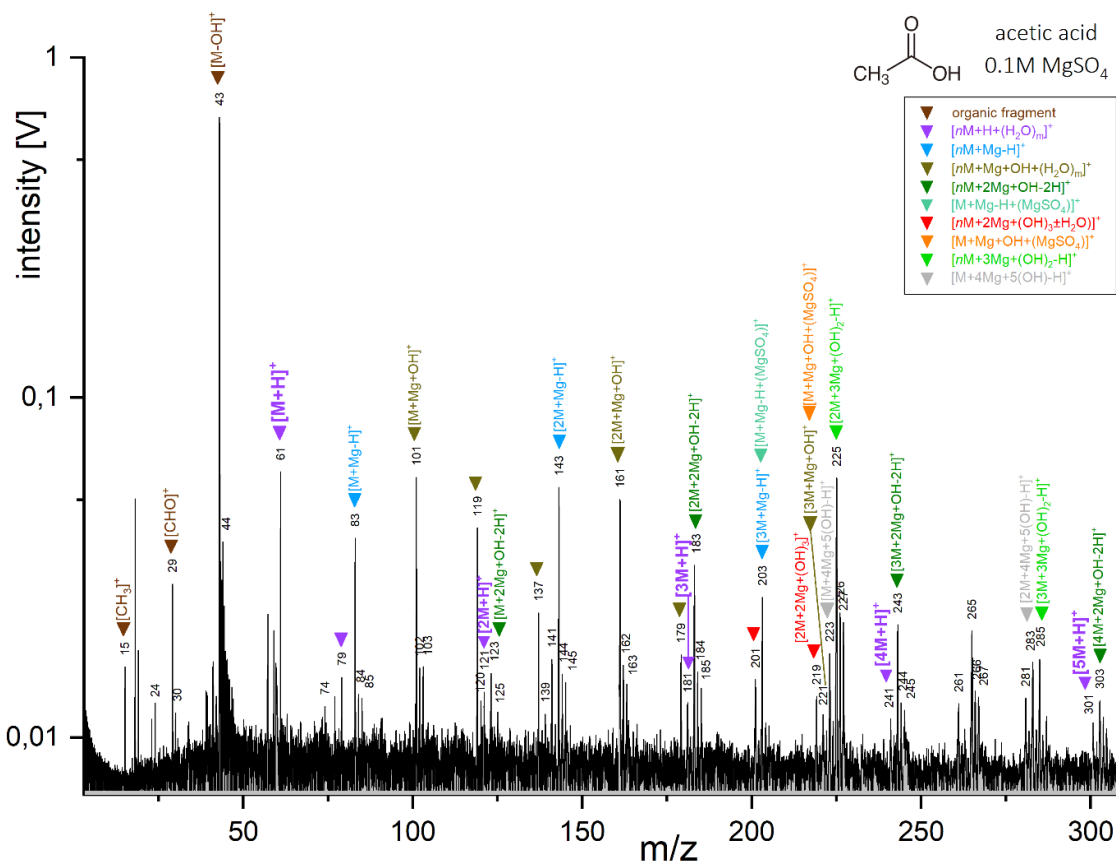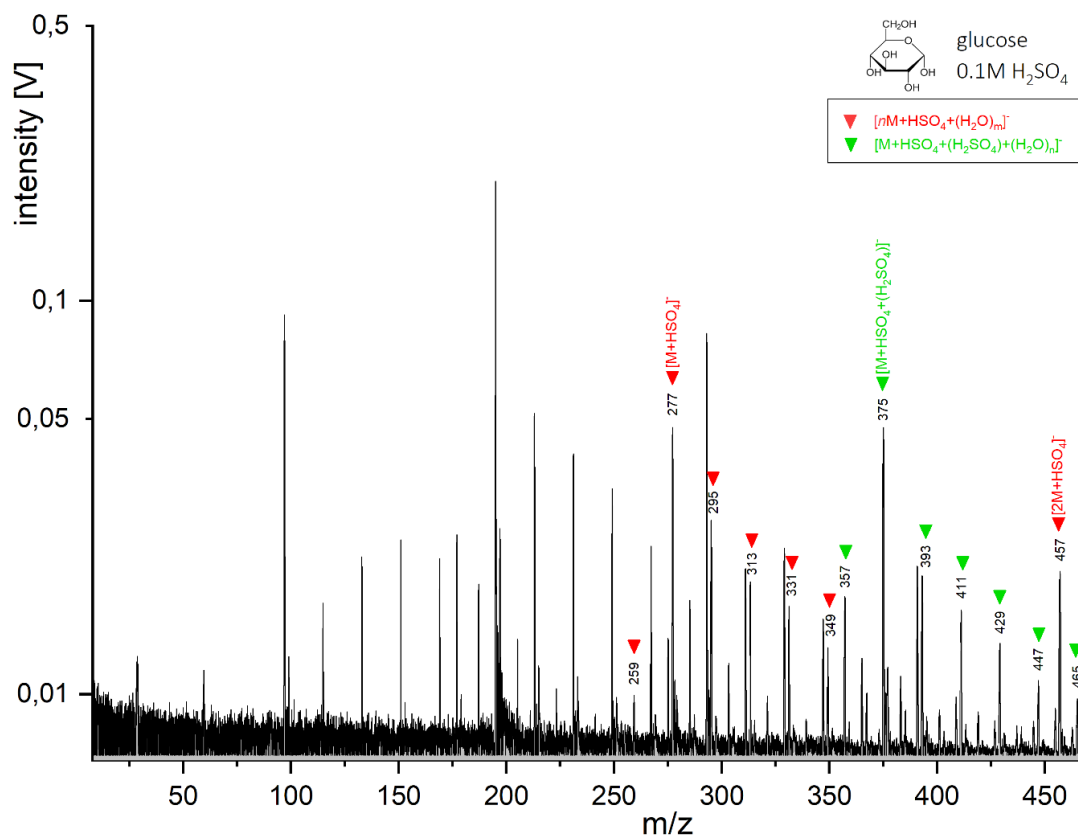
Figure S59. Baseline corrected cation mass spectrum of acetic acid (concentration 5 wt%) in 0.1M magnesium sulfate (MgSO₄), generated with a delay time of 5.0 µs. Unlabeled peaks originate exclusively from the MgSO₄ matrix.
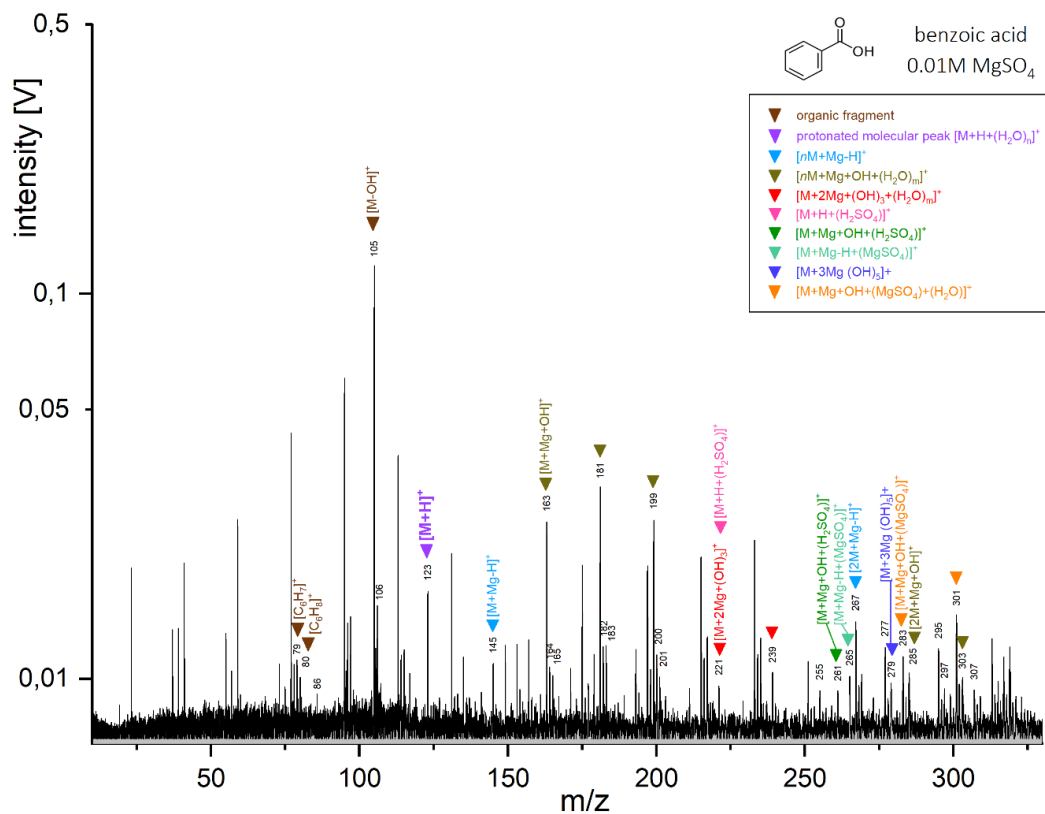
Figure S60. Baseline corrected cation mass spectrum of benzoic acid (concentration 0.17 wt%) in 0.01M magnesium sulfate (MgSO₄), generated with a delay time of 5.8 µs. Unlabeled peaks originate exclusively from the MgSO₄ matrix.
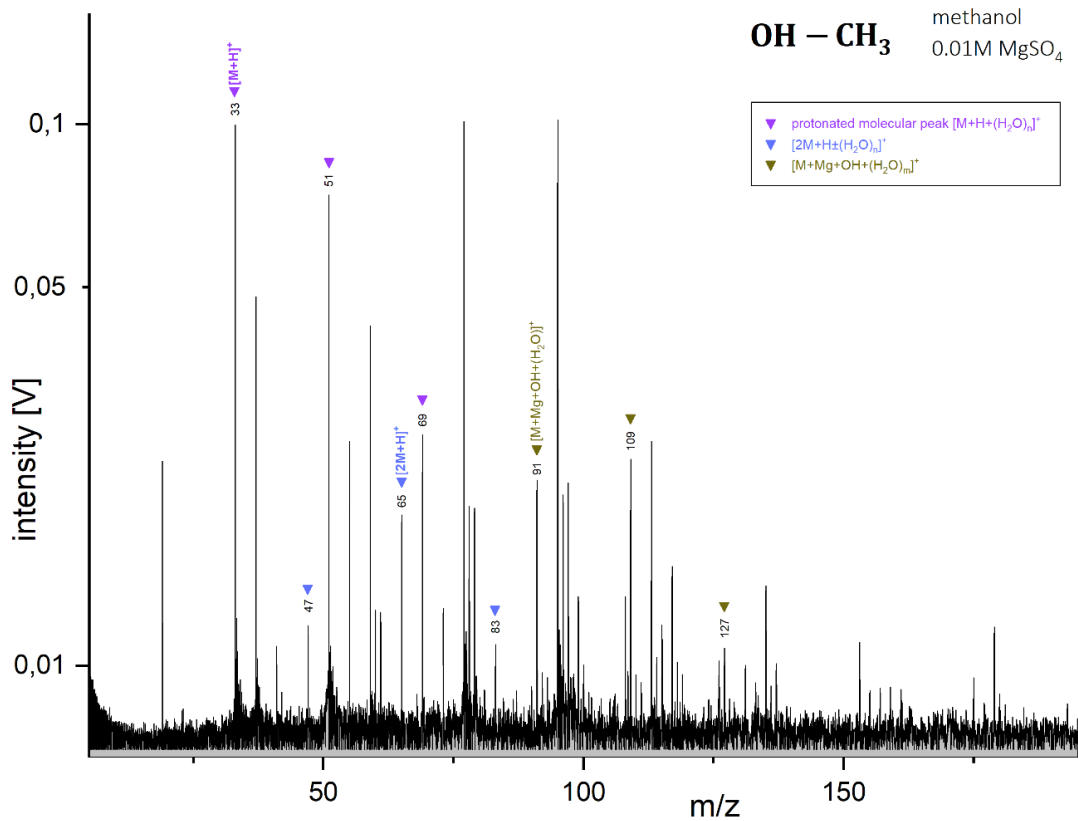
Figure S61. Baseline corrected cation mass spectrum of methanol (concentration 5 wt%) in 0.01M magnesium sulfate (MgSO₄), generated with a delay time of 5.5 µs. Unlabeled peaks originate exclusively from the MgSO₄ matrix.
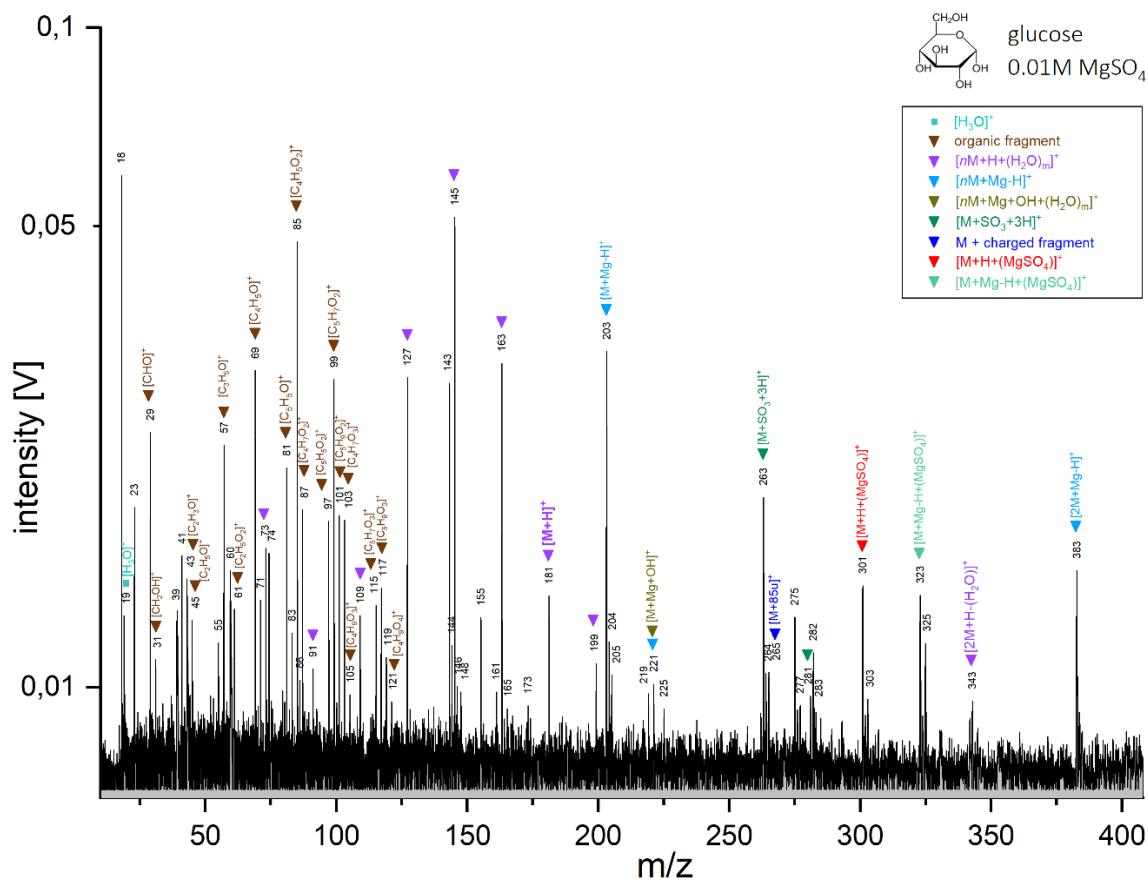
Figure S62. Baseline corrected cation mass spectrum of glucose (concentration 5 wt%) in 0.01M magnesium sulfate (MgSO₄), generated with a delay time of 6.0 µs.
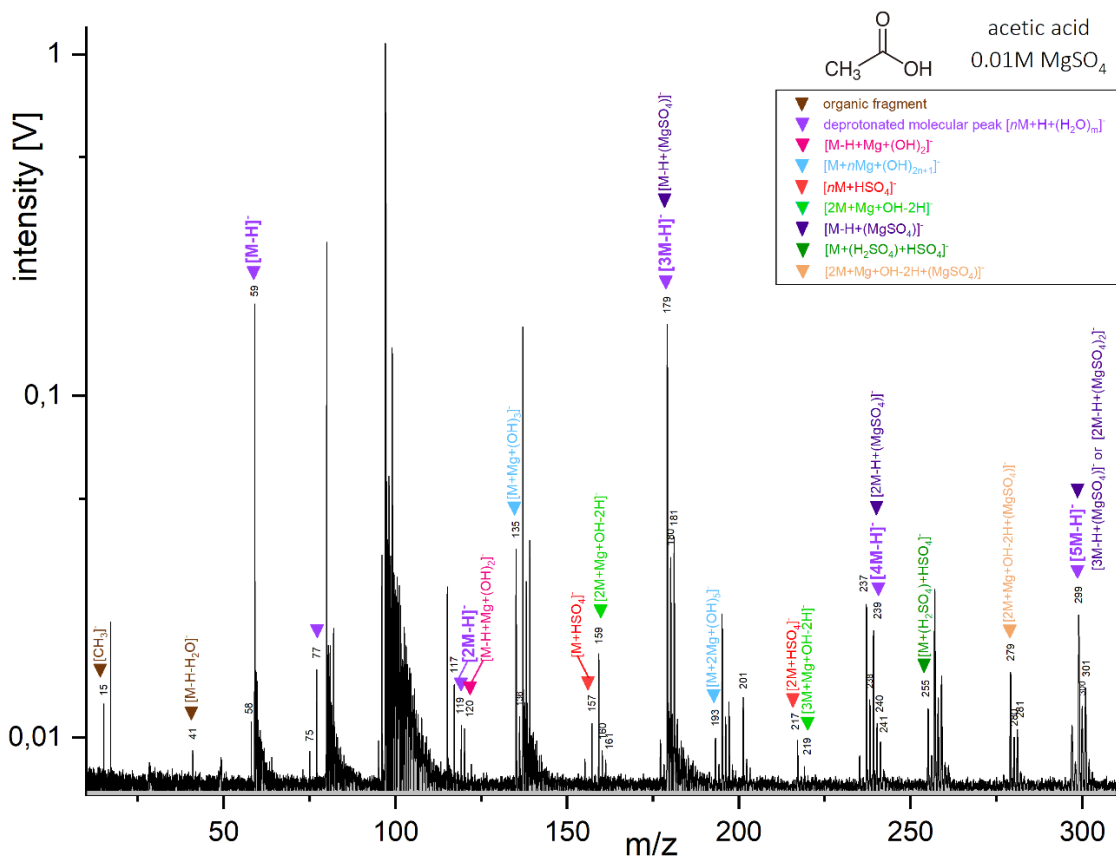
Figure S63. Baseline corrected anion mass spectrum of acetic acid (concentration 5 wt%) in 0.01M magnesium sulfate (MgSO$_4$), generated with a delay time of 5.0 μs. Unlabeled peaks originate exclusively from the MgSO$_4$ matrix.
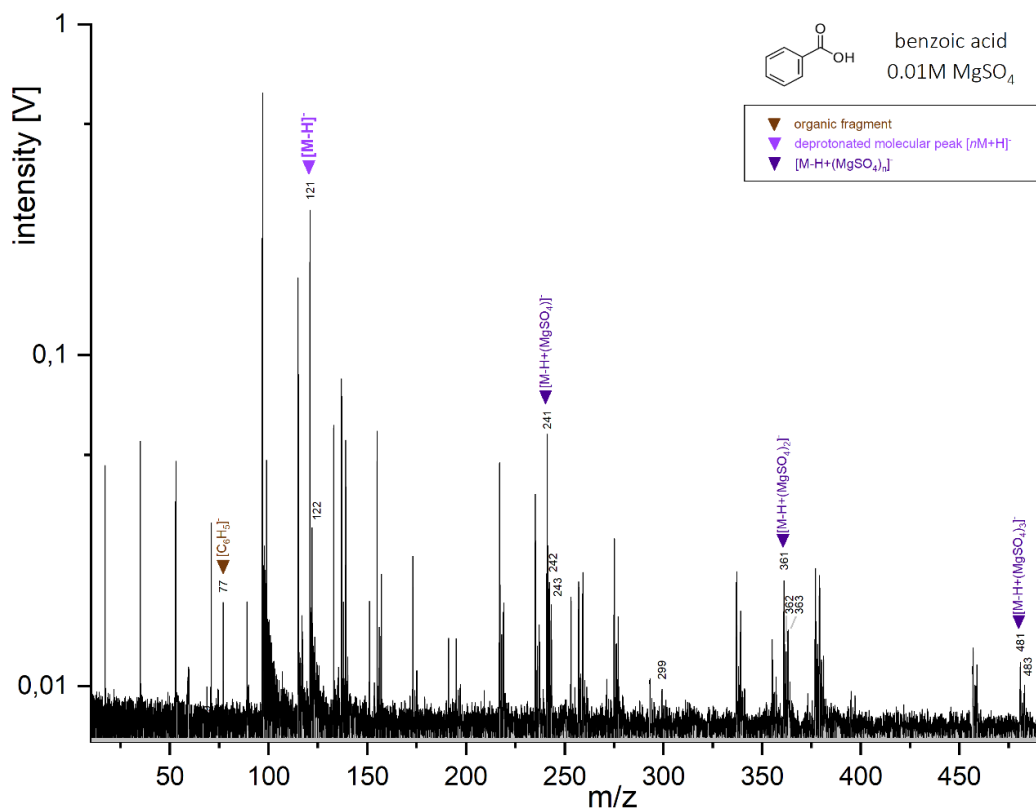
Figure S64. Baseline corrected anion mass spectrum of benzoic acid (concentration 0.17 wt%) in 0.01M magnesium sulfate (MgSO$_4$), generated with a delay time of 5.8 μs. Unlabeled peaks originate exclusively from the MgSO$_4$ matrix.
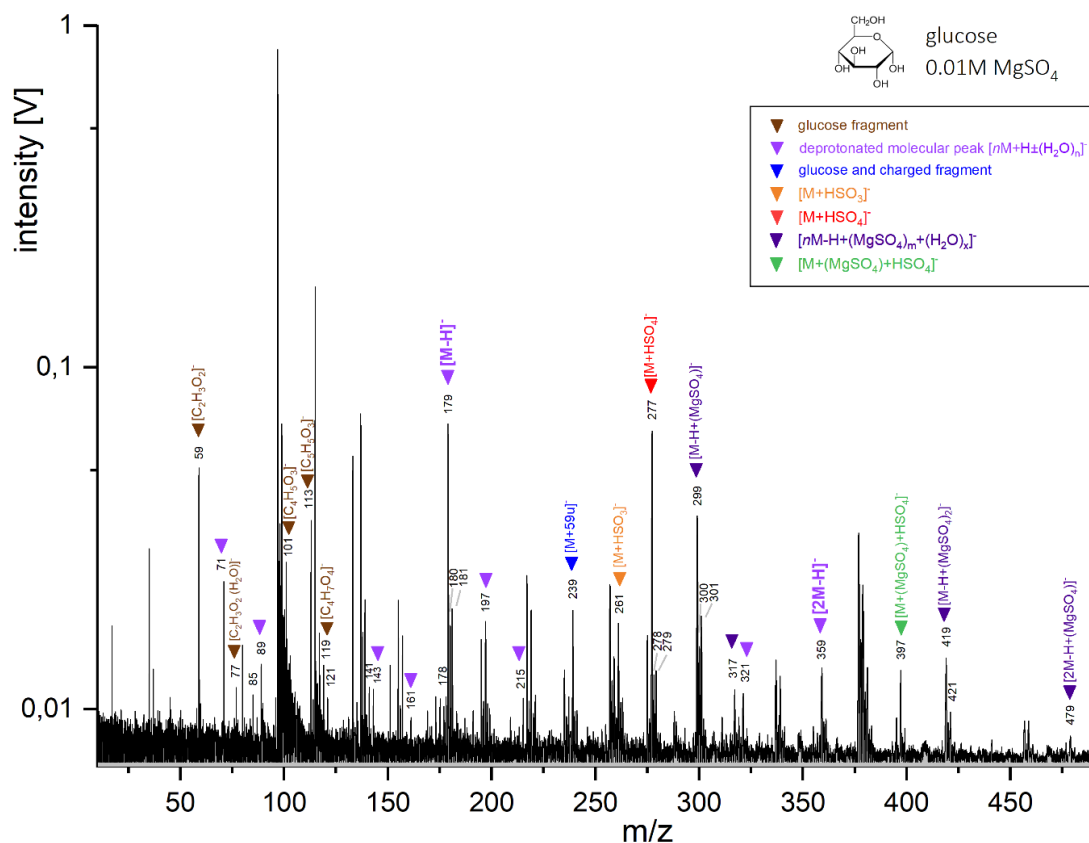
Figure S65. Baseline corrected anion mass spectrum of glucose (concentration 5 wt%) in 0.01M magnesium sulfate (MgSO₄), generated with a delay time of 6.0 μs. Unlabeled peaks originate exclusively from the MgSO₄ matrix.
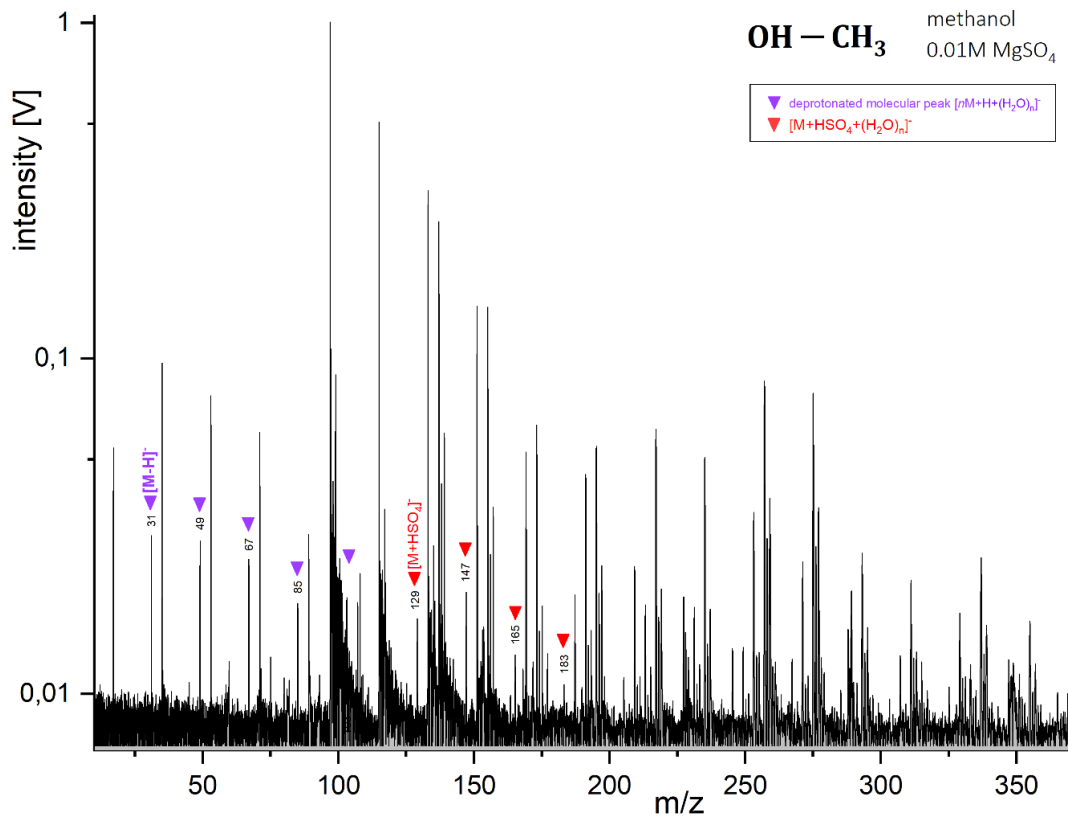
Figure S66. Baseline corrected anion mass spectrum of methanol (concentration 5 wt%) in 0.01M magnesium sulfate (MgSO₄), generated with a delay time of 6.3 μs. Unlabeled peaks originate exclusively from the MgSO₄ matrix.
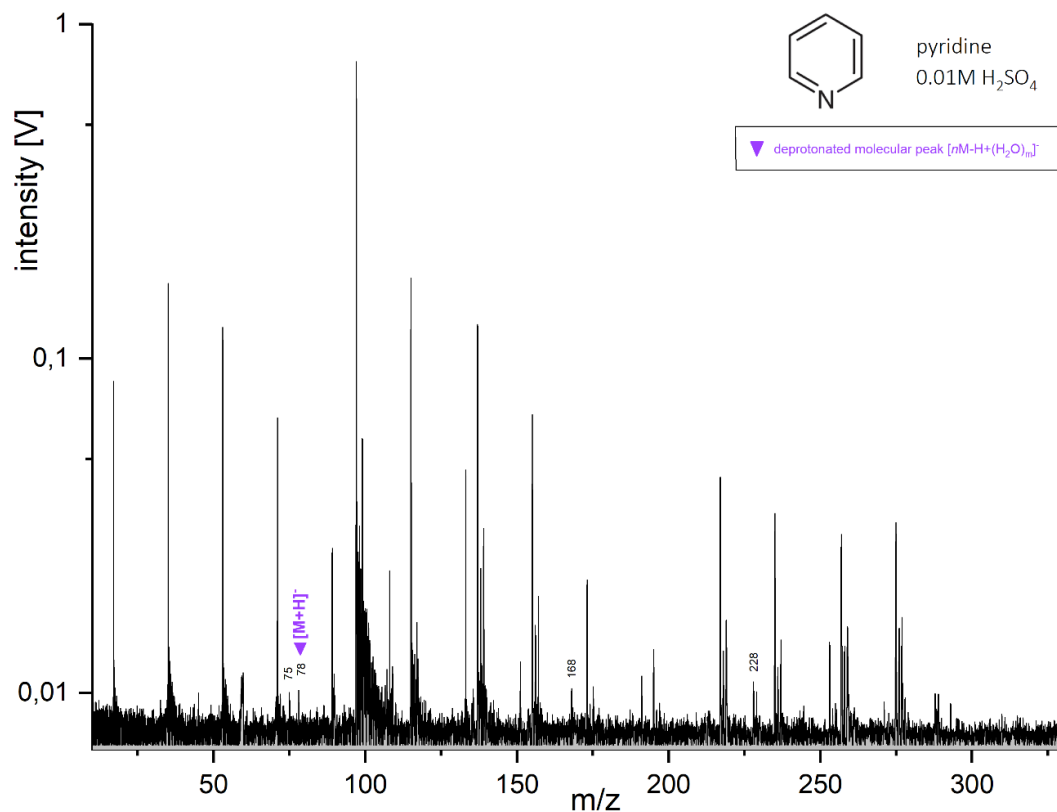
Figure S67. Baseline corrected anion mass spectrum of pyridine (concentration 5 wt%) in 0.01M magnesium sulfate (MgSO$_4$), generated with a delay time of 5.8 µs. Unlabeled peaks originate exclusively from the MgSO$_4$ matrix.
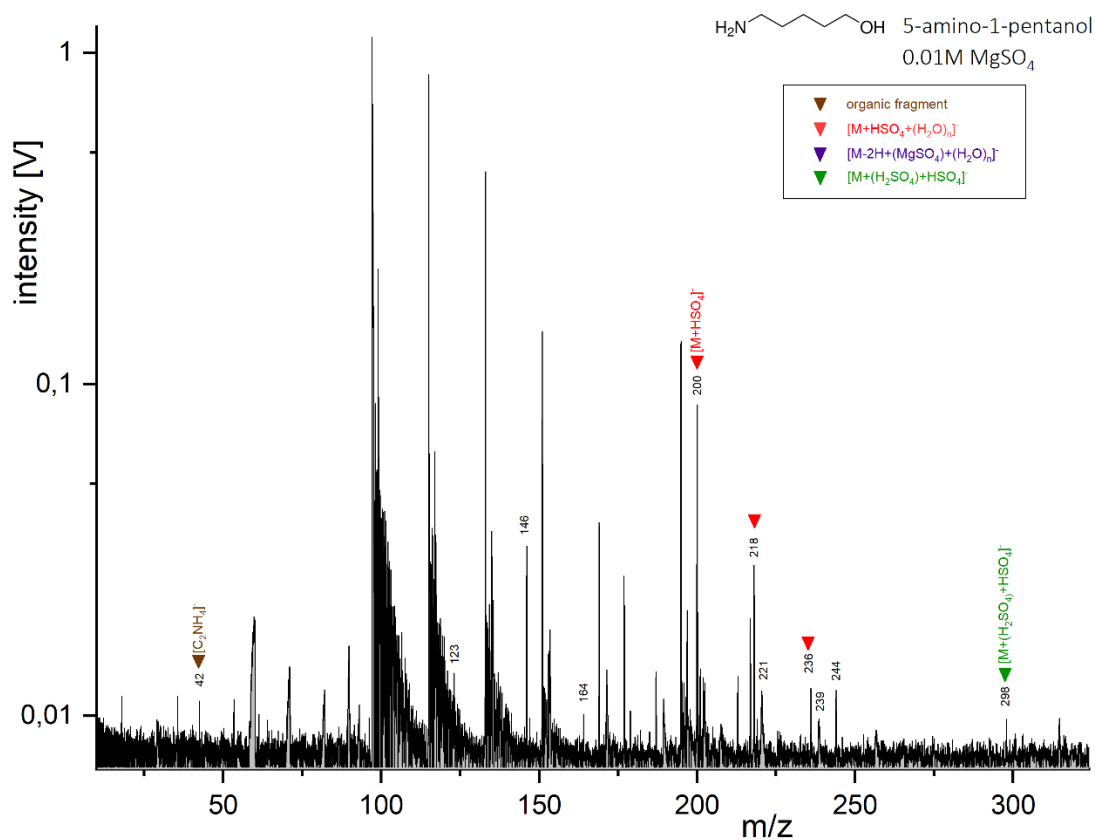
Figure S68. Baseline corrected anion mass spectrum of 5-amino-1-pentanol (concentration 5 wt%) in 0.01M magnesium sulfate (MgSO$_4$), generated with a delay time of 6.1 µs. Unlabeled peaks originate exclusively from the MgSO$_4$ matrix.
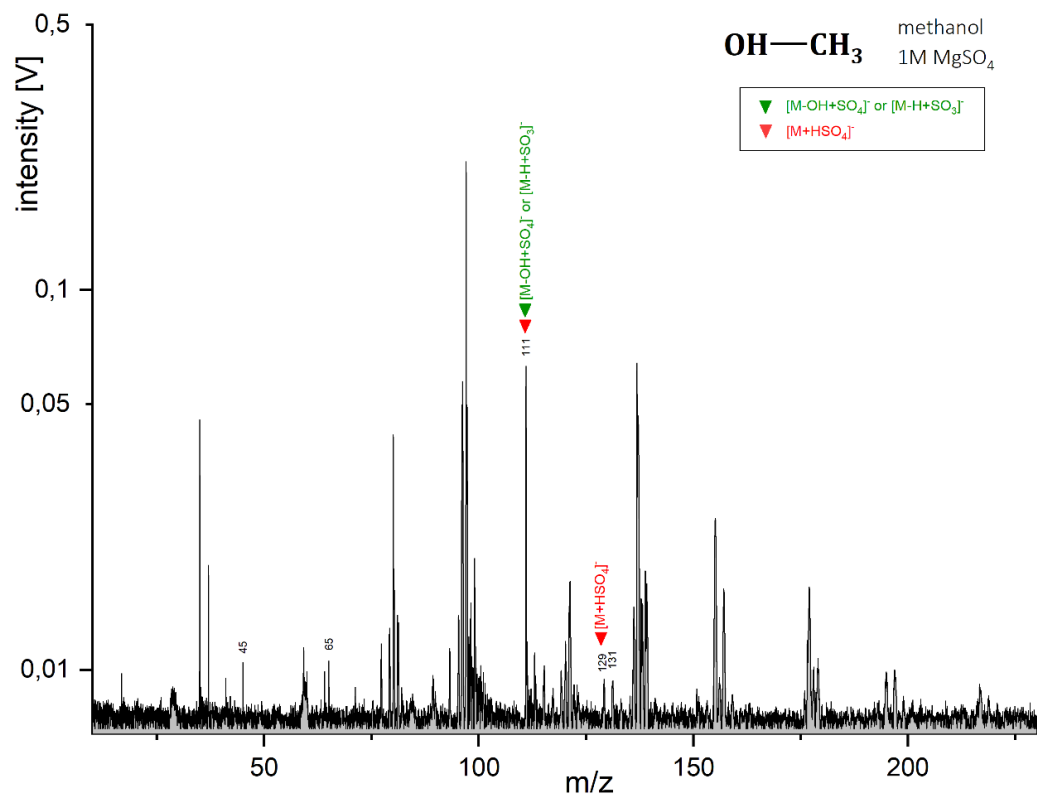
Figure S69. Baseline corrected anion mass spectrum of methanol (concentration 5 wt%) in 1M magnesium sulfate (MgSO₄), generated with a delay time of 9.3 µs. Unlabeled peaks originate exclusively from the MgSO₄ matrix.
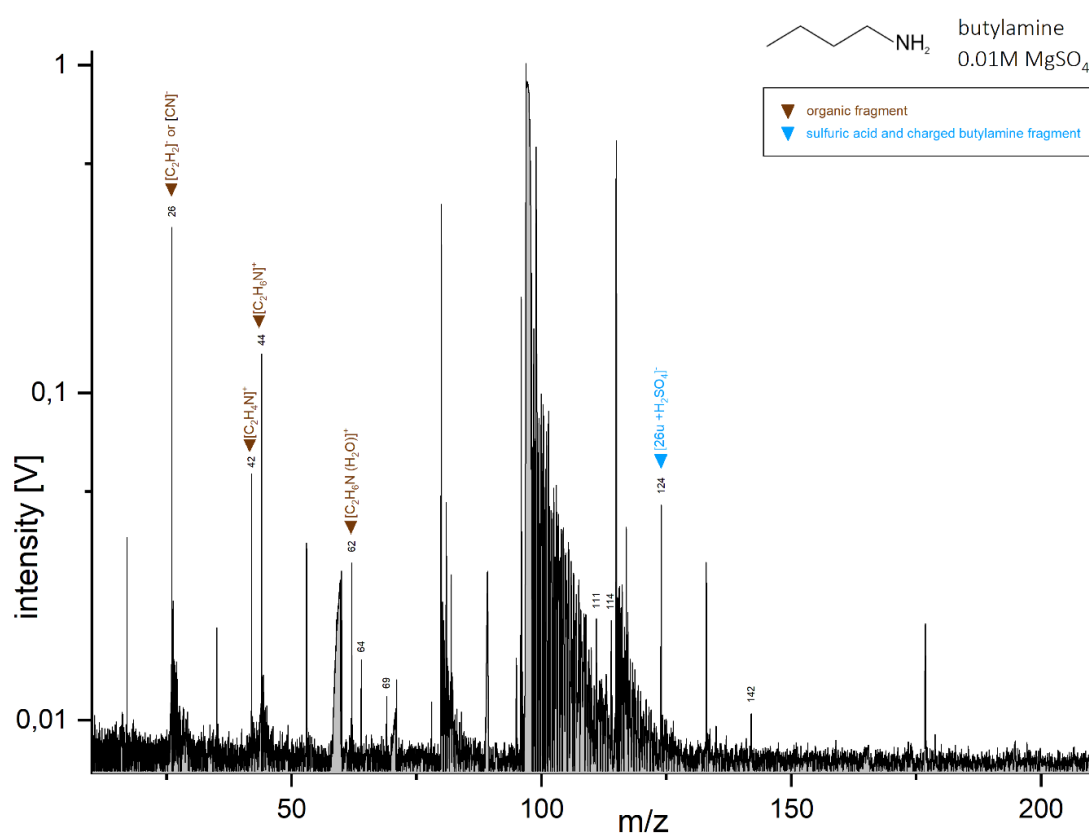
Figure S70. Baseline corrected anion mass spectrum of butylamine (concentration 5 wt%) in 0.01M magnesium sulfate (MgSO₄), generated with a delay time of 5.5 µs. Unlabeled peaks originate exclusively from the MgSO₄ matrix.
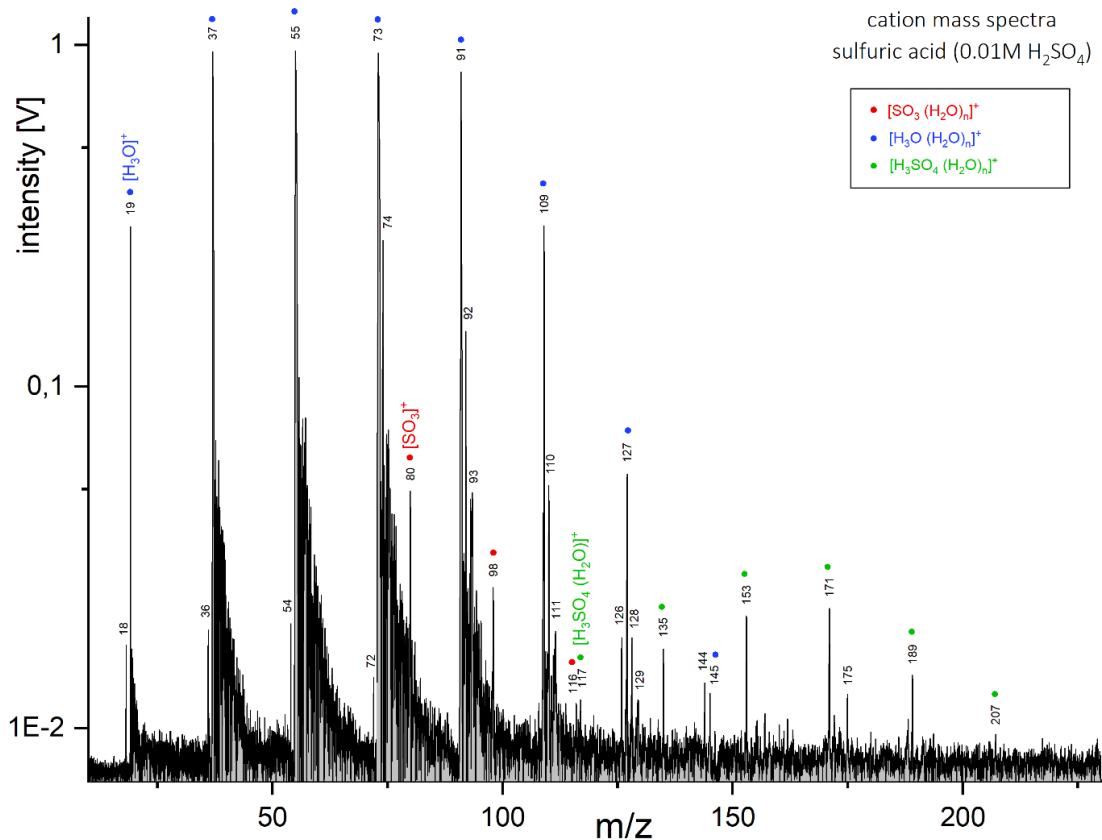
Figure S71. Baseline corrected cation mass spectrum of sulfuric acid (H_2SO_4) at a concentration of 0.01M, generated with a delay time of 6.0µs.
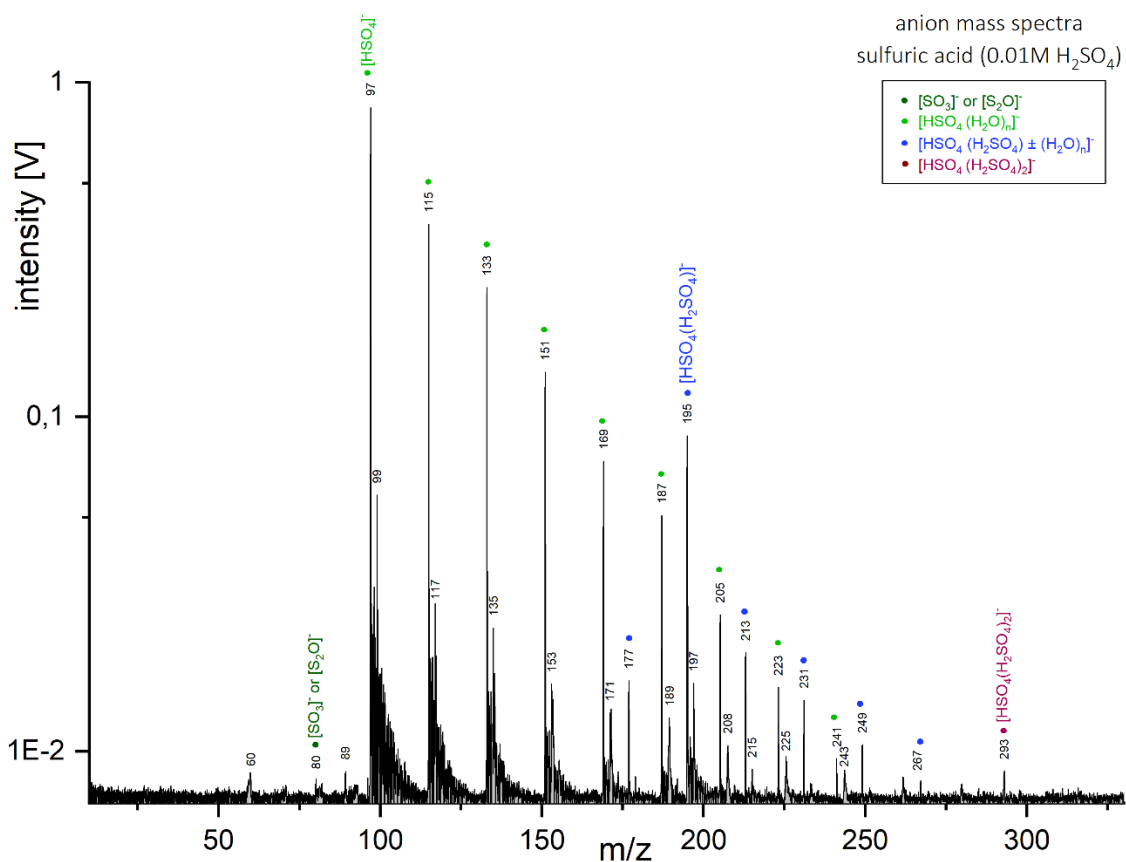
Figure S72. Baseline corrected anion mass spectrum of sulfuric acid (H_2SO_4) at a concentration of 0.01M, generated with a delay time of 6.2µs.
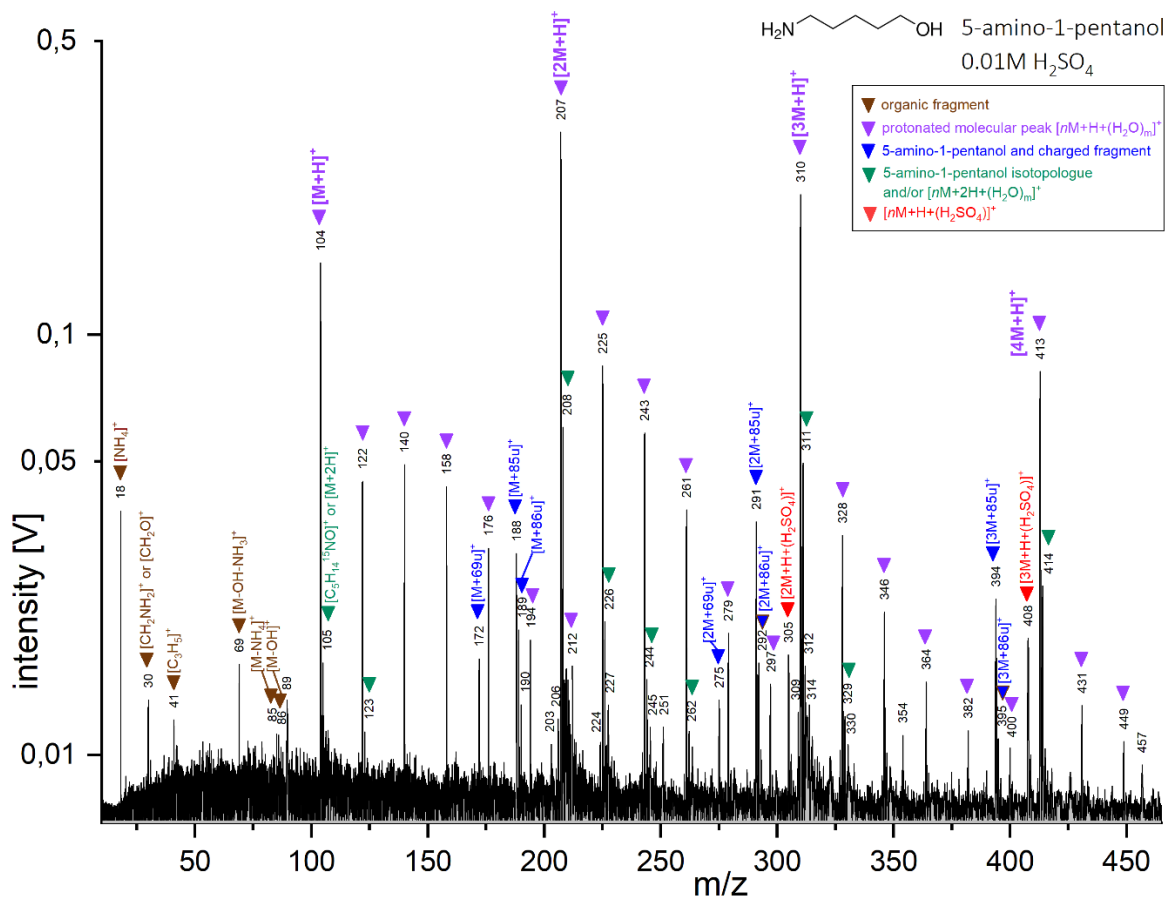
Figure S73. Baseline corrected cation mass spectrum of 5-amino-1-pentanol (concentration 5wt%) in 0.01M sulfuric acid (H_2SO_4), generated with a delay time of 6.8µs.
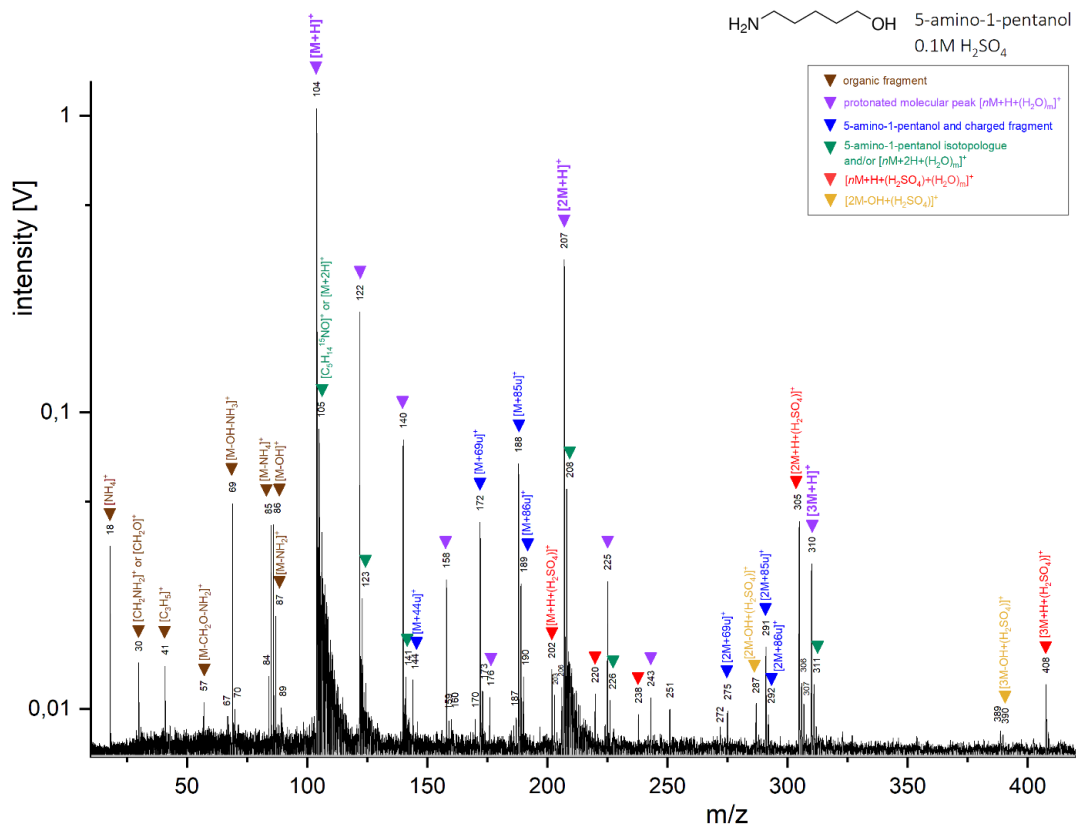
Figure S74. Baseline corrected cation mass spectrum of 5-amino-1-pentanol (concentration 5wt%) in 0.1M sulfuric acid (H_2SO_4), generated with a delay time of 6.8µs.
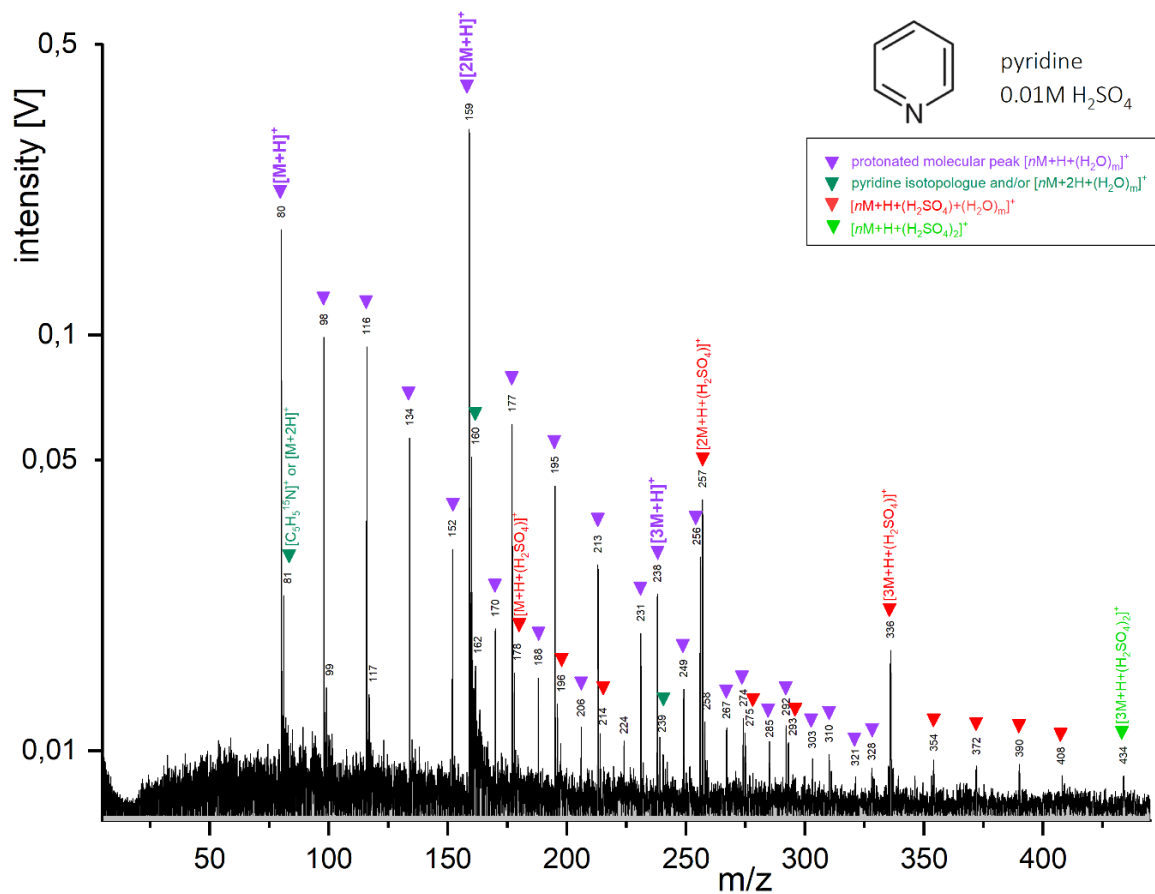
Figure S75. Baseline corrected cation mass spectrum of pyridine (concentration 5wt%) in 0.01M sulfuric acid (H_2SO_4), generated with a delay time of 6.2µs.
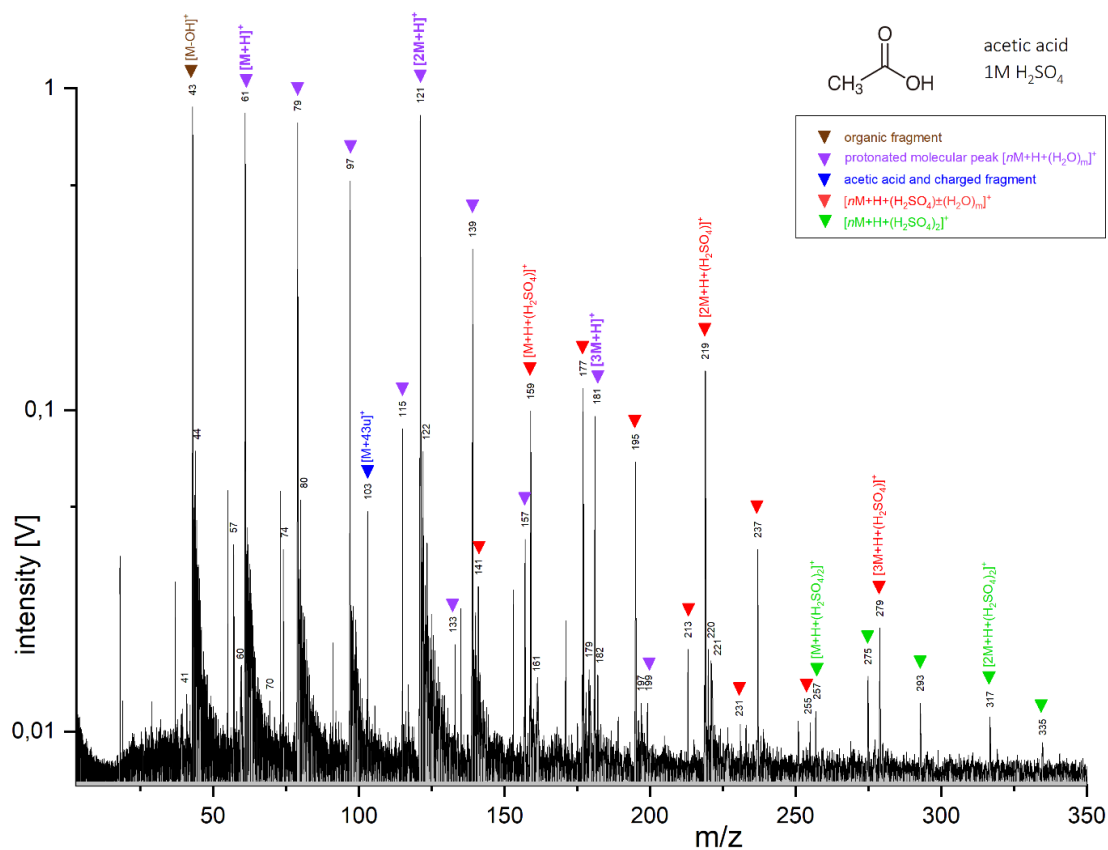
Figure S76. Baseline corrected cation mass spectrum of acetic acid (concentration 5wt%) in 1M sulfuric acid (H_2SO_4), generated with a delay time of 6.4µs.
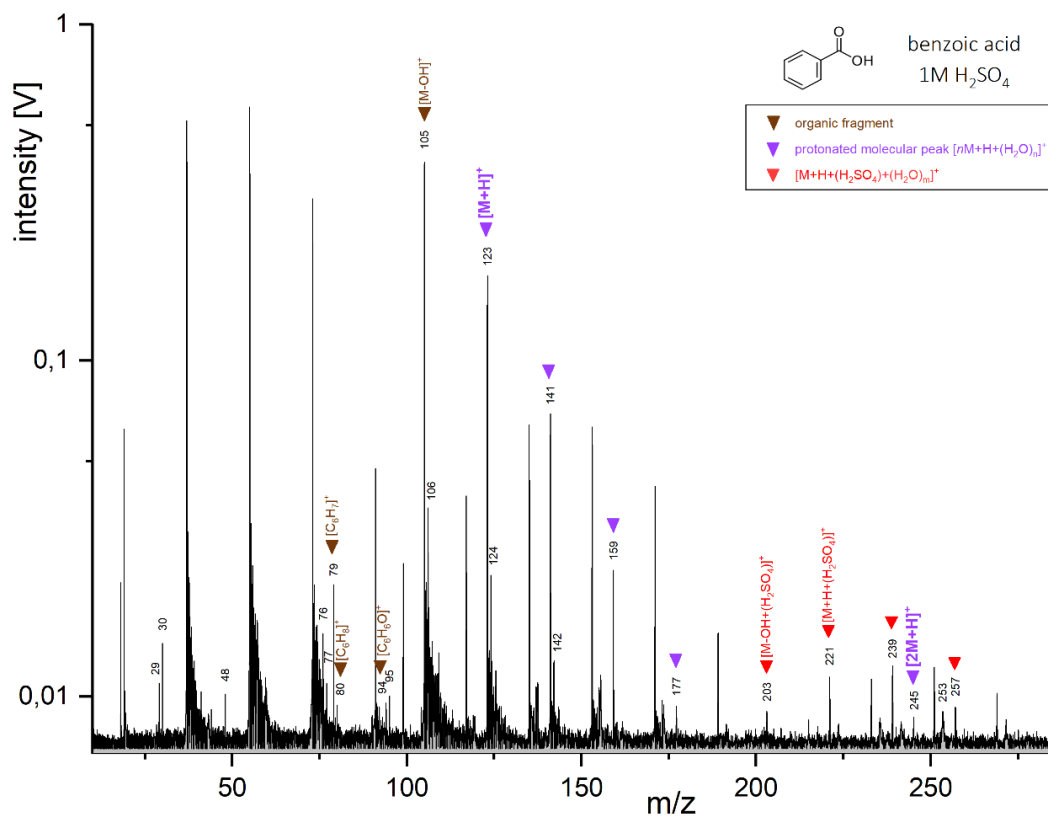
Figure S77. Baseline corrected cation mass spectrum of benzoic acid (concentration 0.17wt%) in 1M sulfuric acid (H₂SO₄), generated with a delay time of 6.0 µs. Unlabeled peaks originate exclusively from the H₂SO₄ matrix.
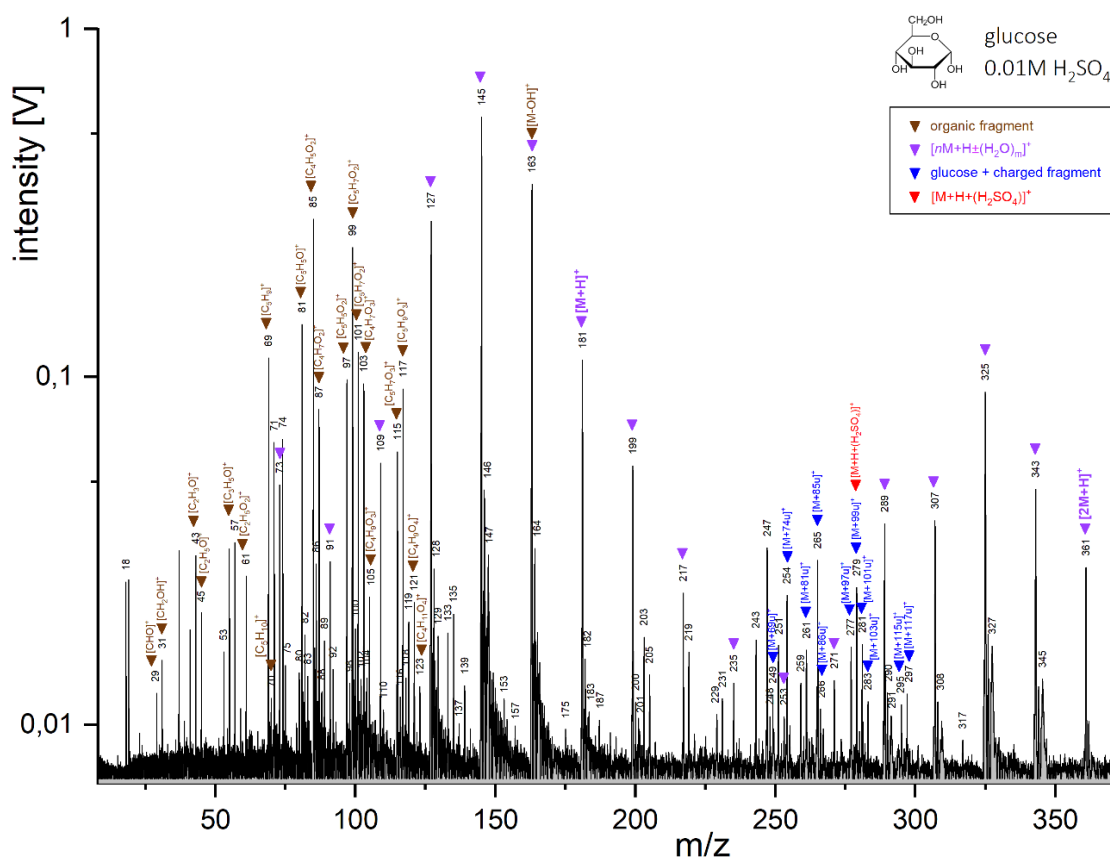
Figure S78. Baseline corrected cation mass spectrum of glucose (concentration 5wt%) in 0.01M sulfuric acid (H₂SO₄), generated with a delay time of 6.0µs. Unlabeled peaks originate exclusively from the H₂SO₄ matrix.
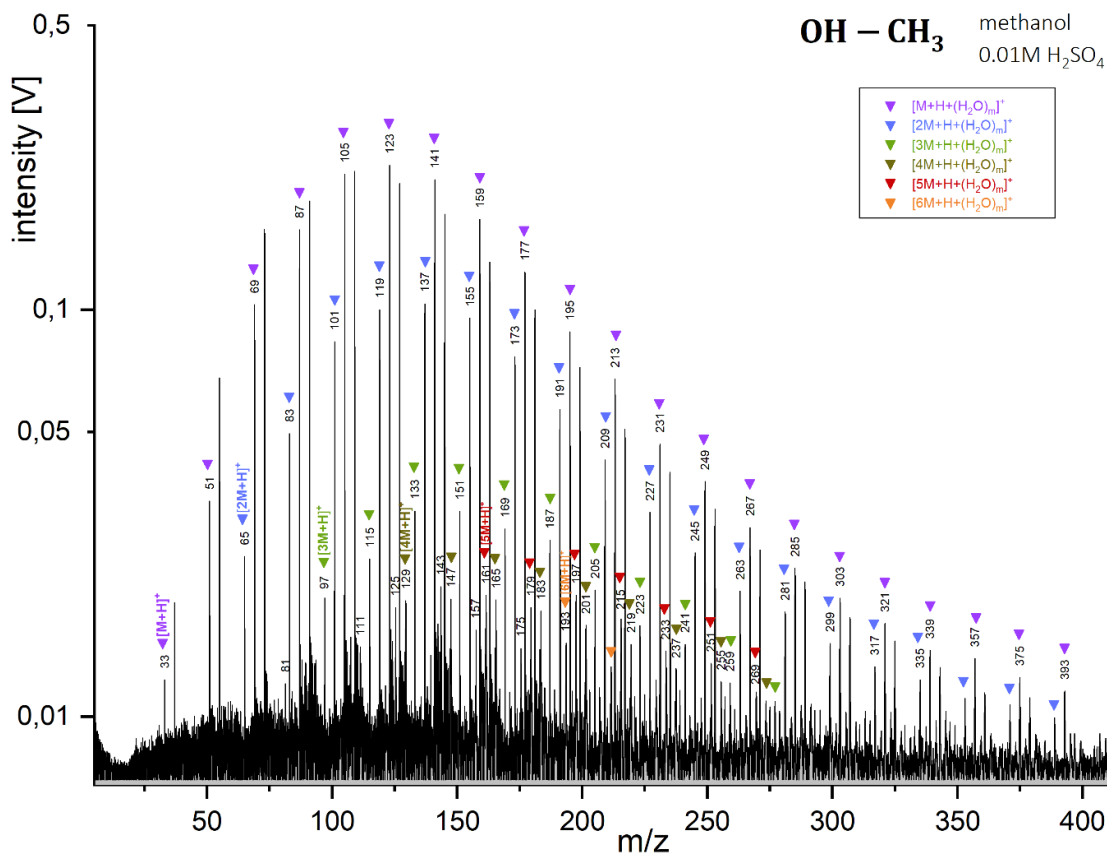
Figure S79. Baseline corrected cation mass spectrum of methanol (concentration 5wt%) in 0.01M sulfuric acid (H_2SO_4), generated with a delay time of 6.7μs. Unlabeled peaks originate exclusively from the H_2SO_4 matrix.
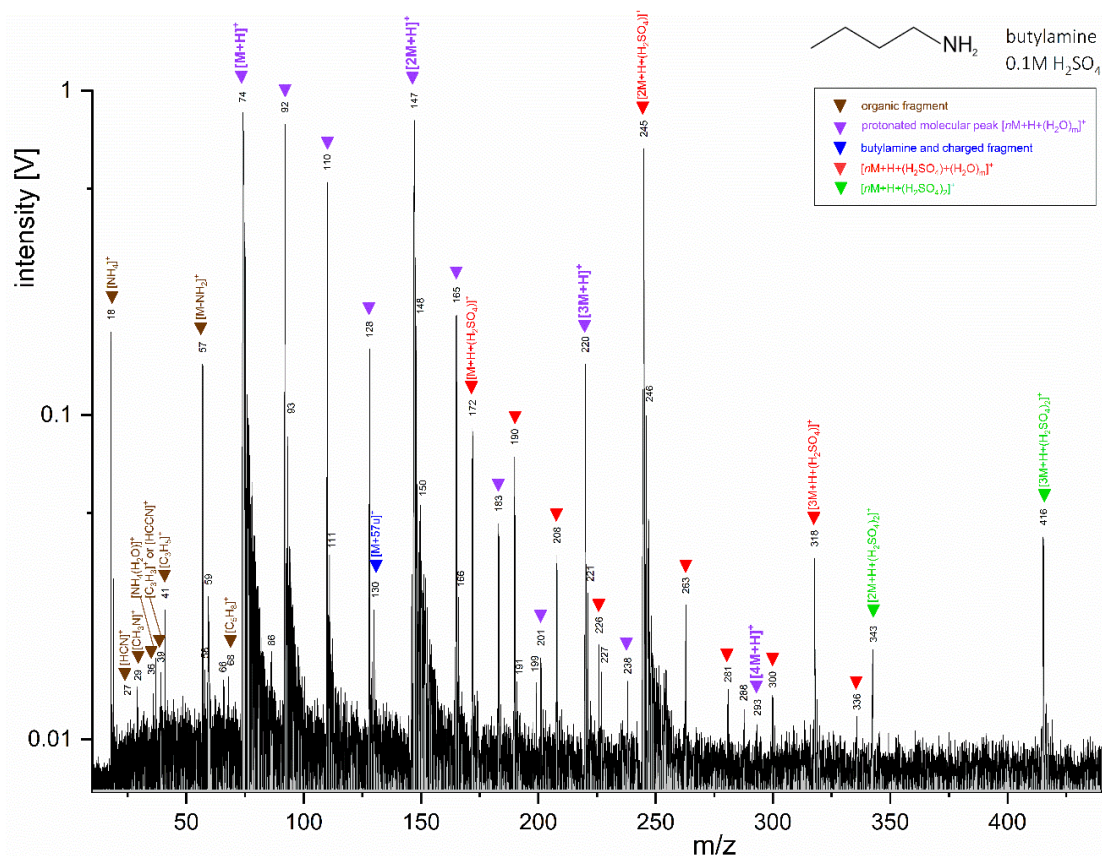
Figure S80. Baseline corrected cation mass spectrum of butylamine (concentration 1.3wt%) in 0.1M sulfuric acid (H_2SO_4), generated with a delay time of 6.4μs.
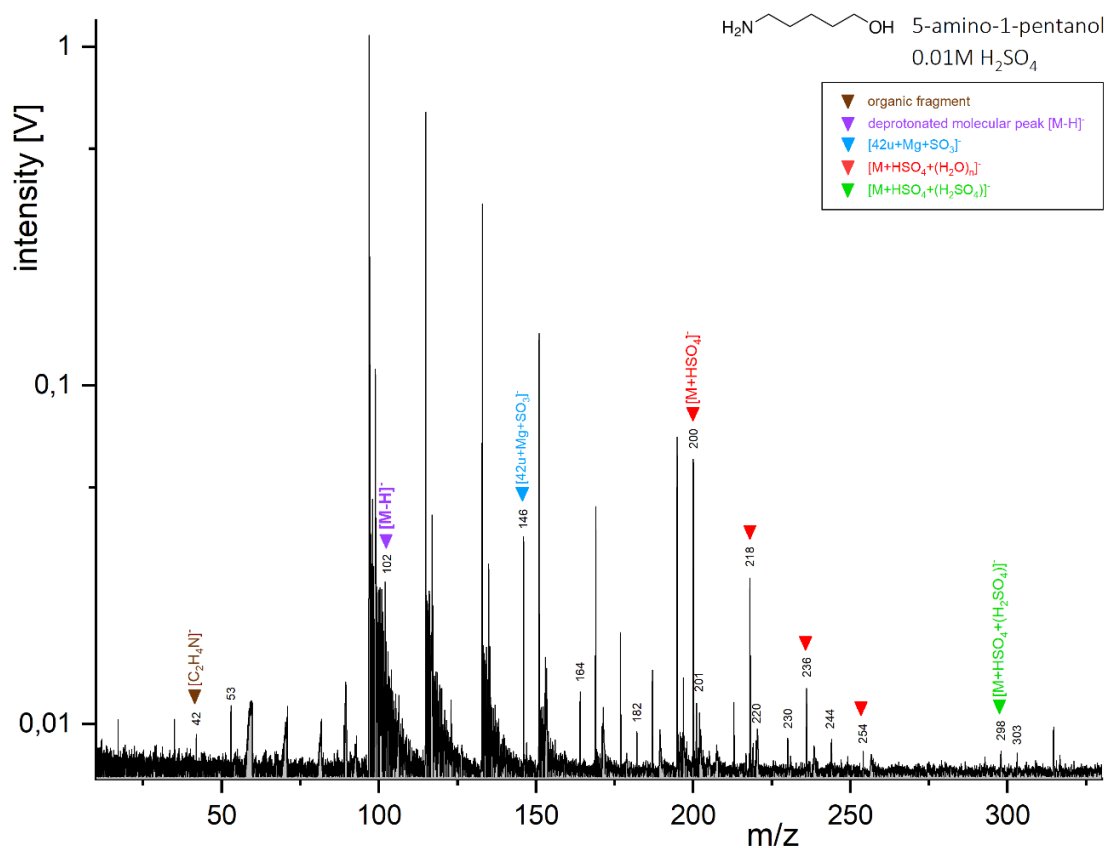
Figure S81. Baseline corrected anion mass spectrum of 5-amino-1-pentanol (concentration 5wt%) in 0.01M sulfuric acid (H_2SO_4), generated with a delay time of 6.2µs. Unlabeled peaks originate exclusively from the H_2SO_4 matrix.
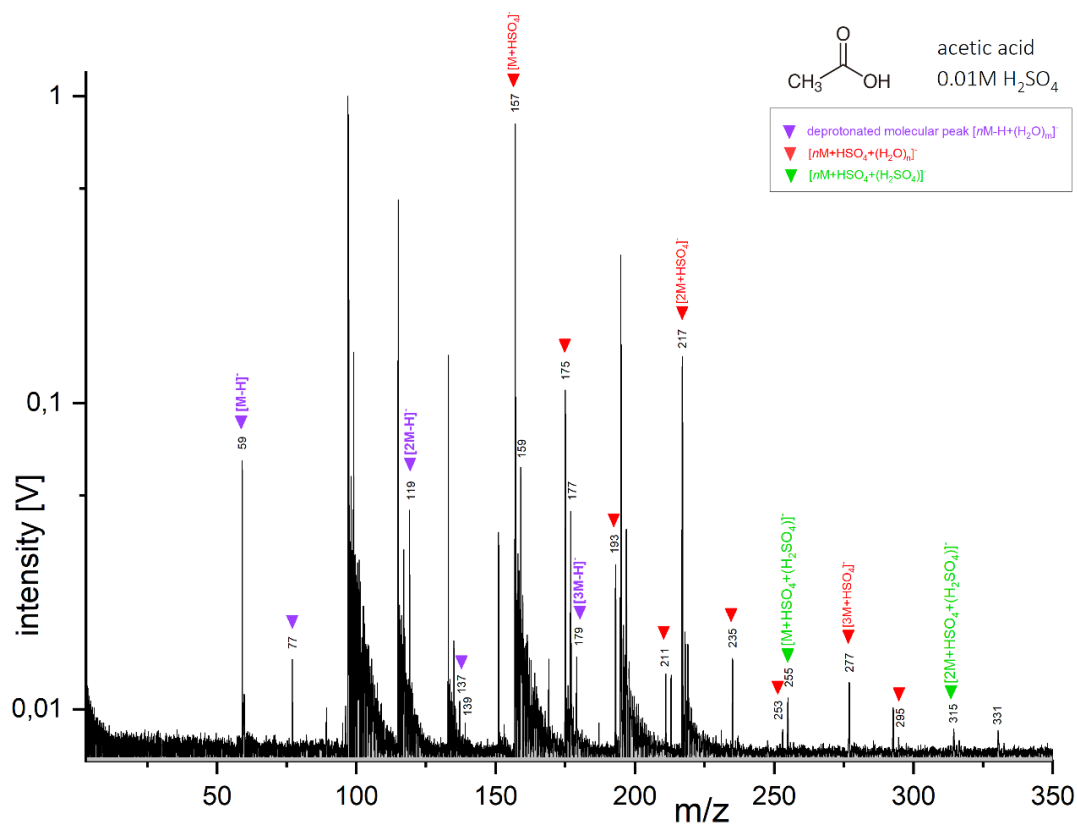
Figure S82. Baseline corrected anion mass spectrum of acetic acid (concentration 5wt%) in 0.1M sulfuric acid (H_2SO_4), generated with a delay time of 6.4µs. Unlabeled peaks originate exclusively from the H_2SO_4 matrix.
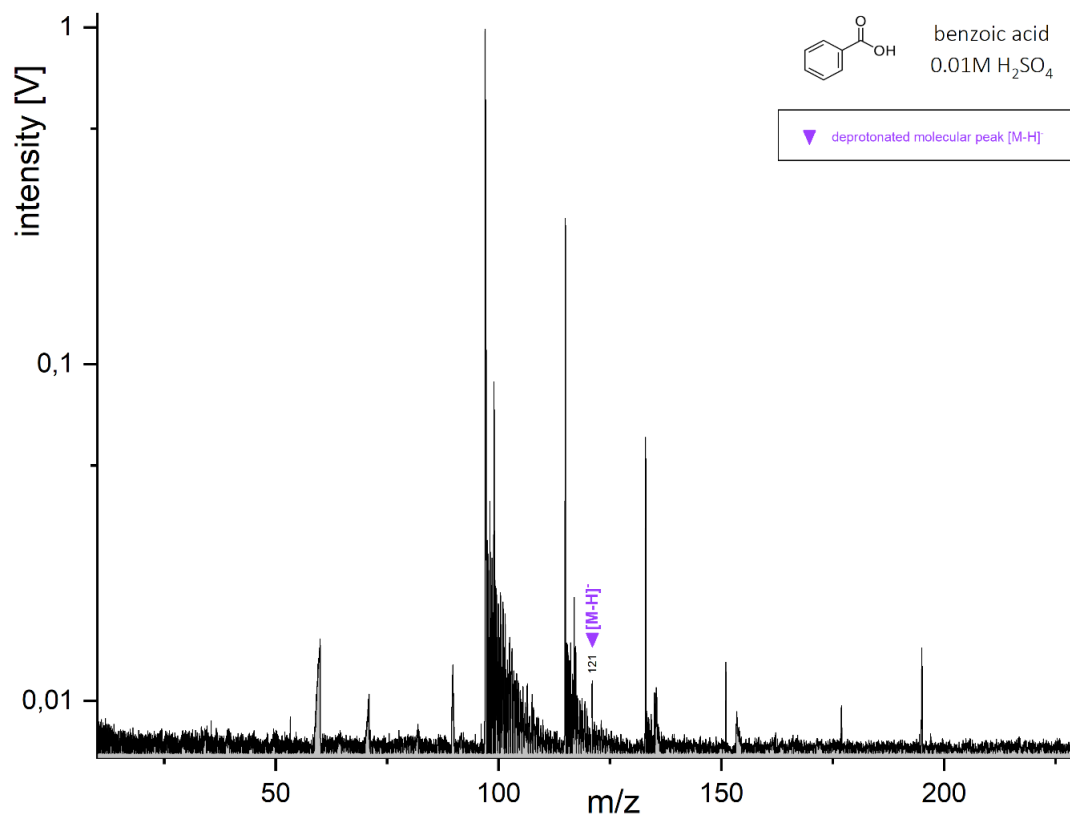
Figure S83. Baseline corrected anion mass spectrum of benzoic acid (concentration 0.17wt%) in 1M sulfuric acid (H_2SO_4), generated with a delay time of 5.7 µs. Unlabeled peaks originate exclusively from the H_2SO_4 matrix.
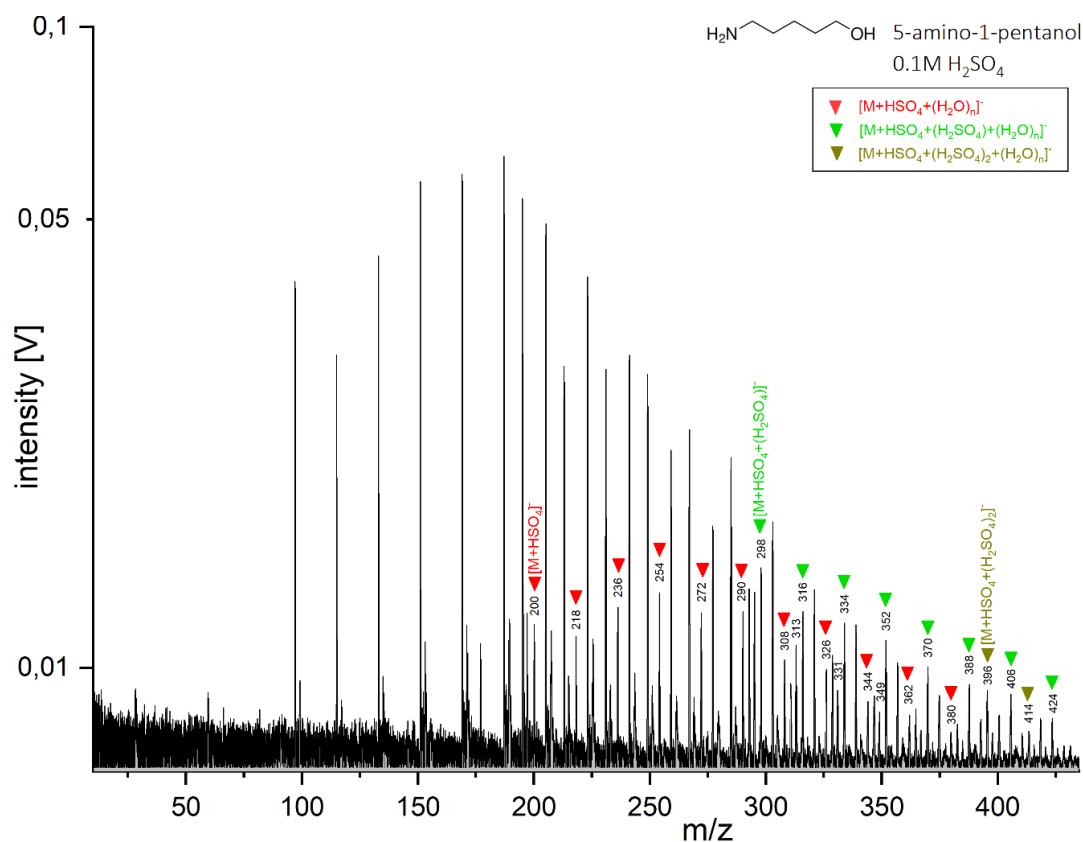
Figure S84. Baseline corrected anion mass spectrum of 5-amino-1-pentanol (concentration 5wt%) in 0.1M sulfuric acid (H_2SO_4), generated with a delay time of 6.8µs. Unlabeled peaks originate exclusively from the H_2SO_4 matrix.

Figure S85. Baseline corrected anion mass spectrum of glucose (concentration 5wt%) in 0.1M sulfuric acid (H₂SO₄), generated with a delay time of 6.9µs. Unlabeled peaks originate exclusively from the H₂SO₄ matrix.
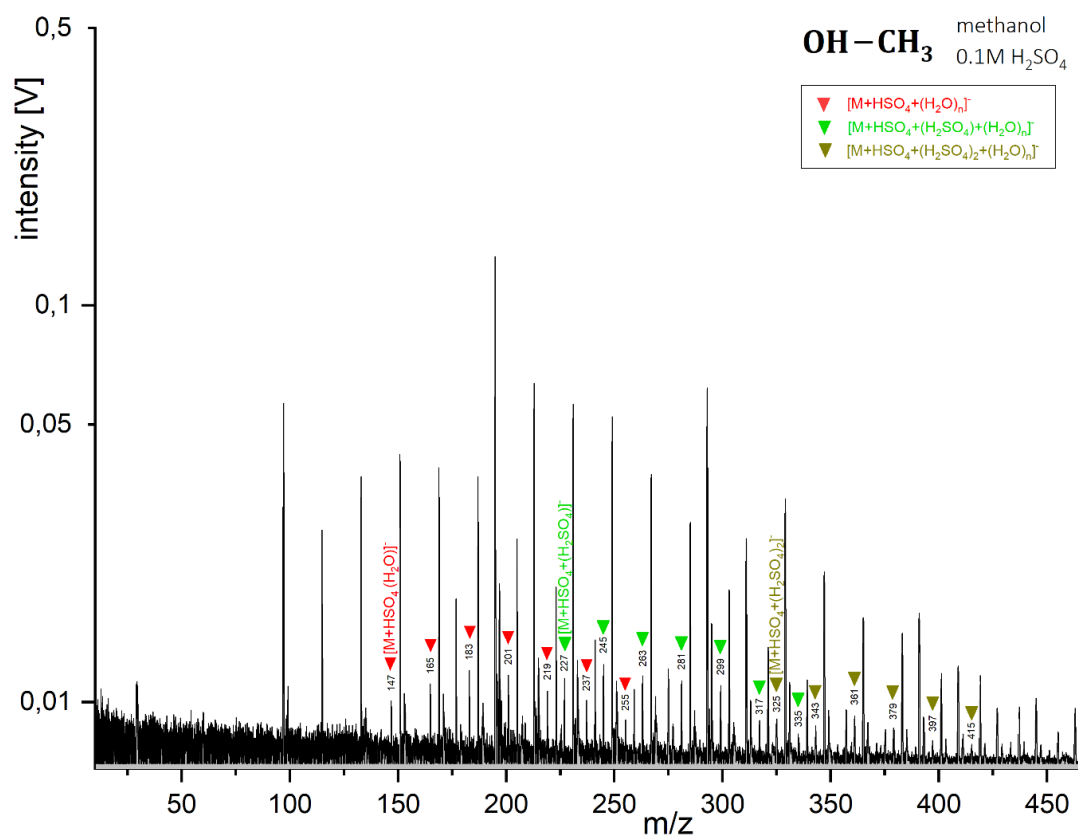
Figure S86. Baseline corrected anion mass spectrum of methanol (concentration 5wt%) in 0.1M sulfuric acid (H₂SO₄), generated with a delay time of 6.8 µs. Unlabeled peaks originate exclusively from the H₂SO₄ matrix.
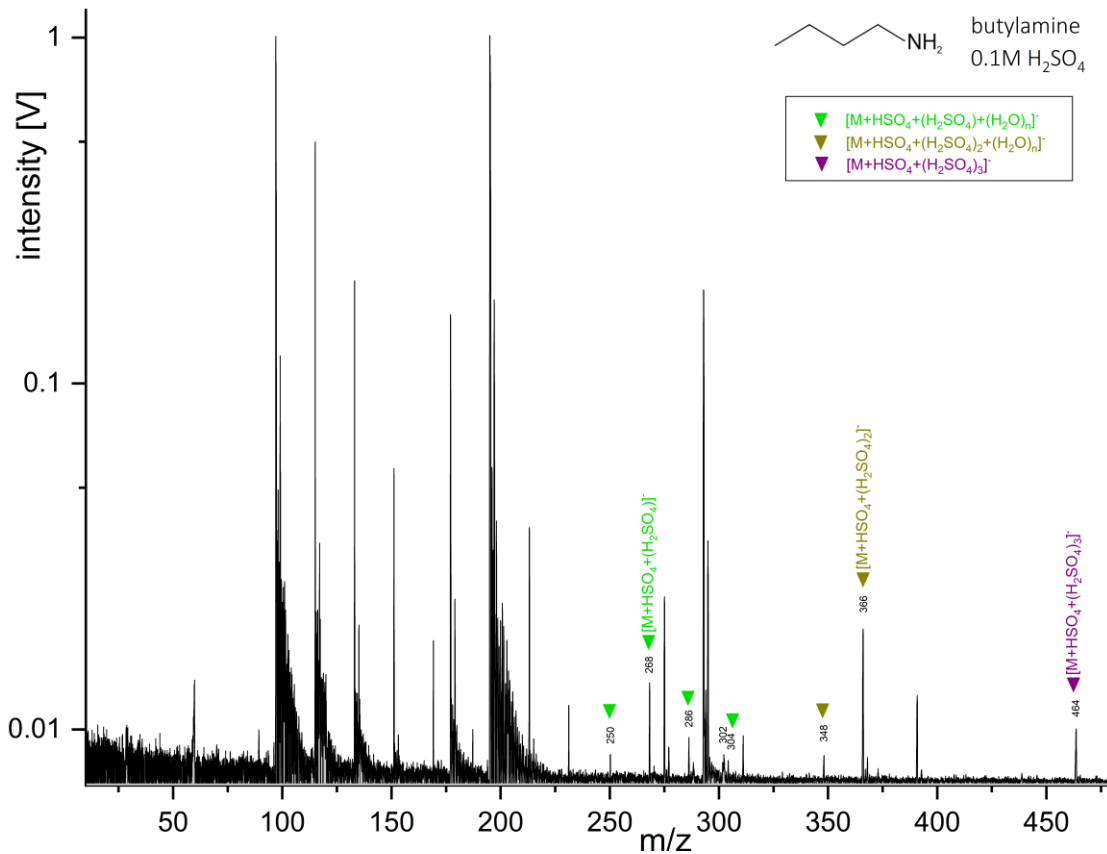
Figure S87. Baseline corrected anion mass spectrum of butylamine (concentration 5wt%) in 0.1M sulfuric acid (H_2SO_4), generated with a delay time of 6.4 μs. Unlabeled peaks originate exclusively from the H_2SO_4 matrix.

NaCl concentration	m/z	pure H$_2$O	0.01M	0.1M	1M
5-amino-1-pentanol	18	[NH$_4$]$^+$	[NH$_4$]$^+$	[NH$_4$]$^+$	
	30	[CH$_2$NH$_2$]$^+$ or [CH$_2$O]$^+$	[CH$_2$NH$_2$]$^+$ or [CH$_2$O]$^+$	[CH$_2$NH$_2$]$^+$ or [CH$_2$O]$^+$	
	36	[NH$_4$ (H$_2$O)]$^+$	[NH$_4$ (H$_2$O)]$^+$		
	41	[C$_3$H$_5$]$^+$			
	47			UI	UI
	48	[CH$_2$NH$_2$ (H$_2$O)]$^+$	[CH$_2$NH$_2$ (H$_2$O)]$^+$		
	54	UI			
	57	[M-CH$_2$O-NH$_2$]$^+$	[M-CH$_2$O-NH$_2$]$^+$		
	66	UI			
	69	[M-OH-NH$_3$]$^+$	[M-OH-NH$_3$]$^+$	[M-OH-NH$_3$]$^+$	
	70, 72, 80, 84	UI			
	85	UI	UI	UI	UI
	86	[M-OH]$^+$	[M-OH]$^+$		
	87, 88, 90, 102, 103	UI			
Acetic acid	28			[CO]$^+$	
	42	[C$_3$H$_6$]$^+$			
	43	[M-OH]$^+$	[M-OH]$^+$		
	44, 57	UI			
Benzoic acid	23	UI			
	39			[C$_3$H$_3$]$^+$	
	41	[C$_3$H$_5$]$^+$			
	43, 59, 61, 77	UI			
	79	[C$_6$H$_7$]$^+$			
	80	[C$_6$H$_8$]$^+$			
	93	[C$_7$H$_9$]$^+$			
	95, 104	UI			
	105	[M-OH]$^+$	[M-OH]$^+$		
Butylamine	18	[NH$_4$]$^+$	[NH$_4$]$^+$		
	29	[CH$_3$N]$^+$			
	36	[NH$_4$(H$_2$O)]$^+$			
	41	[C$_3$H$_5$]$^+$			
	54	[NH$_4$(H$_2$O)$_2$]$^+$			
	57	[M-NH$_2$]$^+$	[M-NH$_2$]$^+$		
	58	UI			
	63		UI	UI	
	72	[NH$_4$(H$_2$O)$_3$]$^+$			
Glucose	29	[CHO]$^+$	[CHO]$^+$		[CHO]$^+$
	31	[CH$_2$OH]$^+$	[CH$_2$OH]$^+$	[CH$_2$OH]$^+$	[CH$_2$OH]$^+$
	43	[C$_2$H$_3$O]$^+$	[C$_2$H$_3$O]$^+$		[C$_2$H$_3$O]$^+$
	45	[C$_2$H$_5$O]$^+$	[C$_2$H$_5$O]$^+$	[C$_2$H$_5$O]$^+$	[C$_2$H$_5$O]$^+$
	57	[C$_3$H$_5$O]$^+$	[C$_3$H$_5$O]$^+$		
	61	[C$_2$H$_5$O$_2$]$^+$	[C$_2$H$_5$O$_2$]$^+$		[C$_2$H$_5$O$_2$]$^+$
	69	[C$_4$H$_5$O]$^+$			
	70	[C$_5$H$_{10}$]$^+$			
	73	[C$_3$H$_5$O$_2$]$^+$	[C$_3$H$_5$O$_2$]$^+$	[C$_3$H$_5$O$_2$]$^+$	[C$_3$H$_5$O$_2$]$^+$
	75, 79	UI			
	81	[C$_5$H$_5$O]$^+$			
	82, 83	UI			
	85	[C$_4$H$_5$O$_2$]$^+$			[C$_4$H$_5$O$_2$]$^+$
	87	[C$_4$H$_7$O$_2$]$^+$			
	88, 89	UI			
	91	[M+H-(H$_2$O)$_5$]$^+$			
	93	UI			
	97	[C$_5$H$_5$O$_2$]$^+$			

	Mass				
Glucose	99	$[C_5H_7O_2]^+$			
	101	$[C_5H_9O_2]^+$			
	103	$[C_4H_7O_3]^+$			
	105	$[C_4H_9O_3]^+$	$[C_4H_9O_3]^+$	$[C_4H_9O_3]^+$	$[C_4H_9O_3]^+$
	109	$[M+H-(H_2O)_4]^+$			
	115	$[C_5H_7O_3]^+$			
	117	$[C_5H_9O_3]^+$			
	119	UI			
	121	$[C_4H_9O_4]^+$	$[C_4H_9O_4]^+$	$[C_4H_9O_4]^+$	
	123	$[C_4H_{11}O_4]^+$	$[C_4H_{11}O_4]^+$	$[C_4H_{11}O_4]^+$	$[C_4H_{11}O_4]^+$
	127	$[M+H-(H_2O)_3]^+$		$[M+H-(H_2O)_3]^+$	$[M+H-(H_2O)_3]^+$
	128, 130, 133, 135, 139	UI			
	145	$[M+H-(H_2O)_2]^+$			
	146, 148	UI			
	163	$[M-OH]^+$	$[M-OH]^+$	$[M-OH]^+$	$[M-OH]^+$
	164	UI			
	165	UI			
Methanol	15	$[CH_3]^+$			
Pyridine	23, 41	UI			
	53	$[C_3H_3N]^+$			
	59, 77, 79	UI			

Table S1. Fragment peaks, and their respective mass, detected in cation mode for the investigated organics in pure water matrix and at 0.01M, 0.1M and 1M NaCl concentrations, at all investigated delay times and laser power intensities. UI stands for unidentified ion species.

NaCl concentration	m/z	pure H$_2$O	0.01M	0.1M	1M
5-amino-1-pentanol	16	[NH$_2$]$^-$			
	26	[C$_2$H$_2$]$^-$ or [CN]$^-$			
	42	[C$_2$H$_4$N]$^-$	[C$_2$H$_4$N]$^-$		
	43, 44, 45, 46	UI			
	57		UI		
	59	UI	UI		
	60 61, 62, 63, 64, 77, 78, 79, 80, 81, 83	UI			
	86, 88		UI		
	95, 97, 98	UI			
Acetic acid	15	[CH$_3$]$^-$	[CH$_3$]$^-$	[CH$_3$]$^-$	[CH$_3$]$^-$
	36	UI			
	41	[M-H$_3$O]$^-$			
	54, 58	UI			
Benzoic acid	59	UI			
	77	[M-COOH]$^-$	[M-COOH]$^-$	[M-COOH]$^-$	[M-COOH]$^-$
	95	[M-COOH+(H$_2$O)]$^-$			
	113	[M-COOH+(H$_2$O)$_2$]$^-$			
Butylamine	16	[NH$_2$]$^-$			
	26	[C$_2$H$_2$]$^-$ or [CN]$^-$		[C$_2$H$_2$]$^-$ or [CN]$^-$	
	32	[N$_2$H$_4$]$^-$			
	44	[C$_2$H$_6$N]$^-$			
	49	UI			
	57		[M-NH$_2$]$^-$	[M-NH$_2$]$^-$	
	58			UI	
	61, 62, 66, 70	UI			
Glucose	31	UI			
	43, 45	UI		UI	
	55, 57	UI			
	58	[C$_4$H$_{10}$]$^-$	[C$_4$H$_{10}$]$^-$	[C$_4$H$_{10}$]$^-$	
	59	[C$_2$H$_3$O$_2$]$^-$	[C$_2$H$_3$O$_2$]$^-$	[C$_2$H$_3$O$_2$]$^-$	
	62	UI			
	71	[C$_3$H$_3$O$_2$]$^-$ or [M-H-(H$_2$O)$_6$]$^-$	[C$_3$H$_3$O$_2$]$^-$ or [M-H-(H$_2$O)$_6$]$^-$	[C$_3$H$_3$O$_2$]$^-$ or [M-H-(H$_2$O)$_6$]$^-$	
	73	[C$_3$H$_5$O$_2$]$^-$			
	75	UI			
	77	[C$_2$H$_5$O$_3$]$^-$	[C$_2$H$_5$O$_3$]$^-$		
	78, 83, 84, 85	UI			
	87	[C$_4$H$_7$O$_2$]$^-$	[C$_4$H$_7$O$_2$]$^-$	[C$_4$H$_7$O$_2$]$^-$	
	89	[C$_3$H$_5$O$_3$]$^-$ or [M-H-(H$_2$O)$_5$]$^-$	[C$_3$H$_5$O$_3$]$^-$ or [M-H-(H$_2$O)$_5$]$^-$	[C$_3$H$_5$O$_3$]$^-$ or [M-H-(H$_2$O)$_5$]$^-$	
	90, 95, 97, 99, 100	UI			
	101	[C$_4$H$_5$O$_3$]$^-$	[C$_4$H$_5$O$_3$]$^-$	[C$_4$H$_5$O$_3$]$^-$	
	102, 103, 105	UI			
	107	[C$_3$H$_7$O$_4$]$^-$ or [M-H-(H$_2$O)$_4$]$^-$	[C$_3$H$_7$O$_4$]$^-$ or [M-H-(H$_2$O)$_4$]$^-$	[C$_3$H$_7$O$_4$]$^-$ or [M-H-(H$_2$O)$_4$]$^-$	
	112	UI			
	113	[C$_5$H$_5$O$_3$]$^-$			

	Mass	0.01M	0.1M	1M
Glucose	114	UI		
	116			UI
	117		[C$_5$H$_9$O$_3$]$^-$	[C$_5$H$_9$O$_3$]$^-$
	119	[C$_4$H$_7$O$_4$]$^-$	[C$_4$H$_7$O$_4$]$^-$	[C$_4$H$_7$O$_4$]$^-$
	120	UI		
	125	[M-H-(H$_2$O)$_3$]$^-$	[M-H-(H$_2$O)$_3$]$^-$	[M-H-(H$_2$O)$_3$]$^-$
	131	UI		
	135	[C$_5$H$_{11}$O$_4$]$^-$	[C$_5$H$_{11}$O$_4$]$^-$	
	137	[C$_4$H$_9$O$_5$]$^-$	[C$_4$H$_9$O$_5$]$^-$	
	143	[M-H-(H$_2$O)$_2$]$^-$	[M-H-(H$_2$O)$_2$]$^-$	[M-H-(H$_2$O)$_2$]$^-$
	149, 155	UI		
	159		UI	UI
	161	[M-H-(H$_2$O)]$^-$	[M-H-(H$_2$O)]$^-$	[M-H-(H$_2$O)]$^-$
	167	UI		
	171		UI	
Methanol				
Pyridine	22, 33	UI		
	42	[C$_2$H$_4$N]$^-$		
	44, 45, 59	UI		
	61	[C$_5$H]$^-$		
	63, 77	UI		

Table S2. Fragment peaks, and their respected mass, detected in anion mode for the investigated organics at 0.01M, 0.1M and 1M NaCl concentrations, at all investigated delay times and laser power intensities. UI stands for unidentified ion species.

	m/z	pure H₂O	MgSO₄			H₂SO₄		
			0.01M	0.1M	1M	0.01M	0.1M	1M
5-amino-1-pentanol	18	[NH₄]⁺	[NH₄]⁺	[NH₄]⁺		[NH₄]⁺	[NH₄]⁺	[NH₄]⁺
	25, 29							UI
	30	[CH₂NH₂]⁺ or [CH₂O]⁺	[CH₂NH₂]⁺ or [CH₂O]⁺	[CH₂NH₂]⁺ or [CH₂O]⁺		[CH₂NH₂]⁺ or [CH₂O]⁺	[CH₂NH₂]⁺ or [CH₂O]⁺	[CH₂NH₂]⁺ or [CH₂O]⁺
	31							[CH₃O]⁺
	36	[NH₄ (H₂O)]⁺		[NH₄ (H₂O)]⁺				[NH₄ (H₂O)]⁺
	41		[C₃H₅]⁺	[C₃H₅]⁺		[C₃H₅]⁺	[C₃H₅]⁺	[C₃H₅]⁺
	42							UI
	43		UI	UI				UI
	44							UI
	45							[C₂H₅O]⁺
	48	[CH₂NH₂ (H₂O)]⁺		[CH₂NH₂ (H₂O)]⁺				
	54	[NH₄ (H₂O)₂]⁺						[NH₄ (H₂O)₂]⁺
	56			UI				
	57	[M-CH₂O-NH₂]⁺	[M-CH₂O-NH₂]⁺	[M-CH₂O-NH₂]⁺			[M-CH₂O-NH₂]⁺	[M-CH₂O-NH₂]⁺
	58			UI				UI
	62			UI				
	66	UI						
	67		UI				UI	
	69	[M-OH-NH₃]⁺	[M-OH-NH₃]⁺	[M-OH-NH₃]⁺	[M-OH-NH₃]⁺	[M-OH-NH₃]⁺	[M-OH-NH₃]⁺	[M-OH-NH₃]⁺
	70	UI	UI	UI			UI	UI
	72, 80	UI						
	84	UI	UI	UI			UI	UI
	85	[M-NH₄]⁺	[M-NH₄]⁺	[M-NH₄]⁺		[M-NH₄]⁺	[M-NH₄]⁺	[M-NH₄]⁺
	86	[M-OH]⁺	[M-OH]⁺	[M-OH]⁺	[M-OH]⁺	[M-OH]⁺	[M-OH]⁺	[M-OH]⁺
	87	[M-NH₂]⁺	[M-NH₂]⁺	[M-NH₂]⁺	[M-NH₂]⁺		[M-NH₂]⁺	[M-NH₂]⁺
	88	UI						UI
	89		UI			UI	UI	
	90	UI						UI
	98							UI
	102	UI	UI	UI				UI
	103	UI	UI					UI
Acetic acid	15		[CH₃]⁺	[CH₃]⁺				
	24		UI	UI				
	29		[CHO]⁺	[CHO]⁺				
	30, 34			UI				
	41		[C₃H₅]⁺					UI
	42	UI	[C₃H₆]⁺			UI		UI
	43	[M-OH]⁺	[M-OH]⁺	[M-OH]⁺		[M-OH]⁺	[M-OH]⁺	[M-OH]⁺
	44	UI	UI	UI		UI	UI	UI
	57	UI				UI	UI	UI
Benzoic acid	23	UI						
	29							UI
	30							UI
	41	[C₃H₅]⁺						
	43	UI						
	48							UI

	m/z						
Benzoic acid	59, 61	UI					
	74				UI		
	76						UI
	77	UI			UI	UI	UI
	79	[C₆H₇]⁺	[C₆H₇]⁺		[C₆H₇]⁺	[C₆H₇]⁺	[C₆H₇]⁺
	80	[C₆H₈]⁺	[C₆H₈]⁺		[C₆H₈]⁺	[C₆H₈]⁺	[C₆H₈]⁺
	86		UI				
	92					UI	
	93	[C₇H₉]⁺					
	94				[C₆H₆O]⁺	[C₆H₆O]⁺	[C₆H₆O]⁺
	95	UI			UI		UI
	104	UI					
	105	[M-OH]⁺	[M-OH]⁺	[M-OH]⁺	[M-OH]⁺	[M-OH]⁺	[M-OH]⁺
	106	UI			UI	UI	UI
Butylamine	17		[NH₃]⁺	[NH₃]⁺			
	18	[NH₄]⁺	[NH₄]⁺	[NH₄]⁺ ?	[NH₄]⁺	[NH₄]⁺	[NH₄]⁺
	25						UI
	27					[HCN]⁺	[HCN]⁺
	28		UI	UI			
	29	[CH₃N]⁺	[CH₃N]⁺			[CH₃N]⁺	[CH₃N]⁺
	30		[CH₂NH₂]⁺ or [CH₂O]⁺	[CH₂NH₂]⁺ or [CH₂O]⁺			
	31		[CH₅N]⁺	[CH₅N]⁺			
	32		UI	UI			
	33						UI
	34			UI			
	35		UI	UI			
	36	[NH₄(H₂O)]⁺	[NH₄(H₂O)]⁺	[NH₄(H₂O)]⁺		[NH₄(H₂O)]⁺	
	39					[C₃H₃]⁺ or [HCCN]⁺	[C₃H₃]⁺ or [HCCN]⁺
	41	[C₃H₅]⁺	[C₃H₅]⁺		[C₃H₅]⁺	[C₃H₅]⁺	[C₃H₅]⁺
	42		[C₂H₄N]⁺	[C₂H₄N]⁺			
	43		UI	UI			UI
	44		[C₂H₆N]⁺	[C₂H₆N]⁺			
	45, 46, 47, 48		UI	UI			
	49		UI				
	50, 53		UI	UI			
	54	[NH₄(H₂O)₂]⁺	[NH₄(H₂O)₂]⁺	[NH₄(H₂O)₂]⁺			
	56		[C₃H₆N]⁺	[C₃H₆N]⁺			
	57	[M-NH₂]⁺	[M-NH₂]⁺	[M-NH₂]⁺	[M-NH₂]⁺	[M-NH₂]⁺	[M-NH₂]⁺
	58	UI	UI	UI		UI	UI
	59		UI		UI	UI	
	60		UI	UI			UI
	61-65		UI	UI			
	66		UI	UI		UI	
	67-71		UI	UI			
	68					[C₃H₅N₂]⁺ or [C₅H₉]⁺	
	72	[NH₄(H₂O)₃]⁺	[NH₄(H₂O)₃]⁺				
Glucose	15					[CH₃]⁺	
	18				UI		
	27					UI	
	29	[CHO]⁺	[CHO]⁺	[CHO]⁺	[CHO]⁺	[CHO]⁺	[CHO]⁺
	31	[CH₂OH]⁺	[CH₂OH]⁺	[CH₂OH]⁺	[CH₂OH]⁺	[CH₂OH]⁺	[CH₂OH]⁺
	33					UI	

	m/z						
	39					UI	UI
	41				UI	UI	UI
	43	[C₂H₃O]⁺	[C₂H₃O]⁺	[C₂H₃O]⁺	[C₂H₃O]⁺	[C₂H₃O]⁺	[C₂H₃O]⁺
	45	[C₂H₅O]⁺	[C₂H₅O]⁺	[C₂H₅O]⁺	[C₂H₅O]⁺	[C₂H₅O]⁺	[C₂H₅O]⁺
	53					UI	UI
	55		UI	UI			
	57	[C₃H₅O]⁺	[C₃H₅O]⁺	[C₃H₅O]⁺	[C₃H₅O]⁺	[C₃H₅O]⁺	[C₃H₅O]⁺
	58					UI	UI
	59				UI	UI	UI
	60		UI			UI	
	61	[C₂H₅O₂]⁺	[C₂H₅O₂]⁺	[C₂H₅O₂]⁺	[C₂H₅O₂]⁺	[C₂H₅O₂]⁺	[C₂H₅O₂]⁺
	63					UI	UI
	69	[C₄H₅O]⁺	[C₄H₅O]⁺	[C₄H₅O]⁺	[C₄H₅O]⁺	[C₄H₅O]⁺	[C₄H₅O]⁺
	70	[C₅H₁₀]⁺	[C₅H₁₀]⁺			[C₅H₁₀]⁺	[C₅H₁₀]⁺
	71		UI	UI	UI	UI	UI
	73	[C₃H₅O₂]⁺	[C₃H₅O₂]⁺	[C₃H₅O₂]⁺	[C₃H₅O₂]⁺	[C₃H₅O₂]⁺	[C₃H₅O₂]⁺
	74		UI		UI	UI	UI
	75	UI	UI		UI	UI	UI
	79	UI				UI	UI
	80				UI	UI	UI
	81	[C₅H₅O]⁺	[C₅H₅O]⁺	[C₅H₅O]⁺	[C₅H₅O]⁺	[C₅H₅O]⁺	[C₅H₅O]⁺
	82	UI			UI	UI	UI
	83	UI	UI		UI	UI	UI
	85	[C₄H₅O₂]⁺	[C₄H₅O₂]⁺	[C₄H₅O₂]⁺	[C₄H₅O₂]⁺	[C₄H₅O₂]⁺	[C₄H₅O₂]⁺
	86		UI	UI	UI	UI	UI
	87	[C₄H₇O₂]⁺	[C₄H₇O₂]⁺	[C₄H₇O₂]⁺	[C₄H₇O₂]⁺	[C₄H₇O₂]⁺	[C₄H₇O₂]⁺
	88	UI			UI	UI	UI
	89	UI	UI		UI	UI	UI
Glucose	91	[M+H-(H₂O)₅]⁺	[M+H-(H₂O)₅]⁺	[M+H-(H₂O)₅]⁺	[M+H-(H₂O)₅]⁺	[M+H-(H₂O)₅]⁺	[M+H-(H₂O)₅]⁺
	92				UI	UI	UI
	93	UI	UI	UI		UI	UI
	97	[C₅H₅O₂]⁺	[C₅H₅O₂]⁺	[C₅H₅O₂]⁺	[C₅H₅O₂]⁺	[C₅H₅O₂]⁺	[C₅H₅O₂]⁺
	98				UI	UI	UI
	99	[C₅H₇O₂]⁺	[C₅H₇O₂]⁺	[C₅H₇O₂]⁺	[C₅H₇O₂]⁺	[C₅H₇O₂]⁺	[C₅H₇O₂]⁺
	100				UI	UI	UI
	101	[C₅H₉O₂]⁺	[C₅H₉O₂]⁺	[C₅H₉O₂]⁺	[C₅H₉O₂]⁺	[C₅H₉O₂]⁺	[C₅H₉O₂]⁺
	102				UI	UI	UI
	103	[C₄H₇O₃]⁺	[C₄H₇O₃]⁺	[C₄H₇O₃]⁺	[C₄H₇O₃]⁺	[C₄H₇O₃]⁺	[C₄H₇O₃]⁺
	104				UI	UI	UI
	105	[C₄H₉O₃]⁺	[C₄H₉O₃]⁺		[C₄H₉O₃]⁺	[C₄H₉O₃]⁺	[C₄H₉O₃]⁺
	109	[M+H-(H₂O)₄]⁺	[M+H-(H₂O)₄]⁺	[M+H-(H₂O)₄]⁺	[M+H-(H₂O)₄]⁺	[M+H-(H₂O)₄]⁺	[M+H-(H₂O)₄]⁺
	110				UI	UI	UI
	111				UI	UI	UI
	115	[C₅H₇O₃]⁺	[C₅H₇O₃]⁺	[C₅H₇O₃]⁺	[C₅H₇O₃]⁺	[C₅H₇O₃]⁺	[C₅H₇O₃]⁺
	116				UI	UI	UI
	117	[C₅H₉O₃]⁺	[C₅H₉O₃]⁺	[C₅H₉O₃]⁺	[C₅H₉O₃]⁺	[C₅H₉O₃]⁺	[C₅H₉O₃]⁺
	118				UI	UI	UI
	119	UI	UI	UI	UI	UI	UI
	121	[C₄H₉O₄]⁺	[C₄H₉O₄]⁺		[C₄H₉O₄]⁺	[C₄H₉O₄]⁺	[C₄H₉O₄]⁺
	123	[C₄H₁₁O₄]⁺	[C₄H₁₁O₄]⁺		[C₄H₁₁O₄]⁺	[C₄H₁₁O₄]⁺	[C₄H₁₁O₄]⁺
	127	[M+H-(H₂O)₃]⁺	[M+H-(H₂O)₃]⁺	[M+H-(H₂O)₃]⁺	[M+H-(H₂O)₃]⁺	[M+H-(H₂O)₃]⁺	[M+H-(H₂O)₃]⁺
	128	UI			UI	UI	UI
	129				UI		UI
	130	UI				UI	UI

Compound	Mass						
Glucose	133	UI			UI	UI	UI
	135	UI			UI	UI	UI
	137				UI	UI	UI
	139		UI		UI		UI
	141			UI	UI	UI	UI
	143		UI	UI		UI	
	144		UI				
	145	[M+H-(H₂O)₂]⁺	[M+H-(H₂O)₂]⁺	[M+H-(H₂O)₂]⁺	[M+H-(H₂O)₂]⁺	[M+H-(H₂O)₂]⁺	[M+H-(H₂O)₂]⁺
	146	UI	UI			UI	UI
	147				UI		
	148	UI	UI			UI	UI
	151				UI	UI	UI
	153				UI	UI	UI
	155		UI				
	157				UI	UI	UI
	159				UI		
	161		UI				
	163	[M-OH]⁺	[M-OH]⁺	[M-OH]⁺	[M-OH]⁺	[M-OH]⁺	[M-OH]⁺
	164	UI			UI	UI	UI
	165		UI				
	167						UI
	173		UI				
	169, 175				UI		
Methanol	15	[CH₃]⁺					[CH₃]⁺
Pyridine	18						[NH₄]⁺
	23	UI					
	39						[HC₂N]⁺ or [C₃H₃]⁺
	41	UI					
	43						[C₂H₅N]⁺
	53	[C₃H₃N]⁺					[C₃H₃N]⁺
	59, 77	UI	UI				
	79	UI	UI			UI	UI

Table S3. Fragment peaks, and their respective mass, detected in cation mode for the investigated organics in pure water matrix, in 0.01M, 0.1M and 1M MgSO₄ and 0.01M, 0.1M and 1M H₂SO₄ matrices, at all investigated delay times and laser power intensities. UI stands for unidentified ion species. Species written in blue are tentative identifications.

	m/z	pure H₂O	MgSO₄			H₂SO₄		
			0.01M	0.1M	1M	0.01M	0.1M	1M
5-amino-1-pentanol	16	[NH₂]⁻						
	26	[C₂H₂]⁻ or [CN]⁻						
	27			UI				
	42	[C₂H₄N]⁻	[C₂H₄N]⁻			[C₂H₄N]⁻		
	43	UI		UI				
	44, 45, 46	UI						
	53						UI	
	59, 60	UI						
	61	UI		UI				
	62, 63, 64, 77, 78, 79, 80, 81, 83	UI						
	93						UI	
	95, 97, 98	UI						
Acetic acid	15	[CH₃]⁻	[CH₃]⁻	[CH₃]⁻	[CH₃]⁻			
	36	UI						
	41	[M-H₃O]⁻	[M-H₃O]⁻					
	54	UI						
	58	UI	UI	UI				
Benzoic acid	59	UI						
	77	[M-COOH]⁻	[M-COOH]⁻	[M-COOH]⁻	[M-COOH]⁻			
	95	[M-COOH+(H₂O)]⁻						
	113	[M-COOH+(H₂O)₂]⁻						
Butylamine	16	[NH₂]⁻						
	26	[C₂H₂]⁻ or [CN]⁻	[C₂H₂]⁻ or [CN]⁻	[C₂H₂]⁻ or [CN]⁻	[C₂H₂]⁻ or [CN]⁻			
	32	[N₂H₄]⁻						
	42		[C₂H₄N]⁻	[C₂H₄N]⁻	[C₂H₄N]⁻			
	44	[C₂H₆N]⁻	[C₂H₆N]⁻	[C₂H₆N]⁻				
	49	UI						
	53			UI				
	60			UI				
	61					UI		
	62	UI	[C₂H₄N(H₂O)]⁻	[C₂H₄N(H₂O)]⁻				
	64		UI	UI	UI			
	66	UI		UI				
	67	UI						
	68			UI				
	69		UI	UI				
	70	UI						
	71			UI				
Glucose	31	UI						
	41					UI		
	43	UI				UI		
	45	UI		UI		UI		
	55, 57	UI						
	58	[C₄H₁₀]⁻						
	59	[C₂H₃O₂]⁻	[C₂H₃O₂]⁻	[C₂H₃O₂]⁻	[C₂H₃O₂]⁻			
	62	UI						

|	Mass	Col1	Col2	Col3	
Glucose	71	$[C_3H_3O_2]^-$ or $[M-H-(H_2O)_6]^-$	$[C_3H_3O_2]^-$ or $[M-H-(H_2O)_6]^-$	$[C_3H_3O_2]^-$ or $[M-H-(H_2O)_6]^-$	
	73	$[C_3H_5O_2]^-$			
	75	UI			
	77	$[C_2H_5O_3]^-$	$[C_2H_5O_3]^-$		
	78, 83, 84	UI			
	85	UI	UI		
	87	$[C_4H_7O_2]^-$			
	89	$[C_3H_5O_3]^-$ or $[M-H-(H_2O)_5]^-$	$[C_3H_5O_3]^-$ or $[M-H-(H_2O)_5]^-$	$[C_3H_5O_3]^-$ or $[M-H-(H_2O)_5]^-$	
	90, 95, 97, 99, 100	UI			
	101	$[C_4H_5O_3]^-$	$[C_4H_5O_3]^-$		
	102, 103, 105	UI			
	107	$[C_3H_7O_4]^-$ or $[M-H-(H_2O)_4]^-$			
	112	UI			
	113	$[C_5H_5O_3]^-$	$[C_5H_5O_3]^-$		
	114	UI			
	119	$[C_4H_7O_4]^-$	$[C_4H_7O_4]^-$		
	120	UI			
	121		UI		
	125	$[M-H-(H_2O)_3]^-$			
	131	UI			
	135	$[C_5H_{11}O_4]^-$			
	137	$[C_4H_9O_5]^-$			
	141		UI		
	143	$[M-H-(H_2O)_2]^-$	$[M-H-(H_2O)_2]^-$		
	149, 155	UI			
	159				
	161	$[M-H-(H_2O)]^-$	$[M-H-(H_2O)]^-$		
	167	UI			
	171				
	177			UI	
	178		UI		
Methanol					
Pyridine	22, 33	UI			
	42	$[C_2H_4N]^-$			
	44, 45, 59	UI			
	61	$[C_5H]^-$			
	63	UI			
	75		UI		
	77	UI			

Table S4. Fragment peaks, and their respective mass, detected in anion mode for the investigated organics in pure water matrix, in 0.01M, 0.1M and 1M MgSO$_4$ and 0.01M, 0.1M and 1M H$_2$SO$_4$ matrices, at all investigated delay times and laser power intensities. UI stands for unidentified ion species.

Supplementary Material – Part III.

## Probing the oxidation state of ocean worlds with SUDA: Fe (II) and Fe (III) in ice grains
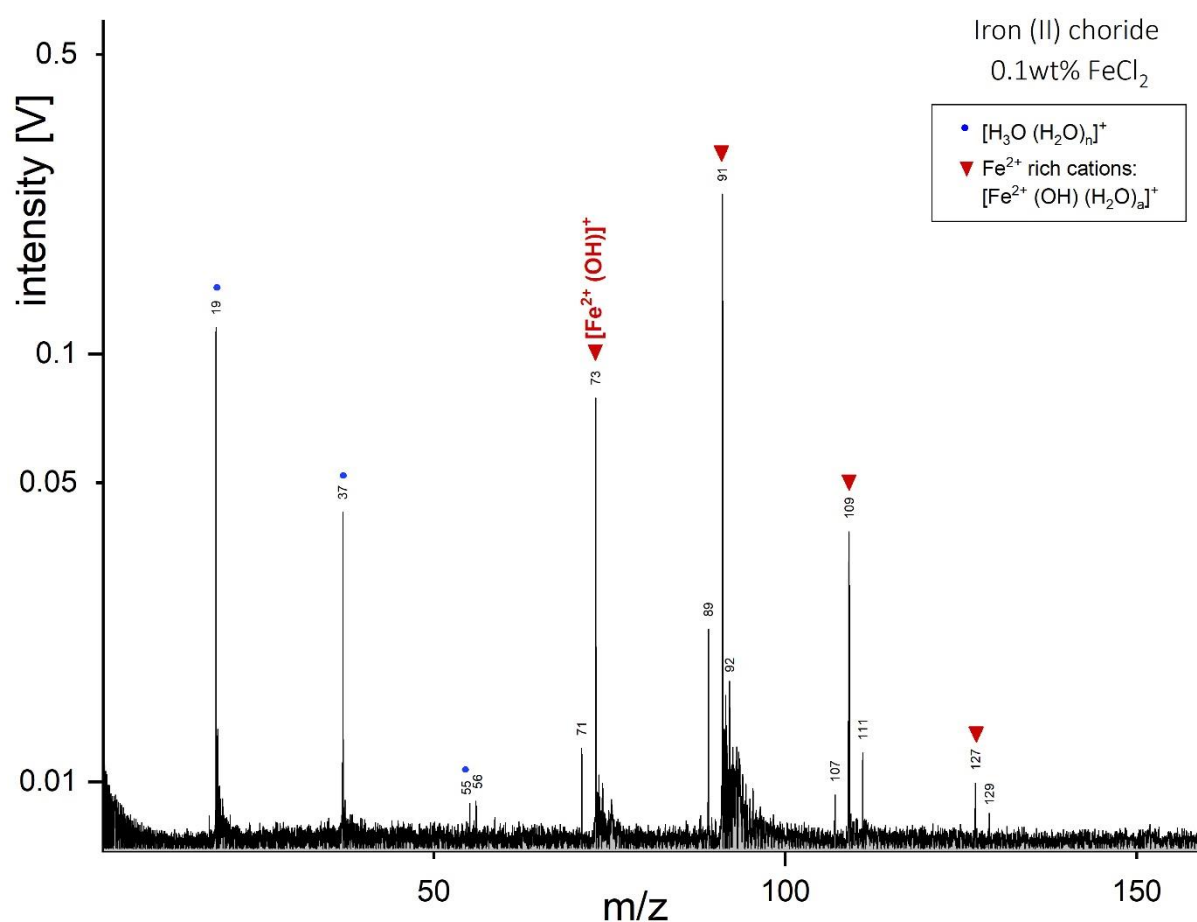
Figure S88. LILBID cation mass spectra of iron (II) chloride (FeCl$_2$), recorded with a delay time of 4.5 μs.
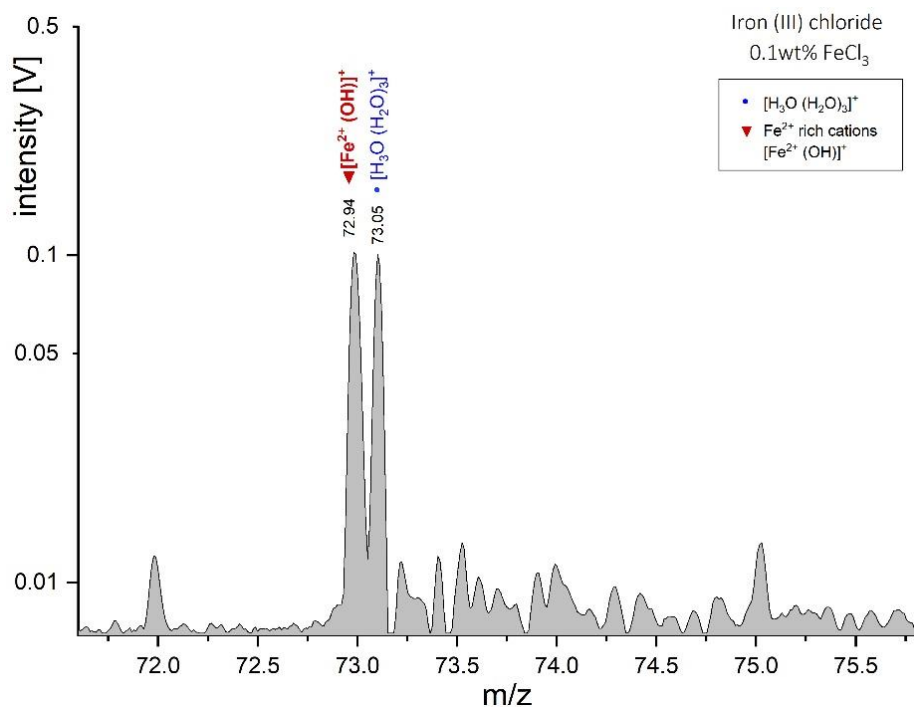
Figure S89. Zoomed-in section of the LILBID cation mass spectra of iron (III) chloride (FeCl$_3$), recorded with a delay time of 5.1 µs. Two distinct peaks are observed at m/z 73 at a similar intensity, corresponding to a pure water cluster [H$_3$O(H$_2$O)$_3$]$^+$ (m/z 73.05) and to [Fe^{2+}(OH)]$^+$ (m/z 72.94). To resolve the two peaks, a mass resolution of about 500 is required.
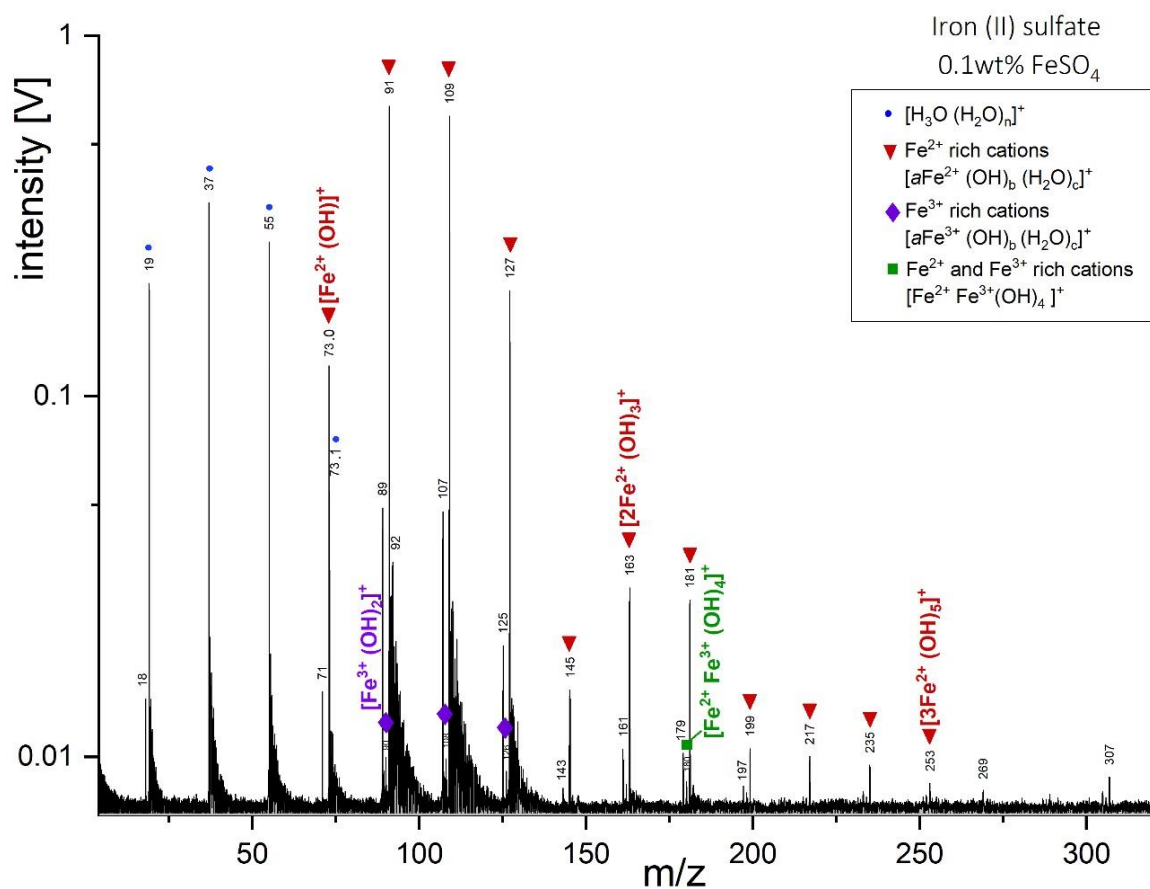
Figure S90. LILBID cation mass spectra of iron (II) sulfate (FeSO$_4$), recorded with a delay time of 5.0 µs.
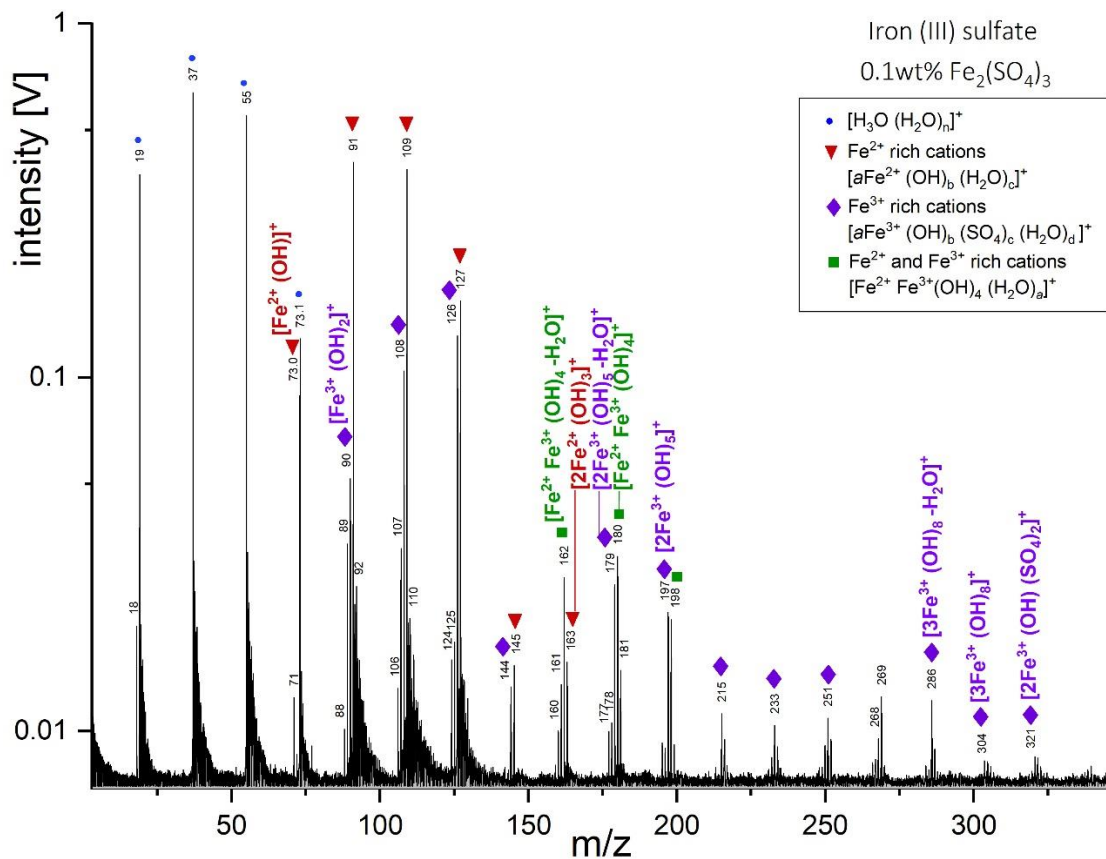
Figure S91. LILBID cation mass spectra of iron (III) sulfate ($Fe^{3+}_2[SO_4]_3$), recorded with a delay time of 5.0 μs.
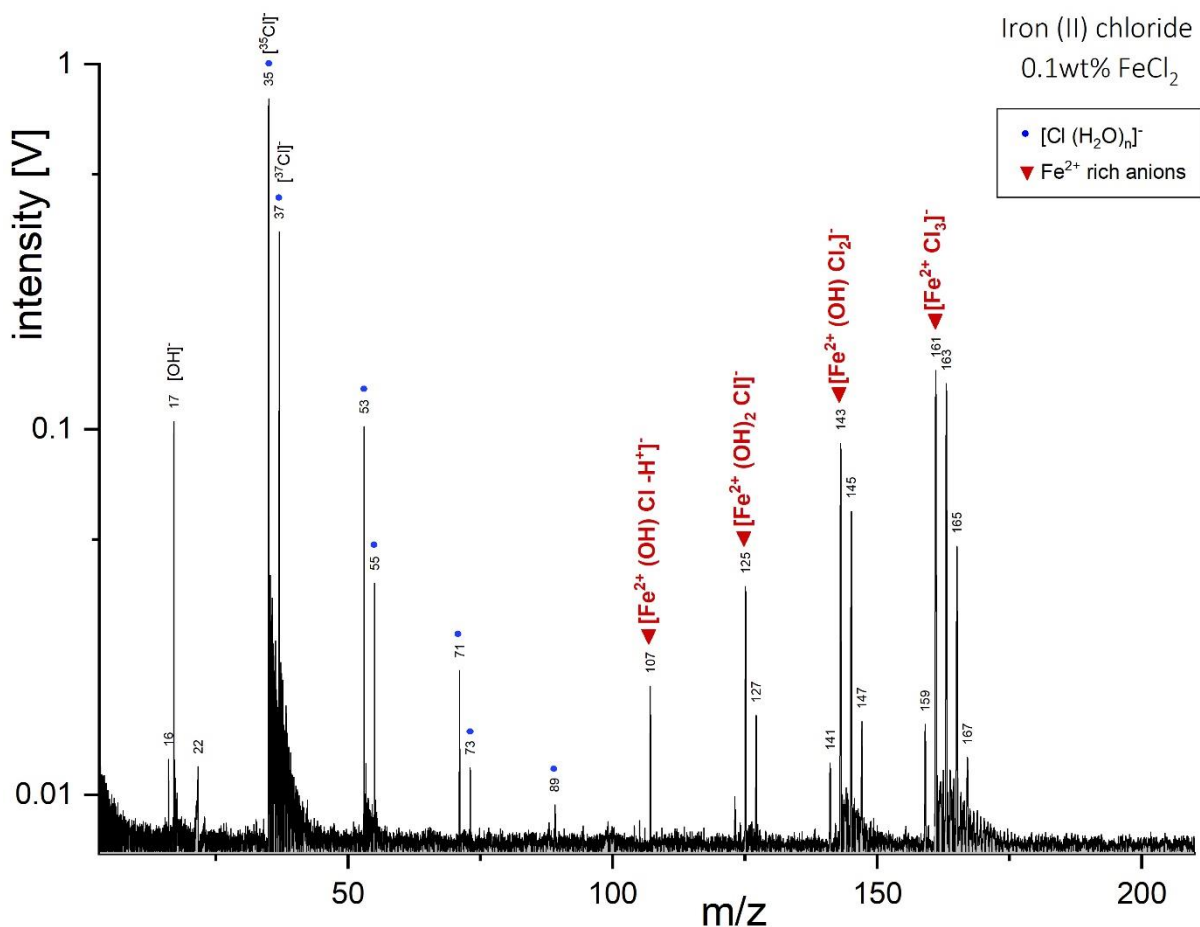
Figure S92. LILBID anion mass spectra of iron (II) chloride ($FeCl_2$), recorded with a delay time of 5.3 μs.

4   Acknowledgments

I would like to express my most sincere acknowledgments to my supervisors Prof. Dr. Frank Postberg, Dr. Nozair Khawaja and Dr. Jon Hillier for giving me the opportunity to work in such a fascinating field for 3 years, with hopefully many more years to come. I would like to express my gratitude for the support, inspiration, and guidance that you all provided.

I would like to thank the reviewers of this thesis, for reading and evaluating this manuscript, and the members of the jury of my phD defense.

I acknowledge all the co-authors of the manuscripts presented in this dissertation for their scientific contributions, and the support provided.

Moreover, I am thankful to many colleagues for allowing me to take part in common projects: Nozair Khawaja, Lucía Hortal, Tom O'Sullivan, and Judith Bloema for developing the hydrothermal experiments at FUB and trusting me with the measurements of their samples; Max Craddock for the opportunity to perform several LILBID analysis with his samples from hydrothermal experiments in Tokyo; Wolfgang Knolle, Evgeny Lugovoy, and Bernd Abel for the opportunity to use the linear accelerator and warm welcome at the IOM in Leipzig, and for sharing their valuable experience with irradiation experiments; Grégoire Danger and Alexis Bouquet for providing several residues from irradiations performed at their lab in Marseille, as well as for having me in Marseille in June 2023 for a seminar talk and visit of their lab; Pablo L. Finkel, Laura Sánchez-García, Daniel Carrizo and Lucía Hortal for the incredible opportunity to go together on a field trip to Antarctica, one of the best terrestrial analogue for the icy moons that we study.

I sincerely thank Lígia F. Coelho for giving me the opportunity to give a seminar talk at Cornell University and making my stay in Ithaca a wonderful time; as well as Taylor Price for the inspiring discussions about astrobiology, and sharing her passion for glacier microbes while hiking in the Picos de Europa. I am really looking forward to future collaborations with you both. I would also like to acknowledge Prof. Lisa Kaltenegger for her warm welcome in Cornell, and the unique chance to sit at Carl Sagan's desk!

A sincere thank you to all members of the Planetology group at FUB, for the friendly atmosphere at the institute. A special, huge thank you goes to Fabian Klenner, for training me in the lab, showing me the tricks of the LILBID, and leading the planetary football team which, despite the lack of success, was much fun to be part of. I'm also especially grateful to René Reviol and Janine Bönigk for their technical support in the lab, and for the chance to often share hiking adventure stories; and to Arnaud Sanderink for making sure that we can always celebrate with crémant. A big thank you to Tom, Marie, and Lucía for taking the time to proof-read parts of this thesis.

A warm thank you to my family, especially my parents Catherine and Christophe for their unconditional support, for transmitting me their energy and sense of exploration; to my sister Raphaelle, especially for often visiting me in Berlin despite the bad weather that seems to follow her anytime she came; to my grandparents for their inspiring lives.

Last but not least, a gigantic thank you to my closest friends: Lucía for the being the most supportive neighbour, the best croqueta (cook) and an inspiring person to follow on adventures to Antarctica; Marwan (or should I call him "Marwan le puissant") for his precious help with LateX, and being always keen to do crazy sports; Pietro for being my travel buddy to conferences, even accepting to do bike polo and making sure I stay hydrated in all circumstances (surtout dans la pénombre); Marina for introducing us to Encephalus, a new icy moon of Saturn; to Simon for sharing his passion of flowers and for the (long) Night in the Museum für Naturkunde; to Judith, André, Fabio, Sara, Ingrid, Lise, Marianne, Camille, Gentiane, Sarah and many others, for bringing joy and happiness in my life.

Eidesstattliche Erklärung

Hiermit erkläre ich, dass ich die vorliegende Dissertation mit dem Thema

Simulation of salt and organic fingerprints in mass spectra of ice grains in the exospheres of the icy ocean moons Europa and Enceladus

selbstständig verfasst und angefertigt habe und keine anderen als die angegebenen Quellen und Hilfsmittel verwendet habe. Geistiges Eigentum anderer Autoren wurde als solches gekennzeichnet.

Des Weiteren versichere ich, dass ich an keiner anderen Stelle ein Prüfungsverfahren beantragt bzw. die Dissertation in dieser oder anderer Form an keiner anderen Fakultät als Dissertation vorgelegt habe.

Berlin, den 15 November 2023